<u>**METAL CERAMIC WEAR MECHANISMS**</u>

by

<u>**WILLIAM MARK RAINFORTH**</u>

A thesis submitted in accordance with the requirements for the degree
of Doctor of Philosophy

This work was carried out under the supervision of Dr R Stevens

School of Materials
The University of Leeds

January 1990

ABSTRACT

Sliding wear of metal-on-ceramic, ceramic-on-metal, and ceramic-on-ceramic have been investigated using a tri-pin-on-disc machine. A technique has been developed for thin foil preparation for transmission electron microscopic examination perpendicular to the wear surface. The role of transformation toughening in the wear behaviour of zirconia ceramics has been investigated. In addition, the role of high strain deformation in a steel surface has been evaluated.

The wear factor of 316L stainless steel pins worn against a zirconia disc was found to decrease as the load was increased, believed to be associated with metal oxide formation. TEM of the stainless steel revealed a worn surface which consisted of a mechanical mixture of metal oxide and heavily deformed metal. Deformation of the metal had occurred by shear banding with a microstructure similar to that observed in rolled specimens, although the texture formed was a wire texture rather than a rolling texture. The crystallite size was found to decrease towards the surface, demonstrating that the shear stress was a maximum at the surface. The shear bands at the surface had always been formed by the passage of the last asperity indicating that contact was plastic over the load range 6-60N/pin. The majority of wear occurred by transfer resulting from plastic overload, although a contribution to the material loss was made by metal extruded off the end of the pin as a result of the high strains. The depth of deformation correlated closely with the wear volume.

The wear of the zirconia discs was found to be dominated by metal transfer. With Mg-PSZ, transformation occurred cooperatively in crystallographically determined bands. Microcrack coalescence led to preferential wear in these bands. However, with a Y-TZP disc transformation appeared to have been responsible for widespread surface fracture.

The wear of zirconia pins against a bearing steel disc gave limited metal transfer. Very little transformation of tetragonal to monoclinic was observed. However, milder forms of the transformation related wear mechanism did occur. Zirconia had formed a solid solution with the iron oxide, leading to the conclusion that the wear mechanism was tribochemically based.

TZP worn against a ZTA disc showed evidence of very high temperature rises at the interface. The surface layer was amorphous and contained a mixture of alumina and zirconia suggesting that melting had occurred at the interface during sliding. At a depth of $0.5\mu m$, the surface consisted of heavily elongated tetragonal grains, with a low dislocation density, indicating a strain of at least 1.7. At a depth of $2-4\mu m$ a layer of monoclinic was found. There was evidence that the stresses imposed by friction extended to at least $8-10\mu m$ from the surface.

TZP containing 20vol% SiC whiskers gave exceptionally low wear rates when worn against a ZTA disc. The greater wear resistance is believed to be a result of the improved load bearing capacity and of the higher thermal conductivity. It is clear that the poor thermal conductivity of zirconia dominates its tribological behaviour. Temperature generation was high enough to substantially reduce the driving force for transformation of the tetragonal to monoclinic, with a high enough temperature for plastic deformation where a low thermal conductivity counterface was used. Where transformation occurred, its effect was to increase the wear rate.

To Elizabeth for her strength and support and to my parents for their faith in my career.

ACKNOWLEDGEMENTS

CONTENTS

LIST OF ABREVIATIONS AND SYMBOLS USED

TZP	Tetragonal Zirconia Polycrystals
Y-TZP	Yttria-TZP
Mg-PSZ	Magnesia Partially Stabilised Zirconia
ZTA	Zirconia Toughened Alumina
t	Tetragonal phase in zirconia
m	Monoclinic phase in zirconia
C	Cubic phase in zirconia
o	Orthorhombic phase in zirconia
δ	δ phase in zirconia
α'	BCC phase in steels
δ	Ferrite phase in steels
γ	Austenite phase in steels
M_s	Martensitic start temperature
SPG	Secondary Precipitate Growth
DSI	Diffuse Scattering Intensity
APB	Anti-Phase Domain Boundary
MOR	Modulus of Rupture
HIPing	Hot Isostatic Pressing
ISE	Indentation Size Effect
SFE	Stacking Fault Energy
FCC	Face centred cubic
BCC	Body centred cubic
HVEM	High Voltage Electron Microscope
SENB	Single Edge Notched Beam
XRD	X-ray diffraction
EDS	Energy Dispersive Spectroscopy
WDS	Wavelength Dispersive Spectroscopy
TEM	Transmission Electron Microscopy
SEM	Scanning Electron Microscopy
BEI	Back Scattered Electron Image

K_{1C}	Critical fracture toughness
K_R	Applied stress intensity factor
Y	Geometrical factor
F^*	Nucleation barrier for transformation
C	Crack length
β	Constant
V_f	Volume fraction transforms from t to m
V	Volume dilation on transformation
E	Young's Modulus
υ	Poisson's ratio
H	Hardness
d	Transformation zone size
C_f	Critical flaw size
r	Radius
a_f^c	Critical stress to initiate transformation
τ_o	As above (different author)
σ	True stress
ϵ	True strain
h	Transformation zone width
λ	Non dimensional constant
L	Load
L_{cr}	Critical load for fracture
R	Radius of indentor

d	Indentation diameter (section 2.2.2)
k	Constant
n	Indentation size effect
P_n	Normal load
V	Wear volume
d	Abrasive grit diameter (section 2.2.7)
a	Constant
n	Work hardening index (section 2.3.2)
m	Work hardening capacity
x	Distance slid
α	Standard deviation of the profile heights
R	Radius of curvature of asperities
τ	Shear stress
γ	Shear strain
G_x	Fraction of diffracted intensity contributed by a surface layer of depth x
μ	Linear absorption coefficient (section 3.2)
θ	Diffracted angle
P	Experimental constant (chapter 3)
I	Intensity of diffracted X-rays
X_i	Volume fraction of phase i
G	Shear modulus
b	Burgers vector
γ	Stacking fault energy (chapter 4)
μ	Friction coefficient
T	Temperature
r	Radius of contact spot (chapter 5)
v	Velocity
v_r	Characteristic velocity
κ	Thermal diffusivity
d	Mechanical density (chapter 5)
c	Specific heat capacity (chapter 5)
N	Number of contact spots
λ_i	Relative thermal conductivity of material i
z_s	Thickness of the wear particle
a_b	Area of the contacting asperity
N_m	Number of contact spots per metre of sliding
S	Total distance slid
z_o	Depth of deformation
j	Fraction of contact spots covered by oxide
N_m'	Number of contact events per metre which lead to transfer
δ	Displacement
δ_s	Displacement at the worn surface
V_e	Volume of extruded metal
W	Wear rate
a_t	True contact area
t	Time
w	Width of extruded metal
σ_y	Yield stress
λ	Angle made by compression axis with the active slip direction.
χ	Angle made by compression axis with the slip plane normal.
m_s	Schmid factor at the surface
m_b	Schmid factor in the subsurface regions
$_b\tau_y$	Critical resolved shear stress in the subsurface layers
$_s\tau_y$	Critical resolved shear stress at the surface
c	Multiplication factor
F_t	Friction force

CHAPTER 1

INTRODUCTION

Although alumina has been used as a wear resistant material for many years, it is only recently that the potential of ceramics in tribological applications have been fully realised. Despite this, little is known about their wear behavior and many observations remain unexplained. For example, ceramics can show higher wear rates than metals despite high hardness. Poor wear resistance of oxide ceramics tested in water is found despite their chemical inertness. Given the commercial potential for ceramics in tribological applications, study of their wear behaviour merits further effort.

Many workers have highlighted the importance of fracture toughness in wear resistance of ceramics [1]. Zirconia engineering ceramics offer high K_{1C} as well as high hardness and good chemical inertness [2]. Moreover, the K_{1C} can be systematically varied over a wide range within one system. They therefore provide a useful system for a study of wear, both from an academic point and because of their technological importance.

Wear behaviour has traditionally been related to material properties such as strength, fracture toughness, hardness, and to microstructure. Despite the wear of metals being inextricably related to deformation processes, little detailed work has been done to examine the microstructure right up to the worn surface. Moreover, the deformation mechanism can vary from homogeneous to highly heterogeneous depending on the stacking fault energy, but this has not previously been related to the wear mechanism.

Few authors have attempted an examination of the near surface microstructure of worn ceramics. Hockey [3,4] has investigated the abrasive wear of alumina by TEM and Page and co-workers [5-7] have examined the near surface microstructures generated by a sliding indentor in non-oxide ceramics. No reports are available from sliding wear studies. A major aim of this study, therefore, is to examine the near surface microstructure generated by wear using detailed analytical transmission electron microscopy.

Wear tests rarely indicate quantitatively what may be expected in

practical applications. Instead, a wear test may be regarded as a means of investigating the wear mechanisms taking place within each load/speed/state of lubrication regime and of relating this to microstructure. This understanding can then be used to evaluate processes occurring in field trials. It is on this premise that the project was conducted. Thus, major emphasis was placed on the investigation of the development of microstructure at the worn surface, rather than exhaustively establishing wear rate data. Both metal and ceramic surfaces have been examined in detail to permit an understanding of the couple as a whole.

The literature survey (chapter 2) covers several topics. A fairly detailed review of the principles of transformation toughening is presented, since it was felt that, unless a clear understanding of this is attained, the complex changes occurring at the worn ceramic surface could not be evaluated. This section is followed by a review of the literature on the wear of zirconia ceramics. In addition, the wear of all ceramics is considered. The literature on the high strain deformation of metals is reviewed fairly briefly as the background to the microstructures at the worn surface of metals.

The experimental procedure (chapter 3) describes in detail the method used for the preparation of thin foils perpendicular to the worn surface. This technique was crucial in obtaining meaningful results about the near surface microstructure.

Chapter 4 reports the results of a study on the microstructure generated by rolling a stainless steel. This was conducted in order to provide a comparison of the microstructure generated by sliding contact. In addition, this investigation acted as a comparison to the microstructures reported for the deformation of other metals, such as 70/30 brass.

In chapter 5 the results of the wear of 316L stainless steel pins against zirconia discs are reported. The stainless steel was chosen as a medium to low stacking fault energy, single phase, FCC metal. The specific stacking fault energy was similar to that of 70/30 brass for which the deformation behaviour is well characterised. The wear of the zirconia discs is covered briefly in this chapter, the main discussion being metallurgical.

Chapter 6 starts by considering the wear mechanisms on the zirconia discs used in the experiments reported in chapter 5. However, the majority of this section reports the findings of the wear of zirconia

pins (TZP and Mg-PSZ) against a hardened bearing steel disc. The materials were chosen to provide a range of toughness values such that the role of transformation of tetragonal to monoclinic during sliding could be evaluated.

The final results and discussion chapter (7) reports ceramic on ceramic wear. These tests were conducted to examine the change in wear mechanism under low adhesive force conditions. Two additional toughening mechanisms were examined, namely microcrack-toughened zirconia toughened alumina (ZTA) and whisker toughening in a TZP/SiC composite. These tests provide an important basis for comparison with the wear of zirconia.

It is important that the philosophy adopted in this study and the critical issues which have been addressed be reiterated. An assessment of the literature has clearly highlighted the inadaquate use of TEM in the investigation of wear. Therefore, this study has concentrated on detailed TEM of the worn surfaces (rather than exhaustive wear testing) in order to answer the following critical issues: During the wear of metals, what is the exact role of plastic deformation, in particular the importance of the ductility limit and whether deformation is heterogeneous or homogeneous?; how does metal oxide form during sliding and how does it interact with the deformation of the metal?; what are the important microstructural features which should be incorporated into a wear equation?; with regard to the wear of zirconia, what is the role of transformation of the tetragonal to the monoclinic?; does it increase or decrease the wear rate?; what is the importance of tribochemically-based wear mechanisms in the wear of ceramics?; and finally, does any dislocation flow occur during the sliding wear of ceramics?

CHAPTER 2

LITERATURE SURVEY

This chapter provides an extensive literature survey of zirconia ceramics since it is considered that, unless a comprehensive understanding of the basic science is obtained, the wear behaviour of these materials cannot be understood. However, the survey is restricted to those materials under investigation, namely the yttria TZPs and Mg-PSZ materials. The general absence of an appreciation of the basic principles of transformation toughening in any of the published literature on wear is demonstrated in the subsequent section on wear of ZrO_2. A survey of the high strain deformation of metals demonstrates the inadequate understanding of the deformation structure below a worn surface. A section on the high strain deformation of metals provides a basis on which to consider the likely microstructures which will be developed by wear. No attempt is made to discuss the individual wear mechanism, rather, a survey has been made in an effort to rationalise the range of applicability of the different mechanisms.

2.1 ZIRCONIA ENGINEERING CERAMICS

The following provides a summary of the literature on Y-TZPs and Mg-PSZs. The first section deal with microstructure/ property relationships, a clear understanding of which is necessary to optimise toughening. This is followed by an outline of the particle size dependency of the martensite start temperature (M_s). These sections are used as the basis for a discussion of strength/ toughness relationships in zirconia ceramics. The discussion demonstrates the wide range of ceramics available, exhibiting behaviour from flaw-size controlled strength to transformation-controlled strength. It is this ability to vary the microstructural control of strength and toughness within one ceramic system which forms the basis of this study.

2.1.1 Microstructures of Mg-PSZ

It is well known that Mg^{2+}, Ca^{2+}, Y^{3+} and virtually all the rare earth ions stabilise the cubic flourite structure of zirconia. The $MgO-ZrO_2$ phase diagram is shown in fig 2.1 [8].

In common with many ceramic systems the diffusion kinetics are sluggish so that equilibrium is rarely attained [9]. Metastable phases are therefore common. An understanding of the phase equilibria and metastable extensions is crucial to the production of useful engineering ceramics. The many possible variations in microstructures will be presented in the following sections, which are restricted to the commercially important Mg-PSZ materials which contain 8 to 9 mol% MgO.
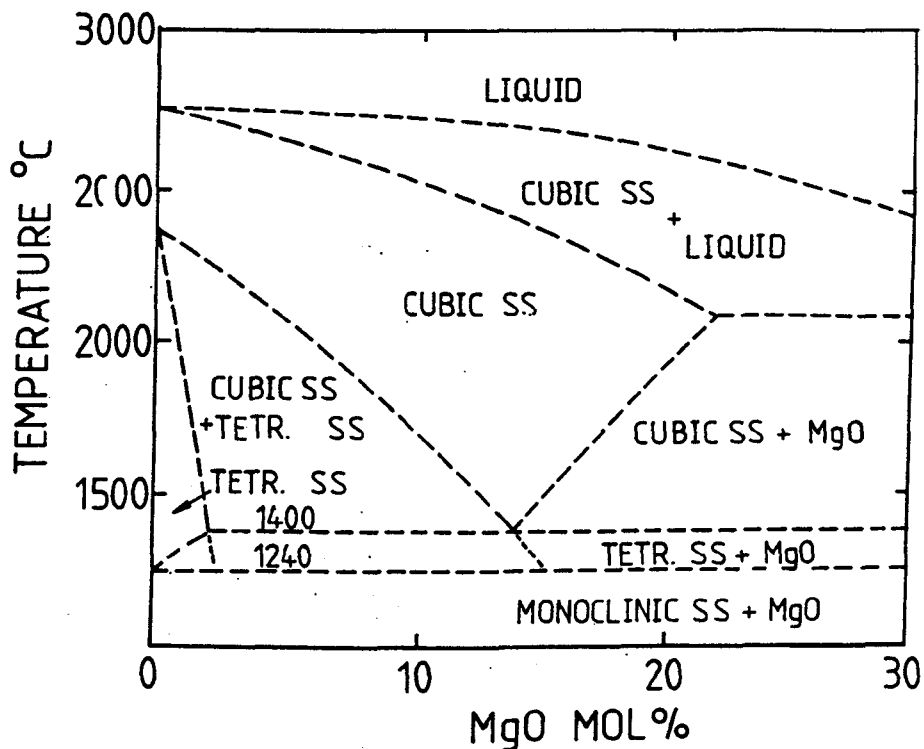
Fig. 2.1. The ZrO_2 rich end of the ZrO_2-MgO phase diagram [8].

2.1.1.1 Solution Treated

All commercially important PSZ materials require a solution treatment to develop a supersaturated solid solution prior to an ageing cycle which developes the transformation toughened structure. The exact temperature used varies, but the solution treatment is carried out in the cubic single phase field, i.e. above about 1750°C, often 1800°C, for 2-4 hrs . This is followed by a 'quench' to retain the

supersatured solid solution. The presence of monoclinic, especially at grain boundaries, reduces strength and so it is important that the solution treatment is sufficiently long to re-dissolve all second phases and that the quench is sufficiently fast to prevent precipitation of the tetragonal phase at grain boundaries (which would transform to monoclinic on cooling). Grain sizes after sintering are typically 40-70μm with a modest growth during solution treatment [10]. During the quench some transformation of cubic to tetragonal occurs resulting in extremely small (5-10nm) precipitates, resolvable using dark field imaging in the TEM. The even distribution of the precipitates indicates that nucleation is homogeneous.

2.1.1.2 Ageing of Quenched Material.

Porter & Heuer [12] classify the possible products of ageing a supersaturated cubic solid solution (ss) as follows:

A) $C(ZrO_2)(ss) \text{---> } t(ZrO_2) + C(ZrO_2)$

                        $\text{-->Cool--> } m(ZrO_2) + C(ZrO_2)$

B) $C(ZrO_2)(ss) \text{---> } t(ZrO_2) + C(ZrO_2)$

                        $\text{-->Cool--> metastable } t(ZrO_2) + C(ZrO_2)$

C) $C(ZrO_2)(ss) \text{---> } t(ZrO_2) + MgO$

                        $\text{-->Cool--> } m(ZrO_2) + MgO$

D) $C(ZrO_2)(ss) \text{---> } m(ZrO_2) + C(ZrO_2)$ $<1240^oC.$

E) $C(ZrO_2)(ss) \text{---> } m(ZrO_2) + MgO$ $<1240^oC.$

These classifications will be used in the following discussion:

2.1.1.2.1 Age at 1600°C

This produces heterogeneous precipitation of tetragonal phase (hereafter referred to as 't') at the grain boundaries, which transforms to monoclinic on cooling, thereby degrading mechanical properties (scheme A).

2.1.1.2.2 Age at 1400 to 1500°C

With ageing times of 4-5 hrs the t nuclei formed during cooling grow by conventional diffusional mechanisms and follow an Ostwald ripening process. The precipitates form as oblate spheroids which lie on the cubic {100} planes and are coherent with the matrix. Below a well defined critical size (about 0.25μm) the tetragonal phase is retained on cooling, constrained from transforming by the matrix (scheme B) (the precipitate size dependency of the martensite start

temperature will be discussed later). The structure produced contains about 0.25-0.3 volume fraction t and is usually referred to as optimally aged [1].

As the particles grow they reach a stage where it is suggested that coherency can no longer be maintained and they transform spontaneously to monoclinic on cooling, with associated microtwinning [11] (scheme A). The twinning is believed to occur in order to reduce the compressive stresses generated by the volume expansion accompanying transformation [11]. Twinning may occur perpendicular or parallel to the habit plane of the particle, with the former more likely to lead to microcracking. The crystallography of the martensite reaction and the origin of microcracking is given in appendix 1.

The change in fracture toughness and modulus of rupture (MOR) with ageing time at 1420°C is given in fig 2.2 [12]. The numbers in parentheses give the ground surface monoclinic levels. The fall off in fracture toughness in overaged materials is not as steep as may be expected, partly because of the residual matrix compressive stresses (although these are reduced by twinning and microcracking) and the possible contribution of microcracking, albeit small. In addition, some metastable t particles remain in overaged materials. In heavilly overaged materials a contribution to toughness may also arise from crack deflection [13].

The effect of temperature on fracture toughness of such materials is given in fig 2.3 [14]. The curves reflect the reduced transformability as the test temperature is raised.

2.1.1.2.3 Age at 1200-1300°C

A homogeneous distribution of t precipitates is still formed at this temperature in accordance with the metastable extension on the phase diagram (fig 2.1). The extension appears to be primarily a result of nucleation kinetics of the equilibrium eutectoid product [10]. The eutectoid reaction may proceed within the grains through the formation and breakdown of a number of metastable compounds, such as δ phase, $Mg_2Zr_5O_{12}$, (discussed later) with MgO only being produced in the grain interiors after an extended ageing time, e.g., 90 hours at 1300°C [10].

Normal ageing times give direct eutectoid decomposition (Scheme C) which is restricted to heterogeneous sites, such as grain boundaries. Even so, growth is slow, but does result in strength degradation from
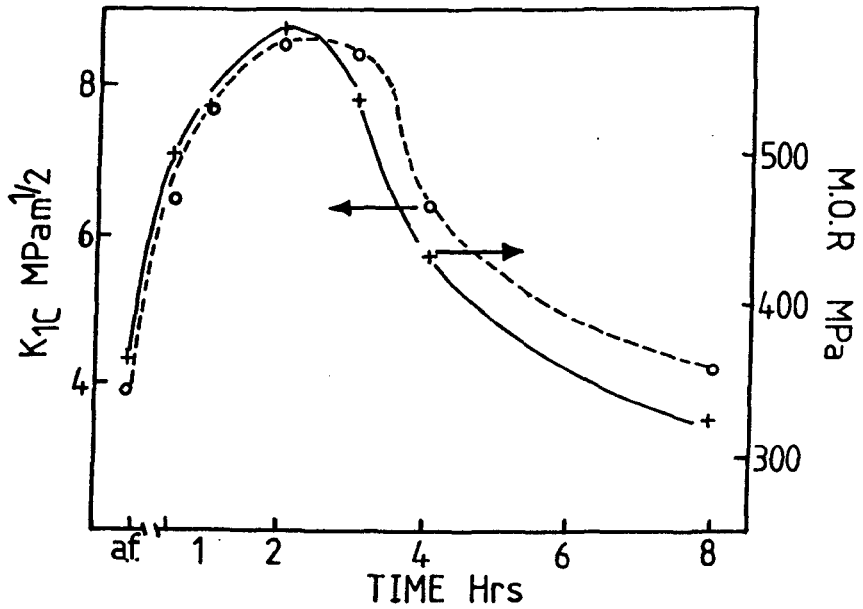
Fig. 2.2. Ageing time dependence of the strength (MOR) and toughness (K_{1C}) of an Mg-PSZ alloy aged at 1420°C [13]
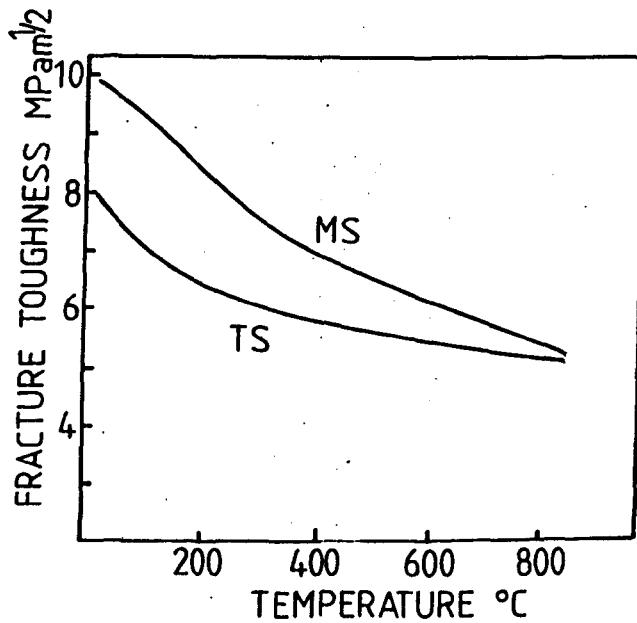
Fig. 2.3. Fracture toughness as a function of temperature for two grades of Mg-PSZ [15].

the microcracking due to the thermal mismatch of the cubic and eutectoid product.

The eutectoid transformation front advances into the grain interior by a 'cellular' reaction involving the co-operative growth of MgO pipes and the low solute ZrO_2 phase with either t or m symmetry (depending on temperature). The rods of MgO, whose spacing decreases as the stabiliser content is increased, grow in well-defined planes along <110> directions [15]. Farmer et al. [15] have observed a modulated structure within the monoclinic constituent indicating that the monoclinic developed by this process possesses a slightly different morphology to that formed, for example, in overaged samples. Eutectoid decomposition is dealt with in detail by Farmer et al. [16].

Long term heat treatment of an optimally aged microstructure in this temperature range also produces eutectoid decomposition. Dworak et al. [17] demonstrated a rapid fall in strength with ageing time, decreasing to about 1/6 the original value after 10hrs. However, a relatively new material was reported by these authors which showed no degradation in strength after 1000hrs at 1200°C. The material contained yttria substituted for 60% of the magnesia but was otherwise processed in a similar manner. An effect of the yttria was to reduce the lattice mismatch between the tetragonal and cubic phases. However, modification in the coarsening behaviour of the precipitates and the eutectoid reaction were not discussed by Dworak et al. [17].

2.1.1.2.4 Age at 1000°C

Porter & Heuer [11] found only eutectoid decomposition, which occurred at grain boundaries, whilst the cubic matrix remained unchanged (following scheme E). However, important microstructural changes can take place if an optimally aged material is given a subsequent heat treatment at 1100°C. This is discussed later in section 2.1.2.

2.1.1.3 Microstructures of Commercial PSZ's

Commercial PSZ's are rarely supplied in the optimally aged condition, being more usually produced by a furnace cool after sintering in the single cubic phase field, or possibly a rapid cool from the sintering temperature to an isothermal hold temperature [2].

Little literature is available on such microstructures although Hughan & Hannink [18] have provided some characterisation, using a 9.1

mol% MgO, 0.28 mol% SrO_2 PSZ. (The SrO_2 acts to remove grain boundary phases by leaching out Al_2O_3 and SiO_2 impurities) [19]. In this work, continuous cooling at 500°C/hr produced homogeneously nucleated t precipitates in cubic grains of 61±26 nm in their largest dimension. In addition, large (about 1μm) random monoclinic ellipsoids were observed, selectively nucleating at pores or other heterogeneities.

Other samples were studied [18] after the insertion of a 90 min isothermal hold in the cooling curve. This produced large changes in the precipitate form, with five different morphologies being identified (excluding those produced at 1100°C, see later):

- primary precipitates - formed by homogeneous nucleation,

- large random precipitates - formed generally on inhomogeneities such as pore surfaces, which grow rapidly above the eutectoid temperature,

- secondary precipitates - formed by rapid growth of certain precipitates, especially those near grain boundaries,

- intermediate precipitates - formed from the growth of primary precipitates,

- δ phase - an ordered anion vacancy phase $Mg_2Zr_5O_{12}$, formed within regions of primary precipitates, as isolated precipitates up to 500nm diameter.

Isothermal holds above 1400°C simply produced Ostwald ripening of the primary t precipitates, and growth of the large random precipitates. However, Ostwald ripening was not uniform with regions of primary precipitates remaining unchanged at about 60nm in their largest dimension.

Isothermal holds in the range 1300-1375°C produced secondary precipitate growth (SPG) at grain boundaries. An etched surface showed spherical spots of primary precipitation within the interior of most grains with SPG covering all grain boundary regions. The spots of primary precipitation, which also contained large random precipitates, decreased in number and size as the isothermal hold time was increased. SPG, which produced an increase in precipitate size as the transition to primary precipitates was approached, had clearly not occurred by an Ostwald ripening process. Hughan & Hannink [18] propose that the growth mechanism is assisted by rapid diffusion at grain boundaries but provide no clear explanation for the phenomena or for the size distribution within the SPG region. The requirement of rapid diffusion appears sound, supported by the observation that SPG is

initially rapid but decreases as the front moves within a grain. The absence of growth in the primary precipitate region is not commented upon but is most probably a result of sluggish diffusion resulting in a solution build up around the particles opposing further growth, discussed also in the section on thermal shock. The size distribution of the SPG is presumably caused by the production of numerous (smaller) precipitates at much higher growth rates. It is interesting to note that SPG was not produced by re-heating the continuously cooled (500°C/hr) material to 1340°C, rather Ostwald ripening was the dominant process.

In addition to the above microstructural changes, δ phase was observed as large blocky grains (500nm) within the primary precipitate regions (δ phase production is discussed under thermal shock) [18].

The isothermal hold treatments at 1340°C, gave a maximum in strength (MOR) comparable to commercial materials. The ageing window of time and temperature was very specific, a factor discussed further in later sections. It is important to note, however, that the SPG provided the bulk of the transformable particles contributing to strength.

2.1.1.4 Grain Boundary Impurity Phases

It is well established that grain boundary structure strongly influences the properties of ceramics, for example, impurity grain boundary phases can provide crack nucleation sites and reduce high temperature strength. With PSZ materials, the starting powders invariably contain 0.1-0.4% SiO_2, some Al_2O_3 together with other impurities [21].

In Y_2O_3 doped zirconia ceramics, a grain boundary phase forms which acts as a sintering aid. In MgO-PSZ, the grain boundary phase, its distribution and wettability, depend on the Mg silicate formed. Leach [21] has studied the formation of the silicates during sintering, and forsterite (Mg_2SiO_4) was found to be the dominant phase. Up to 1550°C the forsterite remained as isolated pockets, in contact with both cubic and monoclinic phases. At 1600-1650°C, however, individual grains became more rounded, and then appeared to wet the monoclinic (tetragonal at the 1600°C) suggesting liquid phase sintering. At 1700°C full wetting had occurred, with enstatite ($MgSiO_3$) also being detected. The abrupt change from wetting to non wetting appeared to be associated with a change in the silicate composition, with MgO being

leached from the cubic phase. The isolated forsterite particles, strongly associated with monoclinic regions, are expected to reduce the extent of microcracking [21] by making nucleation of the t → m transformation more difficult. The loss of MgO from the matrix to the grain boundary does, however, promote the formation of monoclinic to the detriment of mechanical properties.

Recently Australian researchers [19] have discovered that the addition of 0.25% SrO enhances mechanical properties by altering the grain boundary phases. Rather than forsterite, a Sr/Si based glass is formed which aids sintering, but is subsequently rejected from the material to leave internal grain boundaries with reduced levels of impurities. Ageing Mg-PSZ with SrO showed an improvement in MOR and a retardation of eutectoid decomposition compared to materials without the addition [16]. Additionally, SrO appears to reduce the grain size providing a further increase in strength.

2.1.1.5 Surface Grinding

It is now well established that, unlike other ceramic systems, an increase in strength can be achieved by surface grinding [1,22,23]. The grinding induces transformation at the surface which creates biaxial compressive stresses. Swain [22] has examined the mechanism and concluded that maximum strengthening occurs when the grain size is smaller than the transformed zone size, since the grain size is then approximately equal to the critical flaw size. A limit is placed on the transformation zone size by the amount of transformation which itself introduces strength limiting flaws.

In practice, the advantages obtained vary but, in a hot pressed ZTA, the strength (MOR) can be as much as doubled. A gain of 10-20% is typical for an Mg-PSZ [14,24,25].

2.1.2 Thermal Shock Resistance of PSZ's and Sub-eutectiod ageing

The thermal shock resistance is an important property for many existing and potential applications of PSZ's, such as metal extrusion dies. Fully stabilised ZrO_2 shows poor thermal shock because of a combination of high thermal expansivity and low thermal conductivity. PSZ's have lower thermal expansivity than fully stabilised zirconia, but their thermal shock resistance remains poor.

With optimally aged materials a substantial decrease in strength

results from quenching from above 400°C to room temperature [26]. This is associated with a change in mode of fracture from transgranular to intergranular [27], and could be a result of any of three mechanisms, namely, weakening of the grain boundaries by thermal stresses, crack propagation at lower thermal stress, or from thermally induced cracks formed at temperature.

Thermal shock resistance (in particular up-shock) may be improved by an additional age at 1100°C. The microstructural changes associated are [28,29]:

(i) development of an ordered anion vacancy phase $Mg_2Zr_2O_{12}$ (δ phase),

(ii) development of a fine monoclinic structure within tetragonal precipitates,

(iii) transformation of some normally stable tetragonal precipitates to monoclinic symmetry without prior precipitate growth,

(iv) eutectoid decomposition at grain boundaries.

The δ phase nucleates at the tetragonal/cubic interface [30] and is detectable in the TEM after about 1/2 hr at 1100°C. Hannink & Garvie [31] note certain criterion which must be satisfied for δ phase formation namely, the t precipitates must be sufficiently large (>150 nm) for nucleation and growth, and the matrix solute content must be sufficiently high (since δ contains 28 mol % MgO). The nucleation and growth is explained by Chaim & Brandon [32] as follows: the growth of t precipitates leads to rejection of the stabiliser Mg^{2+} into the cubic matrix; because of sluggish diffusion at <1200°C a concentration barrier builds up; in particular, where t precipitates are closely spaced, the barrier opposes further t growth; this, combined with the tendency towards oxygen ion vacancy ordering on flourite-type structures, leads to the formation of δ phase, nucleating at the C/t interface, and growing into the cubic matrix.

The above theory considers, therefore, that the stabiliser concentration profile is the controlling factor (and hence the minimum t particle size). This is contested by Heuer et al. [33] and Farmer et al. [15,34] who obtained δ phase in a solution treated material by a two stage heat treatment of nucleation at 800°C followed by growth at 1100°C but did not find δ phase in a single heat treatment at 1100°C. They considered that the controlling factor was the heterogeneous site of the t/C interface. However, Chaim & Brandon [32] contend that, since δ is not observed with coarse interparticle spacing (and

therefore no large solute gradients), formation is not heterogeneous nucleation controlled. Moreover, δ phase was generated by long ageing times at 900°C indicating the two stage process to be unnecessary. Indeed, these points explain the observation of Farmer et al. [16,34] and Heuer et al. [33]. In addition to the loss of coherency argument, Chaim & Brandon [32] have provided misfit parameter data which indicates a 2.7 times change in misfit between C/t and t/δ, associated with the decrease in lattice volume in going C → δ. This explains the loss of coherency and hence reduction in critical particle size for the retention of t.

The increase in transformability provides an increase in strength whilst the presence of monoclinic imparts thermal up-shock resistance [31]. Two processes improve the thermal shock characteristics: the transformation of some precipitates m → t during heating counteracts some of the thermal stresses and secondly, the presence of very fine m precipitates enhances fracture toughness with increased R-curve behaviour [35]. The latter is a result of crack branching and microcracking imparted by the grain boundary monoclinic [36].

The kinetics of this reaction are dependent on process history, fig 2.4 [31,37]. The maximum increase in thermal up-shock resistance occurred after 12-16 hrs for a conventionaly aged material, although additional processing stages of calcining and milling the mixed powders to improve homogeneity reduced this time to about 4 hrs. Prolonged ageing produces increased eutectoid decomposition. The optimum monoclinic content appears to be about 10%, above which strength is impaired.

The onset of the above microstructural change can first be identified by diffuse intensity scattering (DSI) in the cubic matrix [32,38,39]. This is common in PSZ and other anion deficient oxides [34] and is associated with short range ordering of oxygen vacancies present in the cubic matrix [32].

An interesting observation in quenched materials was the formation of an orthorhombic (o) phase from t precipitates within 10-20 μm of the free surface [27,33]. This is accompanied by a 1% volume expansion which is considered to be important in improving the thermal shock resistance of optimally aged PSZ's. The orthorhombic phase has been found in several studies, for example in the Mg-PSZ system [33,40,41], the Ca-PSZ system [42] and the ternary Mg-Y-PSZ system [43]. In bulk samples, o-phase can only be detected at high pressure [44,45] and at
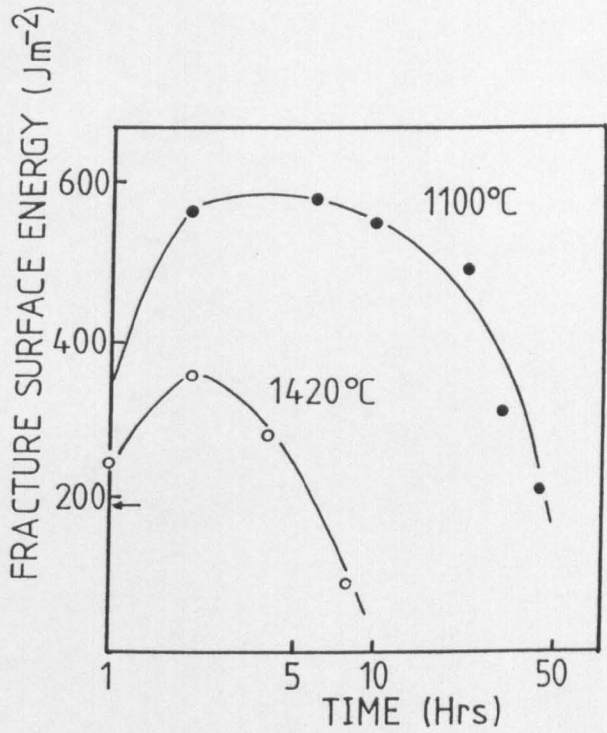
Fig. 2.4. Fracture surface energy as a function of time for an Mg–PSZ aged at 1420°C and 1100°C [53].
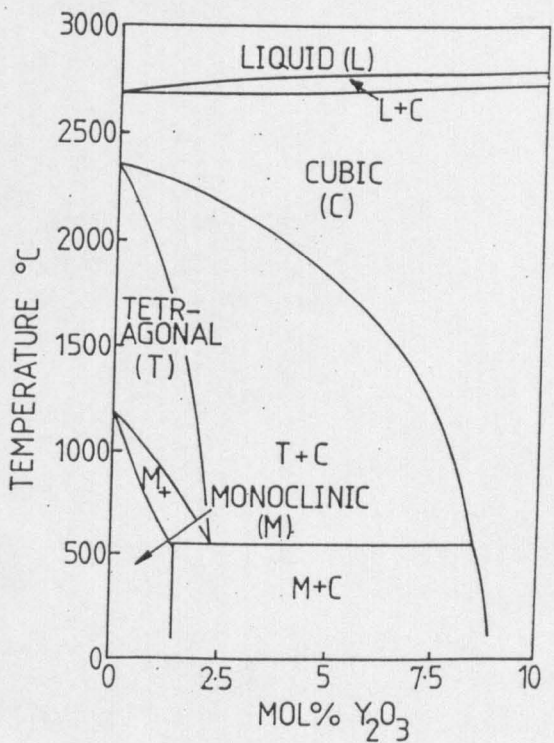
Fig. 2.5. Phase diagram for the zirconia-rich portion of the zirconia-yttria system [66].

very low temperatures [46], and is generally considered to be an artifact of thin foil preparation when detected under ambient conditions. Bestgen et al. [47] have demonstrated that the ordering sometimes observed in monoclinic when examined in the TEM is a result of the monoclinic being formed by transformation from an ordered orthorhombic phase. In their work, the tetragonal was transformed by electron beam heating to the orthorhombic symmetry by a comparatively slow displacive transformation. The transformation front left anti phase domain boundaries (APB) in its wake as it moved through the tetragonal. Transformation of o → m was induced by further electron beam heating of the foil, with the resultant monoclinic retaining the APBs and the ordered structure. In those grains where t → m was induced directly no evidence of ordering in the monoclinic was found. In studies of bulk material, however, Marshall et al. [46] found that there was no tendency for the o → m transformation to occur. Quenching the sample to liquid nitrogen temperatures produced almost total transformation of t → o, but grinding failed to cause any further transformation. Moreover, no toughening increment was provided by the o phase, and the ceramic was essentially brittle.

A detailed analysis of the crystallography of o phase is given by Muddle & Hannink [48].

2.1.3 Microstructure/Property Relationships for TZP

2.1.3.1 Microstructure

The phase relationships in the $ZrO_2-Y_2O_3$ system have been extensively studied [49] and follow the general form given in fig 2.5 [50]. However, the exact position of the t/ t+C phase boundary is still unclear, reflecting the experimental difficulty in achieving equilibrium. Nonetheless, it is clear that a sufficiently large tetragonal phase field exists to be able to produce a fully t structure.

Y-TZP has two advantages compared to Mg-PSZ. Firstly, sintering can be carried out at comparatively low temperatures ($1400^{\circ}C$ c.f. $1800^{\circ}C$) bringing the manufacture of TZPs within the scope of most producers without the need for extra equipment. Secondly, the eutectoid temperature is so low ($500^{\circ}C$) that any diffusional decomposition may be ignored.

The bulk of commercial TZPs contain 2-3 Mol% Y_2O_3 and mainly

consist of fine equiaxed t grains of a diameter, depending on sintering conditions, typically 0.2-2μm. In addition, many materials contain a small amount of cubic phase, whose grain size is usually larger than the t crystals. Although cubic is more common in the more highly stabilised materials, being ubiquitous in 3Y and above, it is also present with lower solute additions especially where inhomogeneous powders are used. The uncertainty of the ZrO_2 rich end of the phase diagram, in particular the position of the t/t+C phase boundary makes an accurate prediction of the amount of cubic difficult. In general, homogeneous powders of 2.5Y will contain about 10% cubic when sintered above 1500°C, (for example, Masaki & Sinjo [51] observed 11% cubic in a 2.5Y TZP prepared from very homogeneous powders sintered at 1450°C). In a survey of 10 commercially available TZPs containing 2-3% Y_2O_3 Ruhle et al. [52] found cubic phase ranging from 0 to 42%. The morphology of the cubic varied but often contained fine (10nm) tetragonal precipitates, believed to form during slow cooling from sintering.

The morphology of the grains varies from faceted to rounded depending on the amount of glass (although all studies have reported an amorphous phase at grain boundaries). The SiO_2 based glass arises from two main sources. In coprecipitated powders, SiO_2 is derived from the precursor $ZrSiO_4$. Careful control restricts SiO_2 to <0.1%, but this still provides a grain boundary glass phase of 1-2nm width. If the powder is further milled the SiO_2 level increases, arising from wear debris of the milling media [53]. Al_2O_3 is also introduced, which produces a glass which has been analysed as SiO_2-Al_2O_3-Y_2O_3 [54,55]. (The phase diagram predicts a eutectic with 45% SiO_2, 20% Al_2O_3, 35% Y_2O_3 which form at 1300-1400°C). TZPs derived from milled powders, therefore, exhibit large amounts of grain boundary glass which collects in easily identifiable pockets at triple points. In TZPs with small amounts of grain boundary glass, microcracks are found in the sintered product due to the thermal expansion anisotropy [56]. This is distinct from microcracking in other transformation toughened ZrO_2 ceramics formed as a result of transformation. In contrast, where a thick grain boundary glass is present, the liquid will accommodate thermal expansion anisotropy on cooling until the glass transition temperature is reached at about 750°C, thereby reducing residual stresses.

The glass appears to play an important role in sinterability [54-56]. With milled, coprecipitated powders the glass phase promotes

liquid phase sintering and the TZP is 99% dense even before the sintering temperature of 1400°C is reached [54,55]. In contrast, TZPs contain little grain boundary glass, so that sinterability is impaired and full density is difficult to achieve.

Before leaving the subject, it is important to consider the variation in microstructure of commercial TZP, highlighted by Ruhle et al. [52]. They found wide solute variations both within grains and throughout the material. The variation within a grain is a result of the slow diffusion of the solute within ZrO_2, although transport is rapid along the grain boundary glassy phases. However, the dramatic variations in solute concentration in many materials indicated that they had not reached equilibrium at the end of sintering and this was thought to be a result of using separate sources of ZrO_2 and Y_2O_3 [52]. It was also suggested that Al_2O_3 had been added deliberately by some manufacturers. The various powders gave a variation in toughness from 5.5 to 11 MPam$^{1/2}$ for nominally identical solute levels.

2.1.3.2 Effect of Grain Size and Stabiliser Content

The strength and fracture toughness of TZP ceramics are controlled by two main variables, namely stabiliser content and grain size. They are also affected by impurities (grain boundary glass and second phase particles), the homogeneity of the compact and the processing route chosen, which determine final density.

The mean grain size may be altered by the sintering schedule [57], or by the stabiliser content [58], although the grain size changes little in the solute range 2-3Y. The reduced grain size with increased yttria was attributed to the role of the cubic phase inhibiting grain growth, and also a solid solution effect on sintering kinetics.

2.1.3.3 Critical Grain Size

Gupta et al. [59] have reported a critical grain size of $0.3\mu m$ above which there is a rapid decrease in strength, surface cracks were observed and the material was largely monoclinic. This observation is consistent with the theory that the tetragonal phase is retained metastably by the matrix constraint, and that the retention of the tetragonal is strongly influenced by grain size.

In contrast Masaki [60] and Masaki & Sinjo [51] failed to show a grain size dependence with materials which had been HIPed (hot isostatically pressed), fracture toughness was invariant for grain

sizes of 0.2-0.75μm for 2-4Y materials. This is assumed to be a result of the greatly increased critical grain size, resulting from crack healing from HIPing, rather than the absence of one. The use of highly homogeneous materials will have helped in this respect. The authors gave no indication of monoclinic content as a function of grain size. The results, however, do give credence to the theory that the critical grain size is determined by the difficulty of nucleation, rather than being inherent. Critical grain size is discussed in relation to transformation theory in a later section.

Lange [57,61] has investigated the effect of stabiliser content on critical grain size, fig 2.6. This shows a sharp rise in critical grain size between 2 and 3Y materials. However, in his work Lange only achieved densities of 80-90% theoretical which will have inevitably reduced the critical grain size [49], and a moderate shift in the curve would place the results of Masaki [60] in perspective.

The effect of stabiliser content on mechanical properties is somewhat clearer. The results of the work of Tsukuma et al. [62], Haberko et al. [63] and Lange [57] are summarised in figs 2.7,8. All show a peak of fracture toughness around 2Y. Masaki [60] also found a peak at 2Y but the values were somewhat higher and the peak far more pronounced. There is wide agreement that with stabiliser contents below 2Y, spontaneous transformation of t → m occurs on cooling after sintering, accompanied by extensive microcracking and a decrease in fracture toughness. Solute contents above 2Y increased the amount of cubic phase thereby reducing the amount of transformable t [22]. In addition, Haberko [47], who failed to identify any cubic in his materials, has attributed the decrease in K_{1C} to a reduction in the chemical free energy driving transformation. However, as Nettleship & Stevens [49] point out, it is difficult to distinguish between cubic and tetragonal.

The effect of yttria content on strength follows a similar trend to toughness but the peak is displaced from 2Y to between 2.5 to 3Y. The reasons for the trend are broadly similar to those for fracture toughness. The resultant fracture surfaces show a change from intergranular for materials with less than 2Y (i.e. largely monoclinic), to irregular transgranular fractures for fully tetragonal TZPs [57]. The disparity between peak strength and peak toughness will be discussed in a later section.
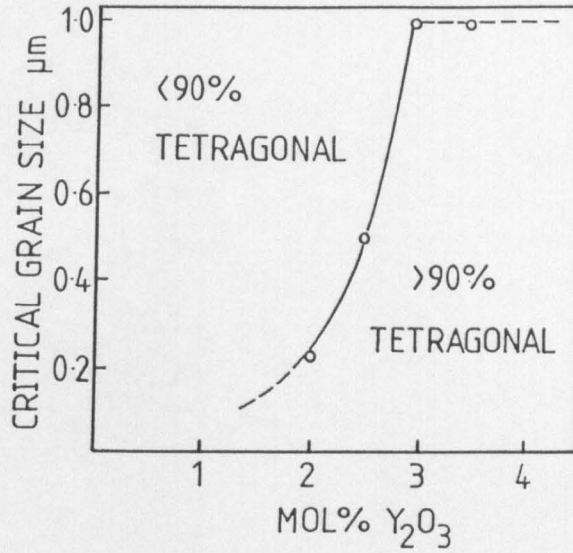
Fig. 2.6. Critical grain size plotted against yttria content in tetragonal zirconia. [61].
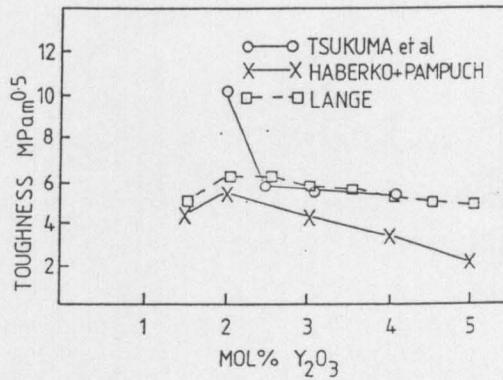
Fig. 2.7. Dependence of fracture toughness on yttria content [42-3,57].
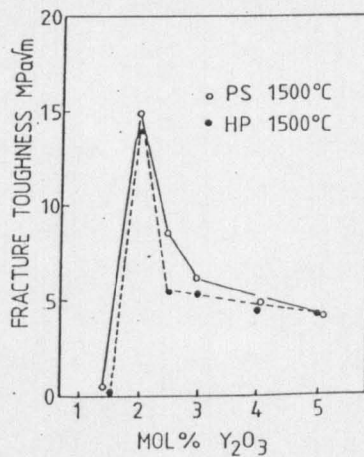
Fig. 2.8. Relation between fracture toughness and yttria content for hot pressed and pressureless sintered samples [60].

2.1.3.4 TZP Ceramics with the Addition of Al$_2$O$_3$

Recently Tsukuma [64,65] has reported that the addition of 20%
Al$_2$O$_3$ to a TZP provides a marked increase in strength, to as high as
2.5 GPa. Such strength levels are only realised in the HIPed product,
whereas little change is observed in sintered composites. The addition
of Al$_2$O$_3$ ($\approx$20vol%) gives a decrease in toughness as transformation is
inhibited. The Al$_2$O$_3$ also greatly improves high temperature strength
[65] with levels of 1000MPa at 1000°C being recorded. The behaviour,
which is independent of Y$_2$O$_3$ level, was attributed to a refined grain
size and HIPing.

2.1.4 Low Temperature Degradation of TZP Materials

A major obstacle to the full exploitation of TZP ceramics is that
spontaneous surface transformation occurs if held at temperatures in
the range of 150-250°C at times ranging from hours to days, which
degrades the material's strength [49]. In the worst case, complete
material disintegration can occur. Since the discovery of this
phenomena by Kobayashi et al. [66], considerable research effort has
been expended on the subject, but the exact mechanism remains elusive
[49].

The low temperature degradation of various TZPs is shown in fig 2.9
with the corresponding surface monoclinic levels in fig 2.10. Note how
the monoclinic content reaches a maximum at about 200°C irrespective of
Y$_2$O$_3$ content, a result found by most workers [eg68]. The degradation
is essentially a surface phenomena [69]. Both microcracks and
macrocracks may be formed [70] depending on the severity of the
reaction.

Most research has demonstrated a grain size and Y$_2$O$_3$ content
dependency for degradation when specimens are annealed in air [eg
69,71]. Watanabe [72] observed a critical size below which no
degradation occurred. Lange [73] and Schubert & Petzow [74] assert
that the critical grain size is that at which microcracking occurs, a
necessary mechanism to permit degradation to penetrate the surface.

In Masaki's [67] work the sintered materials used in figs 2.9,10
were compared to hot pressed and HIPed TZPs of near identical grain
size. This increased the density from about 97% to 99.6% and 99.8%
respectively. Under the same ageing condition only a 2Y-TZP (either
HIPed or hot pressed) showed any degradation. This was attributed to
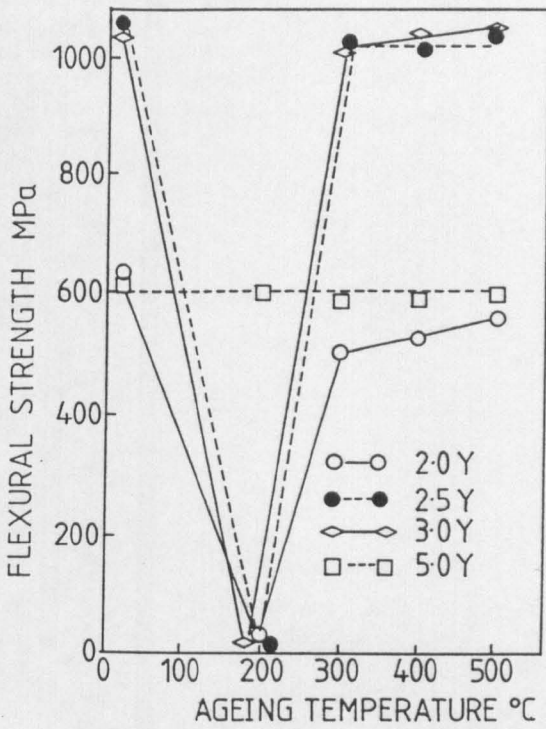
Fig. 2.9. Bend strength as a
function of ageing temperature [67].
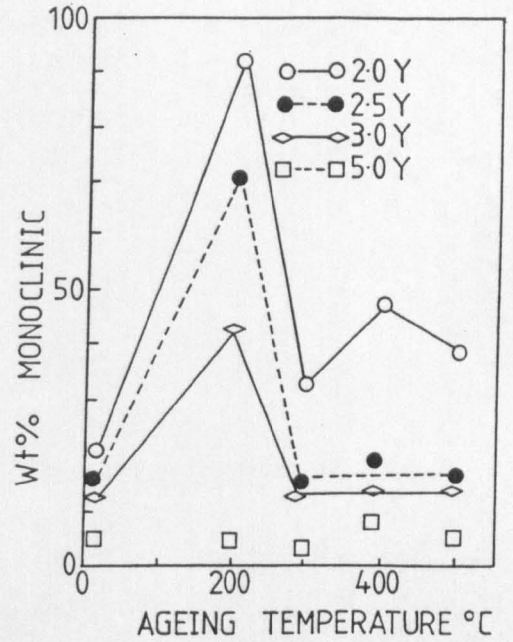
Fig. 2.10. Surface monoclinic
as a function of ageing
temperature [67].
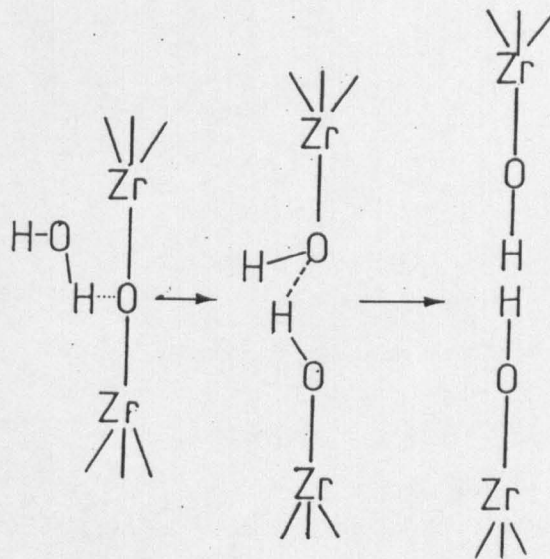
Fig. 2.11. Proposed reaction mechanism between water and the Zr-O-Zr
bonds at the crack tip [77].

the reduced flaw size.

The extent of surface degradation is greatly enhanced by the presence of water vapour at temperatures below 200°C and is accelerated as the water vapour pressure is increased [75,76]. The amount of monoclinic produced at 200°C, however, remains constant, indicating that water vapour affects the rate of degradation rather than the equilibrium. Sato & Shimada [77] have examined the kinetics of the reaction and found that the rate is constant as a function of Y_2O_3 content, provided that only tetragonal grains are examined (ie in materials which do not contain appreciable amounts of cubic). A slight decrease in rate with decrease in grain size was observed.

Sato & Shimada [77] have proposed a mechanism for the degradation illustrated in fig 2.11. This requires a solvent with a proton donor opposite a lone pair of electrons. Their work demonstrated that solutions containing water accelerated degradation rates, but these were unaffected by the presence of acids [70,77]. Interestingly, the temperature of degradation coincided approximately with the range of stability of Y-hydroxide [74]. Non aqueous solutions satisfying the lone pair/proton criterion also accelerated the rate. For a non aqueous solution possessing a lone pair, but not opposite a proton donor, a slight acceleration was observed, attributed to water contamination. Non aqueous solution without a lone pair of electrons showed no acceleration whatsoever. No weight change was observed indicating a dissolution mechanism was unlikely to be operating.

Lange [73] examined a TEM foil before and after low temperature ageing and discovered small (20-50nm) crystallites on monoclinic and cubic grain boundaries. The crystallites were tentatively identified as α-Y(OH)$_3$. The formation of the hydroxide was believed to be due to leaching Y_2O_3 from the tetragonal matrix near the grain boundaries permitting a monoclinic nucleus to form as the chemical free energy driving force was increased. Infra-red and Raman spectroscopy have confirmed the presence of OH$^-$ on a degraded surface [78], although the presence of Y^{3+} would be more conclusive.

Matsumoto [79] has demonstrated that full strength recovery is possible if the degraded sample is annealed at 1000°C for 24 hours. This is little comfort for engineers, however. Alternative strategies lie in the addition of ceria and alumina to the TZP [49,76] or reducing the grain size below that which permits microcracking. Additions of CeO_2 decrease the amount of degradation to the point that no monoclinic

is observed with the addition of 10% CeO_2 to 3Y and 4Y, and 15% CeO_2 to 2Y [76,80]. However, additions exceeding 6-8% CeO_2 decrease the mechanical properties [49]. Additions of Al_2O_3 to TZP reduce transformability by increasing matrix constraint and reduce, but do not eliminate, the degradation [76,81]. However, the advantages of Al_2O_3 TZP ceramics can only be realised by HIPing [65,76]. Alternatively, the yttria content can be increased to reduce transformability, but this obviously degrades toughness. However, an improvement of the homogeneity of yttria distribution will reduce the potential for degradation.

2.1.5 Theories of Tetragonal Metastability and Particle Size Effects

Theoretical analyses of the thermodynamics of transformation toughening must explain the observed dependency of the martensitic start temperature (M_s) on particle size, unless the reason is considered to be kinetic. As noted earlier, the particle size effect is common to all systems whether the ZrO_2 is incoherent within a chemically different matrix (eg ZTA), incoherent in a ZrO_2 matrix (TZP) or coherent (PSZ). In all systems the M_s is affected by the stabiliser content (easily explained in terms of its chemical free energy dependancy [82]), but the size dependency is more difficult to account for [83].

Lange & Green [61] and Lange [84] provide an analysis which introduces the size dependency into the surface area/surface energy terms as a result of:

(i) the volume change of the t → m transformation provides a surface area change and a change in interfacial energy,

(ii) appreciable twin boundary energy results,

(iii) an increase in surface area results from microcracking.

The dilational and shear displacements of the transformation increase the strain energy of the system; this energy needs to be accounted for before transformation can occur [85]. This term is reduced by the surface phenomena (ie twinning and microcracking) which are particle size dependent. The theory also predicts an increased critical particle size for an increased modulus, (which is also observed in ZTA) [86]. Calculations using the above model, however, predict a critical size some 20 times smaller than that observed experimentally at room temperature.

Chen et al. [87] have argued that the size dependence is nucleation controlled and requires some defect to initiate transformation. However, this does not fit with experimental evidence.

Evans et al. [83,88] have suggested that it is the stress component of the strain energy term which is the controlling factor. They assumed that the twin variants produced by transformation are mutually orientated such that there are no long range strain fields. In addition, the nucleation barrier was assumed to be small. Strain is restricted to the particle matrix interface and is therefore much smaller in value, and scales with the particle size. Thus, only large particles whose chemical free energy change on transformation is larger than the strain energy caused by transformation will transform. However, there is no evidence of cancellation of long range strain [89] and the predicted twin spacing has not been confirmed by subsequent work [90]. Indeed, this theory does not allow for shear banding where long range strain is clearly generated.

Heuer [89] and Ruhle & Heuer [90] have represented the transformation by rate reaction diagrams and consider that it is the nucleation barrier, F^*, which is responsible for the size dependency of the M_s, and provide the following as evidence:

(i) t-ZrO$_2$ in dispersion toughened ceramics --incoherent interface, eg ZTA

Intragranular precipitates are frequently spheroidal or ellipsoidal [90]. For 'regular' particles, strain is homogeneous within the particle, and is independent of size. Experimentally, these particles require an external stress to transform and no spontaneous transformation/particle size effect is observed.

In the case of intergranular particles, which are faceted polyhedra, the strain can vary markedly within the particle and is a maximum at edges and corners. Interfacial strains can be generated by thermal expansion anisotropy. Ruhle & Heuer [90] and Heuer [89] argue that these strains are dependant on particle size and are responsible for nucleation.

(ii) t-ZrO$_2$ formed by internal oxidation --incoherent interface

Chen & Chiao [87,91] have studied spherical ZrO$_2$ particles formed by internal oxidation of an Cu-Zr alloy. As with intragranular particles in ZTA, no size dependence was observed, even where the

matrix was dissolved away. This suggests that it is not the matrix constraint per se, but rather the nature of the constraint controlling nucleation which is important. However, the authors assumed a classical nucleation scenario.

(iii) TZP -- incoherent interface

The behaviour of TZP is similar to that of intergranular tetragonal phase in ZTA. Growth of martensite plates has been observed to initiate at grain boundaries [82,92-94] with several nucleation sites being possible in each grain. Here again, thermal expansion mismatch generates the required strain for nucleation. Many lattice defects such as low angle grain boundaries and stacking faults have been observed within tetragonal grains but only occasionally play a part in transformation, discrediting the classical nucleation theory [82]. As noted earlier, Masaki [51,60,67] has demonstrated that the critical grain size can be increased by HIPing. This suggests that there is not an inherent critical grain size, rather it is the nucleation barrier which is important.

(iv) t-ZrO$_2$ with coherent interfaces. (PSZs)

This includes the MgO, CaO, Y-PSZ materials in which a well defined critical particle size has been observed. Hannink [95] has explained this by assuming that above a certain precipitate size coherency cannot be maintained. Misfit dislocations are introduced which then provide nucleation sites for transformation. Theory does predict that a screw dislocation of burgers vector [001] lying in a (100) plane would provide a potent source [82]. However, only edge dislocations can be predicted for the precipitate morphology in Mg-PSZ, which would not provide such a nucleation site [90]. Moreover, no TEM examination has ever shown any misfit dislocations, although it is unlikely that they would be visible after transformation.

Ruhle & Heuer [90] assert that a significant shear stress occurs within the precipitate and nucleation should be similar to that described earlier for t-ZrO$_2$ polyhedra, explaining the critical size effect.

In all the instances where transformation has been directly observed, the nucleation mechanism has proved extremely difficult to elucidate [82]. Classical nucleation theory of a martensitic reaction

requires a heterogeneous site such as an array of dislocations which provides an embryo for the martensitic structure, but this has not yet been observed.

Heuer & Ruhle [82,90] have examined the nucleation theory in detail and have discussed classical and non classical theories. The classical approach involving pre-existing embryos, as favoured by Anderson & Gupta [94] is discounted because of the absence of special defects. Of the non classical approaches they favour a 'localised soft mode' model which provides heterogeneous nucleation at the grain boundary or particle matrix interface, i.e., a region able to act as a stress concentrator. Nucleation is considered to be controlling and always stress assisted, from a crack tip or thermal expansion mismatch.

The above approach is supported by Schubert & Petzow [74] and Schmauder & Schubert [96] who consider that the tetragonal phase does not have any thermodynamic stability in TZP materials. They consider that the factors affecting transformability are the chemical free energy driving the transformation (i.e. the undercooling) and the residual stresses. Thermal expansion anisotropy was shown to increase as the yttria content was decreased. These stresses are further augmented by an increase in grain size and an increase in the anisotropy of the grain shape. The considerable segregation of yttria, which is common in TZPs, and the loss of yttria to the glass phase, further aids the residual stresses which reduce the nucleation barrier for transformation. However, it should be noted that the explanations are not conclusive, reflecting the complexity of the problem.

A final point, which has not been discussed fully in the literature, is the implication of reversible transformation on the above theory. This demonstrates that even if stress is applied to generate a nucleus, the t inclusions can remain in the lowest energy state [97].

2.1.6 Inelastic Deformation

During the tensile testing of an optimally aged Mg-PSZ, Marshall [98] made detailed studies of the 'plasticity' shown by the tougher ceramics. Initial surface transformation was observed at >200MPa, manifesting itself as surface rumpling. The extent of rumpling varied between grains but was constant within a grain. Unloading at this stage caused the surface to return to its original state. At a stress

of >360MPa small cracks appeared, with associated rumpling, which did not disappear on unloading. By carrying out the tests inside an X-ray diffractometer the percentage monoclinic could be evaluated. This clearly demonstrated a reduction in monoclinic level on unloading. The monoclinic content at failure was 19.5% for a material containing 13.5% at the outset [98]. The difference between reversible and irreversible transformation could also be seen with a hardness indentation, which produced stresses well into the irreversible transformation regime. Zone 1, adjacent to the indent, showed the characteristic shear bands and grain rotation, produced by co-operative transformation [99]. The outer zone, only reported by Marshall [99], disappeared if the indent was sectioned so as to remove residual stresses, i.e. this was the reversibly transformed region.

Marshall [99] suggests three possible differences in mechanism to explain reversible or irreversible transformation. These are:

(i) that the particles only partially transform in the reversible case whereas complete transformation leads to irreversibility,

(ii) irreversibility is a result of twin formation and microcrack formation reducing the driving force for reverse transformation, or (iii) stabilisation of transformed state occurs when a certain volume fraction has transformed.

Evans [100] has analysed the role of reversible transformation and noted that transformation is restricted to a region ahead of a crack tip and provides no contribution to toughening.

Whilst beyond the scope of this literature survey, the implications of the above on the thermodynamics and nucleation of transformation are clearly important.

2.1.7 Strength/ Toughness Relationships: Transformation Limited Strength and R-Curve Limited Strength

It has been found that with Mg-PSZ ceramics the maximum strength attainable has been limited to about 800MPa despite extremely high K_{1C} values of 14 MPam$^{1/2}$ [101]. Moreover, the peak strength does not coincide with peak toughness, for either TZP or PSZ materials. The peak toughness occurs for a 2Y-TZP whereas peak strength is found between 2.5 and 3Y, at much lower toughness values. The evaluation of the discrepancy is based on inelastic deformation observed in very tough materials and R-curve behaviour, where stable crack growth may

occur. These theories will be developed in the following sections to explain the strength/toughness relationship in transformation toughened materials and to demonstrate the likely limitations in performance.

The strength of brittle ceramics is usually considered to follow classical linear elastic fracture mechanics:

$$\sigma = K_{1C} / YC^{1/2} \qquad \qquad ...(2.1)$$

where Y is a geometrical factor, and C is the crack length.

Thus, for the same specimen and crack geometry, the strength should scale with fracture toughness for various TZPs and Mg-PSZs. In this instance, as with most ceramics, the stress-strain curve is linear up to failure. In tough zirconia ceramics, for example a subeutectoid aged Mg-PSZ, the Griffith criterion cannot explain the strength, which is found to be far lower than predicted theoretically. The stress-strain curves for these materials show an offset of 0.03-0.05% after a pseudo yield point [102], fig 2.12. The extent of this 'plastic' like behaviour decreases with increasing temperature and the apparent yield stress increases and may not be seen at all. Observations on the polished surface of a stressed, very tough, specimen shows surface rumpling some of which disappears on unloading [98] but with a substantial amount remaining [103]. Small surface cracks are formed by the transformation which amalgamate to form large cracks [102]. The above is a result of surface transformation of the t → m, with the associated volume dilation, giving the apparent plasticity.

Since the departure from linearity in the stress strain curve is a result of transformation, a critical stress for transformation can be evaluated. Before considering this, however, the maximum toughening increment must be calculated. The increase in K_{1C} produced by transformation toughening is given by Evans as [104,105]:

$$\Delta K = \beta.V_f.V.E.d^{1/2} /(1-\upsilon) \qquad \qquad ...(2.2)$$

where: β = constant; V_f = vol fraction t; E = Young's modulus; d= transformed zone size; υ = Poisson's ratio and V is the volume dilation on transformation.

Swain [106] has demonstrated that fracture toughness increased linearly with $V_f d^{1/2}$, by changing stabiliser content for Y-TZP.
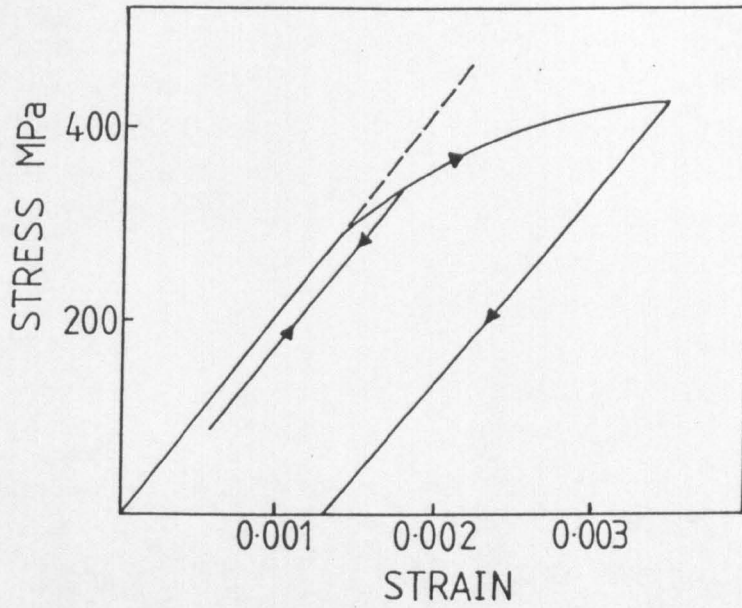
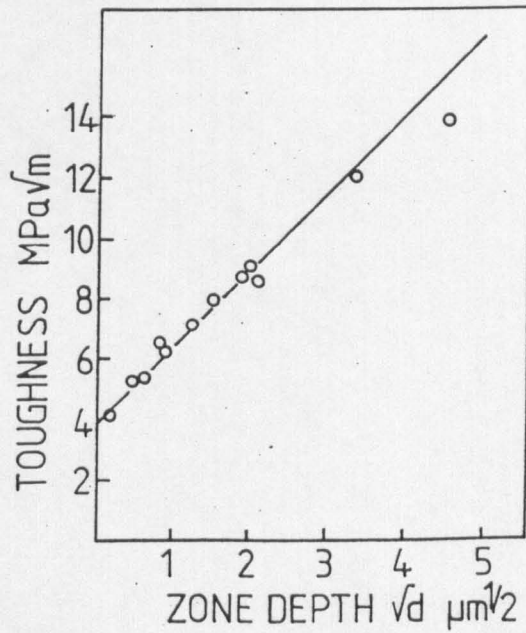Fig. 2.12. Stress–strain curve for a toughened Mg–PSZ in uniaxial loading [102].

Fig. 2.13. Relationship between transformed zone depth, d, and stress intensity factor for Mg-PSZ materials [106].

However, Masaki & Sinjo [51] failed to show any variation in $V_f d^{1/2}$ with a change in grain size, although only a small size range was investigated. Recently, Wang et al. [107] have demonstrated that there is a clear relationship between $V_f d^{1/2}$ and grain size for 2, 2.5 and 3Y-TZPs, confirming that the Evans [104,105] equation (2.2) is also correct for grain size changes.

Given a microstructure optimised with regard to V_f, the equation demonstrates the critical role of the transformation zone size, d. In a sub-eutectoid aged Mg-PSZ, for example, the microstructural change provides an increase in d as a result of the increased transformability of the t phase. Similarly, in TZPs, where V_f reaches 100%, even a moderate increase in d permits a substantial increase in K_{1C}. This is achieved by varying the grain size or solute addition.

Using equation 2.2 it is possible to calculate the expected zone sizes. For example, assuming a base value of K_{1C} of $4 MPam^{1/2}$, E of 200 GPa, volume dilation of 0.04 and V_f of 100% for TZP and 40% for Mg-PSZ, zone sizes of $8.1 \mu m$ and $200 \mu m$ respectively are obtained for zirconia ceramics processed to give maximum toughness. These values depend on the choice of the constant β. In this example 0.22 was used, but if a shear component is taken into account, $\beta /(1-v)$ becomes 0.38 and the zone sizes reduce to $3.2 \mu m$ and $80 \mu m$ for TZP and PSZ respectively. Measurements of zone sizes have been made by several techniques such as TEM, optical microscopy, X-ray diffraction [108,109] and Raman spectrometry [110]. Swain [101] provides values of $0.2-70 \mu m$ for Mg-PSZ ranging in K_{1C} from 4-14 $MPam^{1/2}$ respectively and $0.8-4.6 \mu m$ for K_{1C} of 5-10 $MPam^{1/2}$ for Y-TZP. Measured values are plotted for a Mg-PSZ in fig 2.13. It is interesting to note from these latter results that the constant varies from 0.35 for Mg-PSZ to 0.23 for TZP. This is most probably a result in the difference in transformation mechanism and grain size (i.e. in Mg-PSZ transformation can be co-operative with bands of monoclinic being observed, whereas the random grain orientation in Y-TZPs precludes this).

Based on the above relationship between K_{1C} and zone depth, Swain [101,106] evaluated the critical stress for the initiation of t → m. To do this a simple tensile stress criterion was used, and small scale yield criterion, i.e. that the transformed layer does not modify the elastic stress field. The radial tensile field about the crack tip is then given by:

$$\sigma_r = K_{1C} \ f(\theta)/(2\pi r)^{1/2} \qquad \qquad ...(2.3)$$

where $f(\theta) = 1$, normal to the crack, and r is the radial distance from the crack.

Knowing the zone size, a critical stress may be computed. The level of stress found corresponds closely with observed strength levels.

Using experimental values of the zone depths, (fig 2.13), Swain [106] plotted the critical stress as a function of toughness as shown in fig 2.14. In addition, experimental values of strength against K_{1C} are shown for Mg-PSZ, Y-TZP and (Al_2O_3)-Y-TZP.

Taking the Mg-PSZ curve first. Below the maximum in the graph, strength and fracture toughness are essentially proportional and therefore the Griffith criterion is satisfied, so that the strength is limited by the flaw size. This strength corresponds to a critical flaw size of 100μm. The maximum strength is dictated by C_r^{crit} at the point where this curve intersects the critical stress to initiate transformation. Only a certain amount of transformation is permitted before catastrophic failure of the material, since additional stress provides further transformation, which itself generates strength limiting microcracks [111]. By increasing the transformability of the material, and hence the toughness, the stress at which transformation starts is reduced and, therefore, the stress at which catastrophic failure occurs is reduced, i.e. *transformation limits the strength*.

The 2Y-TZP shown follows the same trend, except that prior to the maximum stress, strength is not proportional to K_{1C}. The additional strength is attributed by Swain [106] to surface transformation from prior grinding.

The above argument possesses several flaws. Firstly, the surface compressive stresses are easier to generate in PSZ than in TZP and so this cannot be used as an explanation for the difference in curve shapes between TZP and PSZ.

Secondly, in the flaw size controlled regime, transformation toughening clearly occurs, as it is this which increases K_{1C} above the base of 4MPam$^{1/2}$. This is not compatible with Swain's curve for critical stress to induce transformation. This curve predicts a stress of 700MPa for a peak aged Mg-PSZ. The work of Marshall & James [98] has shown that transformation may be detected at stresses of 200MPa in a similar material (even allowing for differences in test method this

stress is still much lower), whereas initiation of microcracks only started at much higher stresses. However, it is clear that, despite the presence of transformation toughening, the behaviour is still flaw size controlled.

The reasons for the departure from linearity of the Y-TZP are, therefore, not clear. The observation cannot be attributed to R-curve behaviour as this would tend to reduce the strength in the flaw size controlled regime rather than increase it.

Another possible explanation is that the actual flaw size is different between different TZP materials tested. In the case of the Mg-PSZ, grain size and flaw size may be expected to be approximately constant (i.e. heat treatment does not greatly effect this) whereas in the TZP materials this may not be true since small grain size variations greatly affect material properties. However, Swain [102] maintains that this was not the reason for the departure from linearity.

Only one data point is provided in fig 2.14 for an Al_2O_3/TZP and the curve drawn is therefore speculative. Three additional points, not shown in fig 2.14 were later added [102] for higher toughness materials which lend more weight to the curve. The 'super Z' here has a reduced grain size and critical flaw size as a result of HIPing. This, combined, with an increased elastic modulus, accounts for the very high strength levels achieved.

In a later paper Swain & Rose [102] use a different expression for determining the critical stress to initiate transformation which is given by:

$$\tau_0 = \beta^2.\sigma^t \, [K \, /K_c - K_0 \,] \qquad \qquad ...(2.4)$$

Where β=constant; σ^t = transformation induced stress; K_c= steady state fracture toughness; K_0= maximum stress intensity factor sustainable by the matrix within the transformed zone and K= stress intensity factor.

This expression marginally underestimates the actual stress/ toughness maximum. In fact, the predictions, particularly those for Mg-PSZ, agree better if a constant of 0.65 is used, which is the theoretically predicted value for a hydrostatic zone, rather than 1.35, as determined experimentally.

An additional source of strength limitation may arise from R-curve behaviour [102]. R-curve behaviour describes the condition where a steady state value of fracture toughness is only achieved after stable

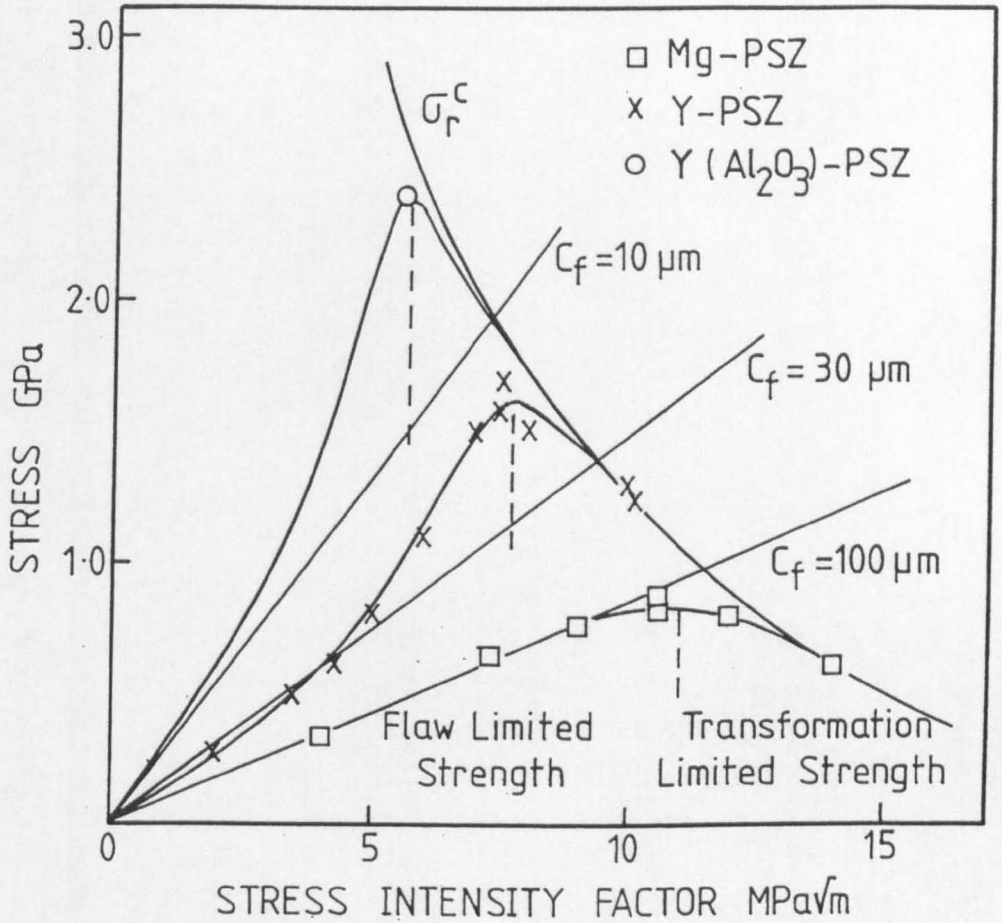Fig. 2.14. Plot of the strength of Mg–PSZ and Y–TZP against measured stress intensity factor. The curve a^c_r is the critical stress to initiate transformation as a function of K. The thin lines radiating from the origin are the anticipated strengths for various critical flaw sizes, C_f. The broken vertical lines indicate the transition from flaw controlled to transformation limited strength [106].

crack propagation as illustrated in fig 2.15. The applied stress may
be superimposed on the R-curve to demonstrate this phenomenon, fig
2.16. For an initial crack of length C_0 the stress intensity factor is
low. As the crack grows, resistance to its growth increases. The
reason for this will be discussed later. The condition for failure is
evaluated as that when the stress reaches $\sigma*$, at which point the stress
curve is at a tangent to K_R (fig 2.16). This defines the critical
crack $C*$. The important point is that this intersection will be
determined by the slope of the R-curve, not by the initial crack size
or by the steady state fracture toughness $K_R^{(C)}$. Note also the stress
intensity factor at failure $K*_R < K_R^{(C)}$, the latter being determined on
materials with much larger cracks.

A schematic of different possible behaviour is presented in fig
2.17. Curve 3 has the highest steady state fracture toughness but the
stress at failure is lower than curve 2, of lower $K_R^{(C)}$ because the
slope is lower. More extensive stable crack growth is permitted in the
lower strength, higher toughness material. Swain & Hannink [13] have
shown how the slope of an R-curve changes with heat treatment. For an
optimally aged Mg-PSZ, a very rapid rise in stress intensity factor was
found over a small crack extension, providing similar behaviour to
curve 2, fig 2.17. Sub-eutectoid ageing, which promotes strong R-curve
behaviour, decreased the slope of the R-curve to something similar to
curve 3, and, as expected, decreased the strength. Similar trends of
strength limited by R-Curve behaviour can be demonstrated for Y-TZP
[101].

To understand how R-curve behaviour limits strength Swain [102]
takes a simplified R-curve construction. Taking:

$$K_C = \beta . \sigma^t (h^{1/2}) \qquad \qquad ...(2.5).$$

and $\qquad \Delta a_t = \lambda h \qquad \qquad ...(2.6)$

the construction gives:

$$\tau_f . Y(a_0 + \lambda h)^{1/2} = K_C = K_0 + \beta . \sigma^t . h^{1/2} \qquad ...(2.7)$$

Where Y is a geometrical factor, dependant on crack geometry equal to
about 2; λ is a dimensionless constant and h is the transformation zone
size; Δa_t is the crack extension; σ^t is the transformation induced
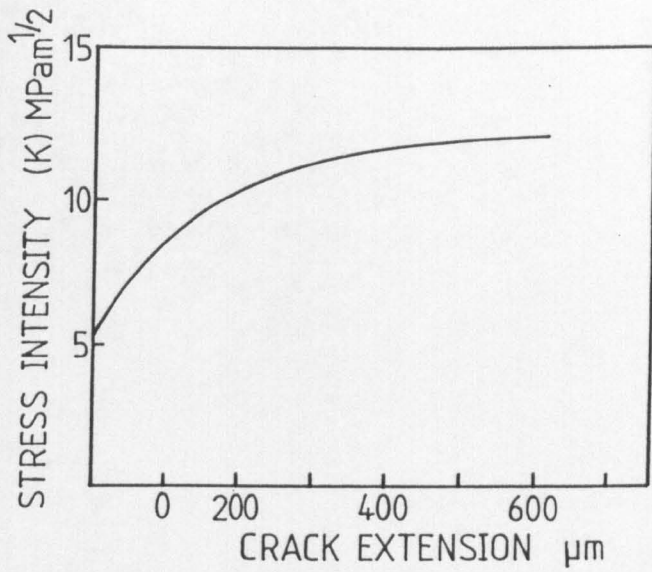stress; σ_f is the failure stress and β is a constant.

Fig. 2.15. Example of the R-curve behaviour in a peak-toughness
Mg-PSZ. The results were obtained by propagating the crack in small
stable increments, followed by annealing and then repropagating [102].
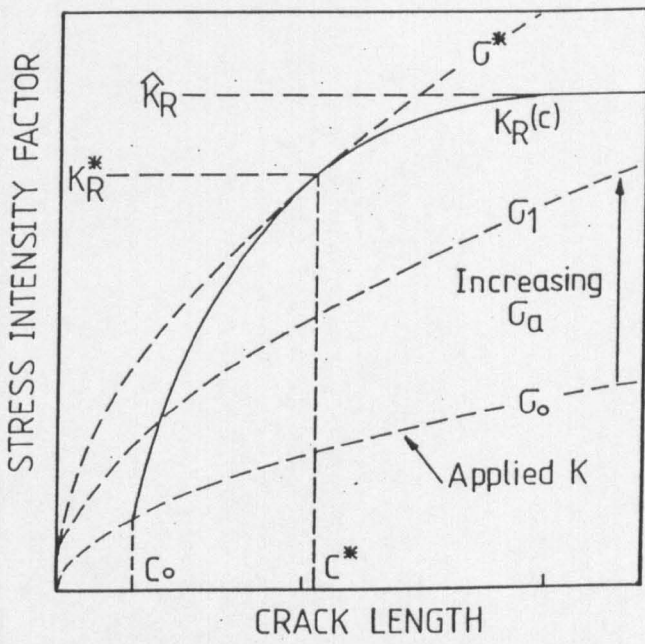

Fig. 2.16. Schematic representation of R-curve (solid line) and
applied stress intensity factors (broken curves) [103].

A plot of σ_f against K_c is provided in fig 2.18 and goes through a maximum at:

$$h^{1/2} = \beta.\sigma^t.a_o \, /\lambda K_o \qquad \qquad ...(2.8)$$

As can be seen the qualitative agreement is good, although, given the simplistic approach, the quantitative agreement is less precise.

An interesting result of the above is that the zone size at maximum strength is dependant on initial flaw size. Thus, maximum strength is achieved at lower fracture toughness as the flaw size is reduced, in agreement with fig 2.14. This has important implications for the behaviour of surface flaws, which are very important in wear, compared to large notches, which are clearly not relevant in wear.

The work of Swain & Hannink [13] demonstrated the mechanisms responsible for R-curve behaviour. Materials containing highly metastable $t-ZrO_2$ show crack extension which is retarded by transformation shielding of the crack tip from remotely applied stresses [102]. In subeutectoid aged Mg-PSZ, the R-curve behaviour was attributed to microcracking and crack branching [36] in addition to the transformation toughening (the contribution of which depends on the extent of subeutectoid ageing). The thin grain boundary decomposition product was found to be very effective in promoting crack branching whilst being thin enough not to affect the strength [36]. In grossly overaged, refractory grade Mg-PSZ, where the microstructure consists of large monoclinic precipitates, the mechanism producing R-curve behaviour is mainly that of crack deflection by the precipitates, analogous to whisker or platelet composites. Again, as with the explanation for maximum strength for transformation toughened ceramics, it is clear that an increase in strength, by an increased R-curve slope, results in decreased stable crack growth and damage tolerance.

The overall conclusion of this section is that, by close attention to processing conditions, it is possible to develop materials close to theoretical strength/ toughness limitations. The consequence of the strength of the very tough ceramics being transformation controlled rather than flaw size controlled is that they exhibit less variability in strength, hence high Weibull moduli are recorded (eg up to 40 for Mg-PSZ [112]). They are damage and process fault tolerant, and consequently design for engineering application must be based on yield stress criterion. It is unavoidable that high strength, low toughness
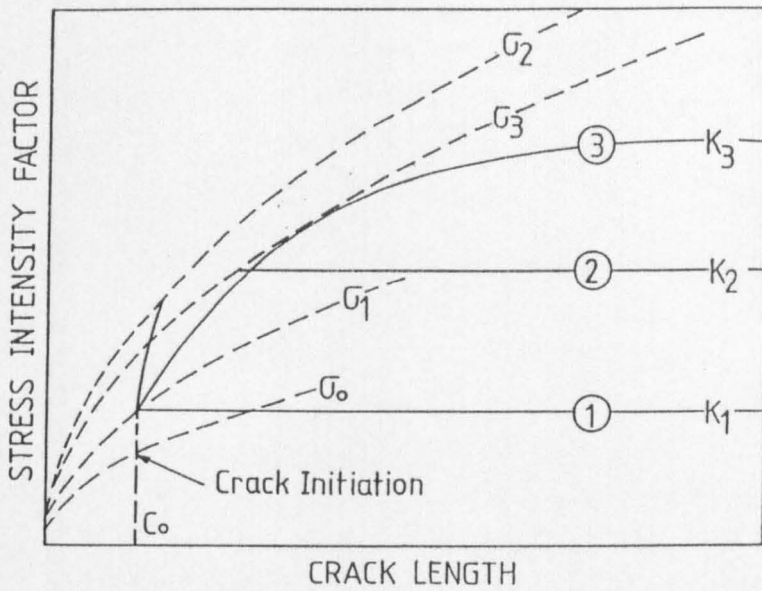
Fig. 2.17. Schematic of R-curves, depicting maximum strength at intermediate steady-state toughness [103].
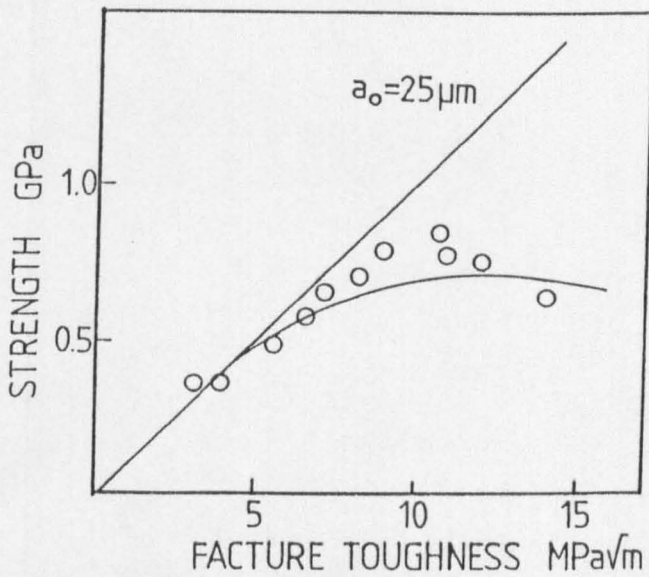

Fig. 2.18. Comparison of the predicted strength vs K_{1C}, with experimental data for Mg-PSZ [102].

materials such as the 2Y(20A)-TZP remain susceptible to damage and processing defects. For example, a 20kg Vickers indent will reduce the peak strength of a 2Y(20A)-TZP ceramic by tenfold, whereas an Mg-PSZ material also of peak strength suffers no degradation even with a 40Kg Vickers indent [102]. Indeed, Marshall [103] found no degradation up to a load of 1000N.

2.2 WEAR OF CERAMICS

2.2.1 Wear of Zirconia Ceramics

The literature on this subject is sparse. This is somewhat surprising given that most workers publishing on structure/property relations assert that this is a 'primary application' for zirconia for which it is 'well suited'. It is rare that studies of wear report the material fabrication route, mechanical properties and, on occasions, they even omit stabiliser type and content. Few appreciate or note the role of transformability. This makes it difficult to draw conclusions and emphasises how little is understood about the tribological properties of zirconia (and all ceramics for that matter).

Table 2.1 gives a list of all field trials conducted to date and Table 2.2 provides a summary of all laboratory wear tests published. These results can be compared to those for other ceramics in Table 2.3

2.2.1.1 Ceramic/Ceramic Wear

In self-mated tests the literature is contradictory. Scott [121] found low wear coefficients at low sliding speeds, which compared favourably with tool grade alumina. Lindberg & Richeson [123] apparently found similar results, although not quantified. Friction coefficients and strength degradation as a result of wear were better for Y-TZP and Mg-PSZ than for SiC and Si_3N_4. Yust & Carignan [134] have examined a range of ceramics, under sliding conditions in dry nitrogen, and found that a self mated Mg-PSZ couple produced virtually immeasurable wear, whilst under the same conditions a self mated SiC pair gave wear rates of 5×10^{-5} mm^3/Nm. Denape et al. [139] confirmed the superior performance of PSZ (type unspecified) to SiC but found sialon greatly superior to both. In contrast to these results, Breval et al. [124,140] found a 3Y-TZP showed an order of magnitude higher wear rate than any other SiC couple (sintered, graphitised etc), a

TABLE 2.1

Field Trials for Zirconia Components

Reference	Material	Application	Present Material	Improvement	Comments
37,113–115	MgPSZ (TS)	Cu/brass extrusion dies High speed steel extrusion	Tool steels	x4	Better dimensional accuracy, more predictable life, less need for lubricants, smoother product finish. PSZ shrunk fit into tool steel.
116,117	MgPSZ	Diesel engine cylinder liners	Cast Iron	not quantified	No measurable corrosion or wear after 100,000km, tested in extreme conditions, shrunk into cast iron block. NB Piston not ceramic.
118	MgPSZ 3YTZP	Cylinder liner and piston; simulated engine	N/A		Not successful. Probably result of self mating. No good vs SiC either. Both oil and dry.
37	Plasma sprayed CSZ	Adiabatic engine	N/A	not quantified	13 month field test. 30–50% fuel saving.
114,115	MgPSZ (MS)	Valve gear eg cam followers	Steel	15%	PSZ works well with oil lubrication – other ceramics may wear less.
116,117	MgPSZ	Valve guide in turbo	Superalloy	x100	Operation at 1000°C under dry condition, low velocities. PSZ far better than any other metal/ceramic (or self/self combination) vs Cr plated steel.
115	MgPSZ (MS)	Screw conveyor bearings	Cast Iron	x10	Unlubricated, abrasive dust. Not successful when PSZ vs PSZ
115	MgPSZ (MS)	Scraper blades (coal conveyor)	WC	not quantified	Improvement
115	MgPSZ (MS)	Metal powder extrusion dies (conform process)	?	not quantified	Temps of 600°C generated, high stresses. Only diamond and MgPSZ successful – all others failed.
37	MgPSZ (MS)	Bioengineering	Various Al_2O_3		Shown to be biocompatible. Could be promising.
37	MgPSZ (MS)	Autoclave nozzle	Stainless Steel	x30	
37	MgPSZ (MS)	Dry bearing	Steel	x6	
37	MgPSZ (MS)	Aqueous slurries	Al_2O_3 SiC	x20 x3	Depends on slurry
119	Y PSZ, TZP	Roller bearings	Si_3N_4	Poor	Bad materials processing evident –not conclusive. Petch type relationship of life, grain size.
119	Y PSZ, TZP	Tools	Al_2O_3	Poor	Too soft, high hertzian stresses → deformed + spalled
120	MgPSZ	Bearing in autoclave (shaft)	?	>x100	vs hard chrome, 450°C, 35MPa. Abrasive dust, hydrocarbons, steam 600 hours, no degradation.

TABLE 2.2

SUMMARY OF THE LABORATORY WEAR TESTS

Ref	Speed	Load	Temp	Test types	vs what	Wear Rate mm^3/Nm $(\times 10^{-9})$	μ	Material Type	K_{IC}	Affect of water or otherwise	Comments
121	1-10mm/s	4.9N	up to 300°C	P on flat	Fe,steel,Cu (not specific) + self	?	0.25-0.3 dry 0.5 wet	Mg PSZ, CSZ Y PSZ including Nilsen MS	varied	↑ greatly	Good at RT, >300°C, severe in between. Wear rate ↑ in H_2O & stearic acid, despite μ0.1. Wear rate higher vs Fe than Cu. Dry comparable to Al_2O_3, much better than SiC
114	2.5cm/s	10N	RT	3 body abrasive	self	?	N/A	MgPSZ TS MS	MS >TS		PSZ (MS) better than Al_2O_3, Cr, cast Fe. TS worst. MS polished
122	[1]92cm/s [2]367cm/s	2.3-40.8 kgf	RT RT		mart steel	?	[1]0.5-0.3 [2]0.2-0.3 [1]0.25-0.6 [2]0.25-0.45 [1]0.3-0.5 [2]0.2-0.4	MgPSZ TS MS Y TZP Y ZTA	not given	N/A	Marked difference between 92 & 367 cm/s esp μ. μ high for high steel wear. Correlation of macrodamage and K_{IC} steel wear↓ as speed↑
123	?	5,4.5, 113, 227 N	RT→ 1200°C	sliding	?	?	RT 0.2→ 0.7 900°C 0.1→ 0.8 0.2→ 0.8	Y-CSZ			little damage, low μ, no strength degⁿ when tested after wear
124	1.5m/s	≈44N		recip flat on flat	self	2.1-2.8×10⁵ 1.35 ×10⁵ 5.1 ×10⁴	0.2-0.4	3YTZP vs self vs αSiC vs CSiC	≈5	–	wear rate order of mag higher than any SiC couple (αSiC, Si-SiC, C-SiC [graphitised
125	1mm/s	9.8N		POD		10⁵-3×10⁵ 10³		3YTZP (0.3μ) 5YTZP (cubic)	11.6 2.5	strong environment effects	wear rate 3Y↑ as: dry N_2 → hexadecane → hex & stearic acid → air → water
121	0.3mm/s	10-55N	ambient		self	?		3YTZP (0.5μ)	5.5-6.5	dry	
118	Engine simulation		ambient		self	2 ×10⁵ 8 ×10⁵		≈3YTZP		dry	up to 54km TZP wore >> Al_2O_3, αSiC
116	0.3mm/s	10-100N		POD	steel	≈0.2μm/hr	≈0.1	PSZ (assume Mg)	8.1	mineral oil	
126	1mm/min	0.05-3.5N	ambient	scratch				Y-TZP,PSZ			abrasive wear threshold ↑ as K_{IC}↑
127	0.3m/s	2.2 - 13.3 N	38, 205 425°C		self	100 mild load 10⁴-10⁵ high load	<0.5 <0.5	PSZ		dry N_2	
128	0.3m/s	12.7N	ambient	POD	self	not quant		MgPSZ		dry N_2	High m in starting material. m% ↓ because of high interfacial temp
129	10-20cm/s	10N	ambient	Ball on disc	bearing steel ball	Steel 6.7×10⁻⁸ PSZ low	0.2	TZP			PSZ better at reducing steel wear of SiC, Si_3N_4, Al_2O_3
130	0.03 -0.3 m/s	10N	20 -1000°C	POD or ring on disc	self	5×10⁻⁸ - 5×10⁻⁴	>0.4	MgPSZ	8.1		Temp effects v strong. Speed influences temp see text.

Ref	Geometry of Test	Load (N)	Ave Speed (m/s)	Total Sliding Distance (km)	Material Specification	(k) Wear (mm^3/Nm) $\times 10^{-9}$
131	Hemispherical pin on recipro- crating plate or rotating disc	50 " "	0.028 " "	1.5 " "	WC-5% Co 99% Al_2O_3 Ti-C	3 6 60
132	Flat truncated crucial pin on rotating disc	85 7.5 15	0.24 " "	7 3962 1671	99.7% Al_2O_3 " "	4600 0.5 0.14
133	Crossed- Cylinder	16 "	1.0 "	NG "	Mixed Carbide RBSC	1000 5000
134	Hemispherical pin on rotating disc	9	0.3	0.2	100% Al_2O_3	400
135	Rotating ring on disc (Folex Model 6)	10 30 50 70 100	0.7 " " " "	up to 54 " " " "	SSiC " " " WC-Co	2300 5300 13000 24000 48
121	Hemispherical pin on recipro- crating plate	4.9 " " "	0.001 " " "	NG " " "	Alumina (Tool grade) Sialon PSZ (Nilson-MS)	7.4 2270 1.5
136	Hemispherical pin on recipro- crating plate	10	0.001	NG	HPSN	31250
137	Flat truncated conical pin on rotating disc or reciprocating plates	8 13 80 8 13 23 43	0.24 " " " " " "	362 886 0.2 609 609 352	Sialon " " SSiC " " "	340 2300 100000 500 2200 2400 3000
138	Flat truncated pin on rotating disc	10	0.24	NG	HPSN	30000

TABLE 2.3 Wear Factors for Ceramics sliding against themselves at low loads and speed under ambient (room temperature, air 40-50% RH) conditions. After Wallbridge [126]. (NG - not given)

result also found for PSZ by Derby et al. [141]. Ishigaki [142] examined self mated couples under a range of speeds and relative humidities for a load of 10N. Relative humidity, (RH), had a strong effect on wear rate tending to increase material removal but also increase friction coefficient. Water gave lower wear rates than an RH of 90%, but these results were discounted because of hydrodynamic effects. These findings are consistent with Fischer et al. [143] who obtained the same value of the friction coefficient in dry nitrogen and air (RH not specified), and only marginally lower in water, a result easily attributable to elastohydrodynamic effects. Thus, zirconia appears to differ from alumina where surface hydroxide effects reduce friction forces [124,140]. Over the speed range 118 to 545mm/s and RH range 20-90%, wear rates of 10^{-5} to 5×10^{-3} mm^3/Nm were obtained by Ishigaki [142] for a load of 5N, confirming that self mated zirconia is a poor couple and that environmental effects can strongly influence results, perhaps explaining some of the variability of the data in the literature.

Woydt & Habig [130] provide evidence for one possible reason for the variable results reported above. They examined self mated Mg-PSZ couples over the temperature range 22-1000°C and speed range 0.03 to 3 m/s. The effect of speed was considered mainly as influencing the flash temperature at the interface. The results are presented in fig 2.18. At speeds above about 1m/s wear was severe at all temperatures (k=10^{-4} mm^3/Nm). In contrast, at very low sliding speeds, comparatively good wear factors of 5×10^{-8} mm^3/Nm were recorded. Clearly, an increase in interfacial temperature increased plastic dominated wear mechanisms, such as adhesion, leading to a rapid increase in the wear rate. The very low thermal conductivity and high thermal expansivity of zirconia meant that this transition occurred at much lower speeds than with other ceramics, thereby making it potentially the worst couple in comparative tests. This has led to observations such as a glow from the sliding interface and thermoelastic instability, both of which ultimately lead to catastrophic failure [eg 118]. Yust & Carignan have confirmed that self mated PSZ couples show a general increase in wear rate with temperature, in contrast to self mated alumina where the wear rate decreases as the temperature is raised from ambient to 450°C. Results such as those from Scott [121] and others were obtained at very low sliding speeds where heat generation is minimal. Whilst the effect of
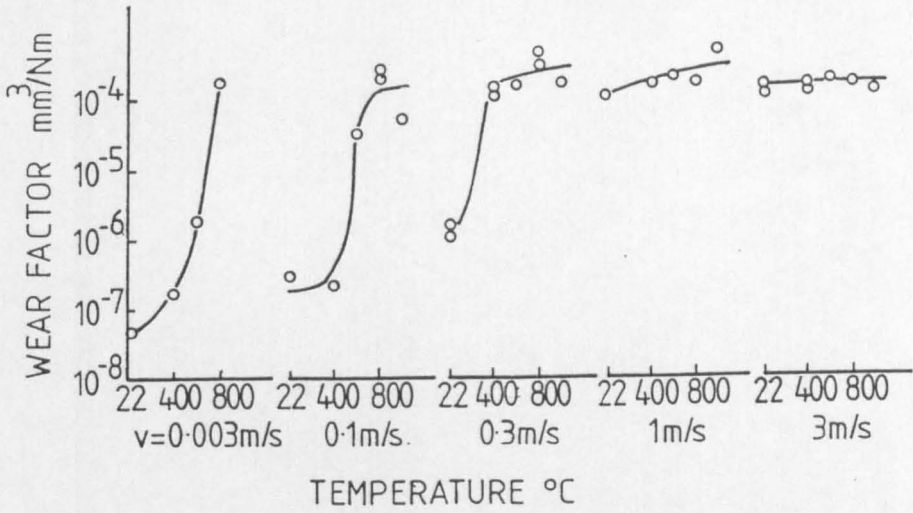
Fig. 2.19. Wear coefficient of self mated Mg–PSZ couples at different temperatures and sliding velocities [130].
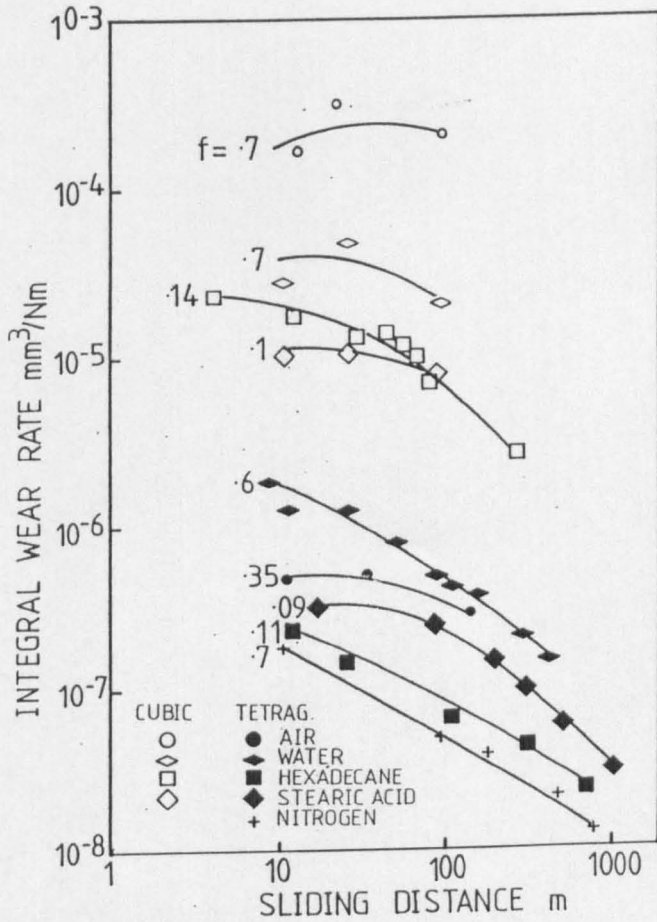

Fig. 2.20. Wear factor against sliding distance for tetragonal zirconia. The numbers represent the friction coefficients [147].

sliding speed is primarily considered to influence the frictional heat
generation, strain rate effects can also be important in some
materials, including zirconias. Moreover, the effect of temperature is
not straight forward since it tends to influence the material hardness
to a greater extent than strength [144,145], and provides complex
changes in chemo-mechanical effects.

Suprisingly, little work has been conducted to establish the role
of transformability on the wear rate of zirconia ceramics. Birkby et
al. [146] have demonstrated that a 2Y wears at a greater rate than a 3Y
as a result of transformation in the 2Y, giving intergranular fracture
and grain 'pop-out'. Fischer et al. [147] have shown that, at very low
sliding speeds, the wear rate decreases from a 6Y to a 3Y material, but
this was essentially a study on the effect of the amount of cubic in
the zirconia rather than the transformability.

It is becoming increasingly apparent that self mated couples of all
ceramics, in particular zirconia, do not operate well under conditions
likely to be found in service (eg see field trials on cylinder liners,
table 2.2). Zirconia mated with other ceramics fare little better than
against itself. The zirconia invariably wears more than the opposing
face, although a zirconia/silicon carbide couple has been shown to be
promising [134].

2.2.1.2 Zirconia/Metal wear

The majority of studies of zirconia against metals are from field
trials and generally give lower wear rates than with ceramic/ceramic
couples. In laboratory trials, Libsch et al. [122] examined various
TZPs, Mg-PSZs, and ZTAs against a hardened steel counterface under dry
conditions. All tests were dominated by transfer of metal to the
ceramic. The authors failed to evaluate the results sufficiently to
provide any clear understanding of the role of transformability.
However, it was evident that a higher toughness permitted a higher load
before the transition to microcracking and material degradation. A
strong sensitivity of wear rate with speed was found for both the Y-TZP
and the Mg-PSZ, but not for ZTA. Testing at temperatures above 300°C
showed a greatly reduced affect of the ceramic microstructure on wear
characteristics.

In metal/ceramic field trials Birkby et al. [146] and Marmach &
Swain [120] have found that TZP (former) and Mg-PSZ (latter)
out-perform all other materials tested in simulated tappets with a cast

iron and steel counterface respectively. Transfer of metal and metal oxide to the ceramic invariably occurred. The relative solubility of the ceramic in the metal oxide has been shown to be an important criterion in determining wear rate [148]. Fingerle et al. [116] showed that transfer of steel to the ceramic was avoided under lubricated conditions. PSZ performed marginally worse than some other ceramics such as SiC, possible because the wear mechanism had changed away from one of dissolution of the ceramic in the metal oxide. However, Mg-PSZ is now being extensively used for extrusion dies, particularily in the copper industry [113-115], as demonstrated in table 2.1.

2.2.1.3 The role of Transformation

Few studies have examined the amount of monoclinic before and after tests, and the morphology of the zirconia wear debris. Birkby et al. [149] found an increase from 0% (sinter + anneal) to 20.1% monoclinic for a worn 2Y-TZP cam follower. Grinding the surface produced 6.4% monoclinic. Harrison et al. [150] found low levels of monoclinic in tests of self mated TZP at a load of 4.8N/pin and a speed of 0.24m/s, for both 2Y and 3Y pins. Extensive line broadening in the XRD trace was attributed to a fine crystallite size and a highly strained structure. The authors concluded that the presence of monoclinic in the debris confirmed that transformation was occurring during wear. No mention of temperature was made although the presence of very fine crystallites in the debris indicates that very high interface temperatures occurred.

The above observations must, therefore, call into question the suggestion that transformation occurs at the surface, rather than in the debris. Ishigaki [142] examined the worn surface of a 3Y-TZP by Laser Raman Spectroscopy for materials worn at 5N and similar speeds to Harrison et al. [150] and found no monoclinic in the worn surface. Two explanations were suggested by Ishigaki [142]. Firstly, the temperature was too high for the $t \rightarrow m$ to take place. Secondly, he suggested that microcracking in the monoclinic would give break-up of the surface so that any monoclinic formed would be immediately removed. The second proposition was favoured on the basis that the heat generation should be low under these test conditions and that the wear debris contained large amounts of monoclinic. Moreover, the wear debris size decreased with an increase in humidity, suggesting that more microcracking was occurring (it is well established that ageing in

humid environments at temperatures of the order of 200°C can promote
spontaneous transformation and associated strength degradation, section
2.4.1.). However, the theory must be suspect since it is unlikely that
such a mechanism would remove all the monoclinic from the surface after
it had formed.

Only moderate temperature rises are required to greatly reduce the
driving force for transformation. Hwang et al. [128] examined the worn
surface by diffraction using syncratron radiation, for a self mated pin
on disc test in dry nitrogen for 12.7N and 0.3m/s. Initially, the
surface contained more monoclinic than tetragonal but the amount of
tetragonal increased during wear. Temperatures were therefore high
enough to give m → t. The question of the role of temperature at the
worn surface and the extent of transformation is, of course, an
extremely important area for future study.

Both Breval et al. [124,140] and Birkby et al. [149] have
demonstrated that grain pull-out can be a major wear mechanism. It is
considered that a grain 'pop-out' mechanism results from surface
transformation [149]. Breval et al. [124,140] examined wear debris in
the TEM, finding a bimodal distribution resulting from grain pull out
(micron sized) and from transgranular fracture and/or comminution of
the former (5-50nm). This result was confirmed by Birkby et al.
[151]. In both cases the bulk of the debris was tetragonal, with
electron transparent areas being almost entirely tetragonal. This
raises two questions. If particle pull out occurred by surface
transformation, why then were the larger particles tetragonal,
especially given that in the unconstrained state, spontaneous
transformation should have occurred? Secondly, why had transgranular
fracture not produced stress assisted transformation? The most likely
explanation for the latter is that reverse transformation occurred at
this particle size. However, in both these studies it should be
emphasised that conclusions were drawn from the electron transparent
wear debris which constituted a minor portion of the whole. The higher
monoclinic percentage measured in both studies by XRD compared to that
found in the TEM indicates the importance of information withheld in
the non electron transparent regions.

The work of Fischer et al. [147] suggests that intergranular wear
mechanisms are not wholly related to transformability. He examined a
3Y (fully tetragonal, grain size 0.3μm) and a 5Y (fully cubic) TZP
under various environmental conditions. The results are presented in

fig 2.20. In all cases the 3Y performed better than the 5Y. For both materials the lowest wear rates were in dry nitrogen, *which will have produced the highest interfacial stresses*, and were the highest in water. The non-polar hydrocarbon hexadecane, with and without stearic acid (a well known lubricant) decreased the friction coefficient (see fig 2.20) but *increased the wear rate*. A change in appearance of the wear surface occurred, being polished in dry nitrogen (under the highest stress conditions), but predominantly intergranular for both 3Y and 5Y in water and other liquids. (The wear factors measured in dry N_2 of 10^{-8} mm^3/Nm approach the lowest values recorded for any ceramic, which were for self mated alumina couples, see table 2.3.)

This work is similar to the results of Scott [121] who observed an increase in wear rate for an optimally aged Mg-PSZ in water and stearic acid. These results suggest a 'stress corrosion cracking' type mechanism rather than a dominant role of transformation. The similarity in behaviour of the cubic and tetragonal, in particular the intergranular fracture, suggests the mechanism was not stress corrosion assisted transformation. However, Birkby et al. [149] demonstrated a change in wear behaviour from intergranular in a highly transformable 2Y, to abrasive grooving in a small grain sized 3Y, clearly demonstrating the similar damaging effect transformation can produce.

Whilst the above behaviour suggests many similarities to low temperature degradation in TZP ceramics, the mechanism clearly has important differences since strong environmental effects are also observed in, for example, alumina.

It has become increasingly apparent that the abrasive wear resistance of Mg-PSZ is superior to many ceramics, certainly well in excess of that expected from its hardness, see for example table 2.1. In abrasive wear, the value of a threshold scratch depth at which lateral fracture occurs, associated with a ten fold increase in wear rate, is a well accepted property. Alexander & McPherson [126] have demonstrated that this threshold increases with toughness for Y-TZPs. Ishigaki et al. [142] have performed scratch tests on various ceramics and found a direct relationship between friction coefficient and fracture toughness, but no correlation with hardness. Above a limiting toughness the value of the friction coefficient was constant, with this toughness becoming smaller the larger the radius of curvature of the diamond pin. The TZP out-performed all other ceramics tested, despite inferior hardness to most.

Ishigaki et al. [142] plotted the friction coefficient as a function of the critical load for fracture, L_{cr}, defined by Warren [152]:

$$L_{cr} = f(E) \cdot R \cdot (K_{1C})^2 \qquad \qquad \ldots (2.9)$$

Where R is the radius of the indenter, and f(E) incorporates Poisson's ratio.

The difference in the critical load for SiC at approximately 0.1N (for a friction coefficient of 0.8) and TZP, which had a critical load of 1N (for a friction coefficient of 0.2) was substantial.

Few firm conclusions can be drawn from section 2.2.1. Laboratory tests have shown both disastrous and good results. Insufficient information is provided to attribute this variation to specific factors such as material processing, although the effect of sliding speed does appear to be of overriding importance. Despite poor laboratory results, zirconia ceramics have survived extremely severe applications, frequently better than other ceramics. Such results tend to be from either abrasive wear or high temperatures conditions. However, evidence is accumulating which suggests that highly transformable materials should be avoided for sliding wear applications, especially when self mated.

2.2.2 Chemo-mechanical Effects in Ceramics

Given the apparent chemical inertness of ceramics it is perhaps surprising to discover that environment can play a major role in their wear behaviour. Chemo-mechanical effects are used to describe the variations in near surface hardness, controlled by the absorption of chemical species at or near the surface (and is distinct from environmentally assisted slow crack growth). This phenomenon was first thought to result from a reduction in the surface free energy because of chemisorption, now known as the Rebinder effect. Evidence is now available which shows that the mechanism is far more complex and that surface energy alone cannot explain such observations [153]. However, the literature is limited and the subject is by no means fully understood.

The variation in near surface hardness is considered to reflect the surface plasticity of ionic and covalently bonded materials [145].

Westwood et al. [154] suggest that chemisorption of species from the environment result in electron transfer which influences ionisation of near surface point defects and dislocations, and, therefore, the interaction of such defects with the lattice is changed. Westwood et al. [154] and Swain et al. [155] have examined the effect of various chemical environments, such as alcohols and aqueous solutions on the hardness of the surfaces of single and polycrystalline alumina. The results were then related to the rate at which the material could be drilled, and to the wear rate. The activity of the environment was measured by the zeta potential and a direct relationship between zeta potential and hardness was found. Variations as high as 25-35% were found in the hardness by a change in the zeta potential. The drilling rate was shown to correlate with the hardness, with a ten fold increase in rate from the softer to hardest surface. The maximum hardness coincided with the point of zero charge (zpc). If this effect was associated with surface free energy the converse would be expected since the zpc coincides with maximum surface energy. Rather, it is suggested that dislocation flow is most difficult at the zpc and so fracture is the dominant mechanism which therefore maximises the drilling rate.

A slight shift in the zeta potential at which the maximum hardness occurred was found between the single and polycrystalline materials, and was explained in terms of the different impurities present. More recently it has been suggested that, at maximum hardness, the frictional forces, and therefore heat generation, would be a minimum, thereby minimizing tool wear and maximizing drilling rate [156]. This explanation is contrary to the findings of Buckley [157] who demonstrated that the minimum frictional force coincided with sliding along the preferred slip plane in the preferred slip direction.

When the abrasive wear rate was examined [154,155], the effect of zeta potential was shadowed by the effect of liquid viscosity, which determined the state of lubrication and therefore the wear rate. By maintaining a constant viscosity it was demonstrated that maximum hardness coincided with minimum wear rate, in contrast to the drilling rate. This result is consistent with models of abrasive wear [158] and the work of Steijn [159], discussed in a later section. Swain suggested that material removal was dominated by plastic flow and therefore the least amount of plastic flow would produce the lowest wear rate. No comment was made on the extent of abrasive blunting or

any discussion of what would happen if fracture was dominant, i.e., would the converse then be true? Whilst increased plasticity often leads to increased wear rates [159], it can also provide an increase in the critical load at which the transition to fracture dominated wear occurs.

More recently Czernuszka & Page [144,145] have investigated the effect of a series of n-alcohols on the near surface hardness and wear rate of glass bonded Al_2O_3 and TiO_2 ceramics. A very strong environmental dependence of hardness was found, although maxima were found at different zeta potentials to Westwood [154] (again explained by different material compositions). The similarity between wear rate and hardness was qualitatively good above N=3 (N= number of carbon atoms in the alkyl group), but poor below. The region of poor agreement was considered to be a result of heating effects with volatilisation preventing surface absorption. Alcohols with N>3 were insufficiently volatile to be prevented from absorbing.

As yet, there has been no investigation into the extent of chemo-mechanical effects on different crystallographic orientations, a factor which could play a role in the grain relief observed on worn surfaces.

Environment has been shown to be an important factor in the sliding wear of ceramics. The wear rate of many ceramics increases under vacuum. Shimura & Tsuya [131] reported an increase in wear rate for chromium and titanium carbides of two orders of magnitude in vacuum compared to air, and an order of magnitude increase for alumina and cemented carbides. The authors concluded that near surface plasticity was suppressed and fracture mechanisms were favoured. Scott [121] and Wallbridge & Dowson [132] have demonstrated an increase in wear rate in water for Mg-PSZ and alumina respectively but a reduction in the friction coefficient. The reduction in the friction coefficient was considered to be associated with absorbed surface species, in particular hydroxides, which act as a boundary lubricant thereby reducing adhesive forces. Buckley [157] has demonstrated an increase in friction as the absorbates are progressively driven off from the surface, by, for example, heating. However, the reasons for an increase in the wear factor for alumina when tested both in water and vacuum rather than air, are not clear. If the absence of absorbed species promotes fracture in vacuum tests, why does the wear rate not reduce in water, especially given the anticipated benefits of boundary

lubrication? This suggests that wear by a tribochemical based mechanism is also important, which becomes increasingly dominant over (or in addition to) plastic based mechanisms as the relative humidity is increased.

The wear of silicon based ceramics can follow the opposite trend to that found with oxides. Horton et al. [160] reported an order of magnitude reduction in wear rate for sintered silicon carbide when tested in water compared to air. Ishigaki et al. [138] and Fischer et al. [136] found similar results for hot pressed silicon nitride (HPSN). Gradual reductions in the wear factor were observed by increasing the relative humidity, demonstrating that the effect was not simply elastohydrodynamic, although the effects must be linked to boundary lubrication mechanisms. Ishigaki et al. [138] demonstrated that dry nitrogen can have similar effects to that of a vacuum, with HPSN exhibiting a dramatic increase in wear factor compared to tests conducted in air. However, the picture is not entirely clear as shown by Sugita et al. [161], who found an increase in wear rate for tests in water compared to air for silicon nitride, provided the wear debris removal characteristics were the same for both systems. Wear was shown to occur by an oxidational mechanism. A similar result was reported by Ajayi & Ludema [161] who found a three fold increase in wear for SiC worn by a spherical diamond indentor.

In all the tests reported above, the comparison between water and air is somewhat ambiguous since the relative humidity can, by itself, significantly alter the wear factor. Moreover, the response to water is different for fracture dominated wear compared to plasticity dominated sliding, and microstructure can have a strong influence on which mechanism dominates. Indeed Fischer et al. [136] found the reduction in wear rate in water compared to dry air was associated with a change from fracture dominated wear (air) to tribochemical wear (water). Clearly, this would be expected to decrease wear irrespective of the increase in surface chemical reaction. The silica layer found by these authors was far thicker than the irresolvable film reported for alumina.

The existence of a distinct tribochemical wear mechanism is not universally accepted, although evidence is certainly mounting. The presence of amorphous wear debris, as found by Wallbridge et al. [132] for example, suggests wear by the removal of a hydrated film. The production of fully amorphous debris from a wearing oxide couple is

usually associated with very low wear rates and predominantly elastic contact. Clearly, such a mechanism is difficult to prove. Similar examples of tribochemical wear mechanisms were found in the grinding of alumina by Hines et al. [163]. The wear debris from grinding tests was shown to be mainly of δ-alumina. δ-alumina can be made by heating α-alumina monohydrate in steam at 1000°C, which suggests that the hydrate might well have been formed during grinding followed by heating to transform the material to the δ form.

The general conclusion is, therefore, that even inert environments can influence the wear mechanism and that the wear rate from tribochemical reactions may be higher than those produced by plastic mechanisms. The oxidation of non-oxide ceramics probably determines the minimum wear rate achievable in the dry sliding of these materials. In the case of oxide ceramics, the minimum wear rate is probably associated with the removal of a hydrated film. However, it must be noted that there is evidence that the subcritical crack growth rate is accelerated by water for alumina ceramics but not for silicon nitride [136].

The interactions between metal and ceramic at a sliding interface also constitute a chemo-mechanical effect. With temperature rises at the interface during wear it is to be expected that, if a ceramic shows any reaction with a material in contact during heating, then similar reactions will occur during wear, probably at somewhat lower temperatures. Such a reaction will promote strong adhesive forces between the surfaces, in addition to those promoted by mechanical keying. With metals, such as copper and nickel, coupled with oxide ceramics, the bonding between the two surfaces can be quite strong [157]. For example, a copper rider slid on a sapphire plate gave spalling in the surface of the sapphire [157], rather than shearing at the metal ceramic interface. In this instance, the friction coefficient was comparatively low. Where extensive transfer of the metal to the ceramic occurred, but with no fracture in the ceramic surface, adhesion between the surfaces was considerable and the friction coefficient high. Thus, the friction force were determined by the deformation characteristics of the metal. Buckley [157] has shown that, under such circumstances, the frictional force can be related to the metal slip systems. The highest value of the friction coefficient was associated with cubic metals with high work hardening coefficients. Buckley [157] also showed that if gold and silver were

worn against sapphire in a vacuum then the friction coefficient was low because of the limited adhesion between the surfaces.   With alumina steel couples, the alumina has been shown to form a continuous solid solution with Fe_3O_4, so that a chemical wear mechanism would be expected to play an important role in the sliding wear of these two materials against each other.   Brown et al. [148] examined such a couple and found that the debris contained a range of compositions, but that $FeAl_2O_4$ was present, confirming that some chemical reaction had occurred.   The same spinel structure was found by Eiss & Fabiniak [164] for a sapphire-steel couple.

2.2.3 Hardness Testing

It is important to note that hardness not only varies with environment, because of chemomechanical effects, but is also found to be a function of the load used for the test, particularily with ceramics.   Czernuszka & Page [144] have demonstrated a considerable rise in hardness at low loads for glass bonded alumina and titania. For a pyramidal indentor:

$$L = k.d^n \qquad\qquad ...(2.10)$$

where L is the load, k is a constant, d is the indentation diagonal and n represents the indentation size effect (ISE) index.   Czernuszka & Page [144,165] have applied this equation, computed the ISE index from their results, and noted the different size effect of different compositions.   Because the hardness is proportional to d^{-2}, a value of $n = 2$ implies that hardness is independent of load.   For $n < 2$ the hardness will increase with decreasing load.   The load/hardness curve may therefore be characterised over a limited range by n and also by the hardness at a given diagonal size (eg $10\mu m$).   It is suggested that the ISE index provides a variable sensitive to microstructure and environment.   In addition, the ISE index can be used to extrapolate hardness values to a constant indent diameter, which should therefore provide a more useful value with which to compare materials.   Indeed, the variation in hardness and extrapolated hardness with temperature [166] was found to be quite different, resulting in changes in the ranking of materials.   Alternatively, the hardness can be extrapolated to the expected size of the asperity interactions during sliding, so

that a material ranking can be produced for these conditions. However, care is required since the hardness at very small indent sizes will be influenced by a number of factors. For example, chemo-mechanical effects become increasingly important. Moreover, microstructural heterogeneities, such as glass phases, will provide scatter, as will the crystallographic anisotropy of hardness.

In general, the measured hardness becomes constant above a material dependant load. This value may be misleading in interpreting wear rate data, given that asperity interactions occur on a finer scale, where the small indent hardness would appear to be more relevant. In addition, the hardness must be determined under the same environmental and temperature conditions as occur in the wear situation.

2.2.4 Surface Plasticity

King & Tabor [167] were the first to point out that during friction experiments the wear of nominally brittle materials may be dominated by plastic mechanisms because of the compressive component of the applied stress. Subsequent to this, it has often been proposed that near surface plasticity plays an important role in wear mechanisms under low load, low speed, mild wear conditions [168-170], even though in bulk studies plastic flow is only considered to be possible above $0.5T_m$ [3]. It is, therefore, appropriate to consider in detail whether plastic flow occurs in surface regions of ceramics during wear.

Evidence for a plastic deformation wear mechanism during sliding wear is indirect, but it is well established that dislocations and twins are generated during abrasion and grinding. Hockey [3,4] has examined the indentation and abrasion of both polycrystalline alumina and sapphire single crystals at various orientations. Back thinned TEM foils were generated, which confirmed the presence of high dislocation densities and twinning on both basal and rhombohedral systems. Chemically polished specimens, which were subsequently ground with $0.25\mu m$ diamond paste, showed arrays of dislocations, with each array corresponding to the contact of a single abrasive particle. The type of dislocations depended on the orientation of the crystal, but half loops on the basal planes were positively identified. Evidence of non-basal slip was also present. Exact identification of Burgers vectors was made impossible by the large residual compressive stresses in the foil, which led to tearing and buckling. It is interesting to

note that such a fine diamond paste can generate considerable residual stresses. With severe grinding (using a diamond impregnated wheel) and hardness indents, twinning was also produced. Again, the extent and type of twinning depended on the orientation of the crystal. For example, rhombohedral twinning was found on (1011) and (1012) single crystal indents, but not on basal plane indents. Basal plane twinning tended to be extended and was believed to be responsible for the raised 'slip bands' found adjacent to indents. Hockey [3,4] has also demonstrated that, where rhombohedral twins intersect a grain boundary, microcracking occurs.

Frei & Grathwohl [171] examined an abraded alumina surface in cross-section by TEM. High dislocation densities and microcracking was produced to a depth of $2\mu m$ by $20\mu m$ SiC powder. Changing the abrasive size to $3\mu m$ did not change the depth of deformation although there was no microcracking. Conversely, $100\mu m$ powder produced no difference in microstructure to the $20\mu m$ paste, except an increase in surface roughness.

The strong orientation dependence of deformation found by Hockey [3,4] is consistent with the findings of Steijn [159] who demonstrated hardness and wear anisotropy for different orientations of sapphire. Sliding on crystals with the prismatic plane parallel to the c-axis produced severe chipping and conchoidal fracture, whereas sliding in other directions in the prismatic planes, and in any direction in the basal plane, produced a smooth surface, and a reduction in wear rate of two orders of magnitude. Smooth sliding was shown to be associated with the activation of slip systems, with the wear rate governed by the ease of deformation. Similar results were found by Eiss & Fabiniak [164], Duwell [38], and Duwell & Butzke [173] for the wear of sapphire on steel. Brookes et al. [174] have demonstrated that the hardness anisotropy can be related to the crystal system and the slip system. Thus, materials belonging to the same class of crystal structure with common slip systems will exhibit the same trend in anisotropy (but not necessarily the same magnitude). The extent of fracture accompanying the indent was not found to greatly affect the anisotropy, except where basal twinning occurred in HCP materials. The effect of crystallographic orientation has been shown to decrease as the sliding speed is increased [175].

McPherson and co-authors [176,177] have demonstrated that, for a range of ceramics, the chips produced by abrasive wear at low loads had

a very fine crystallite size (frequently about 10nm) suggesting that dynamic recrystallisation had occurred. Very large temperature rises were used to explain the microstructure, but some materials failed to show phase changes which would be expected to occur with large thermal transients. The experiments used 1200 grit SiC at a load of 100g and a speed of 10mm/sec, which are surprisingly mild conditions to have generated large temperature rises. It is interesting to note that the appearance of the chip in ceramics when ground under low loads (ie no fracture) is remarkably similar to those produced by metal grinding.

No direct evidence is available to demonstrate that plastic flow occurs at the surface during sliding wear. Various explanations have been proposed to account for the polished 'plastic' appearance of the worn surface. Cranmer [178], when examining the wear of monolith silicon based ceramics, suggests that high flash temperatures occur at the point of contact, permitting dislocation generation. However, the loads and speeds used were high and so large thermal transients would be expected. Griffioen et al. [179] have recorded surface temperatures of over 2000°C using a scanning infra-red camera when investigating a silicon nitride/sapphire couple. Griffioen et al. [179] further suggest that the real contact area is very small and occurs at points of entrapped debris, thereby providing high flash temperatures. Theoretical analyses, such as those performed by Challen & Dowson [180] predict substantially smaller temperature rises, but all such computations give results which are very sensitive to the actual contact area. However, suggestions which assume that plasticity in ceramics during wear is only a high temperature phenomenon, are dubious. Hockey [4] has clearly demonstrated plastic flow under a hardness indent and using $0.25\mu m$ diamond paste where temperature rises are expected to be minimal.

Plasticity is also believed to play a role in crack propagation in ceramics, so that plasticity may also be important in fracture dominated wear. The measured fracture energy of alumina, 6–40 J/m^2, [181] is many times greater than the surface energy of about 1 J/m^2, which suggests that fracture is not entirely brittle but is associated with some plasticity. However, the difference can be partly explained by crack bridging and deflection mechanisms. In addition, the temperature dependence of the fracture energy is much larger than would be expected from the elastic constants or the surface energy. High dislocation densities and extensive twinning have been observed in

flakes removed from fracture surfaces [182] of alumina and X-ray
evidence of plastic deformation near fracture surfaces has also been
reported [154]. Page and co-workers [5-7] have demonstrated the
presence of high dislocation densities below the wear track of various
silicon carbides after the passage of a sharp diamond rider, despite
the dominant material removal mechanism being fracture. Interestingly,
the area of plastic deformation was confined to directly below the wear
scar and did not extend right across the track. This would explain why
attempts to show up slip by etch pitting have failed for this test
geometry. Alternative explanations for surface plasticity are based on
chemo-mechanical effects which are discussed below.

2.2.5 Grain Relief in Sliding Wear

The work of Steijn [159] has been used to explain the grain relief
observed on worn oxide ceramics [132], whereby each grain wears to a
different extent, determined by its crystallographic orientation.
Steijn [159] found 50-80 times higher wear on the basal plane compared
to the prismatic or pyramidal planes, which may be related to the
greater ease of slip on basal planes. This suggests a plastic failure
mechanism for wear debris formation. This observation is consistent
with those of chemo-mechanical effects where increased plasticity (i.e.
reduced hardness) from surface absorbents leads to an increase in the
wear rate. Wallbridge et al. [132] suggest that certain orientations
allow plastic flow, and therefore a low wear rate, whereas others are
not correctly orientated and undergo microfracture. However, the
situation is likely to be far more complicated since chemo-mechanical
effect will alter the near surface plasticity. Moreover, it is not
clear whether conclusions about the benefits of plasticity compared to
fracture, drawn from single crystal studies, are applicable to the
polycrystalline case. For example, twin and dislocation interactions
with grain boundaries tend to produce microfracture in polycrystalline
specimens, but this does not arise in sapphire. Eiss & Fabiniak [164]
found an increase in the extent of brittle fracture in the wear of
sapphire as the number of imperfections such as low angle grain
boundaries was increased. This was attributed to dislocation pile-ups
at these boundaries, which then nucleate fracture. Interestingly, the
wear debris from plastically dominated wear in Steijn's tests was
amorphous.

Grains frequently appear smooth on surfaces which develop grain relief during wear, suggesting that no microfracture has occurred. Indeed, the suggestion that transgranular microfracture can occur on this scale must be questionable. Kendall [183] has shown theoretically and experimentally that fracture is not possible below a certain crack size for compression loading. This effect can be seen experimentally with hardness indents which fail to give fracture below a material dependant indent size. The most probable mechanism for microfracture is that of intersection of slip or twinning with a grain boundary, producing intergranular microcracks. No similar mechanism is likely to produce transgranular microfracture on this scale, although Buckley [157] has demonstrated subsurface cracking by the intersection of two slip systems in single crystal lithium fluoride. However, in the same work, increased plasticity from surface absorbents suppressed this subsurface fracture. Microcleavage has been seen in the wear of SiC, but this occurs across an entire grain and is easy to identify. It is clear that the steady state fracture toughness is not relevant in determining the scale on which microcracks will propagate under high shear forces augmented by tensile forces which are promoted by adhesion.

The hardness anisotropy as a function of crystallographic orientation could be expected to produce grain relief without the need for a microfracture mechanism. However, the mechanism for grain relief could also be partly explained by thermal expansivity and elastic modulus anisotropy, but no data is available to substantiate this and the disappearance of scratch marks at grain boundaries, observed by Wallbridge et al. [132], demonstrates that these factors cannot be entirely responsible. However, such effects will inevitably act alongside hardness anisotropy. In conclusion, therefore, it is considered likely that grain relief arises without microfracture in the plastic dominated regime. The wear anisotropy results from hardness, elastic and thermal expansivity anisotropy. However, the exact mode of debris production in this mild wear regime remains unexplained.

2.2.6 The Effect of Grain Size on Wear

The effect of grain size on wear is an important area of study. The grain size dependence of fracture strength and hardness for many ceramics is well established [183]. The grain size and shape

anisotropy are important in determining the residual stresses in the sintered state. The larger the grain size, the greater the thermal mismatch stresses which promote grain boundary microcracks in many non cubic materials. Cubic systems also show anisotropy although to a lesser extent. Residual stresses add to those stresses imposed by the passage of an asperity and thereby increase the wear rate. Elastic anisotropy also alters the stress response to the passage of an asperity [185]. It is clear, therefore, that for these reasons and those of hardness anisotropy, the mechanical properties based on the bulk material may be inaccurate when applied to asperity contact. Thus, the size of the contact point compared to the size of microstructural features, such as grain size, is an important criterion.

Lawn [186] has demonstrated the importance of the microstructure in determining residual stresses and its effect on wear. Work on alumina ceramics with highly anisotropic microstructures, which exhibit R-curve behaviour, provided a model for predicting residual stresses. This was applied to three microstructures of varying grain size. The model successfully predicted an upturn in the wear rate which was associated with the incubation period for fatigue type fracture. Lawn [186] proposed that the coarsest grain sized material contained the highest residual stresses, which when added to the deformation imposed by wear, gave the shortest time to the wear transition. However, this behaviour is well recognised when selecting ceramics for wear applications. For example, the alumina specified for hip prostheses is high purity, fine grained material in order to minimize residual stresses and therefore its wear rate.

2.2.7 Wear Models for Ceramics

There are few analytical models which predict the wear rate. Those that are available use indentation fracture mechanics to describe fracture processes occurring during friction. The most widely referenced is that of Evans & Marshall [158] which assumes that wear, above a threshold stress, occurs predominantly by lateral fracture. By deriving the lateral crack length from a hardness indent, the material removal rate, V, can be determined from:

$$V = \alpha \; \frac{P_n^{9/8}}{K_c^{1/2} \; H^{5/8}} \; (E/H)^{4/5} \; d \qquad \ldots(2.11)$$

Where P_n is the normal load, α is a material-independant constant and d is the distance of motion. The material removal rate by grinding was determined for a range of ceramics at constant force and provided reasonably good correlation to the equation above. Clearly, the equation predicts improved wear resistance from increased hardness and toughness. Moore & King [186] derived a slightly different model for abrasive wear of brittle materials;

$$V \approx 2 \; \sigma^{5/4} \; d^{1/2} \; K_c^{-3/4} H^{-1/2} \qquad \ldots(2.12)$$

Where σ is the applied load per unit area and d is the abrasive grit diameter. They found considerable scatter in the results, with no apparent dependency of the wear rate on equation 2.12. Evans & Marshall [158] criticize these authors for using wrong values of the fracture toughness, but after taking this into account it is still apparent that the model does not provide a clear fit. A number of reasons can be proposed for the poor correlation. Firstly, the model assumes that plasticity contributes a minor amount to the wear rate compared to lateral fracture. Secondly, the exact role of plasticity remains unclear. Under certain conditions deformation can relieve applied stresses and reduce wear rate. Increased plasticity under such circumstances is therefore expected to be beneficial. However, several authors [4,157] have pointed out that cracks can be initiated by the intersection of slip/twinning systems. In their analysis, Evans & Marshall [158] demonstrated that thermal stress assisted cracking should be minimal in most materials except those with a large thermal expansion anisotropy and a low specific heat capacity. However, many authors have shown that temperature generation can be substantial during abrasive wear. The over-riding reasons for poor correlation are probably a result of the many additional fracture mechanisms which can occur.

The problem with applying indentation fracture mechanics theory to wear is that indent behaviour is essentially macro, whereas fracture

during wear often occurs on the scale of the grain size. Ajayi and Ludema [162] have identified up to eight different mechanisms which can occur in wear, including plastic deformation, grain boundary cracking, fatigue cracking, plastic chip cutting edge microfracture and general intergranular fracture. For example, a hot pressed SiC was shown to give high wear rates through gross intergranular fracture, whereas a hot pressed silicon nitride worn under the same conditions exhibited edge microfracture and a fatigue like mechanism. The important point was that the mechanism varied considerably between different materials, even where macro behaviour was similar, and so a unified analytical equation based on macro behaviour would be unlikely to succeed. Whilst this appears somewhat discouraging, Ajayi & Ludema [162] did demonstrate that the majority of the mechanisms occurring during sliding wear could be related to the micromechanisms found in an indent when examined in the SEM.

One final reason for the failure of analytical models is that they do not account for the effect of the environment on both fracture and plasticity. Even small amounts of water can accelerate fracture processes and, therefore, wear rate [162].

The threshold between the fracture-dominated wear regime and plastic-dominated behaviour is better established. It is broadly accepted that ceramics undergo a transition from mild wear at low loads to severe wear at high loads and that this transition is associated with a change from plastic dominated mechanisms to brittle fracture [168]. Wallbridge & Dowson [132] have demonstrated this transition in alumina ceramics. At loads of up to 15N/pin, the wear rate was of the order of 5×10^{-10} mm^3/Nm, with the surface exhibiting a polished appearance. The very small amounts of wear debris were shown to be amorphous. At a load of 40N/pin the wear rate had increased by four orders of magnitude. The test was characterised by chattering and the wear surface was badly damaged, with widespread fracture. Derby et al. [135] found similar results for sintered silicon carbide, although the transition was less pronounced.

The load at which this transition occurs, P^*, is given by Evans & Marshall [158] as:

$$P^* = a \frac{K_c^{\,4}}{H^3} \, f(E/H) \qquad\qquad ...(2.13)$$

where a is a dimensionless constant, depending on the shape of the abrasive. For lateral cracks f(E/H) is approximately $2x10^5$. Clearly, therefore, a high toughness is advantageous. Ramsey and Page [166] have used a method of predicting P^* from microhardness indents for radial cracks whereby load is plotted against the radial crack length. P^* is obtained by extrapolating the graph to the point where the radial crack length is equal to the indent diagonal. However, as should be apparent from the previous discussion, P^* will be sensitive to the material characteristics such as hardness anisotropy, microstructural heterogeneities, the testing environment and temperature.

2.2.7 Statistical Nature of Wear

The literature on the statistical variation in wear rates is sparse. Wallbridge & Dowson [188] have noted that the available information suggests that wear results always follow a lognormal distribution, irrespective of the material tested. In their own tests, they demonstrated lognormal distributions, with order of magnitude scatter, for the wear of ultra-high molecular weight polyethylene (UHMWPE), and tool grade alumina over many thousand Km of sliding. Two points were evident. Firstly, the use of the arithmetic mean to describe a set of data which is clearly skewed is obviously questionable. Secondly, the analysis of wear trends as a function of load, for example using single datum for each load, can be highly misleading, especially at the very short sliding distances.

Gee & Almond [189] have also considered the variability of results for a pin-on-ring and pin-on-disc geometries. They applied Weibull statistics to the wear results, which gave a Weibull Modulus of 0.25 for the wear rate and 3.06 for the friction coefficient. These values are extremely low even when compared to those found for the strength of ceramics, for example. However, the test duration was short and so high variability is, perhaps, not surprising since it will be dominated by the bedding-in behaviour.

2.3 HIGH STRAIN DEFORMATION OF METALS

It is only recently that attention has switched from the deformation of single crystals and polycrystals at low strains to high

strain deformation. The latter is, of course, far more relevant to metal working processes, where true strains of 3 can be found in rolling and up to 9 in wire drawing. The most dominant variable governing the deformation of single phase metals is the stacking fault energy (SFE). This variable is strongly influenced by composition and temperature, but is only clearly defined for FCC metals [190]. The following discussion will catagorise materials by their SFE, rather than by composition. It will also be confined to low and medium temperature deformation (T<0.3 T_m), and will not consider recrystallisation or recovery mechanisms.

2.3.1 True Stress/True Strain Relationships

Evaluation of the flow stress at high strain is somewhat difficult since very large strains cannot be achieved by any of the standard test techniques. Methods therefore rely on carrying out the deformation process, and then performing a conventional test, such as tensile or plane strain compression, to measure the flow stress. A note of caution is required in that the test method should simulate the original deformation mode, otherwise the results can be misleading. For example, rolling experiments should be followed by plane strain compression tests rather than a tensile test. Hardness is often used on the basis that [190]

$$\sigma = H/3 \qquad \qquad ...(2.14)$$

but this does not exactly simulate the stress state during working, for example the hardness estimate of the flow stress of OFHC copper suggests that a saturation flow stress (ie zero work hardening) is attained at a strain of about 1.3. The true stress, however, shows linear hardening up to the highest strain measured of 3.

FCC metals often show a flow stress curve similar to that in fig 2.21, where a saturation stress is found at high strains [192]. Whether a saturation flow stress exists for all FCC metals and single phase alloys remains unclear. Saunders & Nutting [192] have demonstrated this behaviour for Cu and Ag, suggesting that it is not a phenomena restricted by SFE. Evidence is also available for a saturation flow stress in Al and Al-Mg alloys and 70/30 brass [193,194]. Some authors, such as Nutting & Pollard [193], suggest
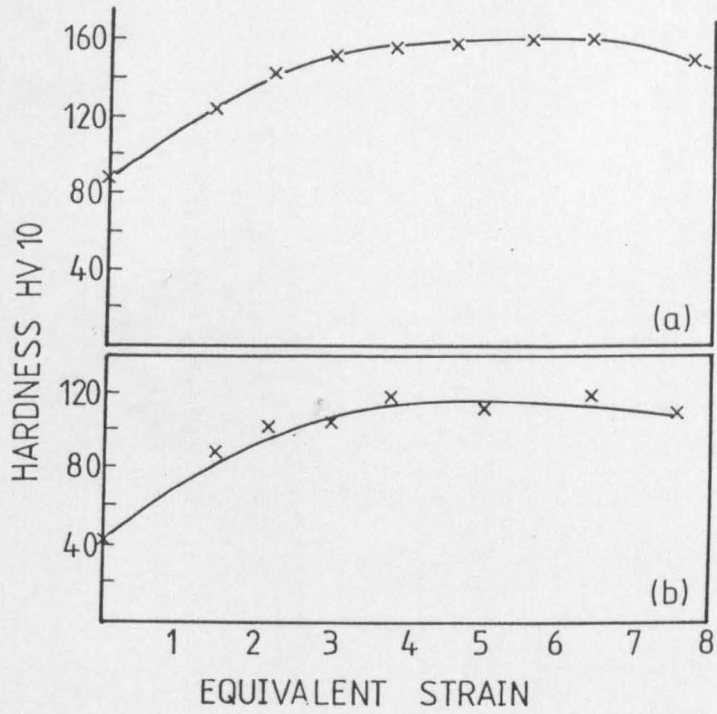
Fig. 2.21. Change of hardness with strain, (a) Cu, (b) Ag, from a totally redundant work machine [192].
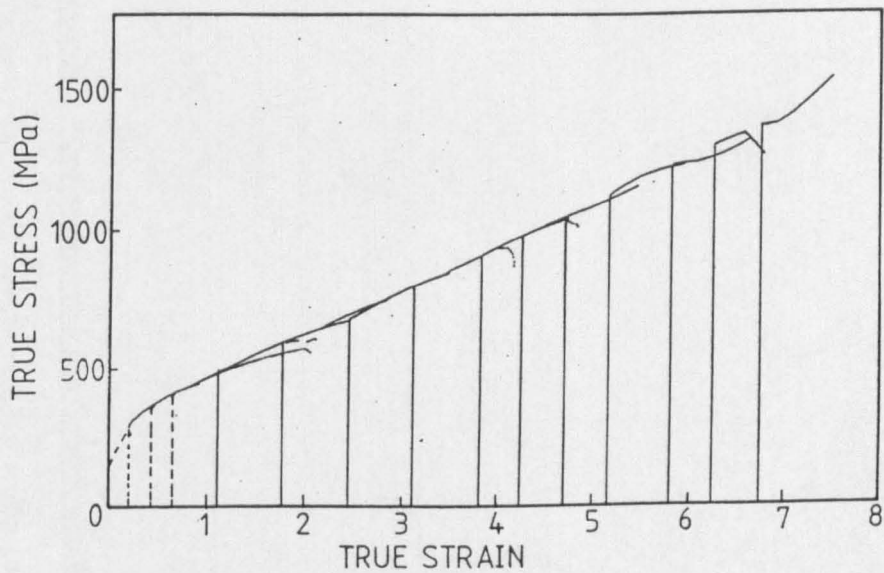

Fig. 2.22. Effect of wire-drawing strain on the tensile stress-strain curves (corrected for necking) of furnace cooled iron, drawn and tested at room temperature [195].

that where saturation is not achieved, higher strains would show a saturation, if these could be generated.

The deformation mode employed can strongly affect the hardening behaviour and influence whether a saturation flow stress is achieved or not. Most deformation modes, with the exception of torsion, tend to give similar flow stress curves. Torsion consistently provides a lower flow stress and will reduce the strain at which saturation starts [194]. Hecker & Stout [194] explain this observation in terms of the texture which is generated. Changing deformation from torsion to compression can re-introduce work hardening after saturation has been achieved.

The purity of the metal or alloy also has a strong influence on whether a saturation flow stress is observed. A reduction in SFE by alloy addition increases the work hardening and delays the saturation stress to higher strains. High purity metals generally show a saturation flow stress [194]. Conversely, commercial purity metals usually show continued hardening up to the maximum strain used. For example, commercial Al continues to harden up to a strain of 6 [194]. Additional differences may arise because of variable temperature generation during mechanical working and differences in the method of measurement of the flow stress, noted above.

With BCC metals a saturation stress is rarely achieved [195], rather linear hardening prevails even up to very high strains, fig 2.22. The nature of the curve is relatively unaffected by solute additions. Surprisingly, there is little literature indicating the effect of deformation mode on flow stress. However, torsion has a pronounced effect, reducing the flow stress and introducing a saturation flow stress, fig 2.23, which is not observed for pure iron using any other deformation mechanism [196]. Langford & Cohen [194] claim that linear hardening is specific to wire drawing where the <110> fibre texture is found in iron. However, the same texture in FCC metals produces a saturations stress. Nonetheless, linear hardening appears to be the norm and the flow stress varies very little between different deformation processes.

Nuttall & Nutting [197] have observed a change of slope in the flow stress-true strain graph, or a plateau followed by an increase, fig 2.24. The reasons for these effects were complex and related to the microstructure. The microstructural reasons for this behaviour and the saturation flow stress will be discussed in the following sections.
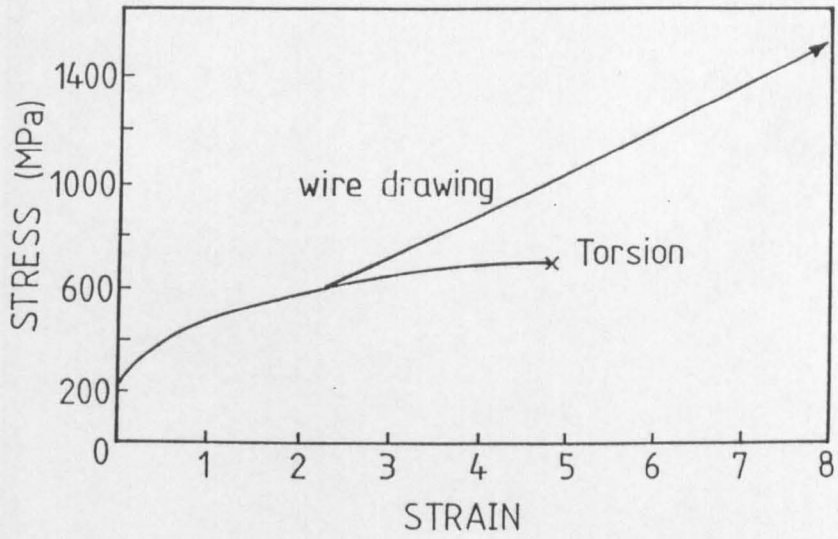
Fig 2.23. 'Equivalent' stress-strain curves for polycrystalline BCC
iron (gettered with 0.17% Ti) in torsion and wire drawing [191].
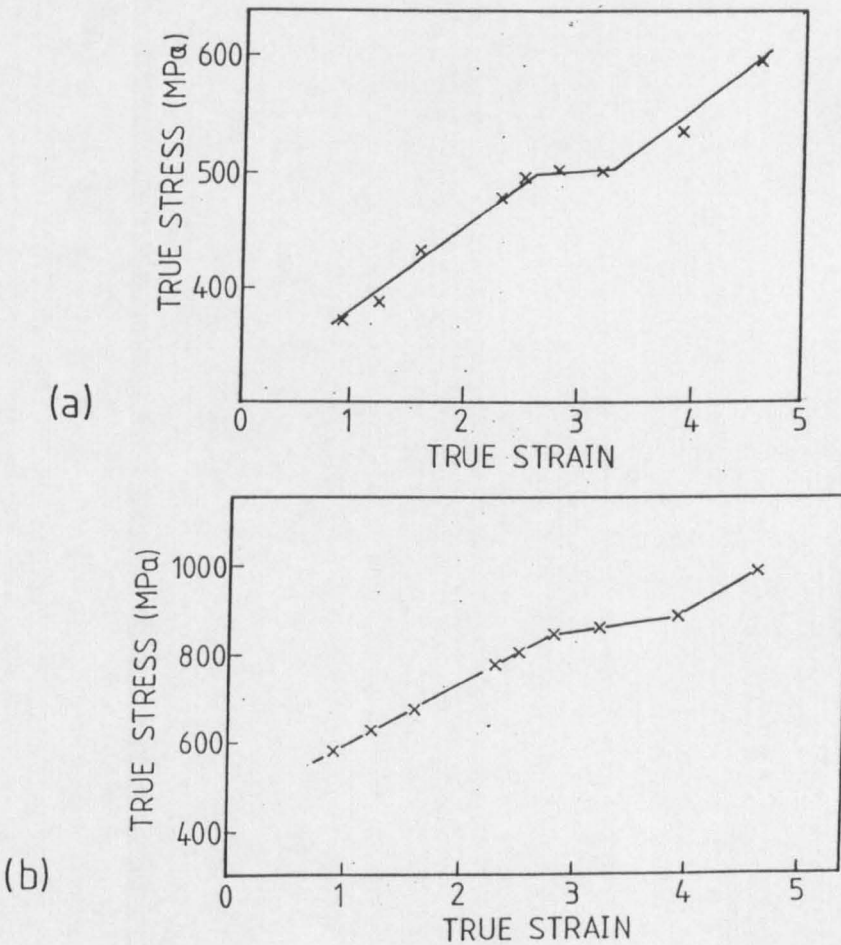

(a)

(b)

Fig. 2.24. True stress, true strain plots for, (a) Cu-10%Ni, (b) Ni
[197].

The effect of grain size on flow stress is well established, with a strong effect being recorded for both both low SFE FCC alloys and BCC metals. With high SFE FCC metals, the Petch slope is low at high strains.

2.3.2 Equations Predicting Stress Strain Relationships

On the basis that many metals show a saturation flow stress, Nutting & Pollard [190] have presented an expression which describes the stress strain relationship for high strains:

$$\sigma = K \; m^n \; [\tanh(\epsilon/m)]^n \qquad \qquad ...(2.15)$$

Where K is a strength parameter corresponding to the flow stress at unit strain, n is the work hardening index and m is an additional parameter which is a measure of the work hardening capacity (and therefore SFE and solute concentration etc). Values of m lie in the range 1.5–5 depending on the material properties. This relationship reduces to approximately the Hollomon modification of the Ludwick equation at low strains:

$$\sigma = K \; \epsilon^n \qquad \qquad ...(2.16)$$

Where n is often 0.5 giving parabolic hardening.

Attempts have been made to describe a universal temperature scale for plastic flow. It is now recognised that metals deformed at the same homologous temperature do not behave in the same manner, but that it is the SFE which governs the behaviour. Mecking et al. [198] have further suggested that the important factor is the SFE (γ) normalised by the shear modulus, G, and the Burgers vector, b. Using this variable, these authors were able to demonstrate that the influence of SFE could be accounted for by scaling the stress and temperature axes by a material dependant factor (which accounts for the SFE) for the deformation of single crystals along <111>. This allowed the saturation flow stress/ normalised temperature curves to be brought into coincidence for Al, Cu, Ni and Ag. For example, Ag deformed near the melting temperature provides similar behaviour to Al at $2/3T_m$. However, polycrystalline behaviour may well be different because of additional mechanisms such as grain boundary sliding.

2.3.3 Microstructural Aspects

The nature of screw and edge dislocations and related literature is extensively covered elsewhere [199], and so will not be discussed here. The following sections will concentrate on the microstructure formed at higher strains, and will highlight the heterogeneous nature of the mechanisms involved.

2.3.3.1 Medium and High Stacking Fault Energy Metals

Pure metals such as Cu, Ni, Al fall in the class of medium and high SFE materials. Al alloys also belong in this category, whereas Cu alloys generally come under the low SFE class. Pure iron and low carbon steels generally deform in a manner similar to high SFE metals. Whilst the differentiation between low and medium SFE is not clear cut, values of SFE above about 75mJm^{-2} would certainly be in this category.

Initial deformation produces profuse dislocation multiplication, increasing their density by several orders of magnitude [191]. TEM analysis of materials at this stage reveals the characteristic dislocation interactions which lead to the formation of a cell structure. With Cu, for example, a strain of 10% is required to form a homogenous cell structure. This strain is increased by a reduction in SFE resulting from a solute addition such as zinc.

The cell structure, typically 0.5–1.0μm wide, consists of walls of high dislocation density which appear diffuse in the TEM. The dislocation density of the interior is low in comparison, although dislocation arrays may be observed which divide the cell up into domains [200]. X-ray line broadening studies measure this domain size rather than the true cell size. In-situ high voltage electron microscope (HVEM) experiments have shown that the cell walls act as barriers to moving dislocations although bands of dislocations moving co-operatively may penetrate several walls [201].

The conventional view, as suggested by Sevillano et al. [191], is that the cell size decreases in the strain range 0.4–1.5 at a rate faster than the specimen thickness reduction, which they attributed to cell multiplication. At a strain of about 1.5 a transition occurs and cell annihilation becomes the dominant mechanism. This leads to a reduction in the rate of cell size decrease, and at higher strains a constant cell size is attained, for example, about 0.2μm after a strain of 4 for copper. In contrast, iron shows a continuously decreasing cell size [195,202] up to the highest strain measured. These trends
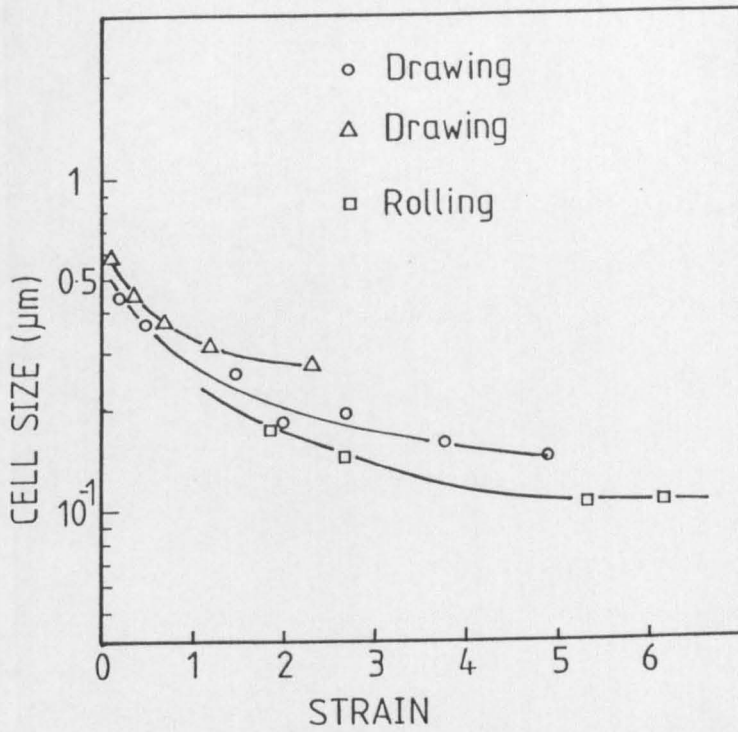
Fig. 2.25. Average cell size as a function of equivalent strain for copper [191].
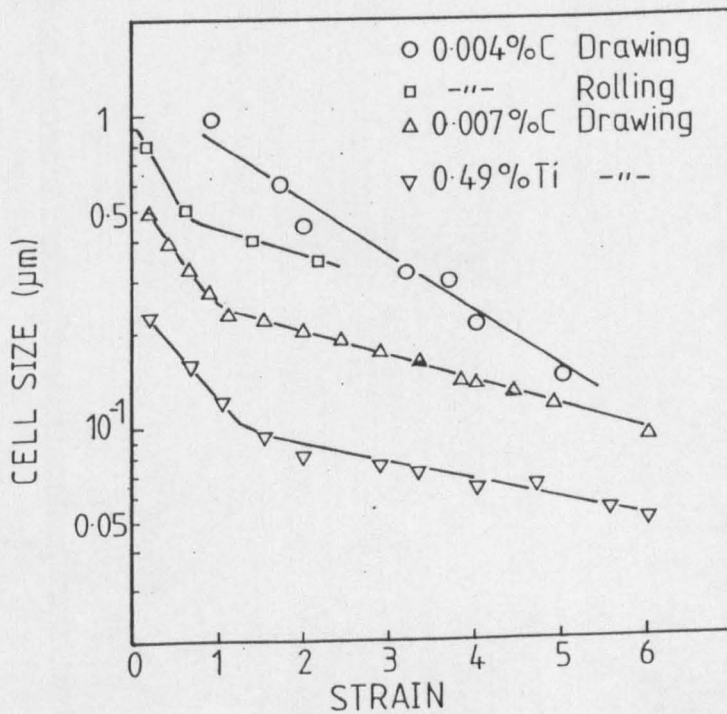

Fig. 2.26. Average cell size as a function of equivalent strain for pure iron [191].

are shown in figs 2.25 and 2.26 [191] respectively.

The above scenario appears to be a good description of high SFE metals such as Ni and Al [194] but is inappropriate for medium SFE metals, as highlighted by Hatherly & Malin [200,203]. They examined the deformation of copper and found that early in the deformation process plate like features were formed, hereafter called microbands. These microbands consisted of parallel sided walls, with a low internal dislocation density, and were invariably about $0.2\mu m$ thick (cf cells of around $1\mu m$). Initially, microbands are always formed on <111> planes at 35° to the rolling plane. Deformation proceeded by the production of new microbands, which tended to cluster with existing bands, then gradually rotated towards the rolling direction. Microband clusters distorted, but did not cross grain boundaries, indicating a significant shear component associated with their formation. Existing cell regions did not change their size or appearance even up to much higher strains (0.5) where the majority of the structure consisted of microbands. Thus, deformation occurred solely by the formation of new microbands rather than slip associated with existing microbands or cells. It is clear, therefore, that the apparent cell size/strain graph (fig 2.25,26) is a result of microband formation, not a reduction in cell size (note the microband thickness is approximately the same as the apparent saturation cell size). Therefore, such graphs and other attempts to relate cell size to flow stress should be treated with caution.

Regions of different orientation can exist within grains during the early stages of deformation [200]. These regions are known as deformation bands and are separated by narrow regions $(2-3\mu m)$ which accommodate the orientation change, known as transition bands. Early descriptions of transition bands considered them to be made up of elongated subgrains although these are clearly microbands. The existence of such bands demonstrates that deformation is heterogeneous despite the apparently homogeneous nature of cell/subgrain deformation. However, Dillamore [204] pointed out that deformation bands may arise not just because of different stress states within different parts of the material, but also because of the operation of different slip systems, which provide locally different strains and rotations. Additionally, the macroscopically imposed shape change may be achieved for a lower energy expenditure if the total strain is subdivided such that different regions undergo different strains and

therefore rotate relative to each other.

If the sample is repolished after a straining to a point where microband formation is dominant, and the cell structure is playing no further role, only slip lines are observed on further deformation. Slip lines are therefore generated by microbands. In the absence of finely spaced slip steps derived from primary slip, it is interesting to consider how deformation is occurring within a microband. Is it by a homogeneous mechanism across the 0.2μm wide band in a manner similar to twinning? Alternatively, slip might be occurring on planes much more closely spaced than previously considered possible, certainly than in primary slip. This latter explanation appears more logical [203].

In relation to this point, Malin & Hatherly [203] highlighted an interesting discrepancy between TEM observations and surface observations which calls into question the nature of cells. During initial deformation diffuse slip steps are formed, about 30nm apart and 1-5nm high. In contrast, the cells have dimensions in the range $0.5-1\mu$m. Therefore, upward of 15 slip planes must have operated within each cell. Thus, either the slip steps are purely a surface phenomena and the cell structure is a fair representation of the dynamic deformation process in the bulk, or the cell structure is a relaxation structure. The latter is more probable because:
- steps are formed well before cells.
- cells persist unchanged to high strains.
- other features such as microbands are easily related to surface features.
- the cell structure cannot be related to the known slip system.

If the cells are a recovered structure, it is not clear whether they are produced during TEM foil preparation or whether they are formed immediately after deformation. Since all other microstructural features appear unaffected by foil preparation, and the cell structure remains unchanged in thicker regions of the foil, the latter theory is strongly favoured.

The nomenclature used to describe deformation microstructures, such as microbands, tends to be variable. Saunders & Nutting for example [192] recently examined the deformation of Cu and Ag to extremely high strains (9) using a totally redundant work machine. In their work they adhere to the cell/subgrain description, although there was no apparent differences in structure to those observed by Hatherly & Malin

[200,203]. Donadille et al. [190] on the other hand use microbands to describe the crystallites formed in a low SFE material which deforms by the production of shear bands. More recently Aghan & Nutting [205] and Osterle et al. [206] have shown that the deformation of a low carbon steel and pure iron follow the same microstructural scheme as found by Hatherly & Malin [119,203] for copper.

At reductions of around 80% the structure of high SFE metals such as Cu and Fe is dominated by microbands which have become aligned with the rolling direction, and have sharpened boundaries as a result of recovery processes. At this stage slip is restricted. Additional plate like crystallites start to form, cutting across the microbands. These are shear bands which show no crystallographic nature. It is now established that the morphology of shear bands are determined by the macroscopic deformation rather than crystallographic slip considerations [204].

In high SFE materials, shear bands only influence the deformation at very high strains (>3) and have a different character to those in low SFE materials where their presence is far more important (see later).

Nuttall & Nutting [197] have examined a range of pure metals and alloys of varied SFE and melting point using rolling experiments. In these studies, strain-free grains, being equiaxed, of diameter 0.25-1μm with a relatively high misorientation of 5-20° were observed. In all cases the grains showed the characteristic deformation texture having <110> planes parallel to the rolling plane. The formation of the grains always occurred in regions of high dislocation density suggesting that their distribution was determined by the prior structure. Measurement of the flow stress indicated that such dislocation free grains were associated with a reduction in work hardening (eg fig 2.24). The exact mode of formation remains unclear, and was not helped by the need to use rolling plane foils rather than transverse sections.

In studies of the deformation of copper to very high strains Saunders & Nutting [192] observed a different type of dislocation free grain, about 0.5μm in diameter whose <100> planes were parallel to the rolling plane. Their formation was associated with a saturation flow stress (fig 2.21). In one of the earliest studies to report this phenomena Nutting [207] noted that the formation of such grains was associated with a change to the recrystallisation texture and ascribed

their presence to a dynamic recrystallisation process which was responsible for offsetting work hardening mechanisms, thus providing the saturation flow stress. Since grains show many characteristics of static recrystallisation it has been asserted by other authors that they may result from frictional heating, especially since some early studies, for example Cairns et al. [208], used commercially deformed materials. Malin & Hatherly [209] failed to observe such grains in cold rolled copper at strains equivalent to those achieved by Nutting [207], for example, where temperature rises were avoided. However, by increasing the rolling temperature to 100°C dynamic recrystallisation did occur. Conversely, Saunders & Nutting [192] removed a specimen from the redundant work machine after a strain of 6.4 and cold rolled the material ensuring no temperature rises. This failed to provide any change in the formation of dynamically recrystallised grains. However, there is some evidence that the temperature for this dynamic recrystallisation is sensitively dependant on metal purity.

Despite these differences it is probable that the formation of equiaxed dislocation free grains is responsible for the saturation of flow stress observed in many FCC metals.

The appearance of dislocation free grains does not necessarily lead to a saturation stress. Nuttall [198] demonstrated that the change in slope for Ni, fig 2.24(a), and the plateau in fig 2.24(b) for Cu-10%Ni, were associated with the first detection of dislocation free grains. As these grains started to deform, work hardening was restored for the latter case. Nuttall postulated that another plateau would exist for Cu-10%Ni at higher strains than he achieved, when the dislocation density would again be high enough to initiate dynamic recrystallisation.

If the SFE or the temperature are reduced, or the strain rate increased, then the following result [191,196]:-

    -cell formation is delayed to higher strains

    -dislocation distribution becomes more even, progressively replacing cell formation

    -twinning is more readily actuated, especially at low temperature. More screw dislocation segments are observed reflecting the increased difficulty of cross slip

    -shear bands are more easily formed.

This produces a range of microstructures, from very high SFE materials, such as high purity Al, where the cell structure persists to

very high strains and shear bands are never formed, to the lower SFE materials, such as Cu alloys, where the cell structure is poorly formed and shear bands become important at high strains.

The influence of grain size on flow stress is well established, with a strong effect being recorded for both both low SFE FCC alloys and BCC metals. With high SFE FCC metals the Petch slope is low at high strains. However, the grain size effect on deformation is indirect rather than intrinsic. At a grain boundary region the slip mechanisms are different to those within the bulk. At high strains, smaller cells and higher misorientation have been observed at grain edges than within a grain [203]. Clearly, therefore, if the starting material has a very fine grain size (<10μm) grain boundary mechanisms dominate. This may in fact suppress the formation of a cell structure. Sevillano [203] has shown that, for a fine grain steel (<10μm), a reduction in cell size was produced by a reduction in the initial grain size (fig 2.27).

Crystallographic effects on deformation are well known for studies of single crystals. The picture is far less clear for polycrystals subject to high strains [191]. Studies have failed to show any strong effects. The only useful data is derived from the study of materials which exhibit duplex <100> <111> fibre textures. Subgrain size distribution has been shown to be wider for crystals with the orientation (111)<110> and (110)<110> than (001)<110>. It appears that the rate of cell multiplication and subgrain annihilation may, therefore, depend on orientation.

2.3.3.2 Low Stacking Fault Energy Metals

The structures in low SFE metals are much more complex than in medium and high SFE metals and as a result there has been little quantitative evaluation. Materials which have been partly examined include Ag [191], brass [eg210] and austenitic stainless steel [190,211].

At low strains dislocations pile up in planar arrays, clearly restricted to the slip system, or adopt a more general distribution in slightly higher SFE materials. Many dislocations become dissociated. Slip no longer occurs on the usual (111)<110> system above a fairly moderate strain, giving way to twinning in the form of bands or bundles. The twins are initially within 30° of the rolling direction but become progressively aligned until they become roughly parallel at
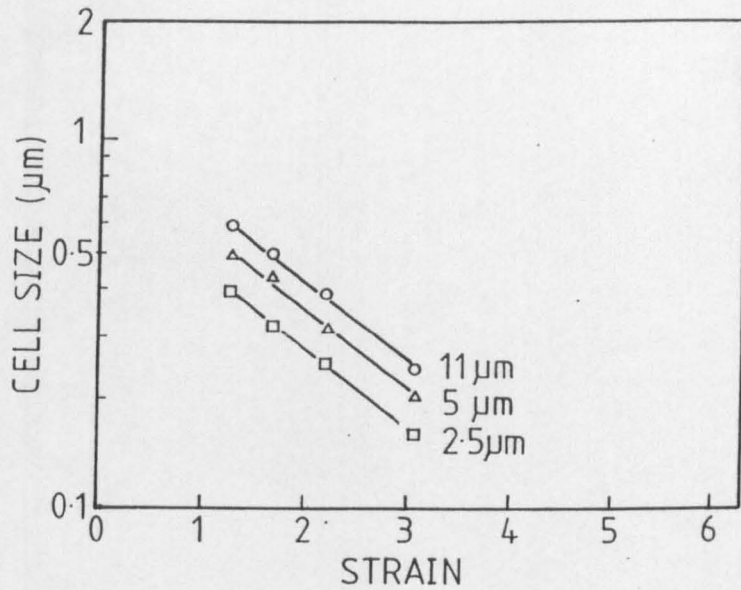
Fig. 2.27. Ultrafine-grain low carbon (0.13%C). Effect of initial grain size on cell size at large strains (wire drawing) [191].
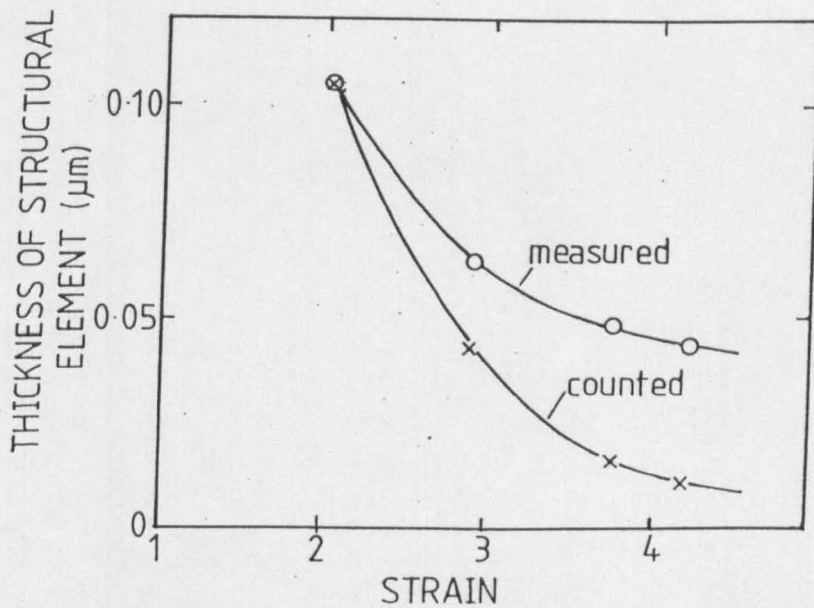
Fig. 2.28. Thickness of structural element as a function of strain. Measured values and those predicted from thickness reductions [211].

strains of about 2.5. The twin lamellae, which are typically 0.02-0.03μm thick and contain fine dislocation arrays, play no further role in the subsequent deformation. Twin band formation has been shown to lead to the strain markings observed on a polished surface [200].

Above a critical strain, when the twinned substructure has fully developed, the structure is crossed by intense shear bands at approximately 35° about the transverse direction [212]. The shear bands consist of small subgrains, with aspect ratios of 2:1 to 3:1, and have a similar appearance in brass, silver and austenitic stainless steel. The subgrains are highly misorientated [211] although they do show some hint of texturing when averaged over many bands, with {110}<uvw> usually being found, and with {110}<001> (Goss texture) being the most common [212]. However, Donadille et al. [190] have reported a strong Goss type texture for shear bands in a 316L, which has a very similar specific SFE to the brass studied above.

Donadille et al. [190] provide evidence for the nucleation of a shear band. A local area of strong curvature was observed within a twin colony, from which a series of 'cells' form step by step in the shear band direction. Intensive glide is then considered possible. Thus, the local distortion of the twins is the first plastic instability by which shear banding starts. The authors use this mechanism to explain the 'microcell' structure which they consider forms progressively. This theory is at variance with the more generally accepted approach that plastic instability leads to an avalanche of dislocations which shear through the structure. The observed structure then represents the 'solidified liquid' [213], i.e. the recrystallised or recovered structure. This latter theory certainly appears to better explain the experimental evidence.

As deformation proceeds, the shear bands divide the structure up into 'rhomboidal prisms' of twinned material, with the twinned units becoming progressively smaller. Crystallites within the shear band are not clearly defined at this stage. Deformation occurs by the generation of new shear bands rather than by homogeneous deformation of existing bands. Once formed, bands tend to be rotated towards the rolling direction so that fresh bands may shear through existing ones [203].

At a strain of about 2.5 only about 25% of the structure remains unsheared. Ultimately, there is insufficient twinned material to generate fresh shear bands, at which point macro-shear bands are found,

crossing the entire sample [212].

Blicharski & Gorczyka [211] have reported areas which remain untwinned and subsequently unsheared in an austenitic stainless steel. Such areas show a stable {110}<001> orientation. The hardness of these regions was shown to be lower than in sheared regions.

At strains >3 the shear bands dominate the microstructure which consists of elongated subgrains. The size of these subgrains decreases slowly (eg from 0.075μm at ϵ -0.78 to 0.058μm at ϵ -3.97 for 70/30 brass [212]) and the characteristic brass texture, {110}<112>, becomes increasingly sharp. The subgrain size decreases with strain for an austenitic stainless steel in fig 2.28. The deformation mode appears to be homogeneous with normal slip mechanisms dominating [200,214]. This suggests a progressive elongation of the crystallites but there is little information at higher strains.

As the SFE is lowered the spacing of twins is reduced, with twins being observed on all four {111} planes in, eg Cu-4.1%Si [200]. There is less tendency for twins to rotate and shear bands with finer crystallites are generated at lower strains. Further deformation induces cracking along the macro shear bands [200]. A detailed discussion of shear bands is provided by Hatherly & Malin [212].

The behaviour in low SFE materials appears to be universal between different metals provided the normalised SFE is considered, although the literature is limited at present.

Table 2.4 provides a summary of the microstructural changes which occur for the spectrum of different SFE metals and alloys.

2.4 METAL WEAR MECHANISMS

The literature on the wear of metals is extensive and spans a number of years. A survey of the wear mechanisms is beyond the scope of this literature survey, but is provided in [215-219]. However, it is important that some rationalisation of the mechanisms is made to place the observations in this thesis in context. This will be followed by an analysis of literature on the microstructure generated by wear.

TABLE 2.4.

SUMMARY OF SUBSTRUCTURAL EVOLUTION FOR SEVERAL
FCC METALS AND ALLOYS. (after [194]).

MATERIAL	T/T_m	SFE	LOW STRAIN	MODERATE STRAIN	HIGH STRAIN
1100 Al	0.32	166	Dislocation tangles; cell network by strain= 0.1. Dynamic recovery and subgrains above 0.2	Cells & subgrains decrease in size, new ones form, some evidence of microbands in edge-on section.	Structure looks very recovered; more subgrains than cells misorientation between subgrains increases. Only occasional microbands at 2.3
200 Ni	0.17	128	Dislocation tangles; cell network by strain of 0.1	Cells decrease in size, definite recovery at >1 with distinct subgrain boundaries. Cells & subgrains continue to decrease Ribbon like structure. Some evidence of microbands.	Continued recovery, cells and subgrains continue to decrease is size (edge-on). No evidence of shear bands
Cu	0.22	78	Dislocation tangles; cell networks by strain 0.1; microbands evident by strain 0.2	Microbands along {111}; rotate towards rolling plane; new microbands form. Much of deformation appears by microband mechanism. Macro shear bands form >1.	Shear bands assume dominant role in deformation. Dynamic recovery occurs. Nutting & co-workers found evidence of dynamic recrystallisation at very large strains (>4)
70/30 brass	0.2	24	Slip by partials; develop planar dislocation array, followed by microbands.	Strains of 0.5 to 1.3, twinning is major deformation mode observed; twins form and rotate to align with rolling plane; by strain of 1.6 most of volume is twinned.	Extensive macro shear banding, especially in twinned areas. Subgrains form in shear band areas and again deform by slip.

2.4.1 Rationalisation of Wear Mechanisms

Table 2.5 provides a brief definition of the more important of the many wear mechanisms. The adhesive theory of wear, sometimes referred to as the Archard theory [220] is the oldest, whilst delamination wear was proposed by Suh in 1973 [221]. After the introduction of the delamination theory, several authors [222] suggested that most adhesive wear situations were in fact the result of a fatigue process and could therefore be classed as delamination. In contrast, many researchers [223] could find no evidence of delamination whatsoever. No worker ever found evidence for both mechanisms, making rationalisation more difficult. Whilst delamination wear clearly does occur, it is now clear that it is only found under limited conditions (related to surface stress, temperature and material microstructure).

The original theory for the production of a delaminated sheet during wear considered that a dislocation free layer existed at the surface which was superplastic, the so called 'Beilby layer'. At the interface between this and the deformed layer, a fatigue process was considered to occur, which promoted voiding at second phase particles. As wear progressed, the voids coalesced to form subsurface cracks which eventually provided a delamination sheet [221]. Whilst such sheets have been shown to form under certain conditions, the existence of a superplastic dislocation free surface layer is unlikely. (The Beilby layer may exist, but on the scale of a few atom layers, not several hundred nm or even larger). The overriding requirement for delamination wear is obviously that the stress is at a maximum below the surface. Such conditions occur for mild wear, where the friction coefficient is low. The delamination theory has now lost the prominence that it once held, but it did at least challenge the assertion that adhesion occurred in all sliding wear situations, even where no transfer of the counterface materials could be found.

Another objection to the adhesive theory was that analytical models consistently failed to predict the wear rate, or even the effect of material parameters on wear. The wear volume, V, was related to material hardness by Archard [220]:

$$V = \frac{K \, L \, x}{H} \qquad \qquad \ldots (2.17)$$

Where K is the Archard wear coefficient, L is the normal load, and x is

TABLE 2.5

SUMMARY OF THE MAJOR SLIDING WEAR MECHANISMS

MECHANISM	ESSENTIAL FEATURES
ADHESION	Defined as the mechanical welding of the two surfaces. Failure of the junction can occur at the original interface or within one of the surfaces. In the latter case, transfer occurs. Promoted by clean, oxide free surfaces. Reduced, but not necessarily eliminated by lubrication. Adhesive forces controlled by nature of electronic forces [216]. Low adhesion from low mutual solubility [217]. However, transfer can occur between totally insoluble surfaces [216].
FATIGUE	Confined to geometries involving rolling contact and those such as gears. High stresses are imposed with repeated loading and unloading. Produces pits on the sliding surface and large debris particles [219].
DELAMINATION.	A fatigue process occurs below the surface leading to microvoid nucleation at second phase particles [221,225]. Coalescence of the voids leads to subsurface cracks. Growth of cracks continues until they emerge at the surface, giving large slab like wear debris. Mechanism requires that stress is a maximum below the surface. Range of applicability fairly limited.
OXIDATION	Heat generation leads to surface oxidation. The oxide is generally harder than the substrate and therefore tends to reduce the wear rate [218]. Oxidation rates are very much quicker at the surface because the oxide film is continuously disrupted by the counterface. Oxide may also reduce friction forces and adhesive forces between the counterfaces. Wear rate dependant on load, i.e. whether film is adherent or broken up. Literature suggests a hard substrate is required for the beneficial effects.
SEVERE	Illustrative of the very loose terminology used in wear studies. Refers to severe adhesive wear.
MILD	Refers to wear dominated by elastic contact. Could include delamination wear. Mechanism of debris formation during mild wear is by no means clear. Includes normal boundary lubricated wear.

the sliding distance. This equation was reduced by Lancaster [224] to:

$$V = K' \ L \ x \qquad\qquad\qquad ...(2.18)$$

This wear coefficient, K', is the one used most frequently in quoting wear data, and will be used throughout this thesis. The Archard equation predicts that the wear rate is expected to decrease with material hardness, which is frequently the case, but the opposite has also been found [225]. The Archard equation does not give any description of the wear mechanism and has been shown to describe delamination wear as well as adhesive wear [225]. Hornbogen [226] considers that the equation only applies when the applied strain is less than some critical value. Above this critical strain there is an increased probability of crack growth and the wear rate can no longer be related to hardness. The important material property then becomes the fracture toughness.

The subject of elastic and plastic contacts is clearly important for rationalising the different approaches to wear and has been dealt with by Greenwood & Williamson [228], who proposed a plasticity index (γ) to predict the state of contact, defined as:

$$\gamma = \frac{E}{H}(\alpha/R)^{1/2} \qquad\qquad\qquad ...(2.19)$$

Where α is the standard deviation of surface profile heights and R is the radius of curvature of asperities. The equation has been subsequently modified, but the general conclusions remain essentially the same, namely, that values of the plasticity index above ≈1 give plastic contact even at low loads, whereas values below 0.5 predict elastic contact even at high loads. It is important to note that the plasticity index is independent of load, clearly dispelling the view that contact progresses from elastic to plastic as the load is increased. Hirst & Hollander [229] have demonstrated that whether a lubricant was effective or not could be predicted by the the plasticity index. However, the authors did find a slight dependence of plasticity index with load, although this may have been related to the state of lubrication. Greenwood & Williamson [228] demonstrated that an increase in wear was associated with an increase in the plasticity

index. Conversely, where a metal mesh was used as the counterface, permitting easy wear debris escape, the wear rate reduced with time, along with a reduction in the plasticity index.

Childs [230] has provided the only clear indication of the range of applicability of the different wear mechanisms. The ratio of the shear stress at the surface (τ) to the flow stress of the material (K) is plotted against strain at the surface (ϵ), fig 2.29. Although not specified, the flow stress is presumably that generated at the heavily deformed surface. The line separating surface smoothing and surface roughening (by transfer, tearing etc), was defined by the equation:

$$\tau/K < Cos\ 2\epsilon \qquad\qquad ...(2.20)$$

The region marked 'normal boundary lubricated wear' (fig 2.29) is governed by surface fatigue (producing 'rubbing wear' particles) but on a smaller scale than with delamination wear. The graph clearly indicates the severity of the conditions required for true adhesive wear.

Oxidational wear is not marked on the graph. However, oxidation has the effect of increasing surface hardness (and therefore flow stress) and reduces adhesive forces between the surfaces, generally favouring elastic contact.

Rationalisation of the different wear mechanisms is complicated by the wide spectrum of testing techniques used. Krause & Senuma [231] have reviewed the requirements of a test capable of producing a qualitative comparison of the results, and noted that 13 variables must be simulated. The number of variables is therefore too high to allow a quantitative comparison of wear test and field test results to be made. Soda et al. [232] have provided a graphic example of the effect of rig design on the wear rate data. By changing the effective rig stiffness by two orders of magnitude the shape of the wear rate/load curves were completely changed. In another example, Rice et al. [233], altered the stiffness of the pin by changing the pin length from 3mm to 6mm. The wear mechanism was totally changed, giving an order of magnitude change in wear rate, for otherwise identical conditions. Other important factors include specimen geometry, which determines the contact stresses and the ease with which wear debris can escape from the interface.
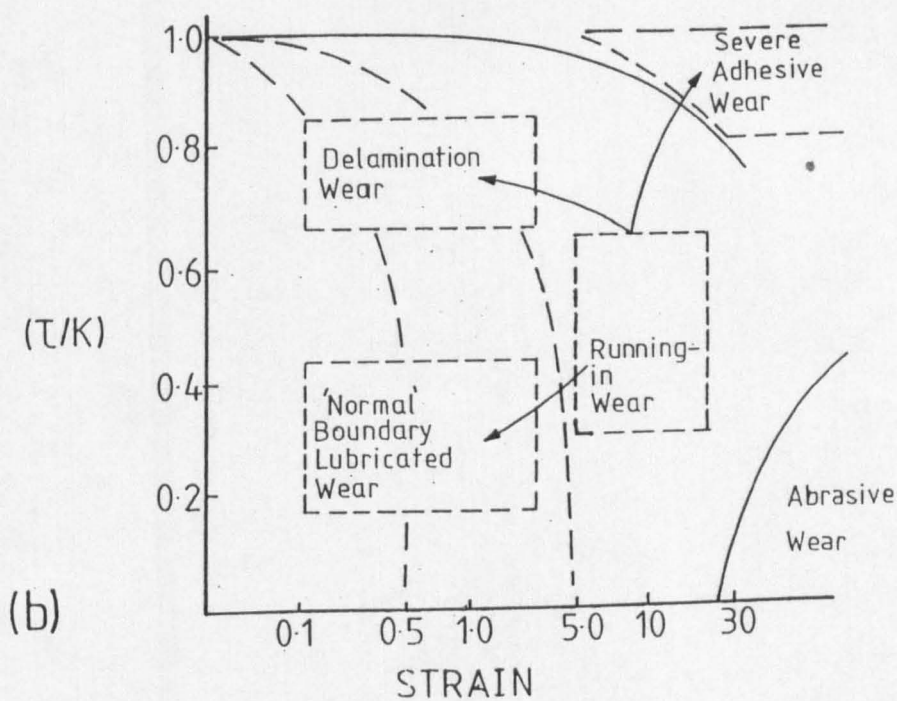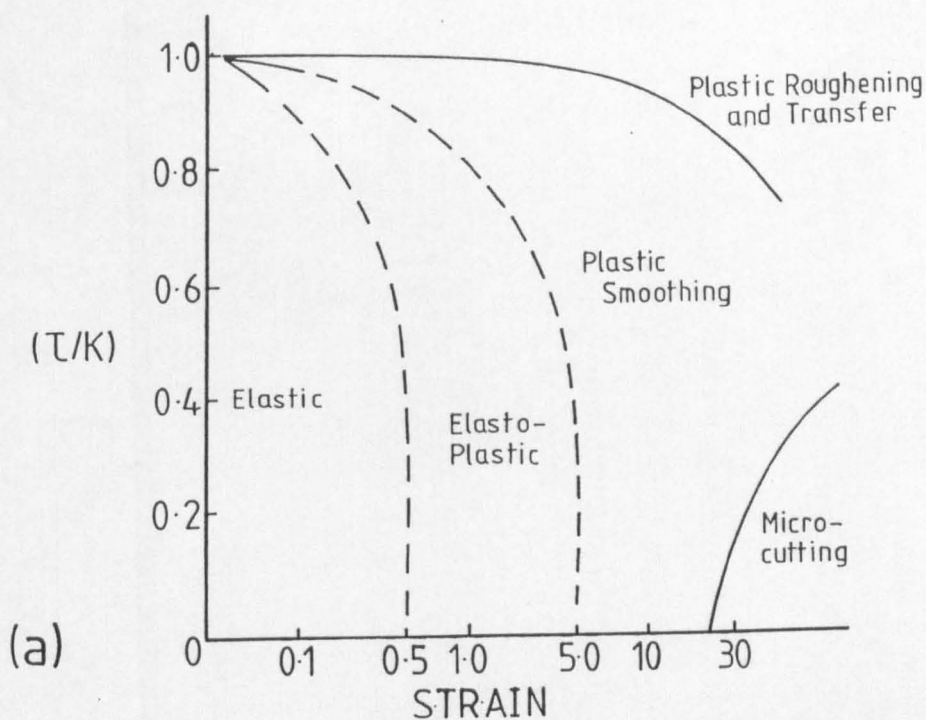
Fig. 2.29. (a) Schematic of the state of contact as a function of the ratio of the shear stress at the surface to flow stress against strain, (b) wear regimes relevant to (a) [230].

2.4.2 High Strain Deformation at the Worn Surface

The following is a brief review of studies of the deformed structure below a worn surface. It serves to establish the inadequate approach taken to date, and the near total disregard of the literature on the high strain deformation.

Estimates of the shear strain at a worn surface have been made using lamellar composites, bending of grain boundaries and measurement of crystallite size. Estimates of the strain varies. Moore & Douthwaite [234] measured a logarithmic strain of 6 by trepanning and 2.5 by abrasion of copper/silver solder composites. Rigney et al. [235] estimated shear strains of 11.4 in sliding wear of copper using TEM measurements, whereas some reported values have been very low, eg 35% by Ruff [236]. Most estimates do not attempt to quantify the outermost few microns but it is clear that very high strains do occur. It is for this reason that the maximum hardness is a more representative variable than the conventional hardness which is usually used [237].

Kuhlmann-Wilsdorf [238] has considered the strain distribution below a worn surface, and assumes that work hardening raises the flow stress to that of the applied stress. The model was compared to the work of Langford & Cohen [195], discussed earlier, who found linear hardening behaviour up to strains of 7.5 for wire drawing of iron. This work hardening behaviour was considered to explain the strain distribution below a worn copper surface [239] shown in fig 2.30, (Here $\delta = \gamma/\sqrt{2}$ and $\epsilon_t = \ln (\gamma/\sqrt{2})$, where γ is the shear strain) but this theory ignores the fact that copper does not show linear hardening to high strains, but rather the flow stress saturates (fig 2.21 previous section). Kuhlmann-Wilsdorf [238] asserts that where there is perfect plasticity (ie a saturation flow stress such as in pure Cu) then the shear strain is expected to show a linear decrease with distance from the surface. However, the deformation will be concentrated close to the surface, so that low wear rates might be expected. Where there is a saturation flow stress, the actual strain at the surface is difficult to estimate since the microstructure remains constant with strain.

The surface structure of worn metals has been examined by many researchers using transmission electron microscopy. The majority of the work has been on copper because of the wealth of background knowledge and the ease of specimen preparation. Much of the work has

been conducted using back thinning to provide thin foils parallel with the worn surface. This has not permitted a comprehensive or accurate view of the operative mechanisms.

Rigney et al. [235] has made extensive efforts to examine the deformation at a worn surface for copper. The sliding of Cu against stainless steel (67N, 1 cm/s) produced a cellular structure, leading to subgrains as the surface was approached. The crystallite size at the surface (300nm) corresponded to a shear strain of about 11.4 (measured by displacement of a grain boundary originally assumed to be straight) and the strain was shown to follow a logarithmic function of depth. Rigney et al. [235] recognises that copper attains a saturation flow stress but fails to relate this to any microstructural reasons (discussed earlier). Much of the work is concerned with dislocation spacing and density at the expense of relating the microstructure to previous work on high strain deformation.

The misorientation of 'subgrains' was systematically measured and is shown in fig 2.31. Extensive study of the rotation of cells about the three axes was made using a computer linked into STEM analysis [239]. Rotation about the z and x axes was negligible. High misorientation at the surface was accounted for by (pre-existing) grain boundaries, but this ignores the possibility of dynamic recrystallisation, and is a mechanism which is very difficult to envisage.

The nature of the surface layer in worn copper has been the focus of some discussion. All workers [238,239,240-250] have found crystallite sizes in the range 0.2-0.5μm (despite differing stress conditions) and many have noted large misorientations. Some have found a smooth transition from cells to 'subgrains' [eg239] whilst others report a definable surface region of fine crystallites [eg241,244,249]. Some authors suggest that dynamic recrystallisation occurred [246,247] which would explain the high misorientation. Certainly, the sharp transition from elongated subgrains with low misorientation (eg 5-8°) [241] to roughly equiaxed grains with random misorientation supports this view. However, the mechanism was not conventional thermally driven recrystallisation as shown by Ives [249]. Ives compared dry and lubricated wear of Cu and found very much larger equiaxed surface grains for the dry wear than the lubricated case. This suggests that the surface layer containing fine crystallites was produced by dynamic recrystallisation similar to that
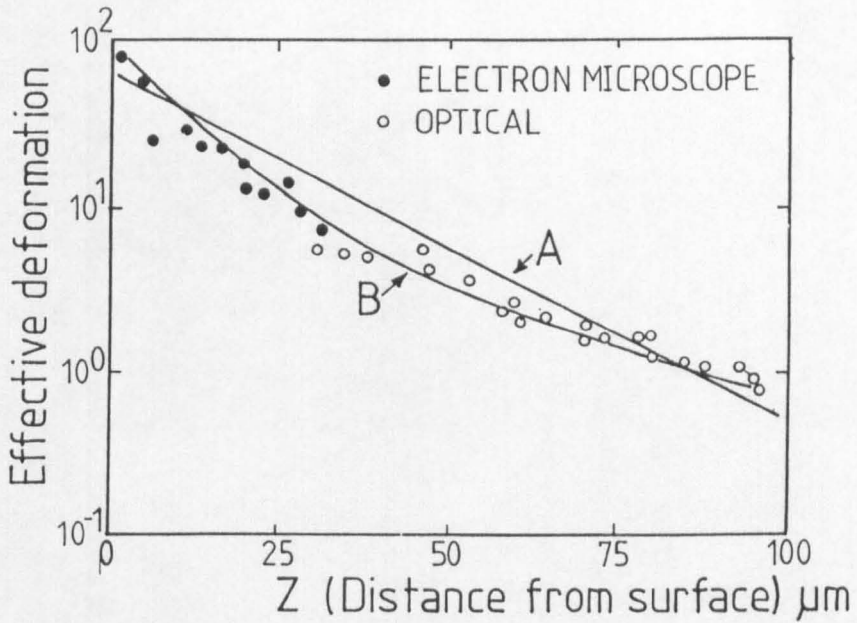
Fig. 2.30.   Subsurface shear strain in a polished OFHC Cu pin slid on a
normalised, polished steel ring at 40N [238].
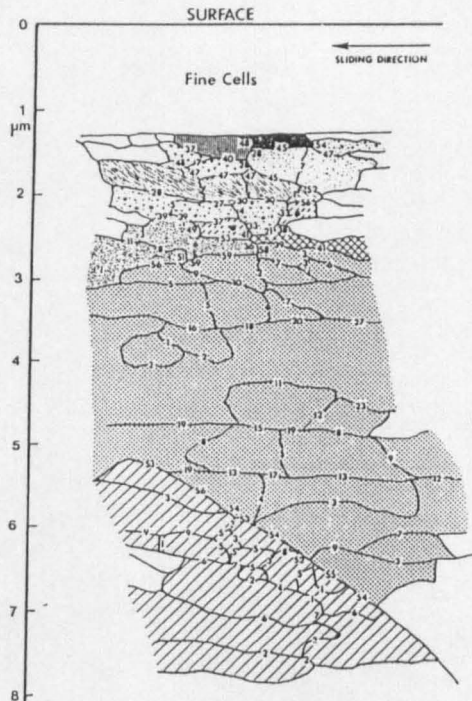
Fig. 2.31.   Pattern of 'cells' at a worn surface.   The numbers are the
misorientation (in degrees) across cell boundaries.   Areas with similar
shading are (considered) associated with the same parent grain [234].

found by Saunders in a totally redundant work machine [192], and therefore the flow stress at the surface had reached a saturation value. However, it was also possible that shear bands had formed, explaining the fairly sharp boundary with the elongated subgrains. Samuels et al. [251] have suggested that the deformation at a worn surface does follow the same scheme as that found in rolling for both Cu and 70/30 brass, but provide no experimental evidence to support this.

Dautzenburg [246], showed that the equivalent strain in such a surface layer was an order of magnitude smaller when measured by TEM analysis of the crystallite size compared to that measured by the displacement of a thin metal foil marker placed in the Cu pin. The latter technique was clearly more accurate, and the authors explained the difference by dynamic recrystallisation which maintained the crystallite size at a constant value whilst the strain increased. Alternative explanations, such as grain boundary sliding, were rejected on the basis that the temperature increase at the interface was too low, and that strain rates were so high that evidence of grain boundary voiding would be present. The authors concluded, therefore, that the very high strains had reduced the temperature for dynamic recrystallisation, although no reference to the literature on the high strain deformation of Cu was made.

Dautzenburg [246] further suggests that dynamic recrystallisation will reduce the shear stresses at the surface. A similar argument is proposed by Ives [249], who cite the work of Thompson [252] as evidence. Thompson demonstrated that the yield stress of Ni was lower for a polycrystalline structure than for a comparably sized cell structure. However, low temperature dynamic recrystallisation has been shown by several authors [eg193] to provide a saturation flow stress at the maximum hardening attained in the material. Again, the problem is one of ascertaining whether the dynamic recrystallisation is the high temperature form or the low temperature, high strain form. If the microstructural changes are similar to other deformation studies such as by Saunders & Nutting [193], then a constant microstructure can be maintained up to very high strains.

Salesky et al. [253] have recently produced a comprehensive study of the surface microstructure generated in pure iron and various steels. Interestingly, they found a 'recovered' layer at the surface of the pure iron which extended to a depth of 200 to 300nm. The

crystallite size in this layer was about 60x80nm, compared to 10-30nm thick by 200-300nm long in the region immediately below. The crystallite sizes were used to estimate the strain as a function of depth, by comparing the measurements with the results of Embury et al. [201] for wire drawing, fig 2.25. However, the crystallite size adjacent to the recovered layer (i.e. 10-30nm) was beyond the scale of Embury et al.'s [201] work, although a small amount of extrapolation would suggest a strain greater than 6.5. If the crystallite size is compared to the work of Langford & Cohen [195], the crystallite size is again smaller than produced by wire drawing, even up to strains of 6. Indeed, a crystallite size of 10-30nm would suggest a strain of the order of 11.5 if Langford & Cohen's graph is extrapolated.

The recovered layer found by Saleski et al. [253] suggests that some form of dynamic recrystallisation may have occurred, although this has never been reported for low temperature deformation of this material. The authors suggest that there is a limiting strain for iron above which the crystallite size does not decrease with increasing strain, and cite the work of Langford & Cohen [195] and Embury et al. [201] as evidence. However, both these authors found a continuously decreasing subgrain size up to the highest strains achieved, which provided linear hardening. This suggests that the 'recovered' layer found by Salesky et al. [253] was thermal in origin, rather than a manifestation of extremely high strains. However, Salesky et al. [253] reported an average misorientation of 15° which is indicative of recovery rather than dynamic recrystallisation. The authors estimated a flash temperature rise of about 500°C, although there was no analytical or experimental evidence to support this. The result of recovery/ recrystallisation in this layer was a reduction in residual stresses. In contrast, the region immediately below this layer would have contained substantial residual stresses. The authors suggest that this promoted tensile forces at the interface between the recovered layer and below, which was responsible for the microcracks observed. These microcracks tended to run along subgrain walls, or were present around second phase particles. The wear debris size coincided with the width of the recovered layer and, therefore, the depth of this cracking, suggesting that debris had formed by spallation of the recovered layer.

None of the researchers, with the exception of Salesky et al. [253] compare their micrographs with those presented by Saunders & Nutting

[192] or other high stress deformation studies. Saunders & Nutting found that the microstructure was constant between logarithmic strains of 4 to 8, consisting of fine (0.2-0.5μm) grains, frequently dislocation free, with high angular misorientation. The micrographs presented by Rigney et al. [235], for example, show similar features to those found by Saunders & Nutting [192], and the have same crystallite size. Saunders & Nutting [192] pointed out that the microstructure is consistent with the formation of new grains followed by strain induced boundary migration. This causes grain growth until dislocation movement within the larger grains once again leads to small grain formation. In other words, the process is similar to dynamic recrystallisation in hot working. This approach clearly explains the high, random, misorientation. As noted above, it also suggests that surface layers were deforming at saturation flow stress.

Limited work has been conducted on aluminium [244,245], where a cellular structure was observed which gave way to a highly recovered subgrain structure as the surface was approached. The morphology in the very near surface region was not evaluated, although large (1-5μm) recrystallised grains have been found in one study [245]. The absence of any driving force for dynamic recrystallisation at room temperature in such a high SFE material suggests substantial temperature rises at the surface.

Where a cellular structure has been found at the surface, several authors [eg254] have suggested that the cell walls act as stress initiators and easy paths for crack propagation. Considerable care should be taken in relating wear debris formation to such a structure, now recognised to be formed by relaxation after the event [201], given that the dynamic structure is unknown. In addition, the cell structure only persists to high strains in very high stacking fault energy materials and therefore cells are largely irrelevant in real wear situations. However, it is reasonable to suggest that low angle grain boundaries in a subgrain structure (or aligned microband, shear band etc) would act as a preferential path for a propagating crack.

Other studies have been made on Ni [247], Ti [255], stainless steel [256-259], and low carbon steels [248,254,257], but these provide little additional information. In the case of Ni [247], a structure similar to that found in Cu is reported, even though high temperatures were generated in this case. The surface of a worn Ti alloy showed a fine crystallite structure with a strong texture. Beneath this,

extensive twinning had taken place. Interestingly, the twins contained dislocations with a 'c' component, which have not been observed during conventional deformation. This suggested that the complex stress state at the wear surface had unlocked an additional slip system. Most studies on stainless steel are on 304 and other alloys which form thick α' martensite layers on the surface. Garbar & Skorinin [254], and Nakajima & Mizutani [248] have identified a 'cellular' structure in a mild steel up to about 5μm below the worn surface.

Limited work has been conducted on the microstructure generated by erosion. Ruff et al. [232] have demonstrated that twinning is produced by the solid particle erosion of Cu, reflecting the effect of high strain rates.

CHAPTER 3

EXPERIMENTAL PROCEDURE

3.1 WEAR TEST METHODS

3.1.1 Wear Rig Design

Two tri-pin-on-disc wear rigs were used in this study, both of the
same design. A schematic diagram of the wear rig is provided in fig
3.1. The design has been shown to give consistent and reproducible
results over many years at Leeds.

The disc was seated on the central drive shaft with the rotation
transmitted by a protruding pin which pushed against the base of the
disc. The head, which contained the three wear pins, was placed on the
disc, located by a central spindle attached to the drive shaft. The
head would have been free to rotate, but was prevented from doing so by
two half-bridge strain gauges.

The pins were clamped into the head by means of collets which were
tighted by grub screws. The design was such that only a few mm of the
pin projected from the lower head surface in order to ensure maximum
stiffness. The pin position was accurately measured after installation
in the head in order to ensure that the pins projected an equal
amount. The pin height was adjusted until all were within 20μm of each
other.

The friction force was measured using the amplified signal from the
combination of the two half-bridge strain gauges. The strain gauges
were calibrated by plotting the amplifier read out against load. The
load was applied by dead weights via a string and pully system.
Readings were confirmed during unloading before the calibration was
considered acceptable.

With the original rig design the load was applied via a cantilever
arrangement. The cantilever was connected to the head via a ball and
race arrangement which allowed the head to rotate freely. However,
this design was found to amplify vibration, (initiated by the wear
mechanism) as a result of the poor rigidity of the system. The loading
arrangement was therefore changed to one of direct clamping of the
weights to the head. This substantially reduced the vibration in the
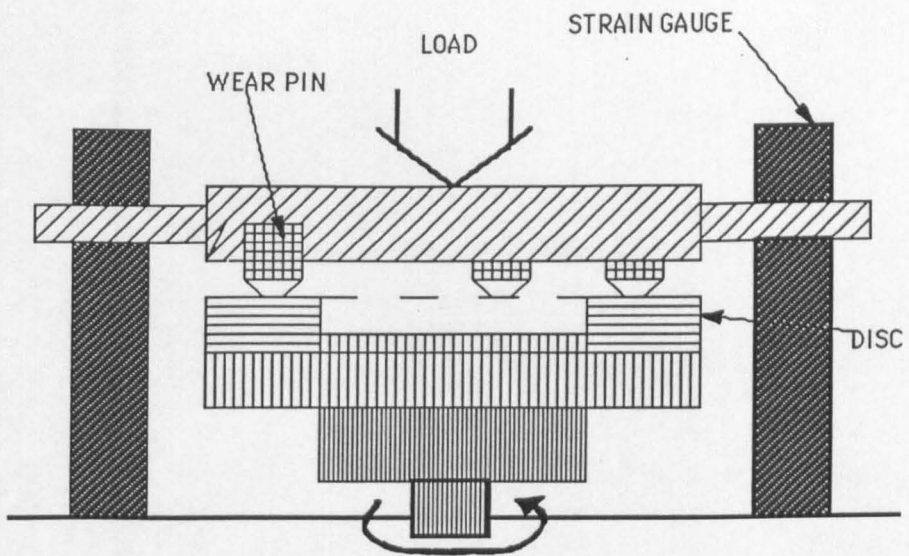
Fig. 3.1. Schematic of the tri-pin-on-disc wear rig.

PIN   DISC
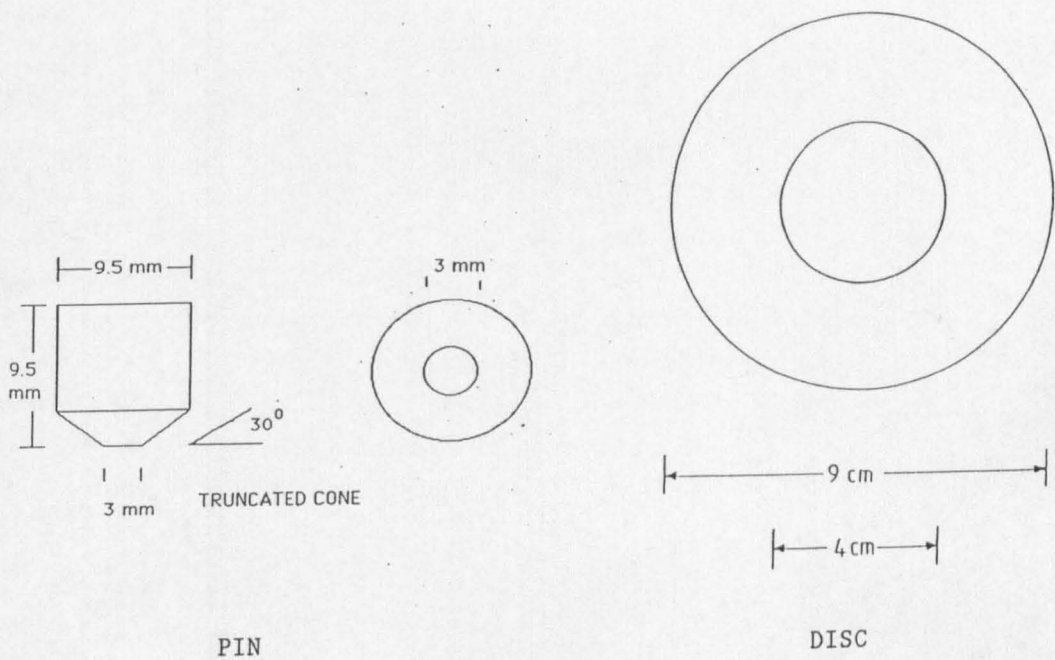
Fig. 3.2. Dimensions of the pins and discs used in the wear tests.

system. The origins of the vibration will be discussed in the results and discussion chapters.

3.1.2 Specimen Preparation and Testing

The pin and disc dimensions are shown in fig 3.2. The surfaces were prepared by lapping prior to testing. The starting surfaces were usually good enough that only 6 and $1\mu m$ diamond pastes were required. This produced a surface finish, R_a, on the ceramic discs of the order of $0.008\mu m$ (individual values are quoted in the following chapters). The starting roughness of the pins could not be measured, because of the small surface area, but it was assumed that they were of the same order as the disc.

The pins were ultrasonically cleaned in acetone prior to testing. The pins were then carefully weighed to ± 0.0004g. Throughout the work a standard was used which was subjected to identical environmental conditions as the wear pins. In other words, the standard was cleaned with the wear pins, weighed at the same time, and placed near to the wear rig during testing. This ensured that any moisture uptake by the ceramic, or other experimental variables, could be corrected. Whilst this was not a problem at some of the very high wear rates encountered, it was essential when wear rates were of the order of 10^{-7} mm^3/Nm, or less.

After clamping the pins in the head, the pin position was carefully located by a marker and checked by a binocular microscope. The mass loss was monitored at regular intervals throughout the tests so that it was important that the pins could be returned to exactly the same position after each measurement. At the start of the test the pins were finally washed in 'inhibsol'.

Wear debris was collected in a bowl which enclosed the disc region. A large glass dome was used to prevent dust getting into the sliding interface or the wear debris. The frictional force, noise and vibration levels were monitored throughout the test.

3.2 X-RAY ANALYSIS

All X-ray analysis was performed on a Philips Diffractometer using Ni filtered Cu K_α radiation. The diffractometer was fitted with a

graphite monochromator. Better resolution traces were obtained from the steel specimens using monochromated Cu radiation (to avoid flourescence) rather than Cr radiation. Calibration checks were conducted using Si standards.

The penetration depth of the X-rays was calculated using the standard equation presented by Cullity [260], where the fraction of the total diffracted intensity contributed by a surface layer of depth x, G_x, is given by

$$G_x = (1 - e^{-2\mu x/\sin\theta}) \qquad \ldots(3.1)$$

where μ is the linear absorption coefficient; the value quoted by Kosmac [261] for yttria stabilised zirconia of 0.0642 μm^{-1} was used .

The fraction of monoclinic in the polished, V_m, ground and worn zirconias was evaluated using the Toraya et al. [262,263] modification to the original equation of Garvie & Nicholson [264], which takes account of the theoretically predicted intensity values and the non linearity of the calibration curve for the integrated intensity as a function of solute concentration:

$$V_m = \frac{P \, X_m}{1 + (P-1) \, X_m} \qquad \ldots(3.2)$$

where P is experimental constant for this system (1.311 ±0.004) and X_m is given by the equation of Garvie & Nicholson [264]:

$$X_m = \frac{I_m(\bar{1}11) + I_m(111)}{I_m(\bar{1}11) + I_m(111) + I_{t+c}(111)} \qquad \ldots(3.3)$$

where I is the integrated intensity of the relevant peak.

In this study, measurements of the integrated intensity were taken using a planimeter. However, overlapping of the monoclinic and cubic/tetragonal peaks, especially with Mg-PSZ materials, led to significant errors in the measurement of the integrated intensity. Errors were estimated to be as high as 20% in some cases, but lower for the TZPs at about 10%.

To account for the preferred orientation in the monoclinic, the correction proposed by Paterson & Stevens [265] was used where the combined effects of the ($\bar{1}$11) and (111) reflections are given by I_M as:

$$I_M = 1.2551 \ (111) + 0.8331 \ (\bar{1}11) \qquad \ldots(3.4)$$

This modification is required because the equations for the fraction monoclinic are based on the assumption that there are an equal number of the possible twin variants. However, because the volumetric expansion tends to occur parallel to the tensile stress field [265] the ($\bar{1}$11) is favoured. This effect tends to be stronger on Y-TZP fracture surfaces than with Mg-PSZ [265].

3.3 TEM SAMPLE PREPARATION

Electolytic thin foil preparation was used for the steel specimens wherever possible (except where geometrical constraints precluded such a method). A solution of 10% perchloric acid in methanol in a Struers 'Tenupol' was used. Optimum conditions were found to be 70 mA at -60°C.

However, in the majority of cases ion beam thinning had to be used. This was essential for all ceramic specimens and in the metal case for cross sections perpendicular to the worn surface and transverse rolled specimens. Ion beam thinning was performed using a Gatan Dual Ion Mill operated at 4-6KV and a gun current of 0.25mA per gun. The lower KV condition were used in association with angles of 12-15° for final thinning and polishing. The higher KV setting was used at an angle of 20° for the first 8 hours of thinning. Such mild conditions were used to minimise temperature generation during thinning. In relation to this point, a foil prepared electrolytically was compared to one obtained by ion beam thinning for the same heavily deformed stainless steel. No difference in the microstructure could be found.

Thin foils of the ceramic were prepared by careful mechanical grinding and polishing of 3mm discs. Initial material removal, down to a thickness of 50μm, was carried out using SiC wet and dry papers. It was found to be important to finish with an extended polish on 1μm diamond paste. This rendered both sides of the disc free from visible scratches and as stress free as possible. The 30μm thick disc was then mounted between Cu grids for ion beam thinning.

The TEM sections perpendicular to the sliding direction were prepared using a variation of the method of Newcomb & Stobbs [266] which was based on that proposed by Manning & Rowlands [267], which is illustrated in figs 3.3-7. The worn surface was first protected and labelled by a coating, fig 3.3. In the case of the stainless steel a two stage Ni coating was used (Watts plating bath). It was essential to use a very low and steady current during initial plating to ensure adaquate adherance. The coating was found to penetrate any surface cracks and even adhere to surface oxide. The ceramic specimens were plated using electroless Ni at 80°C. The solution was less controllable, but still rendered an adherent coating. In all cases, there was no way of identifying the worn surface unless the coating was retained during thinning.

A second surface, of similar material and dimensions to that shown in fig 3.3 was then glued to the first to prevent damage to the coating. This composite was then glued into a slotted steel bar in the manner shown in fig 3.4. Great care was required at this stage. If the composite was too thick, but could still be forced in, the thin foil eventually produced tended to buckle and fall apart. Conversely, if the composite was too small, insufficient mechanical strength was attained in the sectioned disc it also tended to disintegrate. This bar was then glued into a 3mm hollow brass tube with internal diameter of 2mm. The bar was left to dry over several days to ensure full strength in the bond.

$200\mu m$ sections of the bar were removed by a slow speed saw. The resulting cross section of the sample is illustrated in fig 3.5. Thus, the method produced a 2mm longitudinal section of the worn surface. One surface of the disc was then polished in the standard way to a $1\mu m$ finish. Great care was required to ensure the optimum surface finish attainable. A 3mm Cu grid was then stuck to this side and left to cure over 24hrs. The thickness was reduced to about $50\mu m$ by dimpling, finishing with $0.25\mu m$ alumina slurry to ensure a high polish. At this stage, the adherance of the coating was checked by optical microscopy.

The most important step in ensuring success was the ion beam thinning. Conventional thinning invariably eroded the coating at a much higher rate than the substrate so that it was lost before electron transparency was achieved, resulting in some of the original worn surface being lost, often up to $5\mu m$. To prevent this, a blanking arrangement was adopted as shown in fig 3.6. Mechanical blanks were
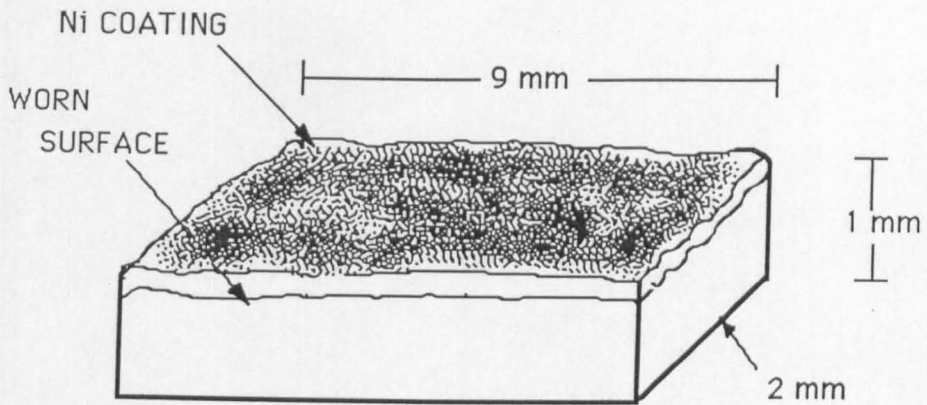
Fig. 3.3. Schematic of the worn surface after Ni coating.
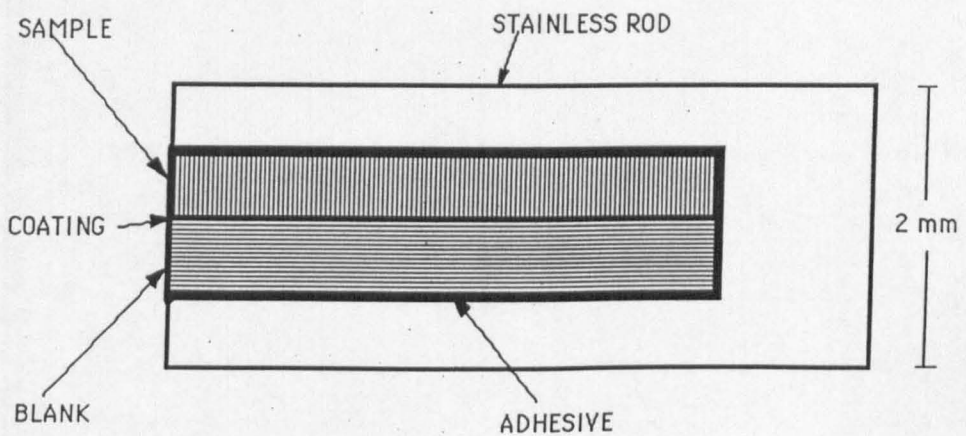
Fig. 3.4. Schematic of the method of cross sectional TEM foil preperation. The composite was glued into a slotted 2mm diameter stainless steel rod.
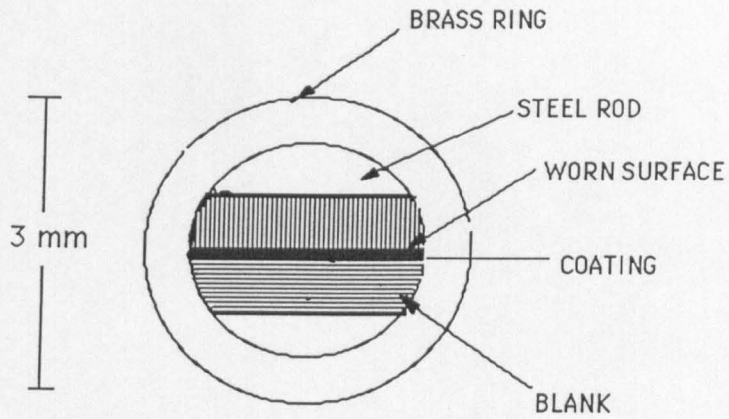
Fig. 3.5. Schematic of the disc cut from the composite bar.
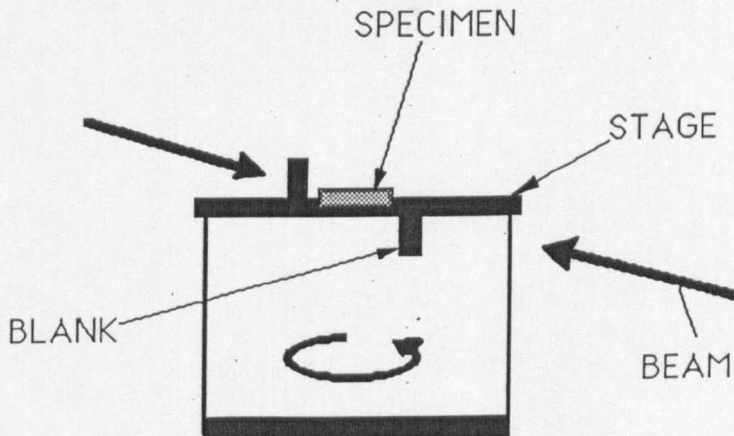
Fig. 3.6. Schematic of the Gattan Ion Mill stage showing the blanking arrangement.

SAMPLE

BLANK
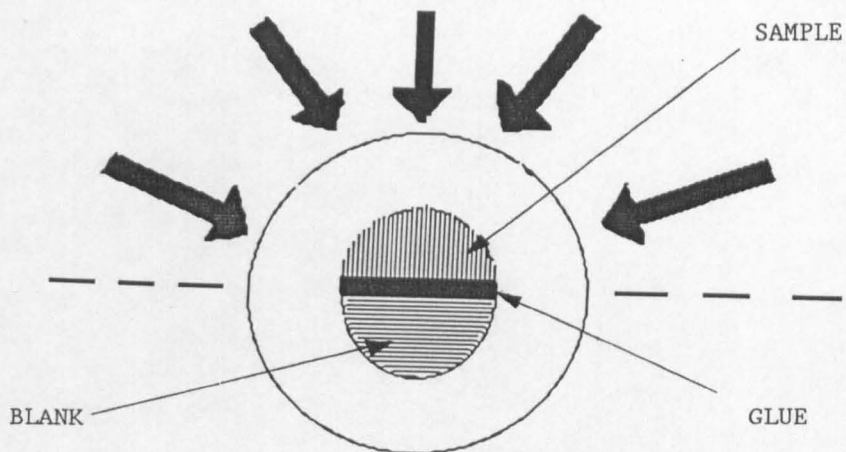
GLUE

Fig. 3.7. Schematic showing the ion beam direction during thinning.

K_{1C}
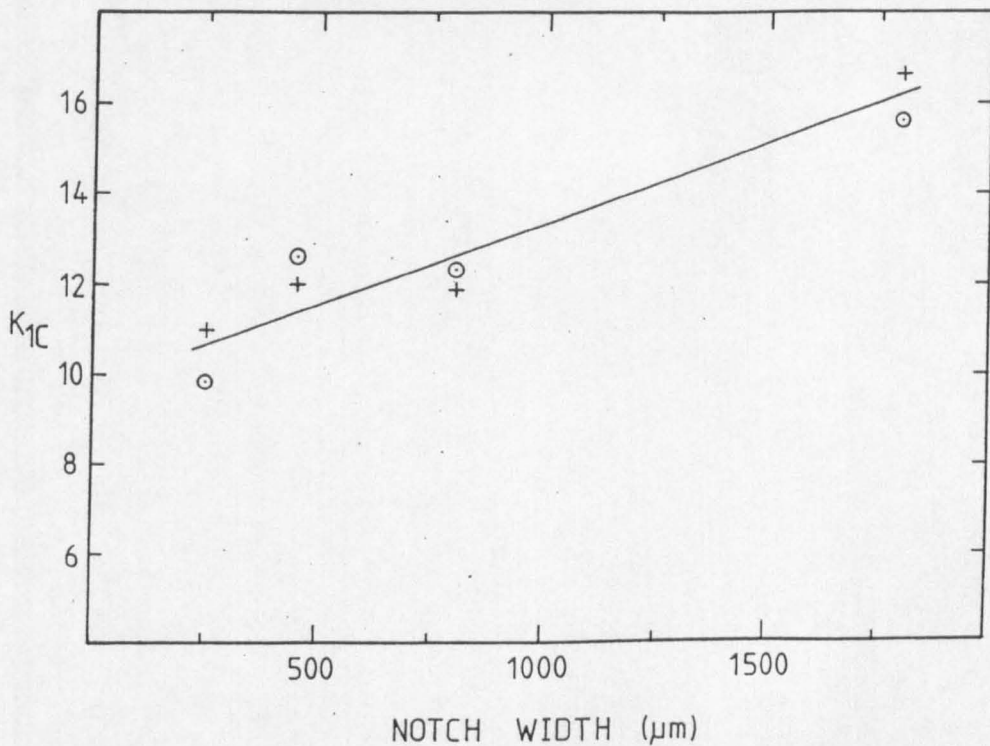
NOTCH WIDTH (μm)

Fig. 3.8. K_{1C} as a function of notch width for SENB tests. Two batches of material were tested, each for five bars.

glued onto the ion mill stage in order to prevent the beam from striking the specimen from the blank side of the composite, fig 3.7. Thinning was only carried out from below the worn surface. Whilst the coating was still eroded at a preferential rate, the last fraction was usually retained so that the worn surface could be identified.

The optimum position for the first perforation was found to be at the worn surface itself. If the thin area was located below the worn surface a tear invariably occurred up to the worn surface, which resulted in the curling up of the thin area or its total loss. Any subsequent thin area was usually very small. Whilst dimpling was used to try and ensure perforation at the surface, the precision of the technique was inadequate and therefore the success rate was low. Although some foils were produced first time, the majority required about five attempts before full characterisation could be achieved. Given that each foil took about 2-3 weeks preparation, characterisation of a particular surface could take several months. However, the potential benefits of this technique over and above back thinning were substantial, so that the additional effort was merited.

The transverse sections of the rolled stainless steel were obtained using this technique, by glueing several specimens together. In this instance the success rate was virtually 100%.

Back thinned specimens were also examined in the majority of cases, prepared using one of the two ion beam guns. The worn surface was protected from redeposition of sputtered material by aluminium foil. However, some redeposition occurred after perforation so that a short cleaning operation using the ion gun was used. This lasted about 5 mins and would therefore have thinned very little of the worn surface.

3.4 MATERIALS

3.4.1 Stainless Steel

The stainless steel used was the low carbon specification of AISI 316, the analysis of which is given in table 3.1. The steel was supplied as 15mm round bar in the solution annealed and quenched state. Wear pins were machined out of the bar to the specification in fig 3.2.

The microstructure was revealed by etching in a solution of 5g CrO_3, 5cm^3 H_2SO_4, and 90cm^3 H_2O at a voltage of 2.8V. Etching times

were of the order of 15s. The time was varied according to the extent of deformation and the specimen type. For example, Ni plated cross sections of the surface required considerably less time because of the galvanic reaction between the worn surface and the coating.

TABLE 3.1

ANALYSIS OF THE STAINLESS STEEL

Wt%	C	Si	Mn	S	P	Cr	Mo	Ni
	0.025	0.29	1.62	0.004	0.022	16.51	2.27	12.27

3.4.2 Bearing Steel

The steel used in these tests was a 1%Cr 1%C steel (EN 31) in the maximum hardness condition. Discs were oil quenched after a carbide coarsening treatment of 1hr at 840°C. Water quenching would have been preferable since it would have provided a higher hardness, but was found to give quench cracking of the disc. The discs were then annealed at 130°C for 1hr. This resulted in a hardness (Vickers) of 790.

3.4.3 Mg-PSZ

The Mg-PSZ used throughout this study was a commercial grade supplied by Coors. The material nominally contained 8.5 mol% MgO, and was prepared by sintering at 1750-1800°C followed by a 16hr furnace cool.

3.4.3.1 Toughness Measurement

The fracture toughness of the zirconia was measured at 7.9 MPam$^{1/2}$ by the microindentation technique, and the hardness at 9.9 GPa. The equation of Anstis et al. [268] was used to evaluate the indentation toughness, which assumes that half penny cracks are formed and is only valid if c>2a, where c is the half crack length and a is half the indent diagonal. However, care should be taken with such results because the crack profile may be Palmqvist, although the final toughness value is little different.

Some difficulty was found in measuring the toughness of this

material by indentation. With small indents grain boundary cracking was common, which tended to give a low value of K_{1C}. If a Vickers indentor was used, at 20Kg for example, the toughness measured was generally marginally higher, apparently because the effect of grain boundary cracking was reduced (the indentation tended to cover several grains rather than just one). Toughness values for the Mg-PSZ were, therefore, also measured using single edge notch beam (SENB) in three point bend at a range of notch widths. The results are presented in fig 3.8 and show that the toughness is dependent on the test technique and the notch width. The difference in toughness values can be ascribed to a difference in the extent of transformation induced and the effect of crack initiation. SENB tends to give larger toughness values than indentation when notch widths of above $100\mu m$ are used [107,269], since greater amounts of transformation are induced. (In non transforming ceramics the opposite is true because SENB does not account for crack initiation, only propagation).

Whilst SENB is considered to give an over estimate of the toughness of transformation toughened ceramics the question must be asked: what is the true toughness? The over-riding point is that the ceramic should be tested under similar conditions to those found in service. This is a very important point with respect to the study of wear since the toughness should be measured under condition which give transformation zone sizes similar to those generated at the wear surface. SENB therefore appears inappropriate since large notches do not simulate the conditions at a sliding interface. Steinbrecht [270] showed that pre-existing flaws could grow at low values of K, ($\approx$2) for an apparently tough ceramic. Clearly, therefore, the absolute toughness measured by indentation or SENB may well be misleading in predicting the stress at which a surface flaw can propagate. This is especially true since sub-critical crack growth (for example where strong R-curve behaviour is present) can cause wear debris formation. None-the-less, the indentation toughness should give an estimate of the extent to which transformation is available to inhibit crack growth.

3.4.3.2 Microstructure

The microstructure of Mg-PSZ has been extensively characterised for materials which have been solution treated, quenched and isothermally aged at 1400°C (section 2.1.1). However, the structure of commercial materials, which have been manufactured using a continuous cool, are

not well characterised. Therefore, the structure of this material will be described.

Optical examination of a polished surface etched in HF revealed a thick film of monoclinic at all grain boundaries. The amount of monoclinic was typical for commercial grade Mg-PSZ, but much higher than would be expected for a laboratory prepared grade, especially if a small quantity of strontia was added. The thick grain boundary monoclinic explained the high prevalence of grain boundary cracking in indentation tests.

The majority of the precipitates in the grain interiors resembled published micrographs of optimally aged materials, showing tetragonal precipitates lying on the {100} cubic planes, fig 3.9. The precipitates, which were typically $0.1-0.2\mu m$ long, were coherent with the matrix as shown by the strain contrast when imaged under two beam conditions. Transformation of t → m was possible by electron beam heating of the foil, suggesting that the precipitates were just below the critical size for spontaneous transformation. The size distribution of the tetragonal precipitates was shown to be larger than for an Mg-PSZ prepared in the laboratory by a rapid cool from sintering followed by an isothermal age at 1420^oC.

Some areas within grains appeared to be fully tetragonal (i.e. no twin boundaries could be imaged) but the diffraction patterns suggested that some monoclinic was present. In addition, extra reflections were present at 1/2(001) positions which were streaked along <001>. These additional reflections appeared to be derived from precipitates which were themselves streaked, such as in fig 3.10. The diffraction pattern is similar to those presented by Heuer et al. [33], Lenz & Heuer [28] and Muddle & Hannink [40], where it was attributed to the formation of an orthorhombic structure (o phase). The streaking has been related to a fine modulated structure with a repeat distance of ≈0.5nm and ≈1nm [28]. The o phase cannot be detected by X-ray diffraction in the bulk phase and is generally considered to be a result of transformation of the tetragonal to monoclinic during thin foil preparation [28]. Muddle & Hannink [40] have shown that the transformation of t → o → m can be induced in thin foils.

Many diffraction patterns showed diffuse intensity scattering which was shown to arise from the cubic matrix, fig 3.11. This is a result of ordering in the cubic matrix [32], a first step towards the formation of δ phase, as discussed in section 2.1.2. Such ordering is
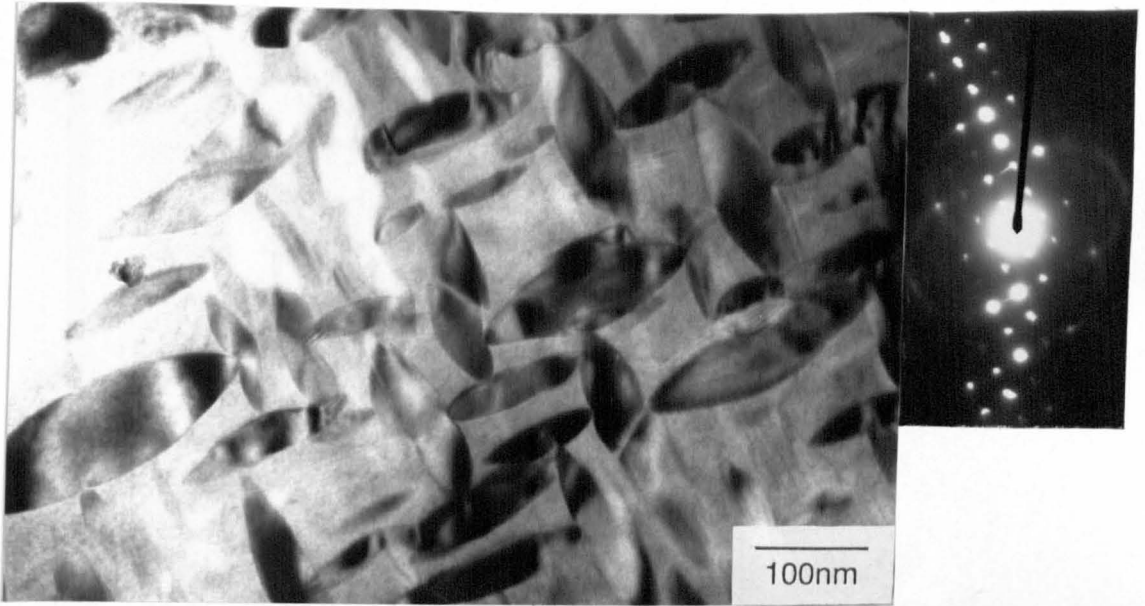
Fig. 3.9. TEM micrograph of the tetragonal precipitates in the cubic matrix for a continuously cooled Mg–PSZ resulting in optimum K_{1C}.

B = [100]
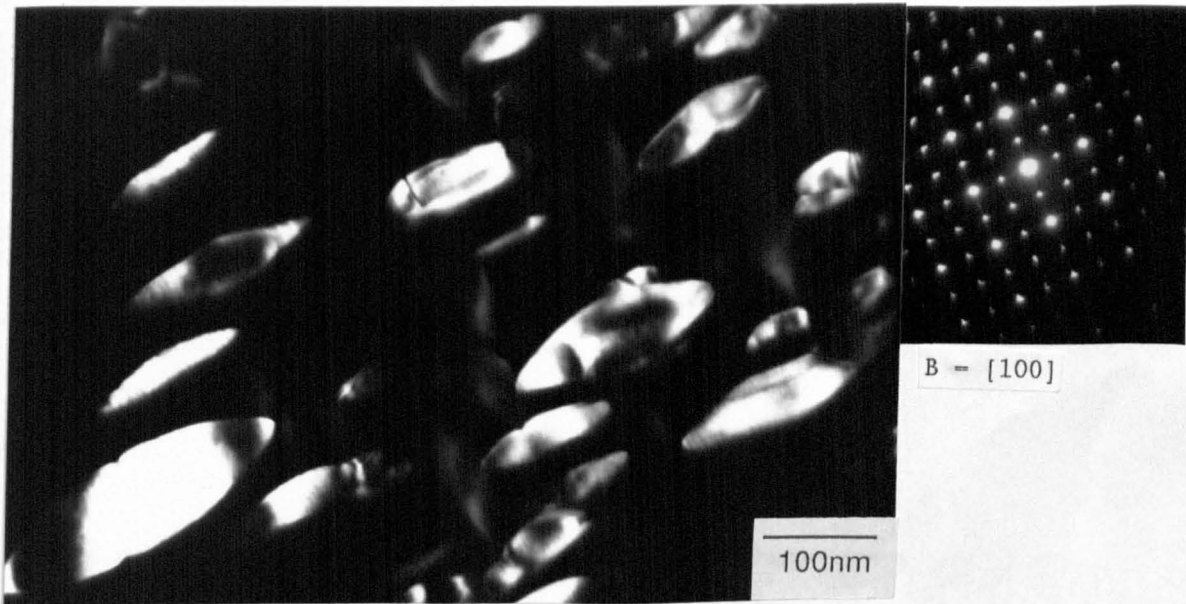
Fig. 3.10. Dark field of the same area as fig 3.9. Note the streaking in the lower precipitates.
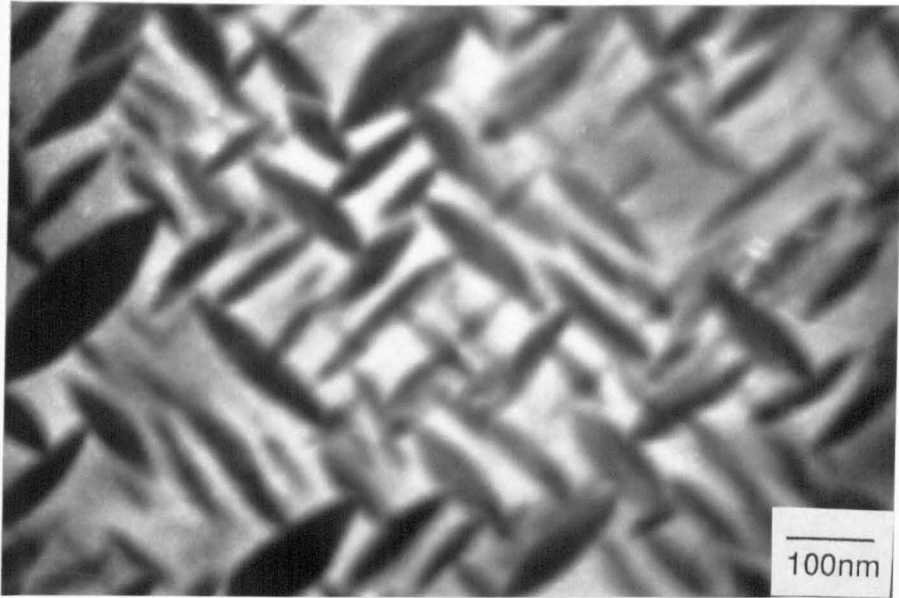
Fig. 3.11. Dark field image formed by the diffuse intensity scattering in the diffraction pattern of fig 3.9.
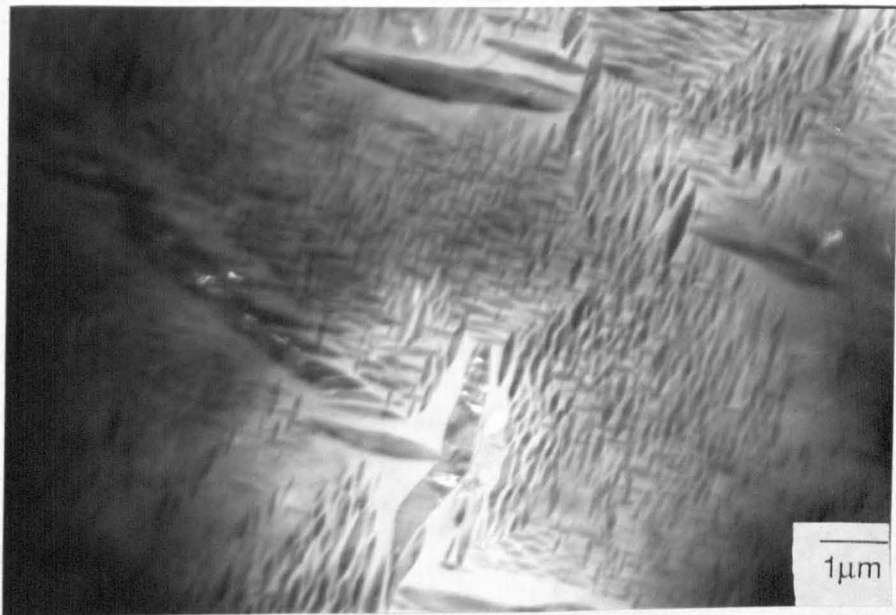
Fig. 3.12. Low magnification dark field micrograph formed from the diffuse intensity scattering, showing the heterogeneous distribution of precipitates.
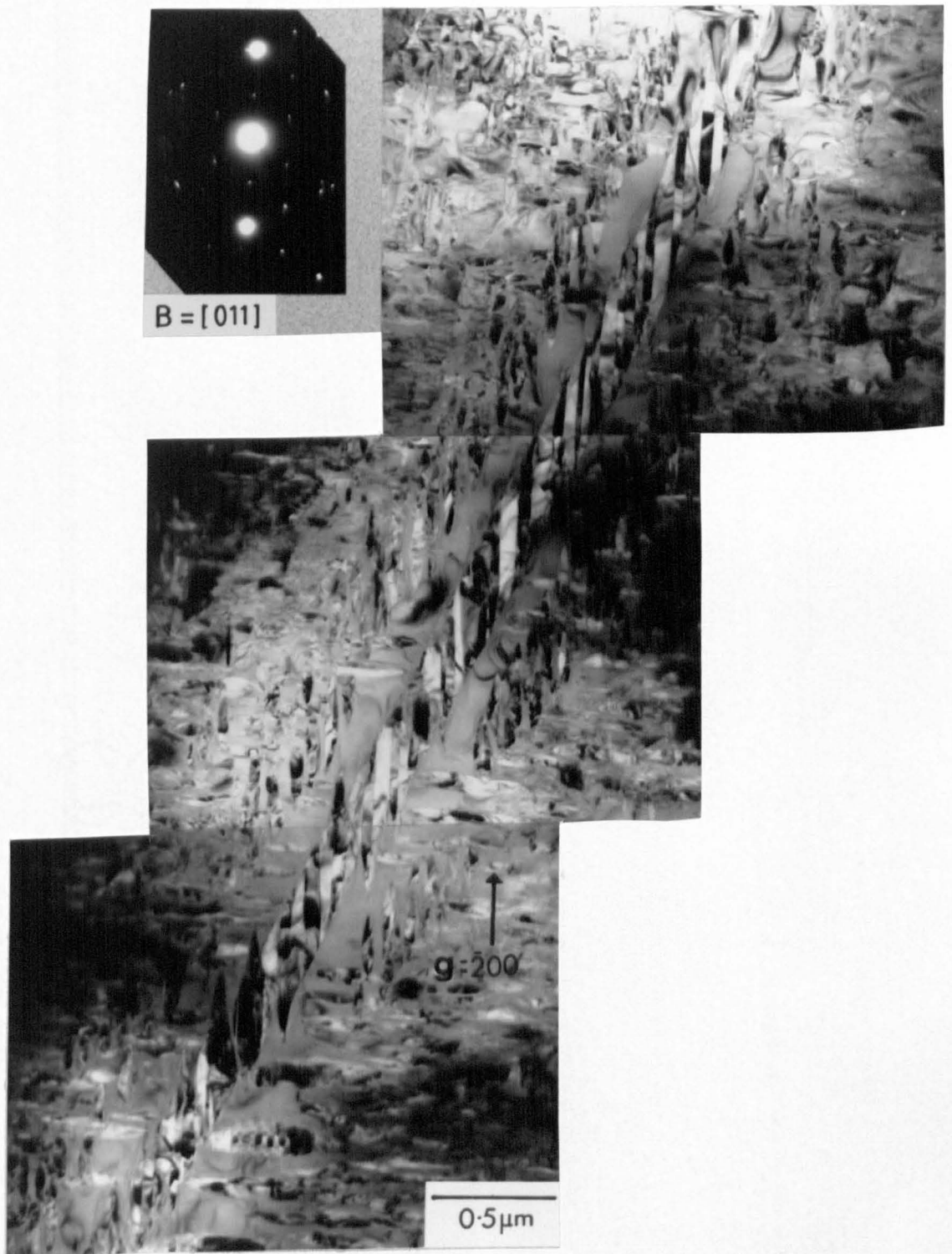
Fig. 3.13. Bright field micrograph showing the mechanism by which a series of precipitates grew heterogeneously to coalesce and form one large precipitate. See text for discussion.

not suprising in a material which has been furnace cooled through the eutectoid temperature.

In addition to the homogeneously nucleated t precipitates, several much larger precipitates were present with monoclinic symmetry, fig 3.12. This dark field image was formed using the diffuse intensity scattering from the cubic matrix mentioned above. Some of these precipitates had formed from the heterogeneous growth of a single precipitate. Others appeared to have formed from the coalescence of numerous smaller ellipsoids. One example of this mechanism is given in fig 3.13.

It is interesting to consider the mode of formation of such a line of precipitates, whilst the neighbouring precipitates appear to have grown homogeneously by an Ostwald ripening process. Bathena et al. [271] have presented SEM micrographs of similar features. Widely spaced arrays of long precipitates, apparently formed from several smaller ellipsoids, were found after ageing at temperatures above 1480°C. The morphology was considered to be a result of nucleation rather than growth. Bathena et al. [271] presented strain energy distribution and chemical free energy graphs as a function of position around the precipitate. These suggested that auto-catalytic nucleation is favoured in specific positions at these temperatures, specifically at about 30° to the longitudinal axis of the precipitate. Rapid growth at this temperature (1480°C) promoted coalescence producing a similar arrangement to that shown in fig 3.13. Rainforth & Nettleship [272] further examined the effect of cooling rate and isothermal holds on the precipitate distribution. A continuous cool from the sintering temperature produced an even distribution of very fine tetragonal precipitates, fig 3.15. No heterogeneously nucleated particles could be found except occasional large precipitates at pores. However, an isothermal hold at 1500°C gave rapid growth of some precipitates whilst the majority remained the size shown in fig 3.14. Clear precipitate free zones were present around the larger particles. Occasional heterogeneous precipitate morphologies similar to that shown in fig 3.13 were found. This evidence suggested that the phenomena was growth controlled rather than nucleation controlled [272]. The number of large precipitates was found to increase with ageing time, which would not be expected for nucleation control.

The presence of these large monoclinic precipitates in the Coors material would be expected to reduce the toughness because of the

reduction in the volume fraction tetragonal available for transformation. Nonetheless, the toughness levels recorded above are respectable for optimally aged materials so that the effect cannot have been substantial.

3.4.4 TZP Materials

The TZP pins and discs were supplied by Danite Hard Metals and Dynamic Ceramic LTD. In both cases, the ceramics were manufactured by isopressing followed by green machining and a subsequent binder burn out treatment. Sintering was carried out at 1400-1550°C for 2hrs, depending on whether the material was 2 or 3Y. The higher temperature generated a larger grain size and, therefore, a higher toughness. The powders were supplied by Toya Soda Corp and the binder was PEG 1000 used at a concentration of 3wt%.

The toughness was measured by indentation at 11.2 and 6.1 MPam$^{1/2}$ for the 2Y and 3y materials respectively. The hardness was 1.1 GPa.

The grain size of the 3Y material is shown in fig 3.15. A corresponding TEM micrograph is given in fig 3.16. The levels of intergranular glassy phase were very low, since none could be imaged either along the grain boundaries or at triple points. No rounding of the grains at grain junctions was ever found. Numerous defects such as low angle grain boundaries were present. The level of cubic phase was low in both materials, reflecting the high purity and homogeneity of the powders.

3.4.5 TZP-20vol% SiC Whisker Composite

The material was manufactured by Yang [273] by hot pressing, the details of which are described in detail in reference [273]. Pins were diamond machined from the hot pressed disc such that the majority of the whiskers were aligned perpendicular to the contact surface.

The microstructure of the material was briefly investigated by TEM, and was found to be very similar to that reported by Claussen et al. [274]. The hot pressing had led to an increase in the 2.5Y TZP grain size over and above the conventional material. The majority of the grains remained tetragonal, although several pockets were found which had completely transformed to monoclinic.

The distribution of the SiC whiskers was found to be uniform,

although at this loading whisker interaction was fairly common. The structure of the whiskers varied considerably. Many whiskers were of a random shape, whilst those having conventional aspect ratios invariably contained undulating sides. A typical example of this is shown in fig 3.17. Therefore, very little contribution to the toughness would have occurred from whisker pull-out.

The internal structure of the whiskers was variable, but contained a high density of planar faults (fig 3.17). The origin of these defects is discussed in detail by Nutt [275]. The whisker/ matrix interface frequently contained a glassy film.

100nm

Fig. 3.14. Dark field micrograph showing very fine tetragonal precipitates produced by a rapid cool from sintering (after Rainforth & Nettleship [272]).

1 μm
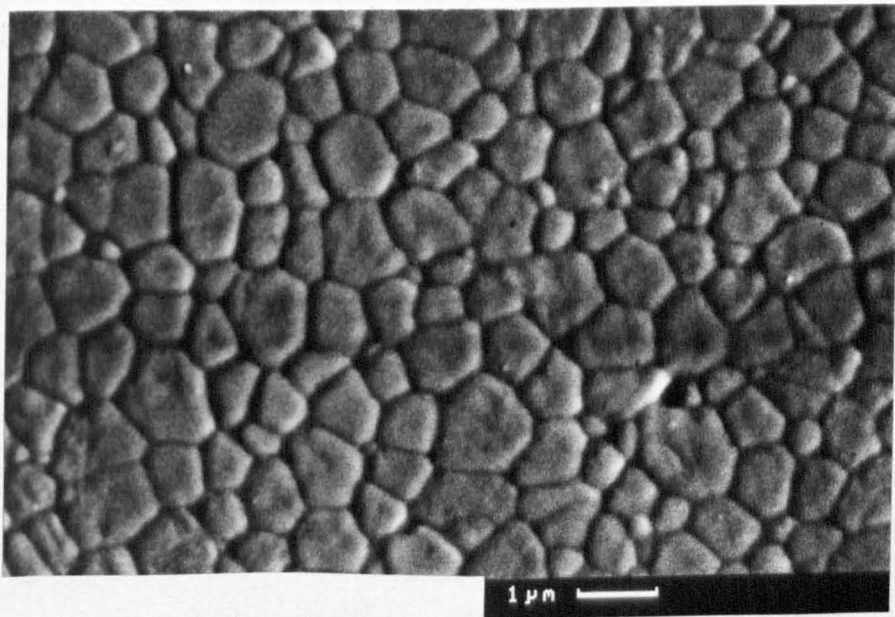
Fig. 3.15. SEM micrograph of the thermally etched surface of the 3Y-TZP.

Fig. 3.16. TEM micrograph of the same material as in fig 3.15. Note the angular triple points and the low angle grain boundary.
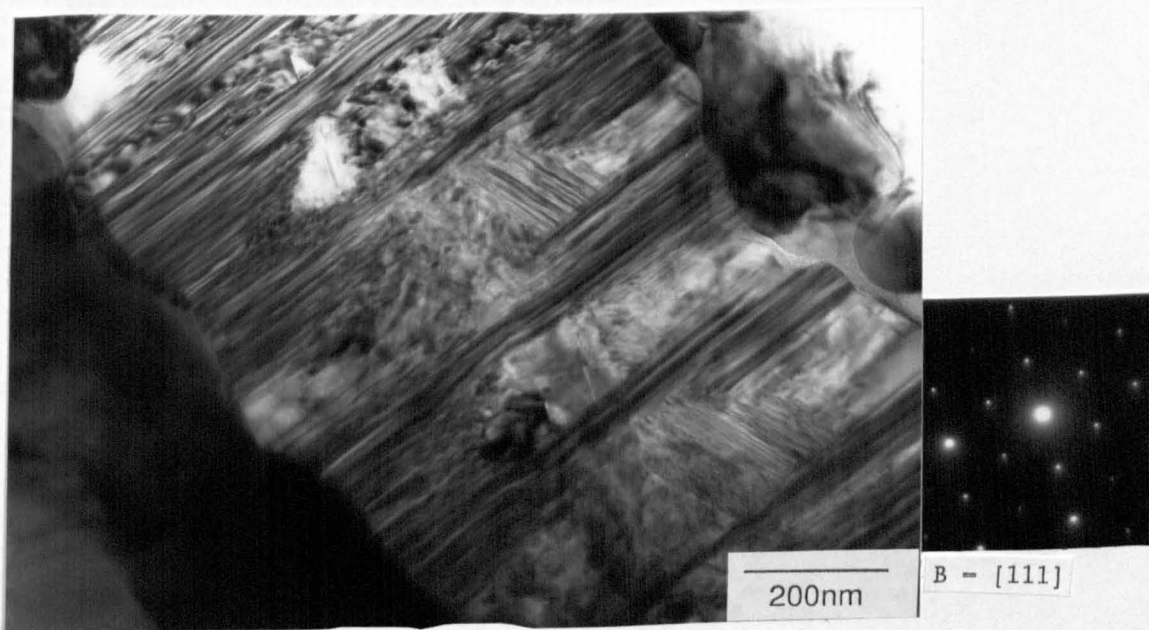
Fig. 3.17. TEM micrograph of the composite material showing the whisker morphology. Note the internal fault structure and the wavy whisker surface.

CHAPTER 4

ROLLING EXPERIMENTS

At the outset of this research, literature was not available on the high strain deformation behaviour of 316L stainless steel. The only comparable work was that of Blicharski & Gorczyca [211], which examined the deformation of a 20%Cr, 26%Ni austenitic steel. However, this material would be expected to have a higher SFE than 316L, because of its higher Ni content. Rolling experiments were therefore conducted on the supplied 316L, to establish the deformation mechanisms operating and also to provide a comparison with the microstructure generated by wear. However, Donadille et al. [190] have recently published detailed results for the deformation of 316L, which provide a useful comparison to the present work.

4.1 STACKING FAULT ENERGY.

Little research has been conducted on the SFE of the low carbon version of 316 stainless steel and, therefore, no clear guideline for the SFE of the material used in the present study is available. Measurement of the SFE by TEM estimates of partial dislocation separation is difficult, especially with 316 because the partials are rarely observable, and when they are found the separation is likely to be very small. Moreover, it is not certain that the equilibrium separation of the partial dislocation is achieved in thin foils. Alternative strategies lie in X-ray diffraction analysis, as detailed by Schramm & Reed [278], but these require very accurate measurement of the microstrain along the [111] direction. The following will examine the various linear regression analyses for austentic stainless steels in order to estimate the SFE of the 316L.

Several linear regression analyses of the SFE as a function of composition have been proposed to predict the SFE of stainless steels. Assessing the SFE of different alloys of varying composition by linear regression is difficult because the effect of individual elements changes when combined with other alloy additions. For example, Cr,Si

and Mn are generally believed to lower the SFE. However, when Ni, Cr, Mn and Mo are considered together, the following equation has been found [276]:

$$SFE= -53 + 6.2(\%Ni) + 0.7(\%Cr) + 3.2(\%Mn) + 9.3(\%Mo) \ (mJ/m^2)...(4.1)$$

which suggests a positive effect for Cr and Mn and also highlights the strong effect which the Mo content can have. The situation is too complex to describe the effect of more than a few of the elements in an individual equation, and therefore requires that the other elements be maintained at constant levels.

Schramm & Reed [276] have proposed the following equation:

$$SFE= 4 + 1.8(\%Ni) - 0.2(\%Cr) + 410(\%C) \ (mJ/m^2) \qquad ...(4.2)$$

Many researchers have found, as suggested in equation 4.2, that an increase in carbon content increases the SFE [276-279], but disagree as to the extent of this effect. Swann [280] examined the dislocation structure for a stainless steel over a range of carbon and nickel contents, and found the role of Ni to be dominant and that of the carbon content to be minimal, although it did have some effect, with a change in dislocation structure from cellular (0.1%C) to a planar array (0.001%C). Brofman & Ansell [277] have criticized the equation of Schramm & Reed [276] because of the high coefficient assigned to the carbon content and provide a modified linear regression:

$$SFE= 16.7 + 2.1(\%Ni) - 0.9(\%Cr) + 26(\%C) \ (mJ/m^2) \qquad ...(4.3)$$

Pickering [281] provides an alternative equation which omits the role of Cr, because the materials he tested contained constant levels, and ascribes a dominant role to carbon:

$$SFE= -1 + 2.02(\%Ni) + 321(\%C) \qquad ...(4.4)$$

One reason for the discrepancy between the above equations may well be the heat treatment schedule used in manufacturing the steels, for example, whether the carbon was dissolved in solid solution by a solution anneal and water quench, or was fixed as carbide.

The analysis of the material used in the present study was given in

the previous chapter (table 3.1). Equations 4.2 and 4.3 suggest SFE values of 39.6 and 28.3 mJ/m^2 respectively for this material. However, these equations do not take into account the Mn, Mo, and Si contents, which would be expected to increase SFE. Using the weight-percent equivalents plotted by Schramm & Reed [276] (which omit Si and C), a value of approximately 58 mJ/m^2 is obtained.

As noted above, the situation is too complex to ever fully describe the SFE by linear regression analyses. Measured values of SFE for 304 stainless steels are generally low, as shown by Schramm & Reed [276], who listed values quoted in the literature as covering a range of 8-30 mJ/m^2. The SFE for 316 is generally higher, reflecting the higher Ni contents and the presence of Mo. For example, Yang & Spruiell [278] measured an energy of 68 mJ/m^2, whilst Schramm & Reed [276] measured a value of 78 mJ/m^2, both from X-ray analysis. The material under consideration in this study contains lower carbon levels than either of the steels used in in the above mentioned work. The reduced carbon levels would be expected to lower the SFE by an amount between 1 and 12 mJ/m^2, depending on whether the carbon was initially in solid solution or tied up as carbide.

The normalised value of the SFE (γ) is given by γ/Gb, where G is the shear modulus and b is the Burgers vector [198]. Mecking et al. [198] have suggested that it is this value which accurately describes the width of the extended dislocations and therefore governs the deformation behaviour. For a 316L, Donadille et al. [190] evaluated this quantity as approximately 3×10^{-3} (although they relied on a SFE derived from one linear regression equation), which is about the same as for a 70/30 brass. Therefore, the deformation behaviour of the 316L should be similar to a 70/30 brass, even though the homologous temperatures are significantly different.

4.2 ROLLING EXPERIMENTS.

Samples of the as-received bar were rolled to strains up to 3. Temperature dependent effects were minimized by cooling the sample in iced water after each pass. The hardness as a function of true strain is presented in fig 4.1, which suggests that a saturation flow stress is achieved at strains above about 2. This contrasts the work of Blicharski & Gorczyca [211] who found that the hardness was still
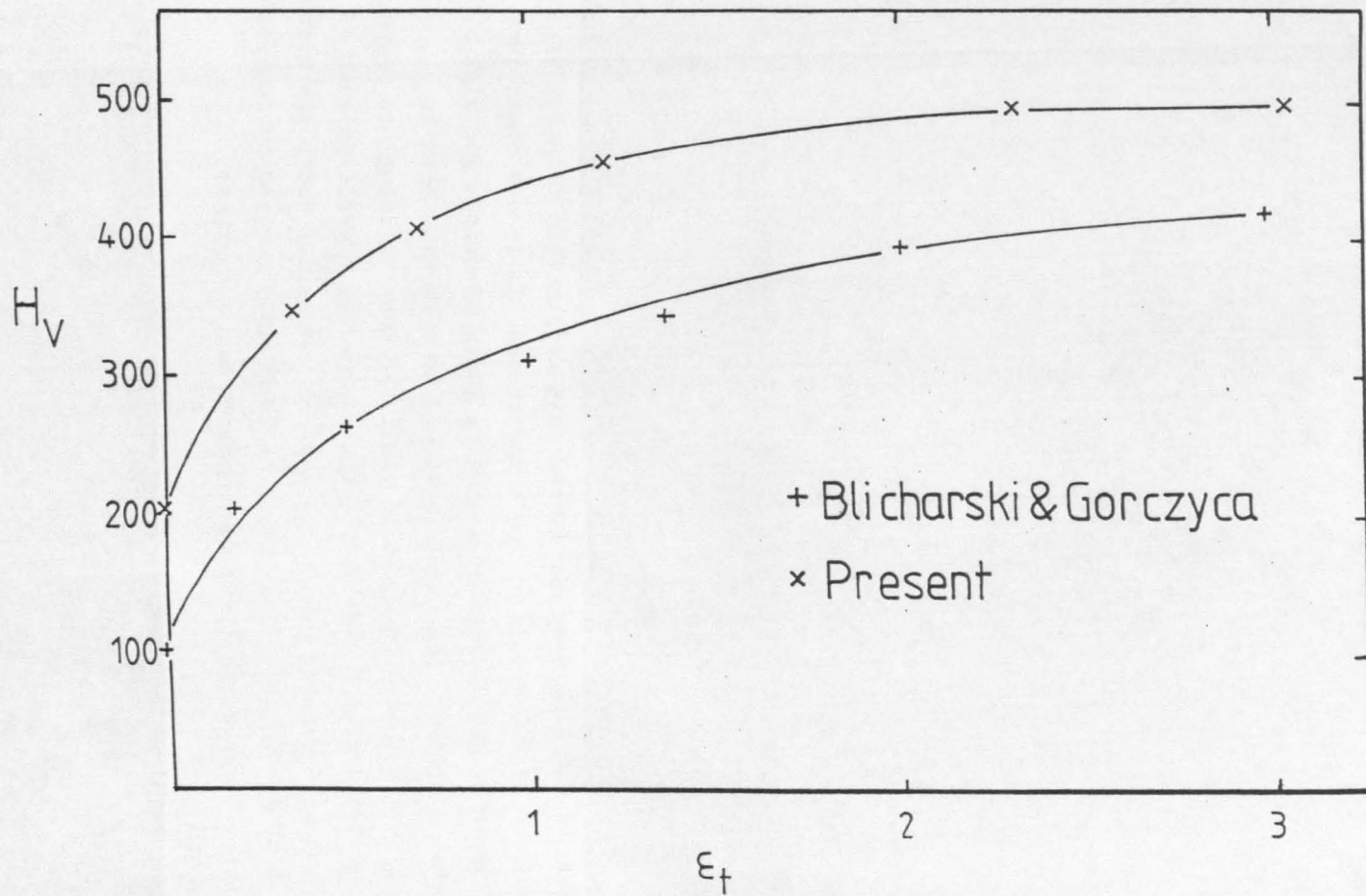
Fig. 4.1. Vickers hardness as a function of true strain, compared to the results of Blicharski & Gorczyca [211].

Whilst it has long been considered that deformation twinning is only observed in FCC metals at low temperatures, it is now clear that this observation was derived from tensile tests of medium and high SFE FCC metals. Moreover, the strain achieved in a tensile test is relatively small. It is now well established that twinning can occur in low SFE FCC metals ($\leqslant 35$ mJm^{-2}) during forming operations such as rolling and wire drawing, where the strains and strain rates are higher than in tensile testing. This point is adaquately covered by Sevillano et al. [191], Honeycombe [283] and Hatherly and co-workers [200,203,209,210,211,214].

rising at a strain of 4 for their 20%Cr, 26%Ni material. The difference is most probably a result of the material compositional differences (the higher Ni content will have increased the SFE compared to 316L). It should be emphasised that the apparent saturation flow stress may not be present when other techniques for measuring the flow stress of a rolled specimen are used. Plane strain compression also tends to produce a saturation flow stress, whilst, for the same material, tensile tests usually show continued hardening up to much higher strains. Tensile tests were not conducted on the rolled specimens since the hardness was considered to better simulate the type of stresses at a worn surface than a tensile test.

4.2.1 Optical Microscopy

Optical micrographs of transverse sections, parallel to the rolling direction, of the rolled samples are shown in figs 4.2-5. The original microstructure consisted of equiaxed grains about 90μm in diameter. The etch used was chosen to reveal the deformation structure, but it also proved sensitive to compositional changes within the material, (attributed to minor segregation of Mc, Ni and Mn during solidification [190]) which tended to partly obscure the deformation structure.

Twinning, which was contained within clear grain boundaries, was observed after a few percent reduction in thickness, at about ±30° to the rolling plane. The extent of twinning increased with strain, and existing twin colonies were gradually rotated towards the rolling direction. Twinning generally occurred on a single system within an individual grain, although occasional examples of twinning on two systems was found, fig 4.2.

At a reduction of 50%, some of the grain boundaries had become obscured, but regions which did not contain any twins were still apparent. Shear bands could be seen cutting through the twin colonies at angles of about 35° to the rolling plane (arrowed feature in fig 4.3). The exact shear band angles are difficult to establish without incrementally deforming a polished cross section. Hatherly & Malin [212] have discussed the angles at which shear bands form, and have noted that bands frequently form at angles below 35°. The reason for the formation at about 35° rather than at the angle of maximum shear stress, 45°, is not completely clear. At the high strains required for

100μm
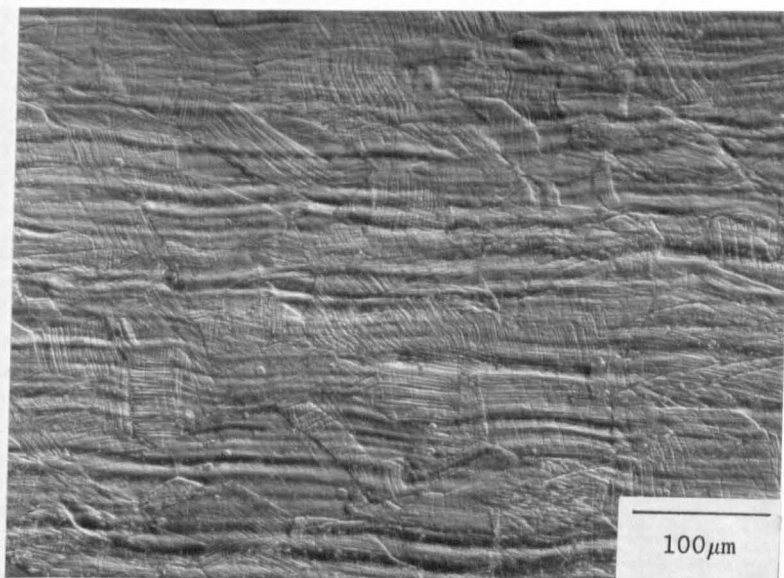
Fig. 4.2. Optical micrograph of a transverse section after a reduction
of 30%. Twin colonies can be seen within many grains but were usually
confined to one system, although examples of twinning on two systems
were present.

100μm
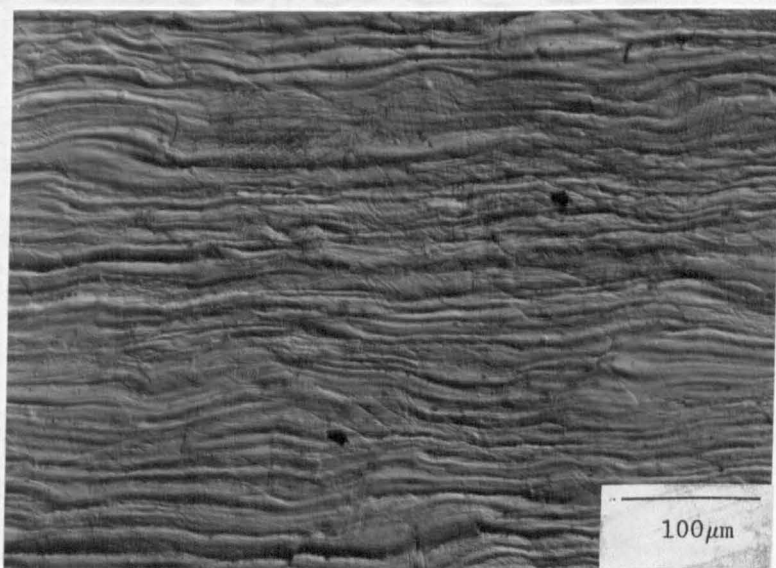
Fig. 4.3. After a reduction of 50% shear bands can be seen crossing
some of the twin colonies (eg those arrowed).
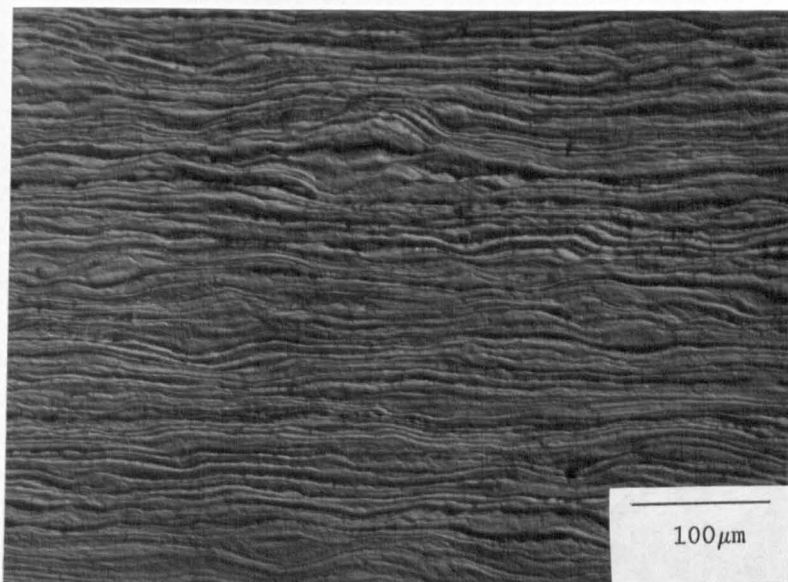
Fig. 4.4. After a reduction of 90% the majority of the twinned
structure had been divided into 'rhomboidal prism' by the shear bands.
Some of the shear bands and twin colonies had become aligned with the
rolling direction.

Fig. 4.5. After a reduction of 96% the majority of the structure had
become aligned with the R.D. but few twin colonies remained. No macro-
shear bands are present.

shear band formation the metal will have acquired a strong texture. Many researchers, as reviewed by Hatherly & Malin [212], have attributed the reduced angle from that at maximum shear stress to the formation of a texture. In a related study, Dillamore et al. [282] examined Luder's bands in hot rolled iron, which contained no texture, and found that the bands formed at the expected angle of 45°, adding to the evidence that texture is important.

At strains above about 2, (reduction of 86%) the twin colonies were either completely consumed by shear banding or were segmented into 'rhomboidal' prisms in a manner similar to that reported by Malin & Hatherly [200], fig 4.4. At a strain of 3, the majority of the microstructure consisted of shear bands aligned with the rolling direction, fig 4.5. Small twin colonies were still present, although greatly reduced in size compared to the 86% reduction sample. There was no evidence of macro shear banding, (bands covering the entire specimen width), although this would be expected to occur at higher strains. Observations by Blicharski & Gorczyca [211] that regions could remain untwinned to high strains, and therefore not consumed by shear bands, could not be confirmed in the present study.

4.2.2 Transmission Electron Microscopy

TEM observations were generally made on transverse sections, parallel to the rolling direction, although rolling plane foils were examined for the specimen reduced by 96%. A typical example of the microstructure at low strains is shown in fig 4.6. Initial deformation produced heterogeneous dislocation structures, in particular planar arrays parallel to the {111} planes. The dislocation structure depended on the orientation of the particular grain, with relatively uniform distributions occurring in many grains. Only a few dislocation arrangements could be described as a rudimentary cell structure. Observation of dissociated dislocations was rare, but some were found at very low strains, for example fig 4.7.

Further strain promoted twinning and a reasonably uniform dislocation distribution. At a strain of 0.36 (30%), twins tended to cluster into bundles. The twin spacing within a bundle was in the range 15-40nm, with gaps between bundles in the range 100-300nm. The twins contained a low dislocation density with dislocations forming a loose tangled structure.
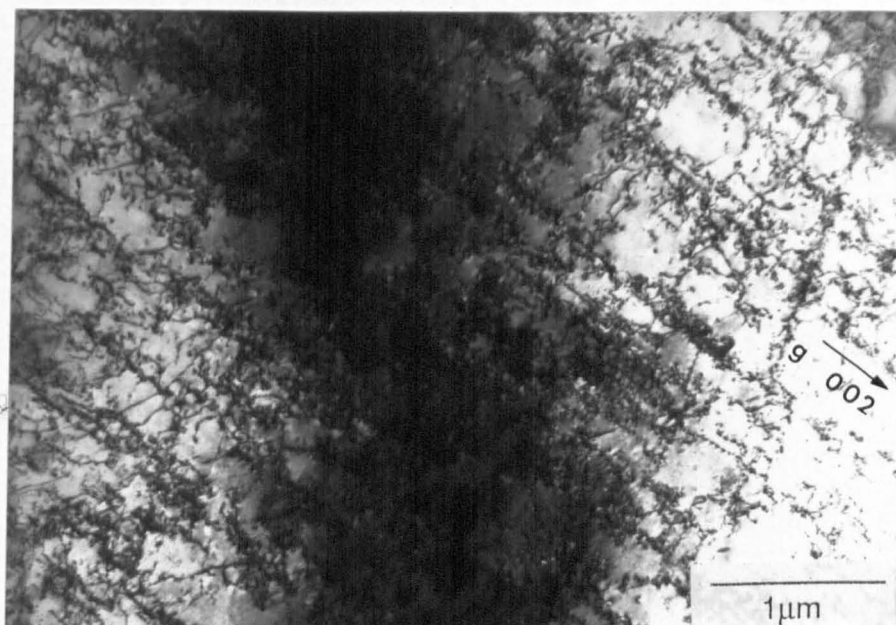
Fig. 4.6. TEM micrograph after a reduction of 4%. The dislocations
were piled up along the primary slip planes. Two beam conditions.
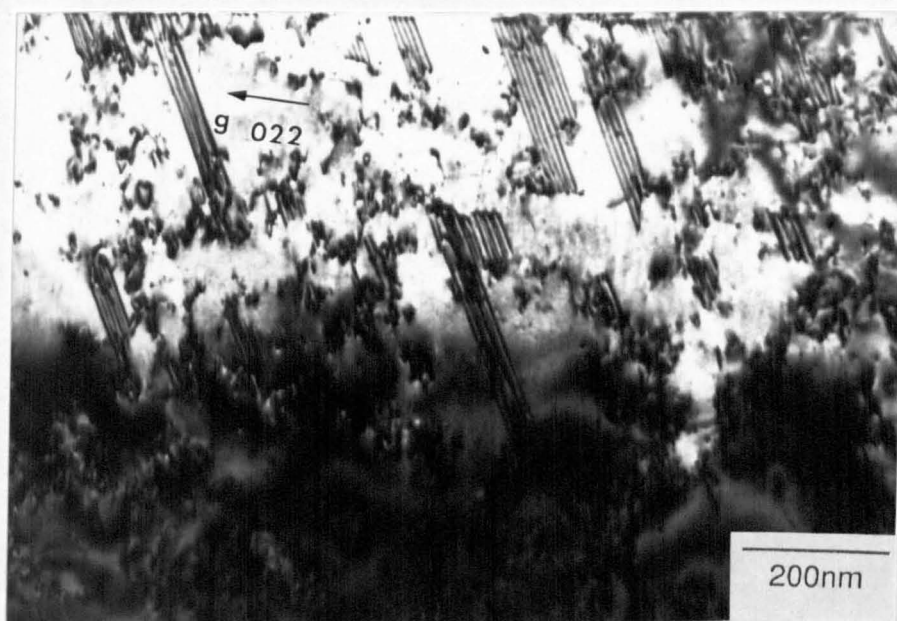
Fig. 4.7 TEM micrograph of stacking faults produced by a reduction of
4%. Two beam conditions.

The diffraction pattern (b) only contains austenite reflections and shows the classical twin orientation {111}<112>. Therefore, these colonies could only be interpreted as twins and not as martensite laths or closely spaced stacking faults.
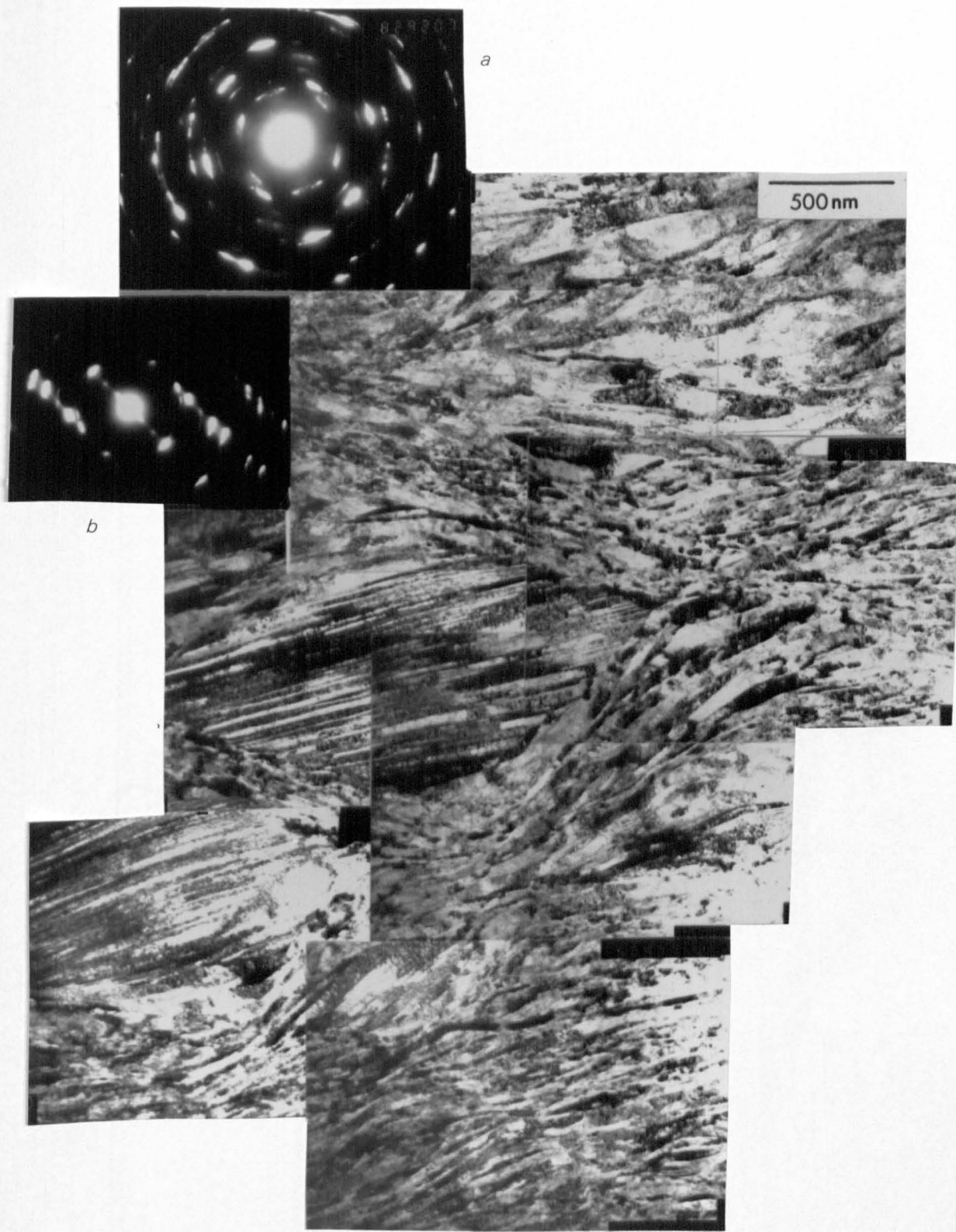
Fig. 4.8. TEM micrograph after a reduction of 90%. Shear bands have
cut through twin bundles to produce a 'rhomboidal prism' appearance.
DP (a) from coarse shear bands, (b) from twin bundle (neither are
corrected for rotation to the micrograph). (a) shows a wide variation
in crystallite orientation, although {110}<001> is strongly favoured.
The twin bundle, (b), exhibits a texture close to {111}<112>.

Homogeneous slip within the twinned structure is inhibited by the twin boundaries except where the glide plane of the dislocations is parallel to the twin plane. Thus, homogeneous deformation is precluded in the majority of the structure at this stage. With continuing stress application a region of instability must develop, capable of circumventing the problem of dislocation glide within the twins. This instability occurs in the form of a shear band.

Shear bands progressively cut through the twin bundles at strains above 0.7, with band widths in the range 0.1-1μm, fig 4.8,9. The twin structure was completely destroyed by the passage of a shear band which was associated with very high local strains. A shear band is believed to develop as a result of an avalanche of dislocations, producing a flow of material which is analogous to that of a liquid [213]. Local curvature of the twins adjacent to a band was frequently found, indicating the manner in which the twins were locally swept into the band. Duggan et al. [213] have shown, by scratch displacement experiments, that the shear strain associated with the formation of a shear band in a 70/30 brass is usually in the range 3-4, but could be as low as 1 and as high as 10.

The structure of those shear bands which had just formed was difficult to resolve, because of incomplete recovery within the crystallites, and the poorly defined boundaries between crystallites. Crystallite sizes were in the range 20-100nm, with an average of about 30nm and aspect ratios of 2:1-3:1, elongated in the direction of the shear band. The observed microstructure does not relate to the dynamic structure of a shear band, but is the recrystallised or recovered state, i.e. when the 'liquid' has 'resolidified'.

The orientation within a newly formed shear band appeared to be completely random, although analysis proved difficult because of the very fine crystallite size, and because of the small width of these bands. STEM microdiffraction patterns failed to show any preferred orientation within the band. Misorientations between individual crystallites was obviously large and there was no tendency towards a cumulative orientation change across a band. However, Duggan et al. [214] have performed a more detailed study and shown that, although the orientation varies considerably, there is a preference for sheet plane orientations near {110} with the {110}<001> being substantially populated.

Duggan et al. [214] demonstrated that a shear band only operates

once, after which it is gradually rotated towards the rolling direction. Thus, new shear bands are formed, which shear through existing shear bands as well as twin bundles, or have their passage arrested by pre-existing shear bands [212]. In the present study, shear bands occurred as two sets of opposite sign, dividing the twinned structure into an array of 'rhomboidal prisms' (fig 4.8). The occurrence of two sets of shear bands of opposite sign is indicative of the low SFE of this material. Each unit of twinned material was progressively divided up into smaller units as deformation proceeded. A strain of 3 (96% reduction) developed a microstructure which consisted of approximately 90% shear banded material. Occasional twinned pockets were still present, figs 4.5,4.10, but these were generally small and aligned with the rolling direction. Very few carbides were found in the material, but where these were present the shear bands tended to flow around them in a manner similar to that of the twin colonies, developing fine voids at the carbide/matrix interface.

At a strain of 3, the majority of shear bands had become aligned with the rolling direction and had become sharper, consisting of elongated crystallites with clearly defined walls and low internal dislocation densities, fig 4.11. Nonetheless, the banded structure was still very 'wavy' as illustrated by the dark field micrograph in fig 4.12. A small crystallite size increase had occurred compared to that of the initial shear bands, and aspect ratios had increased markedly. This indicates that recovery mechanisms had taken place, and that the deformation of the structure had become more homogeneous. Further strain reduced the thickness of these crystallites. However, deformation above a strain of 3 could not be produced (because of the available equipment), and therefore the relationship between specimen thickness and crystallite size reduction could not be established. The crystallite size in the majority of the structure, after a strain of 3, was in the range 35-45nm. The smallest crystallites found were about 15nm with the largest at about 200nm. These values are marginally larger than those in the freshly formed shear bands noted earlier. However, the crystallite size after a strain of 3 was significantly smaller than reported by Blicharski & Gorczyca [211], fig 2.27, which explains the higher values of hardness found in the present work, fig 4.1.

The homogeneous deformation of such a fine crystallite structure
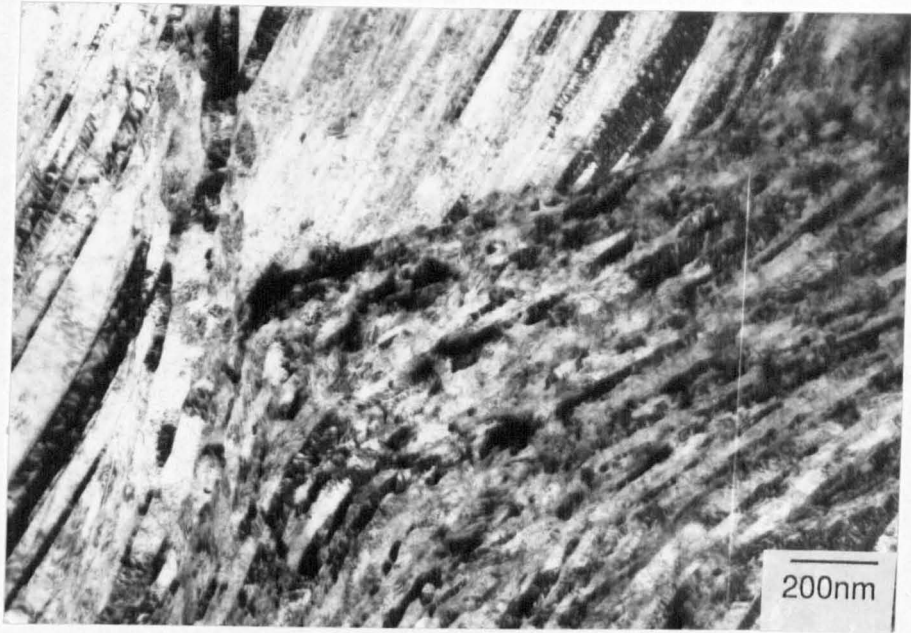
Fig. 4.9   TEM micrograph after a reduction of 90%, showing a shear band cutting through a twin colony, dividing it into two.
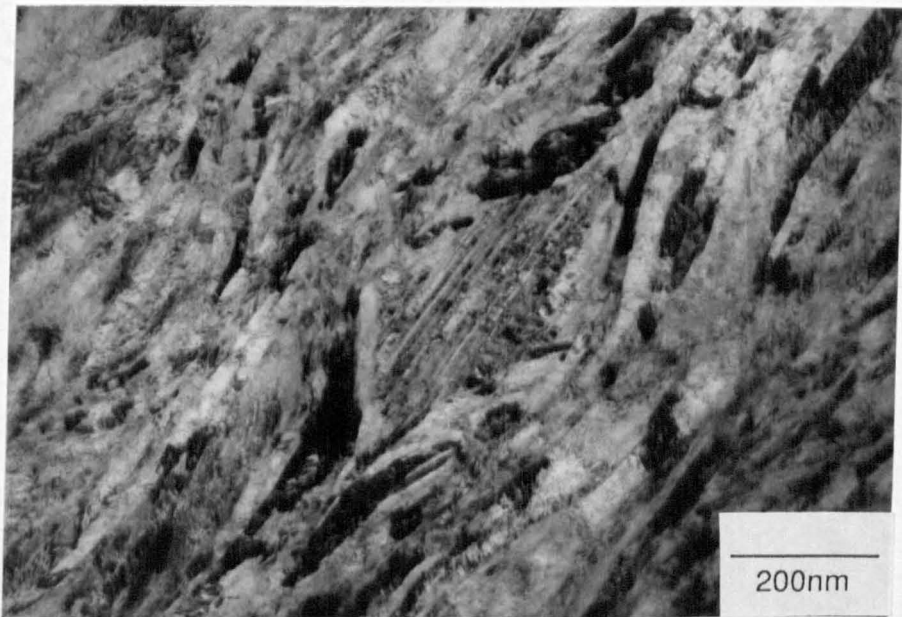
Fig. 4.10   TEM micrograph after a reduction of 96%, showing a small twin colony which is aligned with the rolling direction.   The shear banded structure can be seen flowing around the twins.
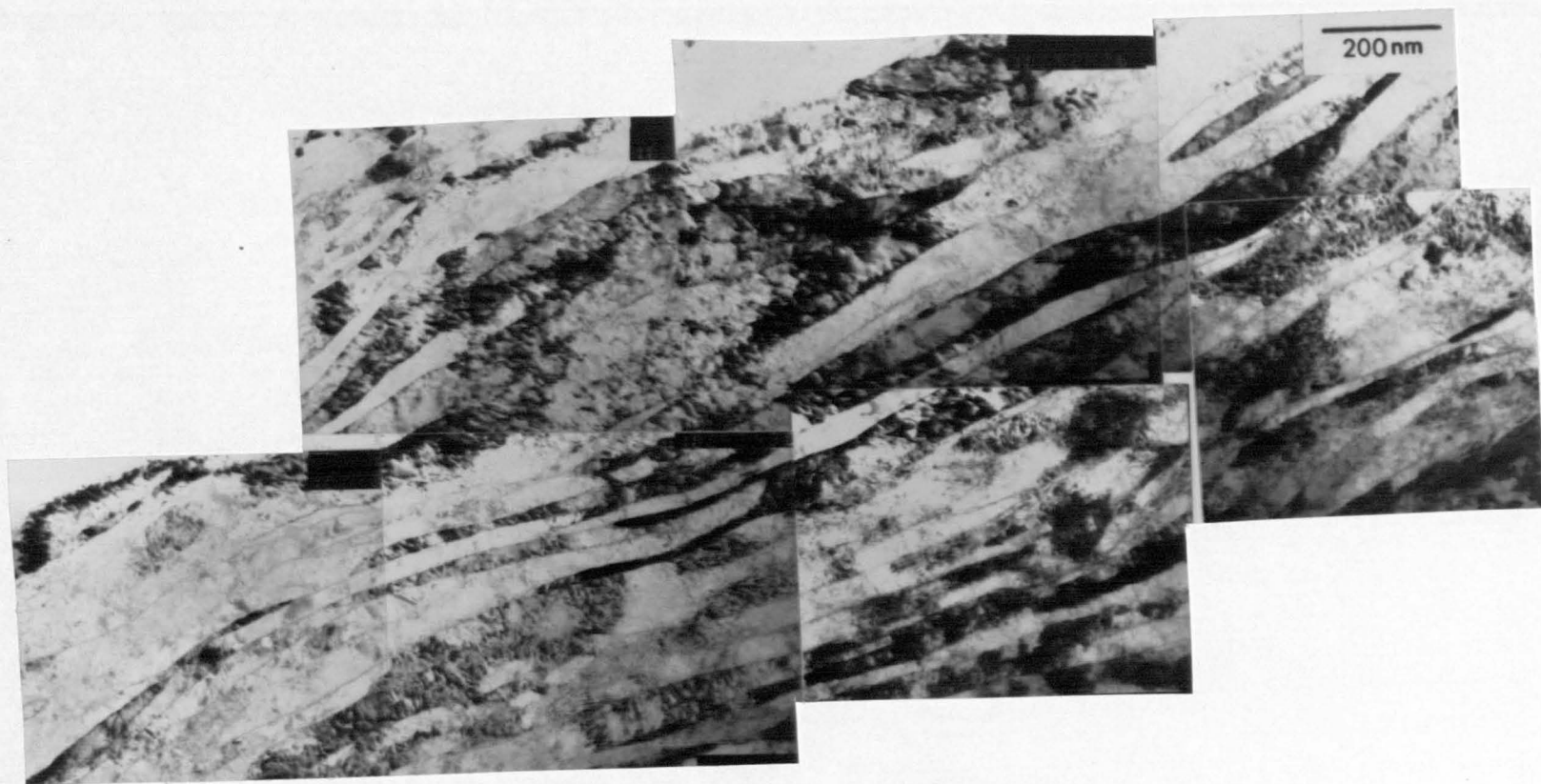
Fig. 4.11. TEM micrograph after a reduction of 96%. The crystallites have become elongated with clearly defined boundaries. The dislocation density was low, but dislocation interactions can be seen in larger crystallites.

might be thought incompatible with twinning at low strains. However, the crystallites are too small to allow significant dislocation interaction, and therefore the glide dislocations encounter few barriers in crossing them. Such glide dislocations are presumably incorporated into the boundaries thereby adding to the misorientation between crystallites and the development of the texture. The larger crystallites in fig 4.11 contained more dislocations, which had become interlocked, than did the thinner crystallites, supporting this assumption. However, occasional very fine twins were found within individual crystallites, suggesting that dislocation glide and recovery was still difficult at times. The ability of the structure to allow dislocation glide reduces the rate of work hardening, and consequently, the rate of formation of macro shear bands tends to be slower than that of the initial shear bands. Since macro shear banding has been shown to be a source of failure [200], the ease of dislocation glide at this stage of deformation would appear to be very important in determining the ultimate ductility of the material.

Whilst 316 is considered to be stable with respect to transformation to martensite during deformation, samples which had been deformed to a strain of 1.5 were magnetic, indicating an increase in the ferritic component with strain. XRD of the rolled materials showed a small α' peak. Close examination of diffraction patterns also revealed faint α' reflections, but these were too diffuse and close to the austenite reflections to be clearly imaged in dark field. No areas could be found with a different structure, suggesting that the α' crystallites deformed in the same manner as the austenite. Some evidence was present in diffraction patterns that the α' formed during formation of the shear band, rather than during subsequent deformation of the shear banded structure. It would appear that the presence of a small volume fraction of α' did not change the mode of deformation.

A rolling plane foil was prepared of the sample deformed to a strain of 3. The structure of the shear bands in this specimen was substantially more difficult to evaluate than with transverse sections. Crystallite boundaries were more obscure, fig 4.13, and generally appeared more rounded. The observation of rounded boundaries, coupled with low internal dislocation densities and high misorientations has led to the suggestion that dynamic recrystallisation was taking place [213]. This was subsequently shown to be incorrect, and the present results confirm this finding.
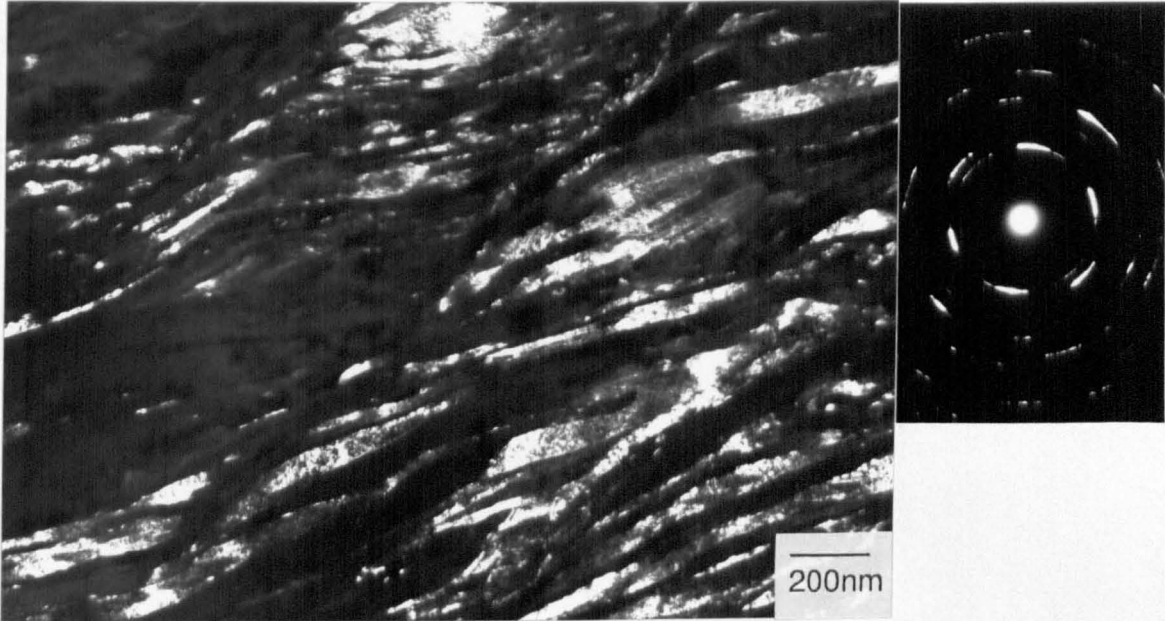
Fig. 4.12. Dark field TEM micrograph of the shear banded region after a reduction of 96%. The flow can be seen to have been 'wavy'. The diffraction pattern indicates a strong {110}<001> texture in this region, but little evidence of {110}<112>.
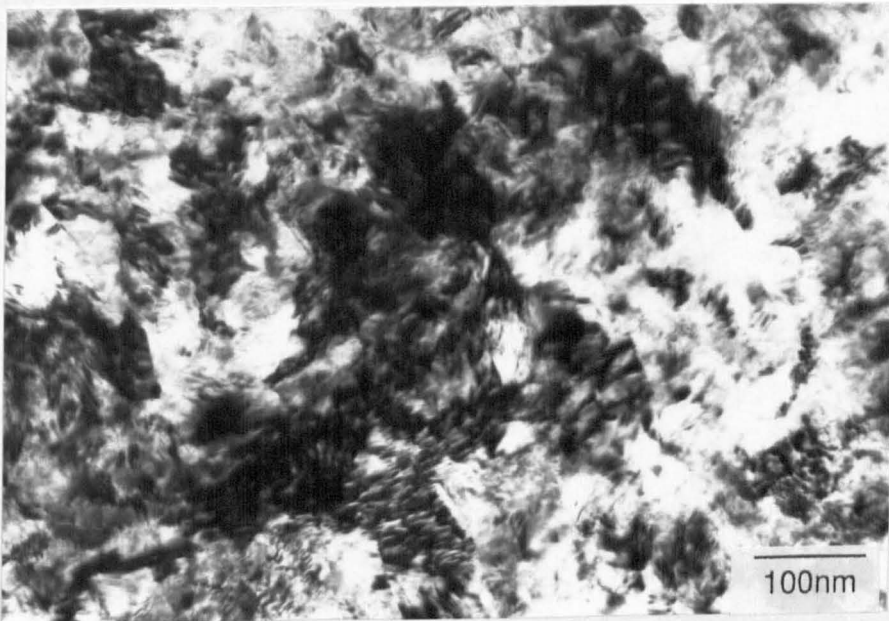
Fig. 4.13. TEM micrograph after a reduction of 96%, rolling plane foil. The structure of the crystallites in the shear banded region was more difficult to discern, although they appeared more rounded than in transverse foils.

B = [111]
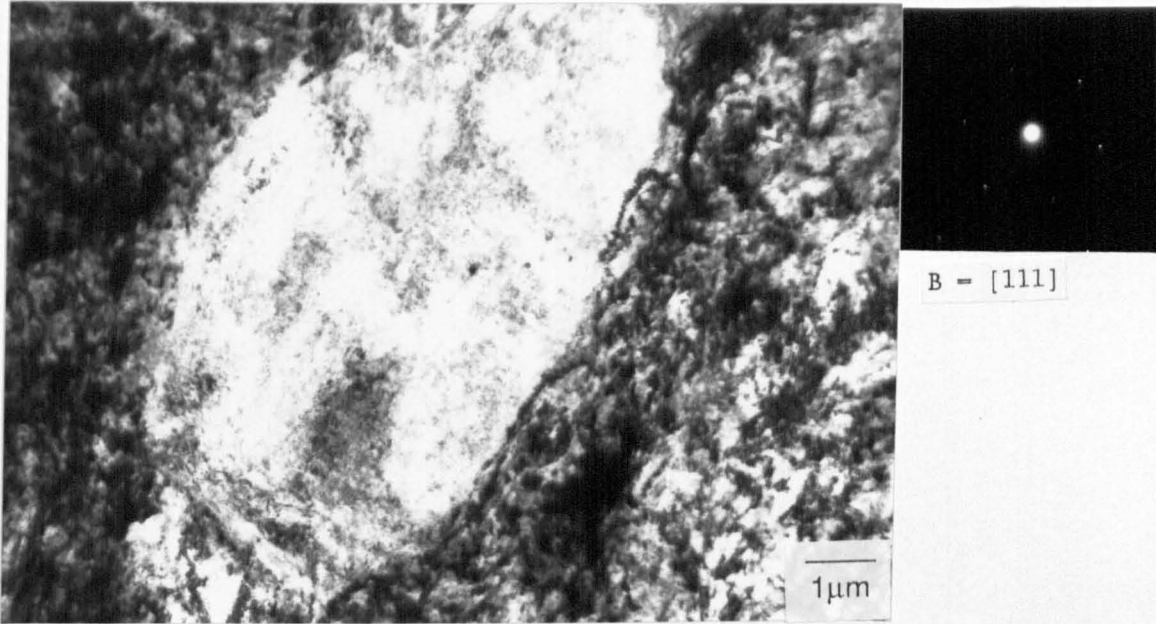
Fig. 4.14. TEM micrograph after a reduction of 96%, rolling plane
foil, showing a small δ ferrite colony which has not been elongated by
the deformation.
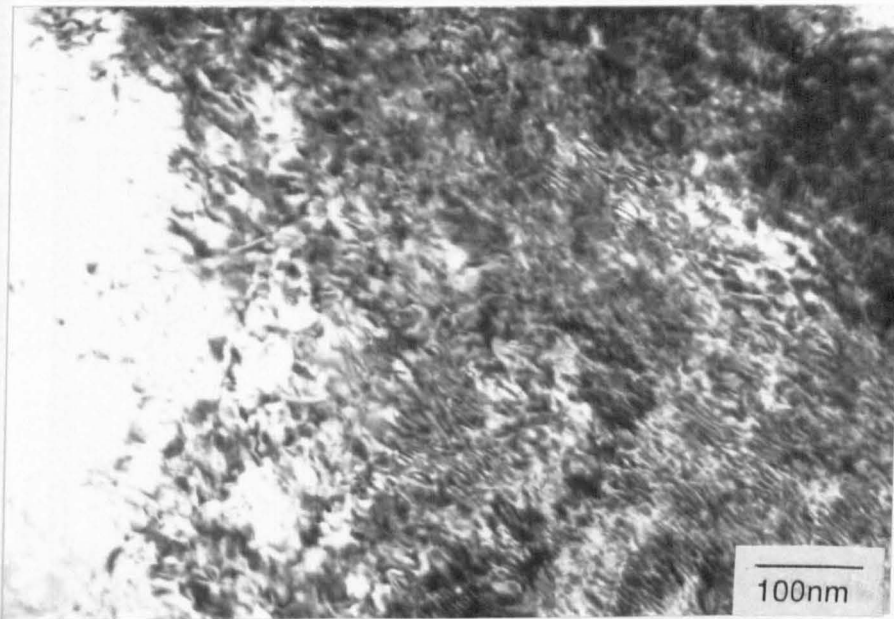
Fig. 4.15. TEM micrograph showing a detail of fig 4.14. The δ ferrite
contained a uniform, high, dislocation density. The colony showed a
clear {111}<112> texture.

Rolling plane foils also revealed a feature not observed in transverse foils, as shown in fig 4.14. The small colonies had a BCC structure and were considered to be δ ferrite. The areas had not been significantly elongated even at a strain of 3, and contained a very uniform, high dislocation density, fig 4.15. The majority of the colonies exhibited a (111)<112> type texture. This is a possible rolling texture for a BCC metal, but (001)<112> is more common [283]. Apparently, since these colonies had remained untwinned, they had not initiated shear bands. However, since their starting dimensions were not known, it is not clear to what extent their size has been reduced by the passage of shear bands initiated in twinned regions. Nonetheless, it would appear that the colonies had undergone very little strain during the deformation, acting in a manner analogous to the very small rhomboidal prism twin colonies.

The δ ferrite colonies were distinct from the regions which did not twin and therefore sustain shear bands, as found by Blicharski & Gorczyca [211] for an austenitic stainless steel. They reported that austenitic grains which were initially orientated with (100) planes parallel to the rolling planes and <100> directions parallel to the rolling direction did not undergo twinning. A similar result was found by Heye & Wassermann [284] for silver single crystals, who reported that this orientation could deform by slip, whilst all others deformed only by twinning. The untwinned areas in the work of Blicharski & Gorczyca [211] deformed by conventional slip mechanisms providing an elongated subgrain structure. These areas were found to be substantially softer than the matrix, a feature attributed to the absence of twinning and subsequent shear banding. At high strain, these regions could only be easily differentiated from the shear banded structure by the orientation relationship. A few areas could be found in the present study which appeared similar to those described by Blicharski & Gorczyca [211], although these were infrequent. This suggests that it is not purely the initial orientation which is important in determining whether homogeneous slip can be sustained to high strains, but also the specific SFE, which appears to be lower in the present case compared to the material used by Blicharski & Gorczyca [211].

In figs 4.9,10 the twins had rotated almost completely towards the rolling direction, with the twin colony showing a 'microtexture' of the form (111)<112>. The texture of the shear banded region was much more

complex, although it can be seen that there was a strong preferential orientation of the {110} planes. Whilst no definitive texture could be ascribed, there was certainly a significant {110}<001> portion, which is also present in freshly formed shear bands. Figure 4.12 also shows strong evidence of the {110}<001>, but the {224} ring was too weak to positively identify whether the second brass texture, {110}<112>, was present.

Duggan et al. [214] have discussed the textures generated by rolling low SFE, FCC metals. They reported that the initial deformation produced {111}<110> type texture as a result of dislocation glide, (which was largely restricted to the primary slip planes). The onset of twinning provided a build up of {111}<uvw>, with <112> and <110> being the most common. The present results confirm their finding that the twin and matrix elements remained coupled and gradually rotated towards {111}<112>. Figure 4.9 shows the remnants of the {111}<112> type texture which was produced by the twin colonies. The majority of the shear banded structure exhibited {110}<001> type texture. As noted earlier, this texture is a result of the average of the crystallites in the shear band, with individual elements deviating significantly. The second component of the brass texture, {110}<112>, is not present in the freshly formed shear bands [214], and develops during subsequent deformation. This component of the texture is believed to be a product of the more homogeneous deformation mechanisms which dominate above strains of about 3 [214]. With the present results no significant evidence of the brass texture was found in selected area diffraction patterns. However, homogeneous deformation mechanisms such as dislocation glide had clearly taken place and it would be reasonable to assume that {110}<112> would be evident in pole figures of material deformed to a strain of 3.

Duggan et al. [214] and Hutchinson et al. [210] recorded the change in pole density with strain for a 70/30 brass. Whilst no rigorous texture measurements were undertaken in the present work, the intensity of various austenite peaks as a function of strain was used as a crude guideline. In agreement with Duggan et al. [214], the (220) reflection showed an initial rapid rise in intensity followed by a slower increase. The (111) reflections exhibited an initial drop in intensity, with the peak becoming very small after a reduction of 30%. The intensity of the peak then increased with strain. Duggan et al.[214] showed that a maximum in the (111) peak intensity occurred

afer a reduction of about 80%, beyond which the intensity started to fall, fig 4.16. The initial depletion of (111) occurred because of the texture developed by conventional slip, which is similar to the texture developed in copper. This provided a rapid initial increase in the (110) pole density. The onset of twinning led to an increase in the (111) pole density as a result of the {111}<uvw> component discussed above. This was further enhanced as the twin colonies were rotated towards the rolling direction. The (311) pole figure represents the copper type texture component {211}<111>, which remained constant during the dislocation glide regime, but was then depleted as twinning became dominant. After a reduction of about 80% the texture was increasingly determined by the shear banding of the type {110}<001> giving an increase in the {110} pole density and a reduction in the (111) pole density. At strains of 3 and above, the homogeneous deformation within the shear banded structure led to an increase in the second brass texture component, namely {110}<112>, which further increased the (110) pole density.

Interestingly, Donadille et al. [190] reported a very sharp texture in the crystallites in freshly formed shear bands. Several examples were given of crystallites having {110}<001> with respect to the normal direction (ND), the rolling direction (RD), and the transverse direction (TD). As noted above, there was some evidence of this texture, both in the present work and in other studies on brass, although this orientation relationship was only seen when averaged over numerous crystallites, and was never as sharp as that suggested by Donadille et al. [190]. These authors only provided STEM microdiffraction patterns of selected individual crystallites rather than any selected area diffraction patterns. It is probable, therefore, that there is no substantial difference between the present results and those of Donadille et al. [190].

The general characteristics of the microstructural development confirms that the 316L behaved as a low stacking fault energy material, and, therefore, that the reduced carbon content has reduced the SFE compared to standard 316. The deformation scheme appears similar to that observed by Donadille et al. [190] who also studied the rolling of 316L, although these authors found no α' martensite.

The reduction in crystallite size reported by Donadille et al. [190] was believed by them to be associated with the formation of cells approximately 10nm in diameter. This was not fully confirmed by the

present study although the absence of microstructural evidence by Donadille et al. [190] makes such a comparison difficult. However, there was certainly evidence in the present work of dislocation structures within the larger crystallites, which undoubtedly contributed to the reduction in the measured crystallite size with strain. Donadille et al. [190] referred to the crystallites produced by shear bands as 'microbands'. Such a description is more usually confined to subgrain formation in high SFE materials. Moreover, these authors suggest that the 'microbands' form as elongated subgrains, rather than the poorly formed low aspect ratio crystallites usually reported for shear bands in low SFE metals. However, it is probable that the authors have not distinguished between newly formed crystallites and those which have been subsequently deformed, in which case there is no significant difference between their observations and the present results.

The deformation scheme is very similar to that reported by Hatherly and co-workers [209,210,212,214], for 70/30 brass. However, twinning was more rigidly confined to one system in 316L than was reported by these authors for brass. Additionally, no evidence of macro-shear bands was found in the present study. In contrast, Hatherly & Malin [209] reported macro-shear bands from a strain of about 2 up to the highest strain of 5. Both these observations suggest that the material in the present study has a slightly higher specific SFE than 70/30 brass. However, there do appear to be some differences, depending on the individual brass studied. Hutchinson et al. [210] observed a poorly developed cell structure in certain areas and found only occasional twins after a reduction of 30%, whereas in the present study twinning was widespread after this strain (fig 4.2). It is possible that the apparent variation in SFE is a result of small differences in strain rates used and temperature rises generated during deformation, and that any difference in specific SFE between 70/30 brass and 316L is small. Had strains above 3 been achieved in the present work, it is likely that macro-shear bands would have been observed.

The 316L showed important differences to the austenitic steel examined by Blicharski & Gorczyca [211]. In the present study, the dislocation configuration at low strains tended to be more heterogeneous than that found by these authors, and the onset of twinning occurred at marginally lower strains. The present study failed to find any areas which did not contain deformation twins, and

subsequently shear bands, in transverse sections. Most significantly, the crystallite size at a strain of 3 was significantly smaller in the present study compared to that reported by Blicharski & Gorczyca [211], confirming that the SFE of the 316L was lower than that of the austenitic steel examined by these authors.
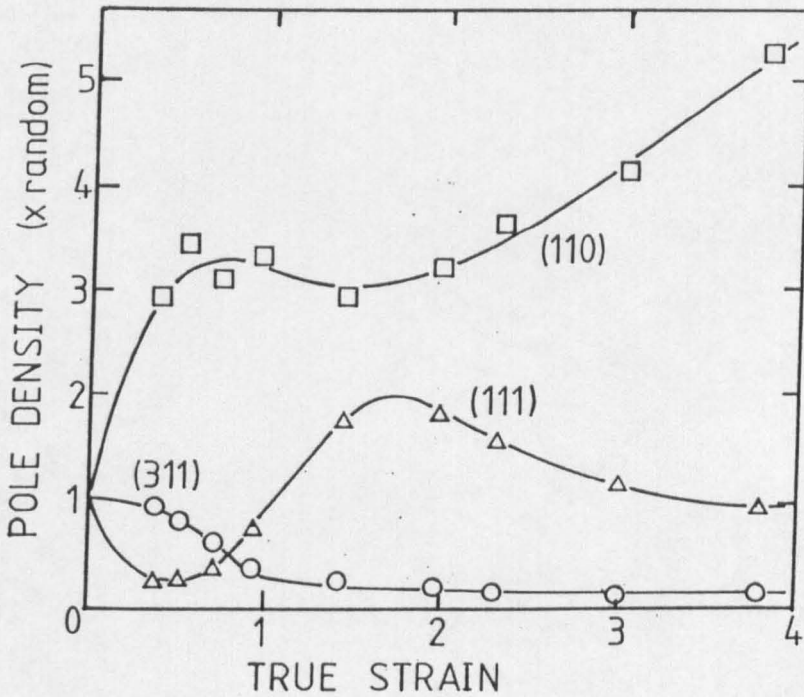
Fig. 4.16. Inverse pole figure data showing densities of selected planes parallel to sheet surface. After Hutchinson et al. [210].

CHAPTER 5

WEAR OF 316L STAINLESS STEEL PINS AGAINST ZIRCONIA DISCS

5.1 INTRODUCTION AND AIMS

Austenitic stainless steels are generally considered to have poor
wear resistance [285], although there are few reports of the wear
behaviour of this material in the literature. Publications are
available on the wear of type 304 stainless steel [256-259] (standard
18%Cr, 8%Ni). The behaviour of this material is dominated by the
formation of a thick martensite layer at the sliding surface, which
impairs its tribological performance. Since 316L generally does not
transform to α' during deformation, the results for T304 will not be
discussed, except where its oxidation behaviour is of interest.

This chapter will consider the wear performance of 316L against
both Y-TZP and Mg-PSZ discs. The effect of load was investigated using
optimally aged PSZ discs whilst the effect of speed was investigated
with 3Y-TZP discs. As noted earlier, the pins were of primary
interest, since these suffered the majority of the wear. Therefore,
the effect of toughness of the zirconia was not considered in these
tests. The effect of transfer to the disc will be discussed in this
chapter so that conclusions can be drawn about the wear mechanism of
the couple as a whole. However, the role of transformation and the
investigation of the subsurface zones in the disc will be considered in
chapter 6, along with the results on the wear of the zirconia pins.

This chapter will start by considering the wear rates of the pins
as a function of load. Surface characterisation by optical microscopy
and SEM, and a full analysis of the wear debris, will be used to
identify the wear mechanism. The main sections of the chapter will
then report the deformation mechanisms which take place at and below
the worn surface of the 316L. These will include an analysis of the
depth of deformation, the texture formed, the crystallite size as a
function of depth, temperature generation and the role of surface
oxides. The above will be used for a general discussion on the
importance of the deformation mechanisms, with comparisons being made
to the literature and to the microstructure generated by rolling. In

addition, the relevance of some of the available analytical equations will be considered and wear equations for the present case postulated. Finally, the results of a brief investigation into the effect of sliding speed will be reported.

5.2 PIN WEAR RESULTS

The details of the test conditions and wear factors are given in table 5.1. The wear factor is defined as the wear rate (mm^3/m) normalised by the load, see equation 2.18. The weight loss was measured at regular intervals during each test, the results of which are presented in fig 5.1. The corresponding average wear factors are plotted as a function of load in fig 5.2. The wear factor was found to decrease with load which is the opposite trend to that found by Smith [285-287], (who studied reciprocating wear of self mated 316). The effect was so pronounced that the wear rate was a maximum for 24N/pin, but then decreased with increased load, fig 5.1. The wear factors though high, are of the order expected for a single phase metal.

The wear factor was found to change with sliding distance for all tests, fig 5.3, with the exception of 7.6N/pin. Therefore, no clear value of the wear factor could be used to characterise the wear rate. The values presented in fig 5.2 are those for the entire test, that is for approximately the same total wear. Values for the wear factor excluding the running-in period (i.e. as close to the steady state wear rate as possible) also showed a similar trend to fig 5.2, although absolute values varied slightly.

The running-in period for each test was comparatively short, invariably less than 1km. During the initial stages of the test, the friction coefficient, μ, was substantially lower than the steady state value, and there was little noise from the wearing couple. As the test proceeded a dull squeak was produced which became louder with time. In the low load tests the squeak appeared only after several hundred metres, whereas at loads above 24N, the squeak was present after about 50m.

TABLE 5.1

TEST CONDITIONS AND WEAR DATA

LOAD (N)	2.23	7.0	7.6	24.1	37.4	55.1
Initial μ	0.2	0.25– 0.35	0.24– 0.35	0.2– 0.3	0.27 0.37	0.2– 0.28
Steady state μ	0.29– 0.33	0.18– 0.29	0.17– 0.33	0.2– 0.33	0.19– 0.31	0.21– 0.33
Peak μ	0.33	0.34	0.47	0.36	0.34	0.33
Dist. to steady state (m)	445	<150	<100	<100	<100	<100
Total dist (km)	109	35	37	13.4	16.8	20
Wear factors						
pin 1	1.8	1.63	1.21	1.37	0.52	0.43
pin 2	1.77	1.68	1.83	1.0	0.76	0.28
pin 3	1.7	1.65	1.47	0.74	0.59	0.26
Average All x10^{-4} mm^3/Nm	1.76	1.65	1.50	1.04	0.62	0.32

The above values are for a sliding speed of 0.24 m/s, against a Mg–PSZ disc lapped to an R_a of 0.008– 0.01 μm.
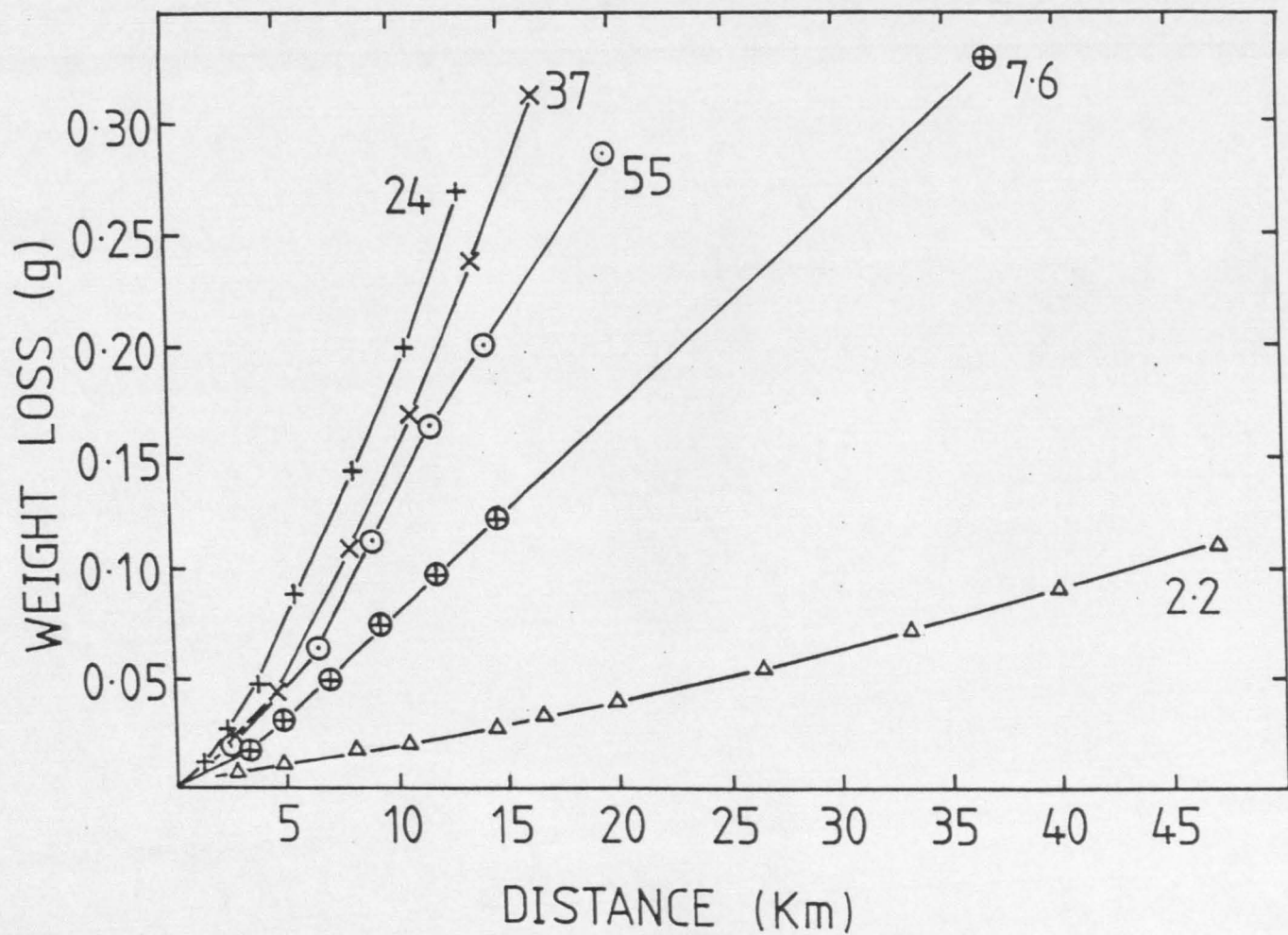
Fig. 5.1. Weight loss as a function of distance for the stainless steel pins worn against Mg-PSZ disc at 0.24 m/s.
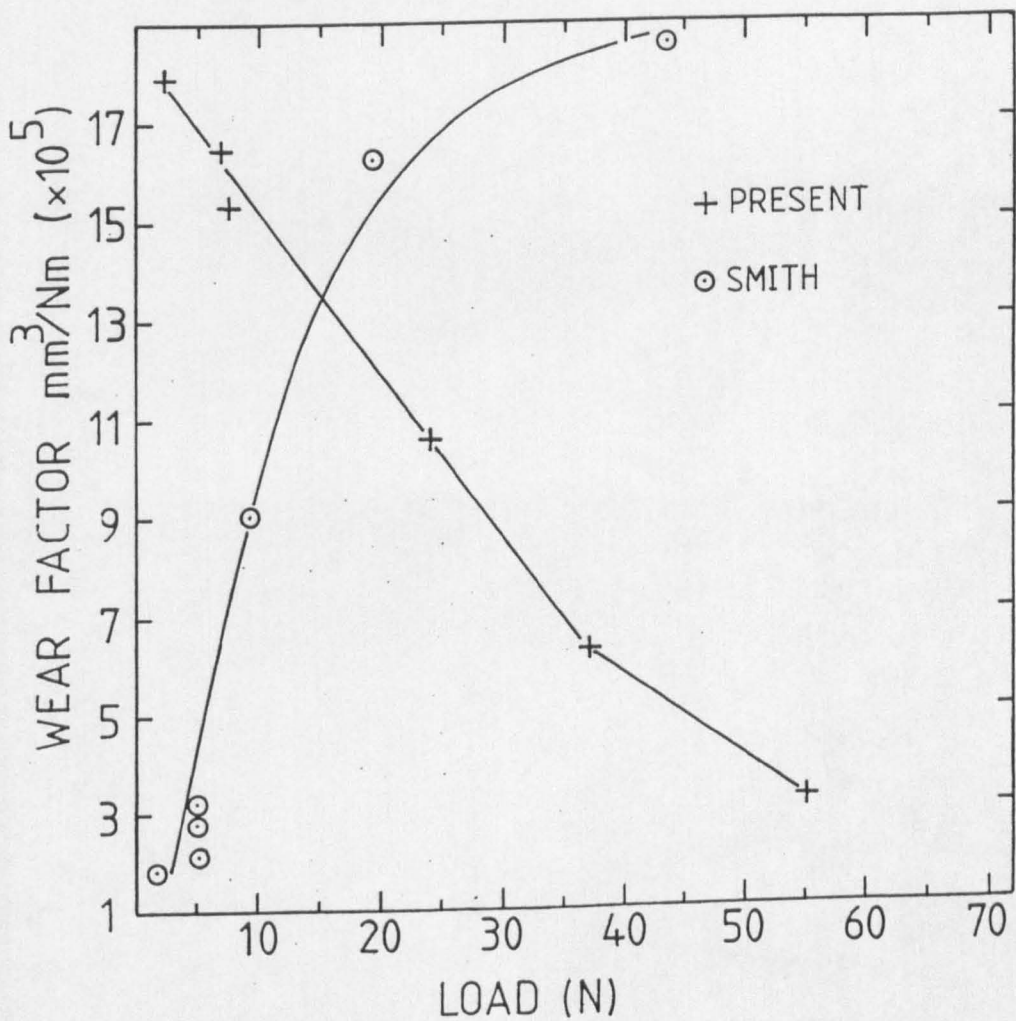
Fig. 5.2. Wear factor as a function of load for the results presented in fig 5.1. The results for Smith [285] are also shown, which were obtained for the reciprocating wear of self mated T316.
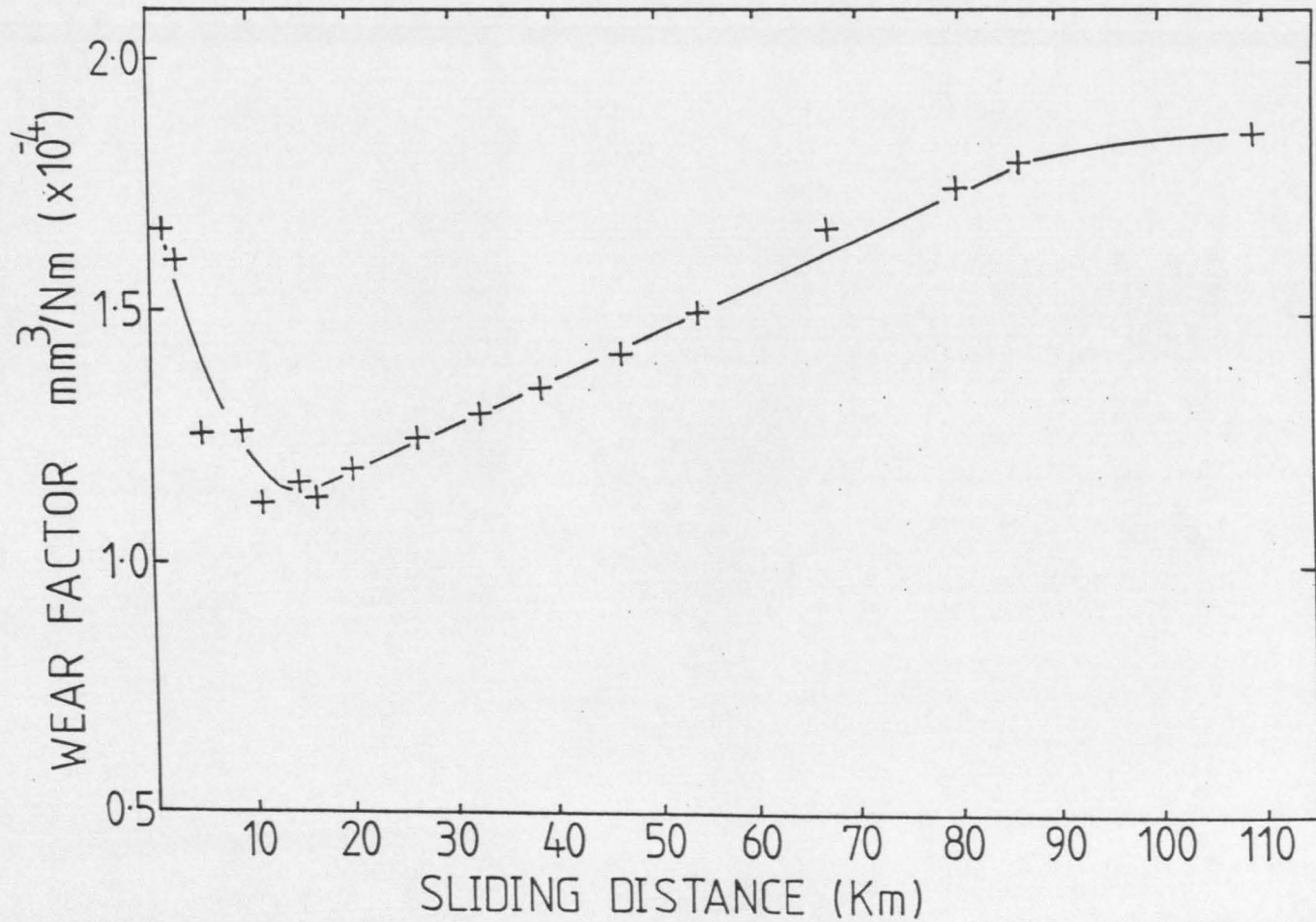
Fig. 5.3. Wear factor as a function of sliding distance for the test
performed at 2.2 N/pin.

The friction coefficient tended to follow the same trend as the noise, starting at very low values (eg 0.06 for 2.2N) but rapidly rising to around 0.2-0.35. This trend, and the values of μ, were essentially independent of load. There was a tendency for the friction coefficient to fall marginally after extended sliding.

With loads of 24N/pin and above an additional noise was heard, which could be best described as a 'grating' sound. This noise was associated with strong vibration from the wearing couple, which was severe enough at 55N/pin to potentially damage the test rig over a long period of time. For this reason no tests were performed above this load.

The friction force showed considerable variability and was generally higher for periods of extended vibration, although this was not always the case. Nonetheless, the values recorded are lower than would be expected for metal on metal tests.

5.3 WEAR MECHANISM CHARACTERISATION

5.3.1 Pin Surface

In all tests, sliding immediately led to an increase in surface roughness. Metallic wear debris became progressively piled up at the trailing edge, and the quantity of this debris increasing with load.

The grooving can be seen in the general views of the wear surfaces, figs 5.4-6. Groove widths and depths tended to increase up to a load of 24 N/pin, thereafter remaining approximately constant, fig 5.7. For example, at 2.2 N/pin the average groove dimensions were in the range 10-20μm wide by 0.5-1.5μm deep. At a load of 24 N/pin, these values had risen to 20-40μm and 2-4μm, respectively. However, considerable variation could be found at different points on the surface, with some grooves as wide as 100μm.

The surface at 2.2 N/pin was predominantly metallic, but contained a small amount of oxide, fig 5.4. The oxide was easily identified in the electron microscope by the low intensity of back-scattered electrons, and was confirmed by windowless energy dispersive x-ray analysis (EDS) (throughout the following sections the word oxide will be used to refer to metal oxide. Where zirconia is involved, its correct name will be used). The proportion of oxide increased with the load, covering approximately 75% of the wear surface at 55 N/pin,

1000µm   S.D.→
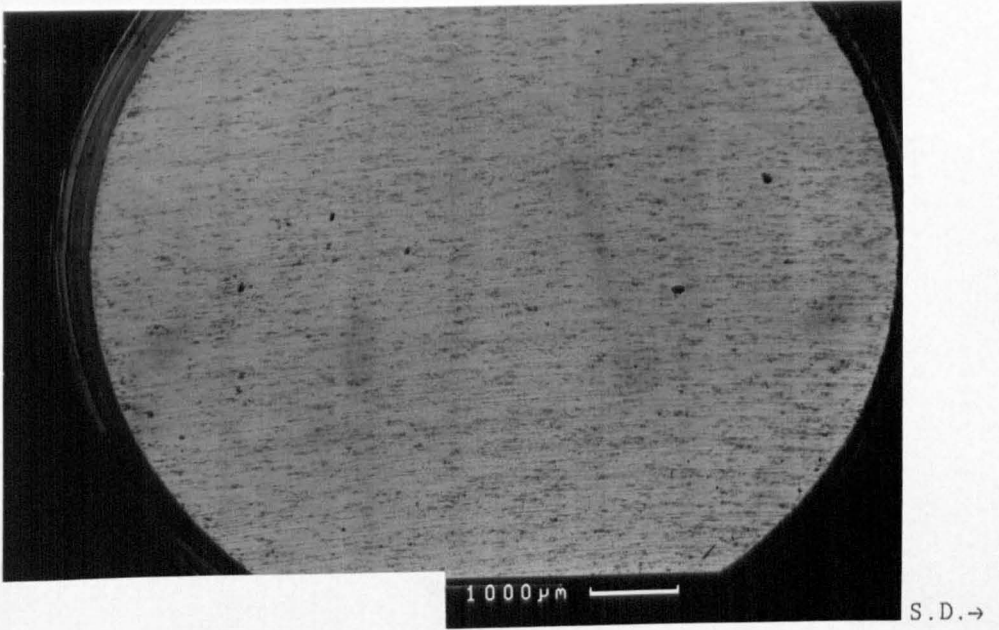
Fig. 5.4. Back-scattered electron micrograph of the pin at 2.2 N/pin.
The dark areas are metal oxide.

1000µm   S.D.→
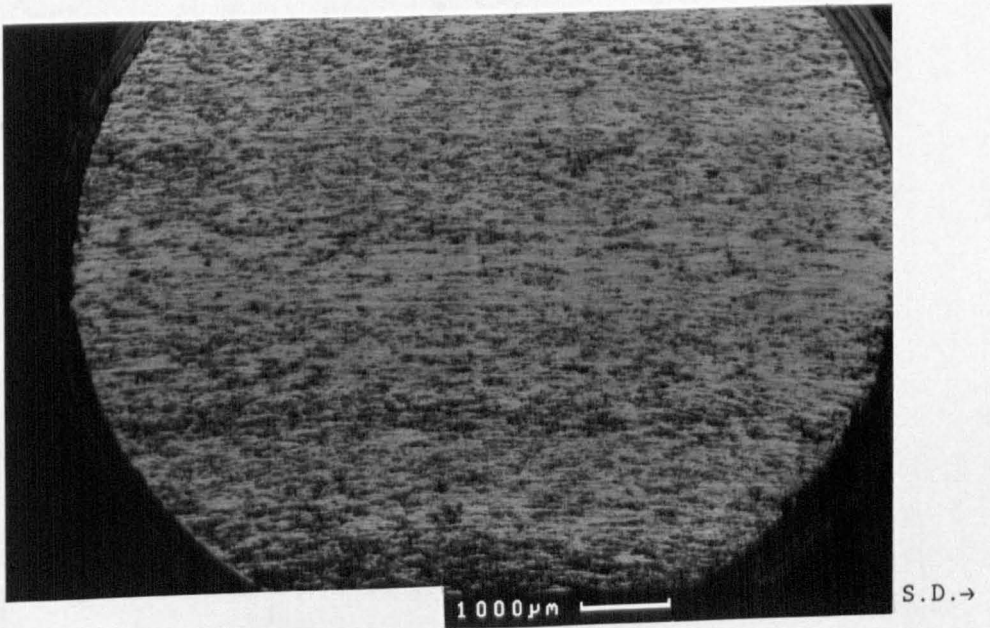
Fig. 5.5. Back-scattered electron micrograph of the pin at 24 N/pin.

1000µ

S.D.→
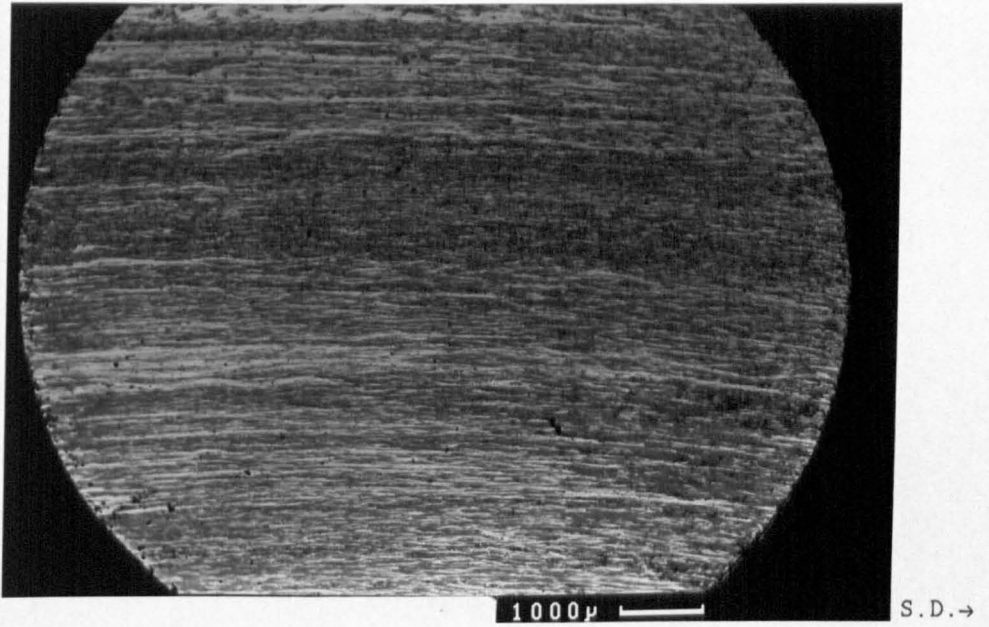
Fig. 5.6.   Back-scattered electron micrograph of the pin at 55 N/pin.

0·1mm | 2 µm

55 N

24 N

2·2N
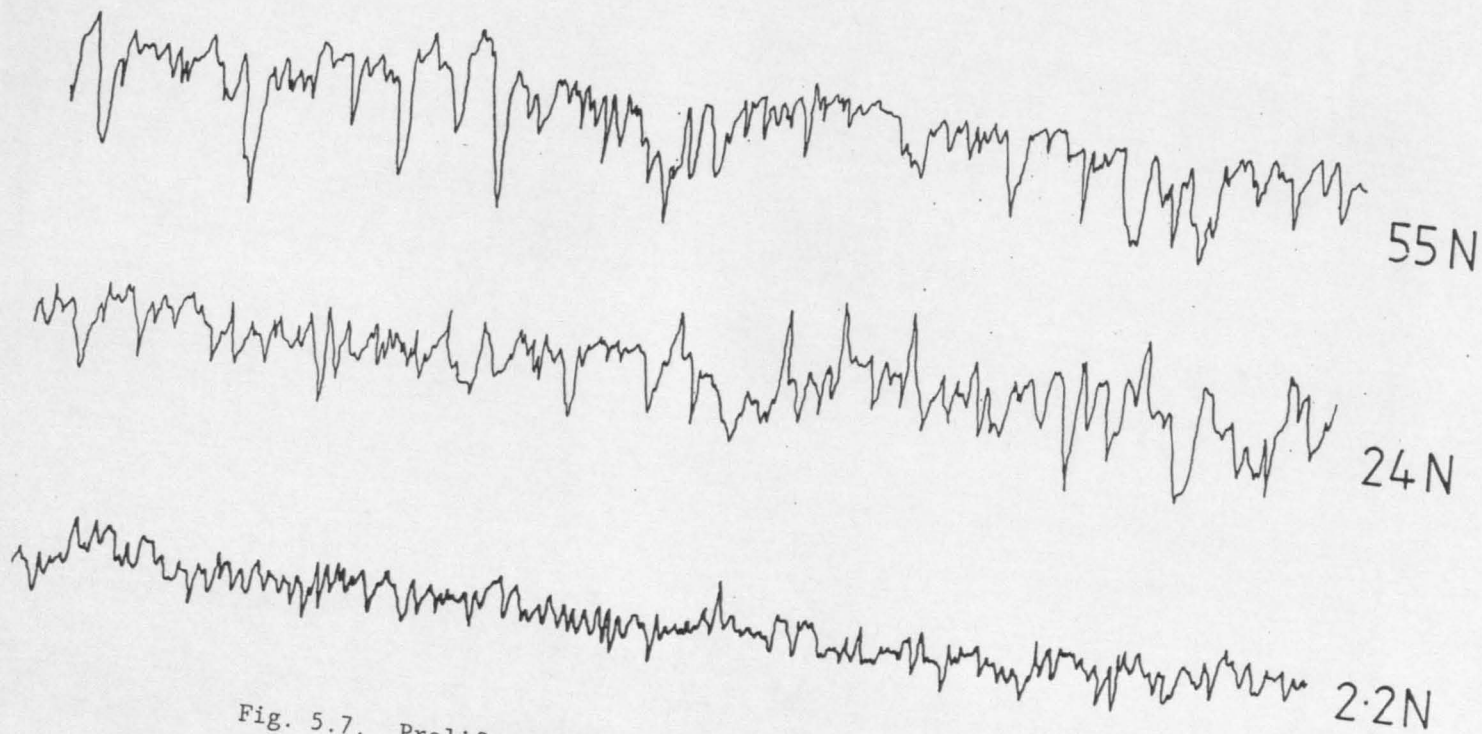
Fig. 5.7. Proliferometry traces, perpendicular to the sliding direction for 2.2, 24 and 55 N/pin.

fig 5.6. The oxide regions tended to be slightly smoother than the metallic areas, possibly explaining the absence of an increase in transverse roughness above 24 N/pin.

Fig 5.8 shows a detail of the surface at 2.2 N/pin. Wear had occurred by a ploughing mechanism, with the edges of grooves frequently folded over to leave loose flaps of metal. The passage of the next asperity would therefore be expected to remove these flaps, producing fairly large metallic wear debris. The mode of formation of the grooves can be seen in figs 5.9,10. In the upper portion of the micrograph a groove ends at a 'prow', which consists of a mixture of oxide and metal. The formation of a prow appears to occur by the progressive build-up of material, both oxide and metallic, in lamellar fashion. It would appear that this prow was pushed through the surface of the pin during contact with the zirconia disc, forming a groove in its wake. Clearly, these prows act as the contacting asperities on the pin surface.

At a load of 24 N/pin about 40% of the surface was covered with oxide, figs 5.5,11,12. The grooves were less frequently aligned exactly along the sliding direction, but tended to be wavy, indicating that the prows were forced around hard obstructions during motion. The noise and vibration produced by the sliding motion would have been associated with this irregular motion. The oxide on the surface was sometimes cracked, figs 5.13. A detail of such cracking is shown in fig 5.14 from the test at 55 N/pin. The cracking indicates the brittle nature of the oxide and the appearance of regular, transverse crazing suggests that it was caused either by thermal expansion transients or by a stick-slip mechanism.

At the higher loads, regions of prow breakdown could be seen, such as in fig 5.15, whereby large slab like particles of wear debris were produced. Such breakdown was invariably associated with prows which were predominantly oxide, rather than metallic.

Extruded wear debris was piled up at the trailing edge of the pin in all tests, fig 5.16, and at the sides of the pin at higher loads. This material usually took the form of slab like particles, which were a mixture of oxide and metal, fig 5.17, but could also consist of large 'fibres' of predominantly metallic material, fig 5.18.

30 μm S.D.←
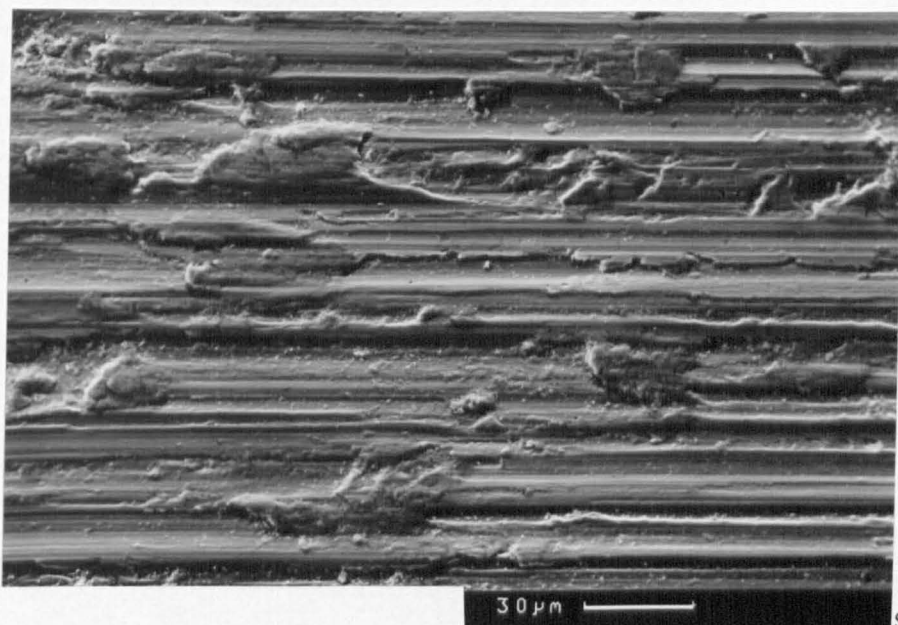
Fig. 5.8.   SEM micrograph of the pin at 2.2 N/pin.   Note the folding over of groove lips.

30 μm S.D.←
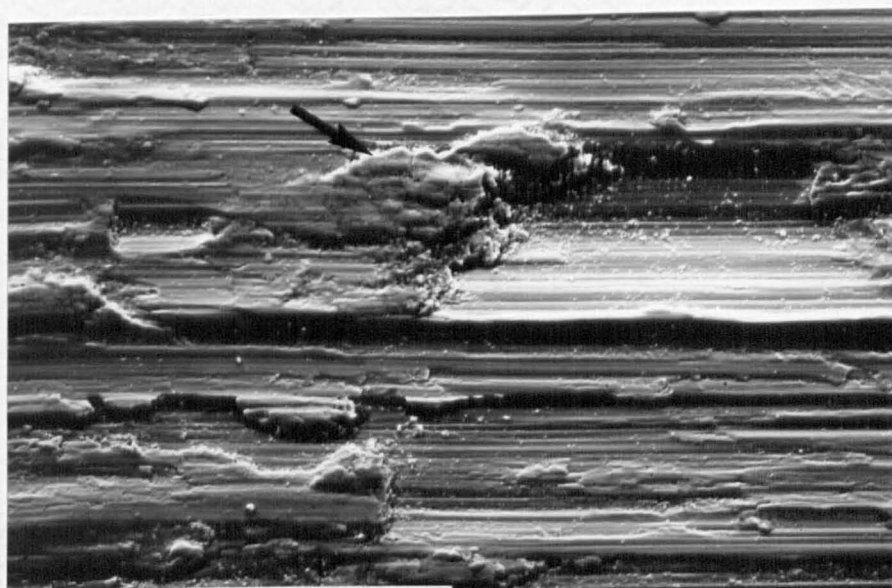
Fig. 5.9.   SEM micrograph of a prow at the end of a groove (arrowed). (6.8 N/pin).
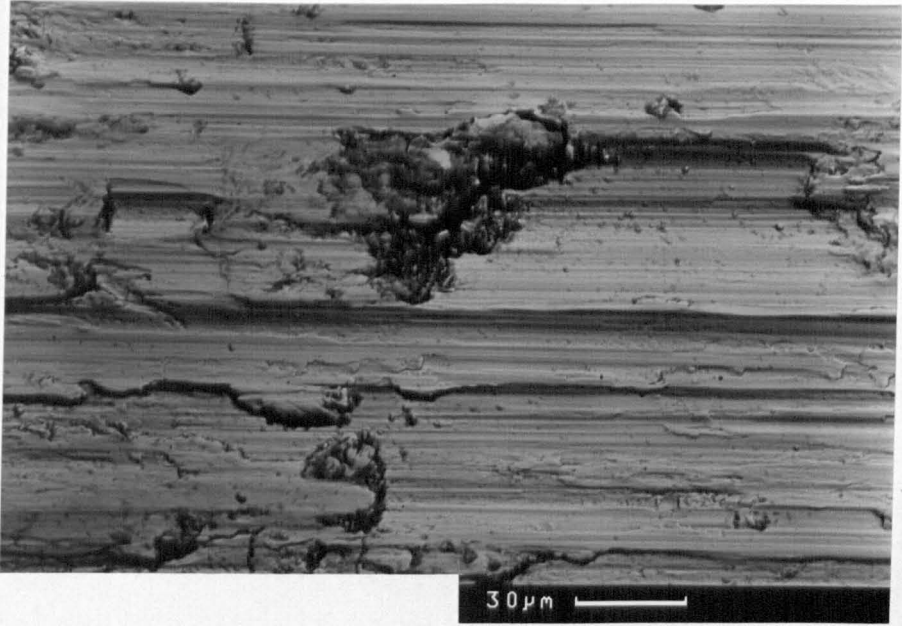
S.D.←

Fig. 5.10.   Back-scattered electron image of fig 5.9.   Note that the
prow is a mixture of metal and oxide. (The oxide is the dark areas).
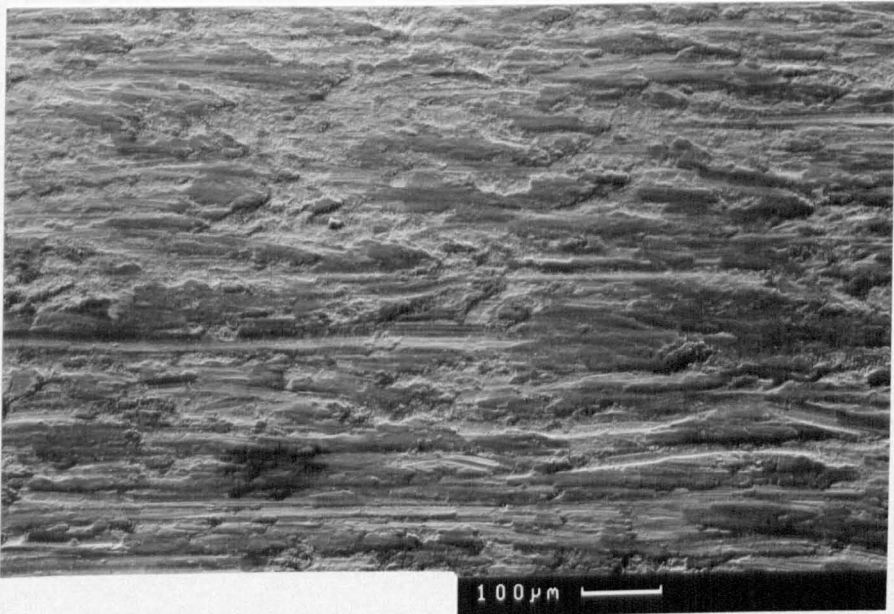
S.D.→

Fig. 5.11.   SEM micrograph of the wear surface at 24 N/pin.   Note that
the grooves are no longer parallel, and are often discontinuos.   This
was clearly related to the chattering and noise.

100μm

S.D.→
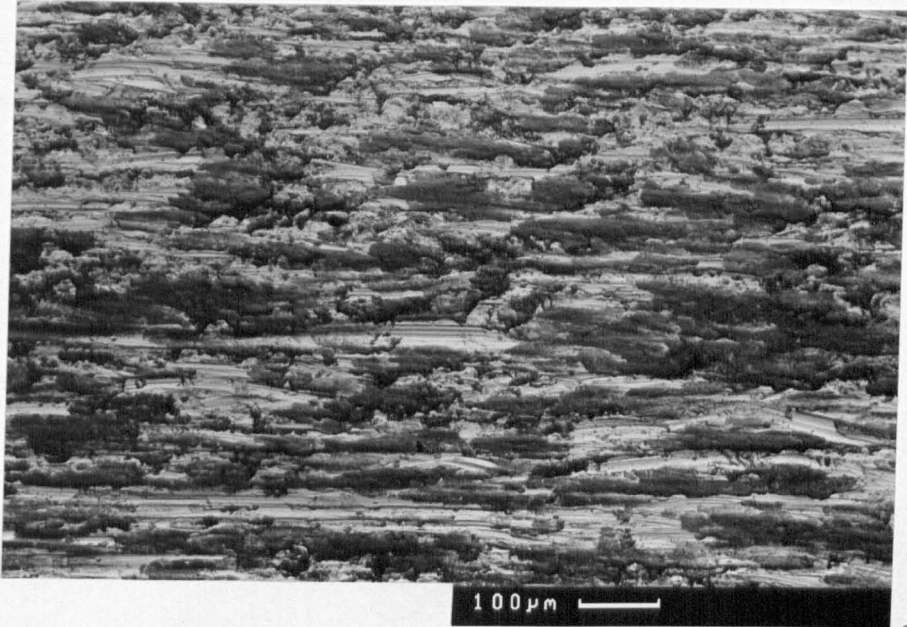
Fig. 5.12. BEI image of fig 5.11, showing the higher proportion of oxide than at 2.2 N/pin.

30μm

S.D.→
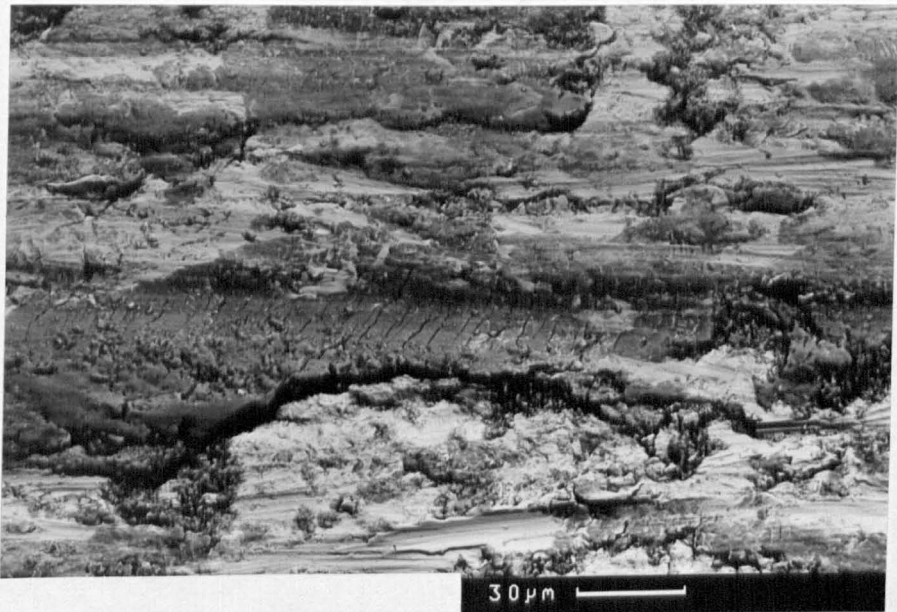
Fig. 5.13. BEI micrograph showing lateral cracking in the oxide. However, much of the oxide was not cracked.

10μ
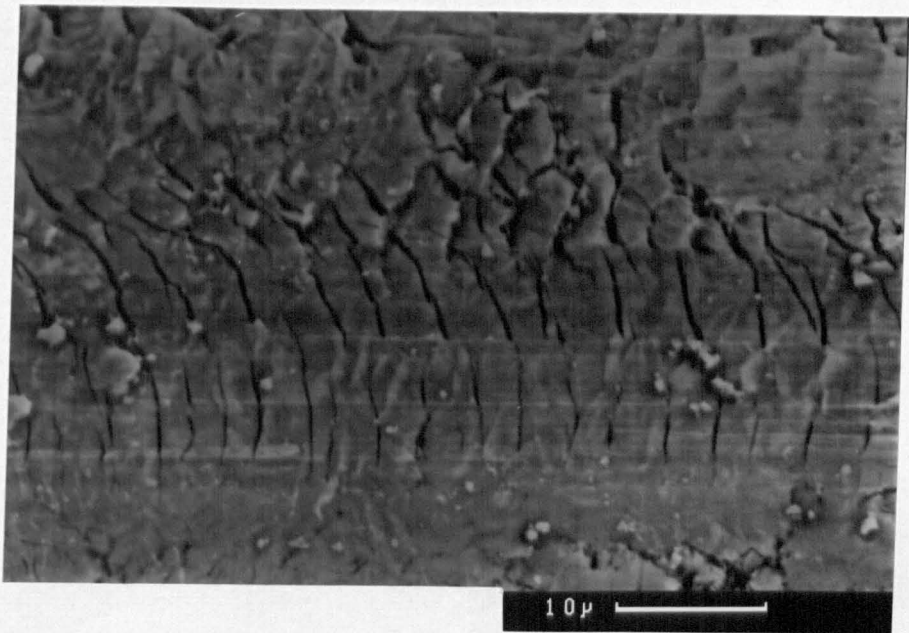
S.D.→

Fig. 5.14. BEI micrograph from the pin at 55 N/pin illustrating cracking in the oxide.

30μm
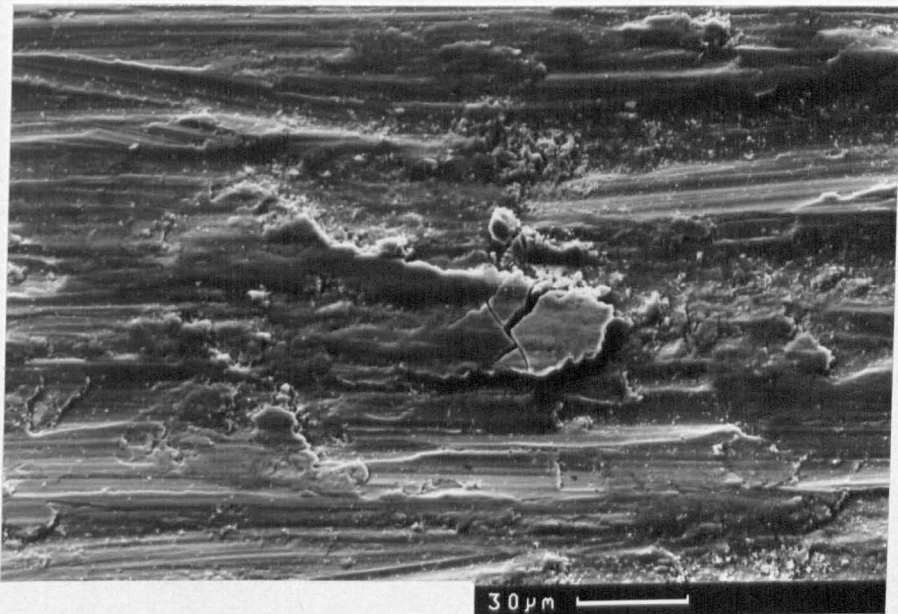
S.D.→

Fig. 5.15. SEM micrograph showing prow break-down. (24 N/pin).
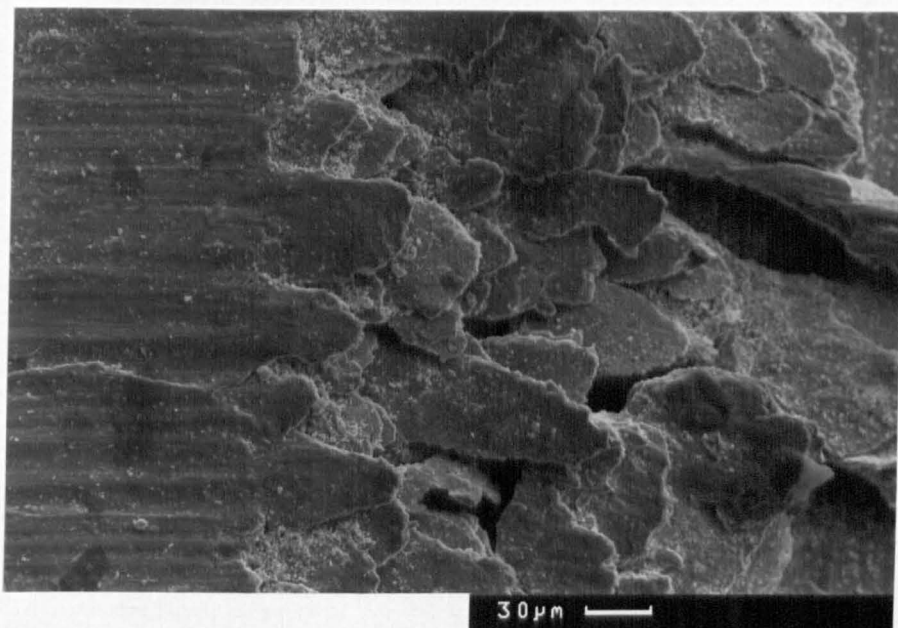
Fig. 5.16. SEM micrograph of the slab like extruded wear debris. (6.8 N/pin).
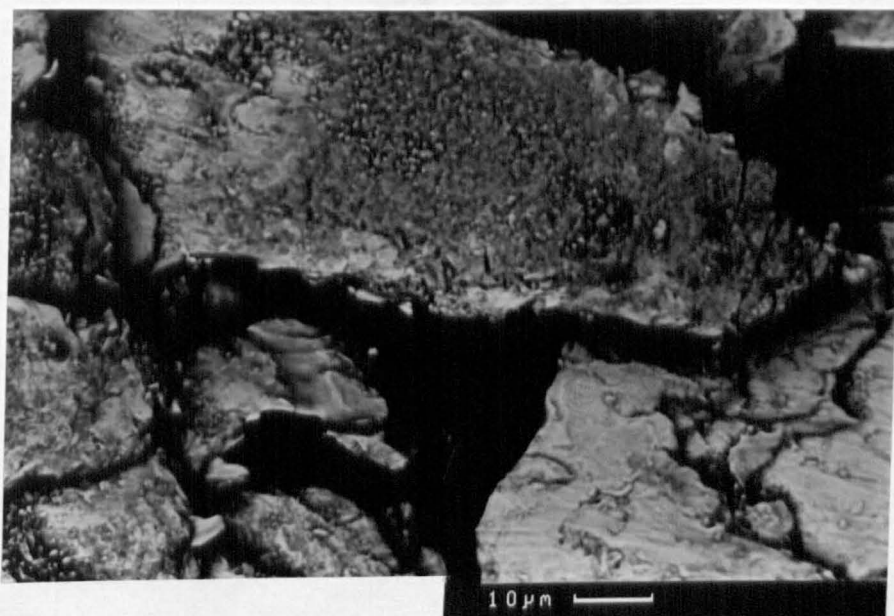
Fig. 5.17. BEI image of the extruded debris, which indicates that it is a mixture of oxide and metal.
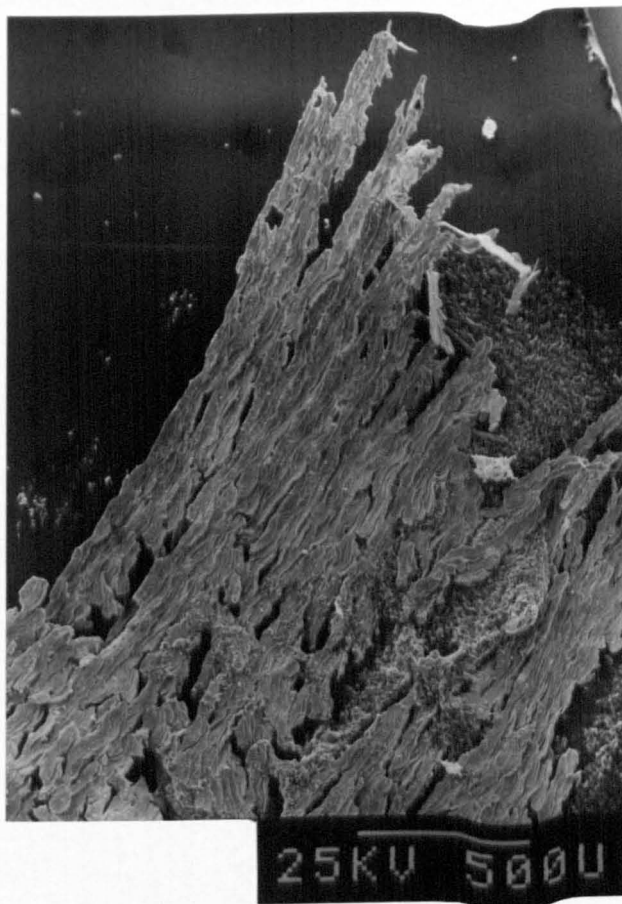
Fig. 5.18. Long fibrous extruded metal wear debris. (7.8 N/pin).
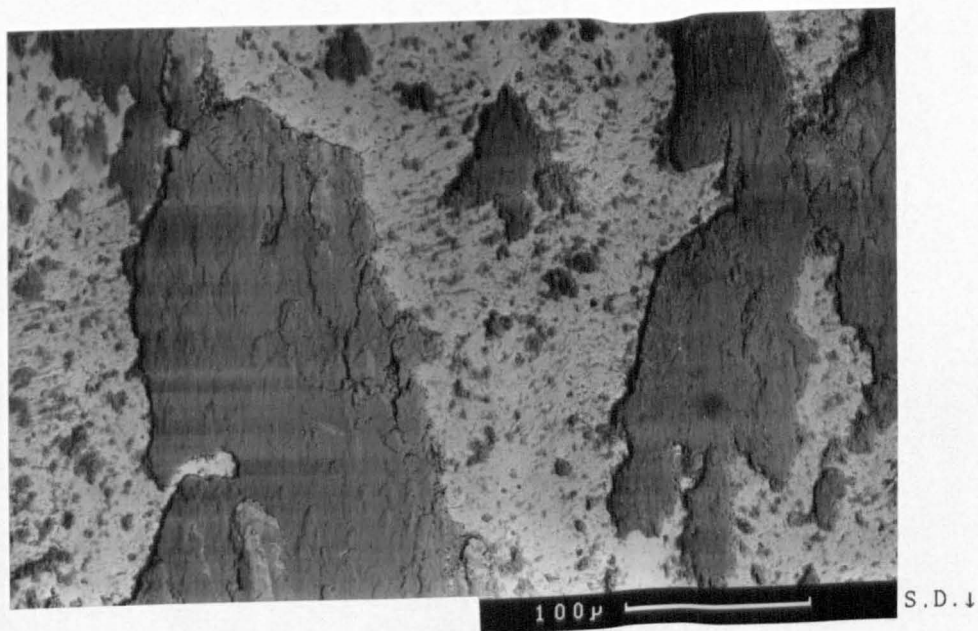
Fig. 5.19. BEI of transfer. Note the lighter metallic transfer and
the thickness of the prows. The size of individual transfer particles
can be seen. (24 N/pin).

5.3.2 PSZ Disc

The surface of the ceramic disc started to darken rapidly as metal was transferred from the pin. The transfer appeared initially as a light brown colouring. As the test proceeded, the coloration changed to a dark brown/black appearance, whence transfer of the metal became easily resolvable by optical microscopy.

A general view of the transfer is given in fig 5.19. Transfer was found to build up preferentially in certain areas leading to prow formation by successive accummulation, whilst other areas were free of transfer. Transferred metal was rapidly oxidised, possibly by the passage of the next asperity, fig 5.20. Thus, more than 90% of the transfer layer was metal oxide. Clearly, the prows provided the contacting asperities, allowing a rough guide to the size of the contact area. Not suprisingly, the prow width on the disc corresponded closely with the groove width values quoted earlier (10-100μm). Prow lengths were variable, in the range 20μm to 300μm. Regions were frequently found where prows had broken away from the disc surface, fig 5.20, leaving bare zirconia. Retransfer in these areas was precluded until the adjoining prow had become detached. It was not clear whether detachment of the prow occurred at the transfer/ disc interface, or within the zirconia. Further evidence will be presented in the following section on wear debris, but it appeared likely that fracture occurred along the original interface rather than in the zirconia.

The prows which had become detached were presumably ejected from the sliding interface. However, several examples were found on the pin which indicated that re-transfer to the pin was also prevalent. Such re-transfer could provide fresh prows on the metal surface. One such example is given in fig 5.21. The back-scattered electron image shows how the slab of wear debris, which has become a prow, is made up of both metal and metal oxide.

The observations above indicate that the sliding contact was essentially a case of metal on metal oxide, rather than metal on zirconia.

5.3.3 Wear Debris Analysis

XRD analysis of the wear debris proved inconclusive. Selected diffractometer traces are presented in fig 5.22. Peaks for austenite and α' were easily identified. However, the peak between about 26° and
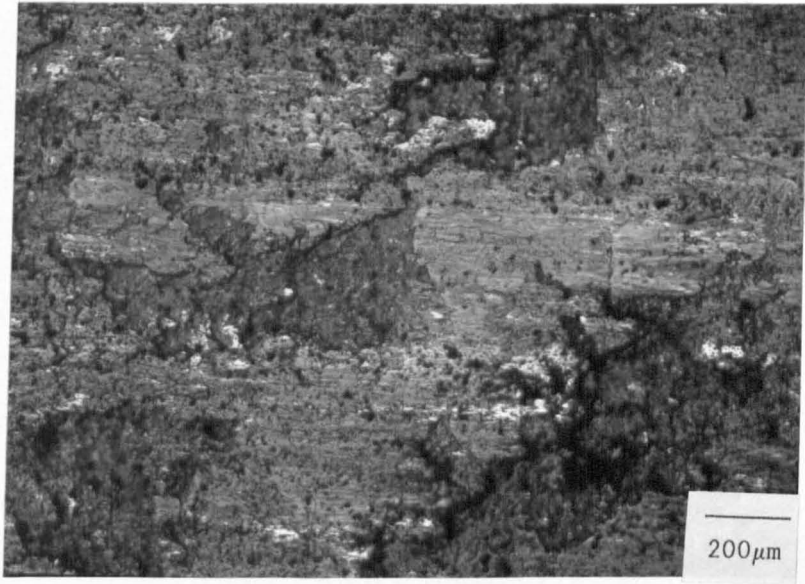
Fig. 5.20. Optical micrograph (Nomarski) showing bright metallic
transfer and areas where thick particles have been detached. (55 N/pin).

200µm

30µm
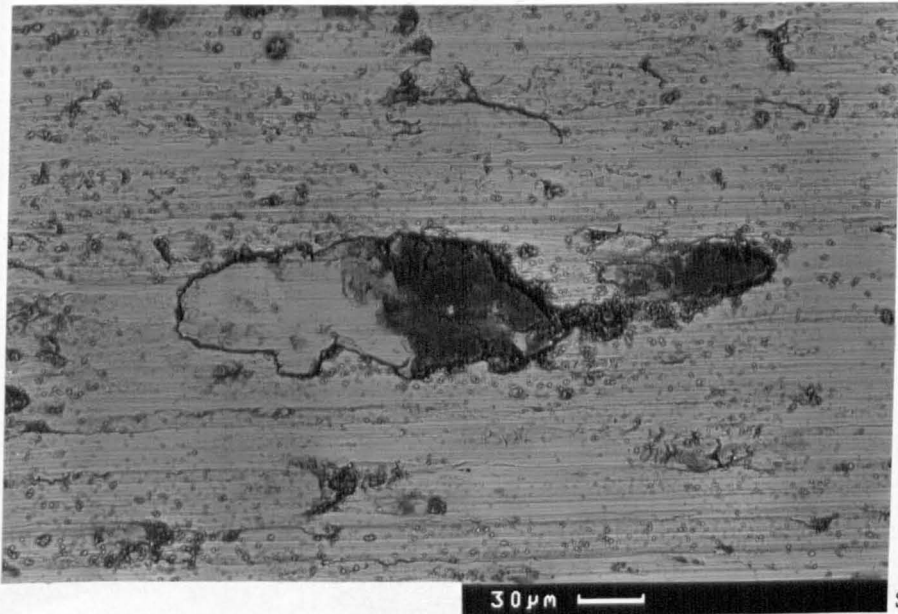
S.D.→

Fig. 5.21. BEI micrograph showing a large particle of debris which has
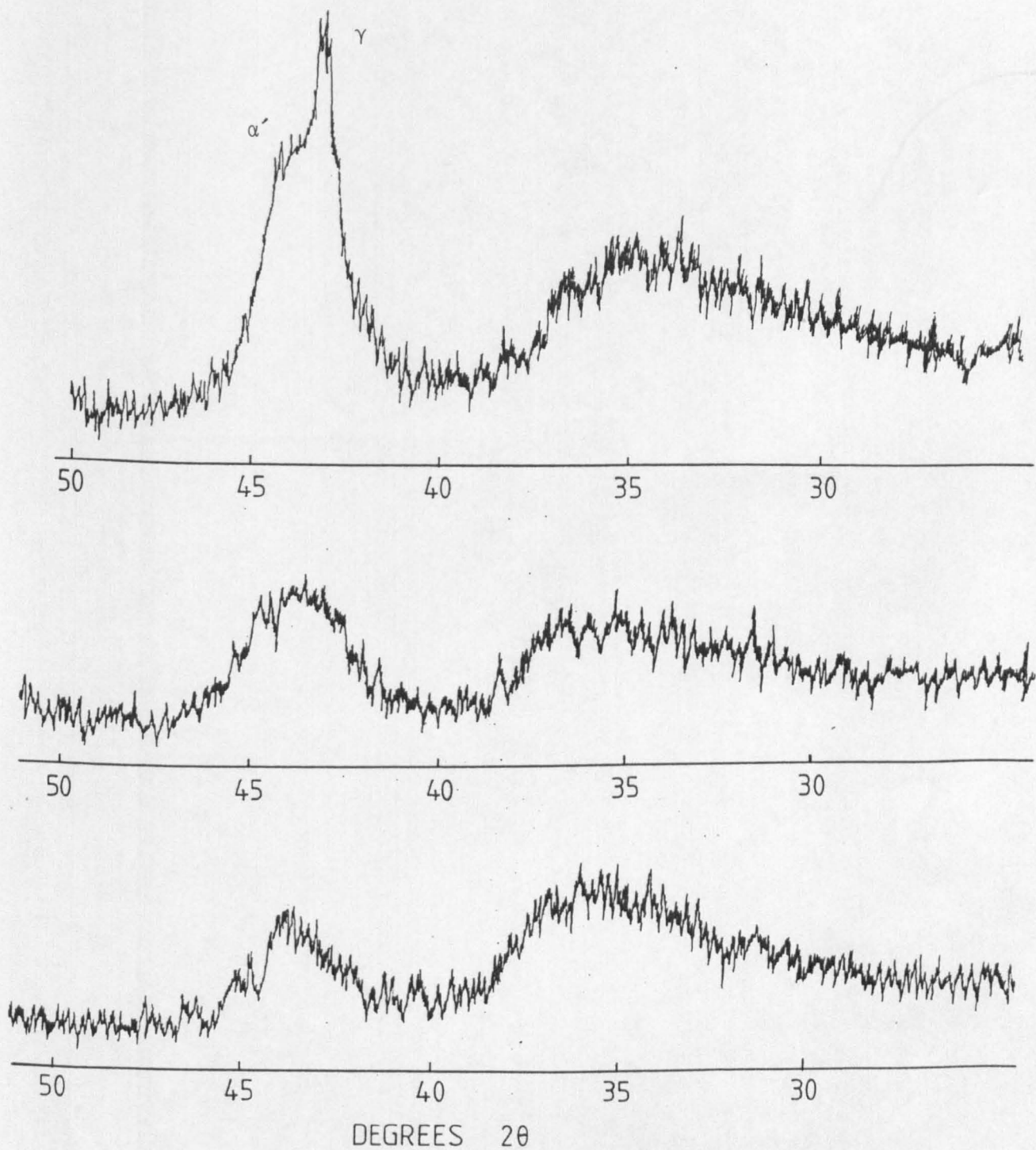become impressed into the surface. (38 N/pin).

Fig. 5.22 X-ray diffractometer traces of the wear debris from tests at 2.2, 24 and 55 N/pin. The broad peak between 26 and 40° could not be identified.

40° was so broad that no positive identification could be made, although it was presumably associated with the oxide portion of the debris. Small peaks corresponding to Fe_3O_4 were found. A further peak for this phase is located within the broad peak noted above, but it would be too small to account for the entire peak. All additional peaks found corresponded to either γ or α'.

The relative intensity of the oxide to metal peaks increased with load, fig 5.22. The α'/γ ratio and the half peak breadth remained roughly constant with load, although there was a small rise in the relative intensity of the (440) Fe_3O_4 peak. The reasons for this were not clear.

A general view of the wear debris is given in fig 5.23, with a detail in fig 5.24. The debris consisted of a complete spectrum of sizes, ranging from large slab like particles such as those shown in figs 5.17,21, which were frequently a mixture of metal and metal oxide, to extremely fine particles, often beyond the resolution of a tungsten filament SEM. The debris could not be categorised into easily identifiable size distributions. This suggests that the fine debris was formed by attrition of the larger particles. The fine debris was entirely oxide, indicating that the attrition process further oxidised any remaining metallic particles.

Microanalysis in the SEM indicated that the ratio of Fe:Cr:Ni:Mo remained the same as in the original 316L, although care should be taken when interpreting such qualitative results. Selected samples were analysed in an electron probe micro-analyser using wavelength dispersive analysis and standards. The debris was compacted into discs in order to present a flat surface to the electron beam. Whilst the results, presented in table 5.2, cannot be considered totally quantitative, the ratios of Fe:Cr;Ni;Mo were almost exactly the same as in the 316L. The average oxygen contents, which were calculated from the balance of the other elements, remained approximately constant with load. However, the ratio of the oxygen peak to the metallic element peaks measured by windowless EDS indicated that the oxygen content of the finer debris particles was higher than for the larger particles. This result should also be treated with caution since the volume producing the X-rays would inevitably be greater for the larger particles, compared to the very fine debris. However, the count rate was standardised for each analysis, and the results do appear to confirm the earlier conclusion that the metallic portion of the debris
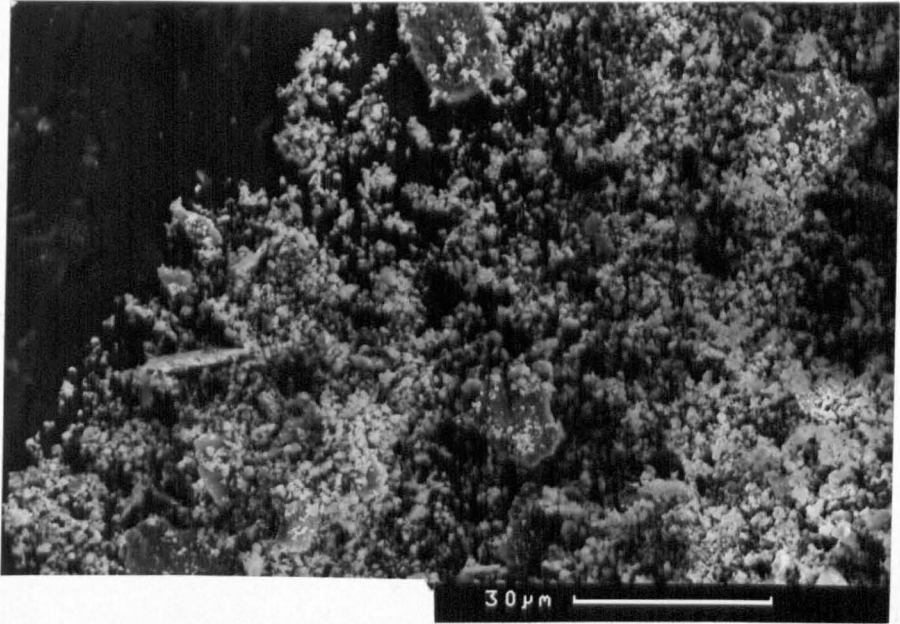
Fig. 5.23. SEM micrograph of the wear debris. Note the wide variation in particle sizes. (7.8 N/pin).
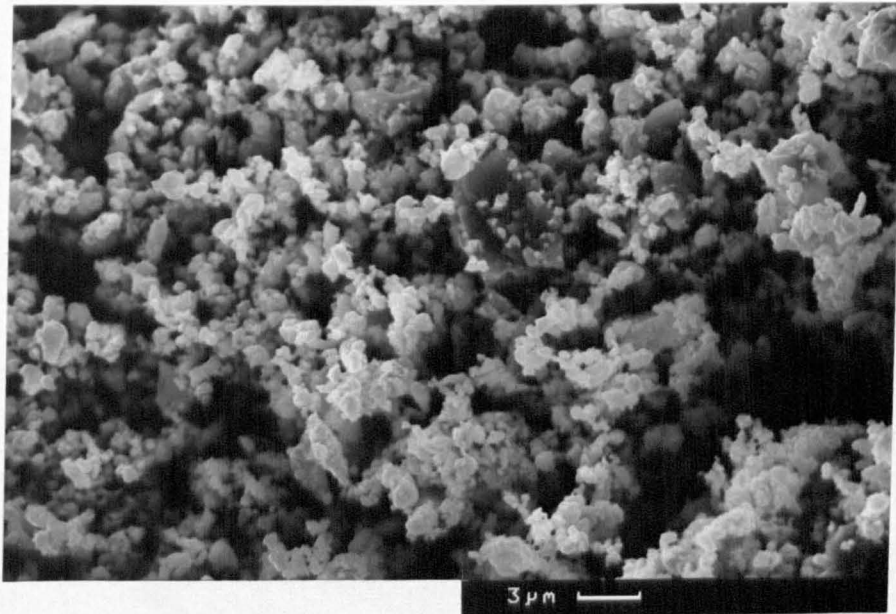

Fig. 5.24. SEM micrograph of the finer wear debris. (7.8 N/pin).

continued to be oxidised as attrition occurred.

Table 5.2

Wavelength Dispersive Analysis of the Wear Debris from Tests Performed at Loads of 2.2 and 55 N/Pin.

Element	Si	Zr	Mo	Cr	Fe	Ni	O
2.2N/pin	0.14	0.42	1.7	12.2	49.3	8.76	27.4 $^W/_O$
55 N/pin	0.25	2.24	1.7	12.1	48.7	8.78	26.2 $^W/_O$

A TEM micrograph of the wear debris is given in fig 5.25. Particle sizes were measured down to 10nm. The majority of the debris contained extremely fine crystallites, of maximum size 10nm, in a matrix which did not appear to contain any structure, fig 5.26. The associated diffraction pattern could not be indexed to any of the known oxides of iron, nickel or chromium or any mixture thereof. If the first diffuse ring is ignored, the remaining rings comform to a BCC structure. Dark field imaging using the first ring proved difficult, but suggested that it was derived from an amorphous portion of the debris. Thus, the majority of the wear debris appeared to consist of a mixture of an amorphous phase and a non equilibrium BCC phase.

Several examples of $(Fe,Cr,Ni)_3O_4$ were found and were easily identified by the larger grain size of the particles, fig 5.27. Such particles tended to clump together, and appeared to be strongly magnetic, being perturbed by the electron beam. Some of the particles appeared to be metastable, since they recrystallised as soon as they were heated by the electron beam. An example of such a recrystallised particle is given in fig 5.28.

Occasional examples of metallic particles were found, fig 5.29. The microstructure of such particles was difficult to discern; the crystallite size was very small and equiaxed (about 5-30nm), and the particle remained wholly austenitic with no evidence of texture. The majority of the metallic debris was present as larger particles which were not electron transparent.

Zirconia particles could not be found in any of the wear debris.
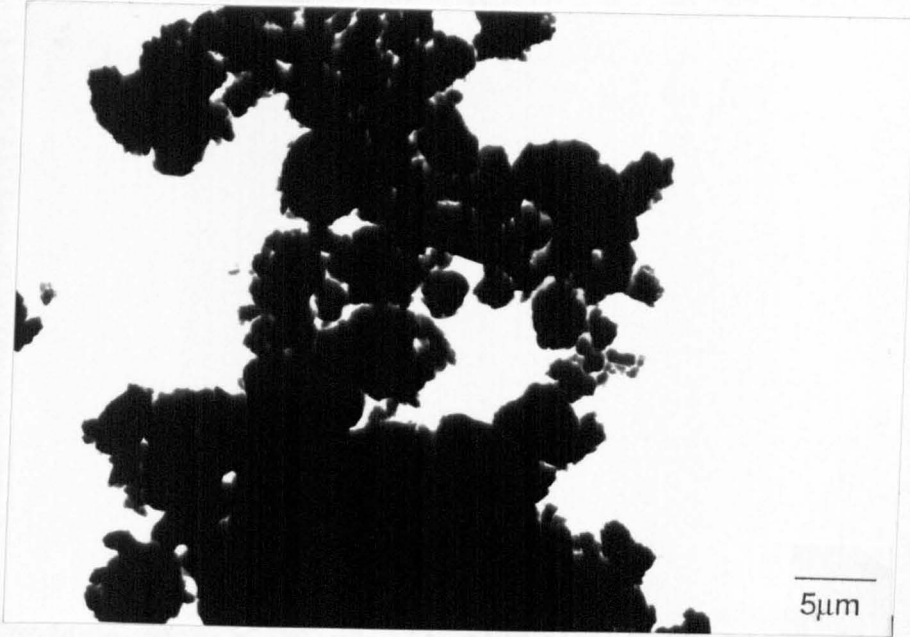
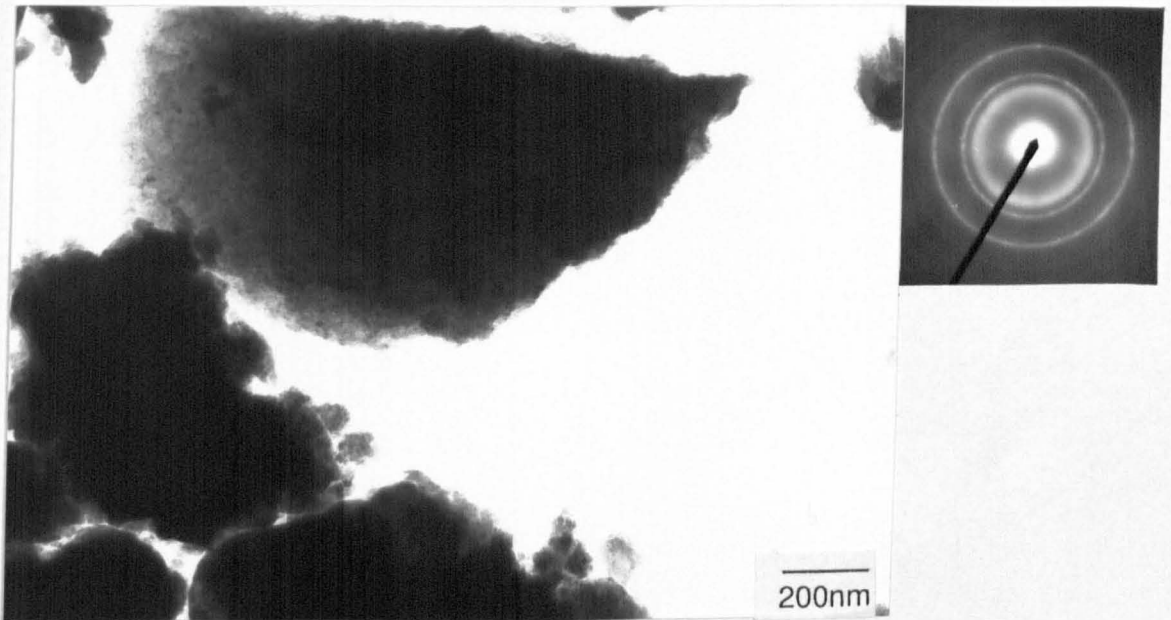Fig. 5.25. TEM microgaph giving a general view of the wear debris.
(55 N/pin).

Fig. 5.26. TEM microgaph of the non equilibrium wear debris. The
phase has virtually no resolvable structure, although was a mixture of
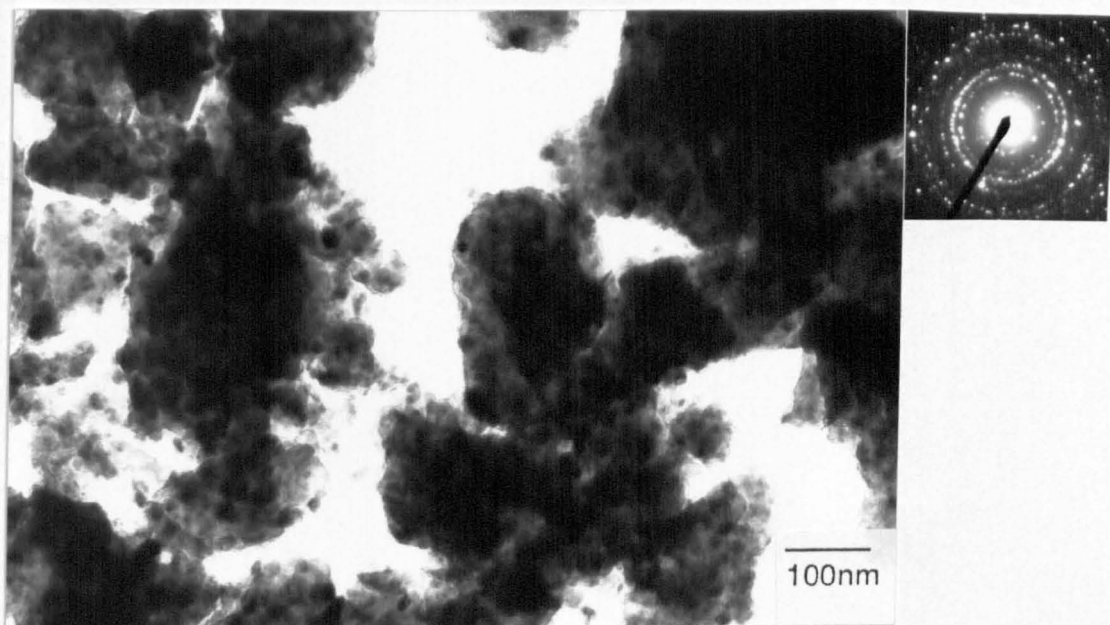an amorphous and crystalline phase.

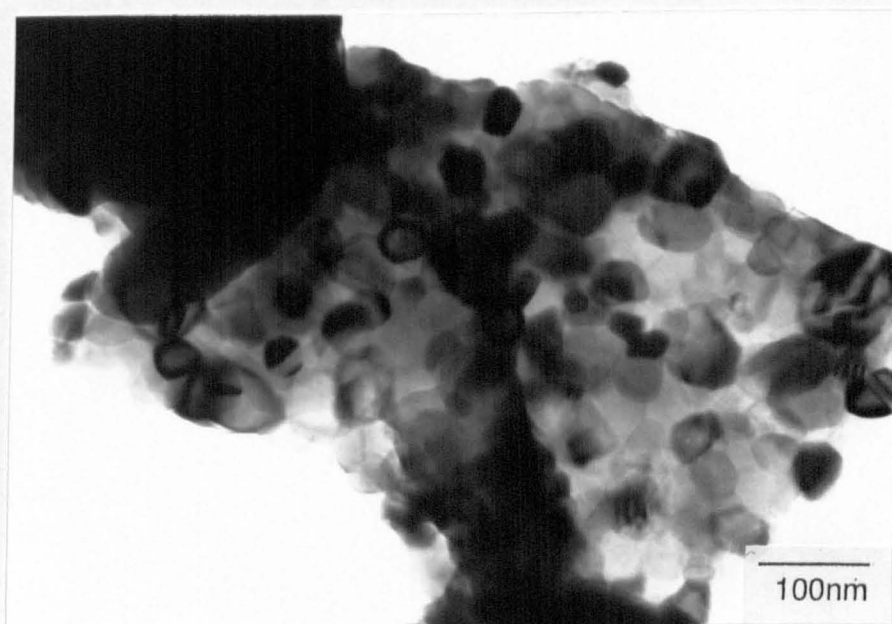Fig. 5.27.   TEM micrograph of Fe_3O_4 particles.

Fig. 5.28.   TEM micrograph of wear debris which recrystallised as a
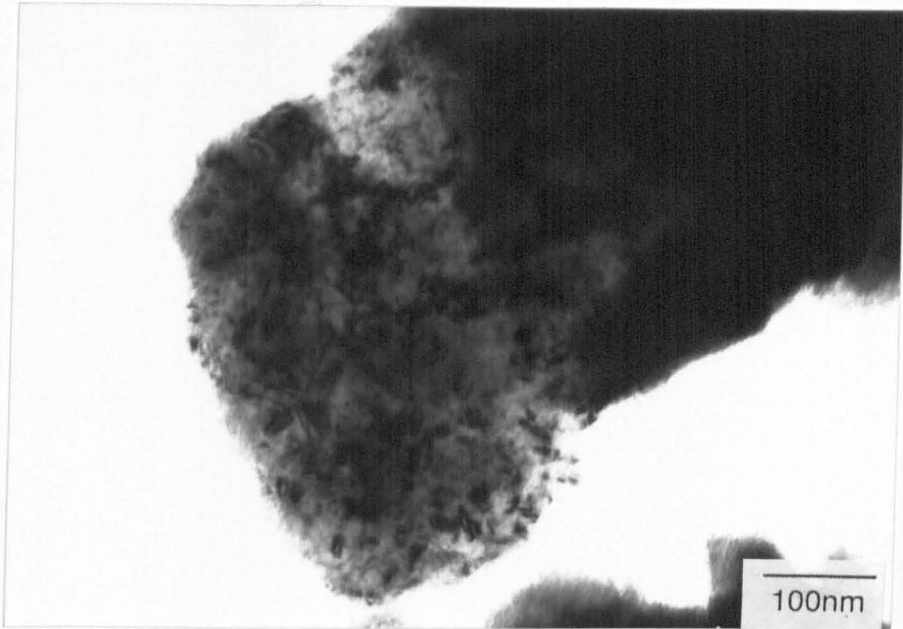result of electron beam heating.

Fig. 5.29. TEM micrograph of metallic wear debris. The crystallite
size is extremely fine and difficult to resolve.

S.D.→
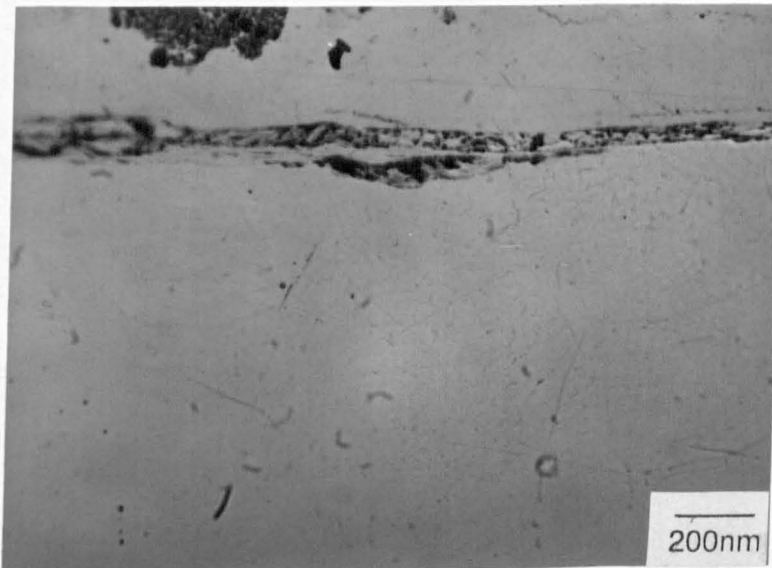
Fig. 5.30. Optical micrograph of a polished cross section showing
sub-surface oxide covered by a metallic lip. Note that the metal is
mixed in with the oxide.

One exception to this was where a few 5nm crystallites of zirconia were incorporated into a metal oxide particle. Considerable time was spent looking for zirconia particles, in view of the information that might be gained about the wear mechanism of the disc. The probe microanalysis results do indicate the presence of zirconia in the debris, namely 0.42% for 2.2 N/pin and 2.24% for 55 N/pin. These levels roughly conform to that expected from the ratios of the wear volumes of each counterface. Larger samples were assessed in the SEM using back-scattered imaging. This allowed identification of small carbides in the debris, but failed to locate any zirconia particles. For specimens tested at the higher loads some of the wear debris showed a very small Zr peak, but in the absence of identifiable particles, it would appear possible that it was present in solid solution.

Samples of the debris were heated in air to assess the stability of the microstructure. Heating for half an hour at 150°C failed to produce any change in either the diffractometer trace or the appearance of the microstructure in the TEM. Heating for 350°C for one hour produced a small change, with the (311) Fe_3O_4 peak becoming sharper on the diffractometer trace, and a possible resolution of the (220) peak of the same phase. This was accompanied by a small rise in the crystallite size of this phase, but no change in the appearance of the non equilibrium debris. Heating at 450°C for 1 hour produced a substantial change in the microstructure. The Fe_3O_4 peaks had become clearly defined, and some of the original broad peak had decreased in intensity but contained definable Fe_3O_4 peaks. The debris, which was formerly a mixture of an amorphous and a BCC phase, had started to undergo a phase change, which had provided an increase in the crystallite size and additional diffraction rings. This evidence suggests that the original debris was formed at a comparatively low interfacial temperature, certainly less than 500°C. (Interface temperatures will be considered in detail in section 5.6)

5.3.4 Discussion of the Wear Mechanism

The wear mechanism appears to have proceeded along the following lines: Initial sliding produced transfer of small quantities of metal to the disc as a result of adhesion between the surfaces. Contact in the surface of the 316L was therefore plastic from the outset of sliding. Transferred particles gradually built up in a lamellar

fashion forming prows. Transferred metal rapidly became oxidised by the heat generated by the passage of the next asperity. The prows acted as contact points and ploughed through the softer steel surface. Further adhesion was promoted with time as contact changed from metal/ceramic to metal/metal and metal/metal oxide. This accounted for the rapid rise in the friction coefficient accompanied by increased vibration and noise.

Oxidation was also believed to occur on the pin surface which lead to further prow formation. These areas were pushed through the surface during contact. Prows on the zirconia surface became detached as they reached a critical thickness and were either re-transferred to the pin surface, or expelled from the interface as debris. Thus, the wear mechanism appears to be essentially that of adhesive wear, with a contribution from 3-body abrasive wear by the action of the wear debris (although this did not produce micro-cutting). The rate controlling step was therefore the rate of prow build-up on the disc to a point where detachment occurred.

An additional mechanism was also responsible for wear, namely extrusion of the surface layer off the trailing edge of the pin, eventually leading to wear debris formation by break-up. The percentage contribution to the overall wear rate was difficult to establish, and will be considered quantitatively later.

Smith [285-287] has published an extensive study into the reciprocating wear of self mated 316 stainless steel. The micrographs of the worn surface presented by Smith are similar to those of the present study for the pin surface, namely a grooved surface with oxidised prows having a lamellar structure. Smith reported that the build up of prows during running-in led to an increase in load bearing capacity and a reduction in the friction coefficient. Smith [285-287] considered that it was the effect of load and speed on prow formation which dictated the wear behaviour. At loads less than 40N a transition in wear rate was observed which gave a 5-10 fold reduction in the wear rate, after a sliding distance which was both load and speed dependent. The distance to this transition increased with load, but the time to the transition remained almost constant. The transition was also associated with an increase in the proportion of oxide in the wear debris [286]. Smith [285,286] attributed this behaviour to the incubation time for the formation of the oxide, which then promoted a lower wear rate. He considered that in the pre-transition stage the

metal transfer was rate controlling whilst in the post-transition region prow breakdown was rate controlling.

No such transition was found in the present case. This was most probably because of the considerably faster oxidation kinetics which resulted from using zirconia as a counterface (discussed in section 5.6). During the initial stages of running-in there would have undoubtedly been a period when prow oxidation was the rate controlling step. However, prows appeared to be fully formed after a sliding distance of only 50-100m, depending on load, indicating that prow breakdown was then the rate controlling mechanism.

The decrease in wear factor with load, fig 5.2, appears to be associated with the increase in the amount of oxide on the pin surface with load. Increasing amounts of oxide would be expected to increase surface hardness and thereby improve the load bearing ability. The difference between this and the trend found by Smith [285-287] appears to be related to the kinetics of oxide formation rather than the mechanical properties of the counterface (i.e. ceramic or metal). Smith reported an increase in metallic content of the wear debris as the load was increased i.e. the opposite to the present results. The wear factor was found to be independent of load above 30N, which Smith attributed to the relative contributions of elastic and plastic contact. This point will be discussed later in the light of the TEM investigation. However, Smith suggested that the presence of oxide reduced the amount of plastic contact. Above a load of 30N, debris was formed too quickly for oxidation to occur, and the contact became fully plastic. In the present case oxidation kinetics were rapid enough to allow an increase in oxide content with load. This would suggest that, if the load was substantially increased above 55N for a zirconia counterface, a point might eventually be reached where the debris would become increasingly metallic.

In relation to the above it is important to consider the stage at which the metallic oxide was formed. The production of oxide was considered by Salesky et al. [252], who examined the wear surfaces of various steels by cross sectional TEM. Using a system where the debris was blown away from the surface during a pin on disc test, a wear surface with a comparatively small amount of oxide resulted. However, the debris was almost entirely oxide. The debris particle size was of the order of $1x2x0.3\mu m$ which corresponds to a surface area of $1.5m^2/g$. Particles with such large surface areas have been shown to be

pyrophoric by Evans et al. [288]. Therefore it appeared that oxidation occurred after the formation of metallic wear debris, which is of course in contradiction to the theory of Quinn [219]. The mode of formation of the oxide will be discussed further during the following sections on the TEM results. The suggestion that oxidation occurs after wear debris production is certainly substantiated by the present results, where the oxygen content was found to increase as the wear debris particles became smaller.

Smith [285] also had difficulty identifying the phases in the wear debris. Considerable transformation to α' had occurred with very little austenite present. All the diffractometer peaks could not be uniquely identified. A spinel type phase was present which was considered to be a hydrated form of heamatite, possibly iron-nickel-hydroxide. However, additional peaks could not be fully accounted for, but gave reasonable fits with $FeCl_3$, $NiCl_2$, $CrCl_3$ and possibly ϵ Fe_2O_3. As with the present results, considerable line broadening compounded the problem. The crystallite size found by Smith [286] in the post transition regime was of the order of 2nm, which was considered consistent with the presence of spinel. Quinn & Wallace [289] reported a similar spinel structure for a sliding T310 stainless steel when tested at 300°C. The same material produced only $\alpha-Fe_2O_3$ when sliding at room temperature. However, the proportion of metallic debris was high, a result of the slow oxidation kinetics of T310 compared to T316.

The values of the friction coefficient shown in table 5.1 are substantially lower than those which would be expected from metal on metal wear. For example, Smith [285] reported values of 0.4-0.5 with transitions to 0.8 for the reciprocating wear of self mated 316 stainless steel. Interestingly, the friction coefficient was higher for Smith's tests compared to the present, for similar wear rate, load, oxide coverage and depth of deformation. This reflects the absence of plowing or deformation on the zirconia surface.

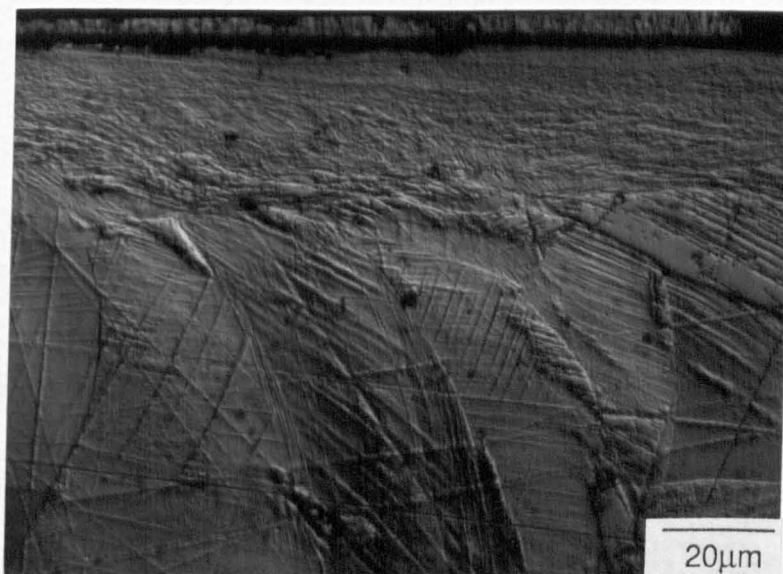## 5.4 HIGH STRAIN DEFORMATION AT THE WORN SURFACE

5.4.1 Optical Microscopy

A polished cross section of the 24 N/pin test is shown in fig 5.30. A large fissure of metal has been dragged over surface oxide,
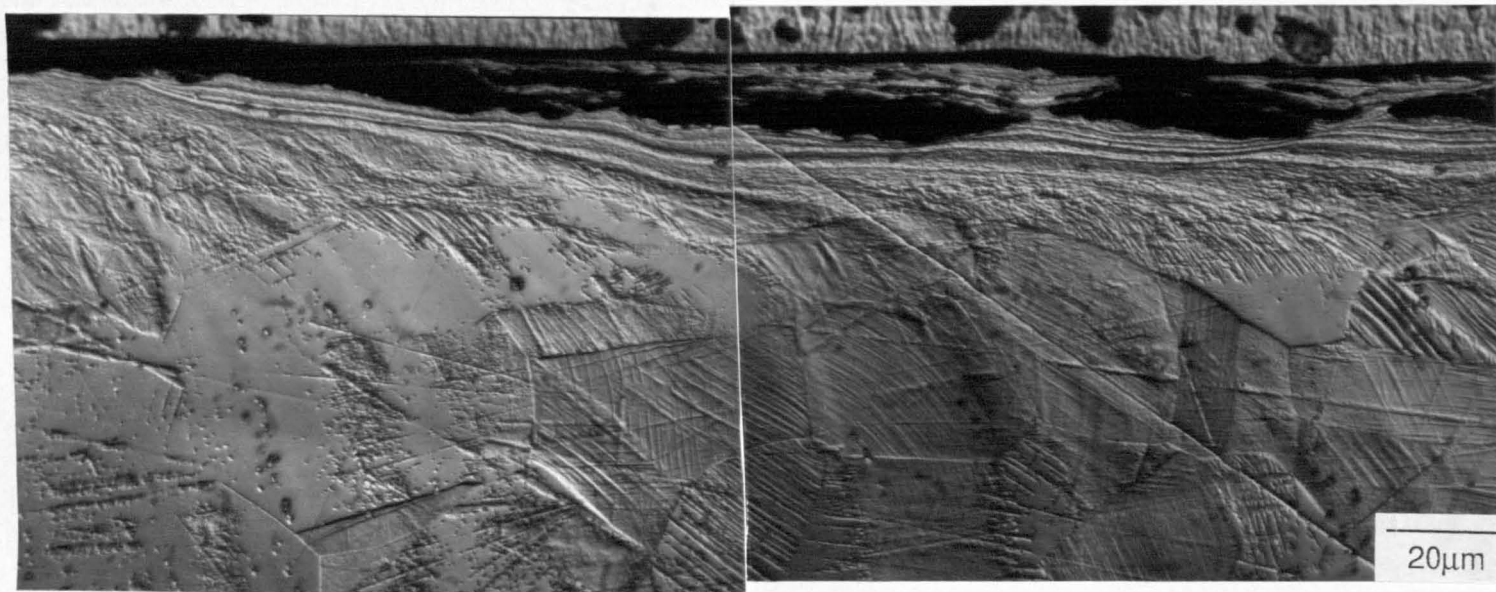
S.D.→

Fig. 5.31. Optical micrograph (Nomarski) of the test at 2.2 N/pin.
Note the bending of the twins and the sharp boundary with the surface
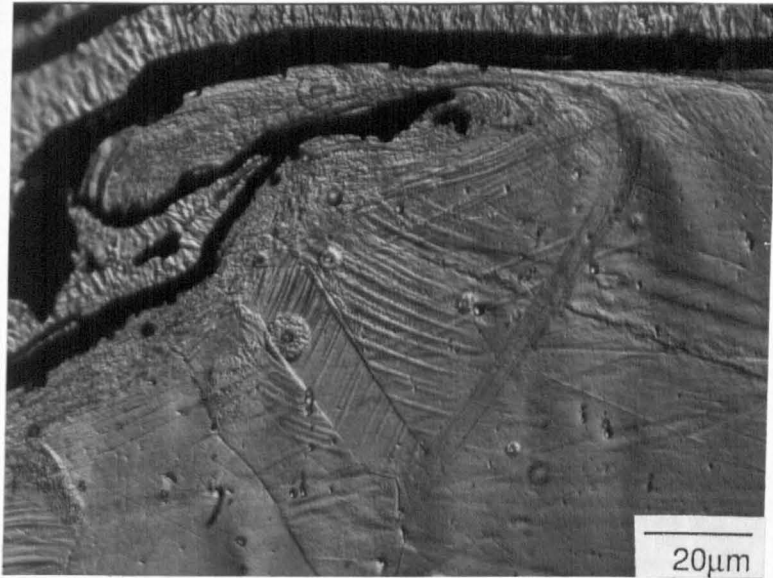shear bands.

S.D.←

Fig. 5.32. Optical micrograph (Nomarski) of the test at 24 N/pin.
Note the thick shear bands and the structure of the transition region
to the twins.

S.D. ←

Fig. 5.33. Optical micrograph (Nomarski) of the test at 55 N/pin.
Note the thick layer of oxide with a long metal fissure at the
surface. Note also the flow lines which can be used for strain
estimates.

20μm

S.D.←

Fig. 5.34. Optical micrograph (Nomarski) of the extruded metal which can be seen to consist entirely of shear bands. (4.8 N/pin).

200nm
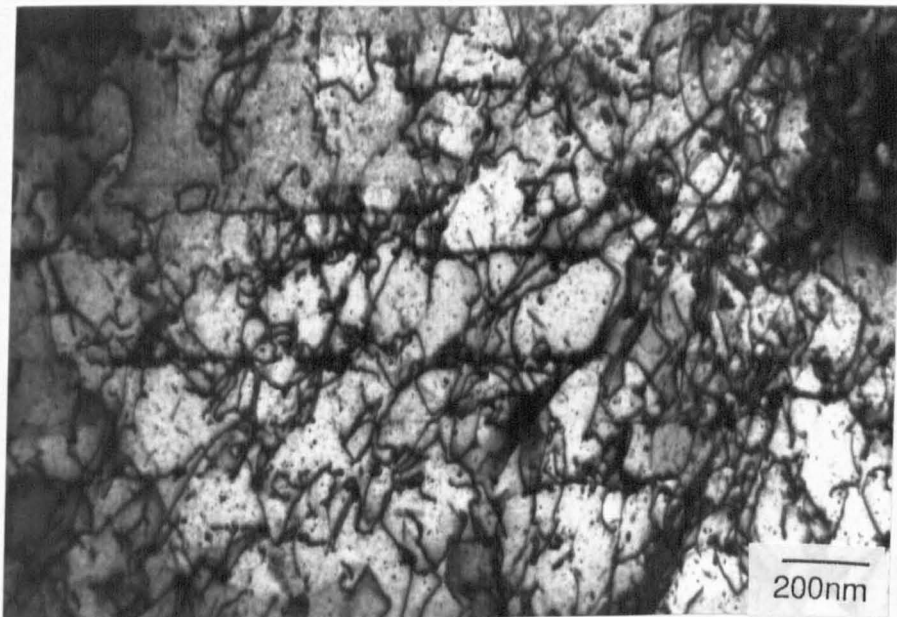
Fig. 5.35. TEM micrograph of the microstructure well below the worn surface, showing the initial stages of dislocation interaction. (Two beam conditions, adjacent to a bend contour).

which itself is an intimate mixture of metal and oxide. This indicates very high strains at the surface and also demonstrates the manner by which oxide can be incorporated well below the surface.

Etched cross sections are presented in figs 5.31-34. At 2.2 N/pin, fig 5.31, the microstructure was divided into two distinct regions namely, a narrow region of shear bands at the surface, and the subsurface twinned region. The boundary between shear bands and twinning was invariably sharp. Shear banding could not always be resolved at the surface, but this was not helped by the galvanic reaction between the coating and worn surface, which inevitably eroded and bevelled the original steel surface. The twins usually showed a curvature towards the sliding direction as the surface was approached.

The depth to which deformation could be resolved increased rapidly with load. At 24 N/pin, fig 5.32, the shear banded region was extremely thick, up to 25 μm. Within this layer the microstructure became finer as the surface was approached. Flow lines could be seen bending to become parallel to the surface, indicating extremely high strains. Possible rhomboidal prisms of twinned material (as described in chapter 4) could occasionally be seen, incorporated into the shear banded region. The interface between shear bands and twinning was no longer sharp, but regions were observed where narrow shear bands had passed through twin colonies. This had produced a different shape of twin colony to that found in rolling, appearing more slab like than rhomboidal prism, and was a result of the different geometry of deformation. As at the lower load, the twins were curved towards the sliding direction. However, the twins were consumed by shear bands before they became aligned with the surface.

With a further increase in load the depth of shear banding appeared to decrease slightly (the depth of deformation will be discussed in greater detail in section 5.5). Surface coverage by oxide increased to a point where entire regions were predominantly oxide. As shown in fig 5.30, the oxide was often covered by metallic lips, drawn over the oxide surface. One example, taken from the 55 N/pin test is shown in fig 5.33. Unfortunately, the etch used severely eroded the oxide, obscuring the manner in which shear bands and oxide interact.

An example of the extruded metal at the trailing edge is given in fig 5.34. In this case the resulting debris was entirely metallic and consisted of shear bands of a similar structure to that of the worn surface. Therefore, this material was produced as a result of high

strains at the surface, leading to considerable physical displacement.

5.4.2 Transmission Electron Microscopy

Cross sectional TEM was performed on the 2.2, 24 and 55 N pins. The difficulty of producing such specimens and the low success rate precluded further study. With all samples it was found that the foil tore just before adequate electron transparency could be achieved, a result of the high residual stresses present in the surface layers. Much of the thin area was lost because of the tearing and subsequent folding up of the foil. Consequently, observations had to be made from a restricted area with a large wedge angle. Nonetheless, the structure could be evaluated with full confidence. An additional problem was that the thinning rate of the nickel was considerably higher than of the stainless steel, so that observations of the surface had to be made in fairly thick regions where the nickel was still present. Otherwise, if the nickel had been removed, there was no way of ensuring whether the area being considered was the original surface or not.

5.4.2.1 Microstructure at 24 N/pin

The pin worn at 24 N/pin will be used to illustrate the microstructure generated by wear, the effect of load being discussed in the next section.

The microstructure followed the same general form as that found in the rolling experiments, with the exception of the region within about 200nm of the surface. The following description of the deformation microstructure will start well below the worn surface and progress to the surface.

The first indication of deformation could be seen with an increase in dislocation density, fig 5.35. This permitted accurate measurement of the depth of deformation, the results of which will be presented in a later section. The dislocations were aligned along the primary slip directions, as with the rolled samples. Examples of dissociated dislocations could not be found. Individual twins gave way to twin colonies with a twin spacing which varied considerably, but was usually in the range 15-50nm (similar to the values found in the rolling experiments, chapter 4), fig 5.36. Twinning was usually confined to one twin system within each grain, but occasional examples of twins on two systems were found.

Shear bands had formed through twin colonies in a similar manner to
those in the rolled samples. The shear bands were almost always
parallel to the surface, or at least parallel to the general direction
of deformation at that point. The thickness of the individual shear
bands, figs 5.37-40, was similar to those in the rolled specimens. The
flow pattern of the material tended to undulate, as shown in the
optical micrographs, fig 5.32. The wavy nature of the passage of a
freshly formed shear band is clearly shown by the dark field micrograph
in fig 5.40. In this example there seems to have been little
perturbation of the twins by the passage of the band, demonstrating the
manner in which the original structure is totally destroyed by such
localised shear. The crystallite size in this freshly formed shear
band was variable, but generally in the range 20-80nm, which was the
same (within experimental error) as in the rolled material.

Several shear bands could be found running parallel to the surface,
but with a small region of twinning in between them, as illustrated in
fig 5.41. The twin colonies divided up by the passage of the shear
bands generally took on a slab like appearance and showed very little
similarity to the rhomboidal prisms observed in the rolled samples
(compare fig 5.41 with 4.8). However, occasional examples of
rhomboidal prisms were found, fig 5.42, but these were invariably close
to the transition region between the shear bands and the twinning.
Interestingly, these colonies never became fully aligned with the
sliding direction, but were totally consumed by shear banding before
this was possible. This is in contrast to the rolling experiments
where several examples of fully aligned twins were found after a
reduction of 95%.

The microstructure in this transition region corresponded,
therefore, to the rolled microstructure after a reduction of about 90%
(strain of 2.3). No evidence of twins were found in regions a few
microns closer to the surface, indicating that the strain had risen to
values above the highest investigated in chapter 4, i.e. a strain of
>3. A note of caution should be made here in that shear bands tend to
form at a point determined by the local orientation (and texture) of
the microstructure and the geometry of the stress system. Therefore,
given a different stress system in wear, compared to rolling, the use
of the microstructure generated by rolling to estimate strains at the
worn surface could be misleading. The issue of the strain at the worn
surface will be discussed in more detail in a subsequent section.

Fig. 5.36. TEM micrograph of a twin colony within a grain which is not fully twinned. Note that individual dislocations can be imaged within the twins.
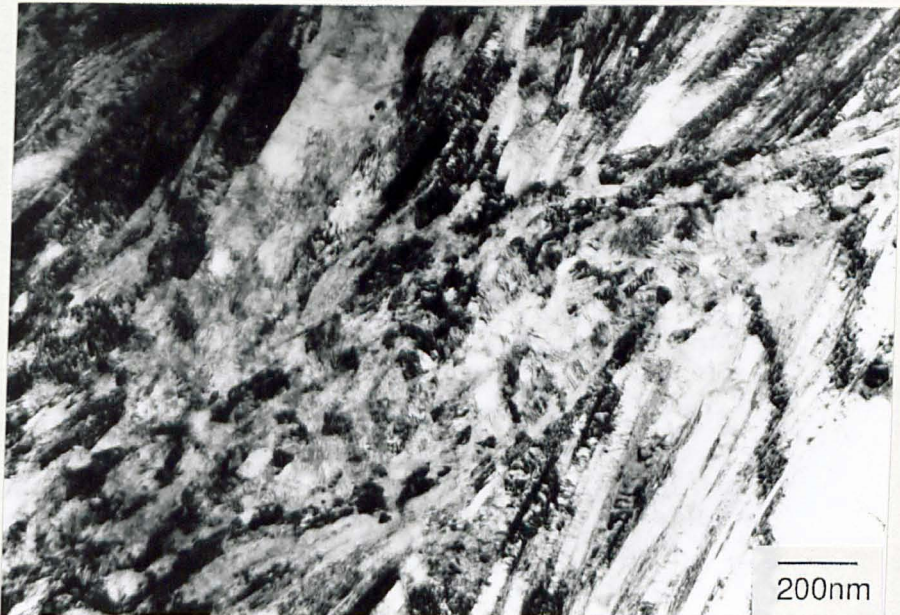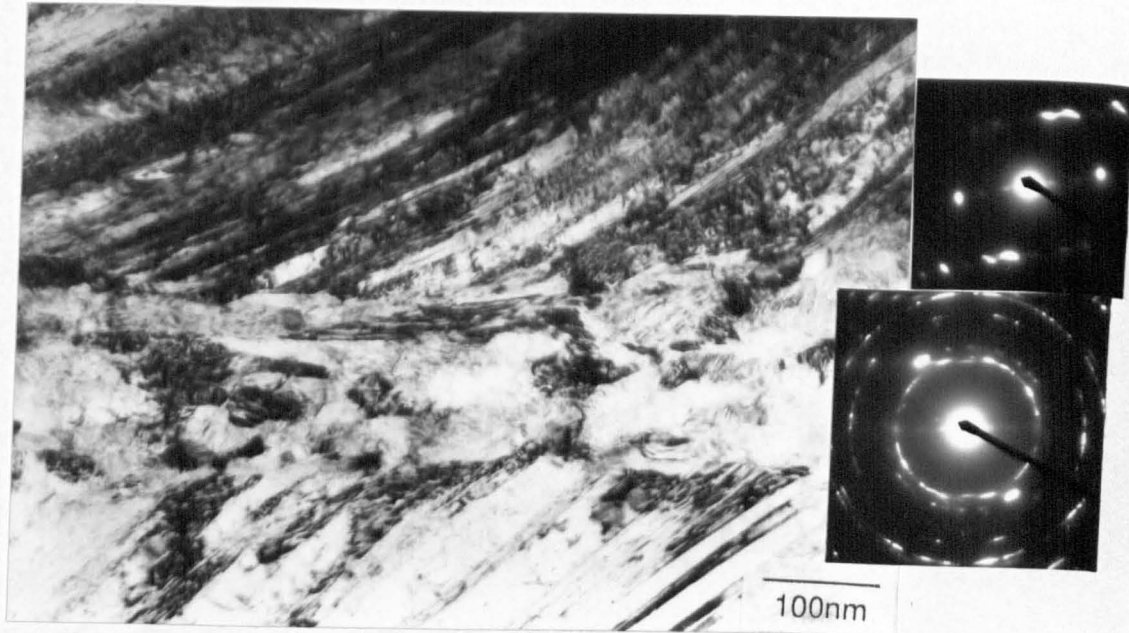

Fig. 5.37. TEM micrograph showing a fresh shear band passing through a twin colony. Note the distortion of the twins lower right. The shear band is running parallel to the surface. $12\mu m$ below the surface.

S.D.←

Fig. 5.38. TEM micrograph showing a detail of fig 5.37, showing the
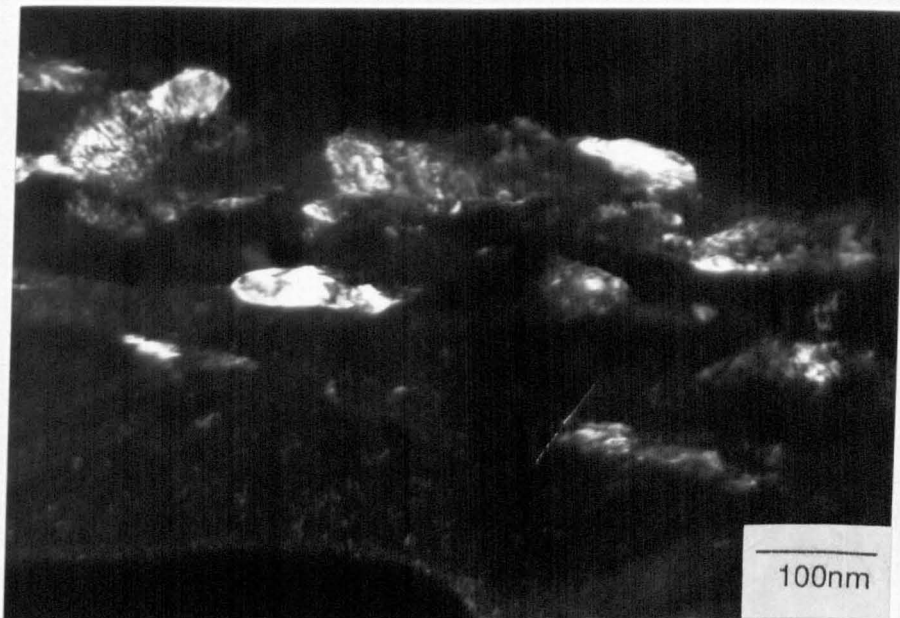interface between shear band and twin colony.

Fig. 5.39. TEM dark field micrograph of fig 5.38, showing the fine
crystallite size.
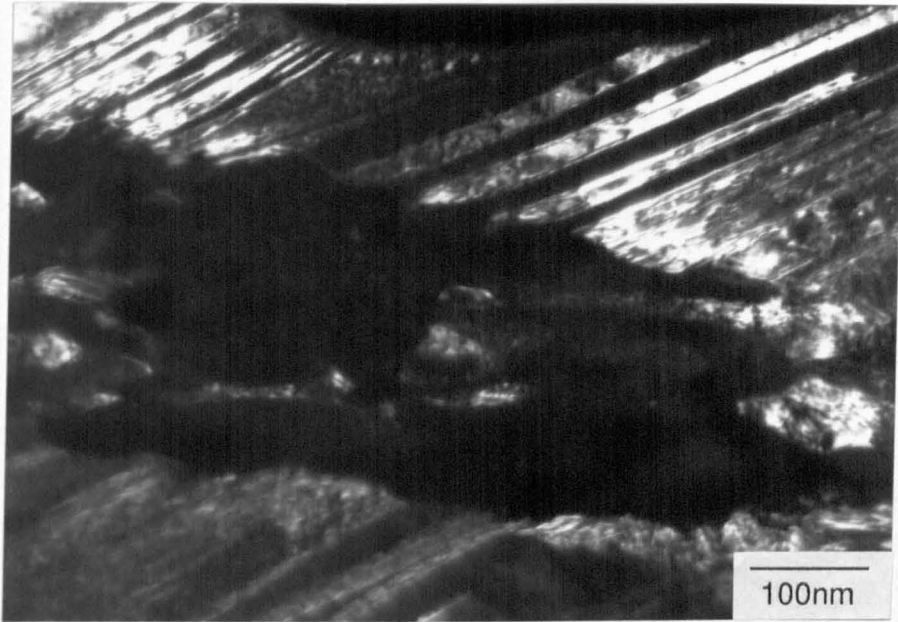
Fig. 5.40. TEM dark field micrograph of fig 5.38 using a twin
reflection. Note the curvature of the twins and the undulating
interface between the shear band and twins.

SHEAR BANDS TO
SURFACE

TWINS
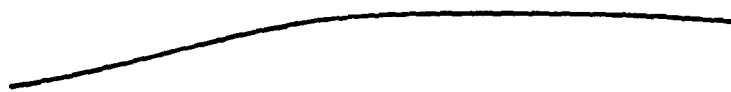
SHEAR BANDS
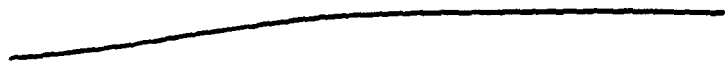
TWINS

SHEAR BANDS

TWINS

S. D.

Fig. 5.41. Composite TEM micrograph showing the typical structure of the transition region. The different regions of twins and shear bands can only be clearly differentiated by the diffraction patterns. A schematic is provided on the facing page.

S.D.↑
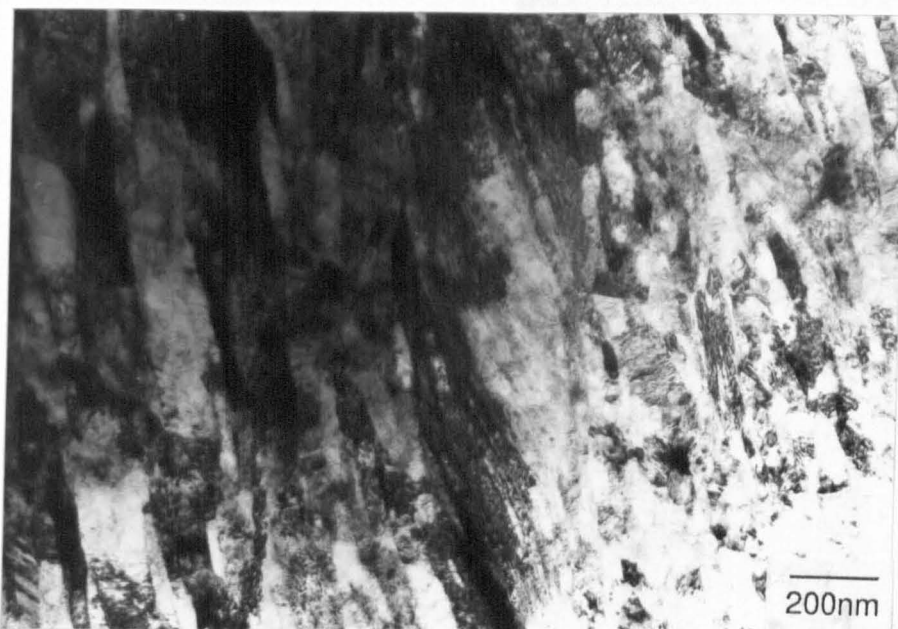
Fig. 5.42   TEM micrograph of a 'rhomboidal prism' of twins lying parallel to the surface at a depth of about 10μm.
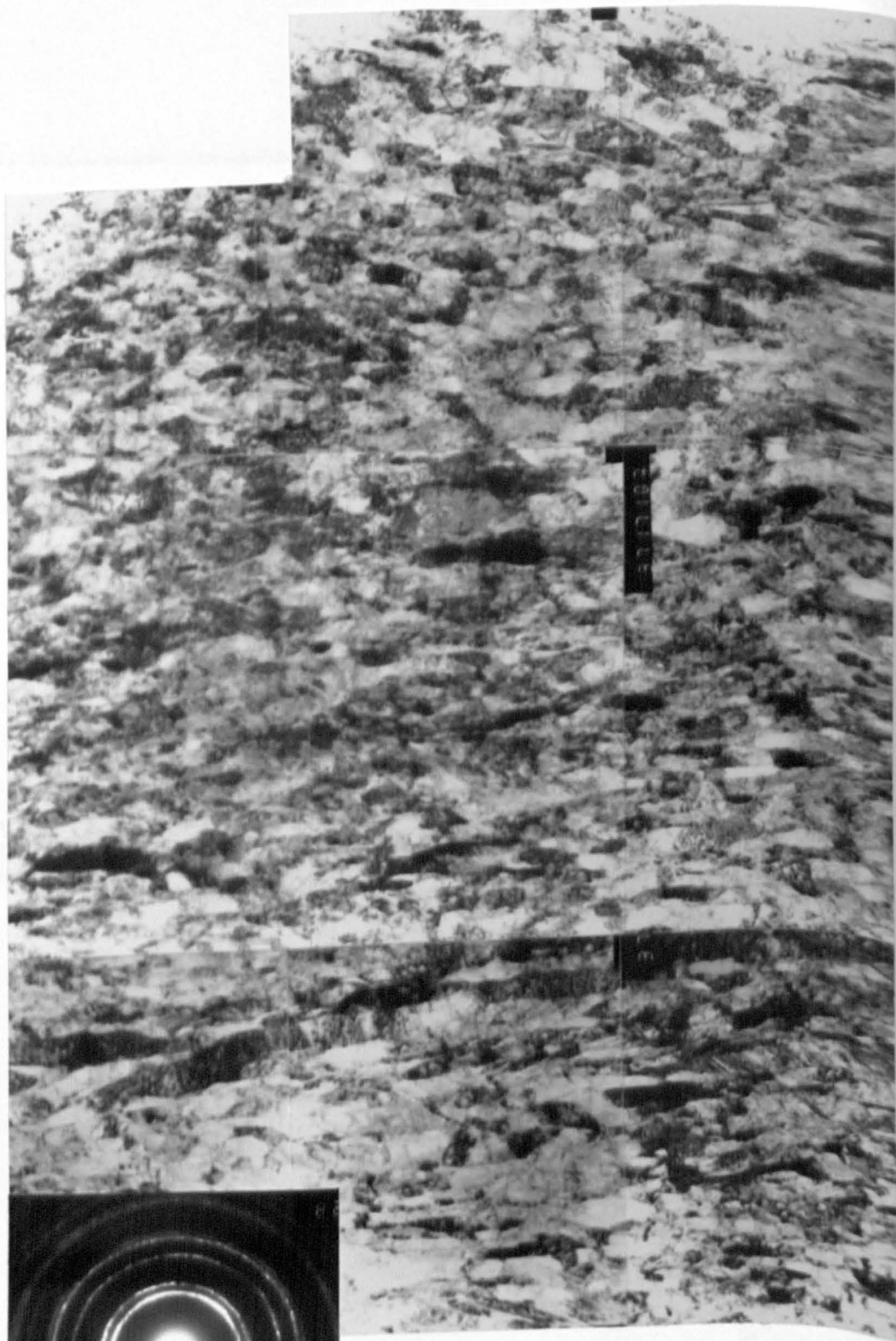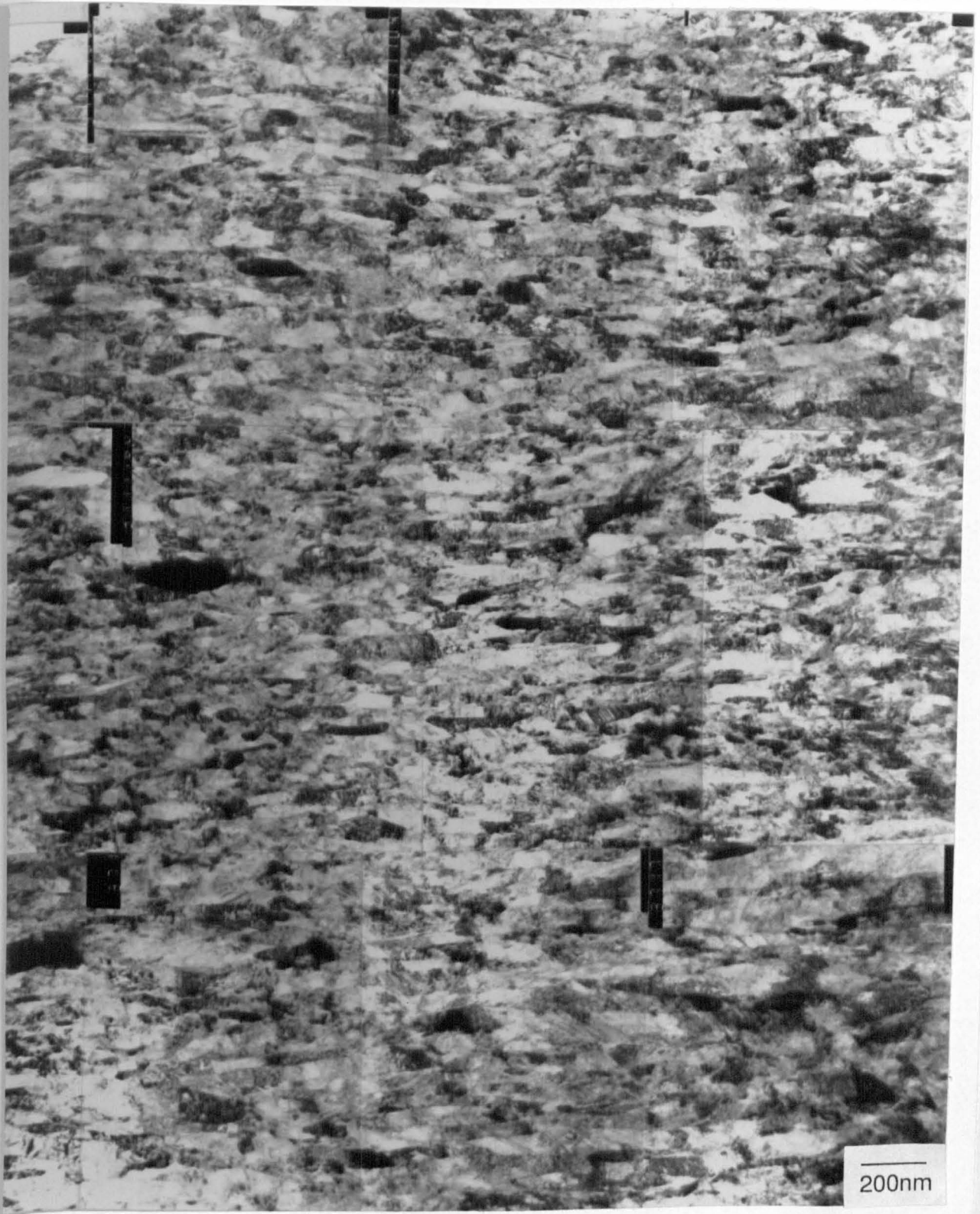

S.D.→
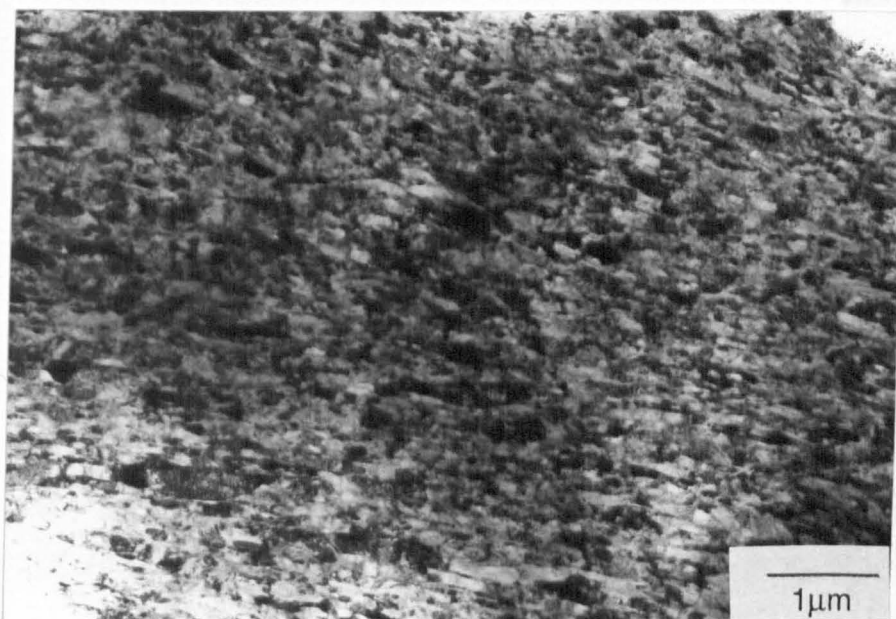
Fig. 5.43.   TEM micrograph of the shear banded region.   Note that the crystallite size and aspect ratio remains relatively constant and that they are uniformly aligned with the sliding direction.

Fig. 5.41. TEM micrograph of...
(titanite) are also not linear...
they are abnormally arr...

200nm
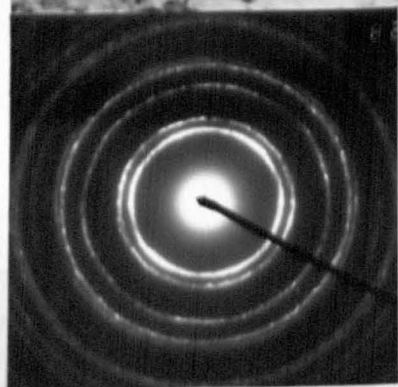
S.D. →

Fig. 5.44. Detail of fig. 5.43 illustrating the uniform nature of the microstructure in the shear banded region.
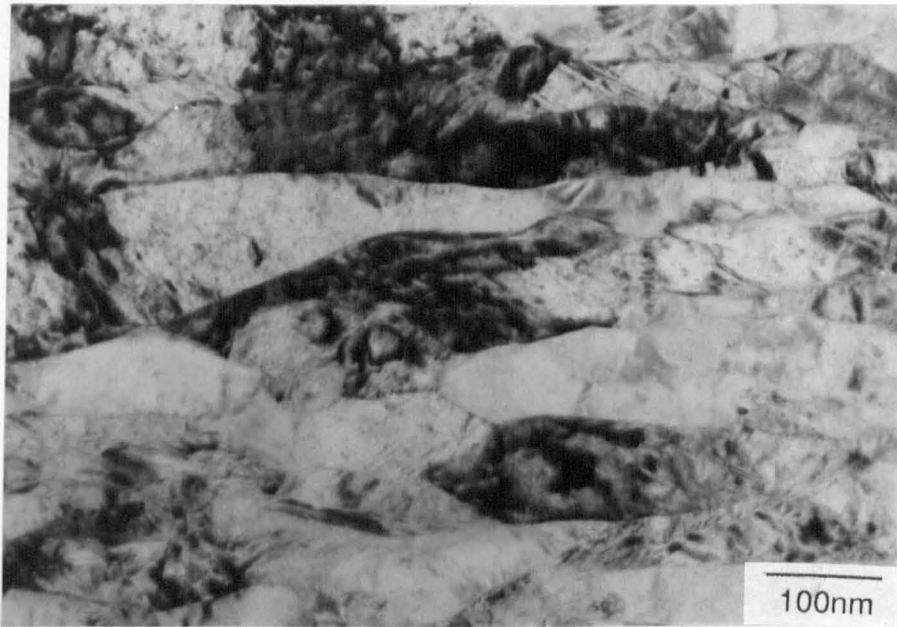
Fig. 5.45. TEM micrograph showing a detail of the crystallites. Note
the low dislocation density and the fine microtwins.

Fig. 5.46. TEM micrograph showing twinning which is most probably
incorporated from the subsurface twins, although they could be a result
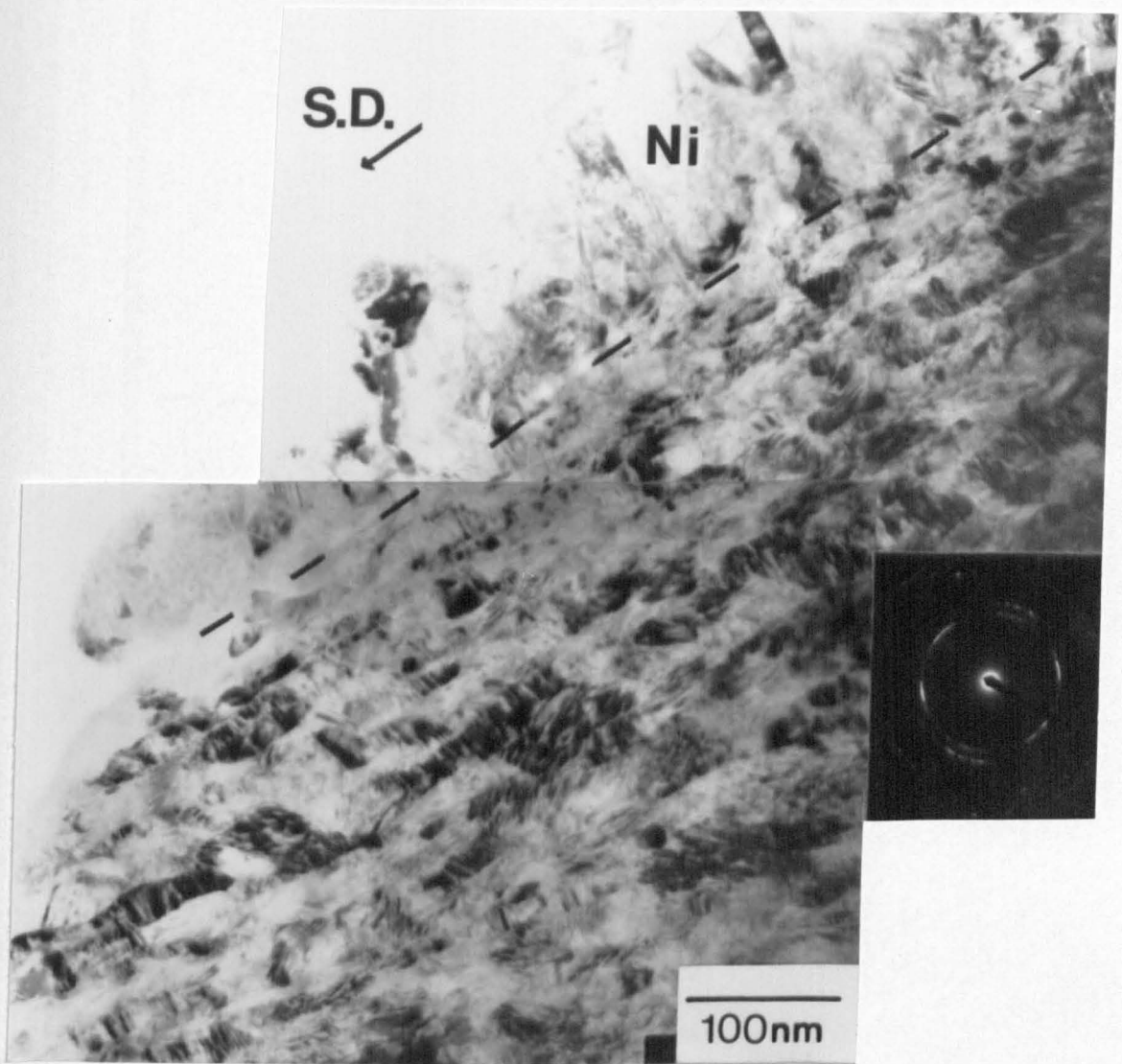of recrystallisation.

Fig. 5.47. TEM micrograph of the freshly formed shear bands at the surface. Note the very fine and rugged appearance of the crystallites.
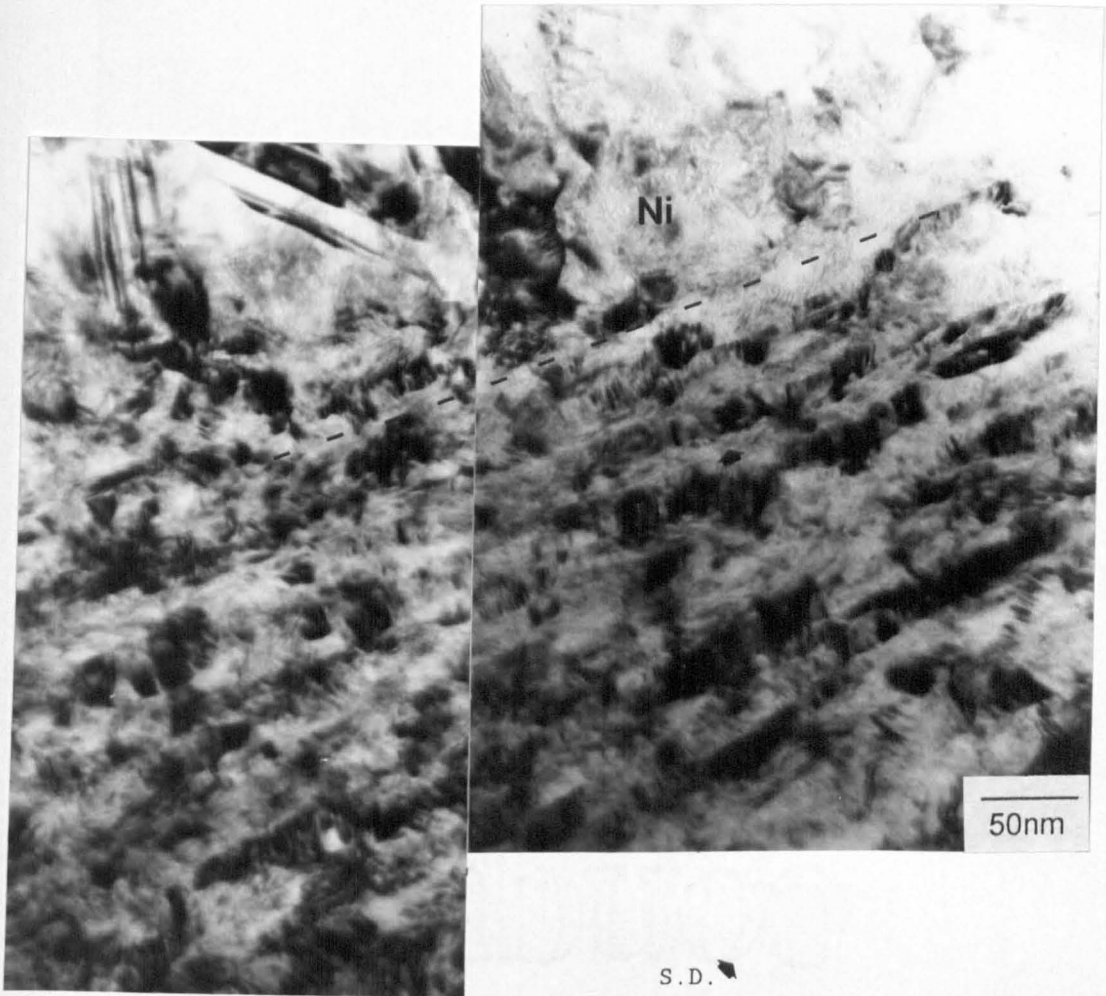
Fig. 5.48. TEM micrograph of extreme surface. Note the very fine microcracks running along some crystallite boundaries (arrowed).
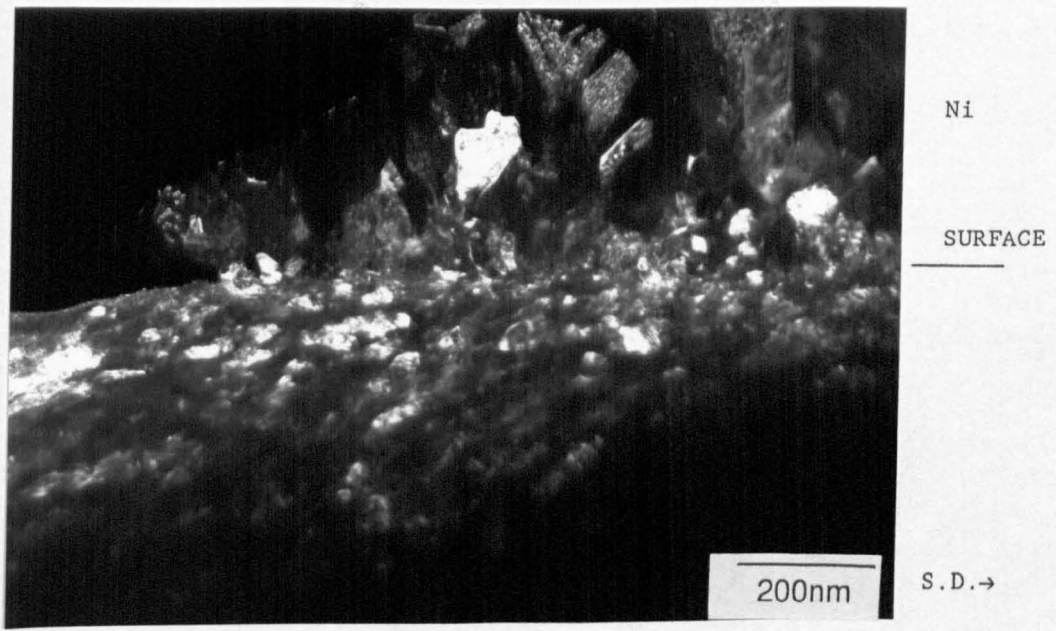

Fig. 5.49. Dark field micrograph of the surface shear bands. As the surface is approached the crystallites become more equiaxed.

The structure of the shear bands between the transition region, discussed above, to within 200nm of the worn surface is shown in figs 5.43,44. The structure consisted of small crystallites, elongated in the direction of sliding, having sharp boundaries and low internal dislocation densities, fig 5.45. High misorientation existed between the crystallites, although when averaged over numerous crystallites a texture was evident (texture will be discussed in detail in section 5.4.2.6). Thus, the crystallites are very similar to those produced by rolling above a strain of 3. The sharpening of the crystallite boundaries, and the increase in their aspect ratio compared with when they have just been formed, indicates that homogeneous deformation has taken place. However, the crystallites were generally less elongated compared with those in the rolled specimen, and the aspect ratio showed very little increase towards the surface. In addition, the structure was less wavy than that with rolling. This was clearly a result of the shear bands being formed along the direction of sliding. In contrast, the shear bands were formed during rolling at both +30° and -30° to the rolling plane, and were subsequently rotated towards the sliding direction.

Some evidence of very fine mechanical twinning was found in one or two of the crystallites, fig 5.45,46. The latter figure also shows larger, parallel sided features. These could either be recrystallisation twins or mechanical twins incorporated into the microstructure, but they were too small to generate fresh shear bands. The former explanation appears unlikely since recrystallisation would produce an equiaxed grain. Further deformation to the aspect ratio of the crystallite in fig 5.46 would have distorted the twins more than had occurred. The latter explanation therefore appears more reasonable.

The region within 200nm of the surface is shown in fig 5.47. This is typical of all the surface where oxide was absent and shows a significantly smaller crystallite size than the region immediately below. The crystallites were ragged, with badly defined boundaries and elongated in the direction of sliding, having aspect ratios in the region 1:2 to 1:3. The appearance of the surface region suggested that the shear bands had just been formed and that they had not undergone any subsequent homogeneous deformation. Also, the thickness of the fine, rugged crystallite region (about 200nm) was of the same order as the freshly formed shear bands in the transition region.

Further examples of the surface region are given in figs 5.48,49.

Note the extremely fine fissures present in fig 5.48. These are most probably microcracks since it would be most unlikely that differential thinning by the ion beam would occur on such a fine scale. This suggests a deformation mechanism involving microfracture and subsequent re-welding.

Several areas contained oxide particles. However, the structure of the oxide was better illustrated by the test at 55 N/pin and will therefore be considered in the next section.

5.4.2.2 Microstructure as a Function of Load

At 2.2 N/pin the crystallites in the shear bands were very similar to that of the 24 N/pin except that the shear banded region was much narrower. One significant difference in the microstructure from that at higher load was the precise boundary found between the shear bands and the twins, fig 5.50. One or two examples of twins swept into the shear banded structure were also found. Fresh shear bands were found at all surface regions, indicating that contact was fully plastic.

The microstructure at 55 N/pin was dominated by surface oxide. A general view of a typical region is given in 5.51,52. It is immediately apparent that the oxide flowed with the metal, producing a lamellar structure. The scale on which the oxide and metal had mixed was remarkably fine, fig 5.53. The flow of the two phases led to the formation of a composite, which was apparently microcracked in a manner similar to some of the surface regions (eg fig 5.48).

The oxide did not contain any Fe_3O_4, but consisted of a mixture of an amorphous phase and a non equilibrium BCC phase, identical to that found in the wear debris. As with the wear debris, no evidence of any zirconia could be found in either the metallic or the oxide regions.

Certain regions where the oxide was present, (as a result of recent incorporation of wear debris), were characterised by the sharp boundaries between metal and oxide, and the equiaxed form of the oxide particles, fig 5.54,55. Similarly, transfer of debris could be found at the surface, fig 5.56. Examples of surface and sub-surface cracking are shown in fig 5.57. Cracks perpendicular to the surface tended to either be arrested in metallic regions, or turn parallel to the surface, propagating along oxide fissures.

The presence of a brittle oxide in the surface regions, with associated cracking, would be expected to increase the wear rate. However, the oxide showed a relatively small amount of cracking and

generally appeared to flow with the metal. No evidence of loss of large particles from the surface could be found. Therefore, it would appear that the compressive forces have prevented widespread failure in the oxide, and have even been sufficient to plastically deform it. The reduced adhesive forces from oxide compared to metal contact will have reduced the tensile component of the surface stress system thereby further reducing the tendency for delamination.

The mode of formation of the oxide remains unclear. Few areas could be found which showed a transition from the metallic to the oxide state. Figs 5.53,55 show examples of such regions of metallic material at the interface between shear bands and oxide which contained an equiaxed structure with a grain size considerably smaller than in the shear banded region, typically 5-10nm. Such areas were considered to be part of a transition from oxide to metal. Unfortunately, facilities were not available to detect oxygen at the required spatial resolution. Such a fine grain size could have been produced by thermal transients leading to dynamic recrystallisation during deformation. However, the absence of a similar morphology at the extreme surface would tend to counter this theory. More probably, the fine grained material had undergone a phase transformation to the oxide.

The general absence of material showing a transition from metal to oxide calls into question the location and mechanism whereby the oxide was formed. The majority of the oxide appeared to have been incorporated into the surface and subsequently deformed, rather than being formed in-situ. This suggests that the majority of the oxide formed on the zirconia surface, or by oxidation of fine debris particles, where rapid kinetics could occur. This issue will be discussed later after estimates of surface temperatures have been made.

In the few regions where metal was exposed to the surface and did not contain any oxide, the deformation characteristics for 55 N/pin followed the same trend as at 24 N/pin. The crystallite morphology and size remained the same as at 24 N/pin. The only notable difference was in the twinned region, as shown in figs 5.58,59. Several examples were found where the dislocations had formed a more pronounced cell structure than in the rolling experiments or in any of the other wear tests. As noted in chapter 4, the appearance of the dislocation arrangement can be a result of the orientation of the grain with respect to the foil surface [290]. However, similar orientations to that in fig 5.58 generated at lower loads, showed a less pronounced
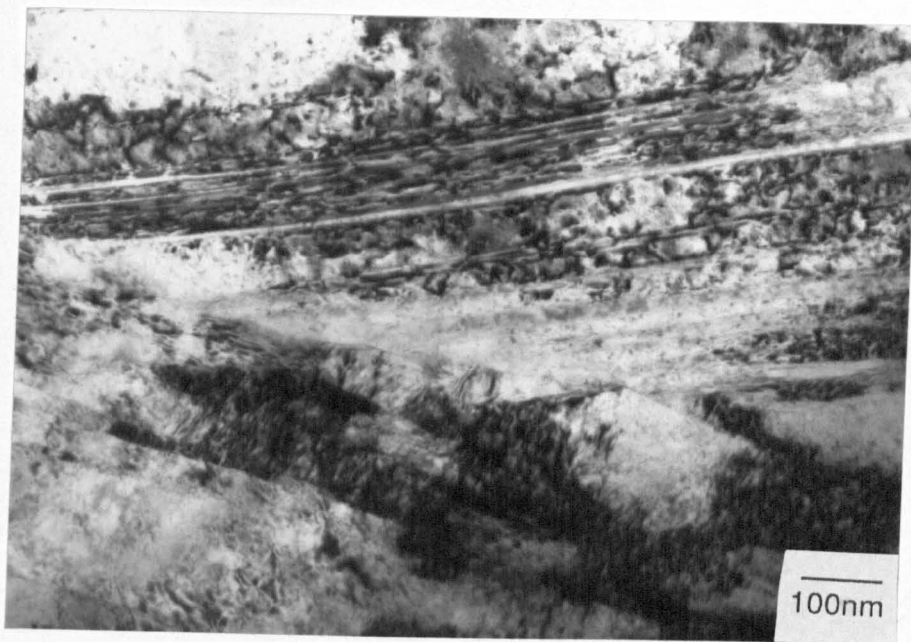
Fig. 5.50. TEM micrograph showing the sharp boundary between the shear bands and twins. (2.2 N/pin).
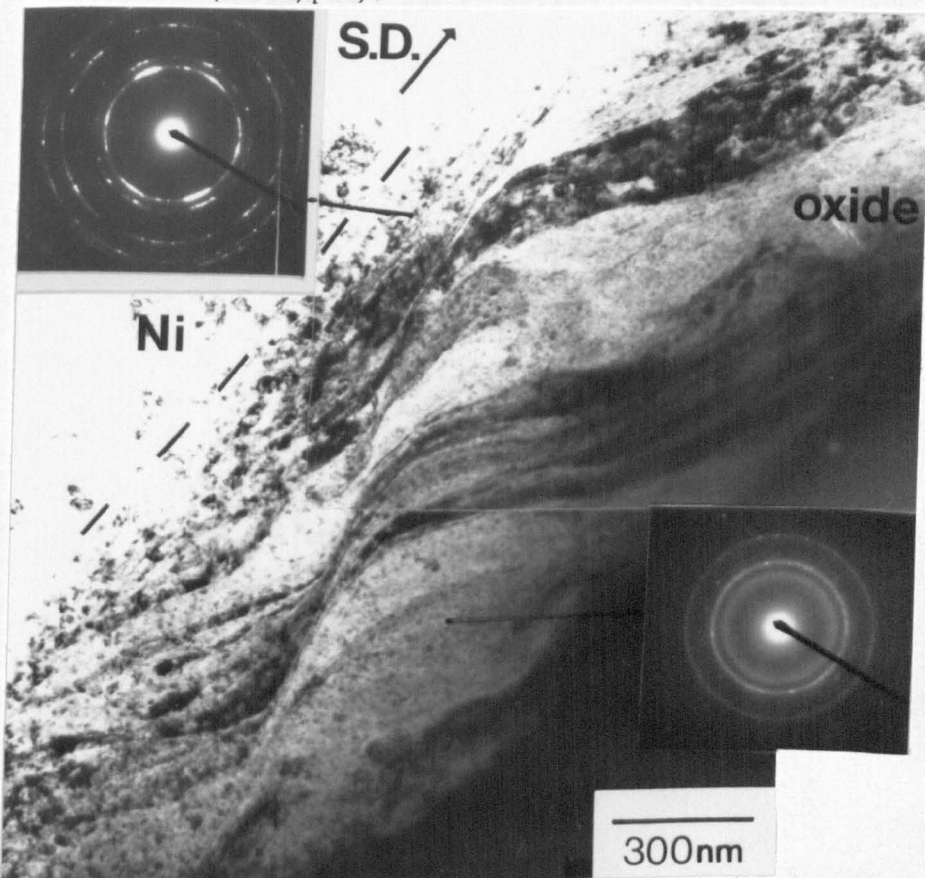

Fig. 5.51. TEM micrograph of the surface where oxide has become intimately mixed with the metal and has been cooperatively deformed. (55 N/pin).
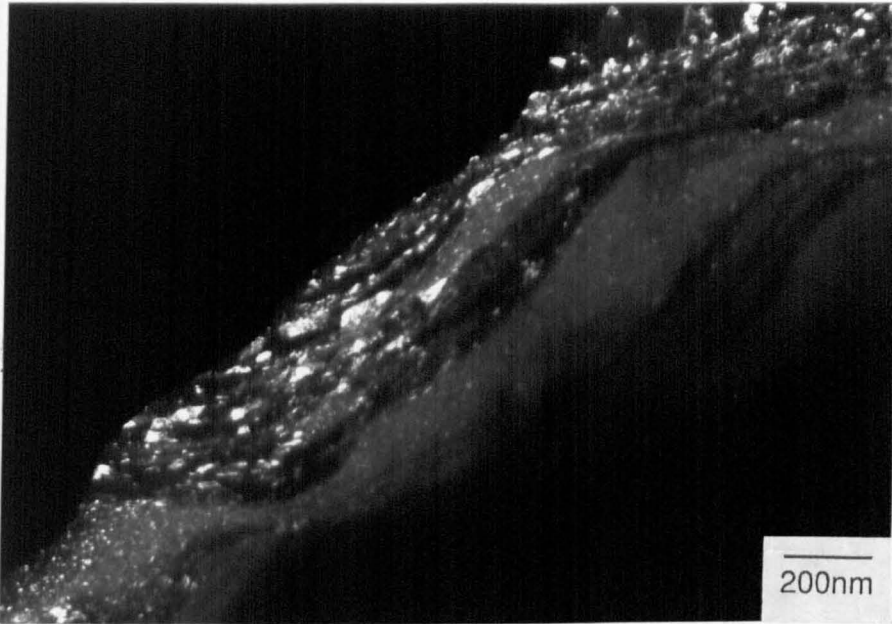
SURFACE

Fig. 5.52. Dark field micrograph of the surface region. Note the fine crystallites within the oxide and the wavy nature of the flow. (55N/pin).
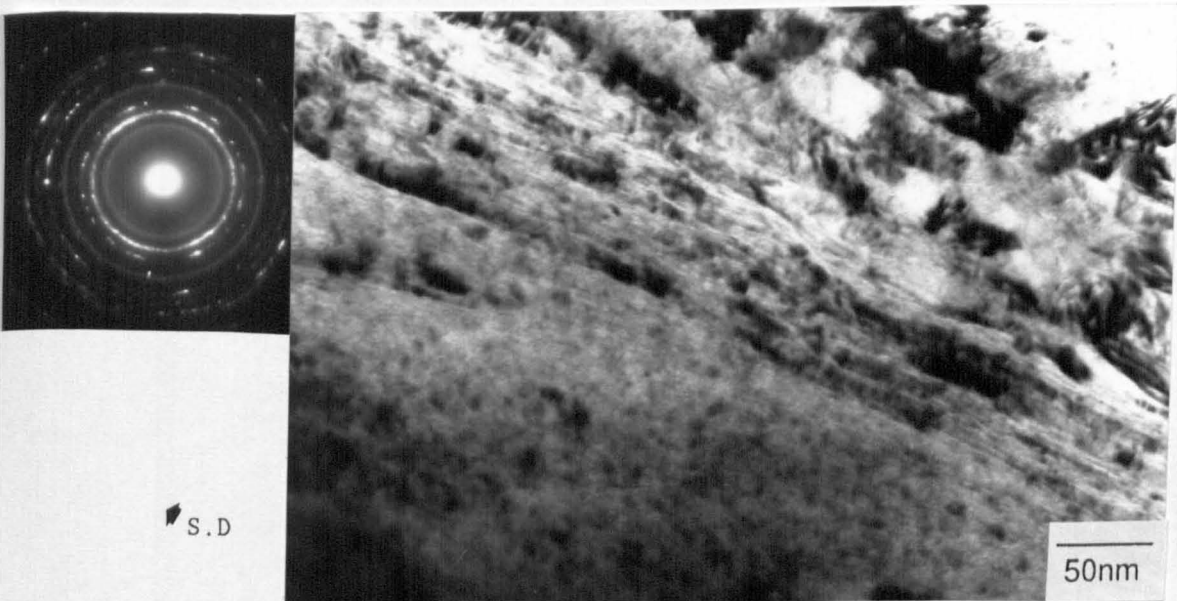

S.D

Fig. 5.53. TEM micrograph demonstrating the fine scale on which the oxide and metal have mixed, forming a composite microstructure. Note the fine microcracks. (24 N/pin).
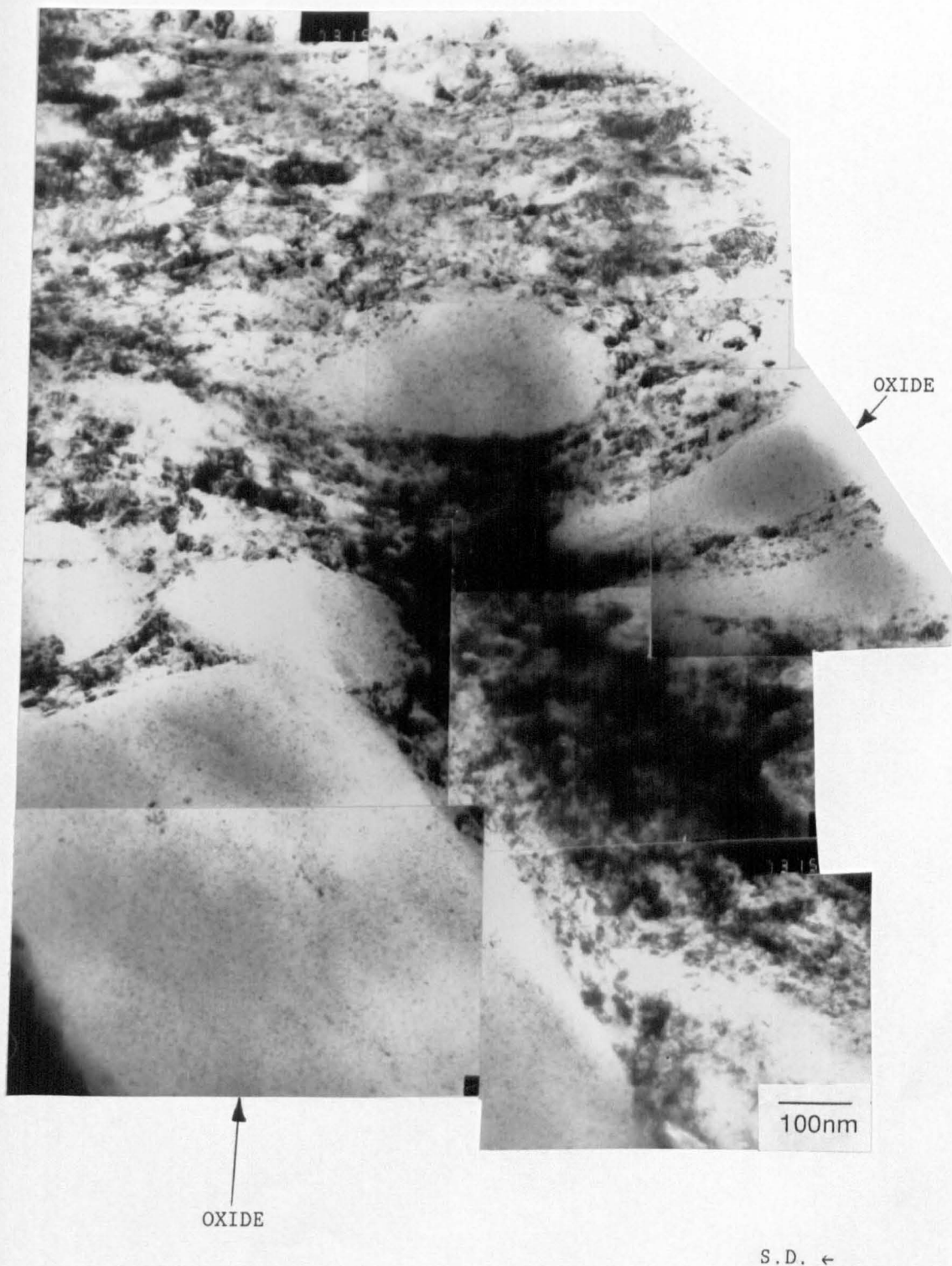
OXIDE

OXIDE

100nm

S.D. ←

Fig. 5.54. TEM micrograph showing a region where oxide has become impressed into the surface, but has not been elongated in the direction of sliding. (55N/pin).
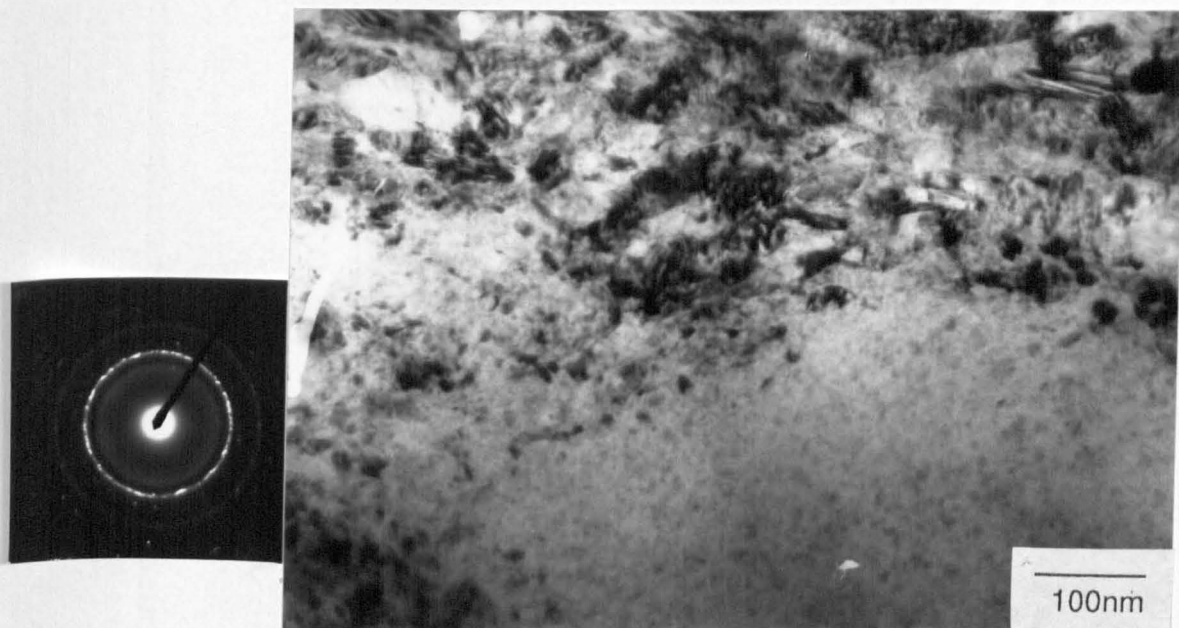
Fig. 5.55. TEM micrograph showing a detail from fig. 5.54. The interface shows a region of equiaxed crystallites which are larger than in the oxide, and could represent a transition from metal to oxide.
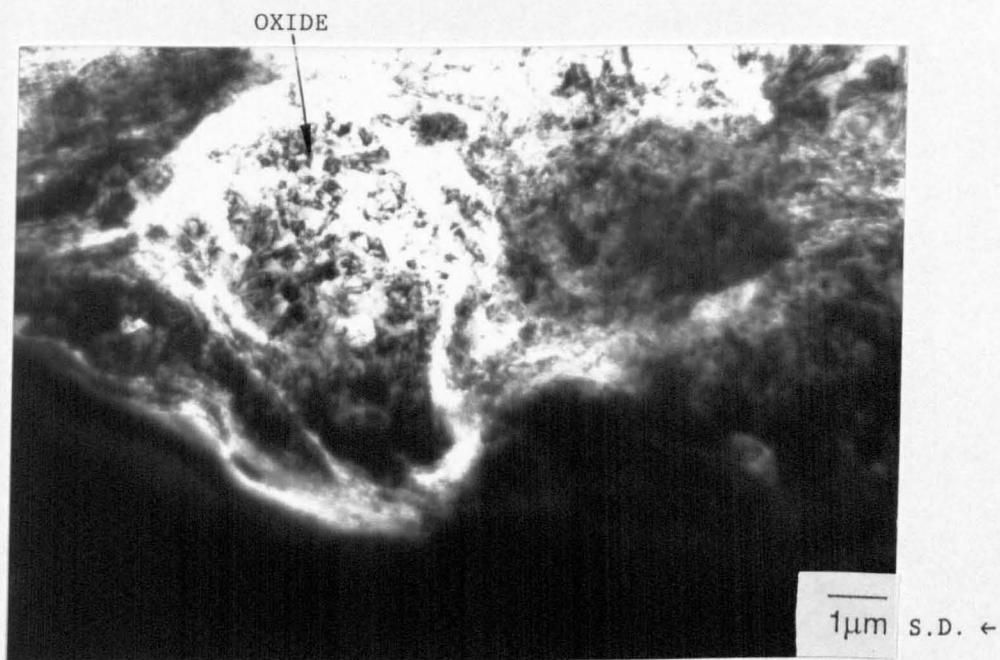

Fig. 5.56. TEM micrograph showing a particle of oxide impressed into the surface. (55 N/pin).
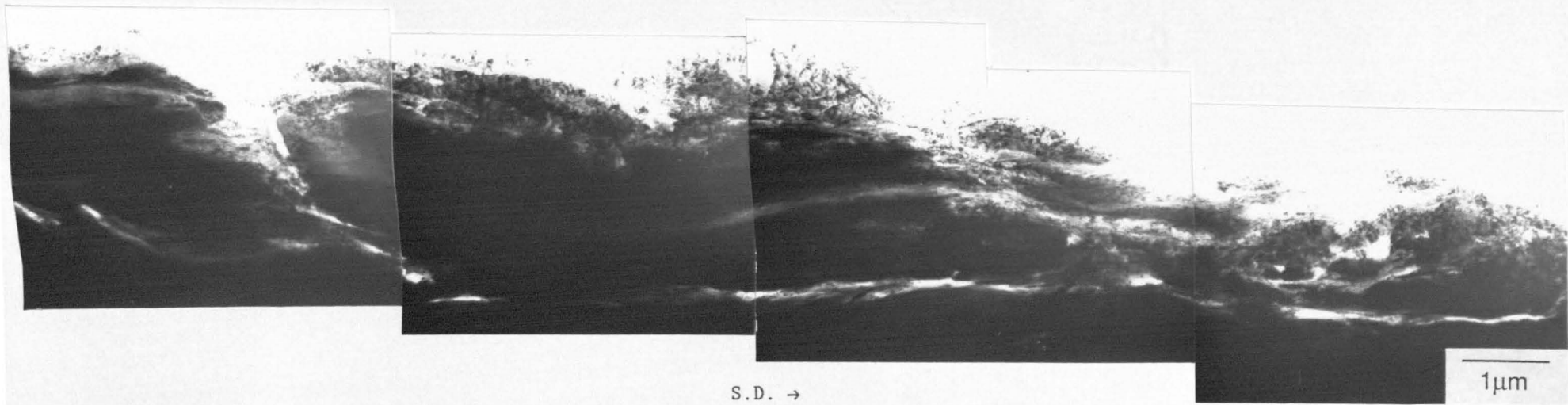
S.D. →

1μm

Fig. 5.57. TEM micrograph showing subsurface cracking. However, this was comparatively rare. (55 N/pin).
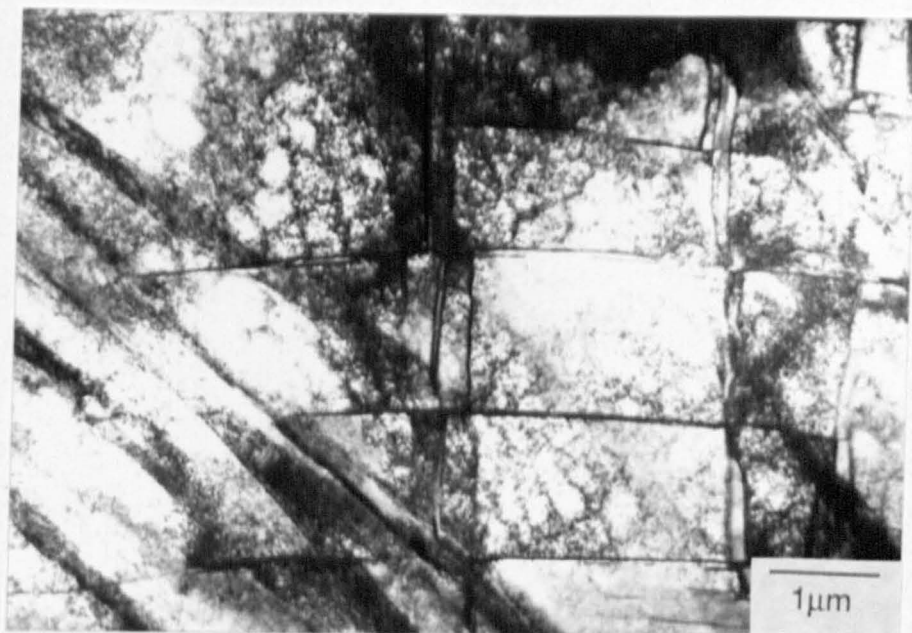
Fig. 5.58. TEM micrograph showing twinning on two systems. Note the
poorly formed cells. (Multibeam conditions, 55 N/pin).
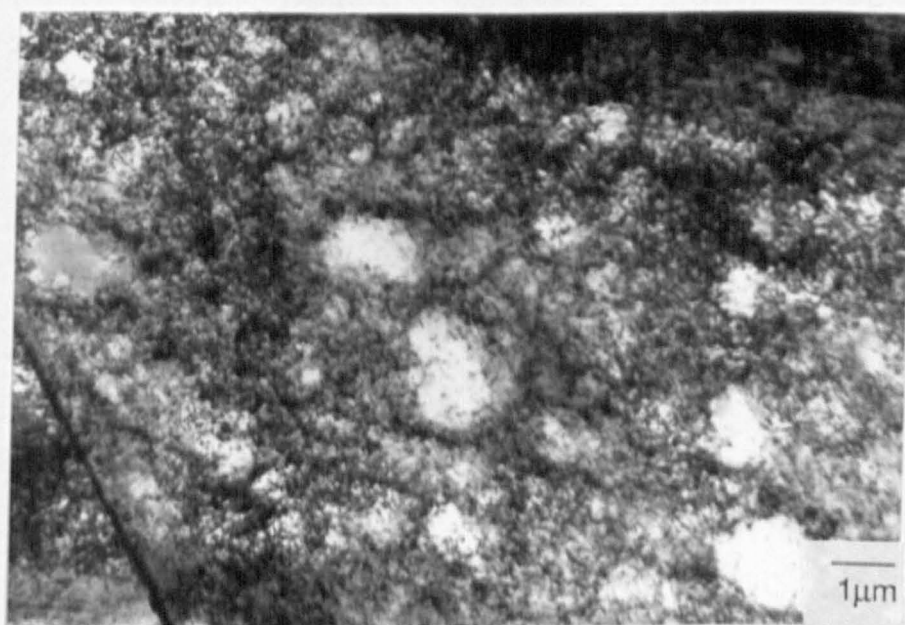

Fig. 5.59 Detail of fig 5.58. Some regions contain a uniform
dislocation density whilst others are arranged in ragged cells.

cell structure. This suggests that a small rise in stacking fault energy had occurred as a result of temperature rises at the surface. Alternatively, the cell structure may have resulted from a different stress system than that imposed by rolling. However, it should be noted that recovery as a result of temperature rises during foil preparation could also provide an explanation.

5.4.2.3 Back Thinned Samples

Back thinning was performed on the samples from 24 and 55 N/pin tests to confirm surface crystallite sizes. An example of the surface structure is shown in fig 5.60. As with rolling plane foils, the structure was difficult to understand, especially since the shear bands are freshly formed and are therefore badly defined. Below the surface the crystallites became sharper, fig 5.61, in agreement with results from cross sectional foils. Occasional examples of equiaxed crystallites were found, fig 5.62. As noted in chapter 4, such observations from rolling plane foils have led to conclusions of dynamic recrystallisation [213], although this was shown not to be the case by the cross sectional foils.

Regions of δ ferrite could not be found in the near surface regions. This was not considered to be a result of sampling, since the ferrite colonies were readily observed in rolling plane foils. This suggests that the ferrite had been swept into the shear banded structure as a result of the very high local strains and the different geometry of the stress system in sliding wear, compared to rolling.

Regions of surface oxide were widespread. Interestingly, the shear bands tended to flow around the oxide regions, fig 5.63. Therefore, the oxides clearly acted to impede metal flow, thereby effectively increasing the degree of work hardening of the surface as a whole.

5.4.2.4 Extruded metal wear debris

Samples of the extruded metal wear debris were removed from the trailing edge of the 24 N/pin test and ion beam thinned. Thin areas were generally small because of the variable starting thickness of the sample. The microstructure was essentially the same as that in the worn surface, as shown by fig 5.64, with the crystallite size the same as in the region >200nm away from the surface. No examples of the surface structure were found, although these would be expected to have been eroded by the ion beam prior to electron transparency being
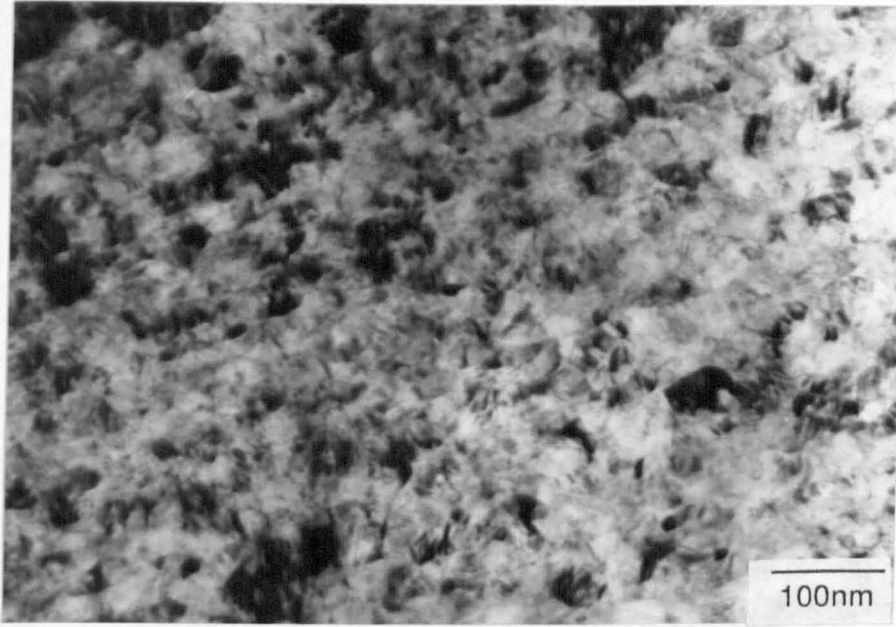
Fig. 5.60. TEM micrograph showing the surface crystallites. The structure is not easily resolvable. (Back thinned, 24 N/pin).
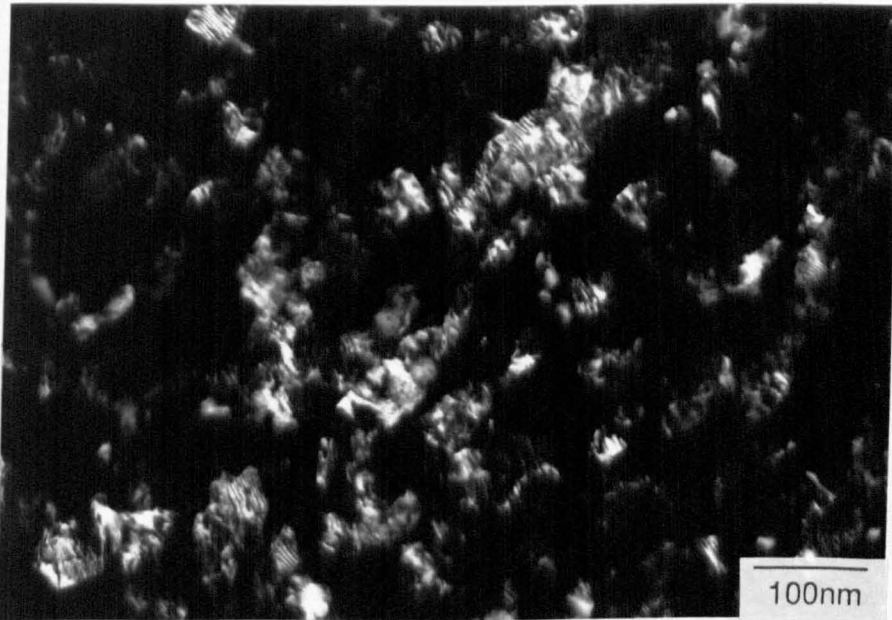
Fig. 5.61. Dark field micrograph from further below the surface (>200nm), where the crystallites are better defined.

Fig. 5.62. TEM micrograph showing an occasional crystallite which appears equiaxed. This was not as a result of dynamic recrystallisation.

S.D. ↑
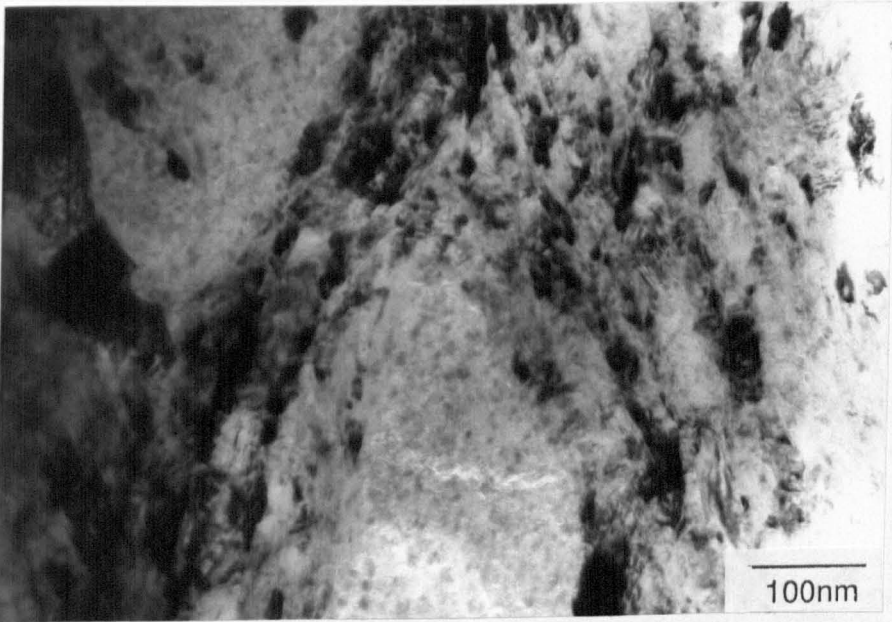
Fig. 5.63. TEM micrograph showing flow of the shear bands around the oxide particles, demonstrating that the oxide impeded flow.

Fig. 5.64. TEM micrograph of the extruded debris. The crystallite structure and size is similar to that in fig. 5.44. (24 N/pin).

100nm

Fig. 5.65.   TEM micrograph of the extruded debris showing grains which may have undergone dynamic recrystallisation.

achieved.

One or two areas were observed which showed a slightly larger crystallite size, but were more equiaxed and rounded, as shown in fig 5.65. This again calls into question the possibility of dynamic recrystallisation. However, comparison of this micrograph with fig 5.62, suggests that the morphology was a consequence of th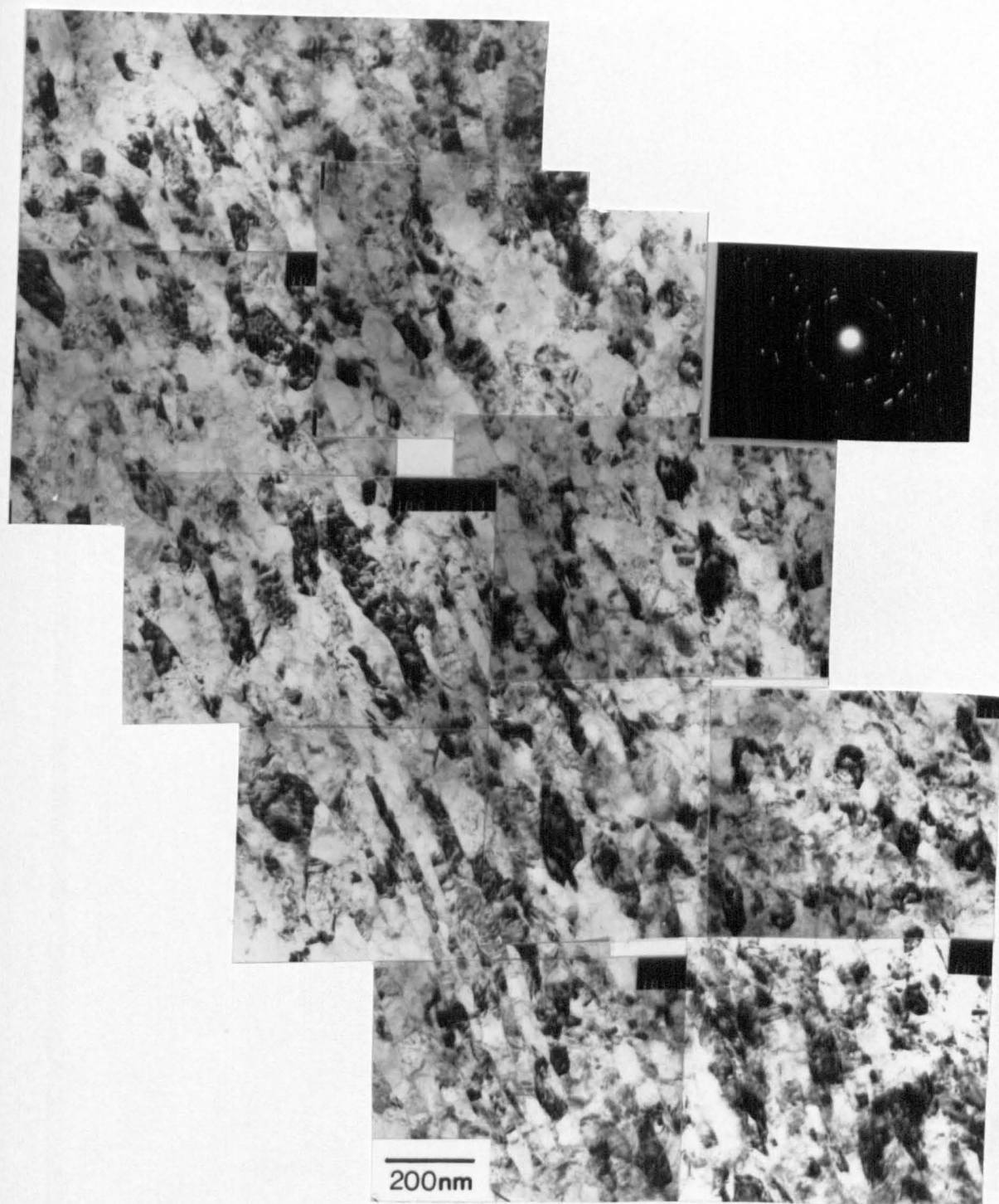e plane of view, and that the crystallite would appear the same as the rest of the shear banded microstructure if viewed in a perpendicular direction. If this were the case, it would demonstrate the manner in which the microstructure is rotated and distorted in the extruded debris, presumably as a result of the lack of constraint from the surface.

5.4.2.5 Crystallite size

The crystallite thickness as a function of depth from the worn surface, for the tests at 24 and 55 N/pin, is shown in fig 5.66. The crystallite thickness at the surface remained within the range 8-23nm over the first 200nm depth irrespective of load or position along the surface.

In the first 200nm, the thickness of the crystallites rose rapidly with depth. This is demonstrated in the montage in fig 5.67. The thickness of the crystallites in the sub-surface region, which had undergone some homogeneous deformation, varied considerably, but showed little tendency to increase with distance from the worn surface. For example, the average crystallite size in the 24 N/pin sample is the same at 700nm as it is at 3.8 μm. The aspect ratio also showed little change with distance from the surface. However, the sample at 55 N/pin showed a more significant rise in crystallite thickness with depth, although the overall thickness of the shear banded region was smaller. Even so, the average value shows only a small increase with depth.

The crystallite sizes outlined above are compared to the results of Blicharski & Gorczyca [211] in fig. 5.68, along with the crystallite sizes recorded in the rolling experiments. The surface crystallite size is considerably smaller than that recorded for freshly formed shear bands in the rolled material, or for any measured by Blicharski & Gorczyca [211]. The crystallites in the sub-surface wear region were slightly larger than those in the rolled samples suggesting that they had been produced either by a lower strain than 3 or at a higher temperature. It is important to note that geometrical differences may also have been important.
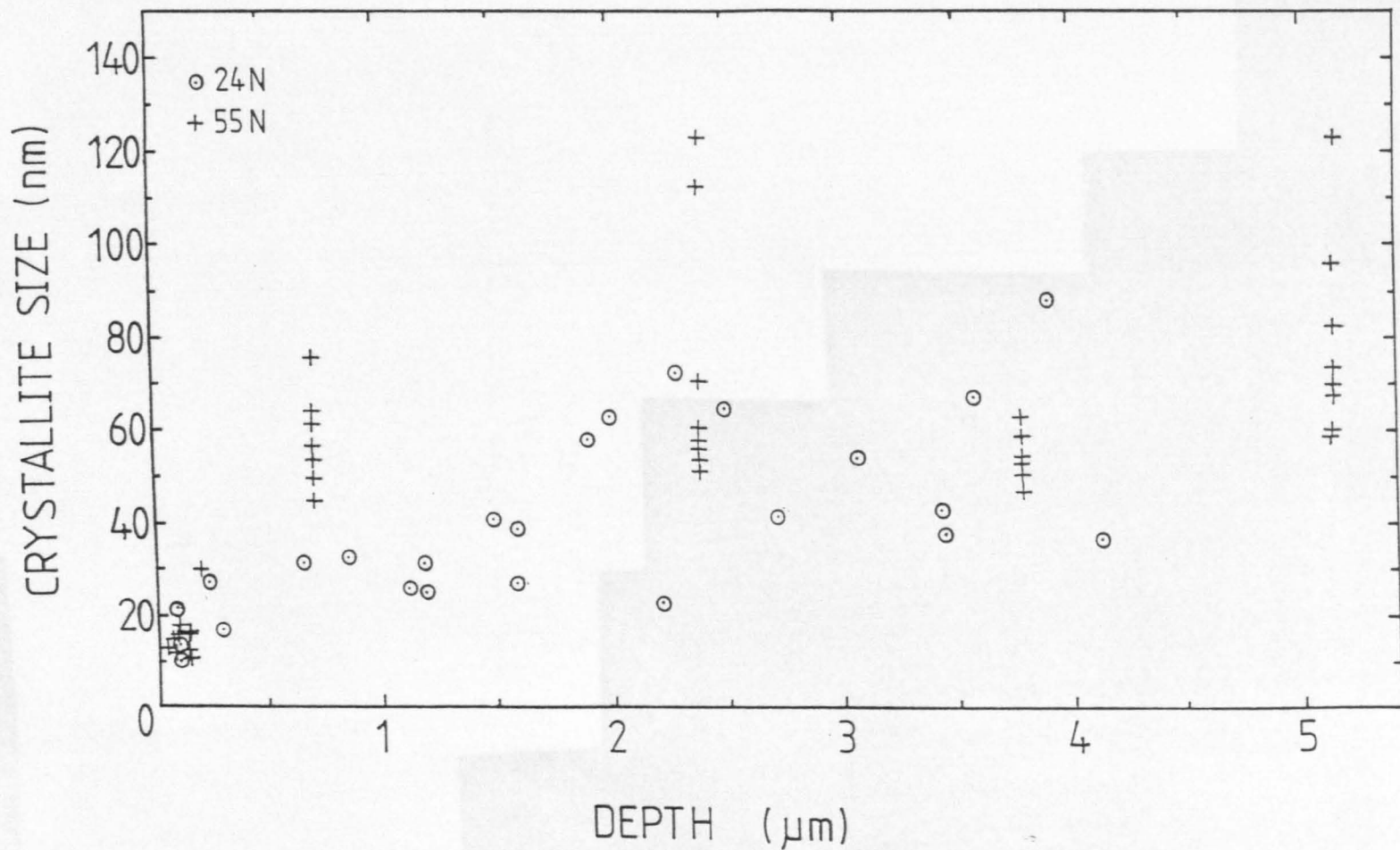
Fig. 5.66. Crystallite size as a function of depth for the tests at 24 and 55 N/pin. Note the very fine surface crystallites.

SURFACE

200nm

S.D. →

Fig. 5.67. TEM micrographs showing the rapid increase in crystallite size in the transition from the freshly formed shear band to the homogeneously deformed crystallites. (55 N/pin).
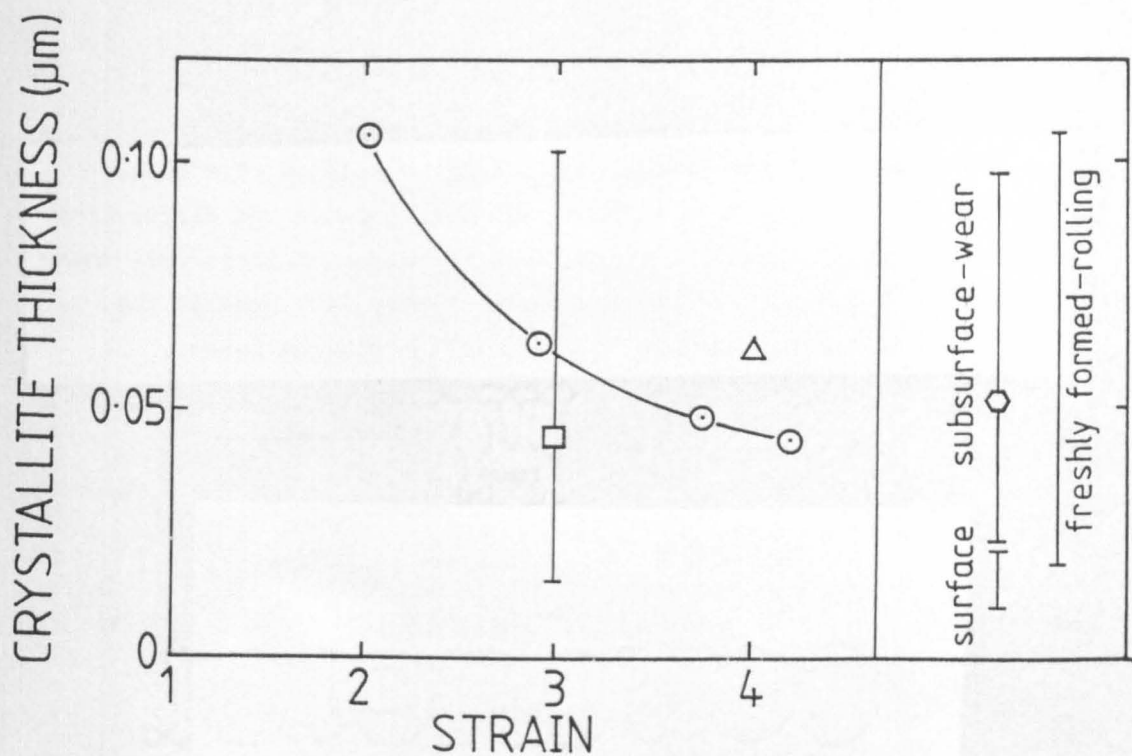
Fig. 5.68. The results from the present study are plotted on a graph taken from Blicharski & Gorczyca [126] (original for rolling). ⊙ [211]; □, ◇ present; Δ [200].
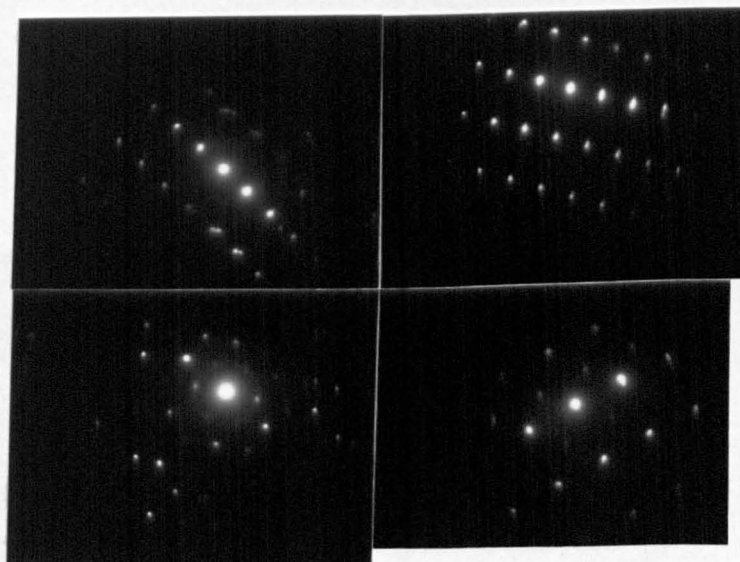
Fig. 5.69. Micro diffraction patterns taken from adjacent crystallites at about 150nm from the worn surface. (24 N/pin).

Measurement of the texture could only be made on thin foils
perpendicular to the worn surface. This is because the diffracting
planes are nearly parallel to the electron beam and it is only those
planes which are parallel to the surface which will exhibit the
texture. An example of this is given in the diagram below.

surface

↑ normal direction

•022̄

•   •1̄11̄

•   .000̣ 002̄ ——→ sliding direction
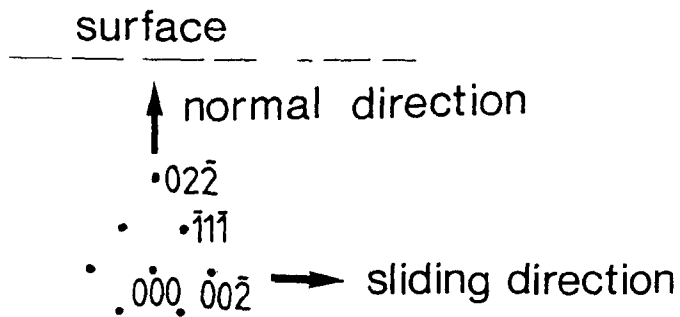
d.p. indicating {110}<001> type

Diagram showing the method of texture assessment. The preferred planes
are shown by those parallel with the worn surface (if present) whilst
the preferred direction is that parallel to the sliding direction.

5.4.2.6 Texture analysis.

Texture analysis was performed mainly by electron diffraction analysis in the TEM. Pole figures were not constructed because of the nature of the texture found in the TEM, namely a wire texture. Such a texture would be difficult to analyse using the reflection diffractometer method since only a limited angle could be covered which would not include the fibre axis. In addition, pole figure analysis would average out a texture changing with depth, possibly giving misleading results. Instead, numerous selected area diffraction patterns were obtained from the deformed region, and careful convergent beam analysis was made of the near surface region.

The twins showed no orientation relationship to the sliding direction. However, (111) was perpendicular to the twin boundaries with the <224> direction along the twin boundaries. Therefore, it would appear that (111)<112> was present, but has not been rotated towards the sliding direction. As noted earlier, the shear bands consumed the twins before they can fully rotate towards the sliding direction.

The shear bands which had just formed at the surface tended to show a stronger texture compared to those in the shear banded region which had undergone some recovery. The strongest texture component at the extreme surface was <111> parallel to the sliding direction fig 5.47-49. In addition, <100> parallel to the sliding direction was also present, but this was never as pronounced. The (022) ring systematically showed preferred orientation, with the (022) planes commonly parallel to the worn surface. In all cases there was a spread of about 15° in the reflections, with numerous reflections not conforming to the texture.

The above data indicates the presence of a wire texture, which is usually a mixture of <111> and <001>, parallel to the deformation axis for FCC metals. The relative amounts of the two directions depends on the SFE of the material [283]. The (220) component of the texture found at the surface was probably coupled with some of the <001> parallel to the sliding direction as a Goss type texture, (110)<001>. This texture was found both in freshly formed shear bands and the recovered shear bands in the sample rolled to 96% reduction, discussed in chapter 4. Unfortunately, the (224) diffraction ring was too weak in the surface diffraction patterns to establish whether (001)<112> was present, (the main component of the brass rolling texture). However,

the absence of any {001} planes parallel to the wear surface suggests that it was not present.

The shear bands formed well below the worn surface in the twin colonies exhibited a similar texture to the surface shear bands, although the preferred orientation was less pronounced, fig 5.38. The textures developed at the worn surface and in the rolled specimens are summerised in table 5.3.

TABLE 5.3

SUMMARY OF THE TEXTURES FOUND IN THE WORN SURFACE AND ROLLED SPECIMENS

Rolled samples:

Twins	{111}<112>	Rotates towards R.D
Shear bands	{110}<001>	(Goss). Initial texture, only evident when averaged over many crystallites.
	{110}<112>	(Brass texture). Very poorly developed in the rolled samples.
δ ferrite	{111}<112>	

Worn surface:

Twins	{111}<112>	Texture does not rotate to sliding direction.
Surface S.Bs	{110}<001>	Only when averaged over many crystallites.
	<111>,<100>	Poorly developed at surface.
Homogeneously deformed S.Bs	<111>,<100>	<111> stronger than <100>. Fibre texture only, no rolling texture.

The shear bands which had undergone some recovery (i.e. all except the transition region and the last 200nm) failed to show any evidence of the {110}<001> orientation found at the surface. Moreover, the texture only became apparent when a very large selected area diffraction aperture was used, when the wire texture was the only one present, fig 5.43. This is in contrast to the surface, where the texture was detected using the smallest selected aperture available.

As with the surface shear bands, the <111> component was stronger than the <001>. The {224} diffraction ring was faint but there was no indication of any <112>, and the {001} planes where not parallel to the wear surface. Specifically, there was no evidence of the brass texture, only that of the wire texture.

Micro-diffraction patterns were obtained from the region about 150nm from the surface for the test at 24 N/pin. These show an almost totally random orientation across the individual boundaries, fig 5.69. This serves to illustrate how many crystallites must be included before the texture becomes apparent.

X-ray diffractometer traces were obtained from the worn surfaces which showed significant changes in the relative intensities of the peaks. Whilst this does not provide a reliable analysis of texture, it does give a crued guide to whether a particular texture is present or not. The {110} peak intensity was found to increase approximately 200% relative to its original value. In contrast, the {111} and {200} reflections decreased, to about 25% of their original values. Whilst a texture could be present which was tilted slightly off the deformation axis (i.e. tilted from parallel to the worn surface), this result appears to support the conclusions from the TEM, i.e., the increase in the intensity of the {110} reflection suggests the presence of a Goss texture. The reduction in the intensity of the {200} supports the view that the normal brass texture, {001}<112> is not present. These results do not give any indication about the fibre texture.

The above textural analysis provides interesting conclusions about the mode of deformation. Firstly, the presence of a strong fibre texture, and the general absence of the brass rolling texture suggests that the surface material is being deformed in a manner similar to extrusion or wire drawing, indicating a large hydrostatic component to the applied stress system. The stress system is obviously different to that in rolling, which can be considered primarily as compressive, with a tensile component.

The freshly formed shear bands showed a strong fibre texture rather than the Goss and brass textures found in rolling. It is interesting to consider the mechanism which determines the shear band texture given that the shear bands form as a result of flow along a geometrically imposed direction, rather than a crystallographically determined system. The conditions for their formation has been discussed in the

literature survey and in chapter 4. The structure observed is that of the recrystallised or recovered state after the passage of an avalanche of dislocations. The implication is that the observed structure forms immediately after the stress is removed. This scenario suggests that the texture in a shear band is determined by the recovery/ recrystallisation process rather than the mode of deformation (whether wire drawing or rolling). The present results clearly demonstrate that the texture within the shear band is determined by the imposed stress state, implying either that the *observed* shear band structure is formed during the application of stress, or that the shear band structure is dependent on the parent structure. The latter explanation cannot account for the observed texture because the twinned region in the present study retained a (111)<112> orientation relationship as found in the rolled samples, and the shear bands were formed at the same angles to the twins as in the rolled samples. Therefore, the texture must be formed during the application of the stress, indicating that the passage of the shear band does conform to the normal slip criteria. Explanations of shear band passage by a superplastic mechanism have been dispelled on the basis that the resultant structure plays no part in subsequent deformation. In other words, fresh shear bands form, consuming the existing shear banded structure, rather than some form of superplastic deformation of existing shear bands taking place.

The third point to arise from the textural analysis concerns the dominance of the <111> over the <001> component. The relative intensities of these two components depends on the SFE [283]. In pure Al, only the <111> component is found. In low SFE materials the <001> component is expected to be dominant. The observation of a much stronger <111> than <001> in the present study is suprising and not commensurate with the estimated SFE of the material. Explanations for this discrepency based on a temperature rise giving an effective increase in the SFE are improbable, since this would removed the driving force for the formation of low SFE shear bands, yielding a distinctly different microstructure.

5.5 DEPTH OF DEFORMATION

5.5.1 Hardness as a Function of Depth

The hardness as a function of depth was measured for all loads. Examples are given for 55N and 8N in figs 5.70,71. Values of the hardness in the near surface region were generally lower than in the samples rolled to a strain of 3. A slightly lower hardness might be expected in the homogeneously deformed region because of the marginally larger crystallites compared to the sample rolled to a strain of 3. However, the lack of surface constraint in cross sectional samples always places a question mark over the validity of data obtained very close to the worn surface. Clearly, hardness values could not be taken from the freshly formed shear bands at the surface.

Hardness values were also obtained from the surface of the worn pins. The metallic regions were measured in the range 4-5 GPa, whilst the oxide was substantially harder at 7-10 GPa. Measurement on such a rough surface proved difficult, with considerable variability being recorded.

The results of Smith [285-287] are also presented in figs 5.70,71 for similar loads. Interestingly, the hardness differences between the present results and those of Smith follow the same trend as the wear rates (fig 5.2). At a load of 7-8 N/pin Smith found a lower wear rate than in the present case. This coincided with a smaller depth of deformation for the self mated tests of Smith [285-287], fig 5.70. In contrast, at 55N/pin the present results recorded a lower wear rate than those of Smith for 48 N/pin. This coincided with a substantially lower depth of deformation in the present case.

5.5.2 Measurement of the Depth of Deformation

Measurement of the depth of deformation was made using optical microscopy of etched samples, TEM cross sectional specimens and from the hardness profiles. The results of these measurements are in broad agreement and are shown in fig 5.72. The total depth of deformation was defined as the point at which a rise in the dislocation density could be observed and the point at which the hardness coincided with the bulk value. The depth of shear bands was taken as that at which the first shear band cut through the twinned microstructure. In both these cases considerable variation was found along the worn surface.
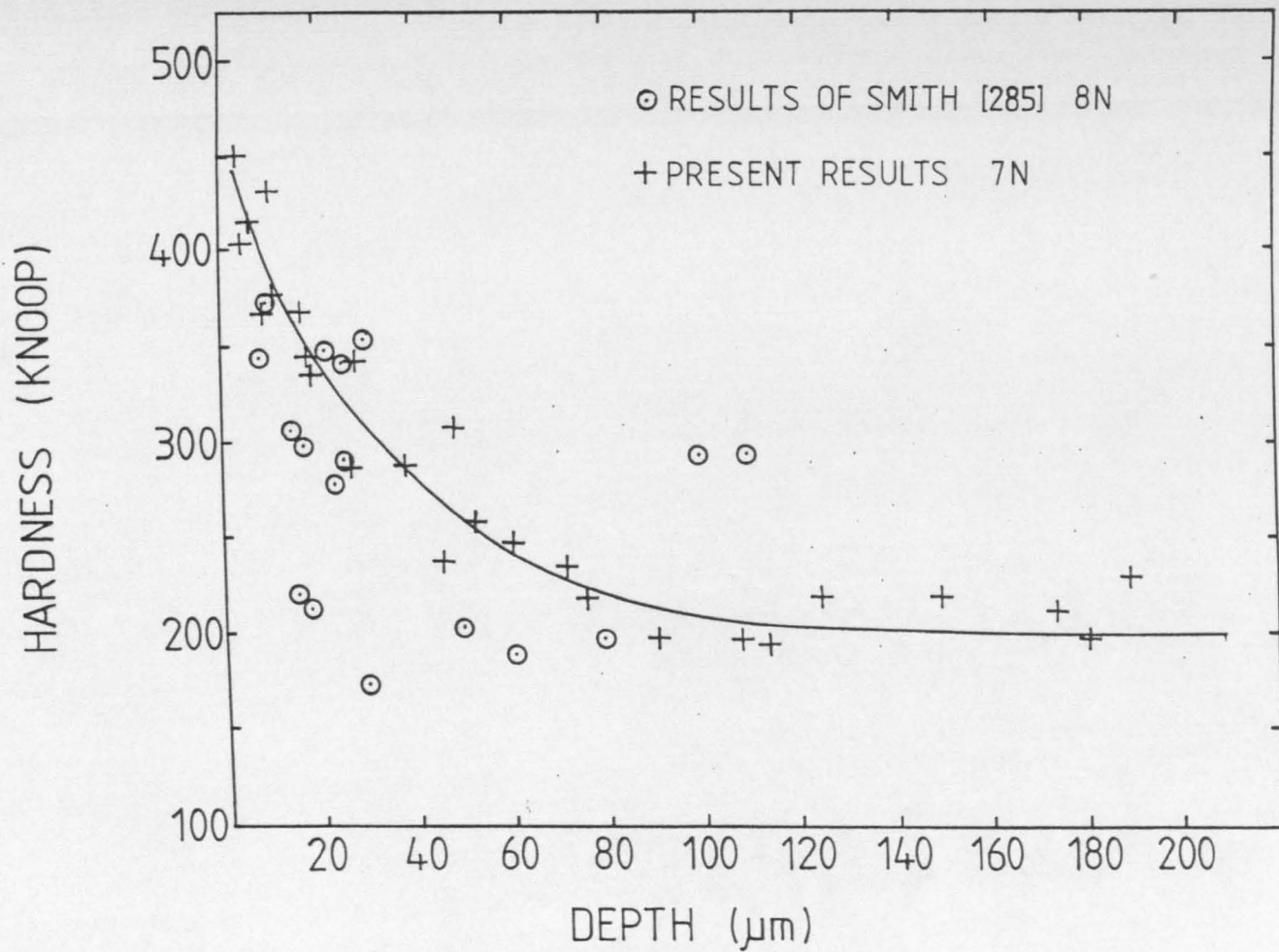
Fig. 5.70. Hardness (Knoop) as a function of depth for the test at 7 N/pin. The results of Smith [285] show a smaller depth of deformation for a similar load.
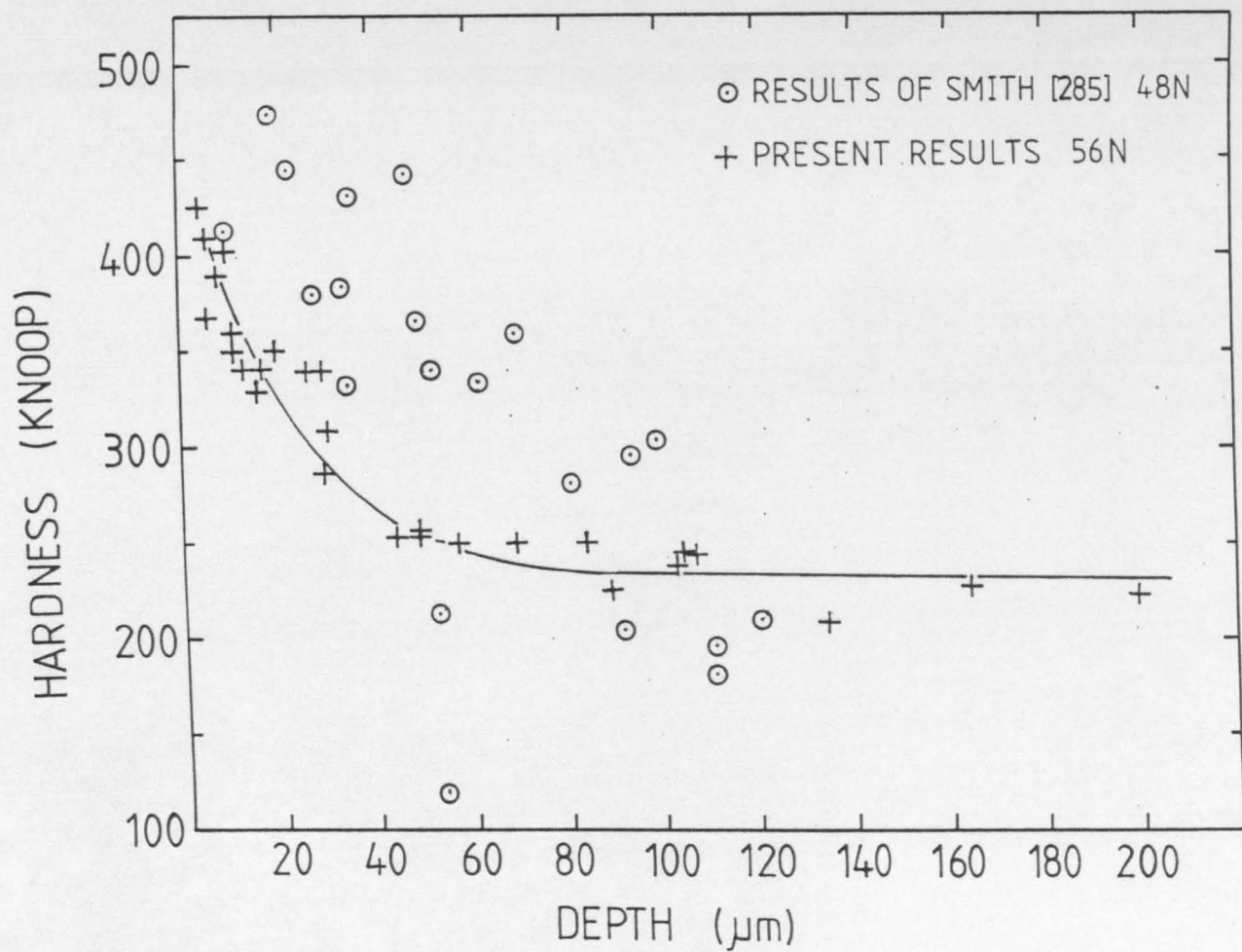
Fig. 5.71. Hardness (Knoop) as a function of depth for the test at 55 N/pin. The results of Smith [285] show a substantially greater depth of deformation at a lower load.

Where large particles of wear debris had been incorporated into the surface the depth of deformation tended to be higher. However, variation in the depth was found irrespective of whether oxide was present or not.

The general trend in fig 5.72 shows that the total depth of deformation does not rise monotonically with load, but falls off at loads above 24 N/pin. The average depth of the shear bands appears to reduce with loads above 24 N/pin, but the range of depth was substantially less at 55 N/pin than at 24 N/pin.

The trend of deformation with load is compared to the wear volume after a constant distance in fig 5.73. This shows that the wear volume follows a very similar trend to that of depth of deformation. This suggests that the depth of deformation plays a dominant role in determining the wear rate. This is in agreement with the comparison of hardness results to those of Smith [285-287], discussed in section 5.5.1. Clearly, this indicates that the increase in oxide content at the surface has led to an increase in the work hardening rate and flow stress at the surface and therefore to a reduction in the depth of deformation.

5.6 TEMPERATURE AT THE INTERFACE

The temperature generated at a sliding interface has been the source of controversy for many years. Estimates have been based on several criteria. Calculations of the temperature by analytical models are often complex, or make simpifying assumptions which run the risk of severely reducing the accuracy. Estimates based on the worn microstructure rely on a comparison of microstructure produced by wear to that of the equilibrium case. However, equilibrium is rarely achieved in the worn surface where rapid thermal transients take place.

The 'white etching layer' formed on rail steels is a good example of the latter point. Many researchers have taken the presence of a martensitic layer on the surface of a pearlitic steel to indicate that temperatures must have been high enough to provide austenatisation of the pearlite [eg 291,292]. However, Newcomb & Stobbs [266] provide an alternative explanation whereby carbon is taken into solid solution as a result of dislocation activity to form austenite at temperatures well below 730°C. Their conclusions were in agreement with calculations of
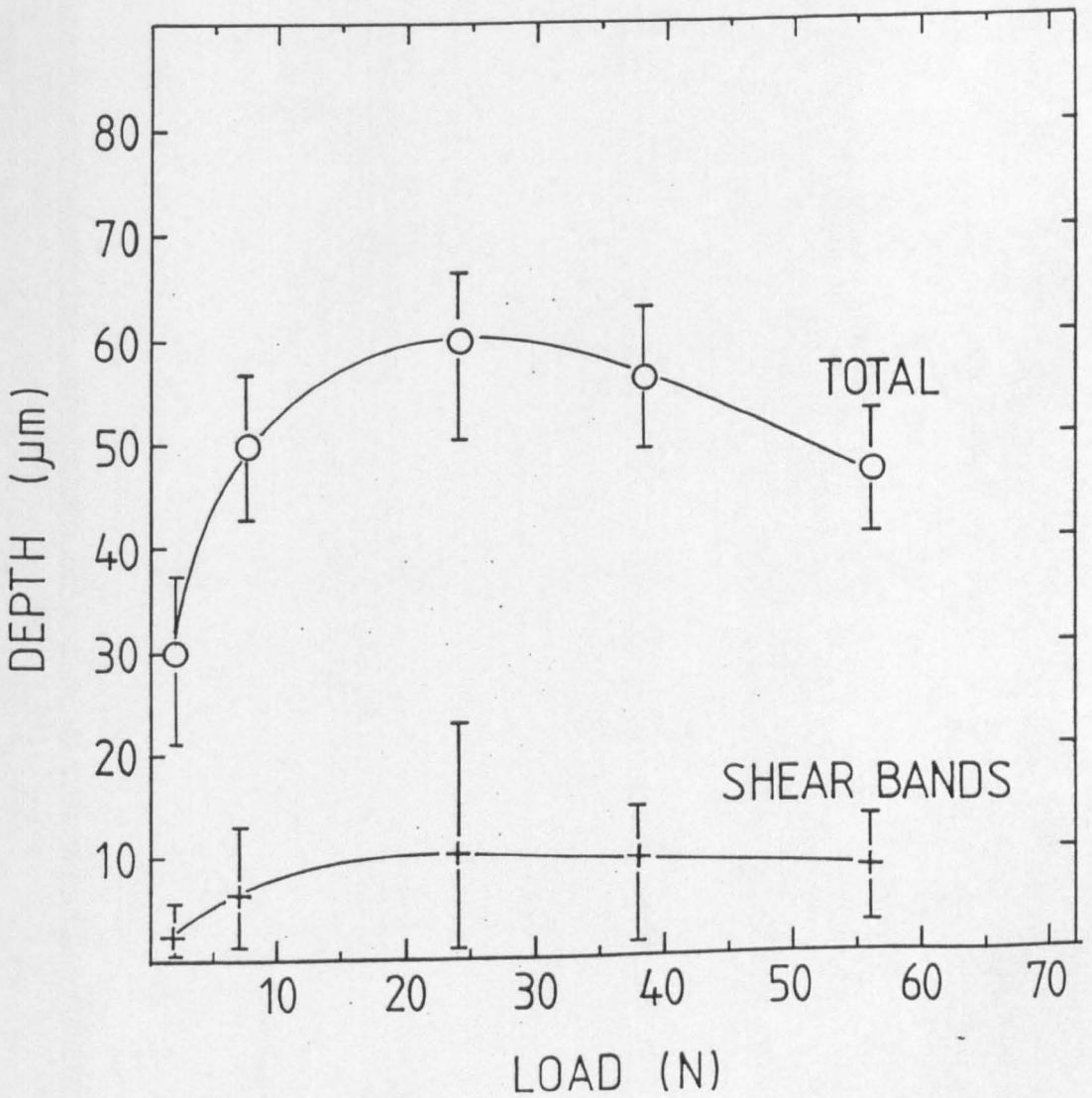
Fig. 5.72. The depth of deformation and shear banding as a function of load. The bars represent the range, not the error.
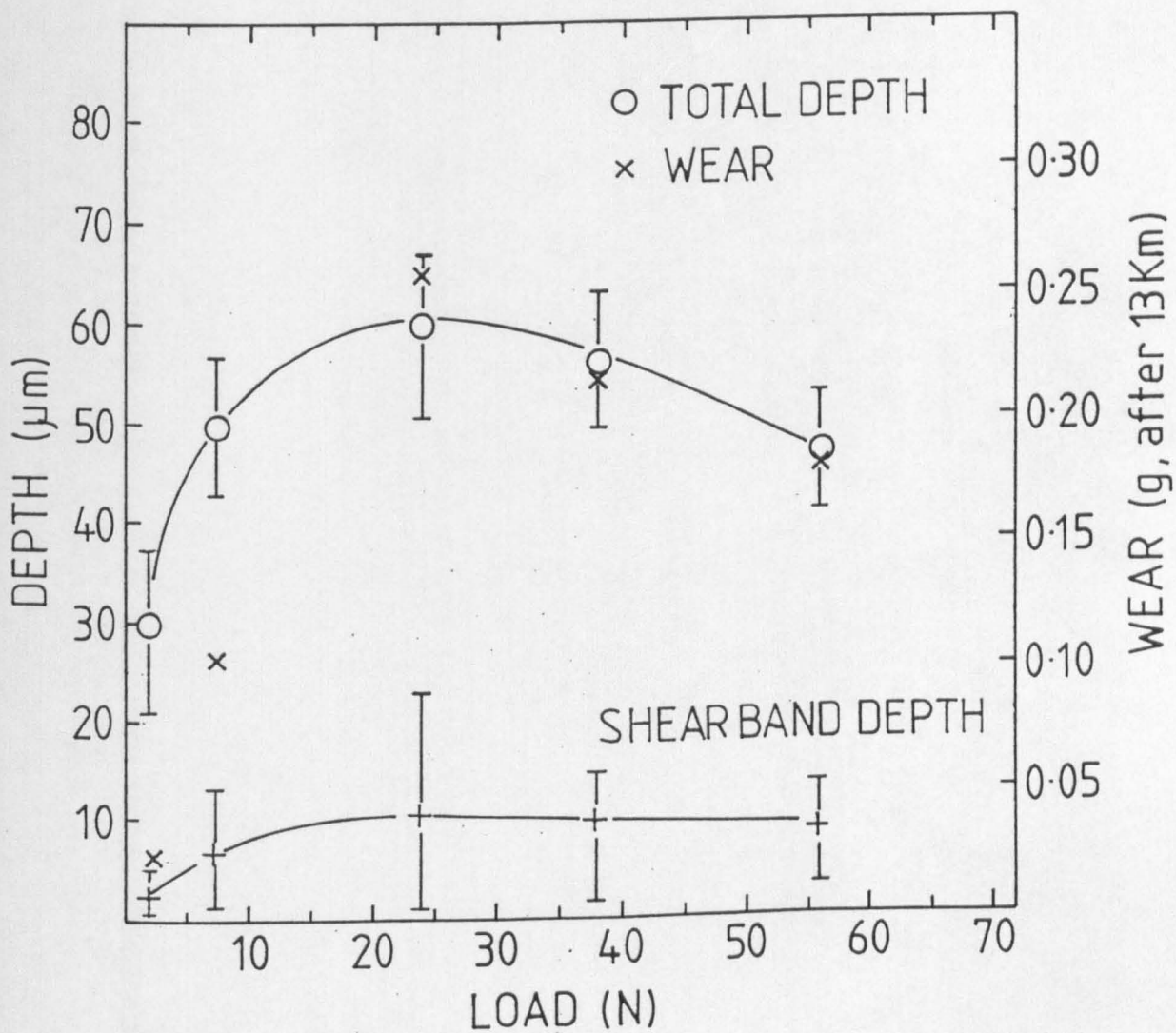
Fig. 5.73. Fig. 5.72 replotted to include the weight loss after 13 Km sliding for each load. This can be seen to follow a similar trend to the depth of deformation.

the maximum temperature rise of 150°C, for the worst case of plastic contact and maximum slip between locomotive and the rail. This example, therefore, demonstrates that the interpretation of the microstructure can give estimates of temperature which differ substantially, in this case by up to 600°C.

The third approach is direct measurement. Data can be obtained by implanting a thermocouple, or from an optical pyrometer. In both cases the objection is that only the steady state surface temperature is measured whereas the flash temperatures occur too quickly to register. Some workers [egl79] argue that a pyrometer can provide the necessary sensitivity, but there still remains an obvious question mark regarding its ability to measure transients at small asperity contacts within the sliding interface.

5.6.1 Direct Measurement

A thermocouple was implanted in one of the pins in a test carried out at 24 N/pin. Careful measurements were made of the distance of the thermocouple from the worn surface so that the temperature as a function of depth could be determined. The thermocouple was glued in place to ensure it did not move and to provide a good thermal contact with the metal.

Even before the sliding couple had achieved the sliding speed of 0.24 m/s (which took about 1sec) a temperature rise of several °C could be registered with the thermocouple 1mm from the sliding interface. The temperature continued to rise over the next ten minutes until a value in the range 36–42°C was reached. This scheme was followed irrespective of distance slid, even to the point where the thermocouple was exposed at the wearing surface.

Interestingly, an additional temperature rise of a few degrees was found to coincide with heavy vibration at the interface. As noted earlier, the friction coefficient did not necessarily increase during these periods.

The rise in temperature indicated by the thermocouple was considerably smaller than had been anticipated. In order to test the reaction time of the thermocouple, the pin with the exposed thermocouple was placed on a hot plate at various temperatures. A temperature rise in the thermocouple was registered instantaneously, reaching 50°C in about a second for hot plate temperatures of 200°C and

above. Therefore, the temperatures measured in the pin during the wear test can be considered to be representative of the average temperature in the surface layers, although presumably it is an underestimate of the flash temperatures at the contacting asperities.

5.6.2 Analytical Models For Temperature Rises

Analytical models have been developed by Blok [293] and Jaeger [294], but these are complicated and it is difficult to apply them to an experimental situation. Archard [292] has further developed equations to predict interface temperatures for slow moving and stationary heat sources, and an equation for a fast moving heat source. As with all the models, a clear estimate of the asperity size and number of contacts is required. On the basis of the Archard model, for the case of steel on steel with a load of 24 N and a friction coefficient of 0.35, a maximum flash temperature of 571°C is predicted.

Recently, Kuhlmann-Wilsdorf [295,296] has provided a comprehensive analysis of flash temperatures based on the original equations of Blok [293] and Jaeger [294], but presented in such a manner that they can be used to make estimates of the surface temperature. In the analysis a distinction is made between circular and elliptical contacts. In the following discussion the former will be used since this simplifies the computation, and the difference in the result between the two is small. Indeed, microstructural observations indicate that whilst prows are probably elliptical, the ellipoidal ratio was small. The model derived by Kulhmann-Wilsdorf assumes that shearing takes place in the softer material; it is this mechanical work which is transformed into heat.

For the general case of unlubricated wear, with plastic contacts between asperities and circular contact spots, the flash temperature is given by;

$$\Delta T_o = \frac{(\pi/4) \; \mu \; H_s \; r \; v}{\lambda_1/z_o + \lambda_r} \qquad \qquad ...(5.1)$$

Where μ is the friction coefficient, H_s is the hardness of the softer material (GPa), r is the radius of the contact spot, v is the speed, λ_1 is the thermal conductivity of the softer material, λ_r is the relative

thermal conductivity which is equal to the ratio of the thermal conductivity of the disc to the pin, and Z_o is given by:

$$Z_o \ (v_r \leqslant 2) = \frac{1}{1 + v_r/3} \qquad \ldots (5.2)$$

Where V_r is the relative velocity, defined as:

$$v_r = \frac{v}{v_o} = \frac{v}{\kappa/r} = \frac{v}{\lambda/r \, d \, c} \qquad \ldots (5.3)$$

Where v_o is the characteristic velocity, κ is the thermal diffusivity, d is the mechanical density and c is the specific heat capacity, each of the softer material. An alternative definition exists for v_r where the radius of the asperity contact area, r, is described by the material hardness, the load applied, and the number of contact spots, (i.e. using the standard expression which predicts the true contact area, equation 5.9) yielding the following for the characteristic velocity:

$$v_o = \frac{\kappa \ (\pi \ N \ H_s)^{1/2}}{P^{1/2}} \qquad \ldots (5.4)$$

Where P is the load, and N is the number of contact spots. Equation 5.1 was further developed by Kuhlmann-Wilsdorf [296] to produce:

$$\Delta T_o = \frac{\mu \ (\pi \ P \ H_s/N)^{1/2} \ v}{4 \ \lambda_1 \ (1/Z_o + \lambda_r)} \qquad \ldots (5.5)$$

At very low speeds $(v_r \ll 1)$ the denominator will reduce to:

$$4 \ (\lambda_1 + \lambda_2)$$

At the characteristic velocity equation 5.5 takes the form:

$$\Delta T_o = \frac{\mu \ \pi \ H_s / 4 \ d_1 \ c_1}{4/3 + \lambda_r} \qquad \ldots (5.6)$$

The first step is to calculate the characteristic velocity, V_r, to establish which equation is relevant. This immediately poses the problem of estimating the number of contact spots and the asperity radius. From microstructural observations, the average prow radius was around $15\mu m$ for the test at 24 N/pin. Equation 5.3 therefore gives V_r = 0.2. At 55 N/pin estimates of prow sizes were more difficult because the oxide tended to be more rounded and cover a larger area. However, a value of r = $30\mu m$ would appear to be reasonable. This yields a V_r of 0.42.

Using equation 5.4, with the hardness taken to be that measured for a mixture of oxide and metal, namely about 9 GPa, the value of the relative velocity depends on the number of contacts. Taking the case of N = 10, the relative velocities were computed as 0.18 and 0.28 for 24 and 55 N/pin respectively. The number of contact spots would need to fall to around 2, to give a relative velocity of one.

Based on this analysis of the relative velocity, it would appear that neither of the simplified equations, namely 5.6 for the case of v_r = 1, or the case for very low values of v_r, are applicable. Therefore, equation 5.5 was used to compute the values of the flash temperature. These are presented in table 5.4 for a range of conditions of number of contact points and metallic or oxide prows. All figures refer to the temperature generated in the pin surface, not the zirconia disc.

The temperatures quoted are all comparatively low. The maximum temperature calculated, 407°C, was for the case of 55 N/pin with only two contact points, which would be highly improbable. A more likely estimate would be based on a larger number of contacts giving a temperature in the range 60-215°C, which is commensurate with the experimentally measured temperature rises.

Also presented in table 5.4 are values for the flash temperature computed for the wear of stainless steel against stainless steel, which was the conditions used by Smith [285-287]. The maximum values shown are lower, but only marginally so, for example the highest temperature for the very worst conditions fell from 407 to 373°C. This temperature difference demonstrates that, *in the steel surface*, the temperatures are largely unaffected by the thermal conductivity of the counterface. This is a reflection of the high thermal conductivity of the steel. However, the increase in surface hardness by the presence of oxide does substantially increase the calculated surface temperature. This temperature would rise further if the oxide significantly reduced the

thermal conductivity of the surface. In the present study the microstructural observations indicated that there was always a metallic component which would provide an good conduction path.

The comparison of temperatures generated in the steel surface in tests on zirconia and self mated tests provides a very important conclusion. In Smith's [285-287] tests the wear debris was reported to be mainly metallic above a load of about 30 N. In the present tests the debris became increasingly oxidised with an increase in load. Since theory suggests that the lower thermal conductivity counterface does not produce an appreciable temperature rise in the steel surface, the increased oxidation kinetics must be a result of oxidation on the zirconia surface and re-transfer of the oxide to the steel. This is in agreement with the findings of Salesky et al. [253], noted earlier, who used compressed air to blow away the wear debris. It was found that the worn surface contained very little oxide whilst the debris was fully oxidised. This was attributed to the pyrophoric nature of the very high surface area wear debris.

Regrettably, the equations presented by Kuhlmann-Wilsdorf [295-296] cannot be used to estimate the temperature on the zirconia surface. This is because the equation assumes plastic contact with subsurface shearing, which is not the case in the zirconia or on the transferred prows (even if there is some plasticity in the prows, the model assumes deformation to a depth equivalent to the contact area). Moreover, the prows on the zirconia surface were only in intermittent contact, further complicating any computation. However, any heat generated in the prows would give rapid surface temperature rises because of the insulating properties of the disc. This view is supported by the observation that immediate oxidation occurred of any metal transferred to the disc, such that for the test at 2.2 N/pin, the zirconia surface was covered with about 95% metal oxide and 5% metal, whereas the pin surface contained about 10% metal oxide and 90% metal.

To demonstrate the potential effect of using two low thermal conductivity counterfaces equation 5.5 was used for the case of zirconia on zirconia. Whilst such a couple would not, at face value, conform to the criterion of plastic contact, the results in chapter 7 will show that contact is indeed plastic. Assuming 10 contacts, although such a number is probably slightly high, the predicted flash temperature for a load of 20 N/pin and a friction coefficient of 0.35 is 2203°C. This point will be considered in much greater detail in

chapter 7, but provides a dramatic indication of the importance of
having one counterface with a high thermal conductivity.

TABLE 5.4

PREDICTED FLASH TEMPERATURES FROM EQUATION 5.5

LOAD (N)	PROW HARDNESS (GPa)	μ	N	TEMP (°C)
PRESENT CASE:				
24	5	0.35	10	64
55	9	0.35	10	85
55	5	0.35	2	215
55	9	0.35	2	407
STEEL ON STEEL:				
24	5	0.8	10	82
55	9	0.8	10	167
55	5	0.8	2	278
55	9	0.8	2	373

5.7 ANALYTICAL EXPRESSIONS FOR THE WEAR VOLUME

The present results demonstrate that the Archard equation [297] is
not applicable to this sliding couple, since the wear rate decreased
with increase in load above 24 N/pin:

$$V = \frac{k}{3} \frac{L}{P} x \qquad \qquad ...(5.7)$$

Where L is the load, x is the sliding distance, P is the flow pressure
(i.e. hardness) and k is the wear coefficient. Many alternative wear
equations [eg298] use linear elastic fracture mechanics to predict the
wear rate, but these are restricted to conditions where contact is

elastic (such as in lubricated wear). Even then, the results are dubious because the near surface region would be expected to be in a condition of plane stress not plane strain. The analytical approach to plastic contact [eg299] generally assumes that hardening is linear up to the surface. This is a specific condition which may apply to pure iron and some two phase metals but does not apply to the present case. Therefore, a wear model has been developed for the present conditions. However, the model is necessarily simple and only applicable to the specific wear mechanisms found in the present study.

5.7.1 Wear By Transfer

The microstructural evidence suggests that a fresh shear band is formed by the passage of each asperity. The dominant mode of wear appeared to be by transfer of the metal to the disc as fine lamellae. The thickness of the small transfer events appears to be similar to that of the freshly formed shear bands. This led to the conclusion that, during the passage of the asperity, the surface material is dragged along with the prow, causing plastic overload within the shear band. Thus, some of the shear band remains in the steel surface, whilst a portion is transferred to the disc. Therefore, a simple relationship for the wear rate can be formulated, based on the criterion that each contact event results in transfer of metal to disc, of a thickness which corresponds to the shear band thickness. Therefore, taking the thickness of this wear particle to be z_s, and the area of the contacting asperity to be a_b, the wear volume from each asperity contact is given by:

$$v = z_s . a_b \qquad \qquad ...(5.8)$$

Taking N_m to be the number of contacts per metre of sliding, the total wear volume, V, is given by:

$$V = z_s . a_b . N_m . S \qquad \qquad ...(5.9)$$

Where S is the total distance slid.

The value of z_s is considered to be of the same order as the freshly formed shear band thickness at the surface, namely 200nm. The value of N_m has to be estimated. Assuming that there are 10 contact

events at any one time (the value used in the temperature calculation, based on a comparison with the measured asperity size and values given in the literature), and that the contact points are continually changing, this gives a total of 1062 contacts per metre (alternatively it can be assumed that each asperity remains in contact throughout 1m, but this yields the same overall area of contact). The value of a_b can be measured from the area of metallic transfer on the disc, which suggests a prow diameter in the range 15-150μm. Alternatively, the value of a_b can be estimated from the expression [300]:

$$a_b = \frac{P}{N\,H} \qquad\qquad ...(5.10)$$

Where P is the normal force and N is the number of contacts at any one time. This equation gives values of a_b as 18μm for a load of 24 N and 37μm for a load of 55 N, each for 10 contact spots. However, this equation provides a simplified approach to estimating the contact area. An alternative approach was suggested by Kuhlmann-Wilsdorf [300] where the contact area of the asperity was related to the total depth of deformation by:

$$a_b = (z_o)^2 \qquad\qquad ...(5.11)$$

Where z_o is the depth of deformation.

Based on the above figures, equation 5.8 predicts a wear volume of 20mm^3 for a load of 24 N and a contact asperity diameter of 100μm. This value falls to 10mm^3 if the approximation for deformation depth is used. The experimental wear rates were recorded as 45, 33 and 24 mm^3 for each of the pins. The relationship, therefore, gives good agreement to the experimental case despite the simplification of the wear conditions.

Two points need to be developed further. Firstly, as the surface becomes increasingly covered in oxide, the number of transfer events will be reduced. Secondly, an expression is required which will predict the wear from ploughing, which includes extrusion off the end of the pin and break-up of groove edges.

Taking the oxide coverage first. The equation presented (5.9) predicts an increased wear rate with load. However, the wear rate was found to fall above loads of 24 N/pin. The equation can be modified by substituting the number of contact events per metre which lead to

transfer of the metal, N_m', for N_m, defined as:

$$N_m' - N_m \cdot j \qquad\qquad ...(5.12)$$

Where j is used to represent the fraction of the asperity surface which is covered by metal, providing an estimate of the probability of a transfer event. This empirical approach could be replaced by adopting the equation presented by Quinn [289], which predicts the oxidation rate, assuming parabolic oxidation kinetics. The probability of forming a wear particle is given by a relationship which accounts for the fraction of oxide which is oxygen, the parabolic oxidation rate and the critical thickness of oxide at which a debris particle is formed. This equation is of little use here because the parabolic oxidation rate of a non equilibrium oxide cannot be estimated. Moreover, the thickness at which an oxide particle is formed is considered to be relevant to the prows on the disc, but not on the pin, as discussed later.

Care must be taken when choosing values of the contact area. If equation 5.9 is used then the hardness chosen should be that of the prow, which is of course a mixture of oxide and metal. In this case a value of 9 GPa would be appropriate for the test at 55 N, compared to about 7 GPa for 24 N. A further problem exists in that the number of contacts as function of load needs to be estimated. As noted earlier, the surface deforms until the saturation flow stress is achieved. The contact area then increases until the applied stress in the asperity equals the flow stress. This infers that a higher flow stress will lead to a reduced contact area. This is, of course, offset by the increased applied stress. To avoid this problem the simplifying relationship between area of contact and depth of deformation (equation 5.10) can be used.

The modification to equation 5.8 introduces a maximum for the wear volume as a function of load, at a load which depends on the value of N_m' chosen for each load. However, by introducing the effect of the oxide the estimate of the wear volume at high load becomes increasingly inaccurate, although still in good agreement with experiment at low load. The reason for this is presumably that the increase in surface hardness does not offset the increase in load so that the contact area increases with load. If the number of contacts is increased to 76, wear values in good agreement with experiment are again predicted. The

true area of contact becomes 0.4% of the apparent contact area, which is a reasonable value.

Experimental results indicate that the thickness of the transfer event remains constant as a function of load, and more significantly, as a function of the depth of deformation. This study has found, in agreement with many others [eg301], that the wear volume is proportional to the depth of deformation. However, this could not be related to any clear microstructural mechanism for a thicker layer being detached as the load was increased. Rather, the equation presented above, and the experimental observations, indicate that the effect is indirect. That is to say that the wear rate is reduced because the number of events which produce debris is reduced. This is a result of a reduction in the amount of exposed metal. Also, the increase in oxide content has increased the flow stress of the prows thereby reducing the depth of deformation. In other words, the wear rate is a result of the amount of exposed metal, not the depth of deformation.

5.7.2 Wear By Displacement and Surface Shear Strain

Consideration of the wear volume produced by the metal extrusion requires a relationship for displacement as a function of depth. Measurements were made of the displacement of flow lines (for example in fig 5.33), the results of which are presented in fig 5.74. The very near surface displacements could not be measured because of the galvanic reaction between the coating and the worn surface. Moreover, a strain discontinuity would be expected at the surface, because of the freshly formed shear bands. In addition, the displacement could only be measured to the depth of the shear banded region, because the shear strain also shows a discontinuity at the boundary between the twinned region and the shear banded region. Therefore, the values for the displacement given in fig 5.74 would need to be adjusted to account for the strain resulting from the initial shear band formation.

The data in fig 5.74 are replotted for displacement (natural log) as a function of depth in fig 5.75. The straight line confirms that the displacement, δ, as a function of depth can be considered to follow an exponential decay:

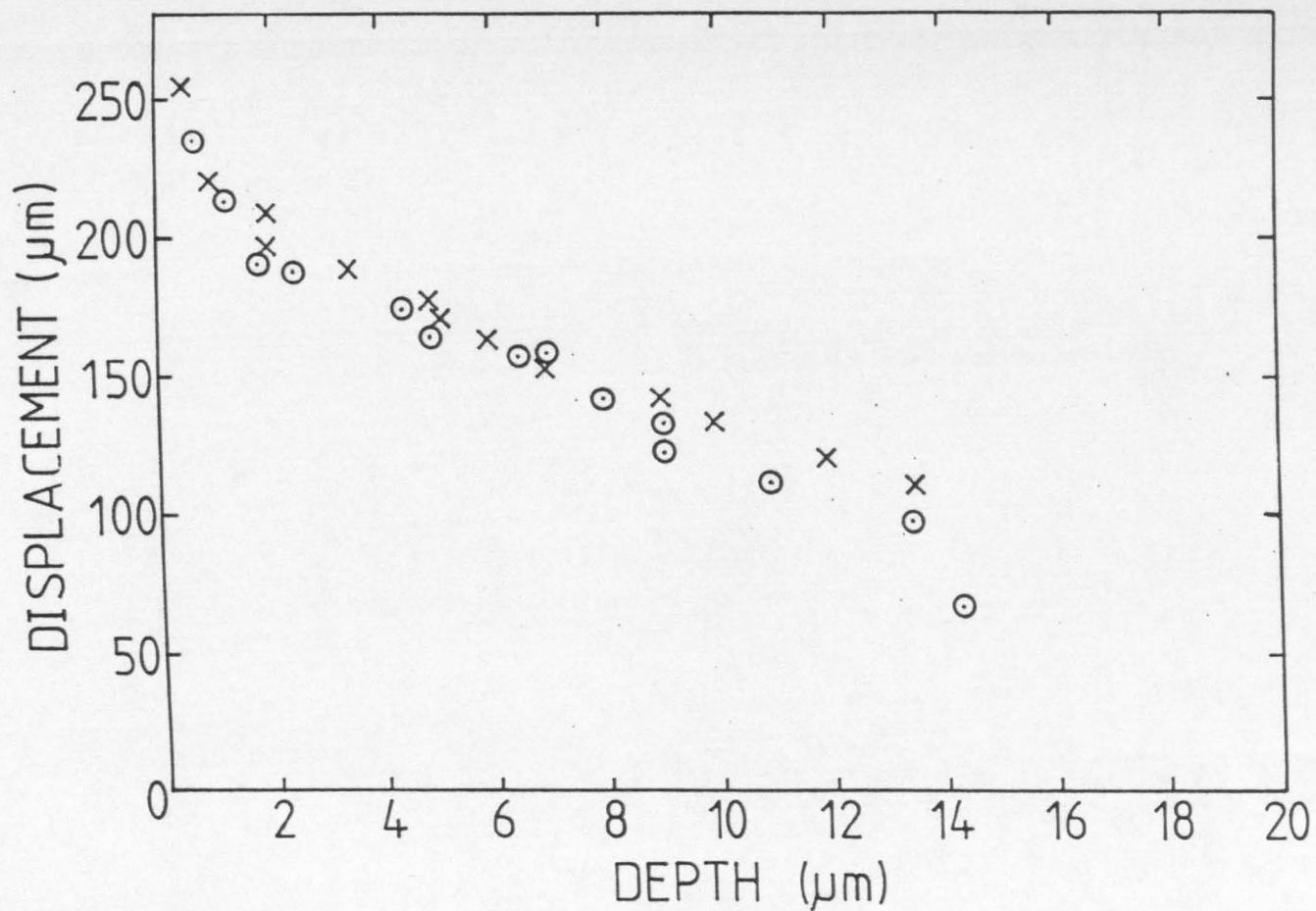$$\delta = \delta_s \exp{(-\kappa z)} \qquad \qquad \dots (5.13)$$

Fig. 5.74. Displacement as a function of depth. Displacement could not be measured with any confidence in the last 100nm.
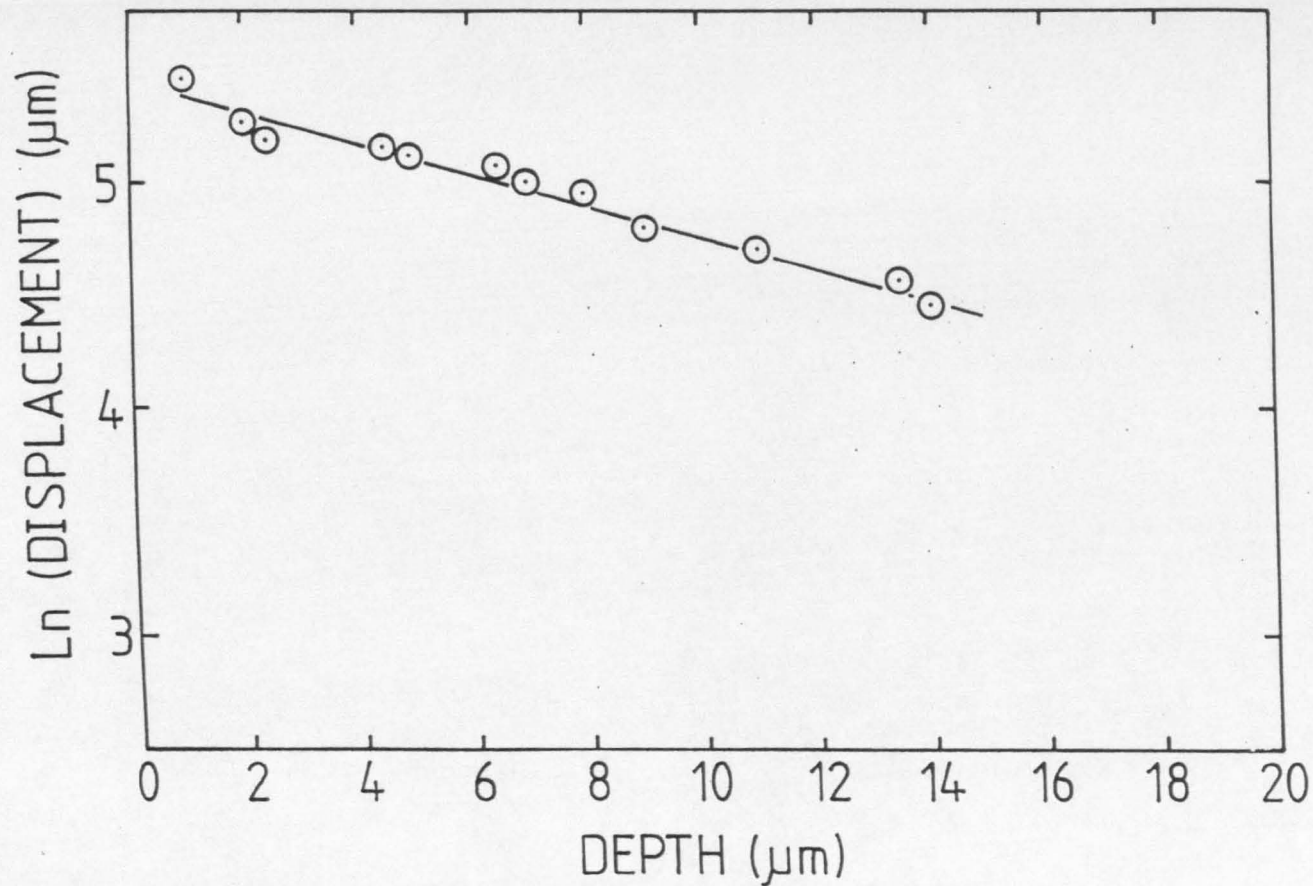
Fig. 5.75. Displacement (natural log) as a function of depth. Only
the results for the homogeneously deformed shear bands are included.
The straight line confirms the exponential relationship between
displacement and depth.

Where δ_s is the displacement at the surface, and κ is a constant. The slope of this graph indicates a value of κ as 6.6×10^4 m^{-1}. Such an expression has also been shown to describe the displacement of a grain boundary below the surface of a Cu pin by Rigney et al. [235], although measurements were only taken to within 4μm of the surface. The shear strain, γ, can also be described by the same relationship, namely:

$$\gamma = \gamma_s \exp (-\kappa z) \qquad \ldots (5.14)$$

Rigney et al. [235] used the expression:

$$\delta = \int \gamma \, dz \qquad \ldots (5.15)$$

with suitable boundary conditions to give the result $\gamma_s = \kappa \, \delta_s$. On the basis of this, with $\kappa = 6.6 \times 10^4$ m^{-1} and a surface displacement of 240μm, a shear strain at the surface of 13.9 is calculated for the present case. As pointed out above, this must be an underestimate of the maximum strain since it does not account for the shear strain from either the surface shear bands or those in the transition region. Specifically, a shear strain of 13.9 has been produced by the homogeneous deformation of the shear banded region (since no fresh shear bands were found in this area). As noted in chapter 2, shear band formation has been shown to be associated with shear strains in the region 1-10, with the majority falling in the range 3-4 and so the shear strain at the surface could be considerably higher.

The displacements measured at the surface are considerably higher than those recorded by Rigney et al. [235] for the sliding wear of Cu. However, the value of the constant κ was nearly an order of magnitude smaller in the present study compared to that found by this author. The lower value of κ suggests that a higher displacement can be achieved by friction in the stainless steel than in the copper pins. Such an apparently higher ductility in the stainless steel compared to copper cannot be explained by the difference in wear test geometries, since these were similar. The load used by Rigney et al. [235] was twice that in the present study, which would be expected to favour the increased deformation in the copper. Therefore, an apparent contradiction exists, with the material being deformed at a higher homologous temperature, but with a significantly higher specific stacking fault energy, giving the lower strain at the worn surface. It

must be reiterated that the effect of shear banding is additional to this arguement since the value of κ was obtained for the homogeneously deformed crystallites. Given that the steel has a substantially higher flow stress, the above observation suggests that the wear mechanism in the copper leads to wear debris formation at a lower strain and/ or to a greater depth. The size of the wear debris found by Rigney et al. [235] would appear to confirm this. The issue is further complicated by the presence of a mechanically mixed layer on the surface of the Cu pin examined by these authors. Unfortunately, Rigney et al. [130] did not provide any wear rate or friction data, so that further conclusions cannot be made.

Returning to the matter in hand, namely evaluating the contribution of the extruded metal to the wear rate. The area of extruded metal may therefore be described by integrating the expression for the displacement as a function of depth (equation 5.13), such that the volume of extruded material, V_e, at any given time is given by:

$$V_e = w. \int_{Z_o}^{surface} \delta \; dz \qquad \ldots (5.16)$$

Where Z_o is the depth of deformation, which in this case would be most accurately described by the depth of the shear bands, since the displacement given by the twinning would be very small. The wear rate would then be computed from the product of the volume of extruded material with the displacement rate, the time of the test and the ratio of the true contact area to the apparent contact area, namely:

$$volume \quad V = w.\dot{\delta}.t.^{a}t/a_a \int_{Z_o}^{surface} \delta.dz \qquad \ldots (5.17)$$

where t is the total time of the test, a_t is the true contact area, a_a is the apparent contact area (which changes with time for the test geometry used) and $\dot{\delta}$ is the displacement rate.

The displacement rate, and the shear strain rate are difficult to estimate. However, the microstructural evidence suggests that the surface shear band becomes welded to the counterface and is dragged along with the pin. Wear occurs by plastic overload within the shear band. Therefore, the displacement rate at the surface should be the same as the sliding speed. The shear strain rate can then be evaluated

from the expression given above, whereby $\dot{\delta} = \kappa\dot{\gamma}$, which yields $\dot{\gamma} = 1.6 \times 10^4$ s^{-1}. Moreover, the shear strain rate should decay with distance from the worn surface in the same manner as the shear strain, as pointed out by Rigney et al. [235]:

$$\dot{\gamma} \leq v \kappa \exp(-\kappa z) \qquad \ldots(5.18)$$

Which assumes that the maximum displacement rate is given by the sliding speed.

From equation 5.17 a wear volume of 6.8mm^3 is predicted for the data presented in fig 5.75. A displacement rate of 0.24 s^{-1} was used and the total test duration was 3.38×10^6 seconds. The pin width was taken as the average between the initial and final sizes. The true contact area was discussed in the previous section concerned with the prediction of the wear rate from transfer, where a true contact area of 0.1% of the apparent contact area (10 contacts of 50μm diameter) was taken as typical. Therefore, the contribution of displacement to the overall wear volume is significant, but smaller than that of wear by transfer.

Values of the extruded metal weight were measured for the 24 N/pin test (the values for which were used in this computation) and were found to constitute about 3-10% of the total debris weight (depending on the pin). This does not account for the extruded metal which has broken off during the test. Furthermore, the figure must be corrected to allow for the weight gain in the wear debris from oxidation, which usually amounted to an increase of the order of 40% (by comparison to weight loss). This adjusted the weight fractions to 5-23% of the total wear, which indicates a wear volume in the range 1.35-8.2 mm^3. Therefore, the theory is in good agreement with the experimental results.

The combined wear rate predicted from the transfer model and the displacement model tends to underestimate the actual wear recorded, especially since retransfer of oxide occurred, which would reduce the wear volume. Some of this shortfall can be explained by wear debris generation by the breaking off of groove lips, and extruded metal which becomes detached during the test. However, this would not be expected to explain the entire shortfall. Whilst the equations are certainly an over-simplification of the real situation, the underestimate does suggest that some of the values used in the calculations are

inaccurate. In both cases, the biggest question mark exists over the real contact area. Theory predicts smaller contact areas than those measured on the wear surface. However, the measured values are considered to be accurate to within 30%. The only value which had to be totally estimated was the number of contacts. Throughout most of the discussion a value of 10 has been used. If the actual wear rates are substituted into the wear equation 5.8 for transfer to the disc, a value of N = 19-76 is obtained for prow diameters of 100-50μm respectively. These values are reasonable and yet still only constitute a real contact area of <1% of the apparent surface contact area.

5.7.3 Flow Stress at the Surface

The manner in which the crystallite size in the shear bands remain approximately constant with depth (with the exception of the outer 200nm) suggests that a saturation flow stress has been achieved in this region, which is only exceeded in the last 200nm from the surface. Therefore, the relationship presented by Nutting & Pollard [190], equation 2.14, which describes the hardening behaviour of metals showing a saturation flow stress should be applicable:

$$\sigma = K \ m^n \ [\tanh(\epsilon/m)]^n \qquad \qquad \ldots(2.19)$$

Where K is a strength parameter corresponding to the flow stress at unit strain, n is the work hardening index and m is an additional parameter which is a measure of the work hardening capacity and lies in the range 1.5-5. Clearly, the tensile stress and strain need to be converted into values for the shear stress and shear strain, using the following equations:

$$\tau_y = \sigma_y \ m_b = \sigma_y \ (\cos\lambda \ \cos\chi) \qquad \ldots(5.19)$$

and

$$\epsilon = \ln(\gamma/\sqrt{2}) \qquad \qquad \ldots(5.20)$$

Where m_b is the Schmid factor, λ and χ are the angles made by the compression axis with the active slip directions and slip plane normals respectively. The Schmid factor rises with the number of possible

crystallographic slip systems, to a maximum value of 0.5. The only metal which approaches the maximum value of 0.5 is Al, deformed above $300^\circ C$, where glide can occur on all {111} and {100} planes in the twelve <110> directions [300]. The next largest value of m_b is for BCC metals when pencil glide takes place so that most, if not all, <111> may be active. Kuhlmann-Wisldorf [300] suggests that taking into consideration the textures formed, a value of 0.44 is appropriate for the non refractory BCC metals. A somewhat lower value of 0.33 is predicted for FCC metals under conditions of multiple glide.

Assuming a Schmid factor of 0.33, the saturation resolved shear stress is about one third the tensile saturation stress. An estimate of the effective shear stress at the surface can be made assuming that the applied stress causes plastic deformation which increases the area of contact to the point where the load can be supported. This does not necessarilly mean that the extreme surface deforms in an elastic manner, because, as shown earlier, this material becomes welded to the counterface and is dragged along with it. Therefore, the shear stress at the surface is given by the applied force divided by the true contact area. Taking estimates of the true contact area ranging from 1.47×10^{-7} to 1.96×10^{-8} m^2 (which were the values used in the calculation in the previous section), the shear stress at the surface is predicted to be in the range 161-1220 MPa for a load of 24 N, and 369-2800 MPa for a load of 55 N. These figures suggest that the true contact area lies somewhere in the range stated, but because this range cannot be narrowed down by experimental results, an accurate prediction of the surface flow stress cannot be made with any confidence.

The hardness of the oxide prows was measured at about 9 GPa, suggesting a shear flow stress of 1 GPa. Unfortunately, the hardening produced by the freshly formed shear bands is very much more difficult to estimate. The crystallite size in the band was much smaller than that in the subsurface region, suggesting substantial hardening. However, the thickness of the surface layer was so small that the effective surface flow stress would not be expected to be that much above the subsurface region. In this region, a hardness of about 4.8 GPa was measured, suggesting a shear flow stress of 533 MPa.

5.7.4 Friction Coefficient

Kuhlmann-Wilsdorf [300] has discussed the effect of the number of

slip systems available at a worn surface on the friction coefficient, and derived the following relationship:

$$\mu = \frac{F_t}{P} = \frac{c \; _s\tau_y \; m_b}{2.8 \; _b\tau_y \; m_s} \qquad \ldots(5.21)$$

where m_s is the Schmid factor at the surface; m_b is the Schmid factor in the subsurface region; $_b\tau_y$ is the critical resolved shear stress in the subsurface layers; $_s\tau_y$ is the critical resolved shear stress at the surface; c is a multiplication factor which accounts for the fact that the area deformed is generally larger than the real contact area; F_t is the friction force and P is the normal load.

Values of m_b have been discussed in the previous section (5.7.3). The values of m_s tend to be larger and less crystallographically dependent than m_b, because the surface is considered to approach simple shear conditions and therefore the number of participating slip systems is less [300]. With single glide the texture would give m_s -1. This is certainly considered to be a reasonable assessment, based on the current findings. Kuhlmann-Wilsdorf [300] suggests that, once running-in has been achieved, the value of m_s is given by $0.8 \leqslant m_s \leqslant 1$.

Equation 5.22 provides an underestimate of the friction coefficient, because it ignores the contribution due to the creation of grooves (which will increase μ by 10-20%), and the increase derived from prow formation which further inhibits sliding motion [300].

Equation 5.21 predicts a constant friction coefficient as a function of load for the present case only if the metallic microstructure of the surface is considered, because values of the surface and subsurface shear stress would remain approximately constant with load. However, the presence of oxide would be expected to increase $_s\tau_y$ but leave $_b\tau_y$ constant, which would provide an increase in μ with load. This would be partly offset by a decrease in c for the higher oxide contents. The disparity between experiment and theory must be explained by a change in the texture and therefore in the Schmid factor. However, there is no way of confirming this assertion.

5.8   EFFECT OF SPEED AND COUNTERFACE

A 3Y-TZP disc was substituted for the Mg-PSZ for the conditions of

7.7 N/pin and a sliding speed of 0.24 m/s. The wear rates of the pins were very similar to those for an Mg-PSZ disc, namely an average of 1.66×10^{-4} compared to 1.5×10^{-4} mm^3/Nm. The wear mechanism was essentially unchanged with extensive transfer of metal to the disc. Where prows had become detached, the wear mechanism in the exposed zirconia could be seen to be by intergranular fracture. This point, and the wear rates of the ziconia, will be discussed further in the next chapter. Such a wear mechanism should provide easily identifiable wear debris. However, no zirconia particles could be found in the debris. This was considered to be for the same reasons as noted earlier for the Mg-PSZ case, namely a sampling problem since the zirconia constituted a small percentage of the total and with particles which were sub-micron sized.

Tests were conducted against the TZP discs at 0.08 and 0.48 m/s. The wear rate of the pins as a function of speed are shown in fig 5.77. As with the wear rate as a function of load, the present results follow the opposite trend to that of Smith [286], who studied the reciprocating wear of T316 stainless steel. The increase in wear with speed which Smith observed was explained by the widely accepted mechanism that suggests that the time between contacts is reduced to the point where the protective oxide film does not have time to heal. The present results show that this is a simplistic approach since the oxide does not form a uniform film, and that contact occurs in prows. Moreover, in section 5.6 on the temperature at the sliding interface, it was shown that oxide was most probably formed in the debris rather than on the steel surface.

The present results not only follow the opposite trend to those of Smith [286], but also the generally expected trend of wear as a function of speed [300]. In the earlier sections it was concluded that the majority of the oxidation occurred on the zirconia disc, much of which was re-transferred to the pin. The increase in temperature from the increased sliding speed would be much higher on the low thermal conductivity counterface than with the steel. The temperature increase in the steel at a sliding speed of 0.48 m/s was not substantial enough to give any change in the shear banded microstructure near the surface, where crystallite sizes were very similar to those presented in fig. 5.67. It would appear, therefore, that the increased oxidation kinetics as a result of temperature rises on the disc have not been offset by the shorter time between contacts. This view is supported by

the increase in oxide content of the pin surface with speed and the increased proportion of oxide in the wear debris, in particular Fe_3O_4.

5.9 GENERAL DISCUSSION AND CONCLUSIONS

The major results from the investigation of the wear of stainless steel have been noted, but it is appropriate to bring these points together to discuss the critical issues.

The wear mechanism has been shown to be a mixture of the two classical models of adhesive wear, producing transfer, and oxidational wear, reducing the wear rate. The frictional force was found to be lower for a non deforming ceramic counterface than the values quoted in the literature for self mated metal wear.

The scheme of deformation in the stainless steel followed similar trends to those found in rolling. The stress system produced by sliding contact had led to an extrusion of the material, rather than a plane strain compression. Therefore, wire drawing would have been a more appropriate comparison than rolling. Moreover, higher strains can be achieved with wire drawing.

The shear band diameter and structure was very similar in the transition region to that produced by rolling, despite the difference in stress state. The observation that the shear bands formed parallel to the surface confirmed that the maximum shear stress was also parallel to the surface. The geometrical constraint imposed by friction was such that no twinned material remained at higher strains (i.e. closer to the surface). The available evidence suggested that with rolling twinned colonies would survive to very high strains.

The shear banded region showed no evidence of fresh shear band formation except at the extreme surface. Rather, the crystallites contained sharp boundaries, indicating homogeneous deformation mechanisms were taking place. The majority of the shear banded region showed very little tendency to change structure towards the surface, with the exception of the last 200nm, despite an exponential strain distribution. Therefore, the steel was deforming at an approximately constant shear stress. The rate of work hardening from dislocation flow was offset by mechanisms such as crystallite multiplication. However, there was no evidence that a dynamic recrystallisation mechanism was responsible. The homogeneous deformation mechanisms were
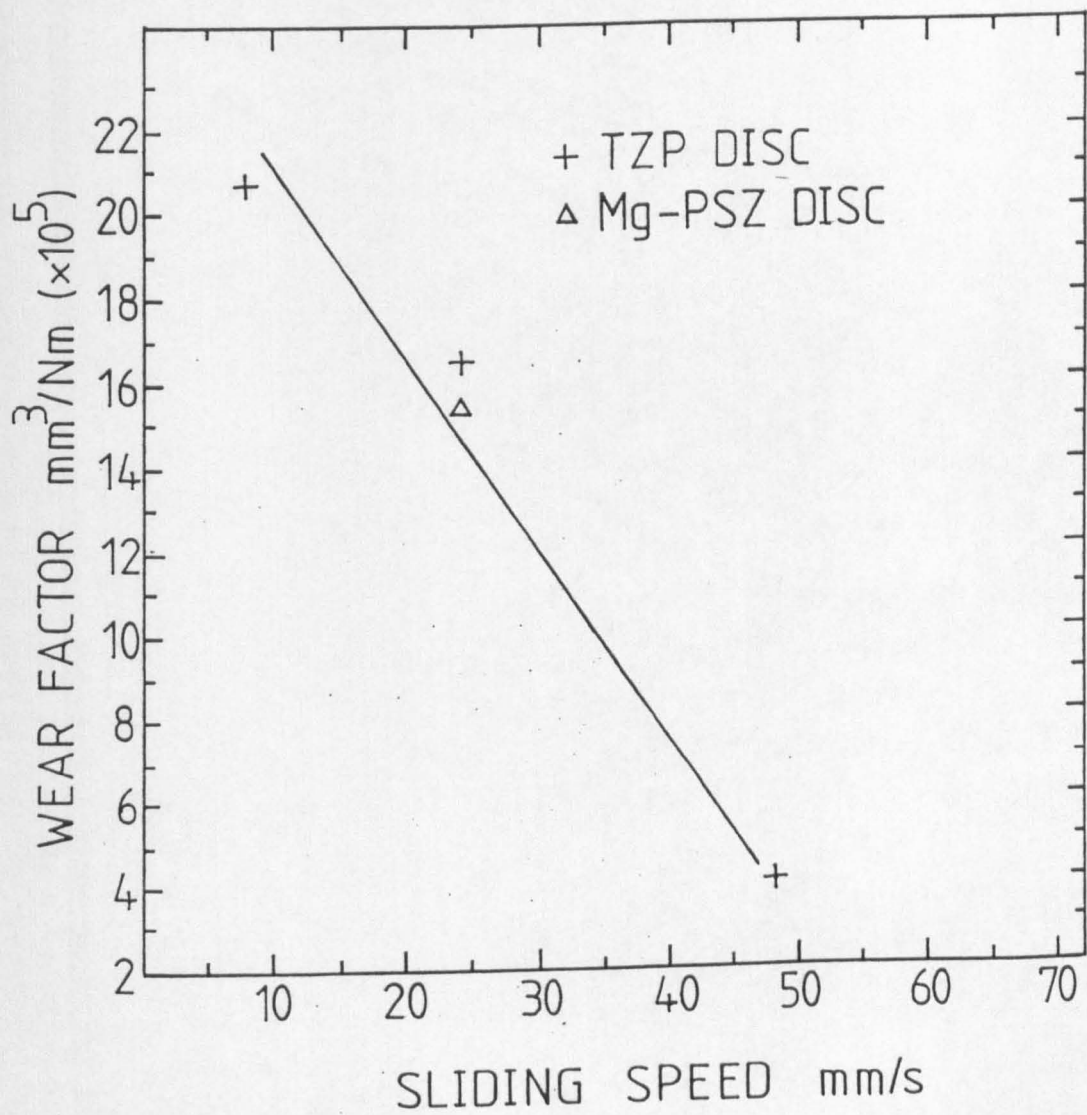
Fig. 5.76. Wear factor of the pins as a function of sliding speed.

permitted because the dislocation path length in the crystallites was too small to permit substantial dislocation interaction, and consequent work hardening. The crystallite size was slightly larger than in the rolled samples, indicating that the saturation shear flow stress would be of the order of 500 MPa.

The constant crystallite size could be taken to indicate that some form of superplasticity was occurring. However, the absence of any microvoiding suggests that no grain boundary sliding was taking place. Microvoiding would certainly be possible under these circumstances given the high shear strain rates and low homologous temperatures.

The observed homogeneous deformation could not be attributed to large temperature rise at the interface. The temperature in the bulk of the shear banded structure was shown to be low both by experimental measurements and theoretical predictions.

The absence of fresh shear bands in the crystallite region is perhaps suprising given that 70/30 brass, which has a very similar specific stacking fault energy [198], shows macro-shear banding after a strain of about 2.5 in rolling [209]. It was assumed that macro-shear banding were not observed in the present rolling experiments because the highest strain achieved (3) was too low. However, macro-shear bands may well be specific to rolling, because of the geometry of the stress system, and would not be found in wire drawing.

The constancy of the microstructure below the worn surface, and the absence of any microcracking (ignoring the last 200nm), suggests that under such a stress system with a large hydrostatic component there would be no limit to the ductility of the material. Failure only occurs when the deforming material is exposed to the adhesive forces at the surface. At this point the stress system must change because the surface material is dragged along with the counterface. Certainly, very high shear strains were developed in the surface, but the ultimate strain was dictated by the depth of deformation, not the limiting ductility of the metal.

The failure at the extreme surface is considered to occur by plastic overload. During the formation of the shear band the metal is believed to act in a manner analogous to a liquid. Under such conditions it is easy to perceive parting of material in the shear band. Walker & Shaw [302] have suggested a microcrack mechanism of deformation which may operate at very high strains. In their work they found a negative strain hardening rate at high strain, just prior to

fracture. Acoustic measurements indicated that microcracking may have been occurring. It was suggested that microcracks form and reweld, possibly many times. In the present study evidence for fine microcracks were found in the freshly formed shear bands at the surface, but nowhere else except in the oxide (fig 5.48). This mechanism is presumably similar to that occurring in Cu-Si alloys with very low stacking fault energies, where failure occurs at relatively low strains during the formation of macro-shear bands.

The relationship between surface roughness and the contact conditions was described by Greenwood & Williamson [228], in equation 2.13, which gives a plasticity index, predicting whether contact is plastic or elastic or a mixture of the two. Unfortunately, the conditions under which the necessary surface roughness variables can be evaluated are exacting, and could not be defined for the present surfaces. However, their theory predicts that the contact conditions are independent of load, dispelling the notion that contact changes from elastic at low load to plastic at high load (although this can still occur if a change in wear mechanism takes place which alters the surface roughness). The present results support this assertion. Contact was found to be plastic throughout the load range studied. The applied load only changed the size of the contact area, the depth of deformation and the quantity of oxide. The presence of oxide increased the flow stress and possibly introduced an element of elastic behaviour, although contact was still essentially plastic.

The surface shear bands contain a finer crystallite size than found in any of the rolled specimens or in the freshly formed shear bands well below the worn surface. This was believed to result from the high shear strain rates imposed by sliding. Studies have shown a decrease in crystallite size within shear bands as a result of an increase in strain rate [191]. Certainly, the strain rates at the surface (a maximum shear strain rate of 1.6×10^4 s^{-1} was calculated, assuming the surface shear band is welded to the disc) are very much larger than those in the rolled material. Therefore, the presence of very fine crystallites at the surface is not taken to indicate some form of stage IV hardening, rather, the saturation stress is considered to continue until some external condition changes (e.g. exposure to the surface).

The presence of surface shear bands which had just been formed indicates that the critically resolved shear stress is a maximum at the surface. This contradicts many wear theories which consider that the

stress is a maximum some way below the surface. Such predictions are based on Hertzian contact theory which was derived for elastic contact under a spherical indentor [303]. A large number of wear situations result in plastic or elasto-plastic contact, where the friction coefficient is high, at least >0.4. Under such circumstances the stress should always be a maximum at the surface and therefore Hertzian theory would not be valid.

Wert et al. [304] have demonstrated an increase in wear rate with decrease in stacking fault energy for a range of Cu-Al alloys having SFE values which ranged from 5-45 mJ/m^2. These findings follow the opposite trend to the predictions of the Archard equation [297] namely, decreased wear with increased hardness. The highest SFE is of the same order as the 316L used in the present study. A decrease in SFE would be expected to produce shear bands (and macro-shear bands) at a lower strain with a reduced crystallite size. At the lowest SFE, behaviour should be similar to that described by Hatherly & Malin [200] for Cu-8.8%Si, where macro-shear banding caused failure after a comparatively small reduction. Therefore, it is postulated that the reduction in SFE which produced higher wear was a result of macro-shear bands being formed at the worn surface, which subsequently acted as failure sites. This would be expected to replace the extended homogeneous deformation found in the present study. A useful extension to the present work would therefore be to study the deformed wear surface of a lower SFE material than was used in the present study.

The above discussion indicates that, although low stacking fault energy materials exhibit heterogeneous deformation, the present material has produced a thick layer that has deformed homogeneously and conforms to an exponential strain distribution in the same way as Cu, for example [235]. The two places where the heterogeneous deformation is important is the surface and the transition region.

Heterogeneous deformation at the surface may well play an important role in the wear mechanism. Soda et al. [138] have demonstrated that the size of the wear debris particles, produced by the sliding wear of Ni, was directly proportional to the depth of deformation. In the present study, a relationship appears to occur between the wear rate and the depth of deformation. However, this has been shown to be associated with the number of contact events which produce transfer, and to the quantity of extruded metal, which is dictated by the strain. Soda et al. [138] considered that there was a direct

relationship between depth of deformation and the depth at which the stress system and microstructure were such that failure could occur. As the load increased, failure could occur at a greater depth. This is a reasonable explanation for a high SFE material such as Ni, where the microstructure would be expected to change uniformly with depth. In the present study, strain localisation in the form of a shear band appears to limit the depth at which failure can take place. The sub-surface regions do not appear to be close to their ductility limit, whereas the thickness of a shear band remained approximately constant in the load range investigated. Therefore, the localisation of shear appears to shield the subsurface regions from failure.

The presence of a strong <111> fibre texture rather than a <001> fibre texture is unexpected and difficult to explain. The former texture is only normally found in very high SFE materials such as Al [283]. This would suggest that a significant temperature rise had occurred at the interface which had effectively raised the SFE. However, this would have undoubtably changed the appearance of the microstructure, certainly to the point where low SFE type shear banding would not have been observed. Therefore, favouring of the <111> above the <001> component must indicate that the stress system was sufficiently different to that in wire drawing to change the slip behaviour and sub-grain rotation.

The literature on textures formed at sliding interfaces is somewhat sparse, which is suprising given that the texture formed can give important information regarding the mode of deformation and can also have a strong influence on the flow stress at the surface. Krause & Ocalan [305] have demonstrated that both the wear rate and the friction coefficient are affected by the initial texture in the material. In their work they examined a steel with a strong fibre texture in three directions, namely along the wire axis and in two directions perpendicular to the wire axis. The minimum wear rate and friction coefficient was associated with a (145)<321> texture which was produced by sliding along the wire axis. The greatest wear was produced by one of the perpendicular orientations which failed to produce a stable texture in the worn pin. It is interesting that none of the textures formed in the worn surface conformed to the normally expected texture for either wire drawing or rolling.

Wheeler & Buckley [306] have also examined the surface textures produced by sliding wear in Cu, Ni, and Fe. For both the FCC metals a

strong texture was found with the (111) planes tilted 10° to the sliding direction (the (111) pole was the only one investigated). The authors consider that this is indicative of the slip planes orientating themselves towards the sliding direction. However, none of the known textures for FCC contain {111} planes parallel to the rolling plane. As Kulmann-Wilsdorf [300] pointed out, the occurance of slip planes orientated such that a single slip system operates is most unlikely. For example, with the FCC fibre texture with <100> and <111>, the <100> provides symmetrical conditions for four <110> slip directions, whilst the three <110> are provided for <111>. In rolling, <112> dominates the texture, which is mid-way between two <110>. Moreover, the slip planes do not align themselves parallel to the rolling plane. However, for the case of the FCC metals, Wheeler & Buckley [306] did not define a direction with the rolling plane.

Hirth & Rigney [307] have noted that the textures generated by sliding are close to, or exactly the same as, the textures generated by rolling. However, the {110}<112> texture quoted was some way off perpendicular to the surface, suggesting that some other low index rolling texture or even a wire texture may also have been present.

The strong fibre texture found in the present results appears at variance with the rolling texture reported by Hirth & Rigney [306], Krause & Ocalan [305] and Wheeler & Buckley [306]. However, the reports of very low index textures suggest that a wire texture may have been present, but was not found because of the experimental difficulties. Therefore, the most reliable method of investigating textures at a worn surface is that used in the present study, namely TEM.

It is interesting that these authors appeared to expect a rolling type texture, rather than a fibre texture. The two textures indicate an important difference in the mode of deformation at the surface, since they reflect the amount of hydrostatic compression. In rolling the amount of hydrostatic compression is lower than in wire drawing and extrusion (depending on the amount of die wall friction) [308]. Therefore, the presence of a rolling texture suggests a significant tensile component of the surface stress, which would promote a delamination type wear mechanism. In contrast, the wire texture indicates a strong hydrostatic component. The absence of subsurface cracking, both in the oxide and metal, demonstrates that the tensile component was low. It is this stress system which has permitted plastic flow and supressed failure in the oxide. It has also enabled

extremely high strains to be achieved at the surface without failure in the shear banded structure. Rolling type stresses would have promoted failure at much lower strains.

Only at the extreme surface does the stress system differ. The strong adhesion promoted failure within the freshly formed shear band. It was only in this region that evidence of microcracking was found. The change in the stress system was reflected in the change in texture to include a Goss component (i.e. a component of the rolling texture). It is interesting that this surface region was so thin (200nm), believed to reflect the manner in which the strain is accommodated in such a small region by shear band formation. In effect, heterogeneous deformation has shielded the subsurface regions from the strong adhesive forces.

The theory of oxidational wear was first described before Bowden & Tabor [309] proposed the adhesive wear mechanism [218]. Since then it has been extensively studied and the general prediction that an increase in the oxide content leads to a reduced wear rate has been confirmed experimentally many times, as reviewed by Quinn [218]. For the case of steels, oxidational wear is associated with the 'mild wear' regime (although this is a very loose term). The transition to the 'severe wear' regime is believed to occur when the load is sufficiently high to destroy the protective oxide film. Furthermore, the oxide is considered to act as a solid lubricant, thereby reducing the friction coefficient. The standard model of oxidational wear considers that the contacting asperities are at a higher temperature than the remainder of the surface, permitting oxidation to take place. Repeated contact provides an increase in the oxide thickness until a critical thickness is reached at which point the oxide spalls off as a wear debris particle. Therefore, the oxidation kinetics at the wear surface can be related to conventional oxidation studies. This view has been supported by good experimental fit to theory, using parabolic oxidation kinetics. The oxidation rate is introduced into an Archard type equation by evaluating the probability of forming a wear debris particle in terms of the rate of growth of the oxide (as discussed in section 5.6).

The present results suggest that this analysis is an over simplification of the oxididation on both surfaces. Considering the oxidation on the disc first. Each transfer event adds to the thickness of the prows on the disc. The transferred metal is rapidly oxidised,

defect density generated during shear band formation. The avalanche of dislocations, which is considered to result in a shear band, would permit substantial quantities of oxygen to be taken into solid solution in the metal. Indeed, it is difficult to see how oxygen would not be taken into solid solution when the driving force for oxidation is so high in this material and the surface is being continually heated and disrupted. Repeated deformation would eventually lead to the point where the oxygen concentration exceeded the solid solution limit thereby driving some form of phase change. This transformation appears to have resulted in the partitioning of the material into an amorphous phase and a crystalline phase. Since the BCC phase contained lattice spacings which more closely conformed to α' martensite than any other phase, it is possible that the partitioning led to oxygen combining preferentially with the Cr, Mo and Ni, depleting the austenite to the point where it was no longer stable and transformed to α'. The significant α' reflection in the XRD traces of the wear debris can only be explained by their presence in the non equilibrium oxide (no clear metallic α' was found). Unfortunately, the microstructure was far too fine to allow any microanalysis to be conducted on the two constituents to confirm this theory.

The temperature generated on the disc was considered to be higher than on the pin because of the low thermal conductivity of the zirconia. However, the small amount of deformation on the disc means that little mechanical work was available to be converted into heat. Therefore, the low thermal conductivity will have been partly offset. Fe_3O_4 could not be found in the steel surface, suggesting that it was produced either on the disc or during debris attrition. Results in chapter 6, where TEM analysis of the disc is presented, show that small amounts of this oxide could be found in material transferred to the disc, but the proportion appeared to be considerably smaller than found in the wear debris. This would suggest that a slightly higher temperature existed on the disc, compared to the pin, had permitted this oxide to form. Even so, this is not the thermodynamically predicted oxide, which would be Cr based. The Fe_3O_4 retained the original proportions of the alloying elements of the steel; again this would not be expected in the equilibrium state. This presumably indicates that the temperatures (or the time at temperature) on the disc were insufficient to allow the necessary diffusion required to form the stable predicted oxide.

CHAPTER 6

THE WEAR OF ZIRCONIA AGAINST STEEL

This chapter will consider the wear of zirconia against steel. In the first section the wear of the zirconia discs used in the tests reported in chapter 5 will be discussed. This will be followed by a discussion of the results of zirconia pins sliding on bearing steel discs. Three different zirconias, providing a range of toughness values, were investigated, each across a range of loads. The general aim of this work was to investigate the interaction of transformation toughening with wear. The wear of the bearing steel discs was only considered with regard to its interaction with the wear of the zirconia.

6.1 THE WEAR OF ZIRCONIA DISCS

6.1.1 Mg-PSZ

6.1.1.1 Optical and Scanning Electron Microscopy

This section will consider the wear mechanisms operating in the PSZ discs used in the majority of the tests reported in chapter 5. The role of transfer of the 316L stainless steel pins to the disc has already been considered. However, this point will be now be related to the wear mechanism in the zirconia.

The wear test data has already been reported in table 5.1. The wear factor of the zirconia discs is shown in fig 6.1. Wear depths were evaluated by proliferometry traces as illustrated in fig 6.2. To compute the wear factor, it was assumed that the disc had essentially slid the same distance as the pins. An alternative value of the wear factor can be evaluated by accounting for the fraction of the distance during which actual contact took place. This gives values of k which are 7.7 times larger than those in fig 6.1.

The wear rates in fig 6.1 do not appear to follow any logical trend, in contrast to the steel pins. Measurement of the wear groove depth was made by proliferometry at three points around the
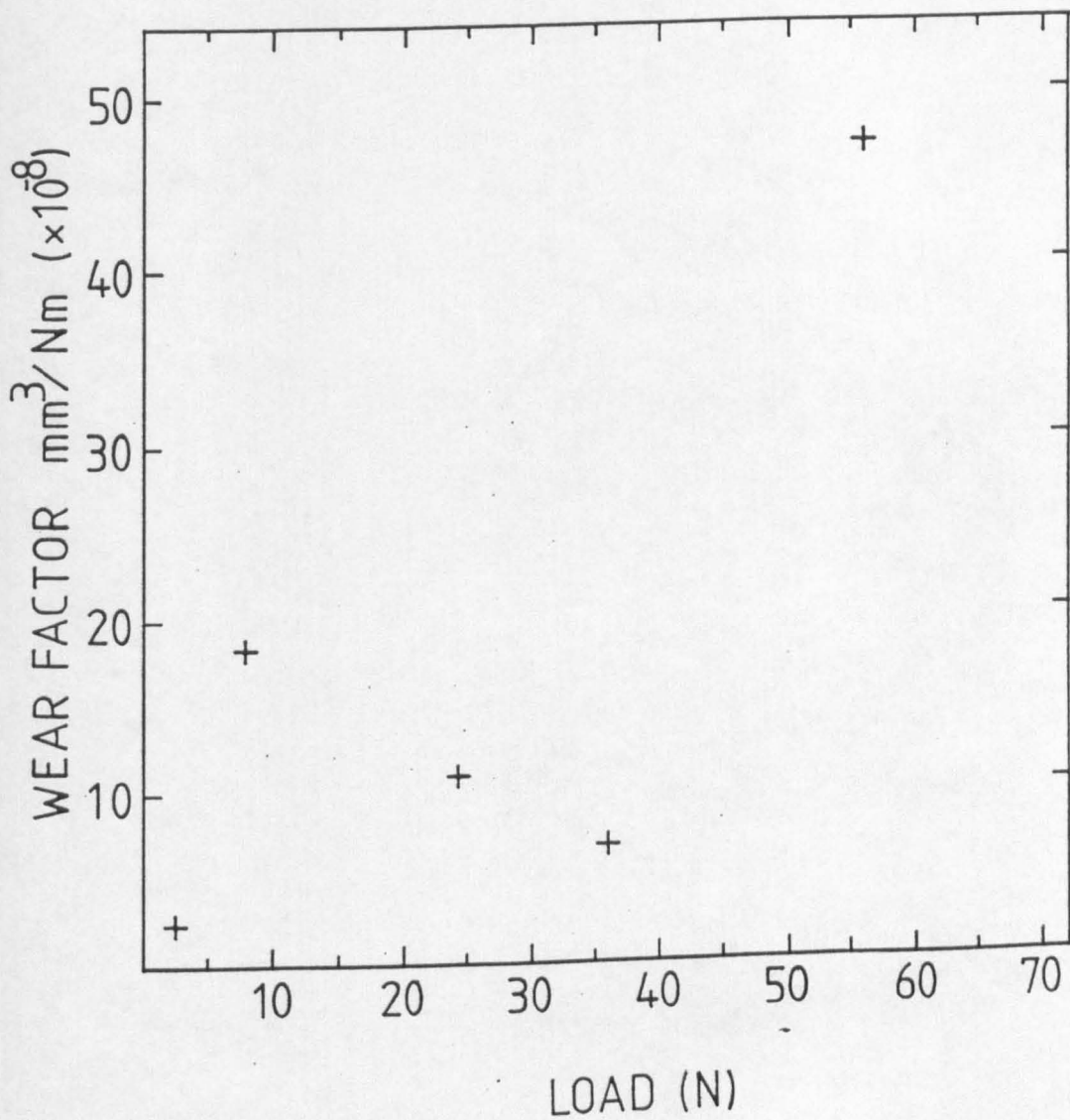
Fig. 6.1 Mg-PSZ disc wear factors as a function of load for the tests described in table 5.1. The wear factors can be multiplied by 7.7 to account for the proportion of time in contact.

circumference and the depth was found to be different at each position. Therefore, small differences in wear factor between 1 and 2×10^{-7} are within experimental error.

The appearance of the disc after sliding against the stainless steel was shown in figs 5.19,20. Some zirconia grains contained only a small amount of transfer, whilst others were covered with a thick layer of metal oxide. Many grains contained parallel sided grooves which were perpendicular, or within about 20° to perpendicular to the sliding direction. The transfer appeared to be strongest where these bands were found, and those grains which did not contain any bands usually exhibited little transfer.

In order to understand the mechanisms operating, the metal oxide was removed from the ceramic surface by immersion in HCl. No resolvable attack of the ceramic surface occurred as a result of this. By measuring the surface roughness before and after removal of the oxide it was possible to make a rough estimate of the thickness of the transfer. For the test at 7.8 N/pin this was found to be of the order of 300nm, whilst at 55 N/pin it was about 500nm. A typical example of the resulting surface is given in fig 6.2 for the test conducted at 7.8 N/pin. Two features were dominant. Firstly, the grooving as noted above. Secondly, the grain relief shown by the Nomarski contrast microscopy.

In fig 6.3 the extent of the grooving can be seen to increase from the edges towards the centre of the wear track, where the majority have undergone severe grooving. The grooves never crossed grain boundaries, and did not necessarily cross an entire grain but maintained the same orientation within each grain. A detail of the grooving from the outer region of the wear track is given in fig 6.4. Further towards the centre of the wear track, fig 6.5, some individual grains remained unaffected even when immediately adjacent to those which had become severely pitted. Note, also, the triangular shaped pits at the bottom of a groove running in the sliding direction. At the centre of the wear track the parallel sided bands could be better described as general pitting, often rectangular or triangular in shape, fig 6.6. The orientation of these pits tended to be $>20^{\circ}$ to perpendicular to the sliding direction, sometimes as high as 45°.

The extent of pitting was strongly load dependent. At high loads the pitting was essentially a general roughness of no particular form, fig 6.7. However, the pitting still gave a different appearance within
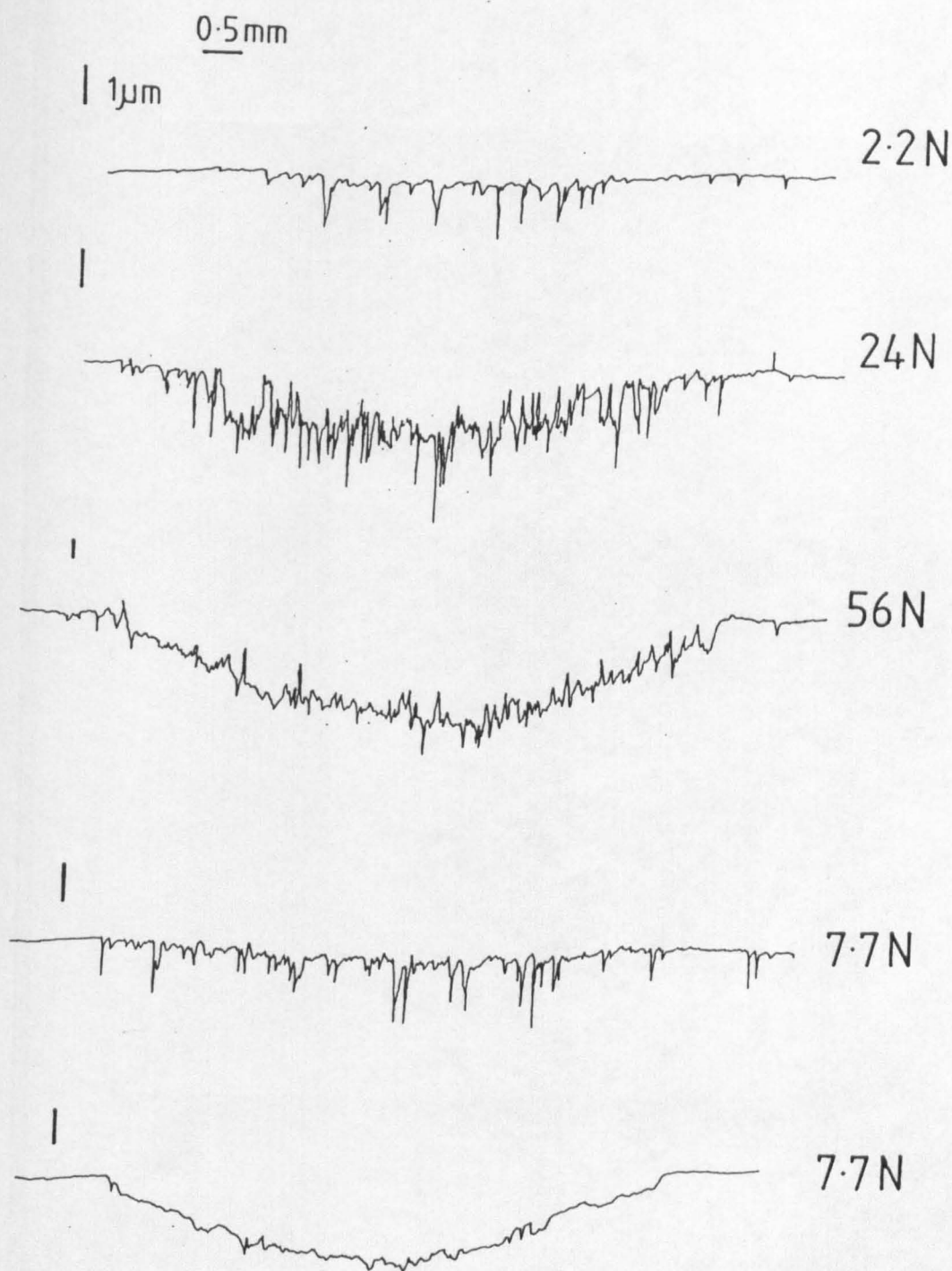
Fig. 6.2. Radial proliferometry traces from the Mg-PSZ discs from which the wear factors were evaluated. Note the change in scale on the vertical axis at the higher loads. The bottom profile is for a 3Y-TZP disc worn under the same conditions.
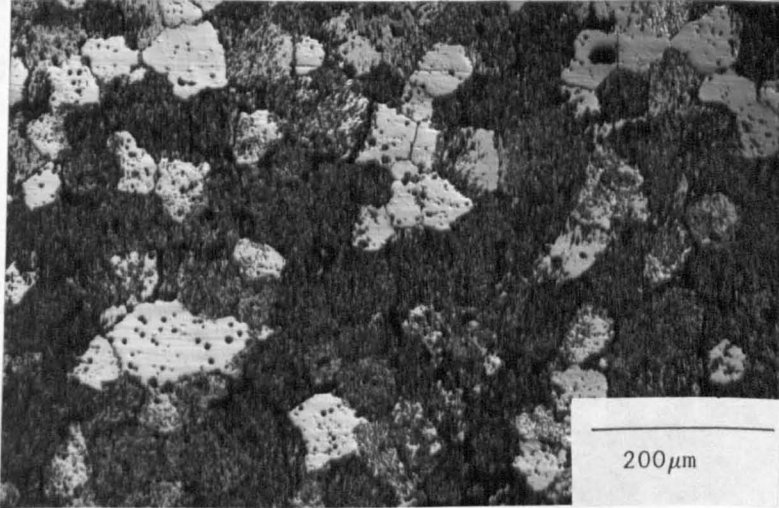
O. D.

CENTRE

Fig. 6.3. Optical micrograph (Nomarski) of a worn disc where the
transfer has been removed by HCl. Little damage occurred at the
outside of the wear track, whilst the centre is heavily pitted. Note
the grain relief and the orientation of the bands. (7.8 N/pin).

10μ   S.D.→
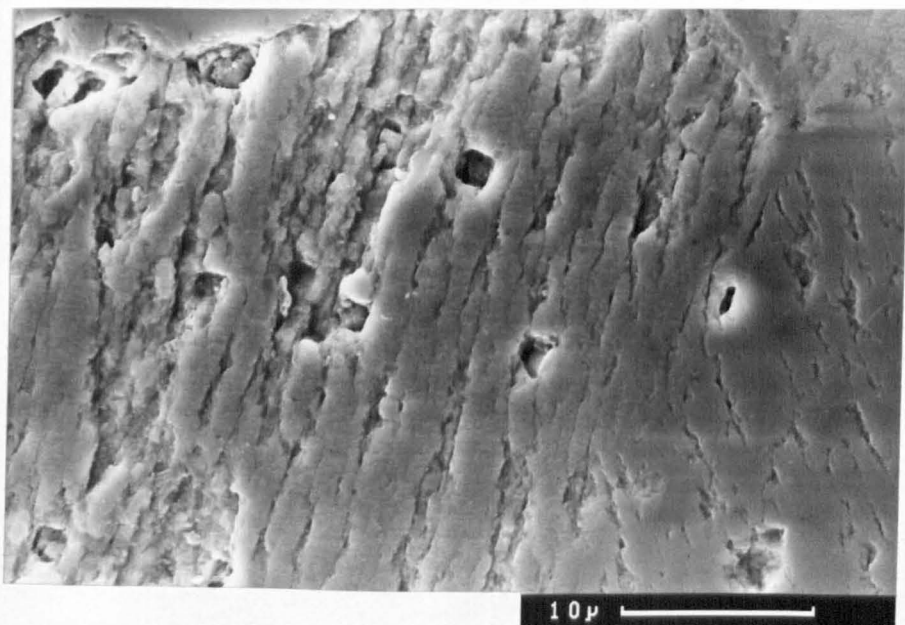
Fig. 6.4. SEM micrograph showing a detail of the parallel grooves. The grooves were sometimes sharp and crack like, whilst often wide and deep, suggesting band coalescence. Note the orientation change across the grain boundary on the right hand side. (2.2 N/pin).

S.D.→
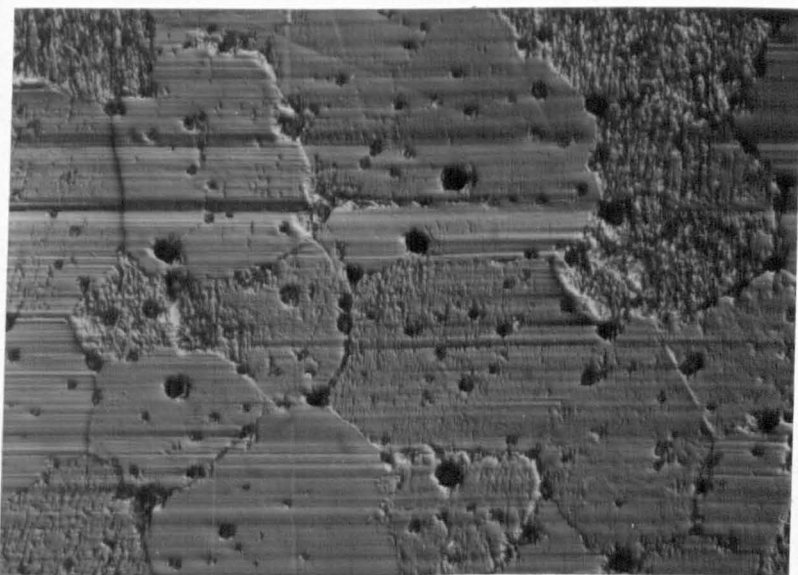
Fig. 6.5. Optical micrograph (Nomarski) of a worn disc mid way between the O.D and the centre of the wear track. Note the heavy pitting in the upper right grain, the triangular pits in the upper centre grain, and the variable grooving in the other grains. (7.8 N/pin).
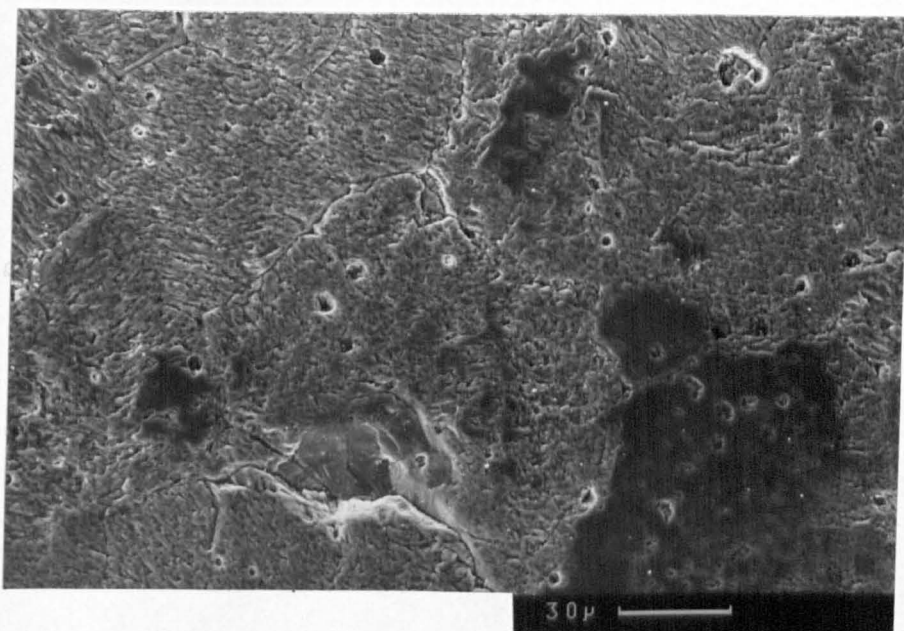
S.D.↑

Fig. 6.6. SEM micrograph of the centre of the wear track. Note the
heavy pitting/ grooving, the grain boundary cracking and the larger
crack initiated at a grain boundary. The grain in the lower right of
the micrograph has undergone significant wear but remains smooth. (7.8
N/pin).
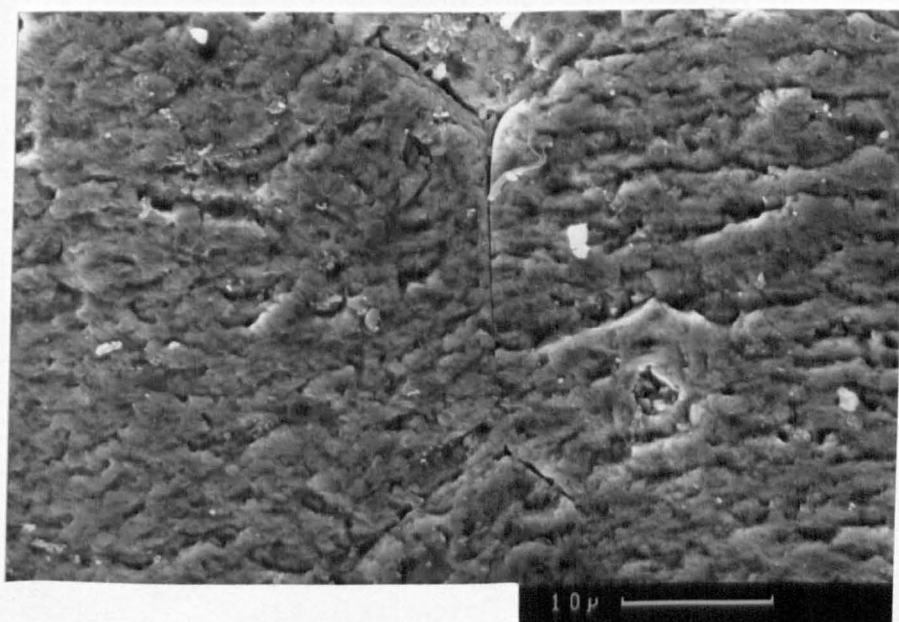
S.D.↑

Fig. 6.7. SEM micrograph of the centre of the wear track detailing the
structure of the pits/ grooves. (7.8 N/pin).

Fig. 6.8. SEM (5KeV) micrograph of the grooves after etching in HF. The precipitates can be seen to run along the direction of the grooves. Also note the coarse precipitates in the upper region. (24 N/pin).
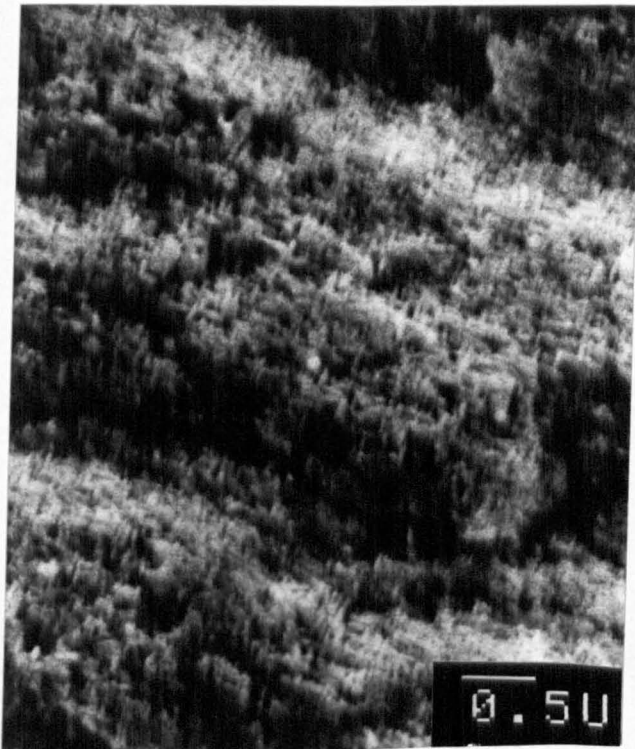
Fig. 6.9. SEM (5KeV) micrograph showing a detail of fig. 6.8.
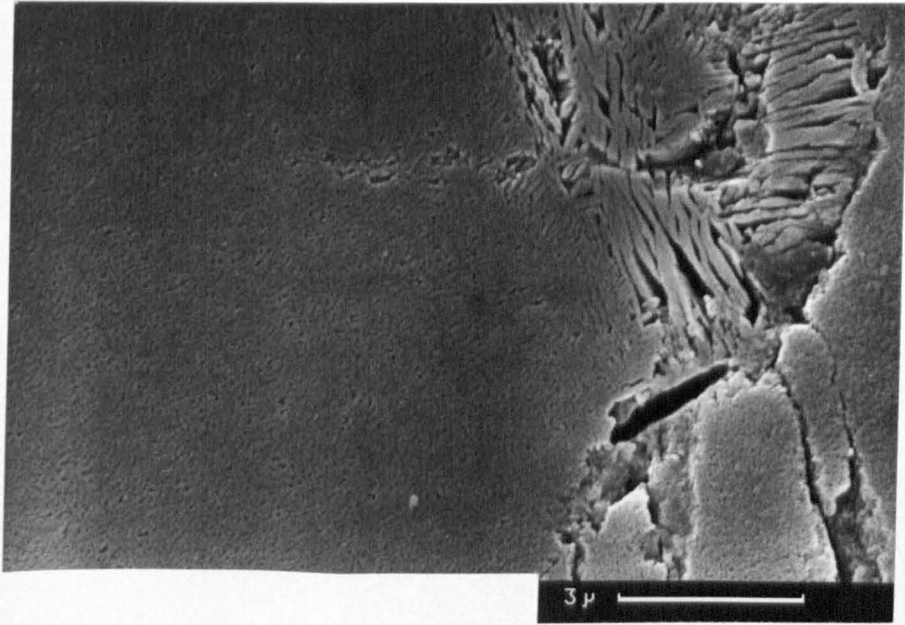
Fig. 6.10. SEM micrograph of a disc etched in HF from a grain which
did not show any grooving. There is no clear orientation relationship
with the surface. Note also the grain boundary monoclinic. (7.8
N/pin).

each grain. Even at the highest loads occasional grains were virtually unaffected by the grooving. In contrast, at the lowest loads, the centre of the wear track still contained a high proportion of grains which did not show any grooving. At all loads the grooving was always light at the edge of the wear track, for example the upper region of fig 6.3. Therefore, the amount of grooving was not only load dependent, but also time dependent.

The grooving/ pitting was clearly associated with the crystallographic orientation of the zirconia grains. In order to verify this the wear surface was further etched in HF. The etch was found to severely attack any prior lapping marks or abrasive grooves, and those grain boundaries which contained monoclinic phase. It proved difficult to resolve the very fine precipitates in the SEM except using a field emission microscope operating at 5 KeV. Fig 6.8 shows a general view of a groove towards the outer region of the wear track. A detail from a similar region is given in fig 6.9. The precipitates can be seen to be orientated along and perpendicular to the wear grooves. Therefore, the grain contained a near [100] orientation relationship with the surface. The larger precipitates in the upper portion of fig 6.8 should also be noted. These are similar to the precipitates shown in the TEM micrograph in figs 3.13,14. The precipitate orientation relationship with the surface could not be established from this technique for grains which did not exhibit grooving, but it was invariably low order, fig 6.10. Therefore, those grains which exhibited a high order orientation relationship with the surface generally contained grooves, whilst those with a low order orientation relationship did not. It is reasonable to assume that the appearance of triangular pits coincided with a [111] orientation relationship, whilst [110] probably produced the rectangular pits.

X-ray analysis was performed on only one disc because an entire disc could not be fitted into the diffractometer and discs were required for further wear tests. The quantity of monoclinic was found to be slightly lower than on the polished surface, 6% compared to 7.2%, although this was within experimental error. The two X-ray traces are shown in fig 6.11. The (111) monoclinic peak was found to have decreased in the worn material whilst the relative intensity of the ($\bar{1}$11) increased compared to the polished state (throughout this discussion the polished material is the same as the lapped state prior to wear testing).
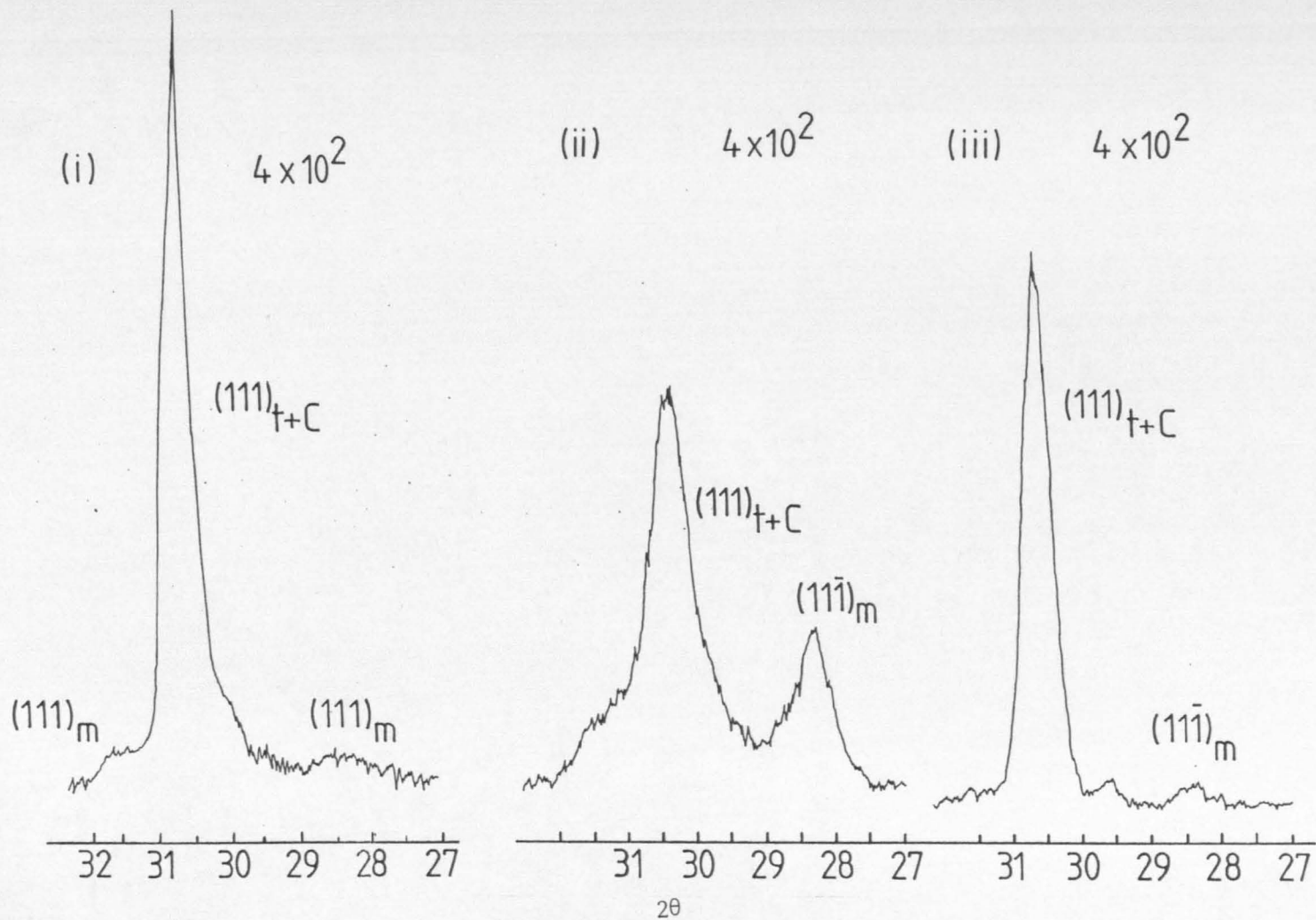
Fig. 6.11. X-ray diffractometer traces from the Mg-PSZ materials for a polished surface (lapped) (i), ground (ii) and from the disc worn at 24 N/pin (iii). Note the low levels of monoclinic in the worn surface and the reduction in the intensity of the (111) monoclinic reflection compared to the polished state.

The majority of the monoclinic in the polished material was from the grain boundary film. This film was shown to constitute about 6% of the total phase content of the Coors Mg-PSZ by X-ray analysis of material which had been re-solution treated in the cubic single phase field and rapidly cooled. Most of the grain boundary monoclinic was removed by wear to a depth of at least 1μm, leaving extensive grain boundary microcracking, fig 6.6,7. The depth of penetration of the X-rays was evaluated using the linear absorption coefficients reported by Kosmac et al. [261] and equation 3.1. This indicated that 60 % of the diffracted beam was provided by the top 1μm of the surface. Therefore, the apparent decrease in monoclinic content during wear may in fact have been a result of a reduced amount of grain boundary monoclinic which was partially offset by an increase in matrix monoclinic. This would explain the change in relative intensities of the (Ī11) and (111) peaks compared to the polished surface.

The parallel grooves and variously shaped pits have also been reported by Hannink et al. [313] for the wear of Mg-PSZ tappet facing under lubricated wear. Whilst these authors also ascribed orientation relationships based on the pit appearance, they did not make any attempt to explain the origins of the pitting.

The appearance and size of the grooves is similar to the transformation bands found adjacent to hardness indents in very tough Mg-PSZs, as reported by Marshall [98]. Rumpling was also found as a result of transformation of t→m on the surface of a tensile specimen and was produced by both permanent and reversible transformation (reversible transformation was discussed in section 2.1.6 and gives transformation of stress induced monoclinic to tetragonal after the applied stress is removed). Uplifted regions on the tensile surfaces were composed of arrays of grains each with a substructure of finer, sharp sided, bands which were confined to individual grains. The orientation of the finer bands within different grains differed but tended to be close to normal to the applied stress. This is a result of autocatalytic transformation (i.e. transformation in one grain initiates transformation in the adjacent grain).

One possible explanation for the pitting observed in the present study, therefore, is that transformation of t→m occurred cooperatively in bands. The resulting volume dilation would have led to the surface being locally raised up, giving preferential wear. However, it is difficult to see why transformation should have been restricted to

bands during sliding contact.

An alternative mechanism can be envisaged whereby microcrack coalescence, leads to preferential wear. This mechanism would operate most rapidly in those grains with a high index relationship because microcracking is favoured along (100), as a result of the precipitate orientation (see appendix 1). This suggestion is the only one which realistically fits with the experimental observations. However, it is possible that it is the combination of the mechanisms outlined which leads to the grooves being formed in certain grains before others.

There is little experimental evidence for the relationship between the stress to initiate transformation and crystallographic orientation. Nonetheless, it is clear that certain grains will transform at lower stress levels than others. For example, in the tensile tests conducted by Marshall [98], the number of grains showing rumpling steadily increased with stress to the point where microcracks formed and eventually coalesced to give failure. However, it was not clear whether this was a result of crystallographic orientation or the effect of residual stresses. Residual stresses have been considered in detail by Schubert [74,312], who suggests that the transformability of TZPs is governed by the level of residual stress, which increase with a decrease in yttria content. In the present case the high order orientations systematically showed banding, which would not have been expected if residual stresses were of over-riding importance.

The subject of the grooves will be further considered after the TEM results have been presented and after the pin wear results have been discussed.

The low monoclinic levels found by X-ray analysis do not preclude the above mechanisms. Marshall [98] reported reversible transformation at tensile stresses as low as 100 MPa. Reversible transformation would be expected to produce surface eruption in the same manner as irreversible transformation, although it is believed that reversible transformation does not result in microcracking. However, some authors such as Ishigaki [142] have suggested that irreversible transformation at the surface during wear leads to microcracking which provides surface break-up to the extent that any monoclinic is removed.

The grooving appeared to play an important role in the transfer process. As noted above, the thickest transfer was associated with extensive surface pitting of the zirconia grain. The mild grooving appeared to act as a key to the transfer of the metal. Once initiated,

further transfer occurred in a lamellar fashion to generate prows. Thus, grains containing more extensive grooves attracted more transfer, for example the grain in the upper right of fig 6.6. Eventually, the prows reached a critical thickness, at which point they became detached from the surface, leaving a considerably rougher zirconia surface. This suggests that fracture occurred within the zirconia surface, rather than at the metal oxide/ zirconia interface. However, as noted in chapter 5, no evidence of zirconia attached to the larger wear debris particles could be found, despite extensive investigation.

One conclusion from the above, therefore, is that the greater the transfer the greater the wear of the zirconia by this mechanism. In addition, the proposed mechanism suggests that the higher the zirconia toughness the lower the stress required for transformation and therefore the greater the amount of grooving at a given load. In other words, high toughness Mg-PSZ should be avoided.

Despite the comparatively high toughness of the Coors Mg-PSZ surface fracture was common at 7.8 N/pin and above. One such example is shown in fig 6.7, where the transgranular cracking was associated with the grain boundary region. As the load increased the cracking covered a larger area, fig 6.12. The crack surface was rough, (characteristic of transformation) and showed branching along what appeared to be grain boundaries. The extent of cracking did not increase at loads above 24.1 N/pin. The cracking was considered to be a result of the thick grain boundary monoclinic in this material, and the strong adhesive forces promoted by metal transfer.

Those grains which had not undergone pitting/grooving wear had still worn to an appreciable extent. The wear in these regions had left the surface very smooth, but had worn different grains to varying extents, giving the grain relief observed in optical micrographs (eg fig 6.3). These grains were frequently covered by abrasive wear grooves running along the sliding direction (fig 6.5), but were often featureless, fig 6.13.

Microfracture has been suggested by several authors (eg Wallbridge et al. [132]) to explain grain relief in ceramics which have undergone very low wear rates, (as discussed in section 2.2.5). Wallbridge et al. [132] proposed that certain orientations undergo plastic dominated wear, whereas others undergo microfracture and therefore wear at a greater rate. In the present study, a two stage replica was made of the zirconia surface before any etching treatment was undertaken. Many
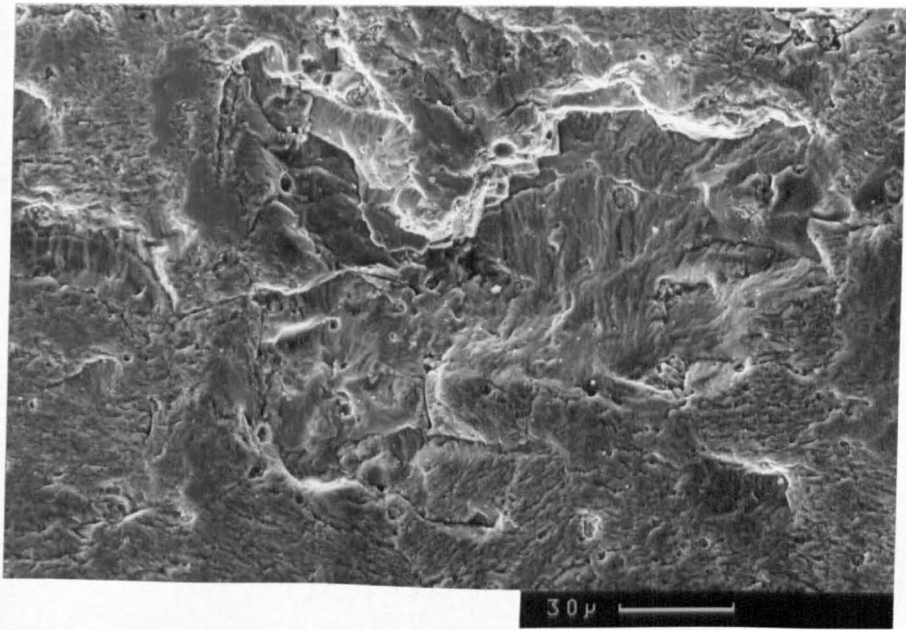
Fig. 6.12. SEM micrograph of a large transgranular fracture at the centre of the wear track. The cracking was believed to be initiated by grain boundary cracking. (24 N/pin).

50μm
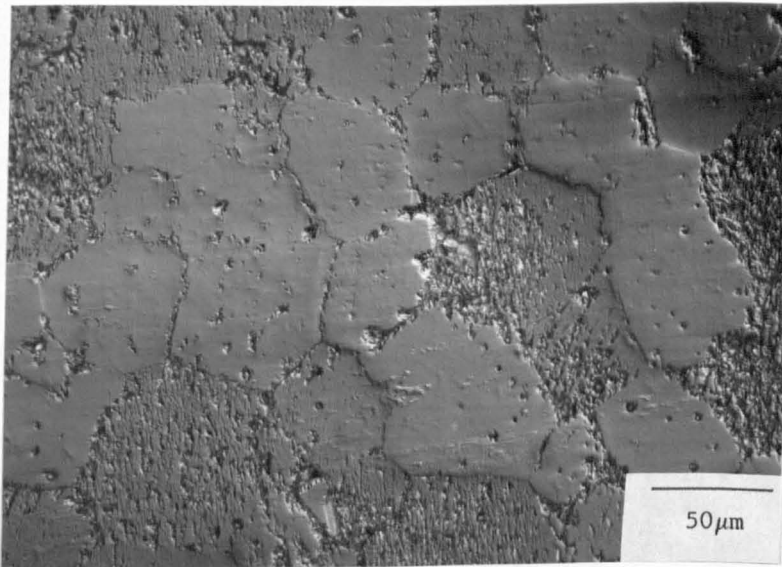
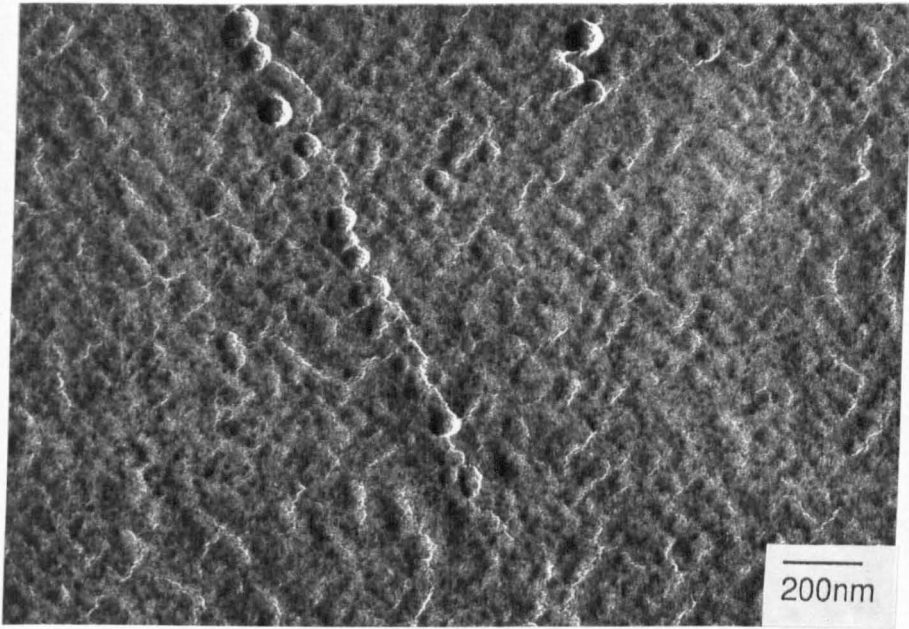Fig. 6.13. Optical micrograph (Nomarski) showing how smooth some of the grains which do not show grooving can be.

Fig. 6.14. TEM micrograph of a two stage replica from the unetched worn zirconia dics. The undulations are considered to reflect preferential wear in the cubic matrix in a similar manner to chemical etching. (7.8 N/pin).

of the grains were extremely smooth, far too smooth to have undergone any form of microfracture mechanism. Moreover, fine fractured particles would have been extracted onto the replica. No evidence was found of any such zirconia particles. To prove this point, two stage replicas were removed from the surface of the worn disc after etching in HF. This produced numerous very fine particles of monoclinic zirconia and tetragonal precipitates extracted from the surface. Particle sizes down to 10nm could be readily resolved. Therefore, it is clear that microfracture did not take place in the present study and that even if it does occur it is not a requirement for the production of grain relief.

Occasional areas on the replica were found which showed a surface structure as shown in fig 6.14. The undulations are on the same scale as the precipitate size and were found to change orientation across a grain boundary. It is reasonable to assume, therefore, that the undulations were produced by the preferential wear of either the tetragonal or the cubic, and most probably the latter. Such a structure could not have been produced by a plastic dominated wear mechanism, which is often considered to be associated with the mild wear regime in ceramics [eg132,167-170]. The only logical explanation for this mcirostructure is based on chemical dissolution of the zirconia surface by the iron oxide, with the cubic being removed at a preferential rate to the tetragonal. In other words, the major wear mechanism is a tribochemical one which occurs in the elastic contact regime. This view is supported by the presence of zirconia in solid solution in the wear debris. The latter point was difficult to prove for these tests, but was clearly apparent in the tests using zirconia pins which will be considered later.

The grain relief found on the worn surface of many ceramics is not suprising given the crystallographic dependency of hardness, stiffness and the variations in residual stresses. However, the actual mechanism which gives the variable wear has never been clearly demonstrated, although it is only found in the mild wear regime. Increased wear has been related to greater plasticity in sapphire by Steijn [158], but this was associated with a surface stress system typical of abrasive wear. No one has ever clearly indicated how wear debris would be formed by such a plastic-dominated mechanism which leaves the surface so smooth. It is clear that plasticity can lead to dislocation pile-ups which then initiate fracture, as discussed by Eiss & Fabiniak

[164], but this would leave a fracture surface. It is also clear that during abrasion of ceramics, considerable plastic flow occurs directly below the indentor, as shown by Hockey [3,4], among others. However, no such evidence has been produced for ceramics which have exhibited grain relief and low wear rates.

It is proposed here that grain relief is produced only by the tribochemical wear mechanism and is restricted to elastic contact conditions. Mechanisms of plasticity and microfracture did not occur in the present case. Mild wear is expected to be associated with elastic not plastic contact. The latter infers temperature rises which would lead to high wear rates. This argument will be considered further in the light of the TEM results in this chapter and the results of ceramic on ceramic wear in the next chapter.

6.1.1.2 Transmission Electron Microscopy

Several attempts were made to obtain thin foils perpendicular to the worn surface, but none of these were successful. The problem was associated with obtaining the thin area at the surface rather than below the surface. In all the attempts the first hole occurred below the worn surface. Further thinning produced fracture of the thin area between this hole and the worn surface. Some attempt was made to examine the thicker regions, but no useful micrographs were obtained. Future work should concentrate on dimpling techniques to ensure that perforation occurs at the worn surface first. Thus, the following results were obtained on back-thinned samples.

Back-thinning is a difficult technique because of the roughness of the worn surface and the re-deposition of the sputtered debris on the the worn surface. Moreover, it is difficult to estimate which is the original surface. However, interpretation of the microstructure was easier for the ceramic specimens, compared to the metallic ones, because of the absence of any significant plastic flow.

The microstructure at the worn surface was difficult to discern because of the extensive residual stresses. Extreme surface regions could be identified by the presence of metal oxide, fig 6.15. The interface between the oxide and the zirconia was always diffuse, apparently a result of considerable interaction. However, this point could not be evaluated with confidence because of overlying metal oxide. Nonetheless, trying to image cubic at the interface between zirconia and metal oxide proved unsuccessful, suggesting that it was

METAL
OXIDE

ZrO_2

100nm
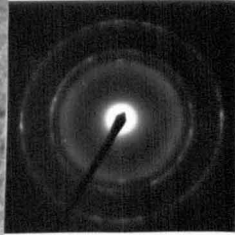
Fig. 6.15. Back-thinned TEM micrograph of the surface of the Mg-PSZ disc. The outer region is the non equilibrium oxide described in chapter 5. Note how the centre consists mainly of precipitates, with a diffuse boundary between the metal oxide and the zirconia. Very little cubic could be imaged in the dark field mode suggesting it has been preferentially eroded. The precipitates are monoclinic even though no twin boundaries could be imaged. (24 N/pin).

not present. In contrast, tetragonal precipitates could be easily
identified in this region. This supports the observation, noted above,
that the cubic is preferentially worn by a dissolution mechanism.

The majority of the metal oxide was found to be the same mixture of
the non-equilibrium BCC phase and an amorphous phase, reported in
chapter 5. Some regions showed trails of Fe_3O_4 within the
non-equilibrium oxide, fig 6.16. Magnetite was never found in the
steel surface, suggesting that temperatures were higher on the zirconia
disc, thereby allowing this oxide to form. However, the quantity of
Fe_3O_4 was lower than in the wear debris which suggests it was also
formed during comminution of the wear debris.

It was difficult to establish whether the precipitates were
tetragonal or monoclinic in this and all other surface regions. The
diffraction patterns usually showed a significant amount of twin
variants which produced arcing of the reflections for large selected
areas. Examples of surface precipitates are given in figs 6.17-19.
The precipitates had lost their distinctive oblate spheroid form and
were extremely difficult to image. It was not clear whether the
residual strain had disrupted the image or whether the precipitates had
genuinely lost their original morphology. The dark field images using
the precipitate reflections never produced an image of an entire
precipitate. Twin boundaries could only be resolved on a few occasions
and only in the dark field images (eg fig 6.19). Microdiffraction
studies were undertaken to try and establish the morphology of
individual precipitates. The convergent diffraction patterns indicated
that the majority of the precipitates were monoclinic. No positive
identification of tetragonal or orthorhombic precipitates was made.

If the selected area aperture was moved across a small distance
within the same grain appreciable rotations in the diffraction pattern
occurred. Examination of this region using secondary electrons in the
STEM suggested that foil buckling was not responsible. The distortion
of the precipitate was not symmetrical, indicating that the Mg^{2+} ions
were not taken back into solution as a result of the high
temperatures. This suggested, therefore, that some (limited)
dislocation flow might have occurred which had led to a local
redistribution of solute. However, no dislocations could be found, and
no subgrains were present to accommodate the rotation. Therefore, it
was probable that the image distortion was caused by residual
stresses. However, irrespective of which of the above represented the

true situation, it was clear that contact had been mainly elastic.

The parallel grooves were found to have been preferentially eroded during ion beam thinning. However, it was possible to confirm that the precipitates were orientated parallel and perpendicular to the groove axis. No changes in the structure adjacent to grooves could be found compared to that described above, for the outermost surface.

At a small distance below the original worn surface (less than 200nm) the precipitates could be imaged with greater ease, fig 6.20, although there was still considerable strain in the cubic matrix, fig 6.21. Many of the precipitates were tetragonal, although significant quantities of monoclinic were also present. However, the twin boundaries were no easier to image than at the surface. This again raised the question as to whether the orthorhombic phase was present, which can give very similar diffraction patterns to the monoclinic. However, no evidence of this phase could be found in microdiffraction patterns. It was possible that the majority of the twin boundaries were parallel to the worn surface, as a result of the shear stress conditions at the surface. The differentiation between monoclinic and orthorhombic will be discussed further in chapter 7.

The above results appear to confirm the X-ray findings which indicate that the amount of monoclinic at the surface was low. The depth to which appreciable transformation had occurred was considered to be less than approximately 300nm by TEM measurements. Since 60% of the X-ray signal was provided by the top $1\mu m$ of the surface any significant transformation would have been clearly recorded on the diffractometer traces. However, the interfacial stresses were shown to be fairly high in the steel surface, with the material shear flow stress of at least 533 MPa being exceeded during contact. Therefore, the asperity contact stress would have been expected to be high enough to initiate widespread transformation where the zirconia surface was exposed. Indeed, such transformation was used to explain the parallel grooving on the worn surface. If the Evans equation (2.2) [104,105] is used to estimate transformation zone sizes, a zone of $3.2\mu m$ is predicted, assuming 40% of the precipitates transform and the major stress component is shear (see section 2.1.7). Measured values of the zone depth were plotted in fig 2.12, which indicated similar zone depths to the calculated values. Whilst the Evans equation was derived for the propagation of a crack it should give a reasonable indication of zone sizes generated during asperity contact. Therefore, the
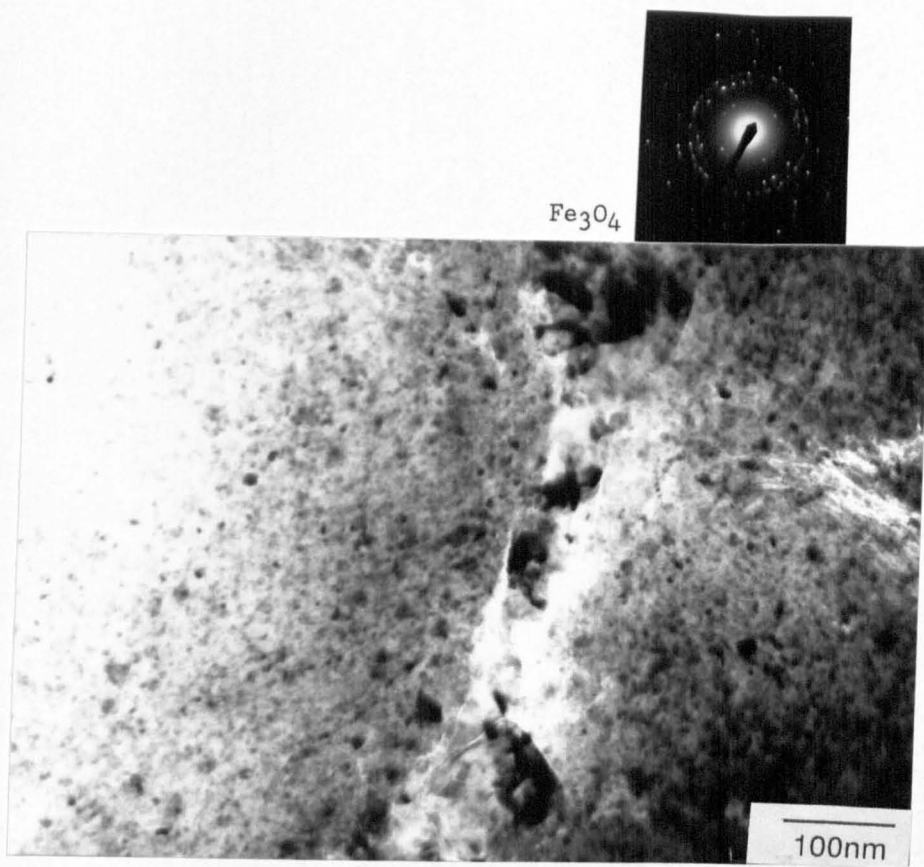
Fig. 6.16. TEM micrograph of the transfer layer showing a thin fissure of Fe_3O_4 passing through the non-equilibrium oxide.
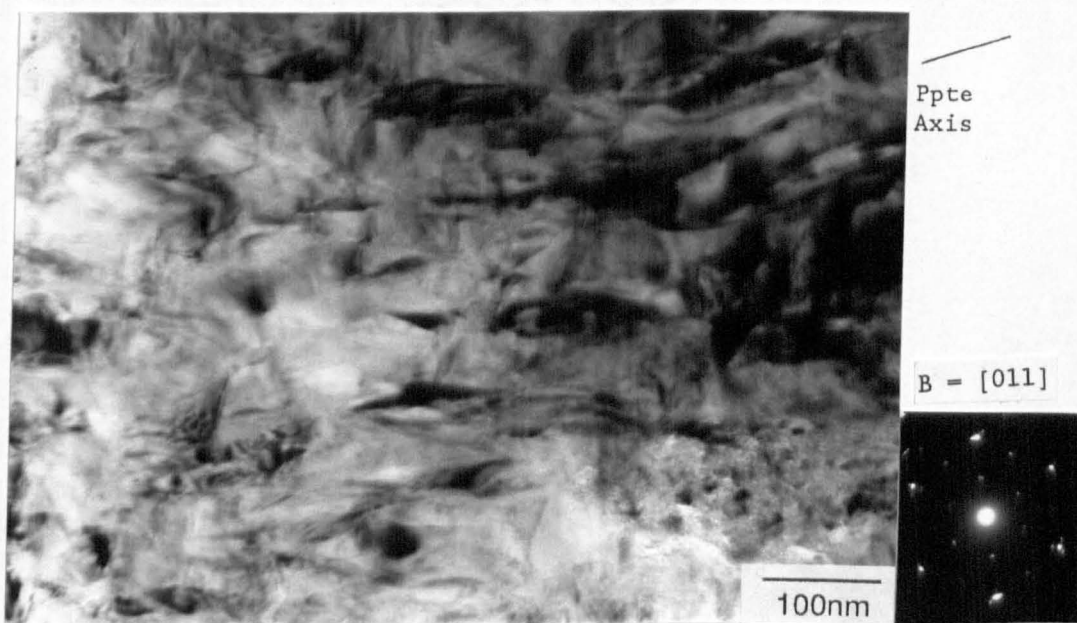

Fig. 6.17. Bright field TEM micrograph of the worn surface of the zirconia. The shape of the precipitates has become obscured, possibly disrupted by dislocation flow. Note the precipitates in the upper right appear to have been rotated to a different orientation. However, the image is difficult to interpret.
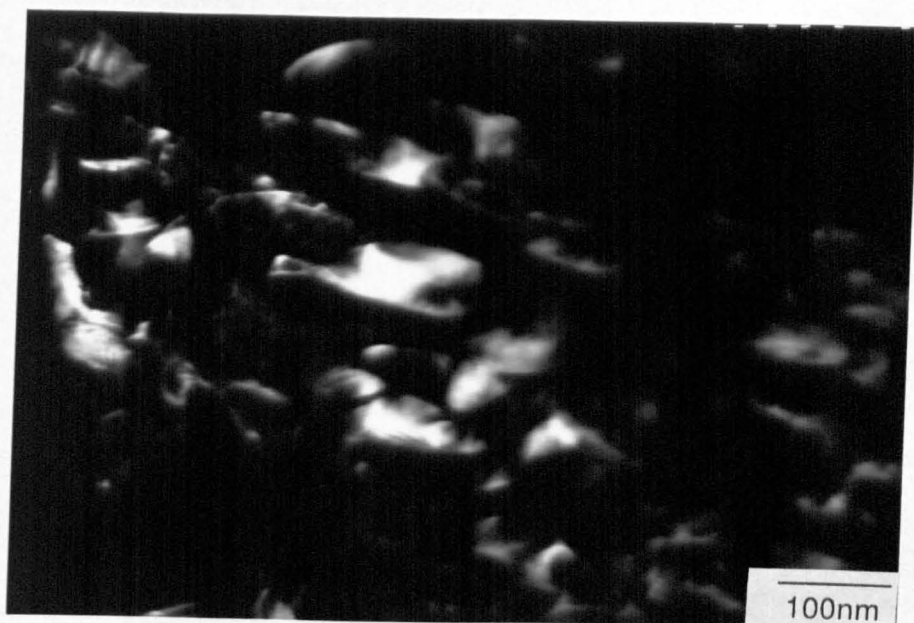
Fig. 6.18. Dark field TEM micrograph using a monoclinic/ tetragonal reflection. Note the distortion of the precipitate boundaries and the absence of twin boundaries despite the evidence of twin variants in the diffraction pattern.

Fig. 6.19. Dark field TEM micrograph from the worn surface using the monoclinic/ tetragonal diffraction spot. Occasional twin boundaries can be seen.

B - [100]
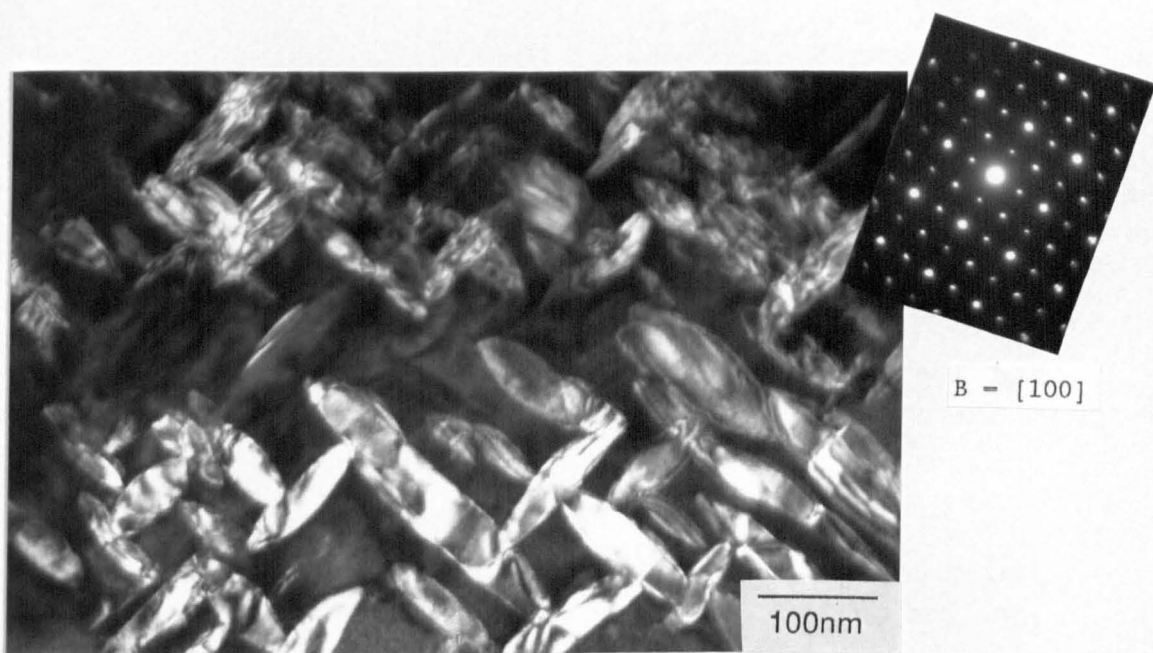
Fig. 6.20. Dark field TEM micrograph using a monoclinic/ tetragonal diffraction spot from about 100-200 nm below the worn surface. The precipitate shape is undisturbed and the majority of the precipitates are tetragonal.

Fig 6.21. Cubic dark field image of the above. There is still considerable residual strain in the matrix induced by the wear process.

monoclinic contents at the worn surface are lower than would be expected.

The low levels of monoclinic can be explained in two ways. Firstly, the temperature rise at the interface, which was considered to be around 300°C in the steel surface and higher in the zirconia, would have substantially reduced the driving force for transformation. Secondly, the explanation suggested by Ishigaki [142] can be used whereby microcracking in the monoclinic was considered to give surface break-up of the zirconia. Cooperative transformation in bands could have led to microcrack coalescence giving preferential removal of the transformed regions. However, no individual zirconia particles were found in the wear debris, although the volume fraction would have been low. In the absence of a good thin area in the banded region this latter suggestion cannot be verified. However, some evidence was found for this mechanism in the examination of the worn pins. Therefore, both the above mechanisms are considered to have contributed to the low surface monoclinic levels.

The wear of the Mg-PSZ discs appears to consist of two main mechanism, namely the formation of grooves/ pits and the removal of material by a tribochemical mechanism involving dissolution of the zirconia by the iron oxide. The former mechanism is considered to be a result of cooperative transformation in bands which generates to dilation of the surface and microcrack coalescence, giving preferential wear. However, problems exist with both theories which preclude definitive statements being made. With the grooving, why was the monoclinic content of the surface so low? Explanations based on microcracking require that some zirconia was found in the wear debris. Temperature rises which reduce the driving force for transformation would also reduce the driving force for cooperative transformation. However, the mechanism was clearly associated with the crystallography of the zirconia, and no other theory can satisfactorily explain the presence of deep parallel grooves and triangular and rectangular pits. For the case of the tribochemical mechanism the difficulty of positively identifying zirconia in the iron oxide wear debris was disappointing. However, in the absence of any evidence of mechanical based mechanisms such as microfracture or plastic deformation, tribochemical wear remains a logical explanation.

6.1.2 TZP Discs

The wear of the discs appeared to occur entirely by an intergranular grain removal mechanism, although some smooth areas were observed at the wear track edge. At speeds of 0.24 m/s and 0.48 m/s the surface appearance varied locally, but was invariably worse where a transferred layer of metal oxide had become detached. A general view of the worn surface from the slowest test (0.08 m/s) is given in fig 6.22. Note that, as with Mg-PSZ, a clean ceramic surface can be seen where the transferred material has just become detached. In addition, a series of parallel bands can be seen which run perpendicular to the sliding direction. A detail across several of these bands, after removal of the transferred material by HCl, is given in fig 6.23, which clearly shows the intergranular nature of the wear mechanism.

The parallel bands are considered to have resulted from either a stick-slip mechanism (evidence of which was mentioned in chapter 5) or from some form of thermal crazing. The former is more probable because the repeat distance for thermal crazing is usually much larger and the cracks more pronounced and deeper [315].

The reasons for the fracture dominated wear are not clear. No evidence of the fractured particles could be found in the wear debris, possibly because of sampling problems (the zirconia constituted 1% by weight). Such an intergranular fracture mechanism has been reported by Birkby et al. [146] for a zirconia die used for the cold drawing of steel and a cam follower sliding against a hardened steel; by Fischer et al. [147] for self mated sliding in hexadecane with 0.5% stearic acid and by Breval et al. [124,140] for unlubricated sliding. Birkby et al. [146] suggest that the intergranular fracture is a result of widespread transformation at the surface. They found an appreciable increase in the surface monoclinic levels for a 2Y cam follower (20vol% compared to none in the starting surface), whilst a 3Y die worn under the same conditions wore by a plastic dominated mechanism with no evidence of grain pull-out. The authors suggest that the absence of transgranular fracture indicates that abrasive wear mechanisms, which promote fracture, were not occurring. However, fracture in 2Y materials and other similar very fine grain sized ceramics is usually intergranular so that this conclusion appears unfounded.

Birkby et al. [146] further suggest that transformation leads to grain boundary microcracking and subsequent grain removal. In other words, a distinction was made between transformation causing fracture

30µ
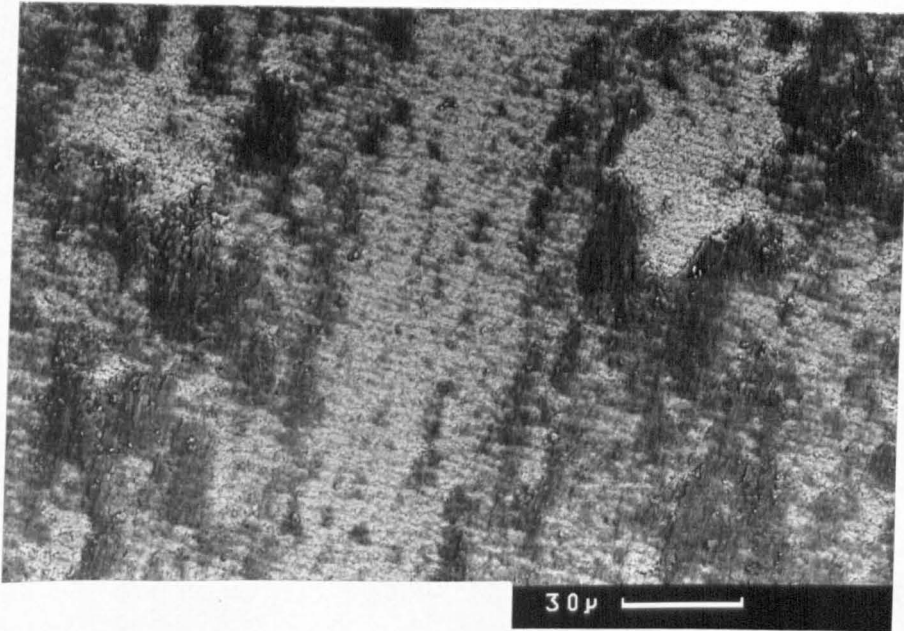
S.D.

Fig. 6.22. BEI image of the TZP disc. Note the region where the transfer layer has become detached in the upper right and the parallel bands which run perpendicular to the sliding direction. These are a result of stick-slip or thermal crazing. (7.8 N/pin, 0.08 m/s).

3µ
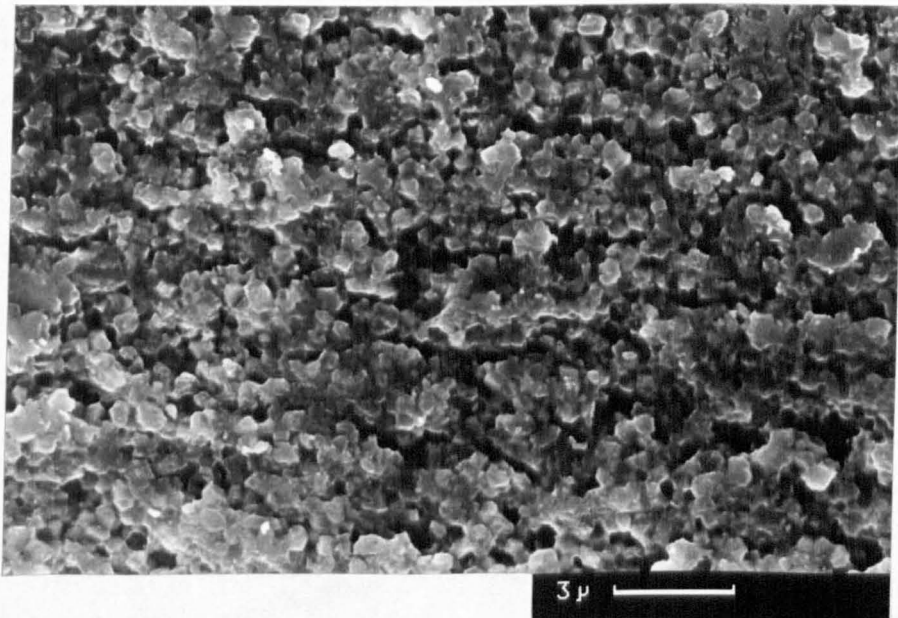
S.D.

Fig. 6.23. Detail of fig. 6.22 showing the intergranular fracture wear mechanism which has promoted a high disc wear rate.

and transformation occurring as a result of fracture processes (i.e. as would be expected in a strength test for example). Certainly, the evidence that the less tough 3Y material worn under the same conditions did not show any intergranular fracture supports this theory. However, it is suprising that transformation should provide surface break-up under sliding conditions but not under machining or grinding of the surface, where monoclinic levels can be much higher. Moreover, a sliding speed of 2.4 m/s under the high stresses associated with cam followers would be expected to generate substantial temperature rises in the surface region reducing the driving force for transformation. Indeed, Birkby et al. [146] show evidence of plastic deformation in the vicinity of the intergranular wear region.

The work of Fischer et al. [147] provides further evidence as to whether the mechanism originates from transformation or fracture. As noted in section 2.2.1.3, they found the intergranular wear mechanism both in a transformable 3Y and a non transformable 5Y. The mechanism was found to occur under lubricated conditions using hexadecane with 0.5% stearic acid. This would have produced very low adhesive forces between the surfaces and comparatively low shear forces. However, minimum wear, with the total absence of intergranular fracture, was found for a test in dry nitrogen. This test would have been expected to produce the highest interfacial stresses and therefore the highest surface transformation. Unfortunately, the authors did not measure surface monoclinic levels. It could be suggested that under dry nitrogen the temperature rises would have been high enough to reduce the driving force for transformation, thereby avoiding any intergranular fracture. However, the wear factors reported by Fischer et al. [147] were very low (10^{-7}–10^{-8} mm^3/Nm) which would not be expected for any substantial temperature rise. The authors concluded that some form of environmentally assisted fracture was occurring in the lubricated samples which was absent in the N_2 tests.

The present results do not provide any firm conclusion as to the mechanism. Unfortunately, it was not feasible to cut up (thereby destroying) a disc, so that X-ray and TEM analysis could be carried out. The results of Fischer et al. [147] suggest that the grain pull-out is possibly associated with some tribochemical mechanism causing intergranular fracture, but not associated with transformation. Birkby et al. [146] certainly provide evidence that transformation can initiate such fracture. This process would be aided

by adhesive forces between the surfaces. In the present study, the adhesive forces between the two surfaces were considered to be quite strong because of the transfer of metal from the pins. Fracture appears to have occurred predominantly where the transferred material was detached. Transformation was shown to have led to material removal in the Mg-PSZ discs and, therefore, it would appear logical that the same could take place on the TZP surface.

If the fracture mechanism was transformation driven, it is not clear why transformation should be so widespread on a comparatively untransformable material. Severe grinding of this material only produced 15.6 vol% monoclinic. One possible explanation is that, during sliding, transformation is cumulative. Each asperity passage led to further transformation and a gradual build-up of damage. Thus, the lower the toughness the longer it would take to create the damage. This would explain why there was comparatively little grain pull-out at the edges of the wear track.

An alternative explanation for the intergranular fracture is that some form of chemical interaction occurred which destabilised the tetragonal grains. A mechanism equivalent to the low temperature degradation of TZPs by water environments at around 200°C could be envisaged (discussed in section 2.1.4). The frictional heating could provide temparature rises to these levels, although higher interfacial temperatures would generally be expected. Interaction of the steel with the zirconia has been shown to be significant (discussed further in section 6.2.4) which could provide a destabilising effect. Such interaction would be expected to occur preferentially along grain boundary regions.

A comparatively soft metal sliding under mild conditions produced extensive damage on a hard, moderately tough ceramic. The greater damage in the TZP compared to the Mg-PSZ is shown by the proliferometry traces in fig 6.2. Thus, under these conditions, it is considered that the Mg-PSZ is a superior tribological material to the TZP discs.

6.2 THE WEAR OF THE ZIRCONIA PINS AGAINST BEARING STEEL DISC

The following describes the wear of 2Y, 3Y-TZP and Mg-PSZ pins against a hardened bearing steel disc (the details of which are given in chapter 3). The wear of the zirconia will be discussed in detail,

whereas that of the bearing steel disc will only be considered briefly.

6.2.1 Wear Data

The details of the wear tests are given in table 6.1. The average wear factor for the three pins in each test is plotted as a function of load in fig 6.24. The wear factor was always found to decrease from the initial value for about the first 20Km after which it reached a steady state value. An example is given in fig 6.25. This is a similar result to that found by Harrison et al. [150] for the self mated sliding of zirconia. Harrison et al. [150] demonstrated that the apparent contact stress followed exactly the same trend as the wear rate, and decreased as the apparent contact area increased. However, the result contradicts the normally held view that it is the load which determines the wear rate, not the apparent contact stress. (This is based on the consideration that the real contact area increases on initial contact to a value at which the load is supported. Since the true contact area is far lower than the apparent contact area, the contact stress based on the apparent contact area is irrelevant.) However, the present results, and those of Harrison et al. [150], indicate that at very small values of apparent contact area, and with hard materials, the rate at which the true contact area can increase to support the load is slow, such that the wear rate does correlate with the apparent contact stress. In other words, during running-in the apparent contact stress is important, but is irrelevant at steady state.

All tests were characterised by an initially quiet period combined with a comparatively low friction coefficient (see table 6.1). Examination of the sliding couple at this stage showed a small region of wear on the pin but virtually no evidence of wear on the disc. As sliding continued, a continious rise in the friction coefficient occurred until a steady state range of values was obtained. The distance to the steady state friction coefficient was a function of load. At low loads the distance was up to 12 Km whereas at the highest load (59 N/pin) distances of 5 Km were more typical.

The increase in friction coefficient was associated with a steady increase in noise and vibration, which coincided with clear evidence of damage to the disc and transfer of metal to the ceramic. In the low load tests the vibration was mild and the noise could be described as a

TABLE 6.1

TEST CONDITIONS AND WEAR DATA

	2Y				3Y				Mg-PSZ		
LOAD (N)	6.6	19.6	37.6	59	6.6	19.6	37.6	59	6.6	19.6	37.6
Initial μ	0.1	0.08	0.09	0.05	0.09	0.1	0.08	0.06	0.08	0.05	0.09
Steady state μ	0.25-0.4	0.2-0.34	0.2-0.28	0.18-0.23	0.19-0.32	0.2-0.28	0.18-0.21	0.16-0.24	0.17-0.26	0.18-0.25	0.18-0.28
Peak μ	0.46	0.34	0.3	0.26	0.33	0.28	0.23	0.26	0.28	0.28	0.38
Dist. to steady state (m)	3400	3500	2800	1600	3500	3900	2500	5600	2800	4300	?
Total dist (km)	300	63	126	47	181	124	27	41	226	108	8
Wear factors											
pin 1	0.85	1.08	2.27	1.71	0.57	1.34	3.58	1.22	0.80	1.83	3.17
pin 2	0.6	1.8	1.22	0.71	0.54	1.1	2.23	1.26	0.60	1.37	1.72
pin 3	0.81	1.25	1.9	1.01	0.21	1.17	2.45	1.03	0.75	1.55	3.04
Average All x10^{-6} mm^3/Nm	0.75	1.38	1.8	1.14	0.43	1.20	2.75	1.17	0.72	1.58	2.64

The above values are for a sliding speed of 0.24 m/s,
against a 1% Cr bearing steel disc, quenched and tempered to maximum
hardness and lapped to an R_a of 0.008μm. The pins were lapped under
the same conditions, but the R_a could not be verified.
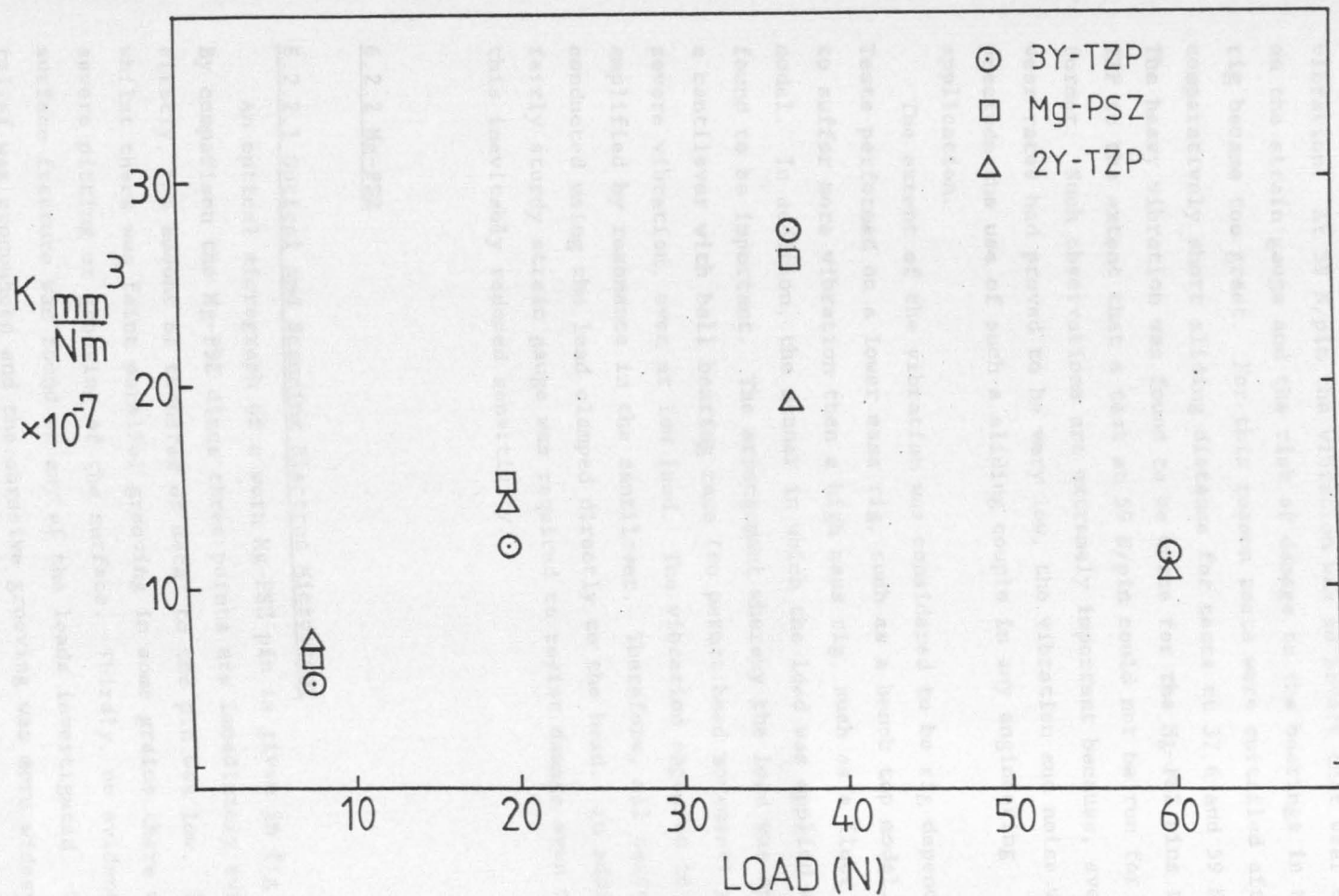
Fig. 6.24. Wear factor as a function of load for 2Y, 3Y and Mg-PSZ
pins worn against a hardened bearing steel disc.
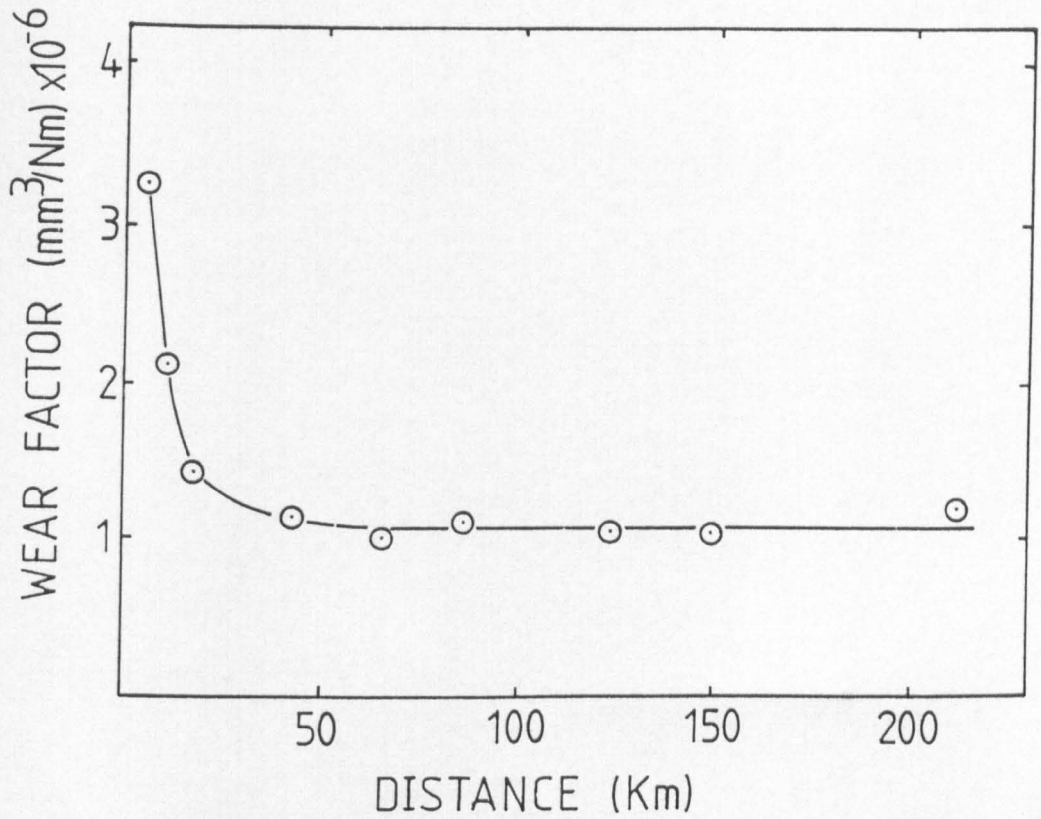
Fig. 6.25. Wear factor as a function of distance for the test at 59 N/pin.

200μm

S.D.←
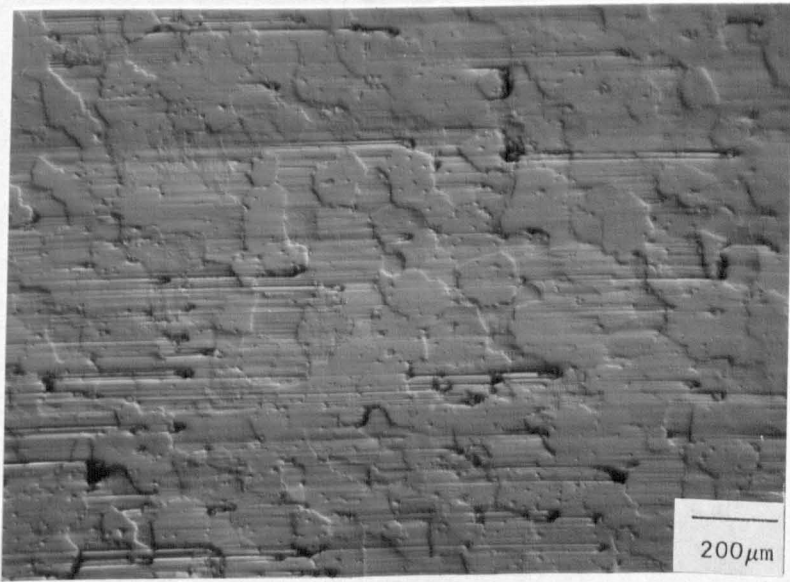
Fig. 6.26. Optical micrograph (Nomarski) of the worn Mg-PSZ pin. Note the grain relief, abrasive grooving and infrequent faint parallel grooves (6.6 N/pin)
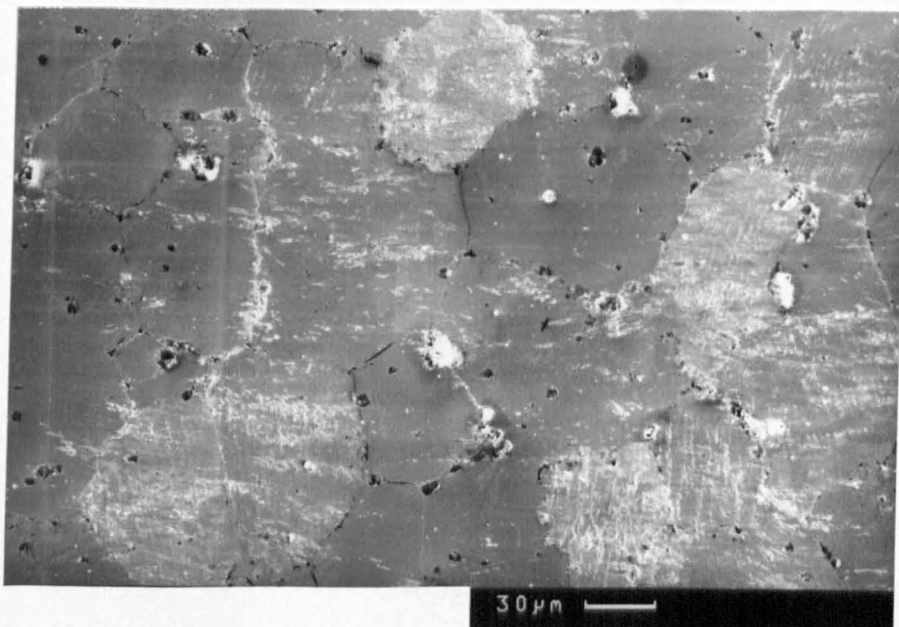
200μm
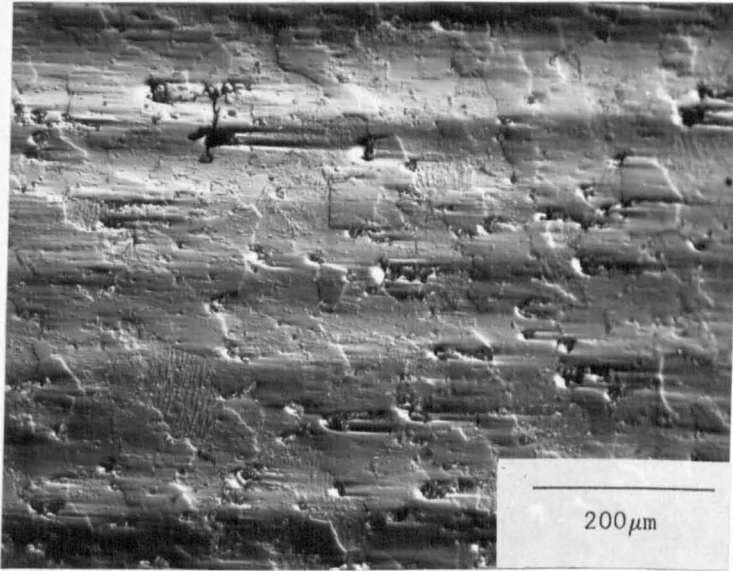
Fig. 6.27. Optical micrograph (Nomarski) showing large wavelength grooving (37.6 N/pin).

50μm
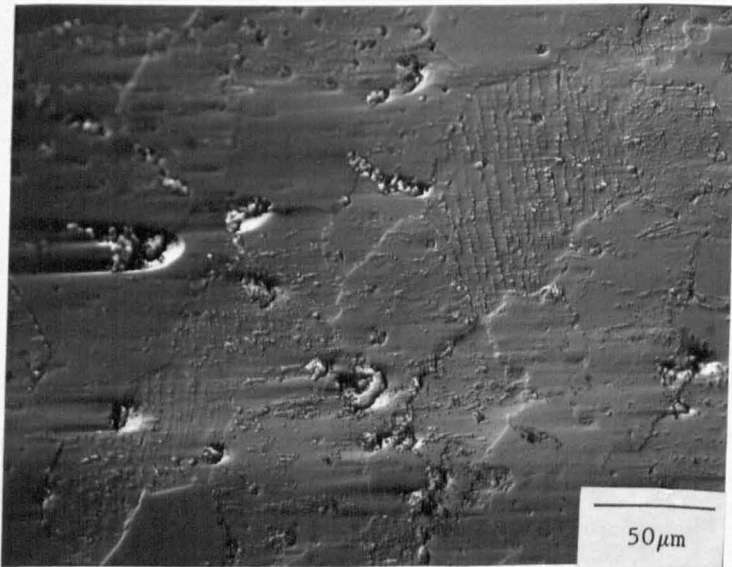
Fig. 6.28. Detail from fig 6.27. Note how the parallel grooves have attracted transferred metal and therefore appear to stand proud of the surface.

S.D.←

Fig. 6.29. SEM micrograph showing transferred metal keyed into the parallel grooves. The other grains were extremely smooth. (19.6 N/pin).
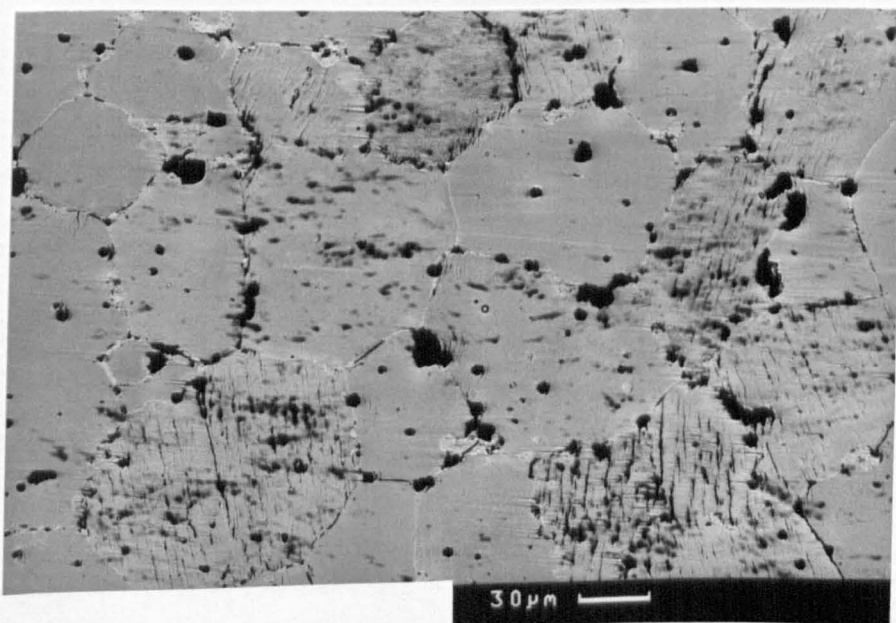
S.D.←

Fig. 6.30. BEI of above. The parallel bands are clearly visible and appear more crack like. Occasional grain boundary cracking can also be seen.
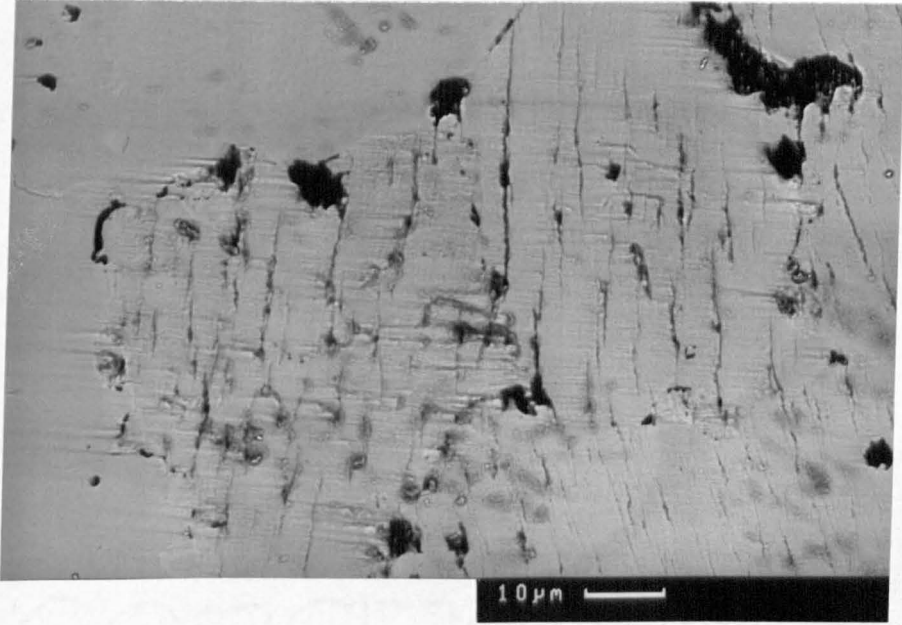
S.D.←

Fig. 6.31. BEI detail from fig. 6.30. Note the abrasive grooves in the wake of the parallel grooves and the apparent crack branching.

However, the grooving could only be seen using Nomarski contrast and was virtually invisible using normal illumination. Only about 20% of the grains exhibited this grooving at a load of 37.6 N/pin, whilst fewer still were grooved at 6.6 N/pin. No evidence of triangular or rectangular pits was found. In fig 6.28 the grooves appear to be standing proud of the surface. This result was confirmed by SEM examination, figs 6.29-31, and was a result of small amounts of metal transfer filling in and standing proud of the grooves. Clearly, as with the disc, the grooving acted as a good mechanical key for the transfer of metal.

Fig 6.31 also shows that the grooves often appeared more like cracks than regions of preferential wear, being considerably sharper than any of those found on the disc. These aspects will be discussed further in the light of the TEM results.

The majority of the wear had occurred by a mechanism which left the surface smooth, with the exception of abrasive grooves. The abrasive grooves frequently appeared to originate from a pit, figs 6.26,28. This was presumably because of the trapping of wear debris and transferred metal in the pits which acted as an abrasive as it broke away.

Grain boundary cracking and preferential wear of the grain boundary monoclinic was far less pronounced than with the Mg-PSZ discs.

6.2.2.2 Transmission Electron Microscopy and X-ray Analysis

The volume fractions of monoclinic found in the worn surfaces are given in table 6.2. The X-ray traces for the tests at 19.6 and 37.6 N/pin are given in fig 6.32 which should be compared with those for the polished surface, ground surface and the disc given in fig 6.11. Some difficulty was found in measuring the worn surface monoclinic levels because of the small area presented to the X-ray beam and the problem of peak overlapping, so that the error in the results was appreciable (about 20% for the Mg-PSZ materials). However, a significant rise in the monoclinic levels was found in most tests. At 37.6 and 6.6 N/pin the worn surface monoclinic was found to be higher than measured on the discs. However, this only represents a rise in the monoclinic of between 1 and 8.6% above the grain boundary monoclinic levels, whereas grinding produced a rise of 26.5%. In other words, the amount of transformation was comparatively low compared to that obtained under abrasive wear conditions. No clear trend in the monoclinic levels with
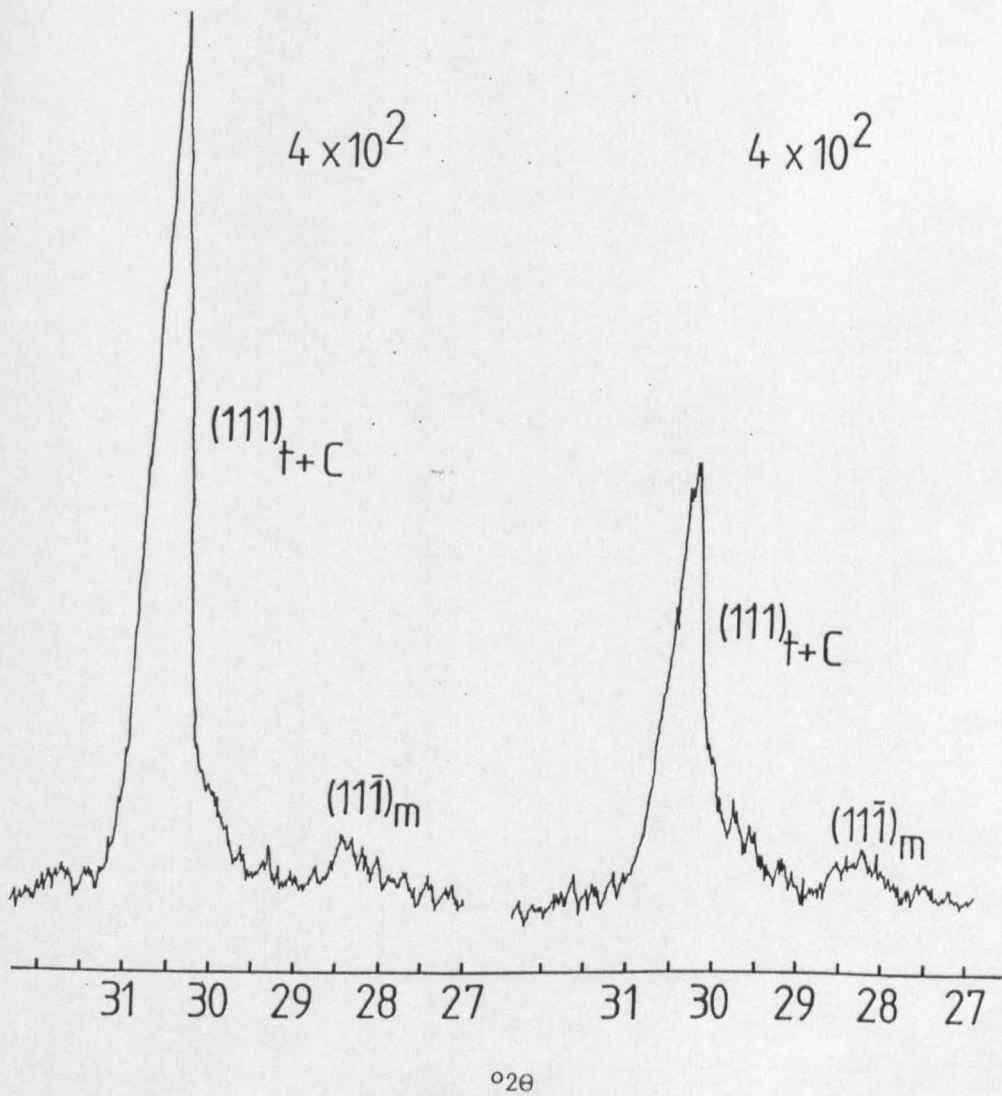
Fig. 6.32. X-ray diffractometer traces from the Mg-PSZ pins worn at 19.6 (left) and 37.3 N/pin (right). The difference in cubic intensity is because of the difference in area presented to the beam.

load was apparent, although any small trend would have been obscured by the experimental errors.

As with the disc, no foils were obtained perpendicular to the worn surface because of premature break-up of any thin area. In this respect, the parallel grooves acted as cracks so that the surface broke away before electron transparency was achieved. However, information was obtained from a series of back thinned foils.

TABLE 6.2

X-ray Analysis of the Zirconia Surfaces Giving Volume % Monoclinic

Material	Volume % Monoclinic		
	2Y TZP:	3Y TZP:	Mg-PSZ:
Polished	1.3	0	10.0
Ground	22.1	15.7	36.5
6.6N	7.5	4.3	18.6
19.6N	8.6	3.1	11.2
37.6N	7.8	6.8	17.7
59N	6.3	0.9	—
Disc			7.9
As sintered			6.9

The structure of the precipitates at the surface was similar to those in the disc, although they were generally easier to image. The majority of the precipitates retained their oblate spheroid form right up to the worn surface. The diffraction patterns indicated that most of the precipitates were monoclinic, although, as with the disc, twin boundaries were difficult to image. One example of twin boundaries can be seen in the large central precipitate in fig 6.34. The depth to which the monoclinic was the dominant precipitate phase appeared to be similar to that in the disc, namely about 300nm. However, further work would be required to give greater confidence in quoting this figure.

The cubic matrix was difficult to image because of the high

residual strain levels. High strain could also be seen within the larger precipitates as illustrated in fig 6.35. As with the disc, the diffraction pattern was found to vary considerably across a small distance within a single grain. This resulted in substantial arcing in the spots for a large selected area diffraction pattern, as shown in fig 6.33. Secondary electron imaging in the STEM mode failed to show any severe foil buckling in this area which could explain the arcing. Thus, as with the disc, this suggests that some form of lattice rotation by the passage of dislocations may have occurred. However, no dislocations could be imaged, although the residual strain would have obscured their presence. Moreover, no evidence of any subgrain boundaries could be found which could have accommodated such a lattice rotation. Therefore, residual strain remains the most likely explanation for the arcing.

A general view of a grain containing the parallel grooves is given in fig 6.33. It is immediately apparent that the grooves could be better described as cracks since they appear sharp and are extensively branched. The micrograph confirms that the cracks run along the direction of the precipitates, that is along one of the {100} orientations. The only obvious reason for certain grains to show parallel cracks whilst others do not was the orientation relationship with the surface. A detail is given in fig 6.34 of a microcrack which was running in the same direction as the larger cracks and was considered to be an embryo of one of the larger cracks. Fig 6.35 shows a crack running through a large primary precipitate (discussed in chapter 3) and apparently unperturbed by its presence.

The interface between the tetragonal precipitates and cubic matrix lies mainly on the {100} planes (see appendix 1). In addition, the twin variants of the monoclinic are highly populated along $(001)_m$, so that maximum strain is generated along $(100)_C$ [12,330]. Consequently, microcracks occur preferentially along this direction, explaining the initiation of grooves in grains with a $(100)_C$ orientation relationship with the surface prior to other orientations.

The above suggests that the mode of formation of the cracks was by microcrack coalescence. Several examples were found, such as that in fig 6.34, where fine microcracks had joined together to produce an embryo for a much larger crack. The mechanism for their formation is proposed as follows: transformation was initiated with the passage of the asperity. At the tail end of the asperity tensile forces were
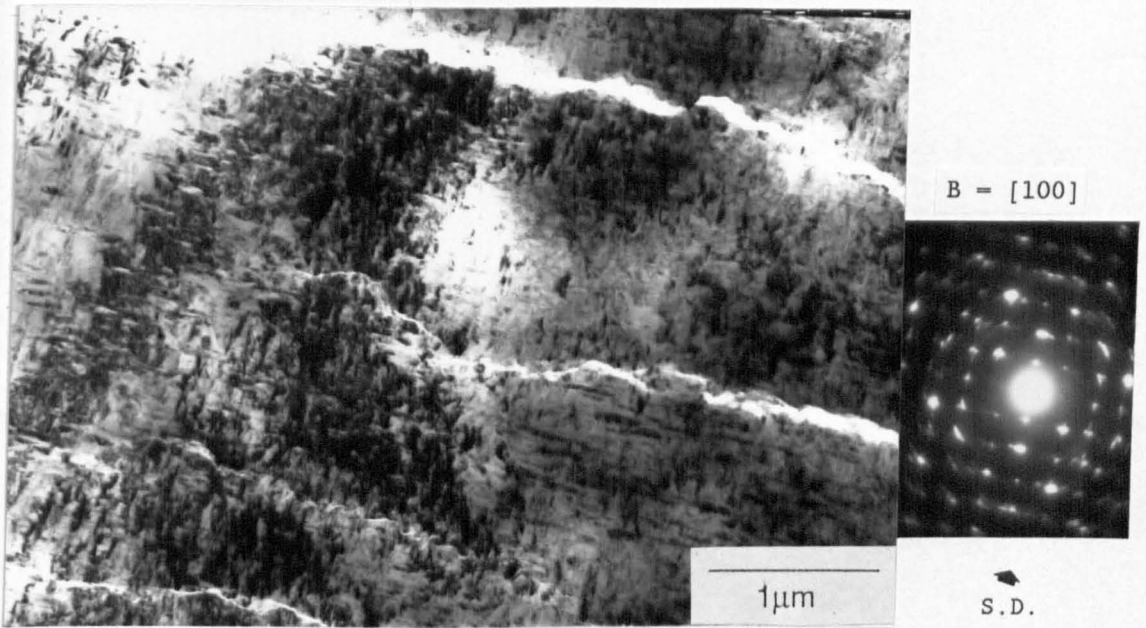
B = [100]

1μm

S.D.

Fig. 6.33. TEM micrograph of a back thinned sample taken from a grain containing parallel cracks/ bands. Note the sharpness of the cracks and the extensive crack deflection and branching. The cracks can be seen to be lying along one [100] direction.
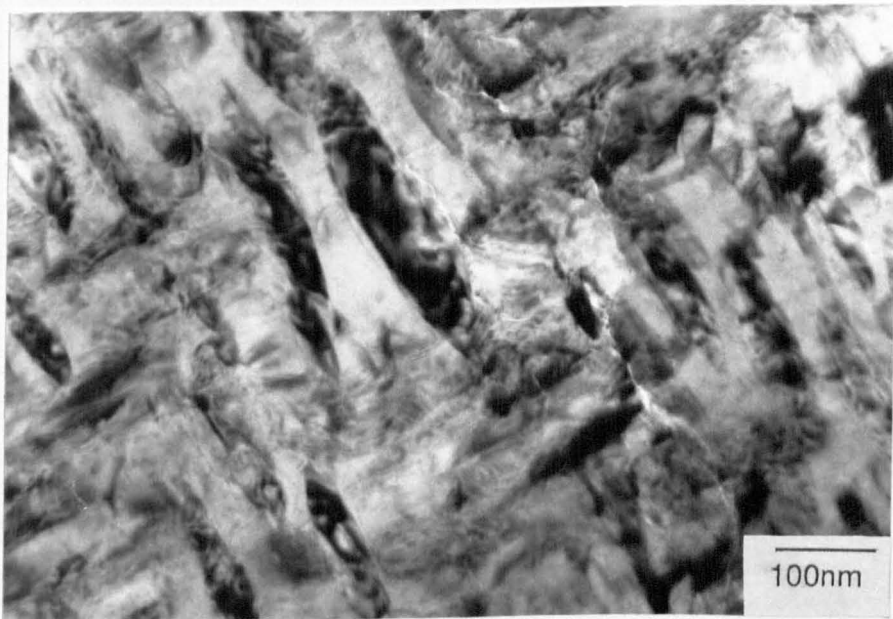

100nm

Fig. 6.34. TEM micrograph taken from the region shown above. Note the fine microcracks which have started to join together. This is believed to be an example of an embryo of a larger crack/groove. Also note the faint twin boundaries in the large central precipitate.

generated by the action of the adhesion between the ceramic and metal surface. This opened up the microcracks formed during the transformation. Microcracks then coalesced to form macrocracks. Grooves were formed by the break-away of material from the crack edges and by the joining of macrocracks during subsequent asperity contact.

Two possible reasons can be suggested as to why more damage was sustained on the disc by this mechanism than on the pin. Firstly, the adhesive forces were higher on the disc, as demonstrated by the greater transfer of metal to ceramic. Secondly, the temperature generation was considered to be higher in the pin surfaces than in the disc, since the disc was only in intermittent contact, whereas the pins were in continuous contact. A lower temperature would have increased the driving force for transformation, thereby leading to more damage.

The occurrence of some transformation places an upper limit on the temperature rise in the zirconia surface of about 500°C. However, as noted in the section on the TZP disc wear (6.1.2), even a small amount of transformation can be detrimental because of the time dependent nature of wear. In other words, even if only a few percent of the precipitates transform with the passage of each asperity this rapidly accumulates to widespread surface transformation. The subject of surface temperatures will be considered further when the results for the TZP pin wear tests have been presented.

The abrasive grooves which were evident in the optical micrographs (eg fig 6.26) could clearly be seen in the thin foil. A low magnification dark field image is given in fig 6.36, which shows a groove running top to bottom of the micrograph, on the left hand side. Notice also how the cubic reflection on the right hand side of the micrograph appear as blocks. The cracks run along the direction of these blocks, namely at about 30° to perpendicular to the sliding direction in this instance. Figs 6.37,38 give details of the transition from the conventional structure to that found in the abrasive groove. The structure within the abrasive groove was difficult to discern, but the original precipitate form had been completely destroyed. Further bright field and dark field images of the groove are provided in figs 6.38-42.

Selected area diffraction patterns suggested that the structure consisted of a mixture of cubic and tetragonal. No monoclinic reflections could be found, although they would have been difficult to differentiate from the cubic and tetragonal in such a pattern.
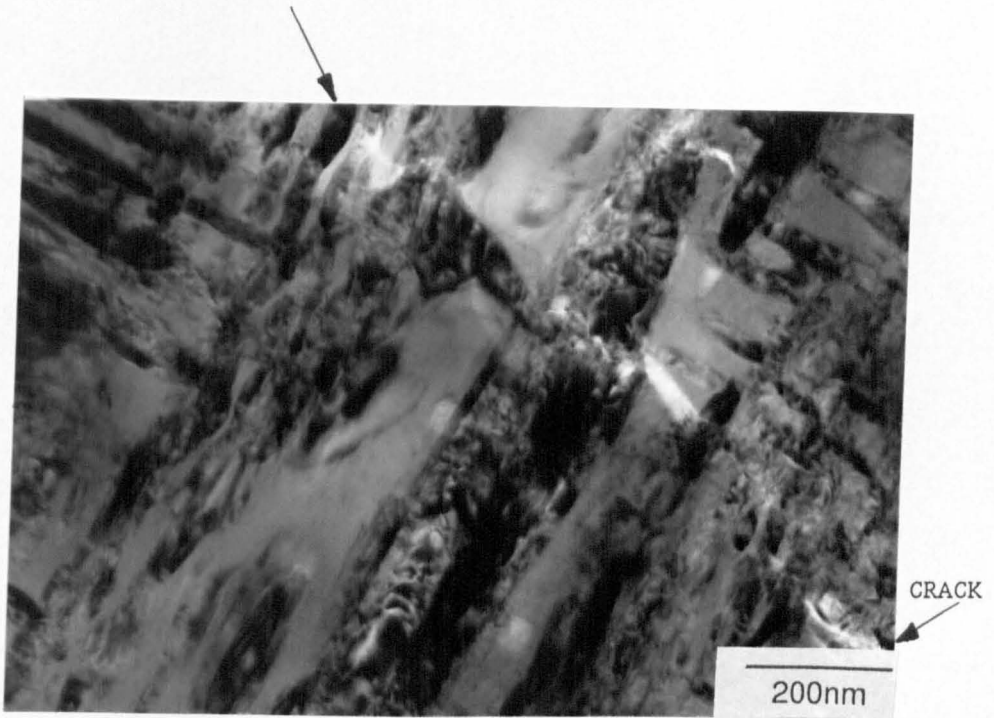
Fig. 6.35.   TEM micrograph from the region in fig. 6.33, showing a fine crack passing through a large primary precipitate. The precipitate, which contains high residual stresses, has not deviated the crack direction.
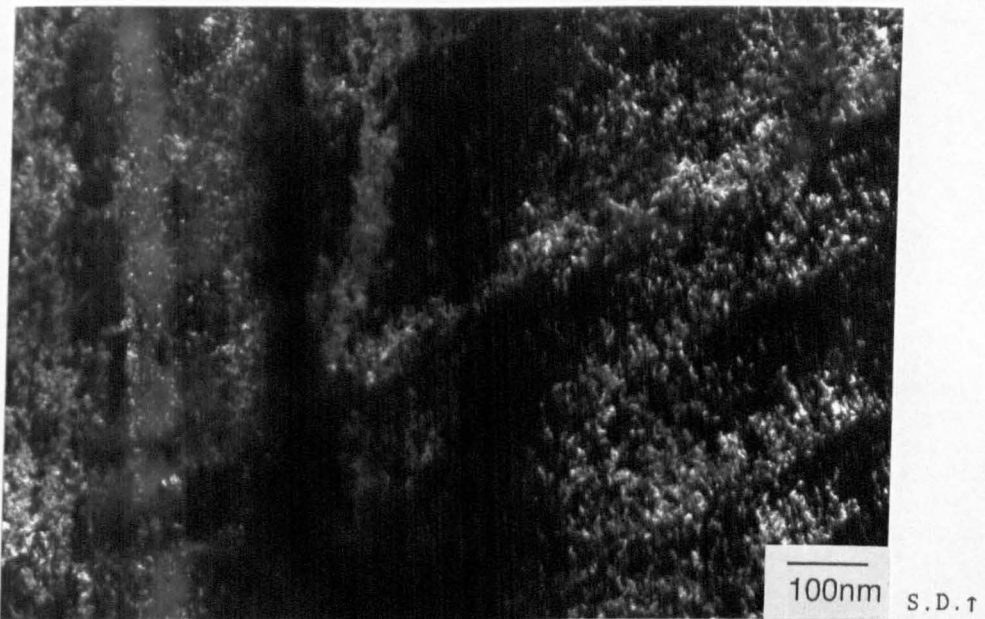

Fig. 6.36.   Dark field micrograph using a cubic reflection from the same grain as in fig 6.33. The right hand side shows the parent microstructure, although the reflections derived from blocks. The left hand side shows where an abrasive groove has been formed.

PARENT MICROSTRUCTURE

ABRASIVE
GROOVE

100nm

S.D.
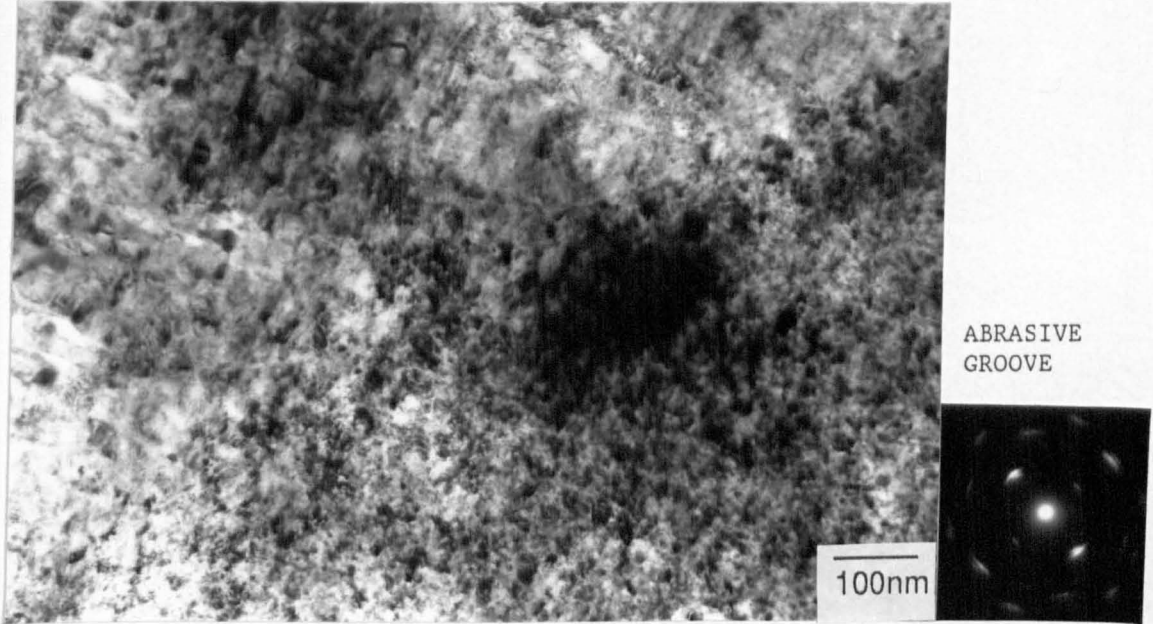
Fig. 6.37. TEM micrograph showing a detail of the above. The upper left region is the parent structure whilst the lower right is the abrasive groove. Note the sharp boundary between the two.

PARENT MICROSTRUCTURE
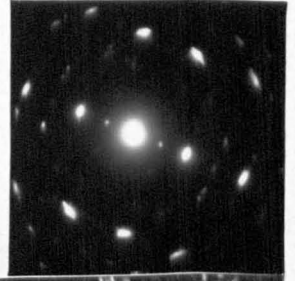
ABRASIVE GROOVE

S.D. →

Fig. 6.38. Bright field (left) and dark field (right) of a more gradual transition from the parent structure to that in an abrasive groove taken from a nearby grain.
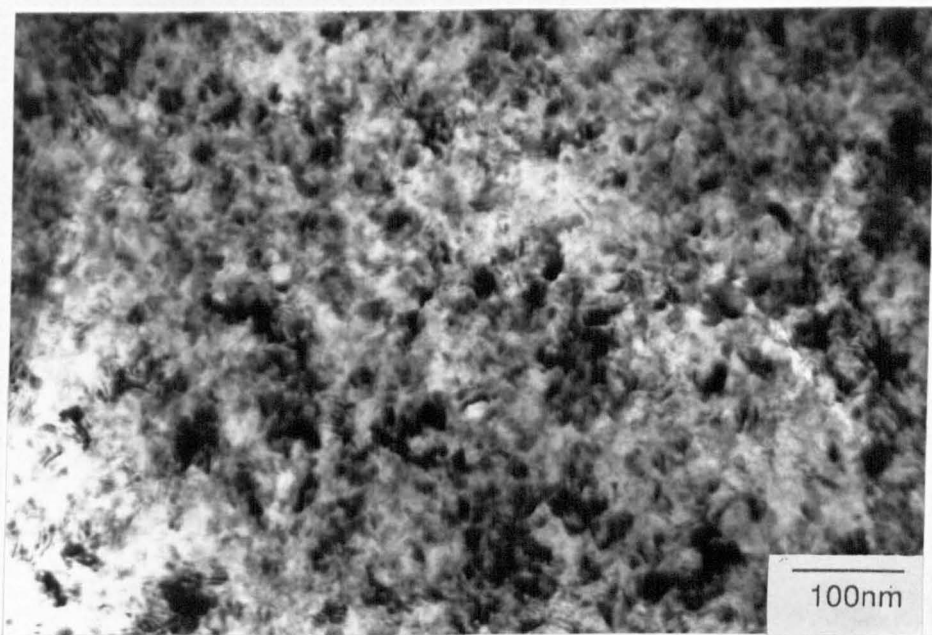
Fig. 6.39. Detail of the abrasive groove in fig 6.37. The structure consists of a mixture of tetragonal and cubic and is microcrystalline. However, phase boundaries or crystallite bounderies were very difficult to image.
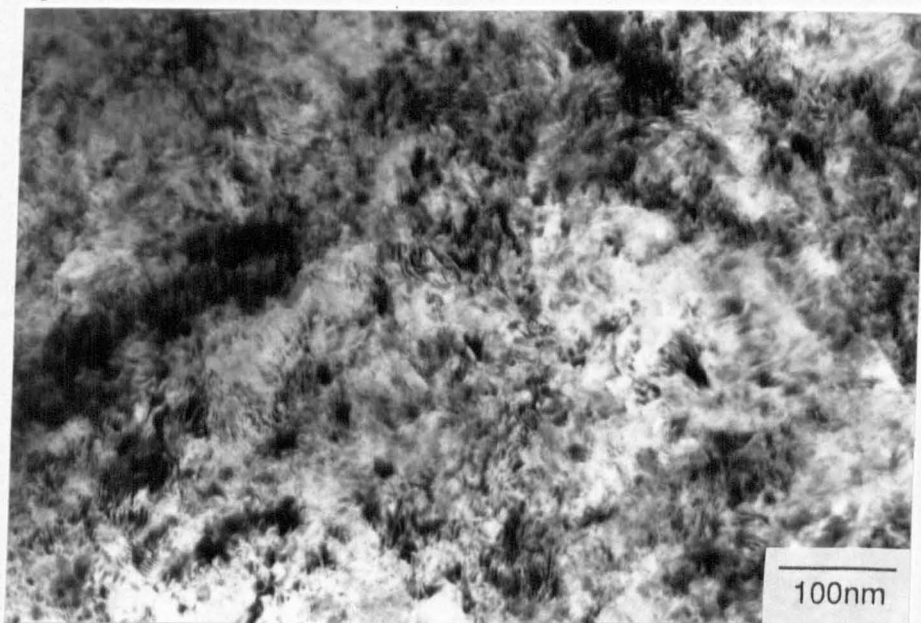
Fig 6.40. Detail of region adjacent to fig 6.39. The region is largely from a single grain, although some crystallites are present as shown by the diffraction pattern. The Moire patterns indicate that the precipitates are contained within the foil and are closely orientated with the matrix.

Fig. 6.41. Detail from the groove in fig 6.38 of a region which
contained no grain boundaries or monoclinic. Some tetragonal is still
present. The structure has undergone considerable rotation compared to
the parent structure.
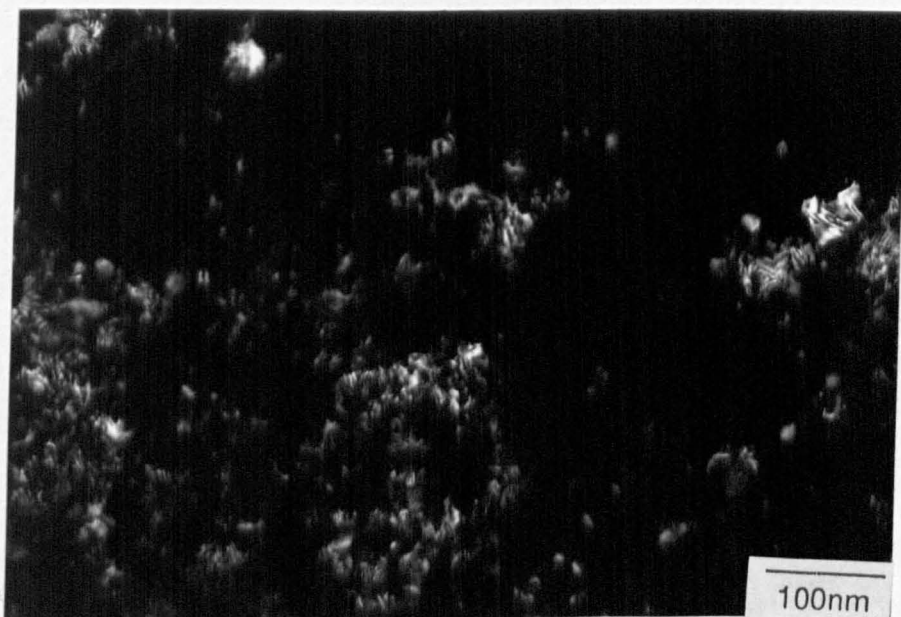
Fig. 6.42. Dark field micrograph from the microcrystalline region.
Individual crystallites are not clear.

However, the monoclinic (100) reflections were never present. Strong texturing was found in all the abrasive grooves although no direction was ever aligned to the direction of the groove. The closest was the [200] direction which was aligned at about 25° to the sliding direction. The texturing gave numerous Moiré fringes in the TEM images, such as those shown in fig. 6.40.

No distinct phase boundaries could be imaged between the tetragonal and cubic, the tetragonal reflections generally being too weak to provide a useable dark field image. However, the image in fig 6.38 does appear to consist of a mixture of two phases with indistinct phase boundaries. No clear indication of dislocation lines could be found, although some of the features in the dark field image in fig 6.41 could be dislocations (they remained stationary during tilting experiments).

Such a microstructure has never been reported in the literature. However, the microstructure does show similar features to that reported for abrasive wear debris from ceramic materials [176]. Indeed, the wear debris produced by grinding this material on standard SiC paper was found to be very similar by the present author [316]. In this instance, the debris had the appearance of a chip with jagged edges such as from the machining of metals.

The mechanism for the formation of the abrasive groove microstructure appears to have been gross plastic flow. Dissolution of the precipitates could be produced by large thermal transients but this would not have produced the rotation of the microstructure. Moreover, the precipitates would have become smaller, but retained a shape dictated by surface energies. The passage of a large number of dislocations would provide break-up of the coherent tetragonal precipitates, and some re-distribution of the solute. The movement of the solute in itself would lead to the loss of the precipitate form and to indistinct phase boundaries. Wear debris would then be expected to form by plastic overload. However, it is remarkable that such deformation could occur without the formation of microcracks at the worn surface.

Evidence for extensive plastic flow by the passage of an asperity has been discussed in section 2.2.4. For example, Hockey [3,4] has provided evidence of dislocation pile-ups and twinning in alumina after grinding with abrasive sized as small as 0.25μm. However, in that instance, the dislocations were easily identifiable.

It is interesting to consider that, whilst such plastic flow has

produced considerable rotation of the microstructure, no evidence of
either recovery, such as sub-grain boundaries, microcrystallite
formation, or dislocation tangles was found. This suggests that
dislocation glide was restricted to a single slip system or that glide
distances were sufficiently small such that dislocation interaction did
not occur. The difficulty of imaging the microstructure did not help
in establishing the mechanism.

In relation to the above, a note is required on the number of slip
systems required to maintain conservation of volume. The Von Mises'
criterion states that five independent slip systems operate. However,
this criterion is based on homogeneous slip considerations. Fleischer
[317] has counted the number of active slip systems for 70/30 brass
deformed in compression and found that in about 40% of the grains fewer
than 5 slip systems were active. The author explained these
observations along the lines that deformation was non uniform,
particularly in the vicinity of the grain boundaries. In other words,
highly heterogeneous deformation does not require 5 slip systems.
Under conditions of the high hydrostatic stress and high strain rates
that prevail during abrasion it has been suggested that a very low
number of slip systems are required, possibly as low as 1 [300]. This
point was made in section 5.7.3. Therefore, it is considered possible
that dislocations passed through the structure without interaction,
although this has been shown not to be the case for alumina [3,4] and
silicon carbide [5-7].

The absence of any dislocation structures, or recovered forms
thereof, makes it difficult to explain how such a large lattice
rotation has been accommodated between the parent microstructure and
the abrasive groove. Certain areas, for example that shown in fig 6.40
are clearly single grains, which cannot provide a rotation. Other
areas are microcrystalline, for example fig 6.38, and appear to consist
of a mixture of both tetragonal and cubic. It is possible, therefore,
that these microcrystalline areas accommodated the rotation for regions
such as those shown in fig 6.40. Indeed, the lattice rotation was
greater in the microcrystalline regions than the single crystal
regions. However, the structure in fig 6.40, which is a single
crystal, tended to be dominant.

Whilst no dislocations or sub-grains could be imaged, it should not
be assumed that they were not present. In chapter 7 results will be
presented which show that the true structure cannot be easily

identified by back-thinning. A back-thinned 3Y pin which had been slid against a ZTA disc, exhibited a very similar microstructure to that shown in this case. The grain boundaries could not be imaged, and the structure generally appeared as that shown in fig 6.38. However, by examining the material in cross section, the grain boundaries were easily imaged. Extensive plastic flow had occurred but the dislocation density was low. Therefore, it is possible that the regions which appear to be single crystal are indeed microcrystalline. However, with such strong texturing it is suprising that Moiré fringes were not observed over the entire surface.

Those areas which were microcrystalline, such as fig 6.38, consisted of a mixture of tetragonal and cubic. Such a microstructure could have been formed either by recrystallisation after deformation or by break-up of the microstructure by the passage of dislocations. A number of problems exist with the recrystallisation scenario. If temperature rises led to recrystallisation, why was the tetragonal not taken into solid solution? In addition, why was the structure not better defined after it had recrystallised? If the tetragonal had been precipitated back out of solution on cooling, then why did it not take on some energetically defined shape, such as fine oblate spheroids?

The most probable answer to these questions is that large temperature transients were not required to form the structure, and the tetragonal particles were remnants of the original oblate spheroids. The observations could be explained by short thermal transients. However, the presence of monoclinic in the adjacent microstructure suggests that temperature rises were limited to <500°C. Hockey [3,4] found no evidence of temperature transients as a result of abrasion. High dislocation densities were produced by the passage of 0.25μm abrasive. Hockey concluded that the temperature was not responsible, rather that hydrostatic stress conditions had suppressed fracture, permitting dislocation flow. Authors who suggest that large temperature transients are responsible for the ability of a ceramic to deform plastically have not been able to provide direct evidence for this assertion. Nonetheless the true mechanism is very difficult to evaluate. However, it is considered here that the microstructures observed provide evidence that deformation has occurred at comparatively low temperatures (i.e. below 1000°C).

The presence of this microstructure provides important information as to why transformation appears to give higher wear rates in sliding

wear, but not in abrasive wear. One explanation has already been mentioned, namely that in sliding wear the adhesive forces coupled with the microcracking in the monoclinic aids surface break-up. In abrasive wear the adhesive forces are considerably weaker. An additional explanation can now be proposed. The action of the abrasive was to destroy the original surface structure, such that there was no question of any precipitates remaining which could transform to the monoclinic, with associated microcracking. The undeformed subsurface layers would transform, but the constraint of the bulk avoided the damaging effects of the microcracking. This layer would be under compressive stress conditions. In contrast, any transformation at the surface of the zirconia during sliding wear would lead to microcracking thereby reducing the surface integrity, despite the presence of the compressive stresses. Further work is required to establish the relative importance of these mechanisms.

The microstructure in those areas which did not show either abrasive grooves or parallel cracks was very similar to that reported for the disc, as illustrated by the cubic and monoclinic dark field in figs 6.44,45. However, one additional feature of the surface region was that certain areas consisted of precipitate skeletons with little or no cubic, for example fig 6.46. It was not clear whether this was a result of ion beam etching or represented the genuine surface roughness produced by wear. However, preferential thinning of the cubic phase was never found in these materials by the present author, except at the worn surface. Moreover, evidence has already been presented for such surface undulations in two stage replicas and of the preferential removal of the cubic phase in the vicinity of the transferred metal oxide on the disc (fig 6.15).

The above was taken as further evidence that the wear involved preferential removal of the cubic, and therefore occurred by a tribochemical mechanism. As with the disc, the TEM results failed to show any evidence of a microfracture or plastic wear mechanism in these regions. This point will discussed in the light of the wear debris analysis.
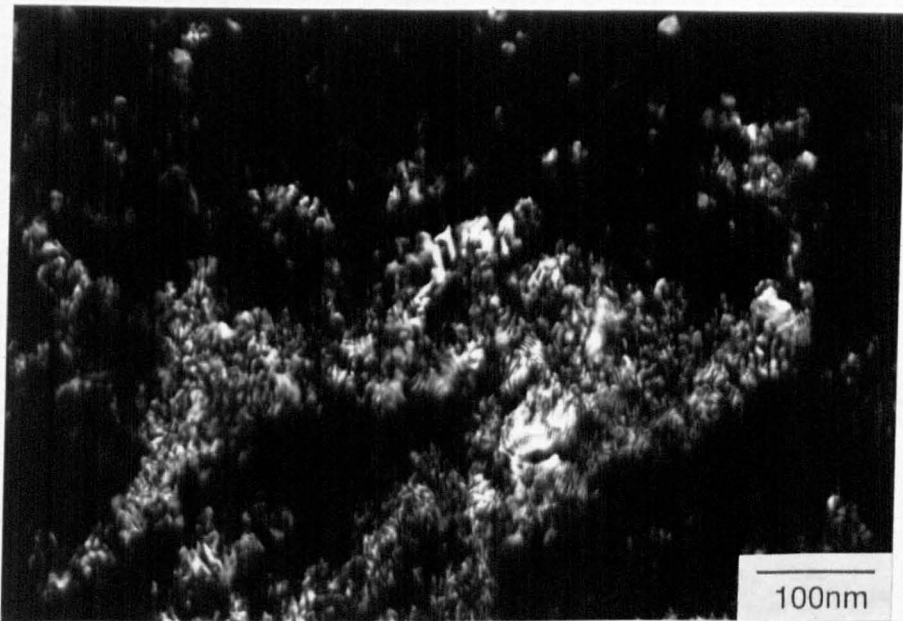
100nm

Fig. 6.43. Dark field micrograph from the general region of fig. 6.40. Numerous strain contours are present and possibly some evidence of dislocation lines.

100nm

Fig. 6.44. Dark field micrograph which has included diffraction spots from the cubic matrix and the precipitates from very close to the original surface. Note the residual strains, the absence of twin boundaries and that the precipitates have retained their original shape.
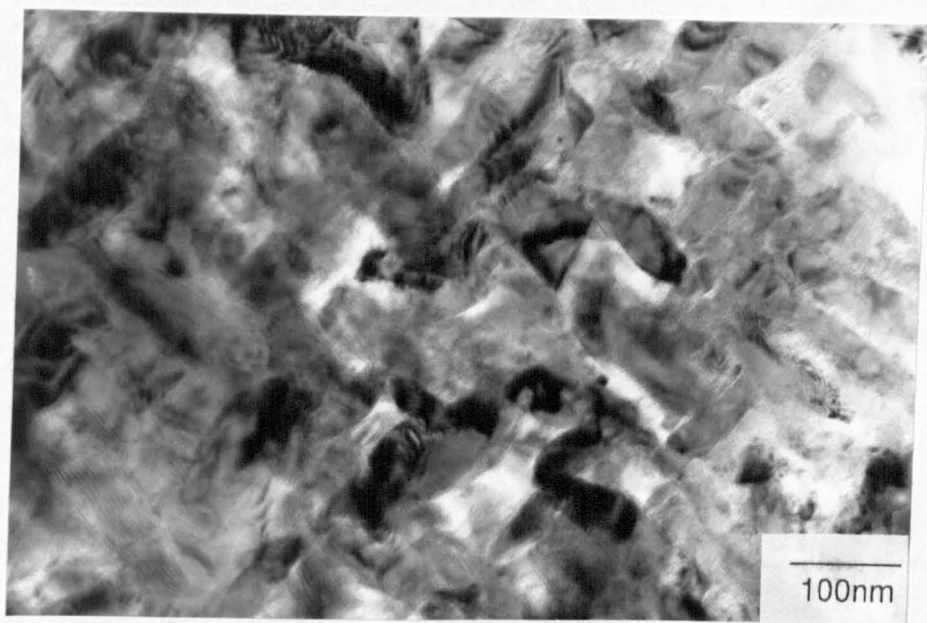
Fig. 6.45. Dark field image from the region in the fig 6.44, showing
possible evidence of twin boundaries.
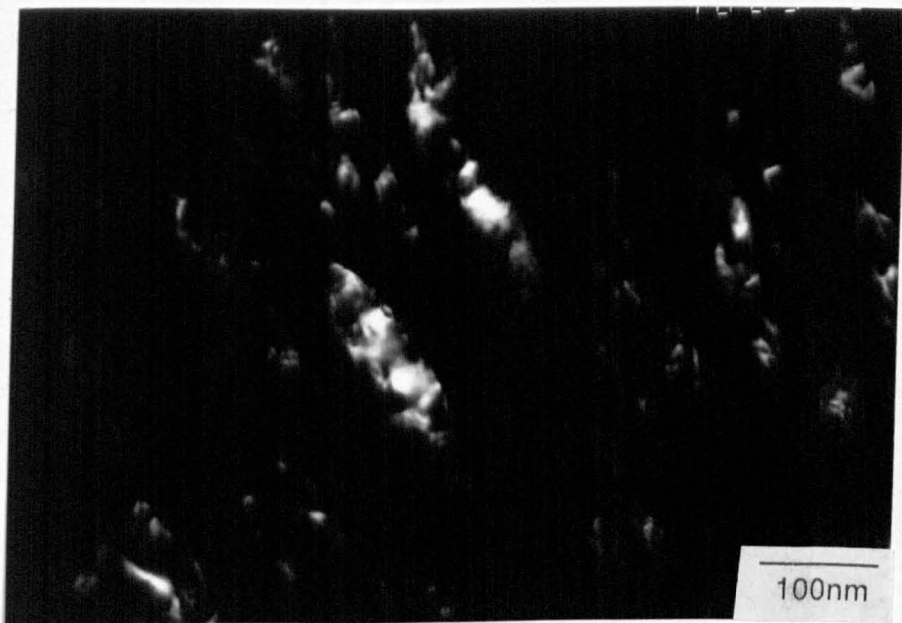
Fig. 6.46. TEM micrograph from a surface region of a grain which did
not contain any parallel grooves/ cracks. The cubic has been
preferrentially eroded either by the electron beam or the tribochemical
wear mechanism.

<u>6.2.3 2Y and 3Y TZP Pins</u>

<u>6.2.3.1 Optical and Scanning Electron Microscopy</u>

Throughout the tests no difference whatsoever could be found in the wear behaviour between the 2Y and 3Y materials. An overview of the typical amount of transfer of metal to the pins is given in fig 6.47. The amount of transfer varied between tests and between pins within a test. No tendency for more transfer at higher loads was found, in contrast to the tests described in chapter 5. The transfer was usually worst at the trailing edge, but this was not always the case.

The TZP pins tended to exhibit the same large wavelength grooving in the direction of sliding as the Mg-PSZ pins, fig 6.48. In addition, this micrograph shows several finer abrasive grooves which originated from a transferred particle. Details of this are given in figs 6.49-51. Transferred material appears to have been impressed into the surface. As fragments were broken away, fig 6.50, zirconia was gouged out in its wake. The transferred material was found to be entirely metal oxide and therefore was of sufficient hardness to abrade the zirconia. Nonetheless, all regions of transfer were not associated with abrasive grooves, for example fig 6.52.

The majority of the pin surface was smooth, although grain relief was always present, as can be seen in the preceding micrographs. No evidence of widespread surface fracture, such as that found on the disc, was observed. The mechanical integrity of the zirconia had been maintained with no evidence of microcracking. This was the same for both the 2Y and 3Y materials. However, on one test, at 6.6 N/pin, some evidence of a grain 'pop-out' mechanism was found, fig 6.53. This micrograph also shows the grain relief found throughout the surface. It would appear that grains were removed, probably in an intergranular manner, but did not generate any abrasive grooving in so doing.

The mechanism for this grain 'pop-out' is considered to be the same as that for the more widespread fracture found on the disc. It would appear improbable that straight forward fracture would occur on such an individual grain basis. What appears more likely is that after transformation of the tetragonal to monoclinic, the associated volume expansion could not be constrained at the surface in certain grains. The transformation would be associated with microcracking which would then weaken that particular grain. In addition, certain grains would be under residual tensile stresses which may not have been offset by
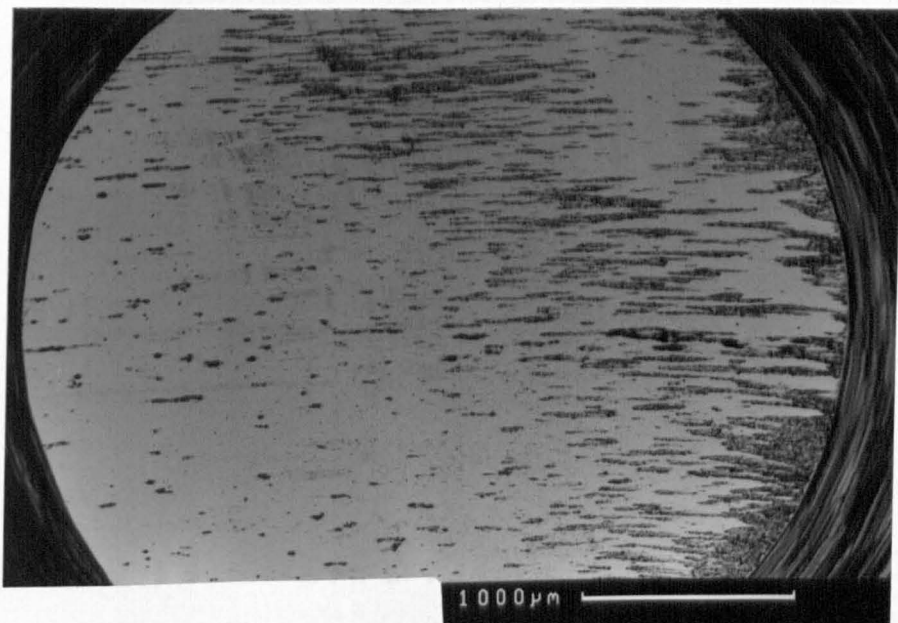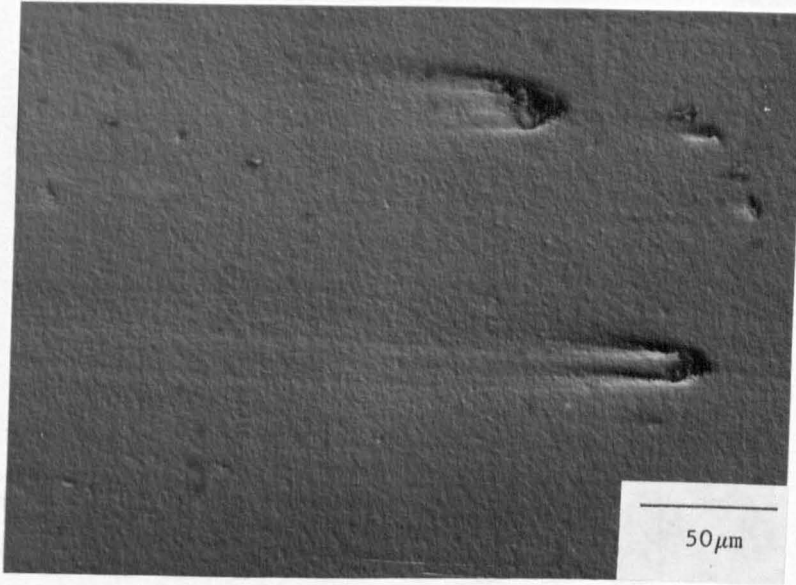
S.D.→

Fig. 6.47. BEI micrograph of a worn 2Y-TZP pin showing the extent of the metal transfer. Some pins showed considerably less whilst others contained more transfer than this example. (6.6 N/pin).
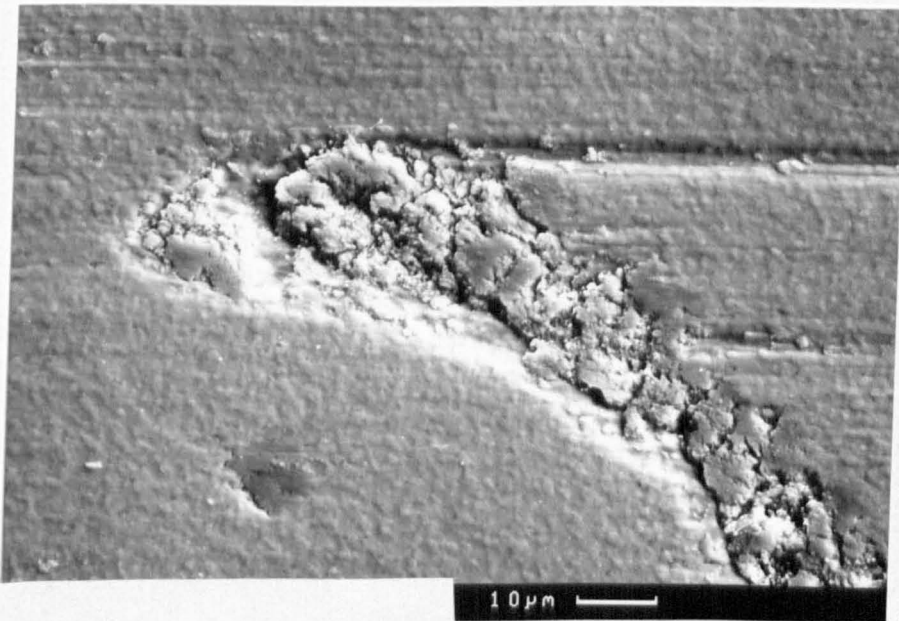

500μm
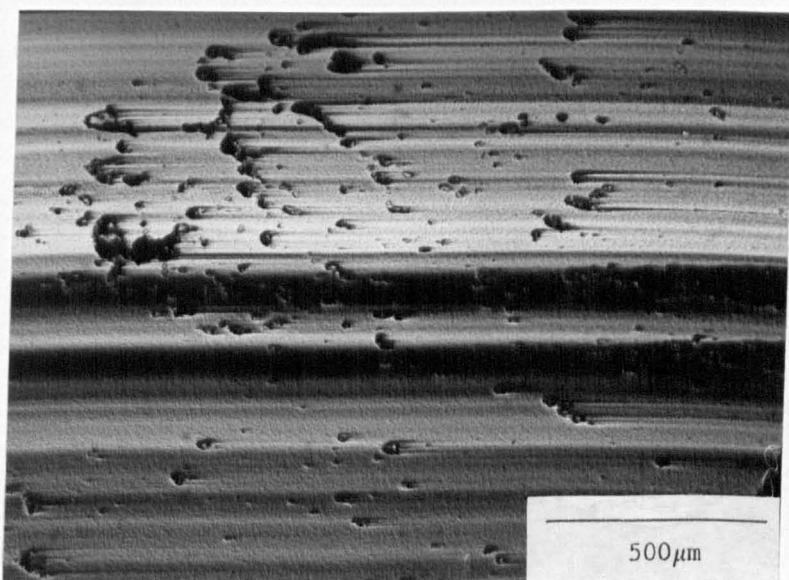
S.D.→

Fig. 6.48. Optical micrograph (Nomarski) showing coarse undulations and abrasive grooves originating from transferred particles. (19.3 N/pin, 2Y).
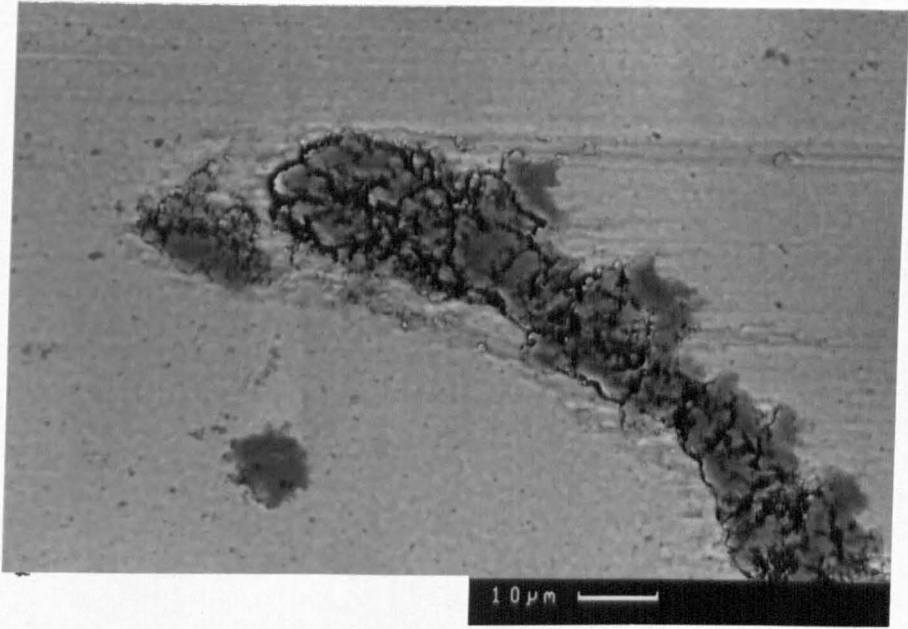
S.D.←

Fig. 6.49. Optical micrograph (Nomarski) showing impressed wear debris with abrasive grooves at the trailing edge. Note also the grain relief, but otherwise generally smooth surface. (59 N/pin, 3Y).

S.D.→

Fig. 6.50. SEM micrograph showing a detail of the impressed metal oxide. Note the grain relief and the points where the debris has become detached. (19.6 N/pin, 2Y).

S.D.→

Fig. 6.51. BEI image of the above. The transfer was present as metal oxide not metal.
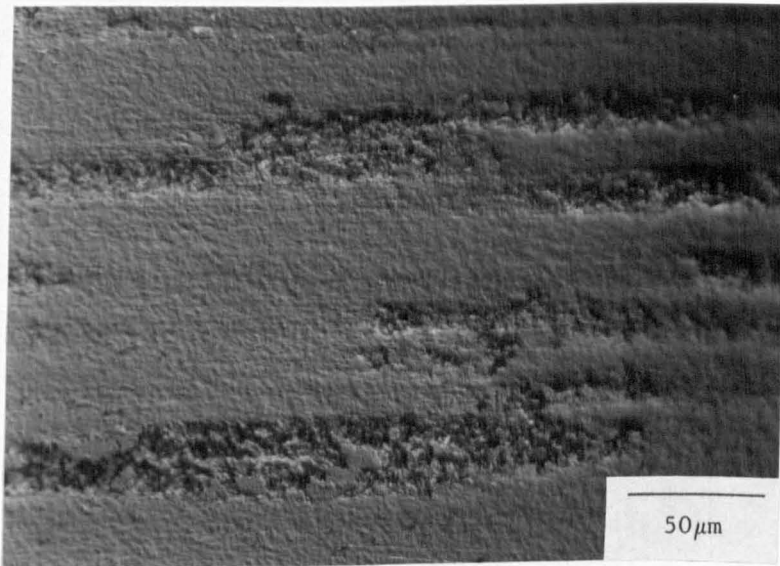
S.D.→

Fig. 6.52. Optical micrograph (Nomarski) of general transfer which was not associated with abrasive grooving. (19.6 N/pin,, 2Y).
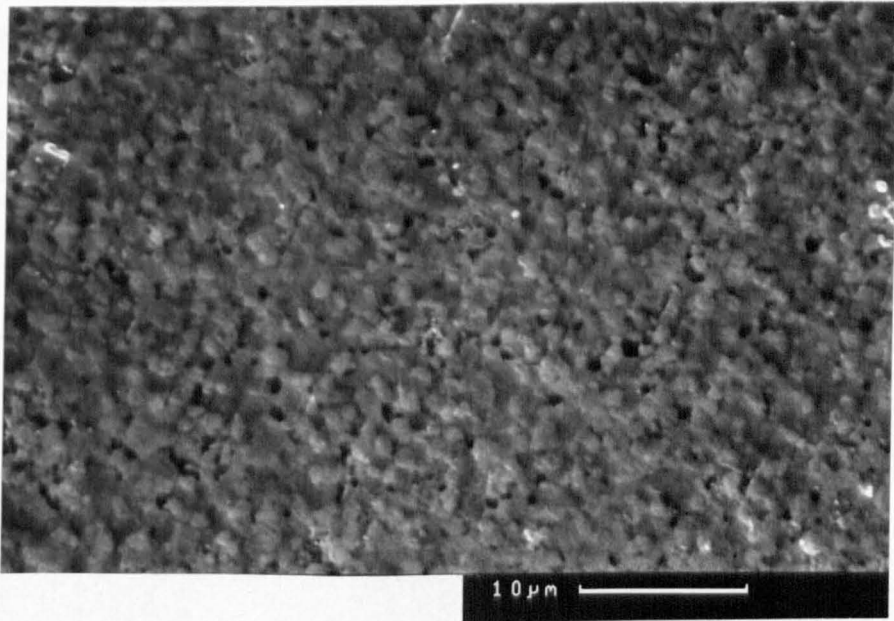
Fig. 6.53. SEM micrograph of a worn pin showing a grain 'pop-out' mechanism, believed to have been a result of transformation of tetragonal to monoclinic. Only a small area of the pin exhibited this mechansim. (6.6 N/pin, 2Y).
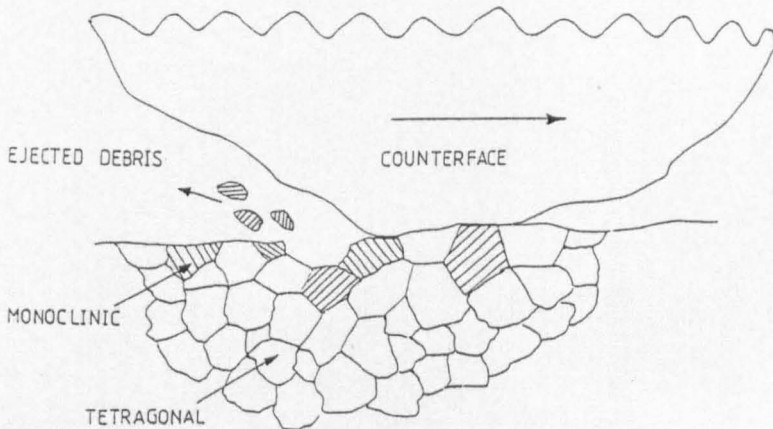

Fig. 6.54. Diagramatic representation of the grain pop-out mechanism. Microcracking in conjunction with adhesive forces and limited matrix constraint cause grain removal.

the compressive stresses resulting from transformation. Adhesive forces between the two surfaces would provide sufficient stress for that grain to become detached, thereby reducing the long range stresses. Such a mechanism is shown schematically in fig 6.54 and is similar to that proposed by Birkby et al. [146]. Thus, transformation has once more been shown to increase the wear rate. This again raises the question as to why transformation is detrimental in sliding wear but beneficial in abrasive wear. This will be discussed further in the final conclusion section of this chapter, but it is considered that the adhesive forces are a highly significant factor. However, it should be noted that the area coverage by the 'pop-out' mechanism was less than 1% and was therefore in no way dominant. The major material removal mechanism was one which gave a very smooth surface but different wear rates within different grains.

6.2.3.2 Transmission Electron Microscopy and X-ray Analysis

The X-ray data has already been presented in table 6.2. The diffractometer traces are presented in figs 6.55-56. Wear provided significant increases in monoclinic levels compared to the polished surface, but far lower than on the ground surface. The average increase was greater for the 2Y materials than the 3Y as might be expected. However, the difference in the amount of transformation did not correlate with any difference in the wear rates of the two materials. The wear rates were found to be near identical for the 2Y and the 3Y *which indicates that transformation was not controlling the wear mechanism.*

The increases in monoclinic levels for the 2Y pins were of the same order as the increase in monoclinic (above the grain boundary monoclinic level) for the Mg-PSZ. The change in monoclinic levels with load for the 2Y materials is within experimental error so that no conclusions about trends with load could be drawn. For the case of the 3Y materials, the reduction in the monoclinic levels at the highest load appears to be significant, and the volume fractions do appear to follow a similar trend to the wear factors (fig 6.24). The very low levels of monoclinic at the highest load suggests that temperatures were high enough to substantially reduce the driving force for transformation. The asperity contact pressure would be expected to have been high enough to have driven transformation at room temperature. In all cases, the amount of transformation was
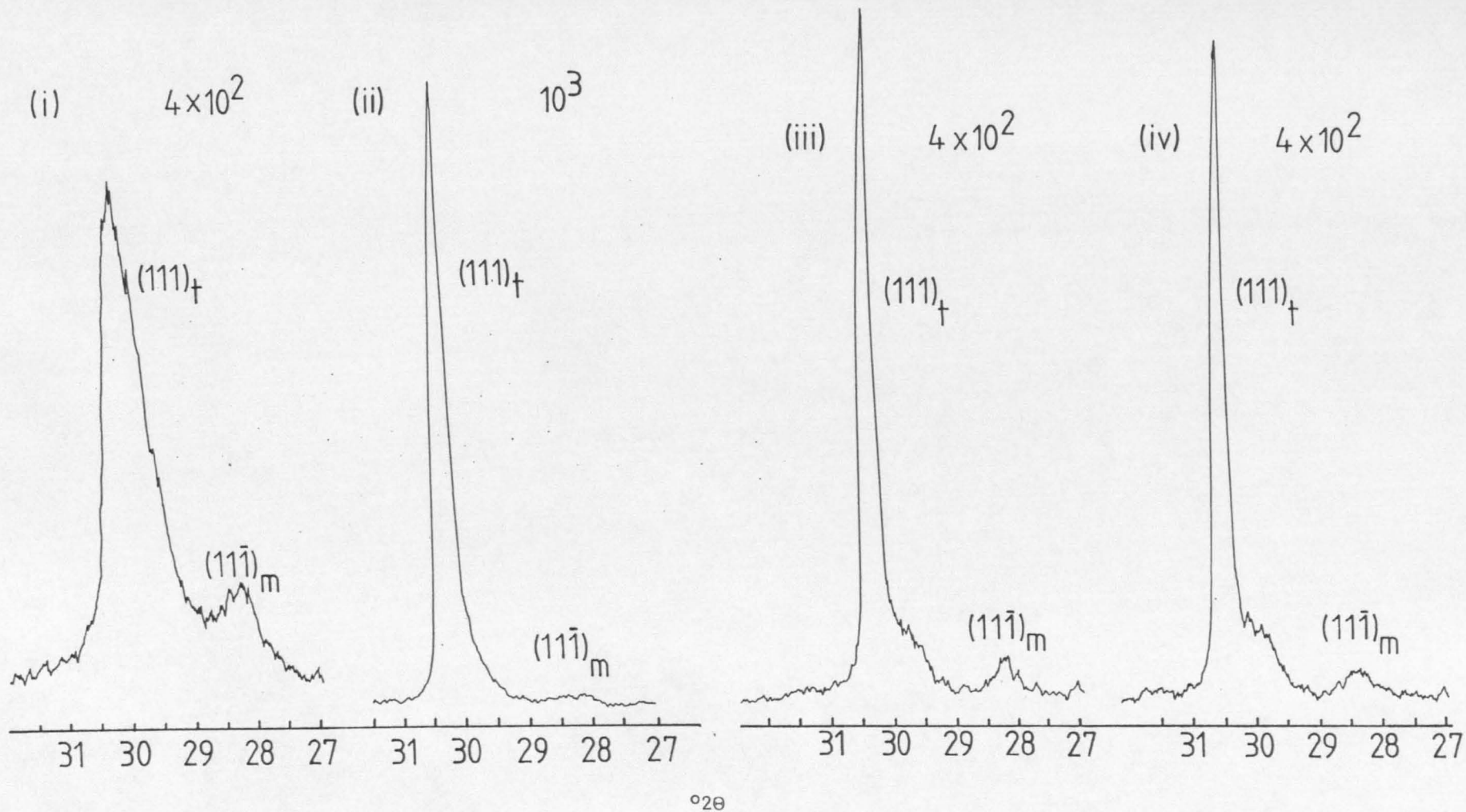
Fig. 6.55. X-ray diffractometer traces for the 2Y-TZP, showing the
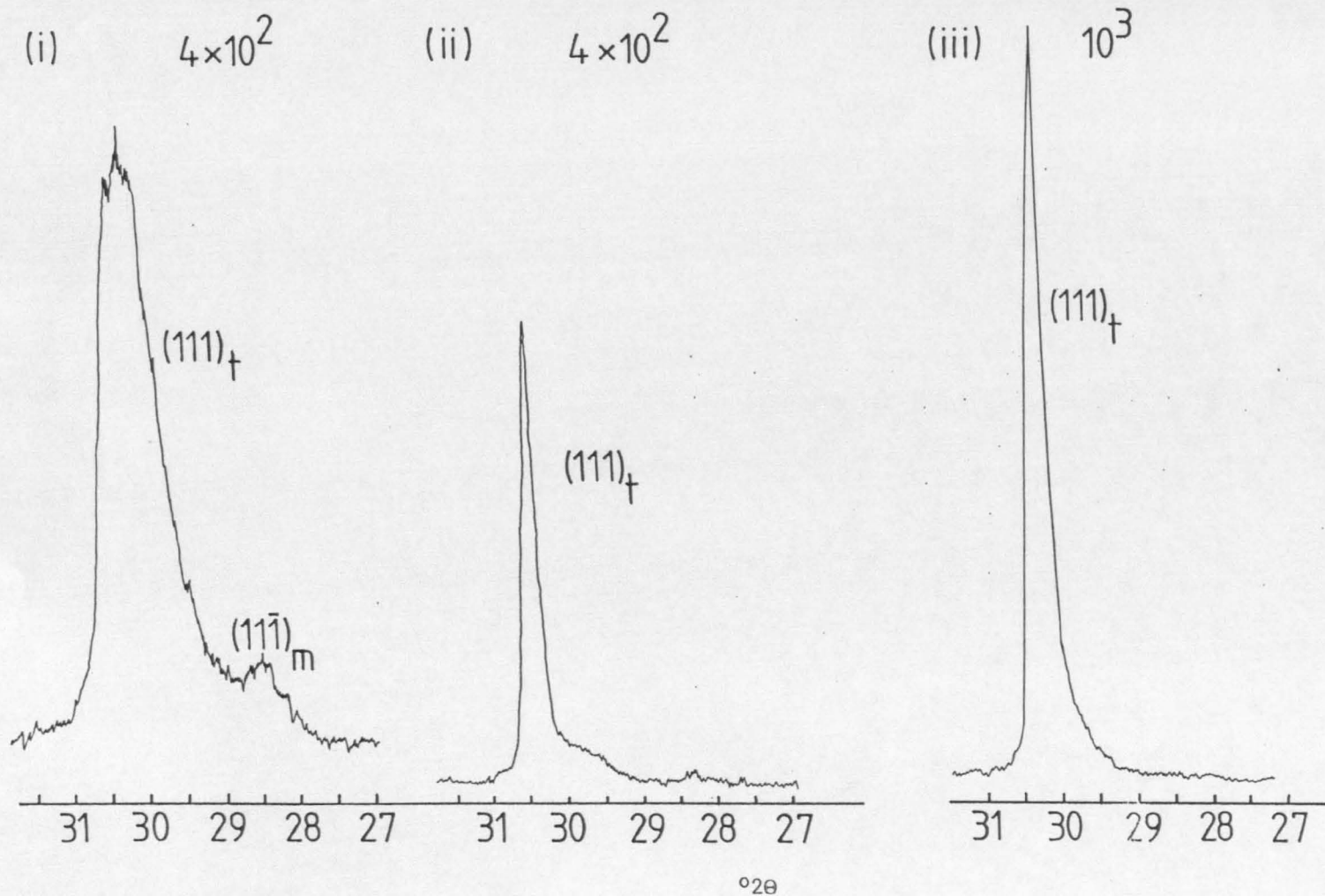ground surface (i), polished (ii), worn at 19.6 N/pin (iii) and worn at
59 N/pin (iv).

Fig. 6.56. X-ray diffractometer traces of the 3Y-TZP showing the
ground surface (left), worn at 59 N/pin (centre) and polished.

considerably lower than the figure of 20% reported by Birkby et al. [146] for a 2Y cam follower.

Thin foils for TEM examination were taken perpendicular to the worn surface for the majority of the 3Y tests and selected 2Y tests. As with the Mg-PSZ case, considerable difficulty was found in obtaining a reasonable thin area. However, less break-up occurred compared to the Mg-PSZ materials because of the absence of surface cracking, so that some limited thin areas were obtained. However, for the 2Y materials, transformation to the monoclinic tends to occur during thin foil preparation so that only tentative conclusions could be drawn about the microstructure at the surface.

The over-riding observation was that there was little change in microstructure at the worn surface compared to the bulk. A montage of a typical surface region from the 3Y test at 59 N/pin is given in fig 6.57 with two dark field images in figs 6.58,59. The surface was found to be entirely monoclinic, although the twins were generally difficult to image. The surface monoclinic contained high levels of residual stress which gave an image which was difficult to interpret. It was difficult to establish whether any dislocations were present, and no direct evidence was found.

The transformation depth varied with load, but never exceeded 2-3μm. At 59 N/pin, transformation only occurred to a depth of a few grains. The distortion of the internal structure of the grain was only evident in the surface grains. It should be noted that transformation depths measured by this technique determine a maximum depth and that the average level could be less. Transformation during thin foil preparation, driven by residual stresses, almost certainly occurred.

Little microcracking was found. One example can be seen in fig 6.57. Surface roughness produced by the grain relief was evident, such as in fig 6.59. The latter micrograph shows how the surface grains can receive only limited constraint from the matrix. Thus, it can be envisaged that the combination of the low surface constraint with microcracking could lead to detachment of an individual grain along the lines discussed above and illustrated in fig 6.54. Unfortunately, no foils were obtained in the region of grain 'pop-out', because of the low area coverage of this mechanism and so this assertion cannot be verified.

Since the amount of microstructural change approaching the surface was comparatively small, back thinned foils were taken to try and
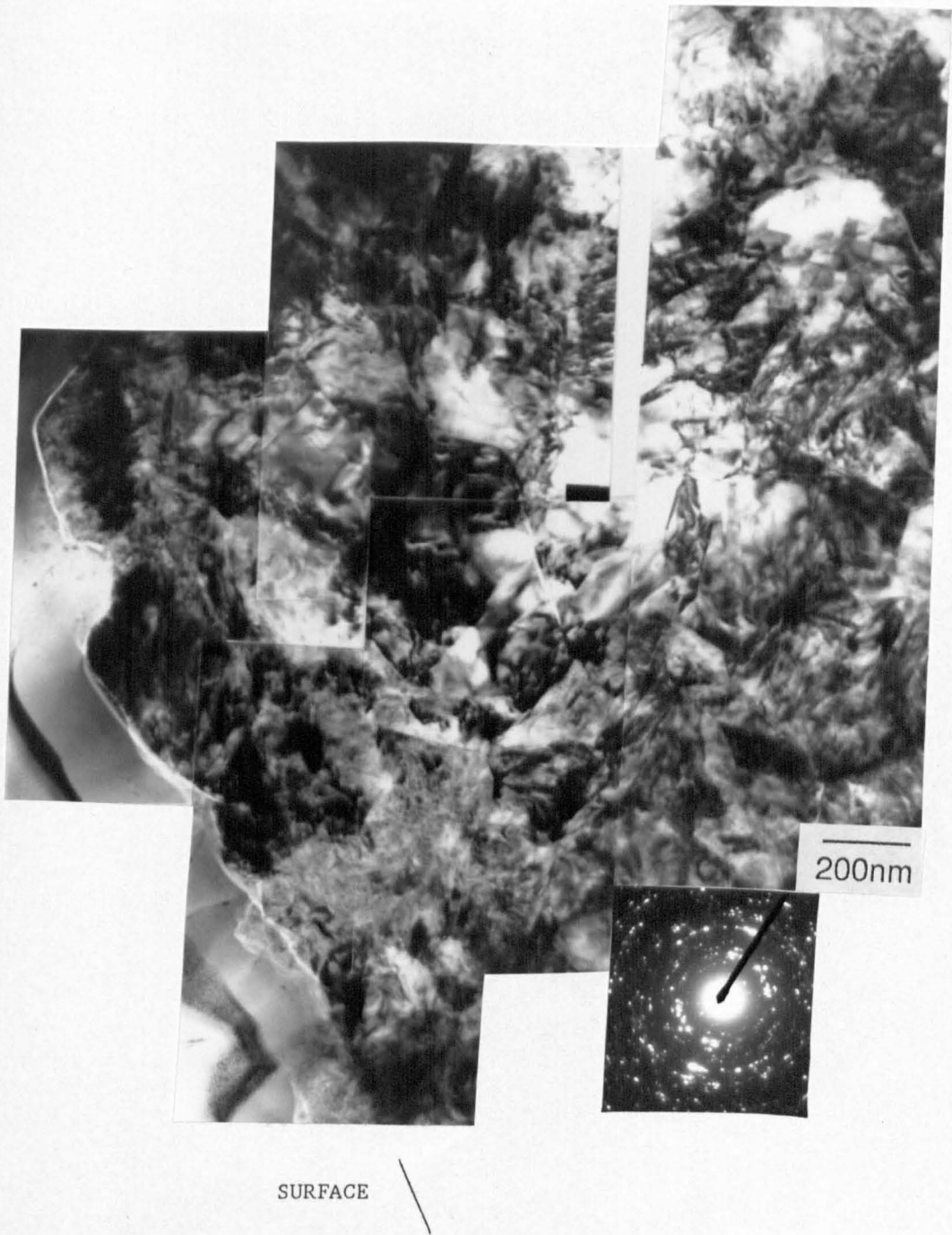
SURFACE

Fig. 6.57. TEM micrograph of a cross section of the worn surface.
Note the high levels of residual strain which become more severe as the
surface is approached. Note the surface roughness but general absence
of microcracking. The outermost surface was entirely monoclinic whilst
the lower end of the micrograph was a mixture of monoclinic and
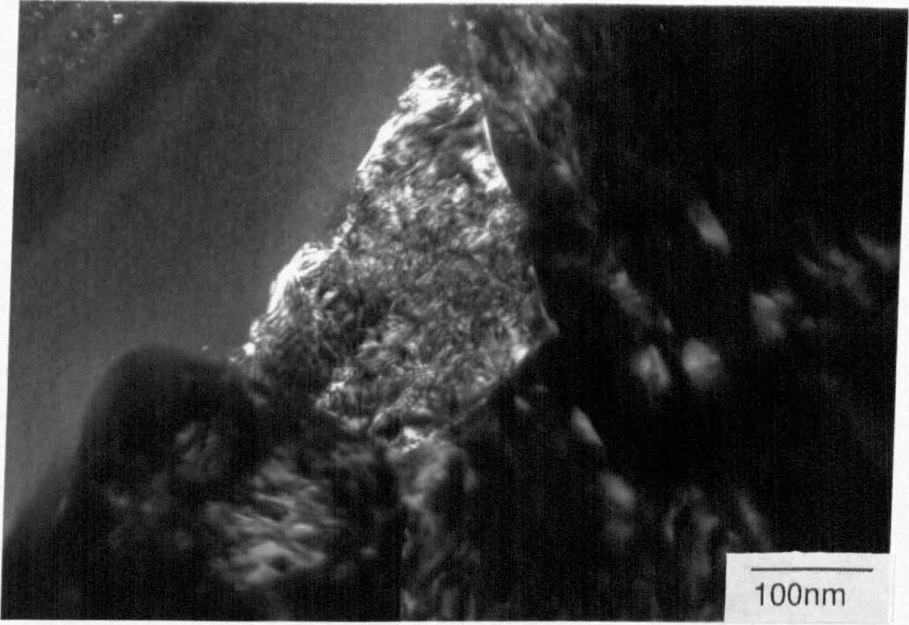tetragonal. (37.6 N/pin, 3Y).

SURFACE

Fig. 6.58. Dark field micrograph showing a detail from fig 6.57.
There is some evidence of dislocations although they were difficult to
image because of the intensity of strain contours.
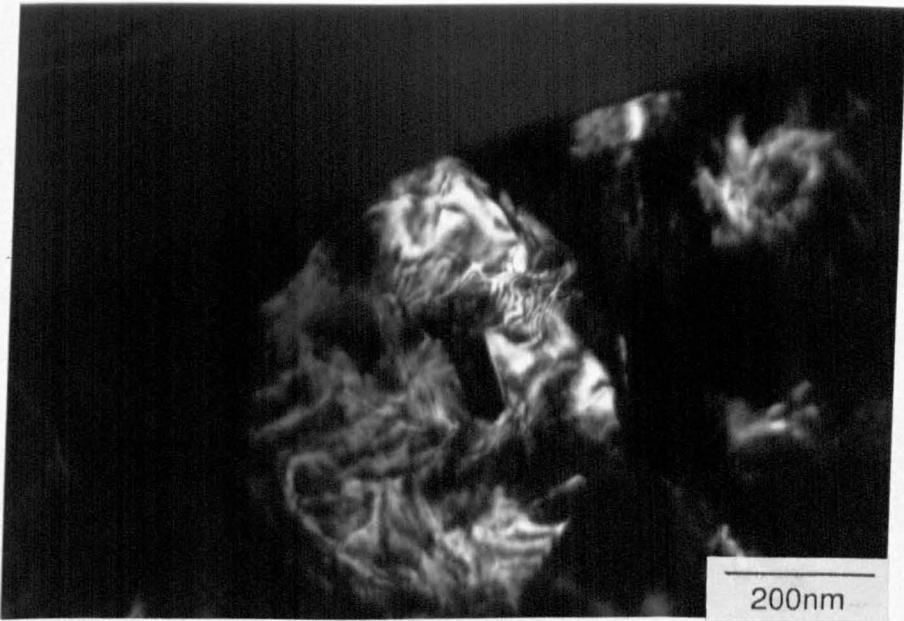

SURFACE

Fig. 6.59. Dark field micrograph from further along the surface. The
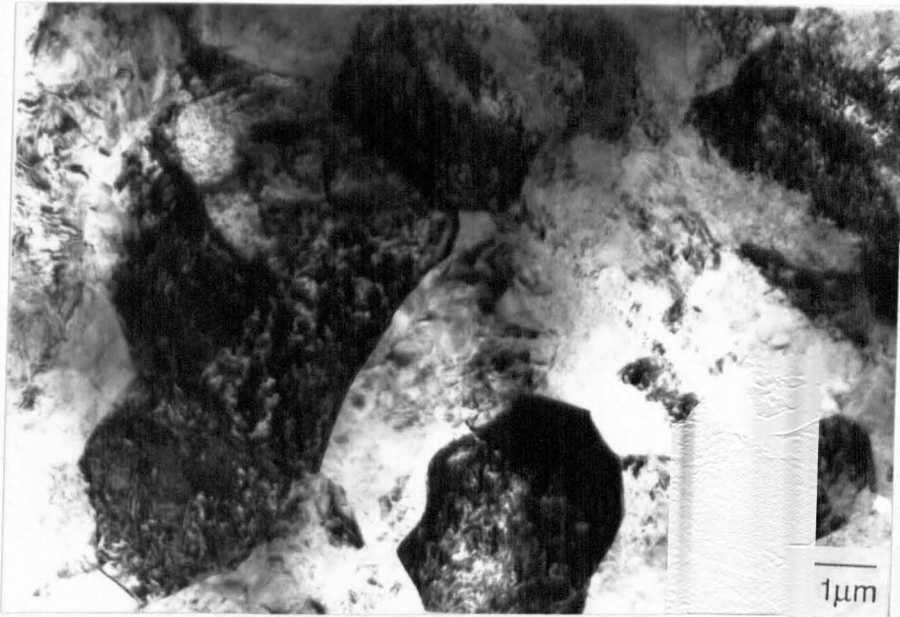morphology was very similar to that found in the as-sintered material.

Fig. 6.60. TEM micrograph from a back thinned foil. The structure
within the grains is similar to that in the surface grains in fig.
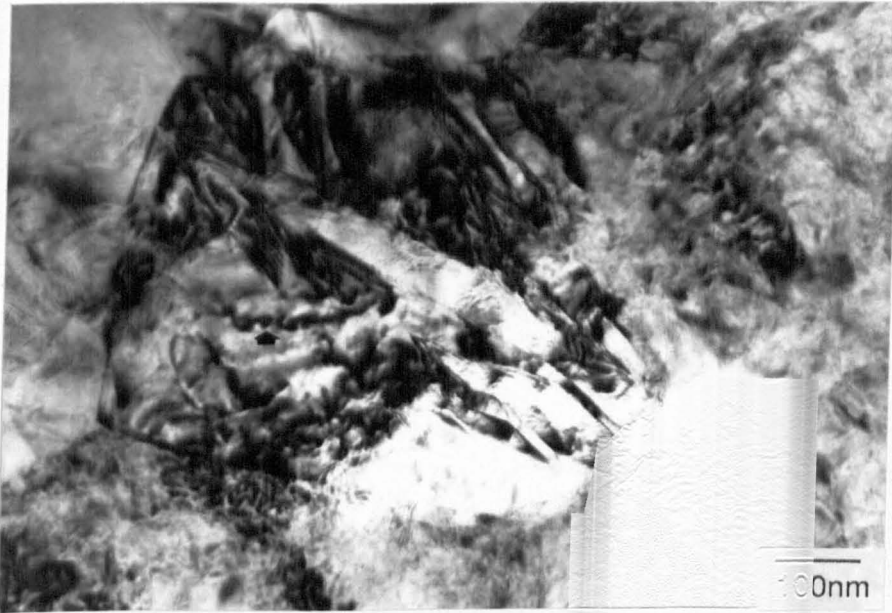6.57. (6.6 N/pin, 3Y).

Fig. 6.61. TEM micrograph of a surface grain containing clear twin
boundaries and what appears to a be a dislocation line (arrowed).

100nm

Fig. 6.62. TEM micrograph showing a detail of the surface
microstructure, which is difficult to interpret because of the high
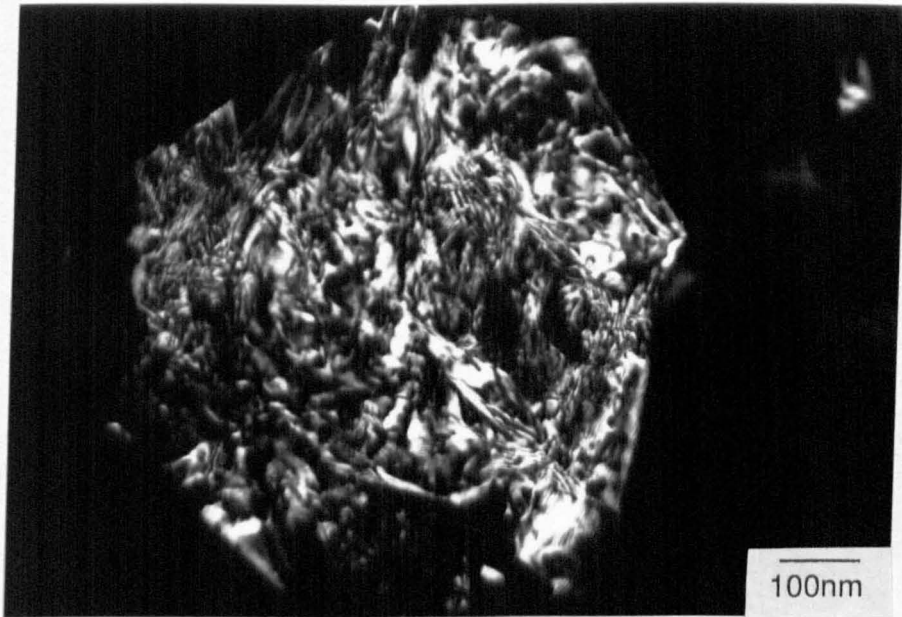density of strain contours. (6.6 N/pin, 3Y).

100nm

Fig. 6.63. Dark field micrograph from an adjacent area. (6.6 N/pin,
3Y).

confirm the microstructural features described above. A bright field image of the surface at 19.6 N/pin (3Y) is given in fig 6.60. Details of the microstructure are given in figs 6.61-63. Only in a few instances could twin boundaries be imaged even with extensive tilting experiments. The high residual strains obscured the structure, but there was some evidence of dislocation lines. For example, the feature in the centre left of fig 6.61 was most probably a dislocation, since tilting moved the line in and out of contrast but failed to move it. However, there was no evidence for dislocation flow that had been sufficient to cause grain shape change.

As with the cross sectional specimens, the amount of microcracking was low. The residual stresses in the surface were insufficient to cause significant foil buckling, which was commensurate with the comparatively low levels of monoclinic found.

The back thinned foils were chosen to include regions of transferred metal oxide. These areas thinned at a substantially greater rate than the remainder of the surface making investigation of them difficult. Diffuse boundaries were found between the zirconia and metal oxide in a similar manner to the Mg-PSZ disc. The residual strains in the adjacent zirconia were considerably higher, which helps explain the higher ion beam thinning rate. Unfortunately, a reasonable thin area could not be obtained in the abrasive groove region, but there was some evidence that plastic flow had led to disruption of the grain structure. Further work is required to verify this.

The TEM results appear to confirm the conclusions from the optical, SEM and XRD work, suggesting a wear mechanism similar to that in the smooth regions of the Mg-PSZ. Transformation of the tetragonal to monoclinic appears to have played a minor role in the wear mechanism. No evidence of a plastic deformation or microfracture was found. The most probable wear mechanism was therefore considered to be tribochemical. The kinetics of such a mechanism were apparently rapid, as shown by the high wear factors obtained. Nonetheless, the wear factors were lower than would be expected for an alumina steel couple, where the formation of a spinel results from rapid reaction rates between the counterfaces.

6.2.4 Wear of the Bearing Steel Disc

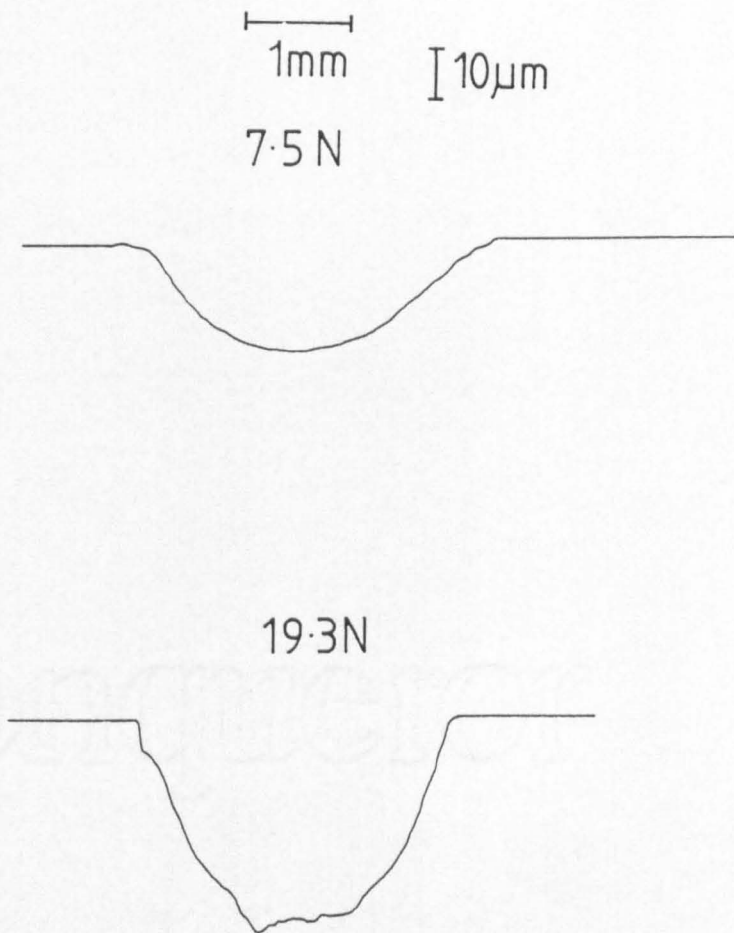The wear groove depth of the bearing steel disc increased with
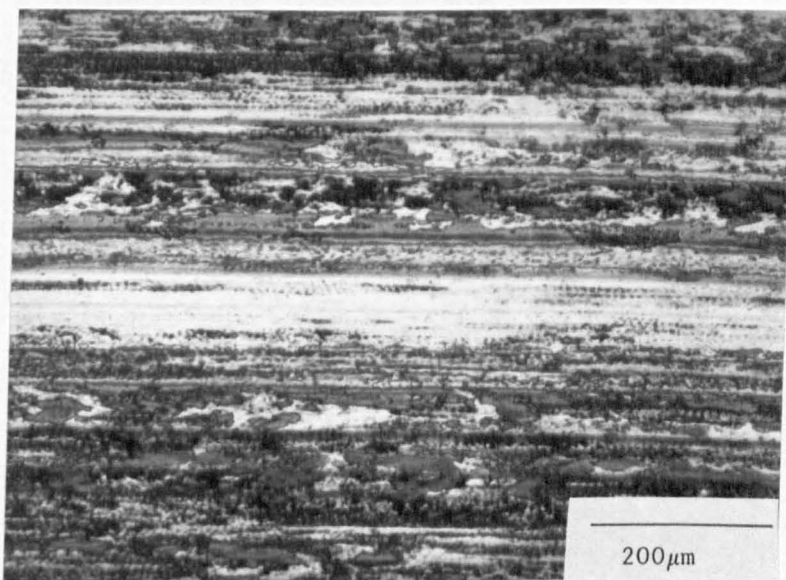
1mm   ⅠⅠ 10μm

7·5 N

19·3N

Fig. 6.64. Radial proliferometry traces from the disc run against the 3Y pins.

200μm

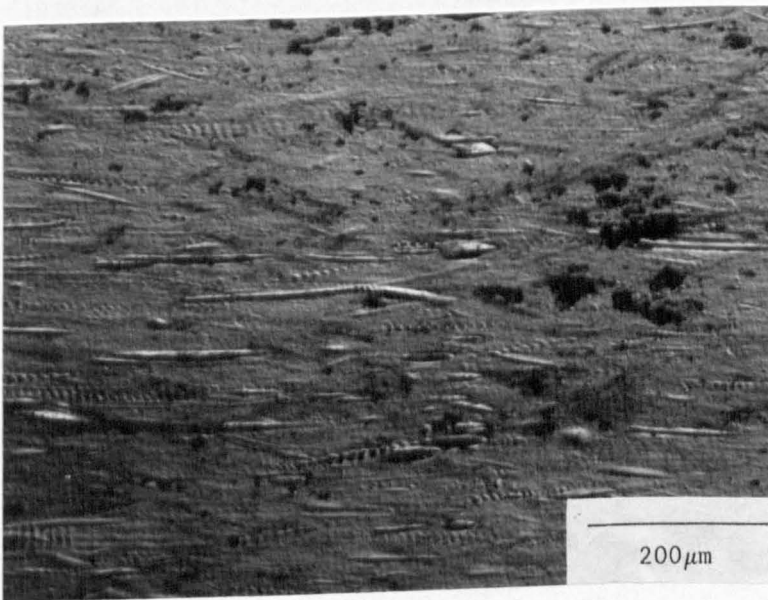S.D.←

Fig. 6.65. Optical micrograph of the worn disc showing widespread coverage of the surface by a thin film of metal oxide. (19.6 N/pin, 3Y).

S.D. →

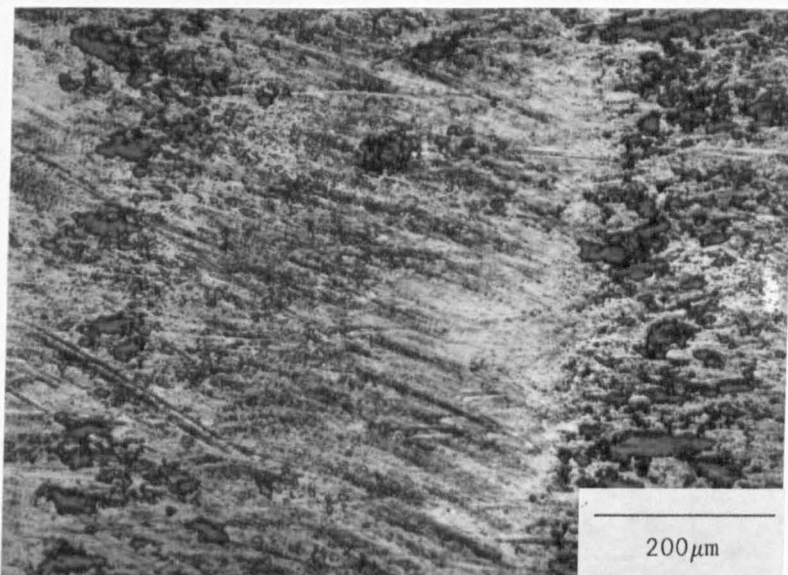Fig. 6.66. Optical micrograph (Nomarski) showing abrasive grooves and evidence of chattering. (59 N/pin 3Y).

S.D.→

Fig. 6.67. SEM micrograph of a worn disc showing 'machining marks' produced by ploughing of the metal oxide. (6.6 N/pin, 3Y).

S.D.→

Fig. 6.68. Optical micrograph of the disc showing intermittent contact
and radial motion of the pin which was a result of the heavy
vibration. (59 N/pin, 2Y).

mechanisms. Firstly, oxidation of the metal led to the formation of a thin film as a result of the frictional heating. This oxide appeared to be fairly adherent, but did become detached and sometimes transferred to the zirconia pins. The metal oxide debris acted as an efficient abrasive causing extensive 3 body abrasive wear of both the pin and, to a greater extent, the disc. No evidence of any smearing of the metal itself or transfer of the metal was found. The rate controlling step was therefore considered to be the oxidation of the metal, in a manner which appeared consistent with the theory of Quinn and co-workers [218,310-312].

6.2.5 Wear Debris Analysis

No difference was found in the morphology of the wear debris between the tests against 2Y, 3Y or Mg-PSZ pins and therefore the debris analysis will be considered in a single section.

The debris was pressed into a flat pellet and analysed in the TI Research electron probe microanalyser using wavelength dispersive analysis with standards (as discussed under the section on wear debris in chapter 5). The results for the Mg-PSZ test at 37.6 N/pin are given in table 6.3.

TABLE 6.3

EPMA Analysis of the Wear Debris From the Test at 37.6 N/pin Against Mg-PSZ PINS

	Cr	Fe	Ni	O	Zr	Light Elements
Wt %	0.94	45.1	0.2	49	4.52	None detected

The amount of zirconia in the debris corresponded closely with the proportion of wear in the respective counterfaces.

X-ray analysis, fig 6.69, suggested that the debris consisted entirely of Fe_2O_3, presumably in the rhombohedral form, although with a slightly larger lattice parameter than given in the powder diffraction file. This result was consistent with the light brown colour of the

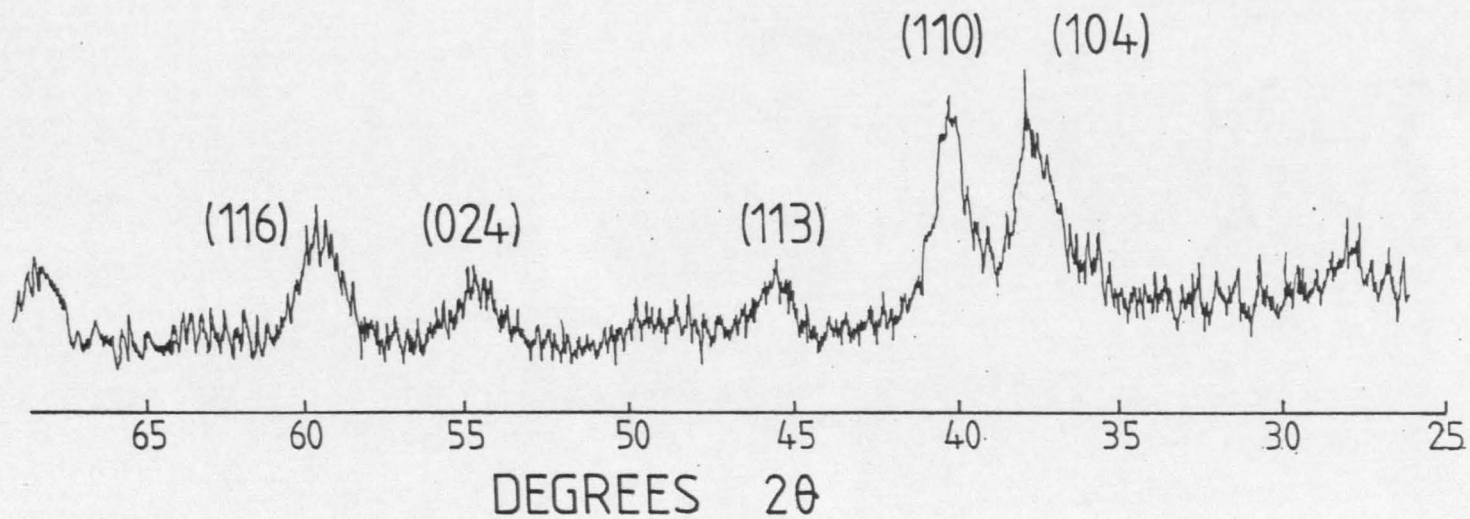Fig. 6.69. X-ray diffractometer trace of the wear debris. The only phase detected was Fe_2O_3 and the profile was unchanged with load or pin type.
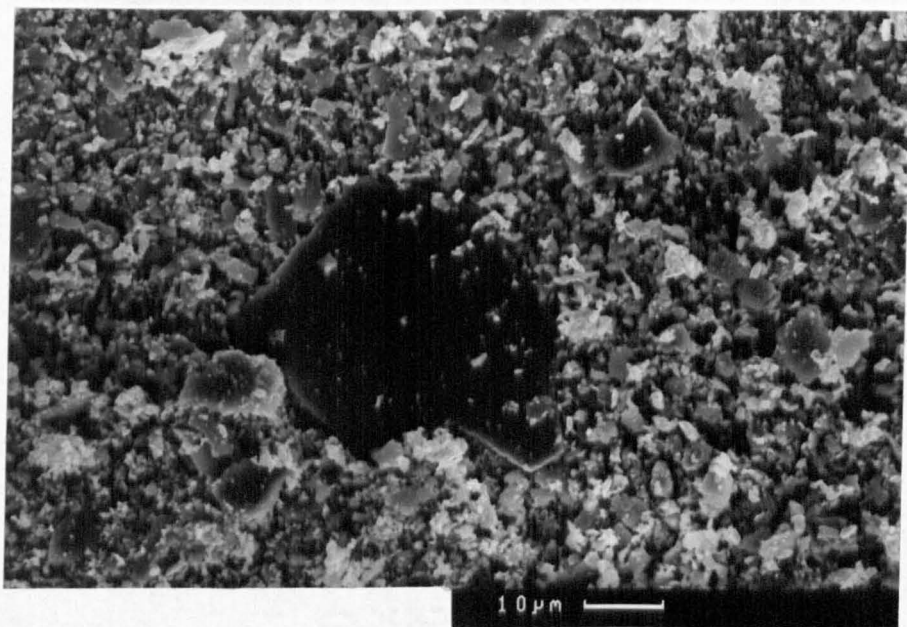
Fig. 6.70. SEM micrograph of the wear debris. The majority was metal oxide but all particles contained some zirconia.
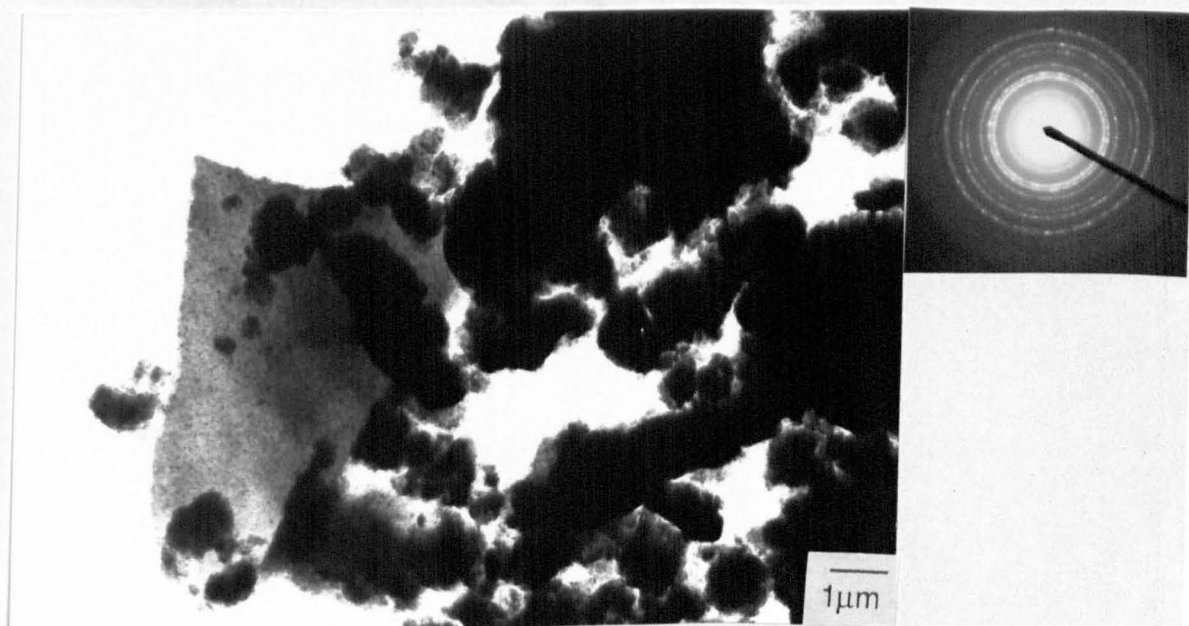
Fig. 6.71. TEM micrograph showing a general view of the wear debris. Numerous thin slabs such as the one shown here were found.

Fig. 6.72. Detail of the slab like particle in fig 6.71. Many
particles exhibited a finer crystallite size. Zironia was detected,
apparently in solid solution.

Fig. 6.73. TEM micrograph of some Fe_3O_4. These particles had a
similar appearance to those described in chapter 5, but were fairly
infrequent.

debris.

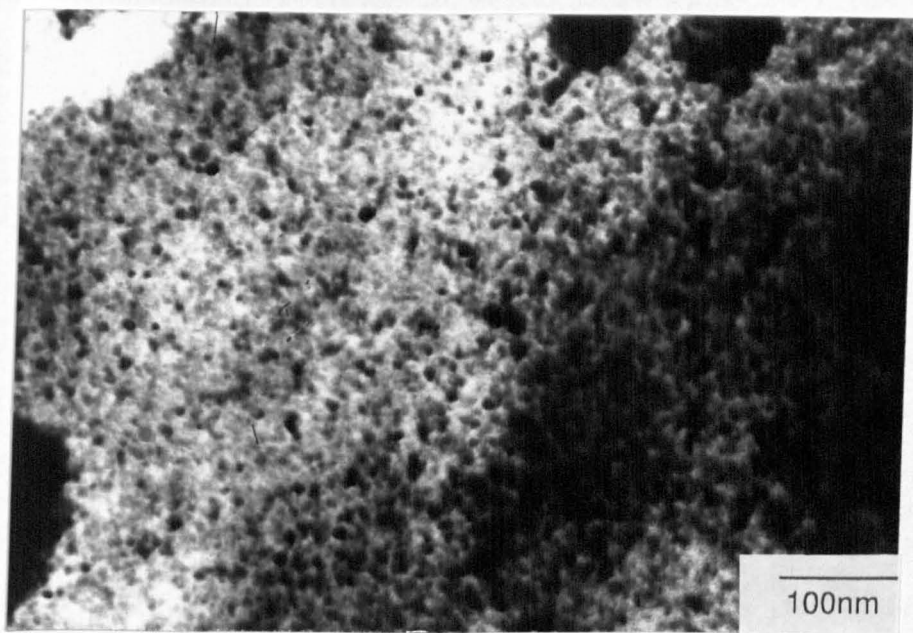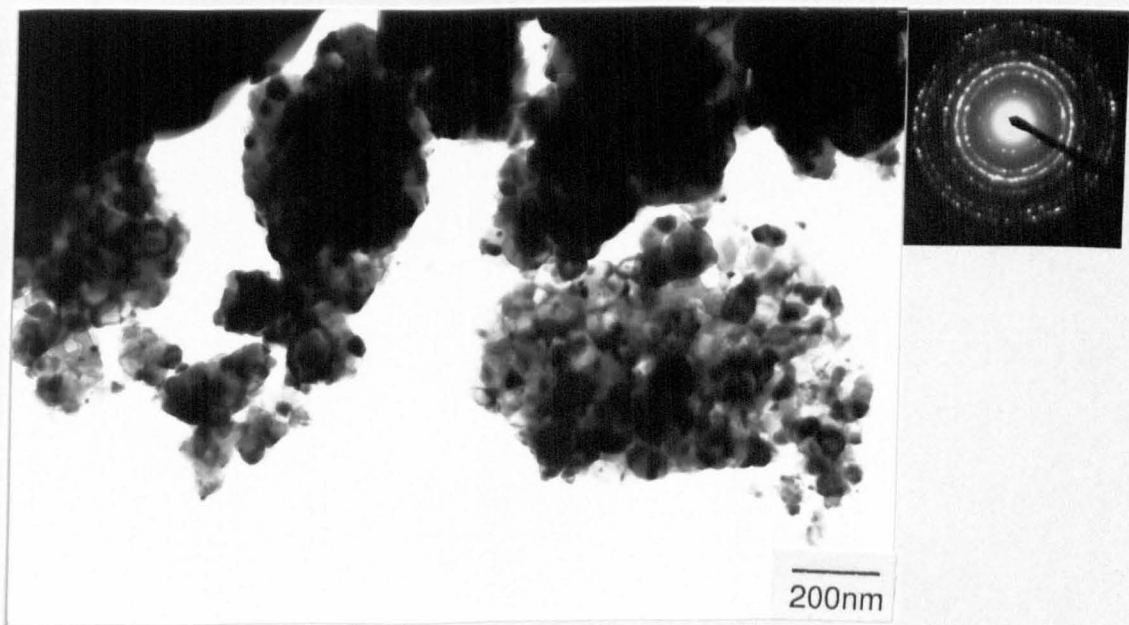A general view of the wear debris is presented in fig 6.70. The majority of the particles were slab like, with a large size distribution of up to 60μm. The finer particles appear to have been formed as a result of attrition of the larger material.

Many of the larger slab particles were thin enough to be electron transparent in the TEM. A general view of the debris, including one such particle, is given in fig 6.71. A detail of the electron transparent slab particle is given in fig 6.72, which was identified as microcrystalline haematite. The majority of the debris exhibited a similar structure, although with a varying crystallite size. The example in fig 6.72 represents the largest grain size found at 35nm, whilst crystallite sizes down to the resolution limit of the microscope were common.

In addition to the haematite, a few particles of Fe_3O_4 were identified in the TEM. These were usually of a similar morphology to the debris in the 316L stainless steel tests, as shown by fig 6.73. However, some of the magnetite appeared very similar to the haematite, as illustrated in fig 6.74. The amount of magnetite was fairly low, as shown by the absence of peaks on the X-ray trace in fig 6.69.

No individual particles of zirconia could be found even though it constituted 4.5% of the total volume. However, all particles contained a significant quantity of zirconia as shown by the energy dispersive microanalysis in the TEM. No diffraction rings other than those from the haematite or magnetite were found. Therefore, it would appear that the zirconia was present in solid solution. This provides strong evidence that the wear mechanism was tribochemically based. In other words, wear appears to have occurred by dissolution of the zirconia into the iron oxide rather than by any fracture or plastic overload based mechanism.

6.2.6 Wear Tests of 2Y-TZP Pins at Low Sliding Speeds

The above results suggest that the temperatures generated at the interface were sufficiently high to reduce the driving force for transformation and allow significant chemical reaction between the metal oxide and the zirconia. Since the over-riding factor in determining the temperature at the interface (for a given material couple) is the sliding speed, a test was undertaken at a very low speed

to try and reduce the temperature at the interface. A speed of 0.016m/s was used which is more than an order of magnitude slower than the tests described so far (0.24 m/s). The test was conducted at 10.64 N/pin and ran for a total of 76,858 Km. The wear rates and friction coefficients are given in table 6.4.

The distance was considered to be the minimum required to give sufficient wear for the wear rate to be evaluated accurately. Because of the slow speed employed the test took 56 days, not allowing for intermediate weighing and examination. Even after this time contact had only occurred on about 25% of the pin. Such a small contact area precluded any TEM examination. The time to give a sufficiently large contact area would have been unacceptably long.

The test produced a high pitched squeak but no significant vibration was observed. A detail of the pin surface is given in fig 6.75. The surface exhibited very similar features to those described for the TZP pins worn at the higher speeds. However, the extent of the grain relief was less and virtually no metal oxide transfer occurred. Occasional examples of surface porosity were found, believed to be a result of grain 'pop-out' as described in the preceding section.

TABLE 6.4

WEAR FACTORS AND FRICTION COEFFICIENTS FROM THE TEST AT 0.016m/s

	Wear Factor	Friction Coefficient	
Pin 1	1.66×10^{-8}	Initial:	0.10–0.12
Pin 2	1.63×10^{-7}	Steady state:	0.27–0.35
Pin 3	1.63×10^{-7}		
Average	1.14×10^{-7} mm^3/Nm		

Very little wear debris was produced, certainly not enough for X-ray analysis. The debris was removed from the disc surface using two stage replica, and found to be haematite with a very similar structure to that described for the higher speed tests. A dark field micrograph
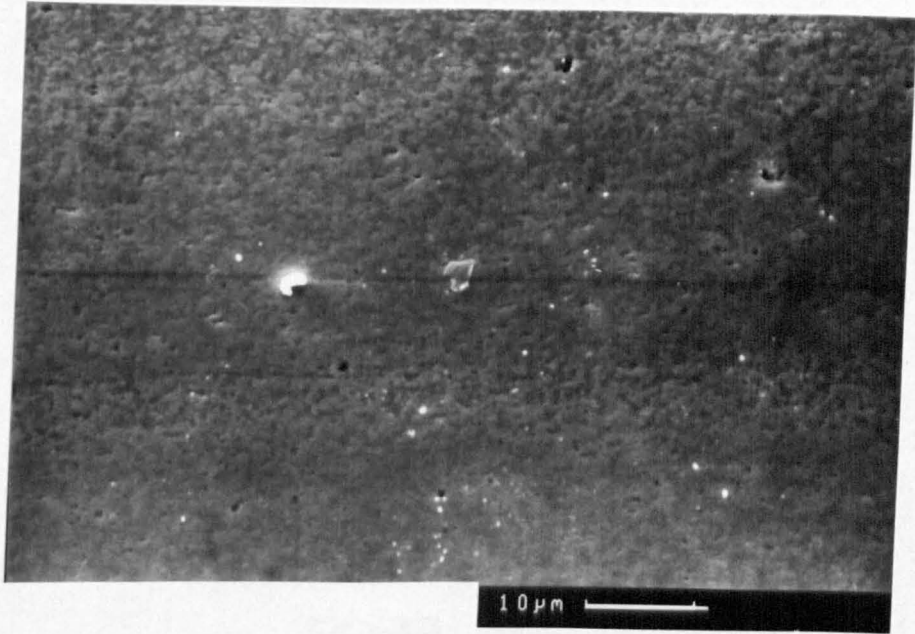
S.D.→

Fig. 6.74. SEM micrograph of the 2Y pin worn at 0.016 m/s. The surface is similar to the test for the same material at 6.6 N/pin and 0.24 m/s.

100nm
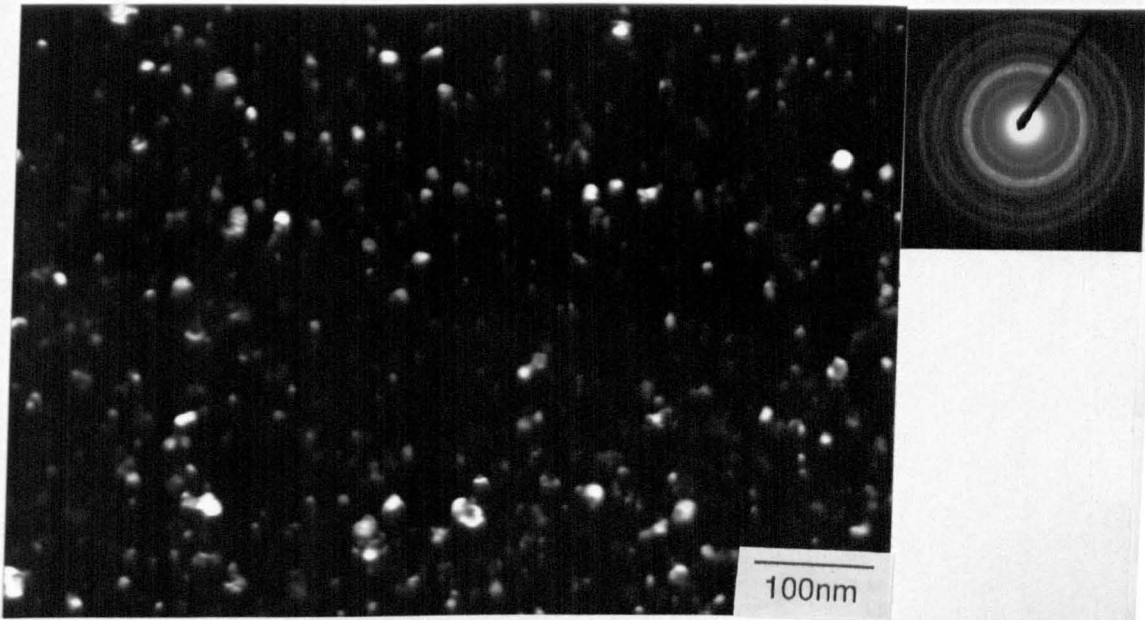
Fig. 6.75 Dark field micrograph of the wear debris removed from the disc surface by a two stage replica. The structure of the debris was the same as that produced at 0.24 m/s.

200nm
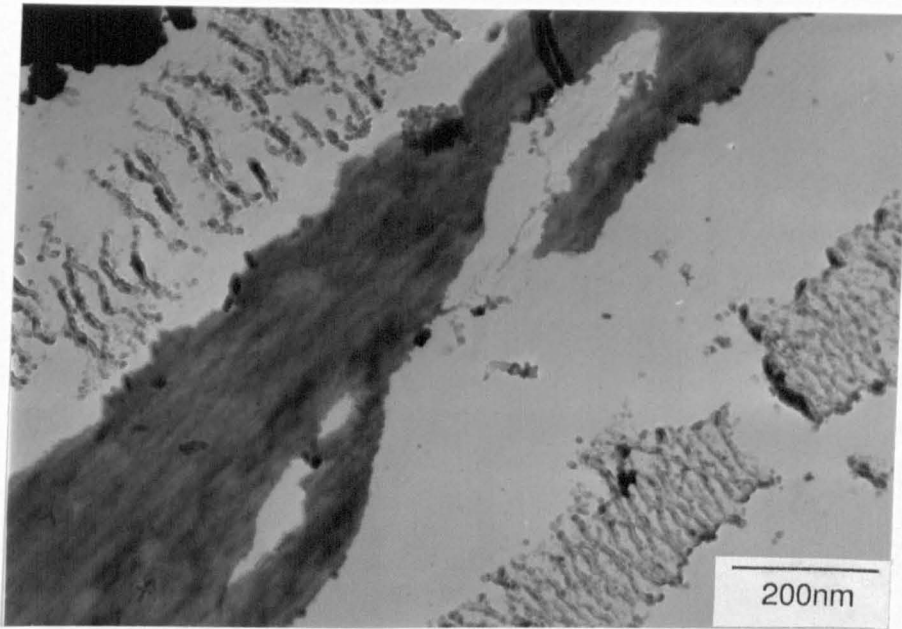
S.D.

Fig. 6.76. TEM micrograph showing a thin film of metal oxide removed from the wear track by the two stage replica. The film was Fe_2O_3 with a crystallite size of about 5nm.
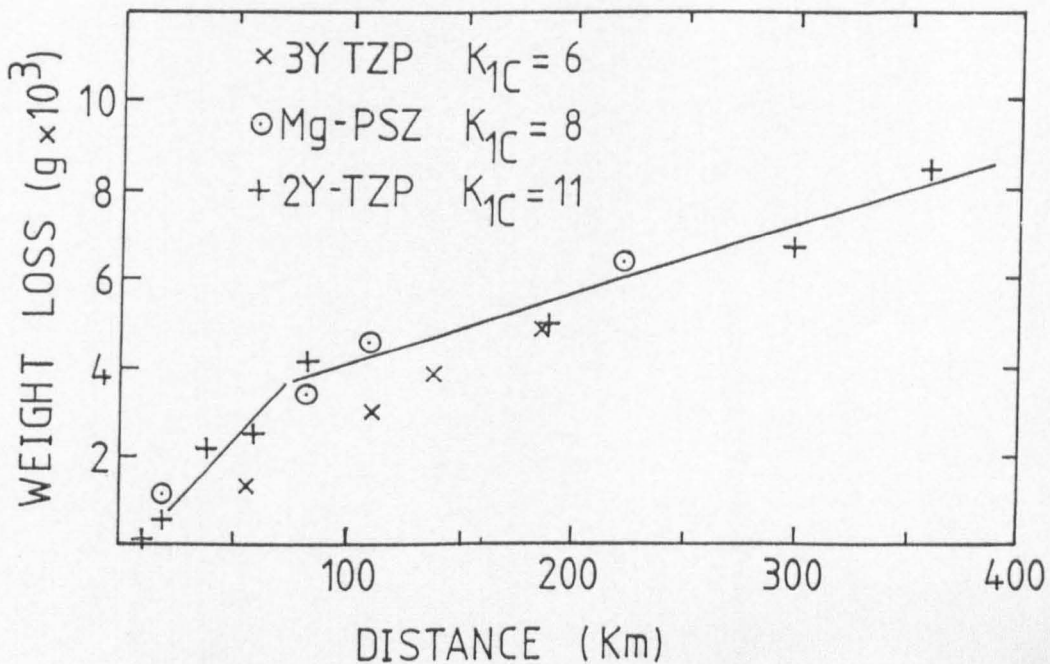
Fig. 6.77. Weight loss as a function of sliding distance for three materials. The toughness did not affect the wear rate suggesting that transformation toughening did not play a dominant role in the wear mechanism.

is presented in fig 6.76. In all cases the debris contained small amounts of zirconia, apparently in solid solution, in approximately the same proportion as that described in section 6.2.5.

The two stage replica also removed thin sheets of metal oxide which had been attached to the disc. One such example is given in fig 6.77. The layer was extremely thin, as shown by its complete electron transparency, and confirmed that it was the build-up and subsequent spalling of this layer which provided the free wear debris and consequently wear of the disc.

Despite the low wear speed employed in this test, no change in the wear mechanism had occurred. Specifically, transformation did not appear to play any major role in the removal of material from the zirconia. However, the lower speed had produced an order of magnitude reduction in the wear factor. Values in the range 10^{-8} to 10^{-7} can be considered to be good for unlubricated sliding wear. This result suggests that the reduced interfacial temperatures had reduced the reaction rate between the metal oxide and the zirconia such that the ceramic was dissolved at a slower rate. There will be a general discussion on the effect of sliding speed at the end of this thesis.

6.3 CONCLUDING DISCUSSION

The wear rates of the zirconia pins were nearly identical irrespective of the toughness of the material and all followed a similar trend with load. This is illustrated in fig 6.78, where it is shown that nearly doubling the toughness between the 3Y and the 2Y materials had not changed the wear rate or wear mechanism. Therefore, transformation toughening did not play a major role in the wear mechanism.

Considering first the wear mechanism which produced the smooth surfaces. The evidence from the wear debris and TEM of the worn surface strongly suggests that wear occurred by a tribochemical mechanism. No free zirconia particles could be found, rather zirconia was present in solid solution in the metal oxide. No evidence could be found of a microfracture wear mechanism on a sub-grain size scale, as suggested by Wallbridge et al. [132]. This study therefore calls into question the existence of such a mechanism. Some evidence of dislocation flow was found, but contact had apparently been
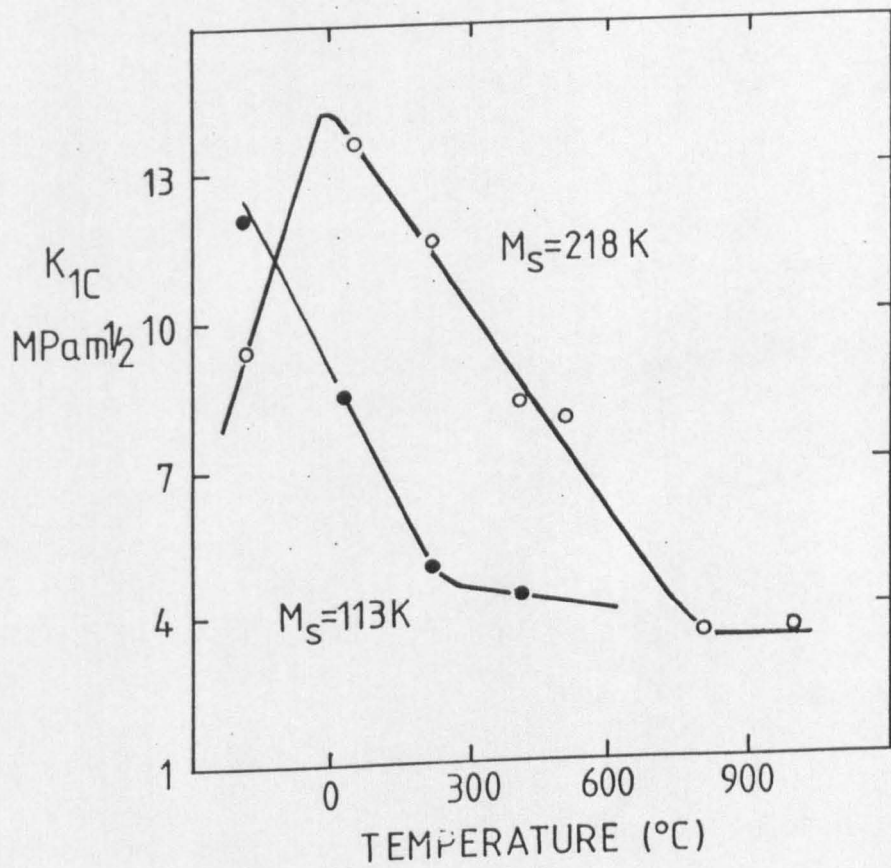
Fig. 6.78. Fracture toughness as a function of temperature for two zirconias with different M_s temperatures. Note the temperatures above which no transformation toughening occurs [318].

predominantly elastic in the zirconia surface. Therefore, no plastic deformation based wear mechanism had occurred. It is proposed here that such plastic wear mechanisms in ceramics are confined to the very high stresses imposed by the passage of an abrasive or where significant temperature rises occur. Thus, it is suggested that grain relief is a result of tribochemical reactions, not mechanical wear mechanisms. The grains are believed to wear to different extent because of the elastic, thermal expansivity and chemical dissolution rate anisotropy with crystallographic orientation.

The wear rate is therefore determined by those factors which govern the dissolution rate of the zirconia into the iron oxide. These include the contact area, the chemical composition of the counterfaces and, most importantly, the temperature at the interface. The temperature is primarily governed by sliding speed which explains why the wear rate was an order of magnitude higher for the tests at 0.24m/s compared to the test at 0.016 m/s.

The trend of the wear factor falling off at high loads, fig 6.24, can not be explained in terms of the surface appearance. For example, the amount of transfer did not change. The fall off in wear factor at the high loads is considered to be a result of the vibration. Microstructural evidence was presented in section 6.2.4 which showes that contact was intermittent. Under such conditions it would be expected that the time for reaction between the zirconia and metal oxide would be reduced so that the wear rate would be reduced.

The increase in wear factor with load up to 37.6 N/pin could not be explained by an increase in monoclinic content of the surface. The rise in wear factor was considered to most probably be a result of an increase in temperature with load, thereby increasing the reaction rate between zirconia and metal oxide.

The small amount of transformation provides an opportunity to estimate the surface temperature. No attempt was made to measure the M_s temperatures for these materials. However, values are available in the literature [318] which are presented in fig 6.79. Although the data presented is for Mg-PSZ materials, the observed relationship between toughness and temperature is the same for TZP and PSZ. The M_s temperature for the optimally aged material would have been very close to 113K, so that no transformation would have been expected above about 250ºC. For the present 2Y material, no transformation would be expected above about 400ºC. Even with an M_s of 218K, (i.e. highly

transformable zirconia) no increment to the toughness is achieved above 750°C. Thus, the presence of some surface transformation indicates that the temperatures must have been low, probably in the range 200-300°C.

The amount of grain 'pop-out' on the pin surfaces was very low. The question remains, therefore, as to why total break-up of the surface occurred for the TZP discs but only very little evidence of this mechanism was present on the pins. Two factors appear to explain this difference. Firstly, the adhesive forces were smaller for the hardened steel disc compared to the stainless steel pins. This was shown by the lower amounts of transfer. It is considered that the adhesive forces played a central role in promoting the surface break-up. Secondly, the surface temperature would have been higher for the pins, reducing the driving force for transformation. In other words, it was considered that more transformation may have taken place on the disc surface.

This latter observation provides important evidence as to whether the banding in the Mg-PSZ and intergranular fracture in the TZP discs was transformation driven or a result of cracking of what was essentially a brittle ceramic. As the temperature at the interface increased the toughness of the material decreased. Therefore, if the mechanism was simply one of brittle failure at the surface, greater break-up would have been expected in the pin surfaces because of the higher interfacial temparatures. However, the opposite was observed. Since increased transformation would be expected the lower the temperature, the present results strongly suggest that transformation initiated the banding in the Mg-PSZ and fracture in the TZP.

The mechanisms which produced the banding in the Mg-PSZ may therefore be summarised as follows. Transformation initiated microcracking such as that shown in fig 6.34. Repeated asperity contact gave microcrack coalescence. This occurred initially in those grains which presented a [100] orientation perpendicular to the surface and close to perpendicular to the sliding direction. The removal of material along this crack was facilitated by the adhesive forces promoted by the metal counterface. Thus, with a stainless steel counterface the adhesive forces were large and greater amounts of material could be removed to give broad bands. With a bearing steel counterface, the adhesive forces were lower so that little material was removed by this mechanism. The cracks therefore remained comparatively

sharp. Thus, it is clear that greater wear would result by this mechanism from a soft counterface and a more transformable ceramic. Even if only a small amount of transformation occurs the repeated contact increases the transformation with time to the point that break-up results.

With this mechanism, the volume dilation at the surface can be seen to be detrimental to sliding wear for the following reasons. Any volume increase raises up the region locally so that it can be swept away by the counterface asperities. In the bulk material the volume increase leads to local compressive stresses because of the matrix constraint. At a free surface this matrix constraint does not exist. During cooling from sintering and during grinding there is sufficient constraint to prevent surface break-up, leading to beneficial compressive stresses. However, in adhesive wear an additional plucking force exists, which leads to break-up of the surface. The mechanism is similar to the total break-up of TZP surfaces as a result of low temperature ageing. In this instance microcracking provides a mechanism for the loss of stabiliser to progress into the material from the surface. In abrasive wear, the adhesive forces are much weaker, and transformation is prevented at the extreme surface by gross dislocation flow.

With the TZP discs, the same mechanism of microcrack coalescence is considered to occur. The plucking forces, in conjunction with the lack of surface constraint, leads to removal of the surface grains. The extent of this was greater on the discs than would have been expected from the transformability of the material. This may have been because of the time dependent nature of wear, but also possibly as a result of destabilisation of the tetragonal by the chemical reaction with the iron oxide. However, these points are speculative.

The wear factors of the Mg-PSZ discs (taking account of the intermittent contact noted earlier) were similar to those of the pins. Had the wear mechanism been identical in both cases, a higher wear factor would have been expected on the pins because of the higher interfacial temperatures and because of the much harder counterface (see experimental details). This demonstrates that wear as a result of transformation was more damaging than that from the tribochemical mechanism.

The over-riding conclusions from this chapter are two fold. Firstly, transformation can be very damaging during sliding wear. The

extent of its importance depends on two factors, namely the temperature and the adhesive forces. High temperature reduces the driving force for transformation and therefore the importance of this mechanism. In the absence of adhesive forces a degree of transformation is generally considered to be beneficial. However, the stronger the adhesive forces the greater the break-up of the surface. Secondly, despite the high chemical inertness of zirconia, significant reaction of the ceramic occurs with the steel. This appears to take place even at slow sliding speed when the temperature rise is at a minimum.

CHAPTER 7

WEAR OF CERAMIC ON CERAMIC

7.1 INTRODUCTION

The following tests were carried out in order to investigate the wear mechanism for a ceramic on ceramic couple, where the adhesive forces should be much lower than the tests in chapters 5 and 6..

A commercial zirconia toughened alumina (ZTA) was used for all the tests described in this chapter. A zirconia disc was not employed because of its low thermal conductivity. The ZTA provided a fine grain size ceramic with reasonable toughness.

Four tests are described in this chapter. In the first test (section 7.2) the wear of 3Y pins at a load of 19 N/pin and 0.24 m/s was investigated. A second test was run for the same materials and counterface but at a speed of 0.016 m/s and load of 10 N/pin, in an attempt to reduce temperature rises at the interface.

Section 7.3 will report the findings of a test of ZTA pins against the ZTA disc. This test was conducted since the couple is known to provide low wear rates and has been characterised in the literature, providing a base line for the other tests. Moreover, the ZTA offered an alternative toughening mechanism to monolithic zirconia.

The last test to be reported employed 2.5Y-20vol% whisker composite pins. This material provided a further toughening mechanism and a higher hardness and thermal conductivity material than the conventional 2.5Y.

7.2 3Y-TZP AGAINST ZTA

7.2.1 Test at 0.24 m/s

7.2.1.1 Wear results

The test conditions and wear rates are given in table 7.1. The mass loss as a function of sliding distance is given in fig 7.1.
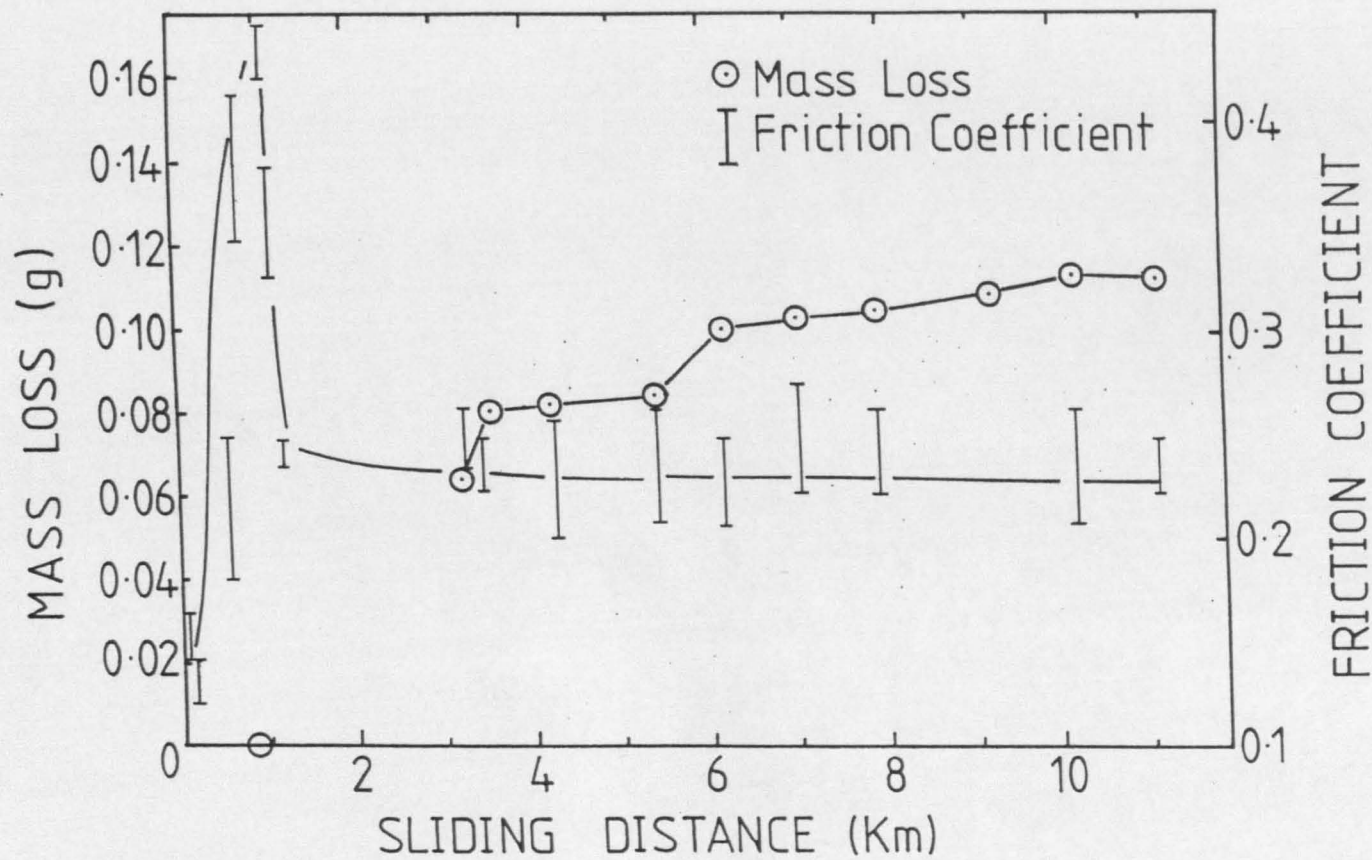
Fig. 7.1. Mass loss (average of three pins) and friction coefficient as a function of distance for the 3Y-TZP against ZTA at 0.24m/s.

During the first 1000m of sliding the test was quiet and smooth. No
visible wear scar could be seen on the disc and only a small contact
area was observed on the pins. The wear on the pin had led to a
smoothing of the surface, but the mass loss was too small to be
measured. The initial friction coefficient values were low at about
0.15 but rose steadily as the test proceeded.

TABLE 7.1

WEAR DATA FOR CERAMIC ON CERAMIC COUPLES

PIN MATERIAL	LOAD (N)	SLIDING SPEED (m/s)	TOTAL DIST (km)	FRICTION COEFFICIENT	WEAR FACTOR (mm^3/Nm)
3Y TZP	19	0.24	11.1	0.12-0.44 0.23 at end	8.9×10^{-4}
3Y TZP	10	0.016	102	0.18-0.39	2.4×10^{-7}
ZTA	19	0.24	159	0.13	3.0×10^{-8}
TZP/SiC	10	0.24	279	0.33	6.2×10^{-9} (n.b. re-transfer)

For the above, the ZTA disc wear was generally immeasurable except for
the 3Y-TZP test at 0.24m/s. In this instance disc wear was measured at
7.4×10^{-4} mm^3/Nm.

At some point over the next 2km of sliding, a massive increase in
wear occurred such that a deep wear scar was produced on the disc and
the pin had worn to give full face contact. The average pin wear
factor after a distance of 3km was very high at 2.5×10^{-4} mm^3/Nm. To

put this in perspective, about 10mm^3 per pin had been removed in the first 3km of sliding, most of which had probably been removed over a much shorter distance. This is $\approx 10^7$ times faster than would be expected for a typical cam follower in a car engine for example.

A rise in the friction coefficient to 0.44 occurred during this period although it was not clear whether it coincided with the catastrophic wear. However, after the initial transition, the friction coefficient was fairly stable at around 0.24. The transition was associated with a rapid increase in noise and vibration.

The wear factor over the remaining 8km of the test was an order of magnitude lower at 2.1×10^{-5} mm^3/Nm, although this is still very high, and can be compared to the wear rates of the stainless steel pins in chapter 5 and the zirconia pins in chapter 6. The noise and vibration occurred in short bursts although the sliding was generally smooth.

If the wear test was examined in the dark, faint orange/white sparks could be seen emanating from the interface indicating very high flash temperatures of at least 1400°C. This effect was similar to the sparking observed when cutting zirconia with a high speed diamond impregnated saw.

The wear track on the disc was found to be deep, with an estimated wear factor of 1.8×10^{-4} mm^3/Nm.

7.2.1.2 SEM and optical observations

A general view of the worn disc is given in fig 7.2. The wear track had worn by a fracture mechanism as shown in the detail in fig 7.3. The majority of the fracture was intergranular although numerous examples of transgranular fracture could be found. The actual contact surface appeared to have been provided by smooth regions which were standing proud of the fracture surface, such as the feature in the centre of fig 7.2. These regions were zirconia rich and appeared to consist of compacted wear debris.

An example of the surface of the worn pin is given in fig 7.4. On each of the pins the surface could be divided into two distinct regions. The upper right hand side was extremely smooth and visually, highly reflective, as shown by the optical micrograph in fig 7.5. The lower left region was rough and partly consisted of agglomerated wear debris, fig 7.6.

EDS analysis indicated that the smooth region, fig 7.5, was predominantly zirconia, although some alumina could be detected.
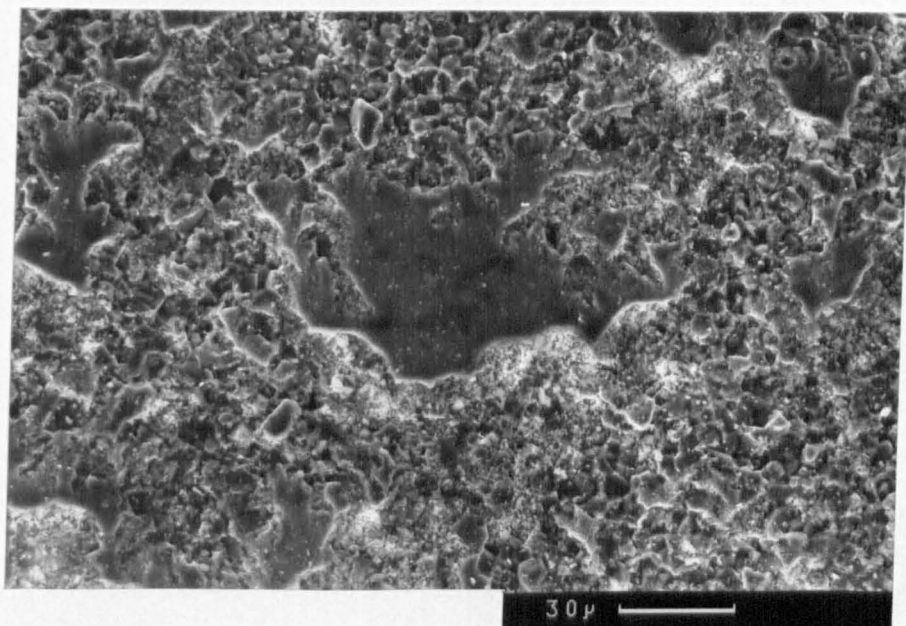
S.D.↑

Fig. 7.2. SEM micrograph of the ZTA disc. The central feature is compacted wear debris (mainly zirconia). The remainder is a fractured wear surface.
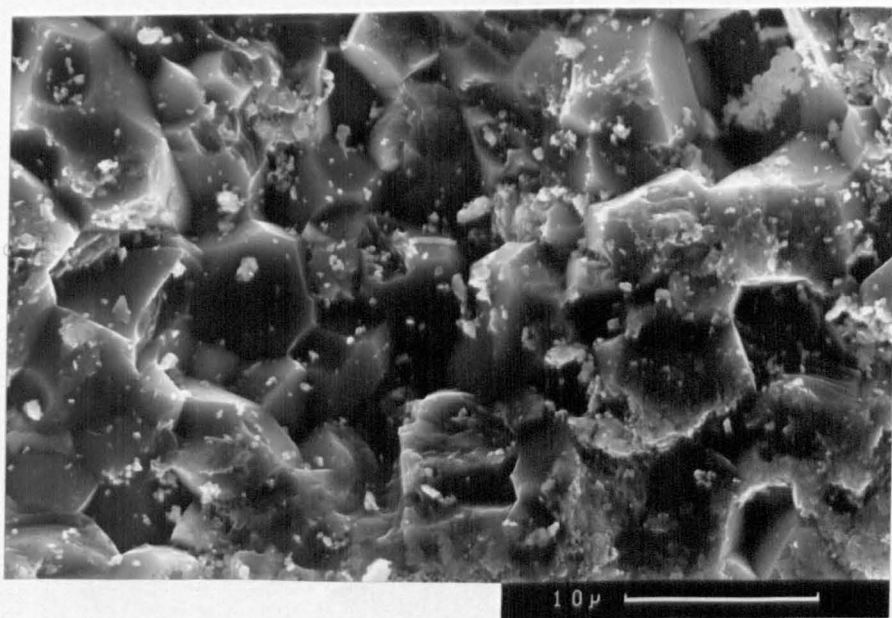
S.D.↑

Fig. 7.3. Detail of the fracture surface. The majority was intergranular, but with some transgranular fracture present.

300μ
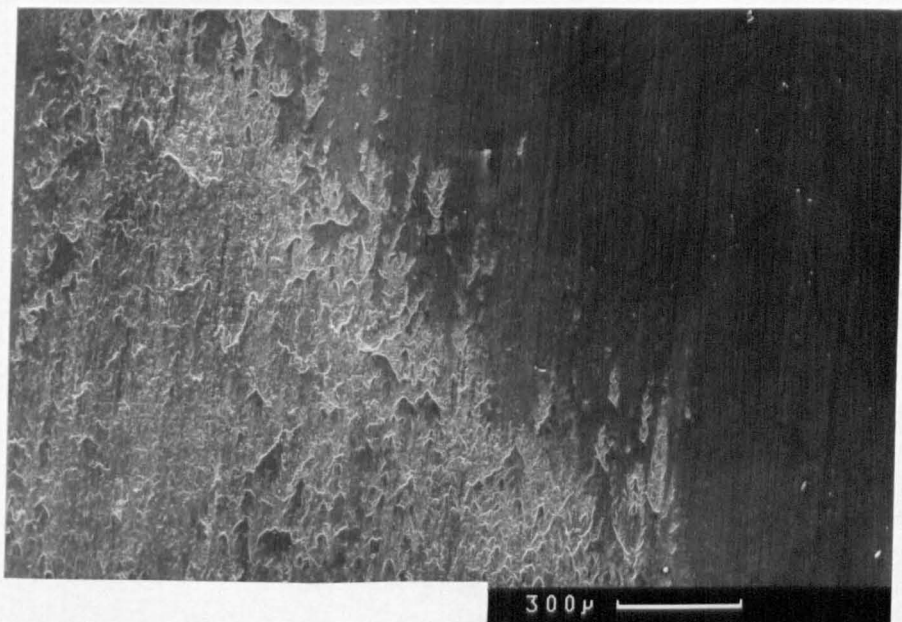
S.D.↑

Fig. 7.4. SEM micrograph of the worn TZP pin surface. The upper right region was smooth and formed the main contact area. Only intermittent contact occurred in the lower right region.

20μm
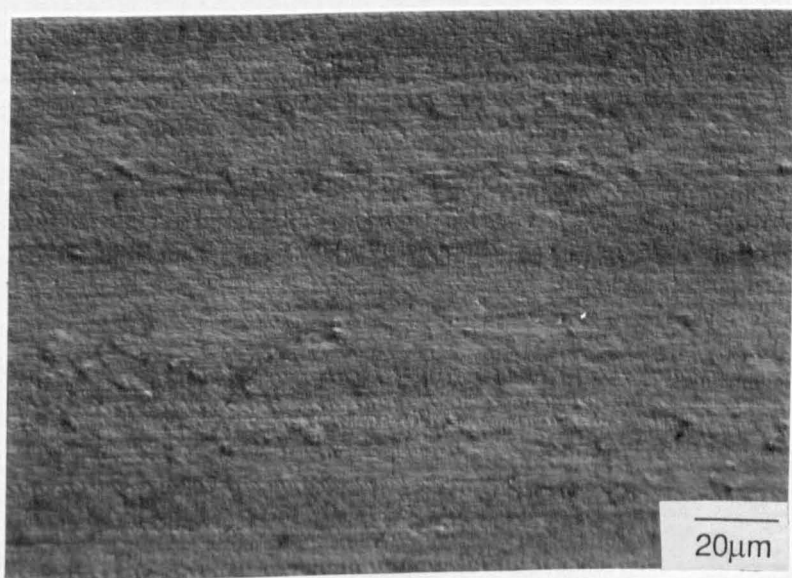
S.D.→

Fig. 7.5. Optical micrograph (Nomarski) of the upper right region in fig 7.6. There was no evidence of grain relief, but micro-abrasion had occurred.
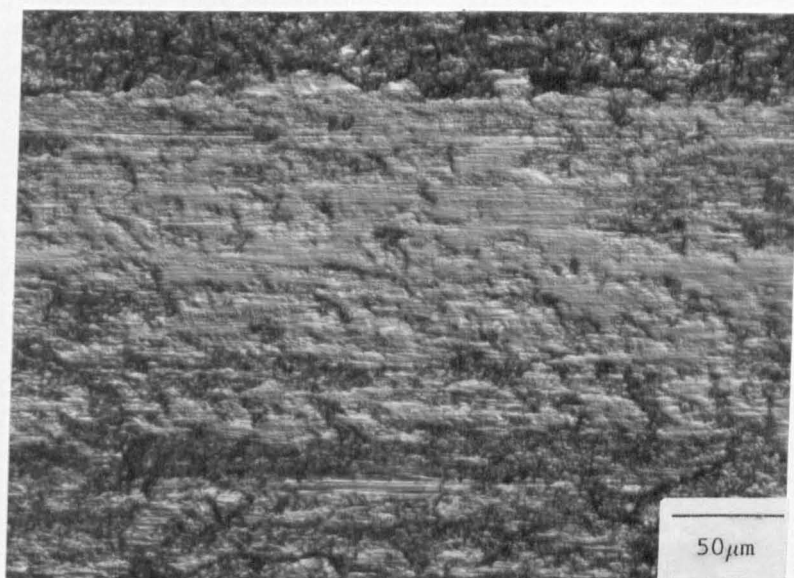
S.D.←

Fig. 7.6. Optical micrograph (Nomarski) of a contact region within the lower left portion of fig 7.4.
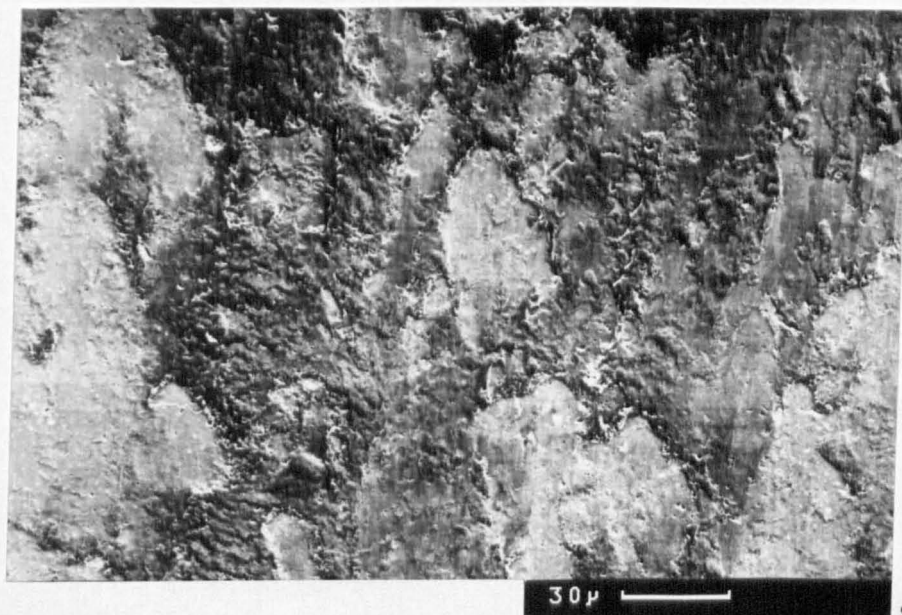
S.D.↑

Fig. 7.7. BEI micrograph of a similar region to fig 7.6. The light areas were zirconia rich whilst the dark areas contained a high alumina content. Mixing of the two had occurred on a finer scale than could be resolved in the SEM.
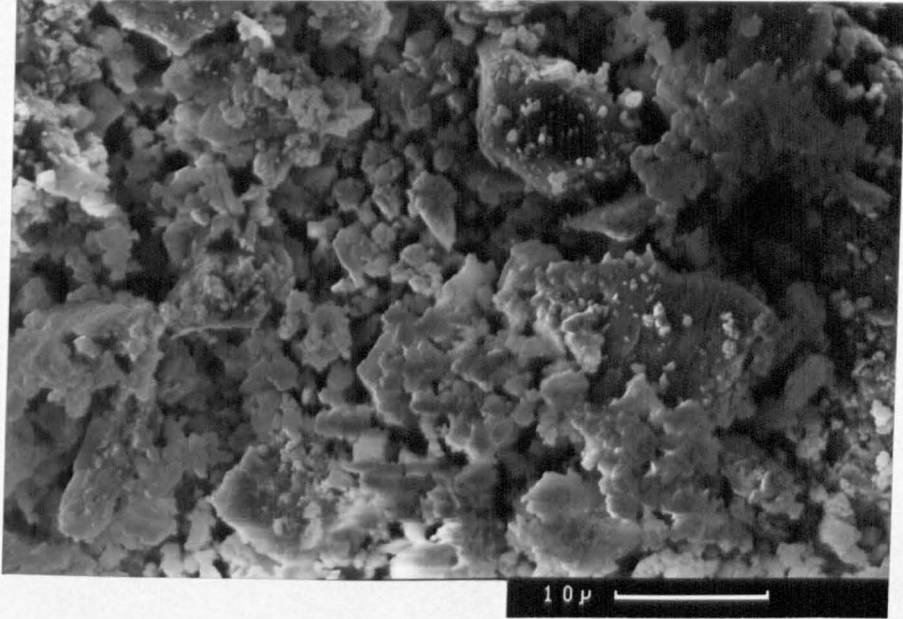
Fig. 7.8. SEM micrograph of the wear debris, which exhibited a wide size distribution.
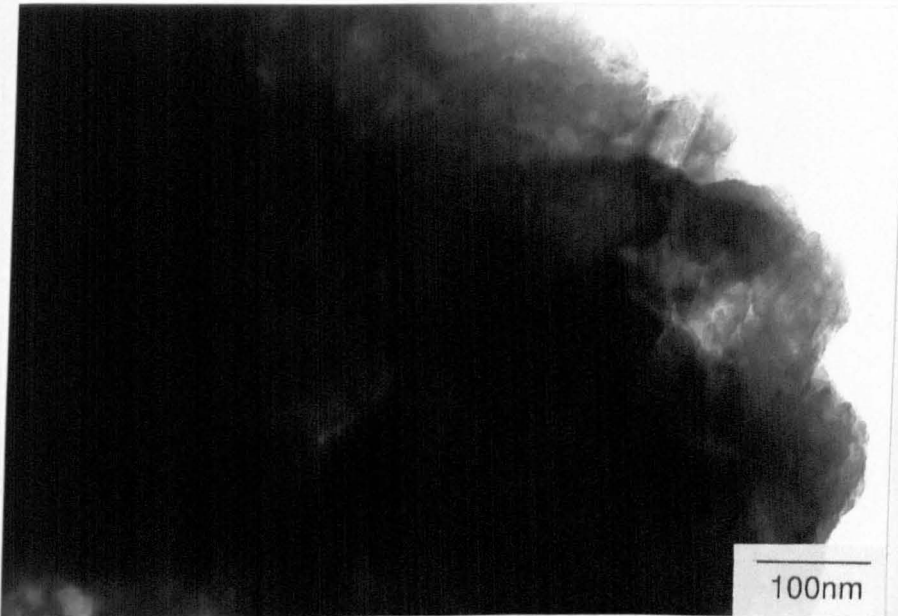
Fig. 7.9. TEM micrograph of the amorphous wear debris, which was a mixture of zirconia and alumina. However, the particles were not rounded, which would have been expected had they originally been molten.
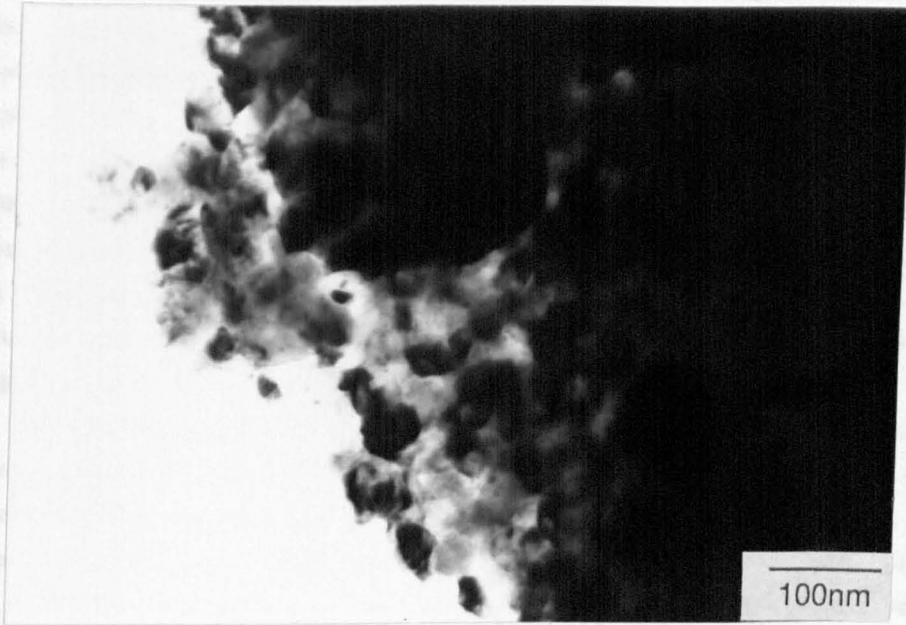
Fig. 7.10. TEM micrograph of a typical crystalline debris particle. The grain size had been reduced by an order of magnitude from the starting material and the tetragonal zirconia contained alumina in solid solution.

Fig. 7.11. XRD traces from polished 3Y-TZP, the worn pin and the wear debris. Note the line broadening and the absence of monoclinic.

Evidence of chatter can be seen in this micrograph. There was no grain relief and the surface appeared to have been plastically smeared. Contact within the rougher region was more localised. The surface contained an intimate mixture of zirconia and alumina as shown by the back-scattered electron image in fig 7.7. The mixing of the two ceramics had occurred on a finer scale than could be r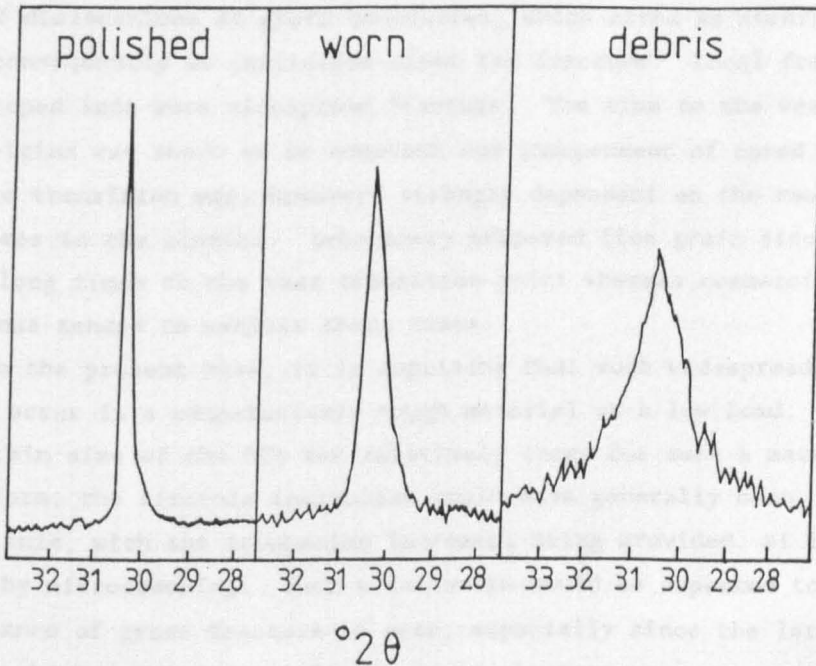esolved in the SEM. Many of the areas appeared to be piled up wear debris, although contact had clearly occurred along smoother grooves such as that shown in fig 7.6. Note in this micrograph the micro-abrasive grooves which show evidence of chatter. Contact within the rougher region also appears to have occurred in the plastic regime.

The manner in which smooth sliding was promoted by the contact of the zirconia pin on zirconia/ alumina compacted debris suggests that the catastrophic wear was initiated by fracture in the ZTA disc. The rapid rise in wear was presumably associated with the abrasive action of the fractured alumina disc. As the debris became broken up and compacted into the disc surface the sliding gradually became smoother.

The reasons for the incubation period for the transition in wear rate are not clear. However, the mechanism suggested by Lawn [186], who reported similar observations in alumina, appears probable. Lawn [186] suggested that the incubation period was associated with the pile up of dislocations at grain boundaries, which acted as stress raisers and consequently as initiation sites for fracture. Local fracture then developed into more widespread fracture. The time to the wear transition was shown to be constant and independent of speed. The time to the transition was, however, strongly dependent on the residual stresses in the alumina. Laboratory prepared fine grain sized aluminas gave long times to the wear transition point whereas commercial aluminas tended to exhibit short times.

In the present case, it is suprising that such widespread fracture could occur in a comparatively tough material at a low load. However, the grain size of the ZTA was relatively large for such a material. Therefore, the zirconia inclusions would have generally been monoclinic, with the toughening increment being provided, at least in part, by microcracking. Such a mechanism would be expected to increase the chance of gross fracture in wear, especially since the larger grain size would have given significant residual stresses.

7.2.1.3 Wear Debris

A general view of the wear debris is given in fig 7.8. The debris varied from large slab like particles to fine rounded fragments. Several examples were found of fractured alumina particles, but these appeared to occupy a smaller volume fraction than would have been expected from the examination of the disc surface. Therefore, the fractured particles had undergone attrition and mixing with the zirconia.

Microanalysis of the debris suggested that a substantial proportion of the particles contained a mixture of alumina and zirconia, with a higher proportion of the latter, on a finer scale than could be resolved in the SEM.

TEM examination of the debris confirmed the presence of several fractured alumina particles. Many of these were too thick to be electron transparent but evidence was found of twinning and of occasional dislocations. The remainder of the debris fell into two broad categories. The first category was amorphous, fig 7.9, and contained variable amounts of zirconia and alumina, although always a substantial proportion of the latter. The second category was microcrystalline, fig 7.10, and was always fully tetragonal with a crystallite size in the range 5-50nm. This type of wear debris contained anything from 0 to about 20% alumina in solid solution. The alumina had distorted the tetragonal lattice, with a decrease in lattice spacing as the percentage of alumina increased. No evidence was found for any monoclinic in the wear debris, rather it was either amorphous or tetragonal.

The microcrystalline tetragonal wear debris contained an order of magnitude smaller grain size compared to the starting material, indicating that some form of recrystallisation had occurred. The microstructure was incompatible with reagglomeration of very fine wear debris, suggesting that high interfacial temperatures had driven recrystallisation. There are no previous reports in the literature on the solubility of alumina in tetragonal zirconia at room temperature. Alumina and zirconia are completely miscible in the liquid state but separate into pure alumina and pure zirconia via a eutectic decomposition at 1845°C [319]. However, Alper & McNally [320] found 7% alumina in solid solution at 1845°C, but the solubility limit fell to negligible levels on cooling. Rapid cooling could account for the solid solubility extension to 7%, but an additional mechanism is

required to account for the higher levels. This will be discussed further in the light of the cross sectional TEM results.

7.2.1.4. Transmission Electron Microscopy and X-ray Results

The X-ray traces of the (111) tetragonal plane are given in fig 7.11 for the polished surface, worn surface and wear debris. No monoclinic was present in either the worn surface or the debris. Considerable line broadening was measured from the wear debris and to a lesser extent in the worn surface. This was attributed both to the fine crystallite size and the residual stresses.
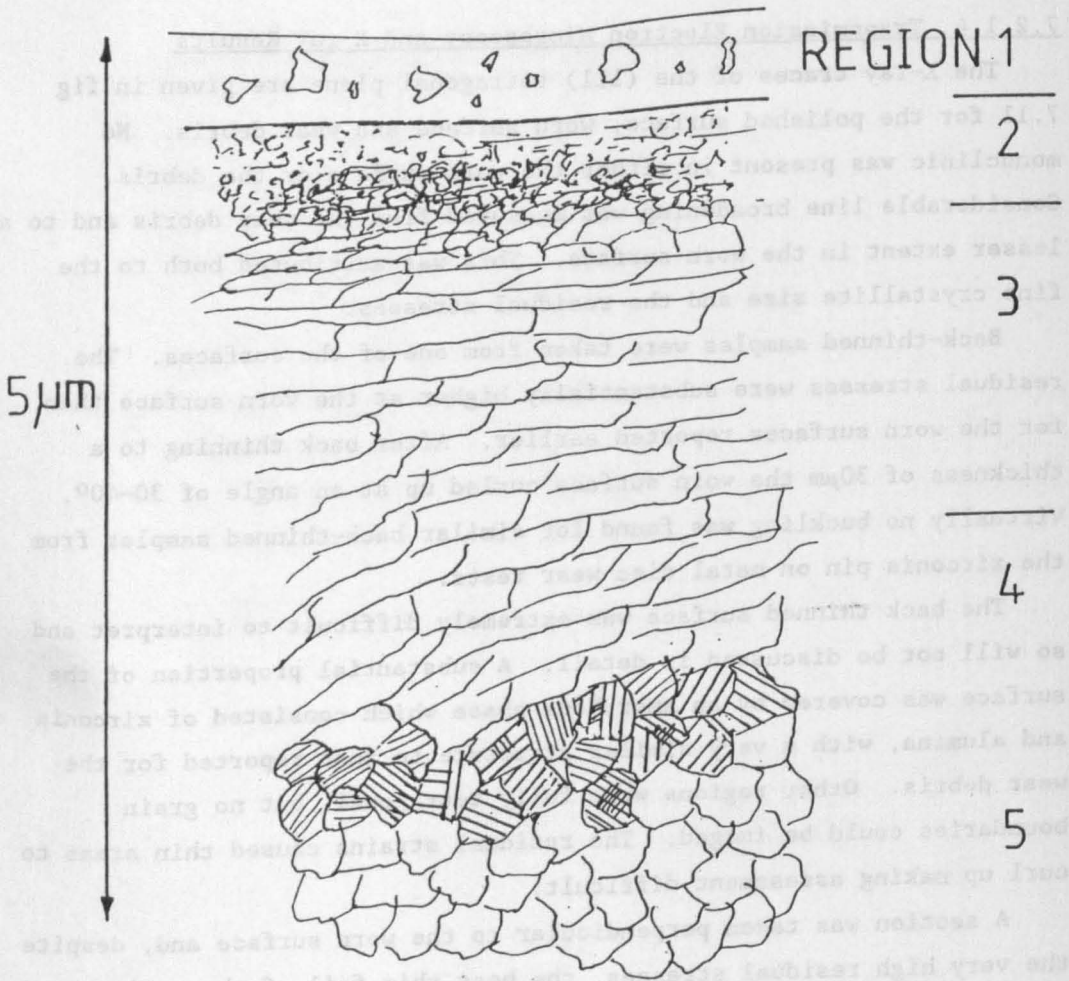
Back-thinned samples were taken from one of the surfaces. The residual stresses were substantially higher at the worn surface than for the worn surfaces reported earlier. After back thinning to a thickness of $30\mu m$ the worn surface curled up at an angle of 30-40°. Virtually no buckling was found for similar back-thinned samples from the zirconia pin on metal disc wear tests.

The back thinned surface was extremely difficult to interpret and so will not be discussed in detail. A substantial proportion of the surface was covered by an amorphous phase which consisted of zirconia and alumina, with a very similar structure to that reported for the wear debris. Other regions were fully tetragonal, but no grain boundaries could be imaged. The residual strains caused thin areas to curl up making assessment difficult.

A section was taken perpendicular to the worn surface and, despite the very high residual stresses, the best thin foil of the entire study was obtained. Even so, the foil tore in several places which gave problems of overlapping material and foil charging.

A general view of the worn surface is given in fig 7.12, along with a diagramatic representation of the surface, divided into sections. The structural changes which had occurred were dramatic, and no such microstructure has been reported in the literature. The following will describe the various features starting at the surface and progressing inwards. The extent of structural changes could in no way be appreciated from SEM observations or back thinned TEM foils, demonstrating the substantial advantages of foil preparation perpendicular to the worn surface.

The outermost surface, (region 1) fig 7.13, was frequently, but not always, covered with an amorphous layer which contained both aluminium ions and zirconium ions mixed on an atomic scale. In addition, the

REGION 1

2

3

4

5

5 μm

S.D. ⟶

SURFACE

REGION 1

REGION 2

REGION 3

REGION 4

200nm

S.D.→
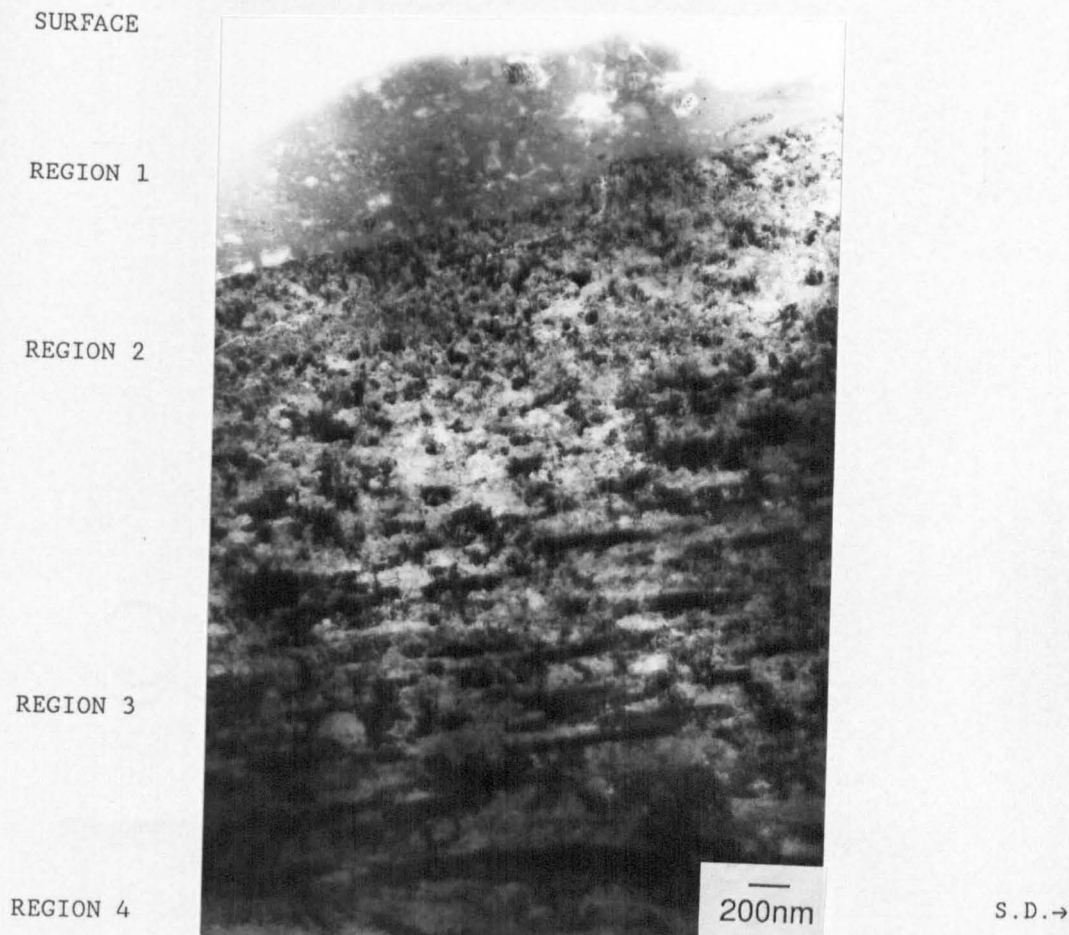
Fig. 7.12. Cross sectional TEM of the surface, with a diagramatic
representation on the opposite page. The outer region (1) consisted of
a mixture of an amorphous phase and fractured alumina particles. Note
the sharp boundary between this region and the crystalline zirconia
substrate. The outer crystalline region (2) exhibits an order of
magnitude reduction in grain size from the starting material. Region 3
consisted of heavily elongated tetragonal grains, with the grain shape
change indicating a strain of 1.7. Below this, region 4, some grain
shape change had occurred, but the structure remained tetragonal. The
first monoclinic phase to be detected, region 5, occurred at a depth of
$5 \mu m$.
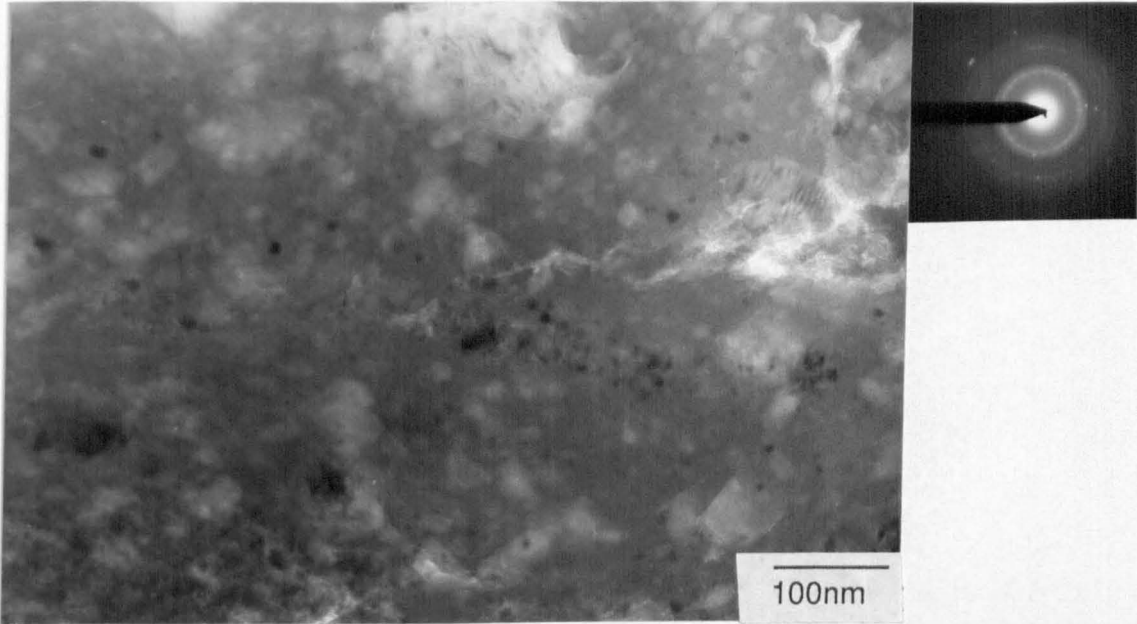
Fig. 7.13. Detail of the outer region (1), which consisted of a
mixture of fractured alumina particles and an amorphous phase. The
amorphous phase contained large amounts of zirconia and alumina. Some
microcracking did occur, but this was rare.
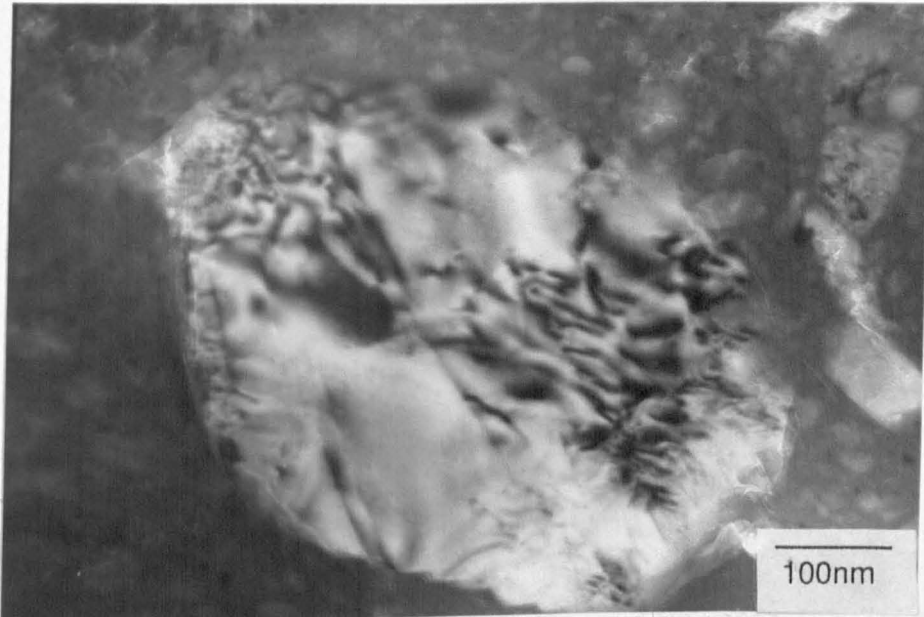
Fig. 7.14. Detail of a large fractured alumina particle. Dislocations
and twins were found within the fractured particles.

S.D. ←

Fig. 7.15. Detail of the transition between regions 1 and 2. Note the extensive microcracking in the crystalline region and the lower portion of region 1. Some areas of region 2 were more equiaxed than this example. The average grain size in this region was about 50nm, representing an order of magnitude reduction from the starting material. Note also, the small dark particles in region 1 close to the interface. This could represent a transition from the crystalline to amorphous state. Alternatively, these could be tetragonal particles precipitated from the amorphous phase on cooling at the end of the wear test.
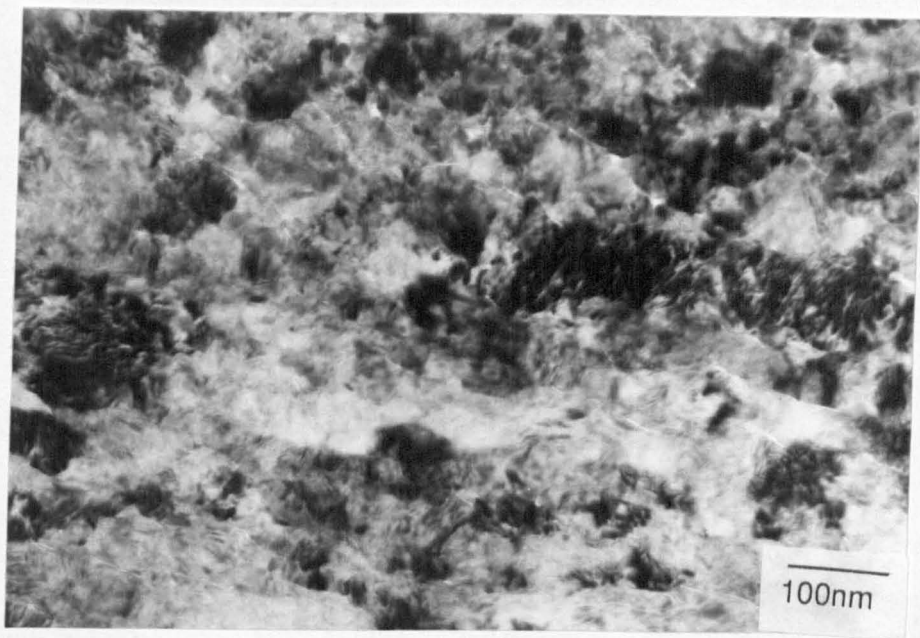
S.D.→

Fig. 7.16. Transition between regions 2 and 3. The high levels of residual strain made interpretation difficult. However, grain elongation is apparent. Extensive microcracking can be seen, which was apparently both inter and intragranular. Note the presence of Moiré fringes.
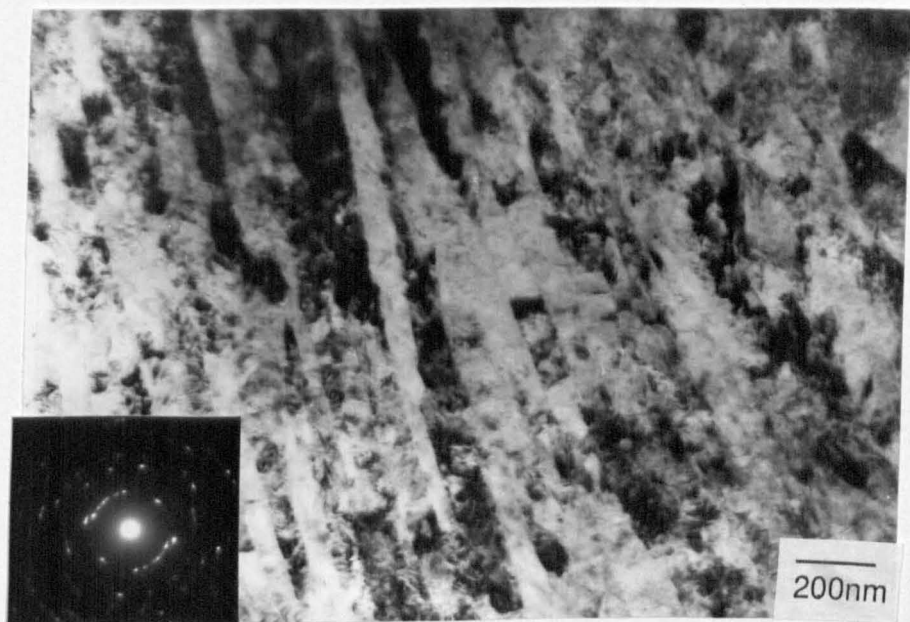
S.D.↑

Fig. 7.17. Detail of region 3 showing the considerable elongation. The structure was fully tetragonal, despite the largest dimension being up to 2μm and the presence of dislocations.

100nm
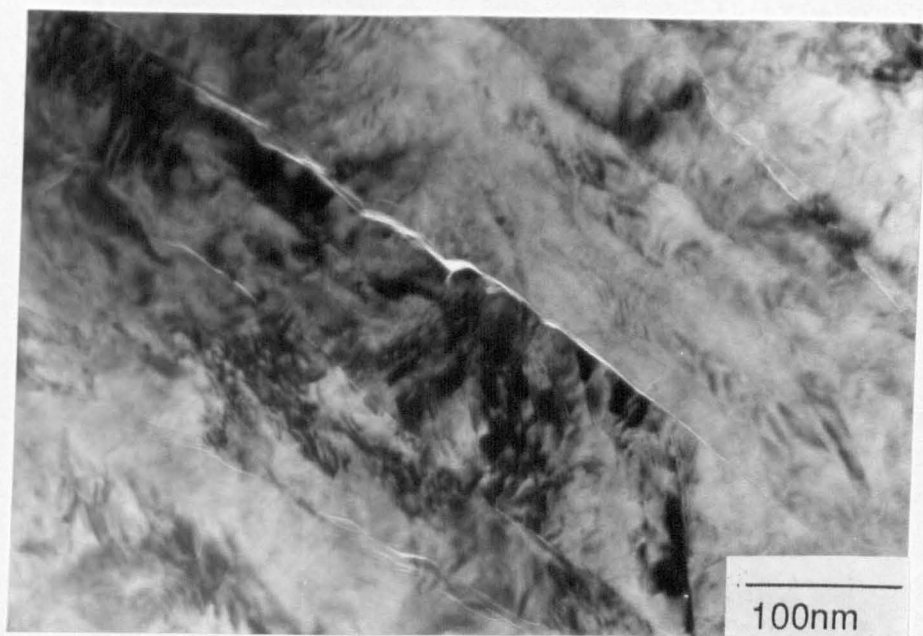
S.D.

Fig 7.18. Detail of the grain boundary microcracking. The grain edges frequently undulated in this manner.

100nm

S.D.↓
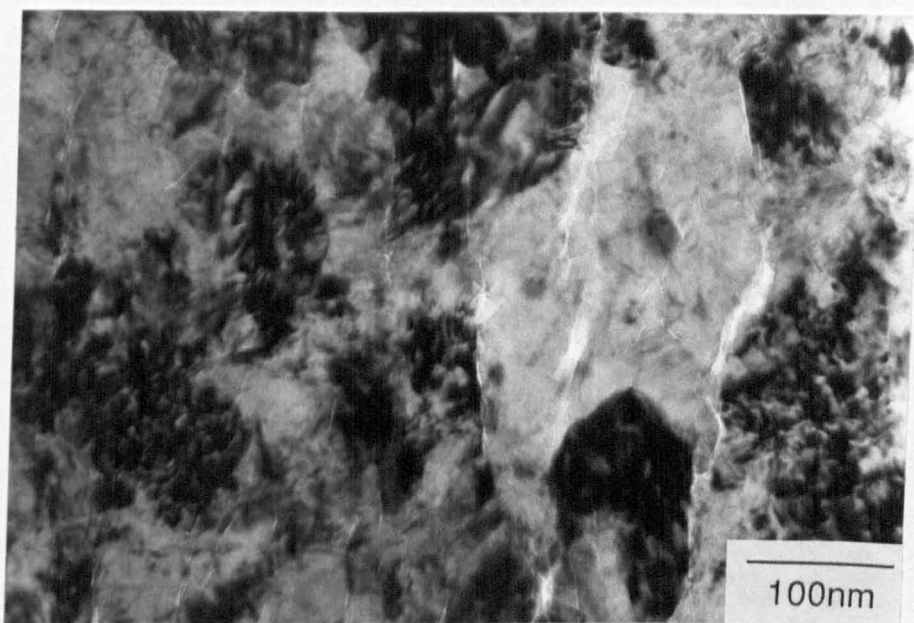
Fig. 7.19. A further detail from region 3 showing extensive intragranular microcracking (right hand grain) which was believed to have been responsible for the reduction in grain size.
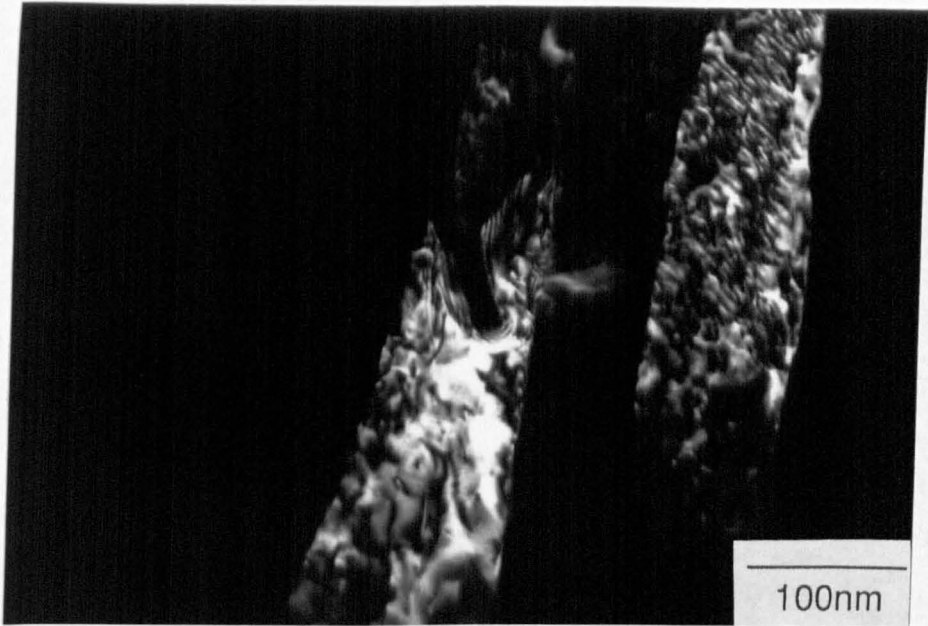
S.D. ↑

Fig. 7.20. Dark field micrograph showing the internal grain
structure. Some dislocation lines were present, but the overall
density was low given the grain shape change which had occurred.

S.D. ↑

Fig.7.21. Detail of the transition from region 3 to 4. Less
microcracking had occurred. The very high strain contrast made it
difficult to establish the dislocation density.

100nm   S.D.↓
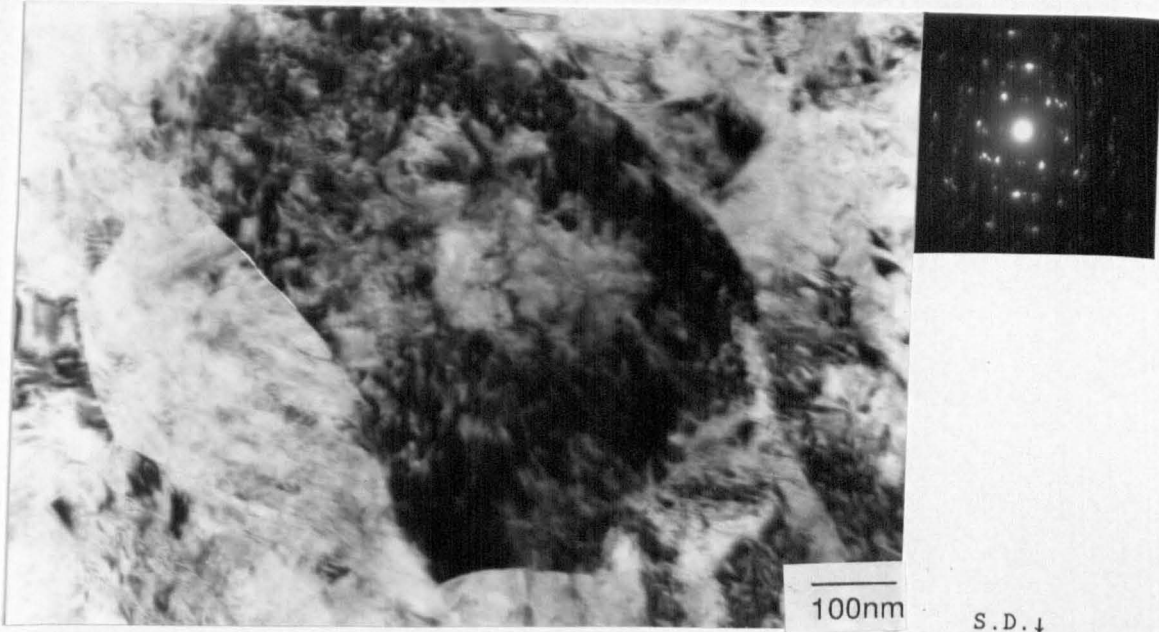
Fig. 7.22. Detail of a grain within region 4. Occasional dislocations could be identified, and some of the grains had partly transformed to the monoclinic state.

200nm   S.D.→
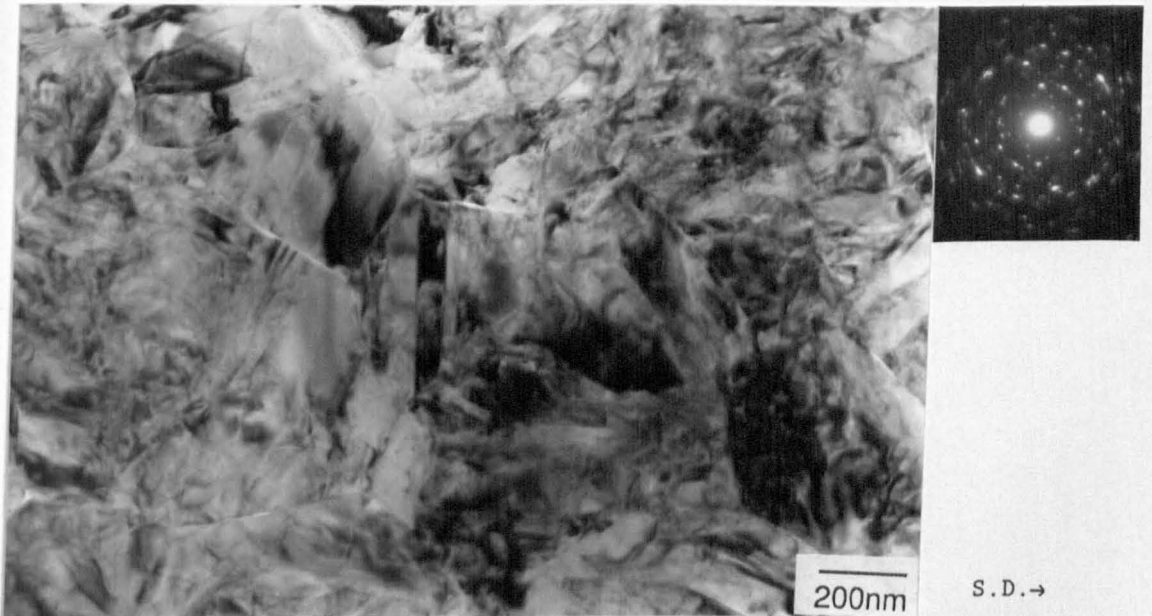
Fig. 7.23. Detail of region 5 which was fully monoclinic. No grain shape change had occurred at this depth, but extensive microcracking at the grain boundaries due to the t → m transformation was evident.

layer contained numerous small fractured particles of alumina. Some of these fragments were quite large, fig 7.14, whilst many were extremely small, down to about 5nm. The layer contained some microcracking but was generally dense and adherent to the subsurface. No individual particles of zirconia could be found in this layer.

The transition from the amorphous layer to the zirconia substrate is shown in fig 7.15. In some regions there was no amorphous layer and, therefore, the lower portion of fig 7.15 would represent the extreme surface. The structure of this region consisted of fine tetragonal grains, typically <50nm in diameter with heavily microcracked grain boundaries. The structure tended to vary locally, with some areas exhibiting slightly elongated grains whilst others had coarser or finer crystallite sizes. It was remarkable that the thin foil retained such integrity, and a considerable shelf life, even though it was so heavily microcracked.

Moving further away from the surface to a depth of about 700nm the crystallites became progressively more elongated, fig 7.16. However, the internal structure of the grains was obscured by strain contrast and was difficult to resolve. The grains had become heavily elongated by a depth of 1μm (region 3), fig 7.17, with extensive microcracking along the grain boundaries. At this depth, grains were aligned parallel to the surface.

Detail of some of the elongated grains is given in fig 7.18. The grain boundaries were rarely straight, showing numerous undulations. A further example of severe undulations is given in fig 7.19, where there was also evidence of intra-granular microcracking. The structure of the grains is illustrated in fig 7.20, showing that the dislocation density was low although some dislocation lines could be identified. No clear evidence of subgrain formation or monoclinic was found at this depth.

Fig 7.21 was taken from a depth of 3-4μm below the worn surface, where the grains were less elongated and heavily curved (transition from region 3 to 4). The grain boundaries were generally found to be smooth and the amount of microcracking was significantly less. The structure was still fully tetragonal, but increased residual strain tended to obscure the image.

At a depth of 4-5μm (region 4) the grain shape was distorted in the direction of sliding, but with less elongation, fig 7.22. Occasional dislocations could be found but these were obscured by numerous strain

contours. Again, no evidence of subgrain boundaries was present. The first monoclinic was detected within these grains at a depth of $4.5\mu m$ from the surface. Some of the grain boundary microcracking, such as that in fig 7.22, was probably derived from the transformation rather than the deformation mechanism.

Over a fairly short distance of one or two grain widths the structure became equiaxed and almost entirely monoclinic, fig 7.23 (region 5). The layer of monoclinic extended up to $10\mu m$ from the surface before the fully tetragonal parent structure was found.

The dramatic changes in microstructure described above extended to $10\mu m$ from the original surface, of which $5\mu m$ had undergone sufficient deformation that grain shape change had occurred. The change in microstructure described reflects the fall in temperature and stress with distance from the interface.

At the extreme surface, region 1, flash temperatures were high enough to give complete mixing of the zirconia and alumina on an atomic scale, leading to an amorphous mixture. Since complete miscibility is found in the liquid state but the two phases only show limited solubility in the solid state at 1845°C, and none at room temperature, this observation suggests that some melting occurred at the interface. Similar amorphous mixtures of alumina and zirconia have been found in rapidly solidified melts by Kalonji et al [321]. The amorphous phase was obtained at both the eutectic composition (42wt% zirconia) and an off eutectic composition (25wt% zirconia). The hammer and anvil technique used by these authors produced a very rapid freezing rate, (estimated at 5 cm/s, but the cooling rate was not specified). Even so, a wide range of microstructures, in addition to the amorphous material, were produced, including the equilibrium eutectic decomposition and fine precipitation of zirconia from the alumina. Therefore, even at the high cooling rates, some equilibrium structures were produced.

In the present study no evidence of any eutectic decomposition was found. The interfacial region between the amorphous phase and the crystalline region 2, could have been interpreted as having been formed by precipitation of zirconia from the amorphous mixture. However, since the surface was clearly at an elevated temperature to a significant depth, cooling rates should have been slow enough to allow some form of equilibrium phase change to occur. Moreover, had the surface been liquid some of the debris might well have taken on a

spherical structure as a result of surface tension rather than the slab-like appearance observed.

The presence of an amorphous phase is therefore difficult to explain. An alternative mechanism to surface melting could be that the high diffusion rates at the high temperatures, coupled with widespread dislocation flow, had led to some alumina being incorporated into solid solution. As the quantity of alumina increased the tetragonal structure would have become progressively distorted. Phase separation was prevented by the continued disruption of the structure by dislocation flow. Ultimately, the increase in alumina content was too great for the crystalline phase to sustain, such that on cooling crystallinity was lost. The cooling rates must have been comparatively rapid to prevent phase separation both in the amorphous material and the distorted tetragonal zirconia. However, such a mechanism is impossible to prove and a mixture of the distorted crystalline tetragonal and amorphous phases would have been expected if this mechanism was occurring, but was not found. The generally sharp interface between regions 1 and 2 certainly suggests that melting had taken place.

The shape changes which had occurred in the tetragonal zirconia below the chemically mixed layer (i.e. region 2) were dramatic and showed many similarities to the deformation of metals. The fine equiaxed layer at the surface had undergone at least an order of magnitude reduction in grain size. This suggests that recrystallisation had occurred, presumably driven by a high dislocation density. In metallic systems recrystallisation results from the passage through the material of a series of high angle grain boundaries, consuming the dislocation structures and resulting in strain free grains. During hot working of metals where dynamic recovery is limited (eg austenitic steels, Ni, Cu) a dynamic recrystallisation process can occur because the dislocation tangles provide sufficient stored energy. A balance is obtained between work hardening mechanisms such as dislocation interaction and the formation of new dislocation free grains. The relative quantities of each depend on the strain rate and temperature. Dynamic recrystallisation is a time dependent process, so that if the strain rate is increased, work hardening increasingly prevails over recrystallisation.

Dislocation flow and interaction is, therefore, a pre-requisite for recrystallisation. In the present case it is considered that the

mechanism of formation of the fine grains took place during sliding at
elevated temperature rather than by static recrystallisation during
subsequent cooling, because of the considerable grain boundary
microcracking. The microcracking indicates that the fine grained layer
had been deformed extensively by grain boundary sliding after its
formation.

Some evidence of dislocation tangles were found which could have
provided sufficient stored energy to drive the recrystallisation
process. However, one problem exists with this scenario. Substantial
shape change was accommodated in the tetragonal grains at a greater
depth. Such a shape change was a result of dislocation flow (as
discussed below). Since the temperature was lower in this region, why
were substantial numbers of dislocation tangles not observed? If
recovery processes were sufficiently easy to give dislocation
annihilation, so that only a low dislocation density was left, why was
there sufficient driving force at higher temperature to drive dynamic
recrystallisation? And if so, why was there no evidence of subgrain
formation. It would be expected that the dislocation back stresses
were sufficiently high to drive the recovery processes, thereby
reducing the driving force for recrystallisation. One possible
explanation for the finer grain size at the surface is that the
increase in strain rate as the surface was approached had led to a
substantial increase in work hardening which had offset the temperature
increase.

An alternative explanation is that the intra-granular microcracking
increased as the surface was approached to such an extent that an
effective grain multiplication mechanism took place. The grain
thickness was reduced to about 50nm at a depth of 700-1000nm (region
3). Fig 7.19 clearly shows extensive microcracking within the grains.
As this material was progressively deformed a point would have been
reached where such microcracks divided the grain in two. Since no
texturing was found in the equiaxed surface region it would appear that
random grain rotation would have been necessary as a result of grain
boundary sliding. Certainly, extensive grain boundary sliding had
apparently occurred in this region.

The microcracking mechanism cannot explain the entire
microstructural change in region 2. In the upper portion of fig 7.15
the crystallite size was further reduced from 50nm to around 5-10nm in
the transition region from the crystalline to amorphous phase (region

1). Moreover, the crystalline portion of the wear debris contained equiaxed grains with no grain boundary cracking and grain sizes down to 5nm. Two possible mechanisms can be proposed to explain this behaviour. Firstly, the strain rate at the surface could have been high enough to give sufficient dislocation interaction to provide numerous nuclei for dynamic recrystallisation. A scenario can be considered whereby the high strain rate gave work hardening during asperity contact and recrystallisation took place statically in between the asperity contacts. Alternatively, these grains could have resulted from precipitation from a supersaturated non equilibrium amorphous phase formed on cooling.

In region 3 (1–3μm below the surface) substantial grain elongation had taken place. The grain dimensions had changed from an average diameter of 600nm, to about 50nm wide by 1.5μm long. This change in aspect ratio corresponds to an equivalent true strain of 1.7 (reduction in thickness of 82%) or a shear strain of approximately 8. A grain shape change can be accommodated by dislocation flow or diffusional creep. The latter could not have accounted for such a shape change at the strain rates and deformation times. To amplify this point the linear wear rate can be established. A total of 0.1 grams/pin was lost over a period of 11km. Thus, the wear volume of 16.6 mm^3 occurred over a period of 10.4 hrs. Such a wear volume corresponds to a linear loss of material of 850μm, which is equivalent to a very high rate of 1.3μm per second. Since the microstructure changed from the undeformed state to the highest elongation recorded in region 3, over a distance of 3–5μm, the shape changes were accommodated over a period of only a few seconds. Clearly such an extensive shape change in such a small time could only be accommodated by dislocation flow.

The grain boundary microcracking indicates that extensive grain boundary sliding also occurred. Therefore, the strain noted above for region 3 could well have been considerably higher than those suggested by the shape change alone.

It is interesting to consider why such a shape change was accommodated without any internal evidence of work hardening. In metallic systems the grains are immediately divided into subgrains/ cells or show a uniform dislocation density (the latter usually indicates the imminent onset of an alternative deformation mechanism such as twinning). The structure is invariably divided into sub-units dictated by the relative importance of the competing mechanisms of work

hardening and recovery. This is equally true at elevated temperature where slow recovery kinetics lead to recrystallisation, whilst rapid recovery leads to subgrain formation. In the present case the absence of any evidence of sub-unit formation suggests that only limited work hardening occurred. This argument is similar to that in chapter 6 regarding the mechanism of abrasive groove formation. Thus, it would appear that slip distances were too small to allow interaction on the number of slip systems operating. Alternatively, the driving force for recovery processes might have been sufficiently high to give extensive dislocation annihilation. This would reflect the high energy associated with dislocations in ceramics compared to metals.

Extensive grain boundary sliding was considered to have occurred as indicated by the widespread microcracking. In the last decade several studies have shown that polycrystalline ceramics with fine grain sizes (below a few micrometers) can be deformed to very large strains without rupture at elevated temperature [322,323]. The mechanisms are not fully understood, but grain boundary sliding is believed to be dominant with dislocation flow providing only a minor contribution, if any at all. Systems are not restricted to single phase materials, as demonstrated by Japanese workers, who reported superplasticity in a zirconia-alumina composite [324].

The majority of work reported in the literature has concentrated on the 3Y-TZP system. Deformation of up to 100% has been achieved in compression in the temperature range 1200-1500°C at strain rates of the order of 10^{-6} -10^{-3} s^{-1} [322,324,325]. Evidence for grain boundary sliding comes from the strong grain size dependency of the flow stress and the strain rate [324,325]. An increase in grain size leads to an increase in flow stress. Thus, it is important that the material does not undergo any significant grain growth during deformation. Duclos et al. [322] found no measurable grain growth during the deformation of a 3Y-TZP in compression, whereas Wakai et al. [324] detected a moderate grain growth during axial tensile tests. It is probable, however, that the temperature was higher in the latter tests. These authors also demonstrated that the rate of grain growth was higher under dynamic deformation than for control samples, an observation which is well known for metals [322]. In the present study, grain growth did not appear to play any role because of the short time over which the microstructure was formed and remained in the surface before being worn away.

Ceria-TZPs have been examined by Wakai et al. [324] and have been shown to display strain hardening during deformation, in contrast to the Y-TZPs. Significant grain growth occurred during the test which provided the increase in flow stress. Indeed, the grain growth in the Ce-TZP prohibited superplastic forming. Under conditions of constant grain size, strain rate and temperature, the flow stress for the Ce-TZP was found to be twice that for the Y-TZP, indicating a fundamental difference in the defect type, although the behaviour could be partly attributable to cubic phase in the Y-TZP.

Lankford et al. [326] have demonstrated that superplastic like behaviour can occur at temperatures as low as 700°C. During compression tests of a 3Y-TZP, shear bands were observed which ran at about 45° to the compression axis. Grain rotation was evident within these bands, with extensive microvoiding at the grain boundaries. Microvoids coalesced to give much larger microcracks, especially at the intersection of two shear bands, which acted as the sites for eventual failure. The superplastic deformation was presumably assisted in this case by the thick grain boundary glass phase observed by these authors.

The extent of microvoiding developed during superplastic deformation has been shown to be temperature dependent. Duclos et al. [322] have demonstrated that microvoiding can be avoided at 1330°C at low strain rates (10^{-5} s^{-1}), but that an increase in strain rate or a decrease in temperature led to an overall loss in material density. Thus, the excessive microvoiding found by Lankford et al. [326] was most probably a result of the slow diffusion kinetics (which is cation controlled) at 700°C.

The tests of Duclos et al. [322] and Okamoto et al. [325] showed that the grain shape remained constant, although grain rotation was presumably taking place, the reasons for which are discussed by Ashby & Verrall [327]. In contrast, Wakai et al. [324] observed a grain elongation during tensile loading, which provided a strain of 0.27. No evidence of significant dislocation activity was found within these grains. Unfortunately, the authors did not specify the temperature at which this test was carried out, although the absence of microvoiding and the presence of elongation suggests that it was at the higher temperature end used in their tests (1450°C). On the basis of this, Wakai et al. [324] attributed 70% of the deformation to grain boundary sliding although the individual contribution of mechanisms such as

mantle climb and glide, grain switching and rotation could not be evaluated.

In the present case, the tetragonal grains which were slightly elongated (region 4, fig 7.21) show some similarity to the microstructure reported by Wakai et al. [324], although these authors did not observe any evidence of dislocation flow. However, it is interesting to note that there was virtually no microvoiding observed at this distance from the worn surface. The similarity in the microstructure in region 4 to that found by Wakai et al. [324] suggests that the temperature at this depth from the surface was of the order of 1500°C. However, this assumes a similar strain rate to that used by these authors (i.e. 10^{-5}–10^{-3} s^{-1}). If the strain rate was higher in the present case (which appears very probable from the linear wear rates), then a higher temperature would be required to avoid significant microvoiding, if grain boundary sliding was the dominant deformation mechanism. However, it is probable that dislocation flow occurred, invalidating such a comparison.

A further problem with this temperature estimate is that the distance from the region of elongated tetragonal (region 3,4) to the monoclinic (region 5) is too small to allow a temperature fall from 1400–1500°C to the temperatures at which complete stress assisted transformation would occur. This discrepancy could be rationalised by assuming that the monoclinic was formed either on cooling after the wear test or during thin foil preparation as a result of the low constraint, augmented by large residual stresses. Indeed, it was considered that the monoclinic layer was too thick to have been entirely formed during sliding.

The presence of extensive elongation demonstrates that dislocation flow and grain coalescence played a very much more significant role in the deformation at the worn surface than was found in the superplasticity studies in the literature. In the present case no evidence of a texture was found, which suggests that grain coalescence would have only played a minor role. It is difficult to establish whether the considerable elongation was a result of higher temperatures than those used in the superplasticity studies, or because the strain rate was high, or because the stress system was so different to that in axial compression or tensile loading. It would appear that the stress system alone would not be so different in wear compared to simple mechanical testing that the deformation mechanism would be changed from

grain boundary sliding to dislocation flow.

The strain rates at the surface would be expected to be substantially higher than those reported in the literature for superplasticity studies. A strain rate of 1.6×10^4 s^{-1} was considered possible in the stainless steel surface worn under similar load and speed conditions. In the present case, the absence of welding between the counterfaces would have led to lower strain rates. However, the strain rate was undoubtedly high as shown by the linear wear rate of $1.3\mu m/s$, and would certainly have been several orders of magnitude higher than those used in the superplasticity experiments (10^{-6}-10^{-3} s^{-1}). Thus, the microstructural response would be expected to be different. In particular, increased probability of dislocation flow and grain boundary voiding would be expected for an equivalent temperature.

From the above discussion it should be clear that no accurate assessment of the surface temperatures could be made. The lower limit appears to be around 1500°C for the surface itself as shown by the sparks which were seen at the interface. An upper limit of 1850°C would be associated with the absence of surface melting. If the presence of the amorphous material is taken to indicate melting, which is perfectly possible, then a much higher temperature may have occurred. These results place the tests of zirconia on zirconia into perspective. With the lower thermal conductivity zirconia, counterface temperatures would have been much higher. Thus, it is considered that reports in the literature which consider transformation toughening as possible, even under slower sliding conditions, are completely unfounded. For example, Harrison et al. [150] reported a grain pop-out mechanism for TZP on TZP at a sliding speed of 0.24 m/s which was attributed to transformation. However, the above results suggest that this would be highly unlikely.

There is one final observation which it is important to consider. The grains in the transition from region 4 to 5 which had undergone significant grain shape change, but without appreciable reduction in grain thickness, were still tetragonal even in the thin foil. These grains contained occasional dislocations which could provide potent initiation sites for transformation to monoclinic. In addition, the longest dimension of the grains was up to $1.5\mu m$ which is in excess of the expected critical grain size for this material [61] (see fig 2.5). Why, then, had no transformation occurred?

Theories of tetragonal metastability were discussed in section 2.1.5. The classical nucleation theory requires some form of defect to initiate transformation, as discussed by for example Chen et al. [87]. Although these theories apply to spontaneous transformation on cooling through the M_s temperature, the current observations appear to contradict the classical nucleation theory. Evans et al. [67,74] considered that it is the stress component of the strain energy term which is important, where the strain energy scales with the particle size. However, the increase in boundary area produced by the deformation suggests that this theory is also unfounded.

Heuer [89] and Ruhle & Heuer [90] consider that it is the nucleation barrier which is important. Of the non-classical nucleation theories they favoured a 'localised soft mode' model whereby a heterogeneous nucleation site is required at a grain boundary which acts as a stress concentrator. Nucleation is considered to be controlling and always stress assisted such as from a crack tip or residual stresses. This approach is supported by Schubert & Petzow [74] and Schmauder & Schubert [96] who consider that the tetragonal phase does not have any thermodynamic stability in TZP materials. They consider that the factors affecting the transformability are the chemical free energy driving the transformation (i.e. the undercooling) and the residual stresses. Thermal expansion anisotropy was shown to increase with decreased yttria content, thereby increasing the residual matrix stresses.

In the present case, the residual stresses may have been reduced by annealing at elevated temperature. However, the grain shape change coupled with the thermal expansion anisotropy would have been expected to increase the residual stresses, thereby driving the transformation. Thus, the present observations tend to conflict with this theory of transformability. However, the objections to this theory raised by the present experimental observations appear less than those for the classical model or that suggested by Evans et al. [83,90].

7.2.2 Test at 0.02 m/s

In the light of the dominant role of temperature generation in the test at 0.24 m/s described above, a test was carried out at low speed in an attempt to avoid frictional heating. The load was reduced to 10 N/pin in the hope that fracture dominated wear of the disc could be
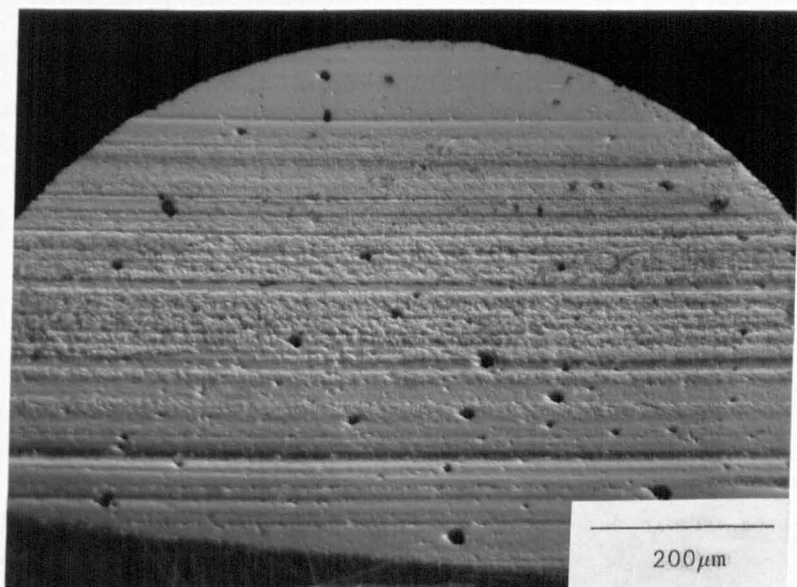
Fig. 7.24. Optical micrograph (Nomarski) of the wear track for the 3Y
tested at 0.016m/s. Note the very flat area at the top and the
grooving in the lower regions.
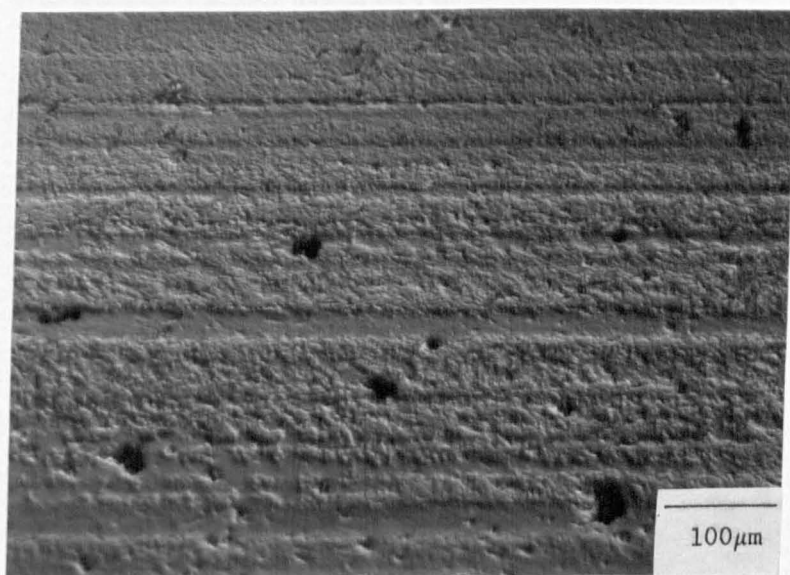
Fig. 7.25. Optical micrograph (Nomarski) giving a detail of the
above. Note the scratch marks.
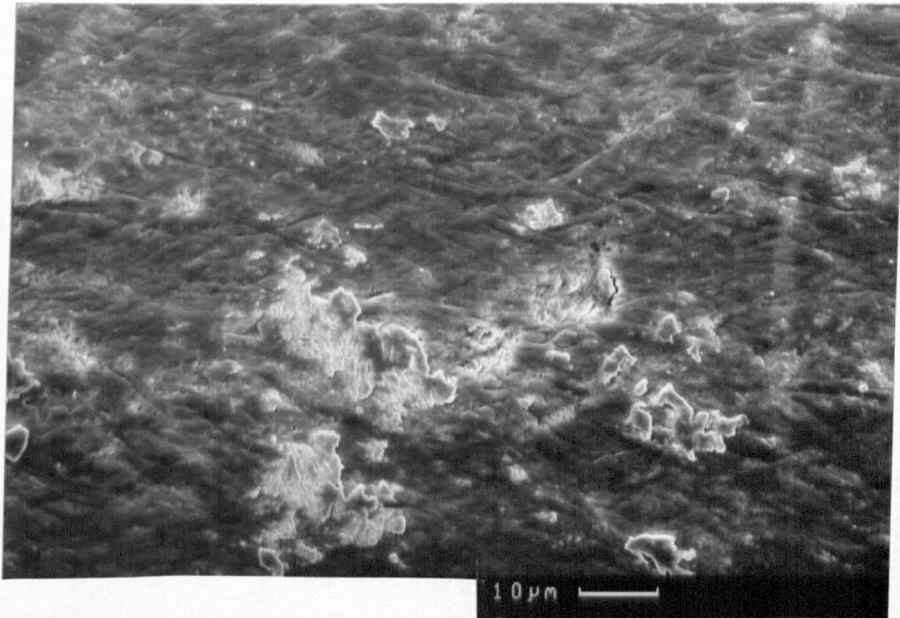
S.D.→

Fig. 7.26. SEM micrograph giving a detail of the above. Note also the morphology of the wear debris.
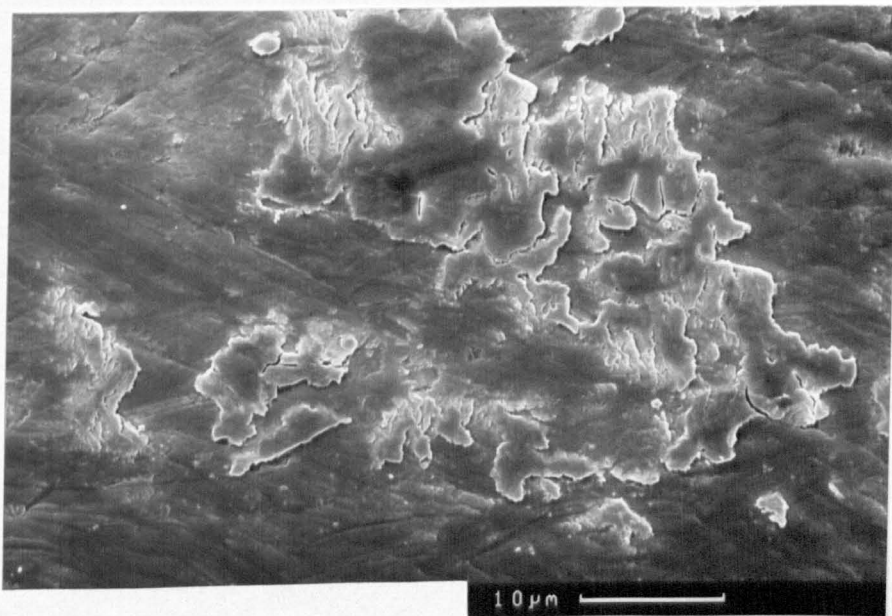
Fig. 7.27. Detail of the wear debris, which has been smeared over the surface.

50μm
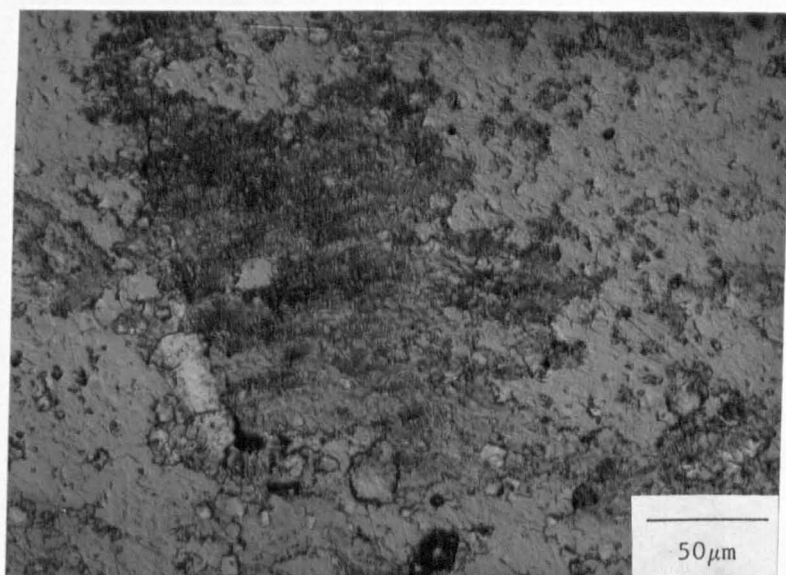
S.D.→

Fig. 7.28. Optical micrograph (Nomarski) of the wear debris on the disc. Note the delamination of the debris in the lower left region.

200n.
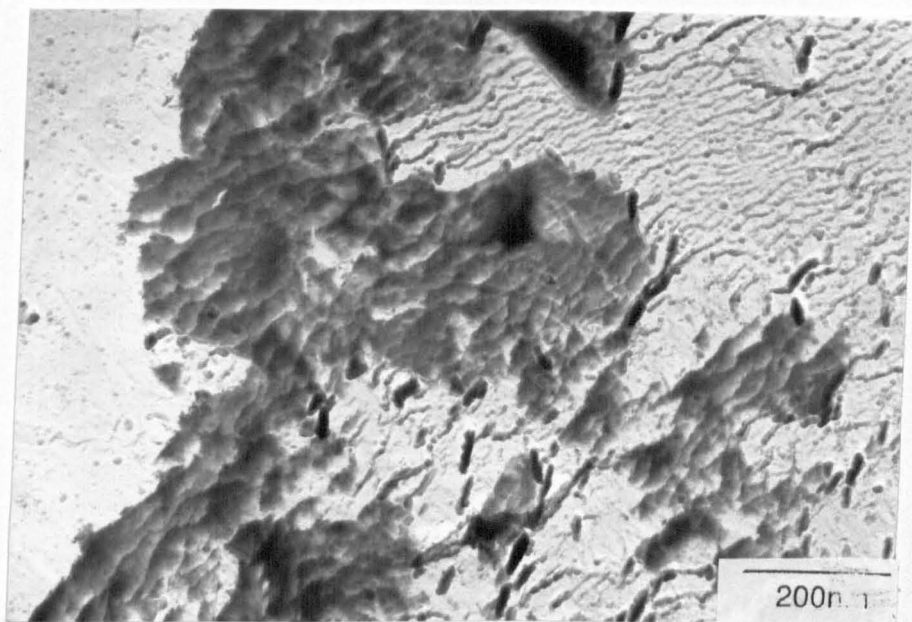
S.D.

Fig. 7.29. TEM micrograph of the wear debris removed from the disc surface by a two stage replica.
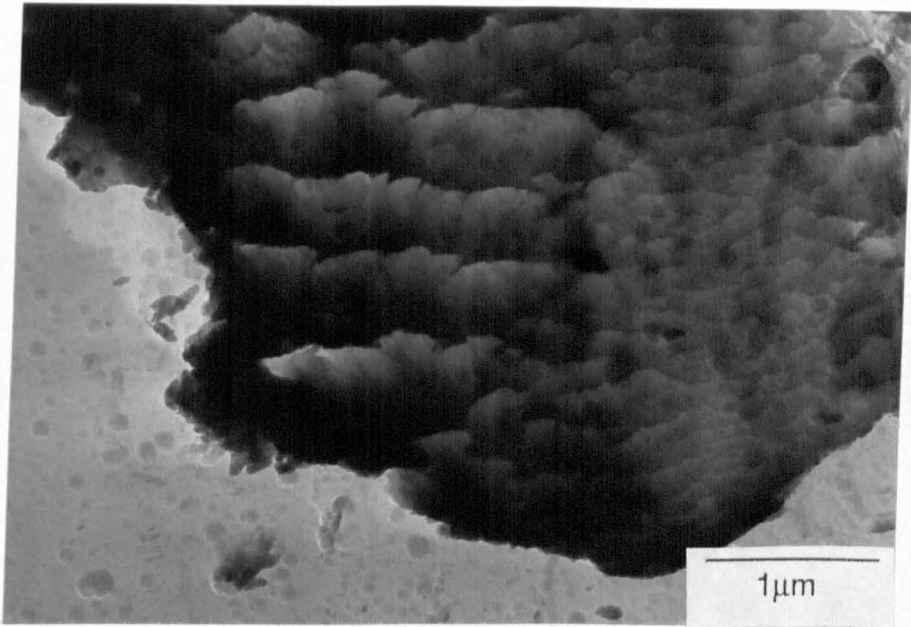
S.D.↓

Fig. 7.30. Detail of the above. The debris was found to be amorphous and consisted mainly of zirconia with a trace of alumina.
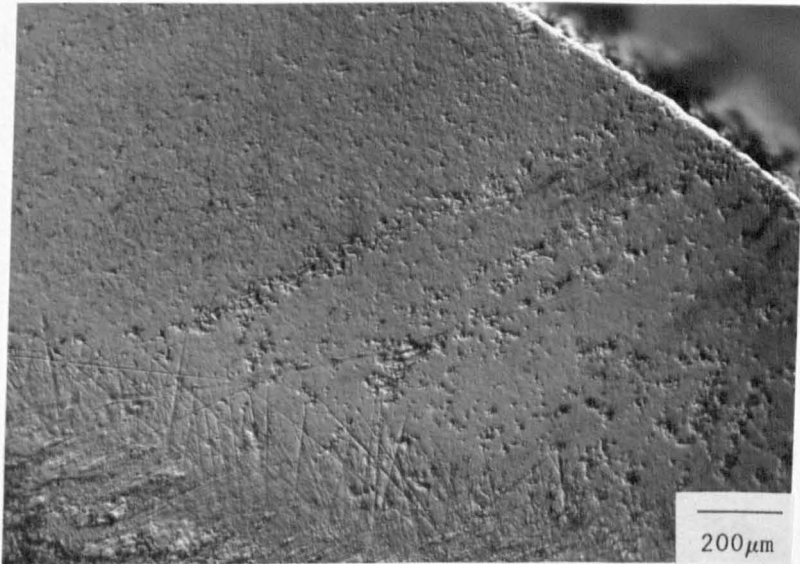
S.D.

Fig. 7.31. Optical micrograph of the worn ZTA pin. The worn area was very small. Note the pitting, but otherwise smooth surface.

avoided.

The conditions and wear factors are presented in table 7.1. The
test was carried out for just over 100km after a running time of 62
days. At the end of this period an apparent weight gain had occurred
in two of the three pins (although the gains were within the
experimental error of measurement). The third pin recorded a wear
factor of 6.2×10^{-8} mm^3/Nm, which is extremely low and four orders of
magnitude lower than the test at 0.24m/s. This figure is comparable
with the value reported by Scott [121] for the reciprocating wear of a
low toughness Mg-PSZ against itself, at a load of 4.9 N/pin and sliding
speed in the range 1–10 mm/sec. However, the majority of the other
wear rates reported in the literature (see table 2.2) are much higher.
Proliferometry traces of the disc failed to reveal any measurable wear.

The friction coefficient started at an initial value of 0.18 but
steadily rose to a steady state value of 0.28–0.39. Such values are
higher than for the sliding of zirconia on the bearing steel disc
(chapter 6). The test was accompanied by an intermittent high pitched
squeak making it virtually unbearable to be in the same room as the
wear test.

The wear scar occupied less than 25% of the initial pin area, as
shown in fig 7.24. A detail of the pin is given in fig 7.25. The
outer region of the pin was extremely smooth, showing no grain relief
and no evidence of plastic ploughing. The centre region of fig 7.24
was grooved with numerous finer grooves running up to 30° to the
sliding direction. A detail of this grooving is given in fig 7.26.
Nowhere on the surface could any grain relief or fracture be found.

Several examples of smeared wear debris were found on the worn pin,
fig 7.26,27. Similar wear debris was found on the disc, fig 7.28. The
smeared layer was mainly zirconia but a trace of alumina was also
present. Local regions where the the smeared film was in the process
of delaminating were found, for example the upper right feature in fig
7.27. The disc showed occasional examples of grain break-up, for
example in the top, centre of fig 7.27. This could have been the
initial stages of surface break-up similar to that found in the test at
0.24 m/s. Alternatively, it is possible that inadequate lapping after
a previous test was responsible, so that some residual damage remained
in the surface.

The minute amount of wear debris was removed from the surfaces of
both the pin and the disc by two stage replicas. A low magnification

micrograph of the electron transparent debris is given in fig 7.29 with
a detail in fig 7.30. The debris was entirely amorphous with no
crystalline material being found anywhere. Microanalysis indicated
that it was mainly zirconia but also contained a small amount of
alumina.

The change in speed had resulted in a dramatic reduction in the
wear rate; two reasons were considered responsible. Firstly, the disc
had suffered only a small amount of fracture. Secondly, the surface
temperatures would have been considerably lower. Attempts were made to
obtain TEM foils by back-thinning but the relevant area was found to be
too small (less than 0.5mm across), and no useful information was
obtained.

The general appearance of the surface suggested that some plastic
deformation had taken place. However, it was considered that this was
similar in nature to that which occurs during abrasion, for example, on
silicon carbide paper, rather than from high interfacial temperatures.
Indeed, it would be difficult to see how such low wear rates could have
resulted from high interfacial temperatures. The origin of the grooves
was most probably from the abrasive particles derived from the break-up
of an occasional alumina grain.

The origin of the amorphous debris is difficult to explain. Low
wear rates in ceramic on ceramic wear are often associated with the
production of an amorphous wear debris [132]. For example, the wear of
alumina in like on like tests produces an amorphous hydrated wear
debris [132]. It is possible that a similar mechanism had occurred in
the present case, but there was too little debris to prove this.

The reason that the disc did not break-up was considered to have
been as a result of the lower load used. However, the observation that
occasional grains had fractured suggested that the load was just below
the threshold value. Whether the speed had any effect was not clear.
It is conceivable that the high interfacial temperatures generated at
0.24 m/s had caused additional thermal stresses which had then reduced
the threshold load.

7.3 ZTA ON ZTA

The ZTA pins employed in this test were made by a different
manufacturer to the disc, and contained a finer grain size (about 1μm

compared to 4μm). The test was carried out under the same conditions as the test reported in section 7.2.1 (i.e. the 3Y pins which gave catastrophic wear rates) and the results and other details are given in table 7.1.

The wear rate recorded was very low at 3×10^{-8} mm^3/Nm and was comparable to the wear rates from the slow speed tests. In addition, the friction coefficient was stable and low at 0.11-0.15. The wear test was characterised by smooth quiet running.

The wear track occupied about 15% of the pin surface. The position of the wear track was different on each pin such that three individual wear grooves were formed on the disc. The worn portion of one of the pins is shown in fig 7.31, with a detail in fig 7.32. The surface was generally smooth and the wear had removed the lapping marks. Faint grain relief can be seen in fig 7.31 along with occasional deeper pits where fracture appears to have occurred on an individual grain basis. There was no evidence that the softer zirconia had worn preferentially.

A general view of the wear track on the disc is given in fig 7.33. Wear was not sufficient to remove the lapping marks. Occasional grains had worn, to give limited grain relief, but other regions had apparently been unaffected. This micrograph provides important evidence as to the wear mechanism. Several grains, for example those arrowed, show an internal structure of criss-cross ridges. Close examination confirmed that the ridges correspond to the original position of lapping marks. Thus, wear has occurred by some mechanism which is related to the deformation structure left by the surface preparation. The mechanism cannot be a result of plastic deformation because it does not show directionality. Micro-fracture would not be so selective, and would be expected to cross the entire grain. The subject of microfracture was discussed in chapter 6 where it was concluded that such a mechanism does not occur on a sub-grain scale. The most probable mechanism, therefore, was tribochemical wear which had resulted in preferential wear of the heavily dislocated regions.

The majority of the wear debris was pushed to the edge of the wear track as shown in fig 7.34, and formed a thin, smeared, layer. Debris within the wear track tended to become smeared at the edges of those grains which were standing proud, fig 7.35. This is an interesting observation since it proves that elastic deflection alone cannot explain grain relief. A third type of debris can be seen in the upper left of fig 7.34 and in fig 7.33. These appear as very small rolls

lying in a random orientation to the sliding direction.

Two stage replicas were used to remove the very small amounts of debris from the disc surface. In all cases the debris was found to be amorphous and consisted only of aluminium ions. An example of the general debris is given in fig 7.36, and an example of the roll type material in fig 7.37. Similar debris has been reported by Wallbridge et al. [132] for the like on like wear of alumina under very similar conditions to the present tests. Wear was considered to occur by the formation of a hydrated alumina film which was then progressively removed, i.e. by a tribochemical wear mechansim.

The origin of the roll type debris is not clear. The general appearance is similar to that reported by Boch et al. [328] for the high temperature wear of SiC. Boch et al. [328] found that the rolls coincided with minimum wear and suggested that they acted as a 3-body bearing. However, there is no direct evidence for this assertion.

No fractured particles of alumina were found. It is considered that the above results further support the assertion made earlier that grain relief is a result of tribochemical wear mechanisms, not from mechanical mechanisms such as micro-fracture. Indeed, it is considered that micro-fracture on a sub-grain scale is not possible. Further, it is proposed that plastic dominated wear only occurs at elevated temperatures and during abrasion. The only effect of significant dislocation flow during sliding wear at low temperatures is to initiate fracture.

It is not clear why no evidence of fracture was found on the ZTA disc in the present test, when under the same speed and load conditions the TZP pins gave extensive fracture of the disc. The explanation most probably lies in the difference in forces in the disc surface or the temperature generated. For the ZTA /ZTA couple the frictional forces were low. However, with the TZP pins the frictional forces were high. The high friction coefficient probably reflected the plastic flow in the pin. In addition, it is reasonable to assume that the high temperatures promoted significant adhesive forces between the two surfaces. The evidence for this is that extensive mixing of the alumina and zirconia occurred. Therefore, it is probable that the stresses within the disc were higher for the TZP pins than for the ZTA pins. Clearly, the effect of having one low thermal conductivity counterface is dramatic.
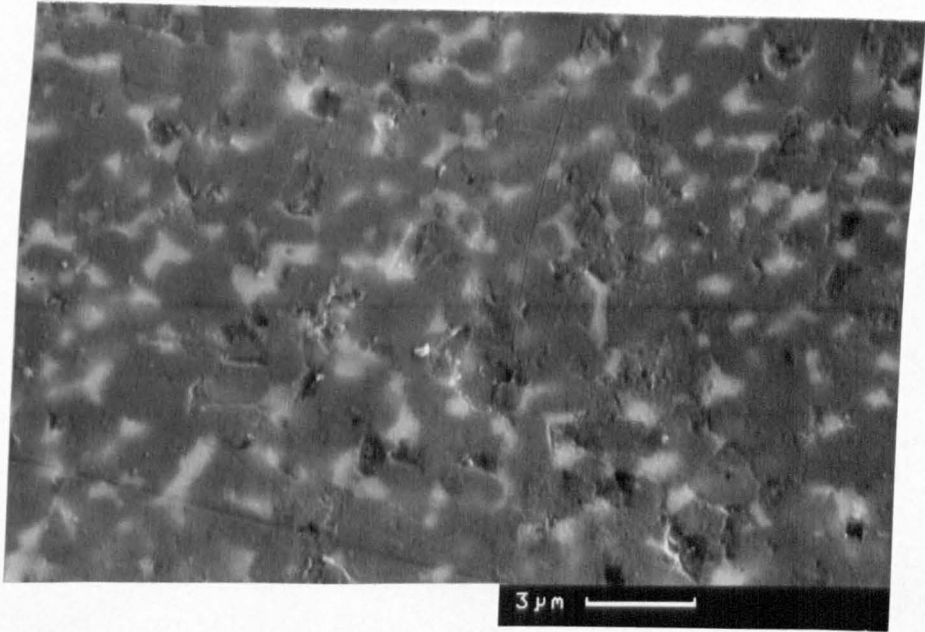
S.D.↑

Fig. 7.32. SEM micrograph of the worn pin surface. The surface was extremely smooth and the remnants of lapping marks could be seen.
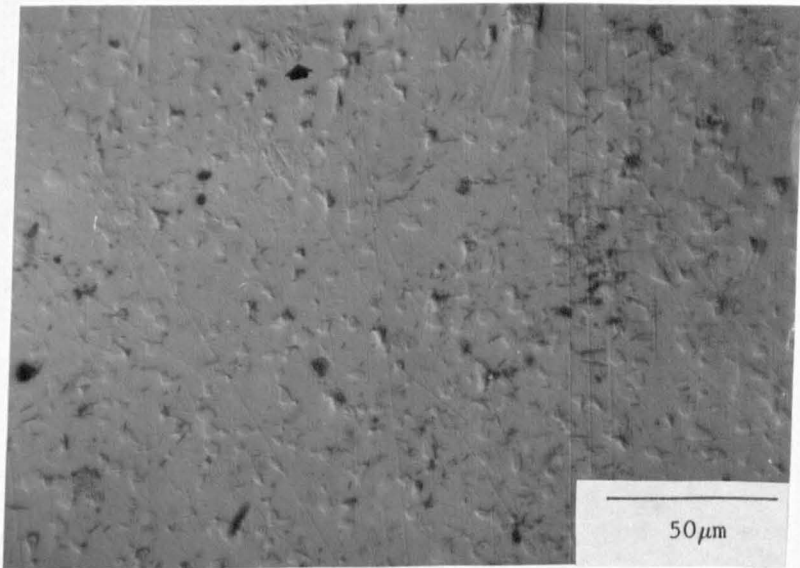
S.D.↑

Fig. 7.33. Optical micrograph (Nomarski) of the disc surface. Most of the lapping marks can still be seen. Note the fine roll like wear debris in the right hand region. Note also, the structure arrowed.
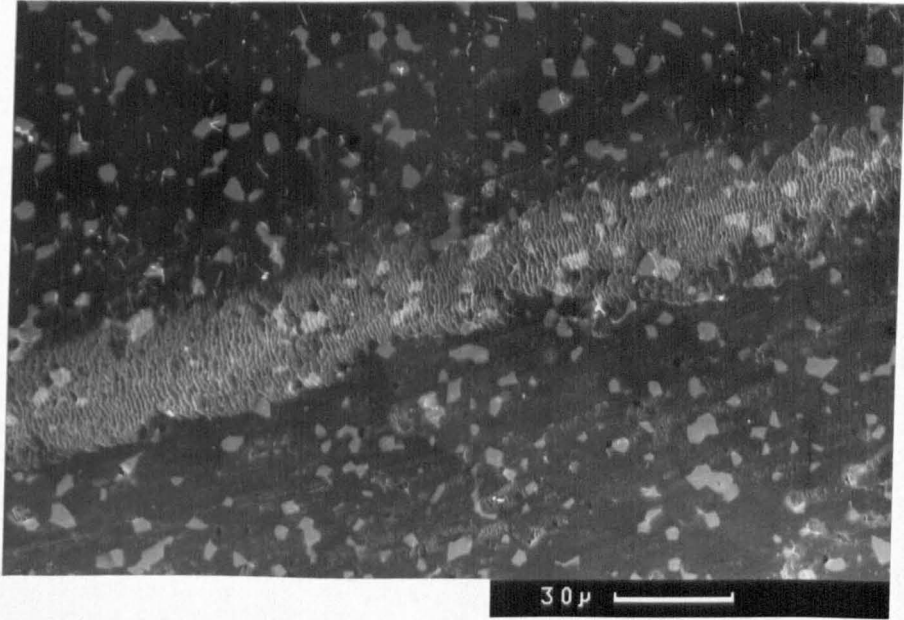
S.D.

Fig. 7.34. SEM micrograph of the smeared wear debris. The appearance was similar to that for the slow TZP test.
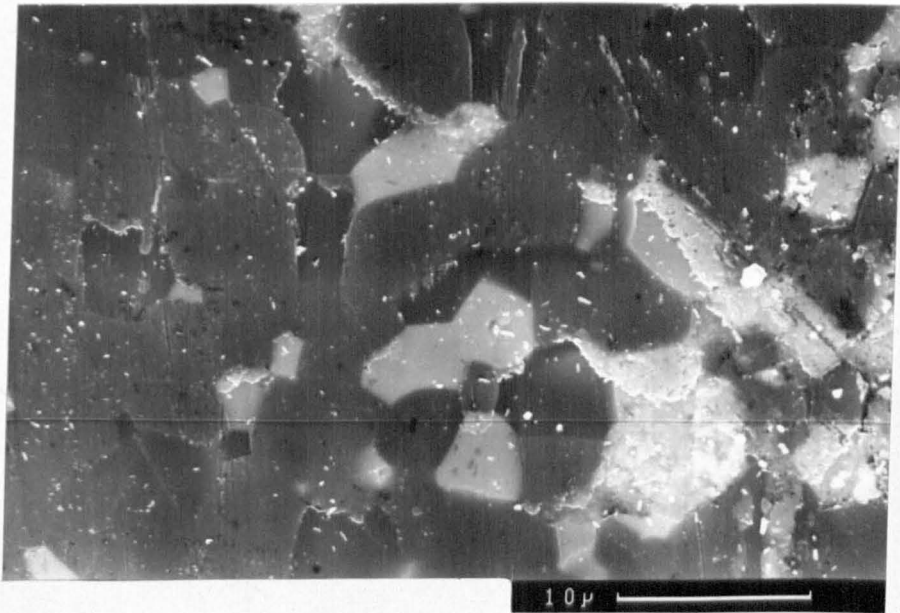
S.D.

Fig. 7.35. Detail of the disc surface. Note the pile-up of debris at the trailing edge of the grains. This proves that grain relief cannot have occurred by different degrees of elastic deflection alone.
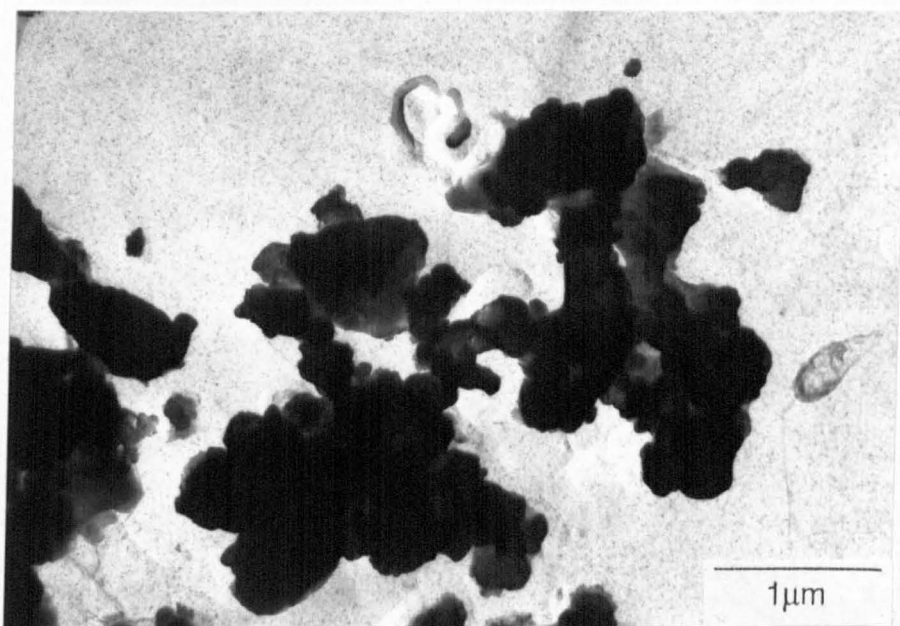
Fig. 7.36. TEM micrograph of a two stage replica taken from the disc surface showing the wear debris. The debris was entirely amorphous.
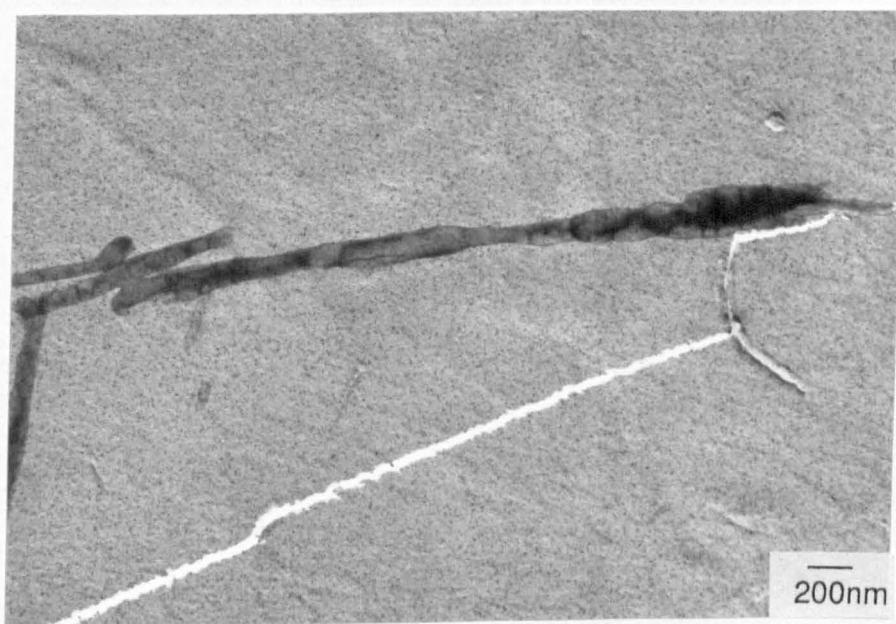
Fig. 7.37. Detail of the 'roll-like' wear debris, which was also amorphous.

7.4 2.5Y TZP-20 VOL% SiC WHISKER COMPOSITE PINS AGAINST ZTA

The details of the composite material were given in chapter 3. A discussion of the mode of toughening in this material is beyond the scope of this thesis, but is amply reviewed by Yang [273]. However, the composite provides a contribution from transformation toughening (although to a lesser extent than a conventional 2.5Y) and a contribution from whisker toughening mechanisms, mainly deflection [273]. The mechanical properties were noted in chapter 3, from which it can be seen that the composite has a higher hardness and higher stiffness for a similar toughness compared to the 3Y or 2.5Y. In addition, the SiC was expected to provide an increase in thermal conductivity. The whisker loading was sufficiently high to provide occasional whisker interaction, especially at agglomerates, thereby providing thermal conduction paths.

The wear results and test details are given in table 7.1. The wear rate of the pins was very low and therefore difficult to measure; the rates were the lowest found in any of the tests reported in this thesis and comparable to the best results for any ceramic on ceramic wear. However, the quoted figure is considered to be an underestimate because the surface contained some wear debris retransferred from the disc, which wore at a significantly higher rate.

High noise levels were associated with the wear test and, towards the end of the test, high vibration levels. The vibration became so severe that the pins started to work loose in their holders. Consequently, wear occurred between the pin side and the collet. Iron particles were liberated onto the interface just before the end of the test, almost certainly affecting the wear mechanism. The metallic wear debris was found to have mixed with the ceramic so that examination of the debris was considered to be pointless. However, the worn pin surface was monitored throughout the test and no evidence of any change as a result of the metallic debris could be found.

A typical region of the worn pin is given in fig 7.38. The surface was generally smooth with occasional abrasive scratches. Interestingly, the SiC whiskers had worn to a greater extent than the zirconia. This was believed to be a result of oxidation of SiC to SiO_2. The distribution of the whiskers is shown in the micrograph in fig 7.39. The majority of the whiskers were perpendicular to the worn surface so that the preferential wear had given the surface a pitted

appearance. Occasional grooves can be seen which were not aligned with the sliding direction as arrowed in fig 7.38. The scale of these grooves suggest that whiskers aligned parallel to the surface had been pulled out.

The disc had suffered significant wear. Limited fracture had occurred on the worn surface, fig 7.40, with particularly severe material removal occurring in radial bands. The bands were equally spaced around the circumference and were probably responsible for some of the excessive vibration. In between the bands, wear had occurred by occasional grain fracture and by a milder mechanism which had led to grain relief. It would appear that the fine abrasive grooves on the pin surface were caused by the debris liberated by fracture on the disc surface.

There was just sufficient contact area for TEM examination perpendicular to the worn surface. Very little thin area was obtained and the wear track only extended about $30\mu m$ along the foil surface. Therefore, only limited conclusions could be drawn because of the small area sampled. A general view of the worn surface is given in fig 7.41 with details in figs 7.42,43. The outer grain was invariably monoclinic. However, the monoclinic never extended more than one grain depth. Very little microcracking was associated with the monoclinic, although one example is shown in fig 7.42. No evidence of surface films could be found although their presence could not be categorically ruled out. The absence of foil buckling suggested that the levels of residual strain at the surface were small.

The general appearance of the surface indicated that wear had not occurred by any mechanical based mechanism, since no evidence of plastic flow or fracture could be found. More probably, wear was a result of a tribochemical mechanism. Such findings from both this and the last chapter suggest that low wear rates only occur when mechanical based wear mechanisms are not significant. That is, where no fracture or plastic deformation occurs. Plastic deformation is only believed to be significant where substantial temperature rises occur, or during abrasive wear.

With tribochemical wear, the reaction rates between the surface and the counterface (or the environment) are considerably higher than under static conditions. Asperity contact provides thermal transients and continuous break-up of any protective layers. Nonetheless, the reaction rates are still slow, such that the wear rates are low. Thus,

20μm
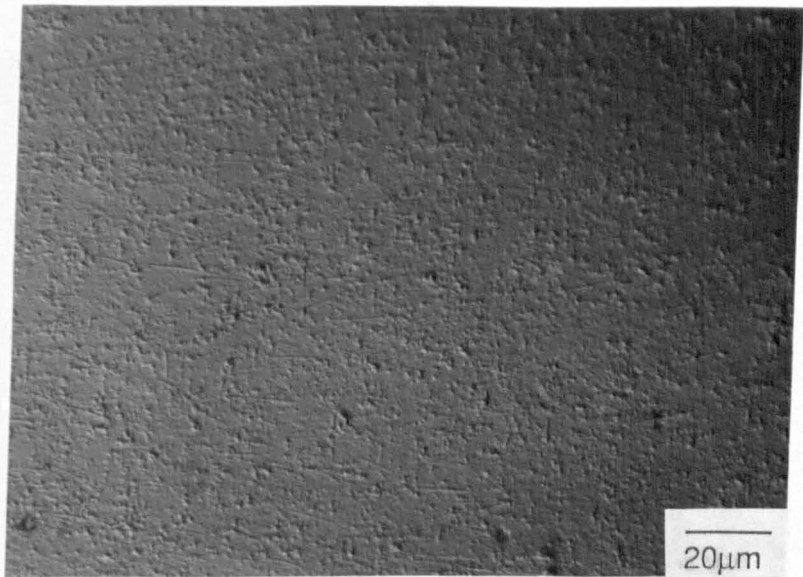
Fig. 7.38. Optical micrograph (Nomarski) of the worn whisker composite pin. Note the scratch marks, probably produced by fractured particles from the disc. Note also the recessed appearance of the SiC whiskers.

30μ
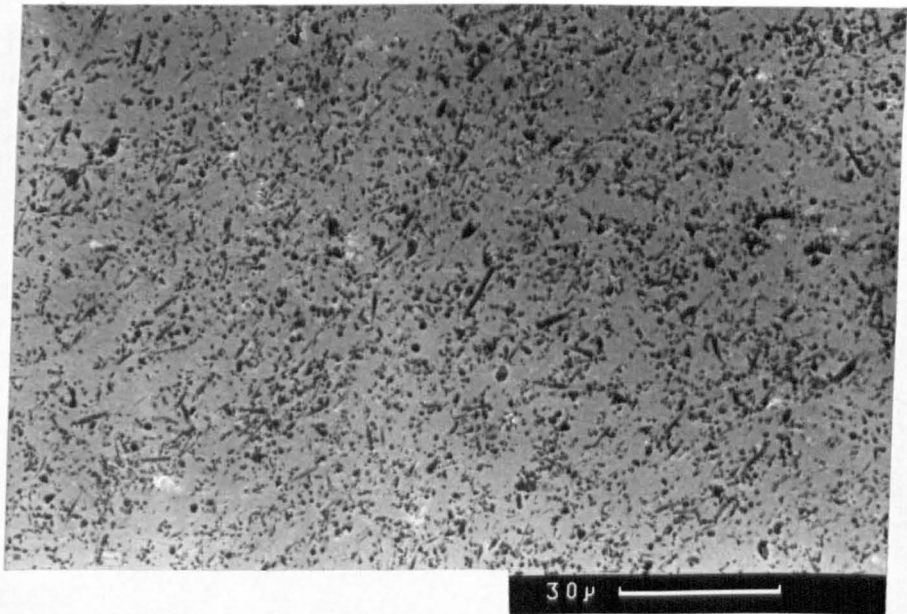
Fig. 7.39. BEI micrograph showing the distribution of the whiskers on the worn surface. The majority were perpendicular to the surface.
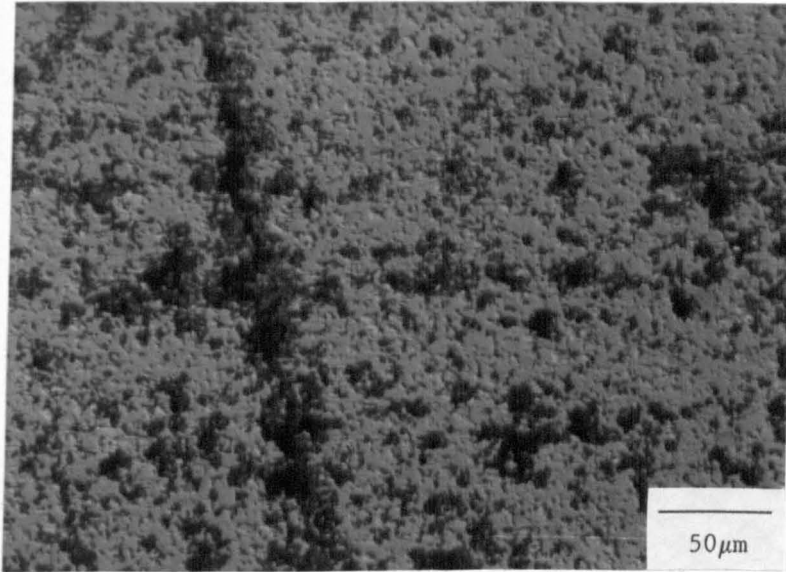
Fig. 7.40. Optical micrograph (Nomarski) of the worn disc. Surface fracture has occurred. However, this might have been due to residual stresses from the previous wear test not removed by lapping.
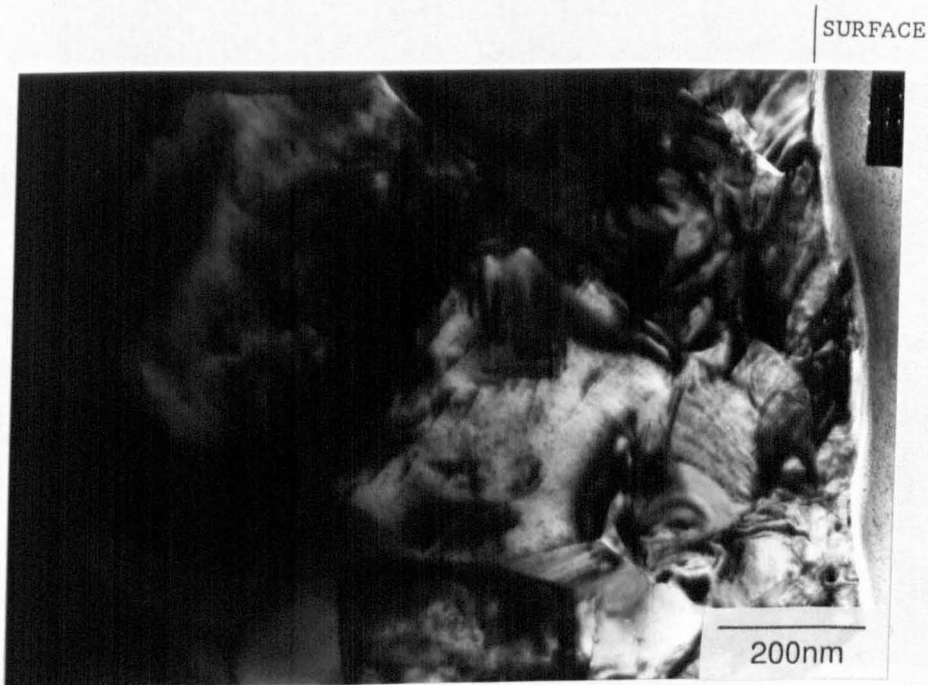
SURFACE

Fig. 7.41. Low magnification TEM micrograph (cross sectional) of the composite surface. Very little microstructural change has occurred at the worn surface.

100 nm
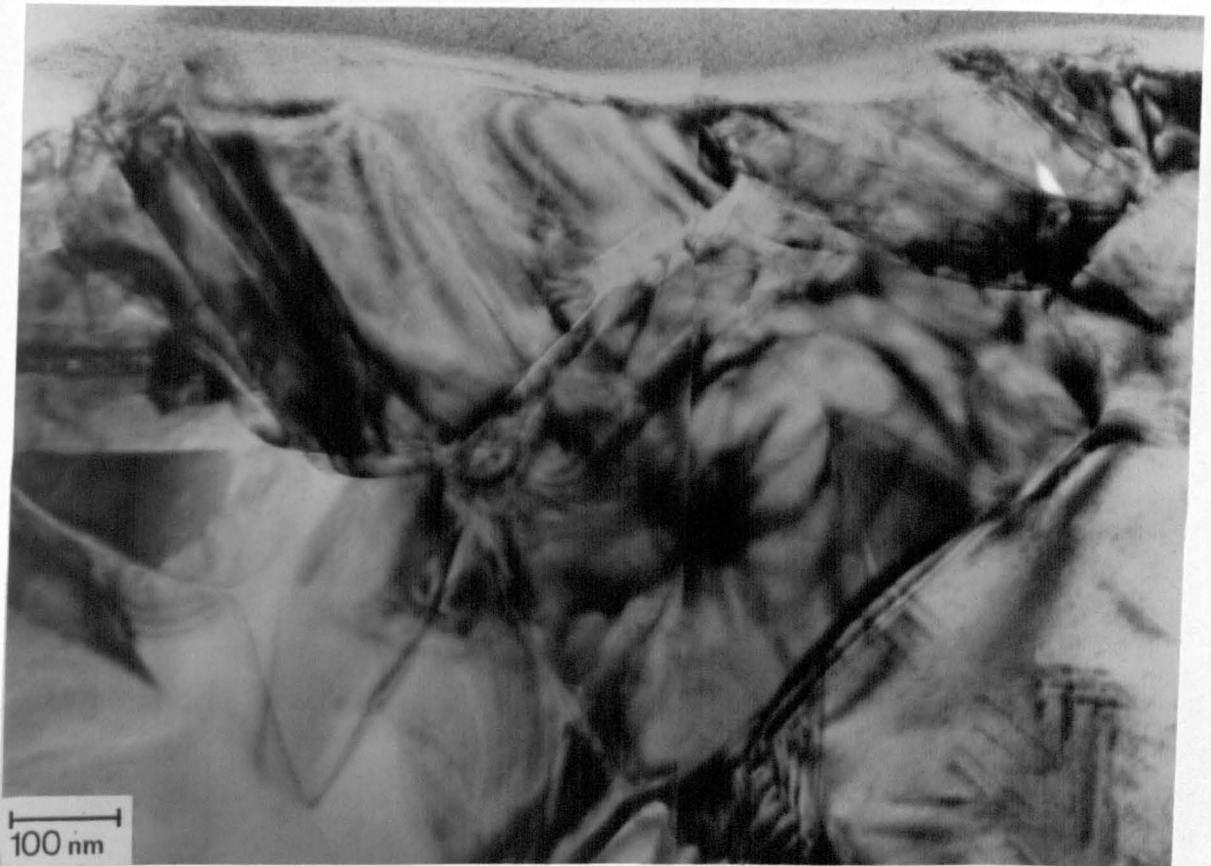
Fig. 7.42. Detail of the worn surface. Transformation to monoclinic had only occurred to one grain depth. Note the large zirconia grain size as a result of hot pressing. Note also, the low level of microcracking. The wear mechanism had clearly occurred in the elastic regime. Consequently, the whisker toughening mechanisms had played no role.
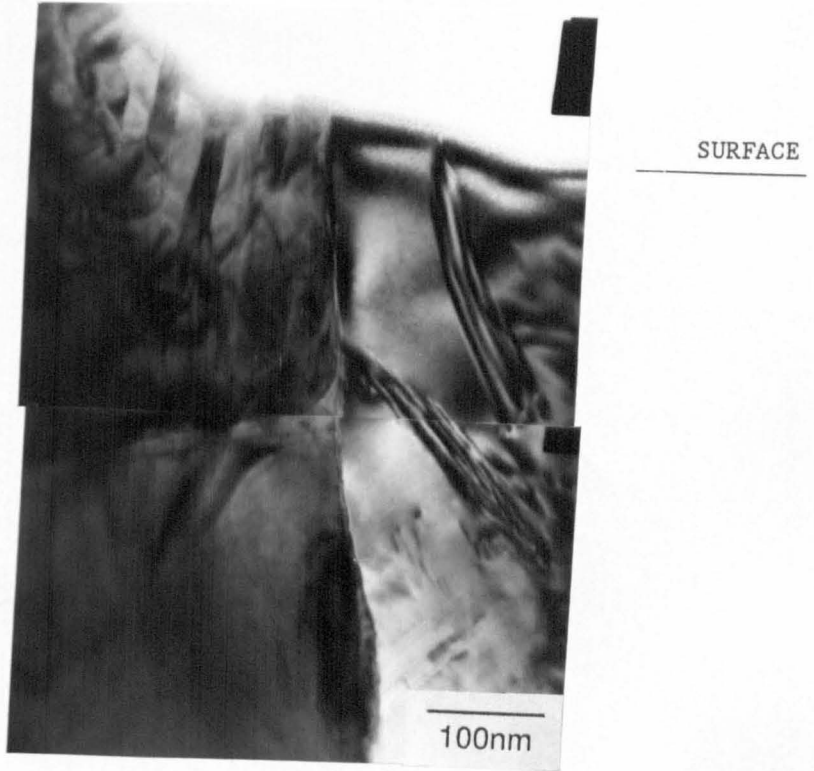
SURFACE

Fig. 7.43. Detail of the surface showing an interface between whisker and tetragonal at the surface.

SURFACE
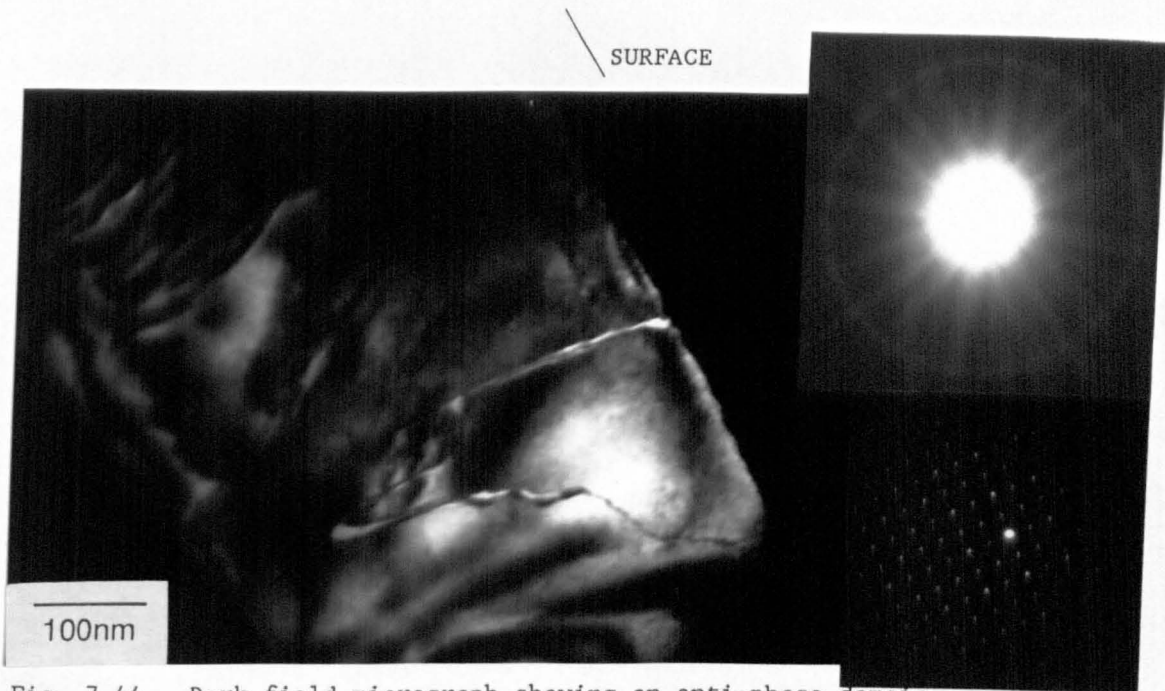
Fig. 7.44. Dark field micrograph showing an anti-phase domain boundary. The convergent beam pattern contains two mirror planes indicating that the grain was not monoclinic and was therefore probably orthorhombic. (The CB pattern was weak because the foil was thin at this point).

this reaction rate determines the minimum wear rate that can be achieved with any particular couple. In the case of zirconia on steel the reaction rates were apparently rapid and therefore the wear rates were comparatively high. Where an additional mechanical mechanism came into play, such as transformation initiated material removal, the wear rate increased. In contrast, the rate of formation of the hydrated alumina wear debris was slow, so that very low wear rates can be obtained in alumina or ZTA couples. The only mechanism by which the wear rate can be further reduced is by reducing the contact area (by lubricating) or changing the environment. Unfortunately, it has often been shown that in a vacuum the lubricating effects of absorbed species is lost and therefore interfacial stresses are increased. Nonetheless, Fischer et al. [147], reported that the lowest wear rate for TZP couples was obtained in dry nitrogen rather than when using one of a wide range of lubricants he had investigated.

The whiskers dramatically altered the tribological behavior of the zirconia. The over-riding difference was considered to be its thermal conductivity. Whilst temperature increases would still have occurred, the extent would have been greatly reduced such that plastic deformation would not have taken place. The general absence of monoclinic at the surface does suggest that the temperature was high enough to reduce the driving force for transformation. Although the constraint on the tetragonal grains was much higher in the composite, such that their transformability was reduced compared to a 2.5Y TZP, the grain size after hot pressing the composite was substantially larger than in a conventional TZP so that some contribution to the toughness was made by transformation. Interfacial stresses would have been high enough to drive the transformation to greater than one grain depth, suggesting that the driving force had been reduced. However, stresses within the zirconia may have been reduced by the load carried by the higher stiffness whiskers. Nonetheless, the preferential wear of the SiC, believed to be a result of oxidation of SiO_2, will have reduced this effect. Little was known about the M_s of this material so that an estimate of the temperature could not be made.

Fig 7.44 gives a dark field image of the worn surface where a anti-phase domain boundary (APB) was observed. This feature was not considered to play any significant role in the wear process but is of interest in the wider study of zirconia ceramics. APBs, which indicate that the grain was ordered, have been identified in monoclinic and

orthorhombic zirconia [37,45,47]. Bestgen et al. [47] have demonstrated that the ordering in monoclinic was a result of the monoclinic being formed by transformation from an ordered orthorhombic phase. In their work, the tetragonal was transformed by electron beam heating to the orthorhombic symmetry by a comparatively slow displacive transformation. The transformation front left APBs in its wake as it moved through the tetragonal. Transformation of the orthorhombic was induced by further electron beam heating of the foil, with the resultant monoclinic retaining the APBs and the ordered structure. In those grains where t→m was induced directly, no evidence of ordering in the monoclinic was found. The orthorhombic phase has been found in many studies, for example in the Mg-PSZ system [40,41], the Ca-PSZ system [42] and the ternary Mg-Y-PSZ system [43]. In bulk samples o-phase can only be detected at high pressure [44,45] and at very low temperatures [47], and is generally considered to be an artefact of thin foil preparation when detected under ambient conditions.

Recently, Pandolfelli et al. [329] have identified APBs in monoclinic grains in which no twin boundaries were present (the twin spacing was very large so that if only a small portion of the grain was examined no twin boundaries were found). The monoclinic and orthorhombic [001] diffraction patterns can be identical if the (001) monoclinic variant is the only plane diffracting. The diffraction pattern in fig 7.44 is such a pattern and therefore the selected area pattern cannot differentiate between whether the surface grain was monoclinic or orthorhombic. However, the convergent beam pattern in fig 7.44 contains two mirror planes. Monoclinic crystals can only produce patterns with one mirror plane and a rotational symmetry of 2. Therefore, the surface grain cannot be monoclinic and is presumed to be orthorhombic (although the convergent beam does not provide full identification in this case).

Attempts to make the orthorhombic grain transform by electron beam heating failed. Such stability has never been reported for orthorhombic formed during thin foil preparation. In the present case no orthorhombic or ordered monoclinic was found in any of the thin foils of this material. This, therefore, suggests that it may have formed by transformation from the tetragonal during asperity contact. If so, the transformation would not have provided any contribution to toughening the ceramic.

7.5 REVIEW OF THE EFFECT OF SLIDING SPEED ON THE WEAR OF ZIRCONIA

The sliding speed has been shown to have a dramatic effect on the wear rate of zirconia against both metal and ceramic counterfaces. At the end of this thesis it is appropriate to briefly review this observation and compare the findings with the literature. The wear factor as a function of sliding speed for the present results and all those in the literature are plotted in fig 7.45. The trend of increase in wear with speed is very clear and little difference is found between the ceramic or metal counterface. The range of wear rates for a given speed is remarkably small given the over-riding effect that the design of the wear rig can have.

Fig 7.45 can be compared to the results of Woydt & Habig [130] reported in section 2.2.1.1 and reproduced in fig 2.19. At speeds of 0.003-0.3 m/s an increase in the ambient temperature in the range 22-800°C produced an increase in the wear factor. However, at 1 m/s and above, the wear rate was independant of temperature. The effect of speed was considered to be almost entirely its influence on the flash temperature. The implication of the results was that the interfacial temperature was the same at 0.03 m/s and an imposed temperature of 800°C as it was at 1 m/s and room temperature.

The over-riding conclusion is clearly that the low thermal conductivity of the zirconia prohibits its use as a tribological material under sliding conditions, unless some mechanism exists for avoiding large temperature rises. At very low speeds and loads it is a viable material. However, this is an unlikely engineering situation. Coupling with a metal undoubtably reduces the interfacial temperatures substantially. This is offset by a high reaction rate between the zirconia and the steel such that the wear rate is still high (although it should be said not as high as alumina on zirconia, for example). The alternative strategy of increasing the material's thermal conductivity by the addition of SiC whiskers undoubtably improves matters, but this creates possible manufacturing problems notably poor sinterability thereby necessitating hot pressing, and potential health hazards. The effect of the temperature rise was to substantially reduce the driving force for transformation of the tetragonal to monoclinic, in many cases to the point where the tetragonal was the thermodynamically stable phase.
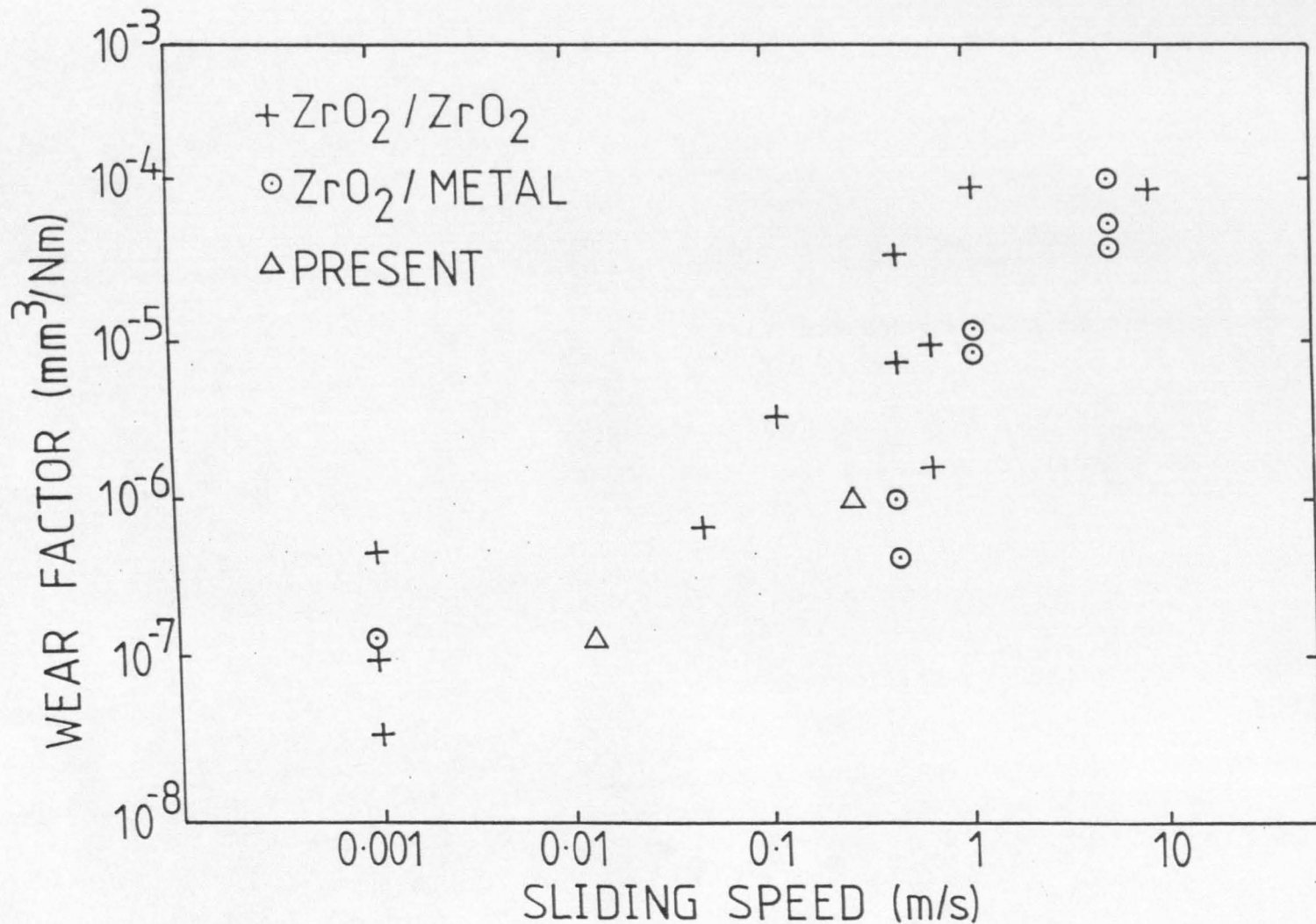
Fig. 7.45. Wear factor as a function of sliding distance for all published results and the current findings (average value). Note the small difference in wear rate between a zirconia and metal counterface. Note also, the fairly small spread in wear factor for different workers who used the same speed.

CHAPTER 8

CONCLUSIONS

8.1 GENERAL CONCLUSIONS

1) Cross sectional transmission electron microscopy has proved an important technique for examining the microstructures generated at a worn surface. A number of new structures have been presented, which could not have been elucidated by any other technique, and which provide important information about the wear mechanisms.

2) The wear surface of the stainless steel deformed in a manner analagous to that of wire drawing or extrusion, rather than rolling. The wear mechanism was closely related to the mode of deformation within the surface, namely whether it was heterogeneous or homogeneous and the ultimate ductility of the material.

3) Transformation of tetragonal to monoclinic phase during sliding wear was shown to increase the wear rate. The extent of this wear mechanism was strongly associated with the adhesive forces at the interface. Sliding against counterfaces which promote strong adhesion should therefore be avoided. Moreover, high toughness zirconias should not be used.

4) All reports in the literature of low wear rates of zirconia are associated with slow sliding speeds. Zirconia shows an almost exponential increase in wear rate with sliding speed in the range 0.001 to 10m/s. For each sliding speed, the counterface and load had a secondary effect but this was generally restricted to an order of magnitude spread of wear factor. Therefore, zirconia will only be a successful tribological material if the temperature generation at the interface is controlled.

5) No evidence was found to support the theory suggested by Wallbridge et al. [132] for the formation of grain relief, which proposed that certain grains underwent microfracture whilst others underwent plastic deformation. The results of the current work clearly indicate that

grain relief is associated with a tribochemical mechanism. For zirconia on steel grain relief was formed as a result of the reaction between the two counterfaces. For self-mated ZTA the dominant mechanism was associated with the formation of a hydrate. Under these circumstances the dissolution rate is a function of crystallographic orientation in a manner similar to that of etching of a metal surface.

6) The tribochemical mechanism is believed to be associated with the minimum wear rate attainable for a particular system. A mechanical based mechanism such as fracture increases the wear rate. Dislocation flow is considered only to occur at high temperatures or with abrasive wear. Thus, its presence in sliding wear is associated with high wear rates.

7) Even where low wear rates were achieved, substantial interfacial noise was generated. At loads of 20 N and above, heavy vibration also occurred. Either of these factors would preclude the use of such couples in engineering applications.

8.2 SPECIFIC CONCLUSIONS

8.2.1 Rolling Experiments
1) The microstructure generated in 316L by rolling is very similar to that of 70/30 brass, although no macroshear bands were observed.

8.2.2 Wear of Stainless Steel Pins Against Zirconia Discs

8.2.2.1 High Strain Deformation in the Pin Surface
1) The wear factor of 316L against zirconia follows a very different trend as a function of load compared with reports in the literature for self mated 316 [285]. A reduction in wear rate and wear factor was found at loads above 24 N/pin. This was attributed to an increase in the surface coverage of metal oxide, the majority of which was derived from re-transfer from the zirconia disc. Therefore, the low thermal conductivity of the disc had led to a decreased wear rate of the pins compared to metal on metal contact.

2) The microstructure of the worn stainless steel was similar to that generated by rolling, but with some important differences. The thick band of crystallites extending from 200nm below the worn surface to the twinned region, originally formed by the passage of shear bands, were subsequently deformed in a homogeneous manner to a high strain. The deformation resulted in a fibre texture rather than a rolling texture. The microstructure in this region differed from that of the rolled material in two important respects, namely, that no fresh shear bands were formed after the first shear bands and that all twins were consumed by the deformation process. This was a result of the geometrical differences between rolling and wear.

3) Fresh shear bands were formed at all positions on the outermost surface, except where oxide was present. The shear bands were poorly defined indicating that little homogeneous deformation had occurred subsequent to formation, suggesting that they were probably formed by the passage of the last asperity. The surface shear bands exhibited a finer crystallite size than shear bands observed in rolling, probably reflecting a higher strain rate. These observations demonstrated two important points. Firstly, contact was plastic in all tests examined in the load regime of 2.2–56 N/pin, where metal was exposed. Secondly, the stress was a maximum at the surface.

4) The strain distribution within the homogeneously deformed shear banded region was shown to decrease exponentially with depth from the surface.

8.2.2.2 Wear Mechanism

1) One major wear mechanism was shown to be the transfer of metal to the ceramic disc. Transfer was believed to be a result of plastic overload in the surface shear band during its formation.

2) A simple theoretical equation was proposed which accounted for the wear by transfer, and which provided good agreement with experimental results. The equation predicted that it was the area of exposed metal and the number, and area, of real contact points which determined the wear rate. Also, that the thickness of the shear band formed at the surface was related to the thickness of transferred material. Thus, a small reduction in stacking fault energy would be expected to reduce

the wear rate as a result of reduced shear band thickness.

3) The wear rate was found to correlate with the depth of deformation, but the relationship was believed to be only indirect. Both the wear rate and the depth of deformation reduced as the oxide content of the surface increased. However, the greater the depth of deformation, the greater the extrusion of metal from the end of the pin. This physical displacement of the wear surface was shown to constitute 5-23% of the total wear volume.

8.2.2.3 Temperature at the Interface

1) The temperature at the interface was considered in detail. The model of Archard [292] suggested a maximum flash temperature of 571°C. The more rigorous model proposed by Kuhlmann-Wilsdorf [295,296] predicted a maximum flash temperature of 407°C for the extreme case, and 200-300°C for more reasonable contact conditions. The latter predictions were in good agreement with experimental results. Firstly, an implanted thermocouple detected a steady state temperature rise of only 20°C above ambient, even when it formed part of the contact surface. Secondly, the microstructure in the shear bands showed no evidence of temperature rises. Microstructural changes would be expected above about 500°C. Thirdly, changes in the wear debris structure were initiated by heating at 350°C, with dramatic changes at 450°C.

8.2.2.4 Metal Oxide Formation

1) In general, the oxide was believed to have been formed on the disc and then retransferred to the pin. However, some oxidation was also believed to have occurred during attrition of the debris.

2) The oxide formed was a mixture of a non-equilibrium BCC phase and an amorphous phase. The mode of formation was not clear. A model was proposed to explain the formation of the oxide at comparatively low temperature. The continuous disruption of the protective oxide layer on the surface of the stainless steel by the passage of an asperity provided a high oxidation rate at low temperature. The oxygen was progressively taken into solution by mechanical mixing and high vacancy concentrations developed during the passage of an asperity. The increase in oxygen content led to destabilisation of the structure.

The oxygen segregated with the Cr, Ni, and Mo ions to form an amorphous structure whilst the remainder formed a crystalline ferrite based phase. The thermodynamically predicted equilibrium oxides were prevented from forming by the low temperature and the disruption of the structure by deformation.

3) The oxide was shown to plastically deform along with the metal despite being brittle (as demonstrated by the localised cracking). The deformation took place on such a fine scale that a lamellar microcomposite was formed. It is considered that this structure is crucial to a reduction in wear rate. A thick monolithic oxide structure would have easily spalled, possibly increasing the wear rate. However, the composite structure would have provided a surface with an increase in flow stress but with good mechanical integrity. These observations are at variance with the model proposed by Quinn and co-workers [218,310-312].

8.2.2.5 Wear Rate

1) The wear rate as a function of load of the stainless steel was reduced by two factors. Firstly, the increase in flow stress at the surface reduced the overall depth of deformation, reducing the wear by physical displacement. Secondly, the oxide prevented transfer of metal to the disc. Evidence was presented which indicated that transfer occurred at each asperity contact with exposed metal. Therefore, an increase in the oxide coverage would lower the transfer rate. This was considered the over-riding reason for the reduction in wear rate with increase in load.

8.2.2.6 Wear of the Zirconia Disc

1) Wear of the Mg-PSZ discs mated with the 316L pins occurred by two mechanisms. The first was shown to be associated with transformation of tetragonal to monoclinic cooperatively in bands. The associated microcracking, coupled with the tensile forces from adhesion between the two surfaces, promoted preferential removal of these bands. The bands formed initially in the grains which exhibited a near [100] orientation relationship with the surface.

2) The second wear mechanism left the surface very smooth, but wore different grains to different extents. Two stage replicas failed to

show any evidence of a microfracture mechanism. However, evidence of preferential removal of the cubic matrix was found. Precipitate distortion had occurred at the worn surface, as shown by back-thinned TEM specimens. This could have arisen from either residual stresses in the thin foil or very limited dislocation flow. However, the former was considered more probable. No evidence was found of a plastic deformation dominated mechanism for the formation of wear debris. It was concluded, therefore, that contact and stressing was mainly elastic and that wear had occurred by a tribochemical based mechanism whereby material was removed by dissolution of the zirconia in the iron oxide.

3) The amount of surface monoclinic was low, despite a transformation driven wear mechanism. TEM suggested complete transformation to a depth of no more than 300nm. X-ray diffraction indicated that there had been no increase in the monoclinic levels. This latter observation was believed to have resulted from the removal of grain boundary monoclinic (about 8% of the total phase content) offsetting the increased surface monoclinic levels.

4) The low monoclinic levels were considered to result from two causes. Firstly, the temperature rises at the surface reduced the driving force for transformation. Secondly, transformed material was rapidly removed by the microcracking mechanism.

5) The presence of some transformation also gave important evidence as to the temperature at the interface. For such a material, an M_s temperature of about 140K would be expected. This would mean that no transformation would be expected above 500°C. Therefore, the flash temperature on the disc surface would have been below 500°C, reinforcing the conclusions presented under 8.2.2.3.

6) A TZP disc worn under similar conditions to the Mg-PSZ discs gave a higher wear rate. Wear occurred by an intergranular fracture mechanism. Whether fracture was a result of the tensile forces initiating conventional fracture or whether fracture was transformation initiated (in a manner similar to the Mg-PSZ) was not clear.

8.2.3 Wear of Zirconia Pins Against a Bearing Steel Disc

1) The wear of zirconia pins on a bearing steel disc followed the same trend of wear factor with load irrespective of material type or toughness. No clear correlation of wear factor with toughness or surface monoclinic content could be found. Therefore, transformation did not play a dominant role in the wear mechanism.

2) For both the Y-TZP and the Mg-PSZ materials, the dominant wear mechanism left a very smooth surface, but with grain relief. TEM of these surfaces failed to find any evidence of a plastic overload mechanism or a fracture mechanism on a sub-grain scale. No individual zirconia particles could be found in the wear debris. Rather, the zirconia was found to be in solid solution in the iron oxide. This was taken to be strong evidence that wear had occurred by a tribochemical mechanism involving reaction between the metal oxide and the zirconia.

3) With the Mg-PSZ pins some transformation induced banding was found. This again provided an upper limit on the interfacial flash temperature. TEM examination of the bands confirmed the crystallographic orientation relationship whereby the bands lay along the axis of the precipitates i.e. along {100}. Evidence was found that the bands were formed by microcrack coalescence. The bands were much thinner and more crack like because of the lower adhesive forces when coupled with a bearing steel disc compared with stainless steel pins. In addition, the temperature in the zirconia pins would have been higher than that of the disc.

4) TEM examination revealed the structure of an abrasive groove. Considerable plastic flow was shown to have occurred which had totally destroyed the precipitate structure. In some areas the magnesia had been redistributed to such an extent that the structure was fully cubic. In other areas, remnants of very fine tetragonal precipitates remained. There was a strong texture within these regions, which had rotated away from the parent structure. Individual dislocations were difficult to image and no subgrains were found. There was little evidence that very high temperature rises had occurred in the abrasive groove.

5) With the Y-TZP materials the monoclinic was found only within the top few surface grains. At low loads, and only in the 2Y materials,

evidence was found of a grain 'pop-out' mechanism. This was believed to be a result of transformation. However, the contribution by this mechanism to the wear rate was very low. Otherwise, very little microstructural change had occurred as a result of the sliding contact.

6) Transformation has been shown to be detrimental in the sliding wear of zirconias. However, with abrasive wear, transformation has been shown to be beneficial because of the surface compressive forces. Two reasons have been provided to explain the difference in behaviour. Firstly, the tensile component of the surface stress, promoted by adhesive forces, is of supreme importance and is lower for abrasive wear. Thus, more damage occurred by this mechanisms as a result of a soft metal counterface (eg stainless steel) than by a hard counterface (such as the bearing steel). Secondly, abrasive wear promotes extensive surface deformation which destroys the original structure. This prevents damaging microcracking, although why no microcracking occurs under such high strain conditions is not clear. Further research is required to establish the relative importance of these two factors.

8.2.4 Ceramic On Ceramic Wear

8.2.4.1 TZP Pins Against ZTA Disc
1) The wear of a 3Y-TZP against a ZTA disc led to high interfacial temperatures. High strains in the zirconia surface were found and possible evidence of surface melting. The surface consisted of an amorphous mixture of alumina and zirconia. Below this, a crystalline layer of tetragonal was found, which had suffered an order of magnitude reduction in grain size. This layer was believed to have been formed by a microcrack coalescence mechanism and would have behaved in a superplastic manner. This gave way to a layer of elongated grains which had undergone extensive dislocation flow. Heavy grain boundary cracking indicated that grain boundary sliding was also important. At a depth of $5\mu m$ the temperature had fallen sufficiently to permit stress assisted transformation of tetragonal to monoclinic. The microstructure described above was not apparent from SEM examination and emphasises the importance of using cross sectional TEM.

8.2.4.2   ZTA Pins Against ZTA Disc

1) Under identical conditions to those in 8.2.4.1, a self mated ZTA exhibited very low wear rates. The wear mechanism was shown to be tribochemical based. This indicated the over-riding importance of the thermal conductivity of the ceramic in determining the wear behaviour.

8.2.4.3   Whisker Composite Against ZTA Disc

1) A 20 vol% SiC whisker-2Y-TZP composite exhibited very low wear rates. The wear mechanism was tribochemical with no fracture occurring. This was attributed to the increased thermal conductivity and load bearing capacity in the presence of the whiskers.

FUTURE WORK PROPOSALS

The use of cross sectional TEM has been shown to be a powerful technique in establishing the true wear mechanism. The technique should be further applied to a metal which shows homogeneous deformation mechanisms and a continued increase in work hardening up to very high strains, such as pure iron. This should be followed by investigation of a material with a lower stacking fault energy than 316L, preferably one with high melting point.

More work is required to examine the worn surface of zirconias. In particular, the low success rate of cross sectional foils meant that conclusions in this thesis were drawn from comparatively few surfaces. These observations therefore need to be verified. In addition, ground surfaces should be examined in order to establish why transformation appears not to lead to increased wear.

At this point further work on required in other ceramic systems. These should include Ce-TZP, SiC platelet-TZP, SiC-fibre composites, sialon and many more. Substantially more work before ceramics will be able to fulfill their potential as tribological materials.

REFERENCES

1) A. G. Evans, D. B. Marshall. Fundamentals of Friction and Wear of Materials. ASME (1980) p439-452.
2) R. Stevens. An introduction to Zirconia. Magnesium Electron. (1986).
3) B. J. Hockey. J. Am. Ceram. Soc. 54 (5) (1971) p223.
4) B. J. Hockey. Proc. Brit. Ceram. Soc. 20 (1972) p95
5) O. O. Adewoye, T. F. Page. Wear 73 (1981) p247-260.
6) O. O. Adewoye, T. F. Page. Wear 70 (1981) p37-51.
7) T. F. Page, G. R. Sawyer, O. O. Adewoye, J. J. Wert. Proc. Brit. Ceram. Soc. No 26 (1978) p193.
8) C. F. Grain. J. Am. Ceram. Soc. 50(6) (1967) p288-290.
9) A. H. Heuer, M. Ruhle. Advances in Ceramics, Vol 12. Science and Technology of Zirconia 2. (1983) p1.
10) D. L. Porter, A. H. Heuer. J. Am. Ceram. Soc. 62(5-6) (1979) p298.
11) B. C. Muddle, R. H. J. Hannink. J. Am. Ceram. Soc. 69 (7) (1986) p547-555.
12) R. C. Garvie. Advances in Ceramics, Vol 12. Science and Technology of Zirconia 2. (1983) p4657.
13) M. V. Swain, R. H. J. Hannink. Advances in Ceramics, Vol 12. Science and Technology of Zirconia 2. (1983).
14) Nilcra Product data.
15) S. C. Farmer, T. E. Mitchell, A. H. Heuer. Advances in Ceramics, Vol 12. Science and Technology of Zirconia 2. (1983) p152.
16) S. C. Farmer, A. H. Heuer, R. H. J. Hannink. J. Am. Ceram. Soc. 70(6) (1987) p431.
17) U. Dworak, H. Olapinski, W. Burger. Advances in Ceramics 24. Science Technology of Zirconia 3. (1986) p545.
18) R. R. Hughan, R. H. J. Hannink. J. Am. Ceram. Soc. 69(7) (1986) p556-563.
19) J. Drennan, R. H. J. Hannink. J. Am. Ceram. Soc. 69(7) (1986) p541-546.
20) J. Drennan, R. H. J. Hannink. J. Aust. Ceram. Soc. 20 (1985) p36.
21) C. A. Leach. Mat. Sci. & Technol. May 1987 p321.
22) M. V. Swain. J. Mat. Sci. Let. 15, (1980) p1577.
23) D. J. Green. Com. Am. Ceram. Soc. Oct 1983 C-178.
24) R. T. Pascoe, R. H. J. Hannink, R. C. Garvie. Science of Ceramics, Vol 9, (1977) p447.
25) N. Claussen, G. Petzow, Proc. 4th CIMTEC, Italy, May 1979.
26) A. H. Heuer, L. H. Schoenlein. J. Mat. Sci. 20 (1985) p3421-27.
27) L. K. Lenz, A. H. Heuer. Com. Am. Ceram. Soc. Nov 1982 C-192.
28) R. H. J. Hannink, M. V. Swain. J. Aust. Ceram. Soc. 18(2) (1985) p53
29) M. V. Swain, R. C. Garvie, R. H. J. Hannink. J. Am. Ceram. Soc. 66 (5) (1983) p358.
30) R. H. J. Hannink. J. Mat. Sci. 18 (1983) p457-470.
31) R. H. J. Hannink, R. C. Garvie. J. Mat. Sci. 17 (1982) p2637-43.
32) R. Chaim, D. G. Brandon. J. Mat. Sci. 19 (1984) p2934-2942.
33) A. H. Heuer, L. H. Schoenlein, S. C. Farmer. Advances in Ceramics Vol 12. Science and Technology of Zirconia 2. (1983) p257.
34) S. C. Farmer, L. H. Schoenlein. Com. Am. Ceram. Soc. July 1983, C-107.
35) G. K. Bansal, A. H. Heuer. J. Am. Ceram. Soc. 58(5-6) (1975) p235.
36) M. V. Swain. Fracture Mechanics of Ceramics, vol 6 p355.
37) B. C. Muddle, R. H. J. Hannink. J. Am. Ceram. Soc. 69 (7) (1986) p547-555.
38) H. J. Rossell, R. H. J Hannink. Advances in Ceramics Vol 12.

Science and Technology of Zirconia 2. (1983) p139.

39) R. Chaim, D. G. Brandon. Advances in Ceramics Vol 12. Science and Technology of Zirconia 2. (1983) p86.

40) B. C. Muddle, R. H. J. Hannink. Advances in Ceramics Vol 24. Science and Technology of Zirconia 3. (1986) p89.

41) L. H. Schoenlein, A. H. Heuer. Fracture Mechanics of Ceramics, Vol 6 (1983) p309.

42) R. M. Dickerson, M. V. Swain, A. H. Heuer. J. Am. Ceram. Soc. 70 (1987) p214

43) R. R. Lee, A. H. Heuer. J. Am. Ceram. Soc. 71 (1988) p694.

44) S. Block, J. A. H. Dajornada, G. J. Piermarini. J. Am. Ceram. Soc. 68 (1985) p497.

45) Y. Kudoh, H. Takeda, H. Arashi. Phy. Chem. Mineral. 13 (1986) p233.

46) D. Marshall, M. James, J. Porter. J. Am. Ceram. Soc. 72 (1989) p218.

47) H. Bestgen, R. Chaim, A. H. Heuer. J. Am. Ceram. Soc. 71 (1988) p826.

48) B. C. Muddle, R. H. J. Hannink, Advances in Ceramics Vol 24. Science and Technology of Zirconia 3. (1986) p89.

49) I. Nettleship, R. Stevens, Int. J. High Technol. Ceram. 3 (1987) pp1-32.

50) H. G. Scott, J. Mat. Sci. 10 (1975) p1527.

51) T. Masaki, K. Sinjo, Ceram. Int. 13 (1987) pp109-112.

52) M. Ruhle, N. Claussen, A. H. Heuer. Advances in Ceramics Vol 12. Science and Technology of Zirconia 2. (1983) p352.

53) M. Ruhle, M. L. Mecartney, N. Claussen. Cer. for Engines, Proc. 2nd Int Conf. on Mat. for Engines. Lubeck-Travemunde. 1986, p593.

54) H. Schubert, Advances in Ceramics vol 11, 1984, p716.

55) M. L. Mecartney, J. Am. Ceram. Soc. 70(1) (1987) p54-58.

56) F. F. Lange, H. Schubert, N. Claussen, M. Ruhle. J. Mat. Sci. 21 (1986) pp768-774.

57) F. F. Lange. J. Mat. Sci. 17 (1982) p240-246.

58) F. F. Lange. J. Am. Ceram. Soc. 69(3) (1986) p240-242.

59) T. K. Gupta, F. F. Lange, J. Bechtold. J. Mat. Sci. 13 (1978) p1464-1470.

60) T. Masaki. J. Am. Ceram. Soc. 69(8) (1986) p638-640.

61) F. F. Lange, D. J. Green, Advances in Ceramics Vol 3, Science of Zirconia 1, 1980, p217.

62) K. Tsukuma, Y. Kubota, T. Tsukidate. Advances in Ceramics Vol 12. Science and Technology of Zirconia 2. (1983) p382.

63) K. Haberko, R. Pampuch. Ceram. Int. 9(1) (1983) p8.

64) K. Tsukuma, K. Ueda, M. Shimada. J. Am. Ceram. Soc. 68(1) (1985) C-4.

65) K. Tsukuma, K. Ueda, K. Matsushita, M. Shimada. J. Am. Ceram. Soc. 68(2) (19850 C-56.

66) K. Zobayashi, H. Kuwajima, T. Masaki. Sol. State Ionics. 3-4 (1981) p489.

67) T. Masaki. Int. J. High. Technol. Ceram. 2 (1986) p85-98.

68) T. Sato, S. Ohtaki, M. Shimada. J. Mat. Sci. 20 (1985) p1466-1470.

69) T. Sato, M. Shimada, J. Am. Ceram. Soc. Oct 1984, C-212.

70) K. Nakajima, K. Kobayashi, Y. Murata. Advances in Ceramics Vol 12. Science and Technology of Zirconia 2. (1983) p399.

71) A. Winnubst, A. Burggraaf, Advances in Ceramics Vol 24. Science and Technology of Zirconia 3. (1986) p1A4.

72) M. Watanabe, S. Iio, I. Fukuura. Advances in Ceramics Vol 12. Science and Technology of Zirconia 2. (1983) p391.

73) F. F. Lange, G. Dunlop, B. Davis. J. Am. Ceram. Soc. 69(3) (1986) p237-240.

74) H. Schubert, G. Petzow. Advances in Ceramics Vol 24. Science and Technology of Zirconia 3. (1986) p21.

75) T. Sato, S. Ohtaki, T. Endo, M. Shimada. J. Am. Ceram. Soc. 68(12) (1985) C-320.

76) T. Sato, M Shimada. Cer. for Engines, Proc. 2nd Int Conf. on Mat. for Engines. Lubeck-Travemunde. 1986, p291.

77) T. Sato, M. Shimada. J. Am. Ceram. Soc. 68(6) (1985) p325-359.

78) S. Somiya, M. Yoshimura, T. Noma, K. Kawabata. Advances in Ceramics Vol 24. Science and Technology of Zirconia 3. (1986) p1P6

79) R. Matsumoto. J. Am. Ceram. Soc. 68(8) (1985) C-213.

80) T. Sato, S. Ohtaki, T. Endo, M. Shimada. Int. J. High Tech. Ceram. 2 (1986) pp167-177.

81) K. Tsukama, M. Shimada. J. Mat. Sci. Let. 4 (1985) p857-861.

82) A. H. Heuer, M. Ruhle. Acta. Met. 33(12) (1985) p2101-2112.

83) A. G. Evans, N. Burlingham, M. Drory, W. M. Kriven. Acta. Met. 29 (1981) pp447-456.

84) F. F. Lange. J. Mat. Sci. 17 (1982) p225-234.

85) A. G. Evans. Fracture in Ceramic Materials. Noyes Publ. 1984 p16.

86) F. F. Lange. J. Mat. Sci. 17 (1982) p247-254.

87) I-W. Chen, Y-H. Chiao. Acta Met. 31(10) (1983) pp1627-1638.

88) A. G. Evans, D. B. Marshall, N. H. Burlingame. Advances in Ceramics Vol 3. Science and Technology of Zirconia 1. (1980) p202.

89) A. H. Heuer, Advances in Ceramics Vol 12. Science and Technology of Zirconia 2. (1983) p98.

90) M. Ruhle, A. H. Heuer, Advances in Ceramics Vol 12. Science and Technology of Zirconia 2. (1983) p14.

91) I-W. Chen, Y-H. Chiao, Advances in Ceramics Vol 12. Science and Technology of Zirconia 2. (1983) p33.

92) S. Wen, L. Ma, T. Yen. J. Am. Ceram. Soc. 69(7) (1986) p570-572.

93) C. A. Andersson, J. Greggi, T. K. Gupta. Advances in Ceramics Vol 12. Science and Technology of Zirconia 2. (1983) p78.

94) T. K. Gupta, C. A. Andersson, 13th Automotive Materials Conf. 1985, Ceram. Eng. & Sci. Proc. vol 7, No9,10, p1156.

95) R. H. J. Hannink, J. Mat. Sci. 13 (19780 pp2487-2496.

96) S. Schmauder, H. Schubert. J. Am. Ceram. Soc. 69 (1986) p534.

97) A. H. Heuer, F. F. Lange, M. V. Swain, A. G. Evans. J. Am. Ceram. Soc. 69(3) (1986) p1.

98) D. B. Marshall, M. R. James. J. Am. Ceram. Soc. 69(3) (1986) p215-217.

99) J. Lankford. J. Am. Ceram. Soc. Nov 1983, C-212.

100) A. G. Evans. Advances in Ceramics Vol 12. Science and Technology of Zirconia 2. (1983) p193.

101) M. V. Swain. J. Am. Ceram. Soc. 68(4) (1985) C-97.

102) M. V. Swain, L. Rose. J. Am. Ceram. Soc. 69(7) (1986) pp511-518.

103) D. B. Marshall. J. Am. Ceram. Soc. 69(3) (1986) pp173-180.

104) R. M. Mecmeeking, A. G. Evans. J. Am. Ceram. Soc. 65(5) (1982) p242.

105) A. G. Evans, R. M. Cannon. Acta Met. 34 (1986) p761.

106) M. V. Swain. Acta Met. 33(11) (1985) p2083-2091.

107) J. Wang, W. M. Rainforth, R. Stevens. Br. Ceram. Trans. 88 (1989) p1-6.

108) R. C. Garvie, R. H. J. Hannink, M. V. Swain. J. Mat. Sci. Let. 1 (1982) p437-440.

109) T. Kosmac, R. Wagner, N. Claussen. J. Am. Ceram. Soc. 64(4) (1981) C-72.

110) D. R. Clarke, F. Adar. J. Am. Ceram. Soc. 65(6) (1982) p284-288.

111) I-W. Chen, P. Reyes Morel. J. Am. Ceram. Soc. 69(3) (1986) p181-89.

112) R. Garvie, M. Goss, C. Urbani. Science of Ceramics 12. Italy. p575.

113) S. Gulati, J. Hansson, J. Helfinstine, c. Malarkey. Tube International, March 1985, p44.

114) R. H. J. Hannink, M. J. Murray, M. Marmach. Wear of Materials. 1983.
Proc. Int. Conf. Reston, Virginia. ASME. p181.

115) R. H. J. Hannink, M. J. Murray, H. G. Scott. Wear. Aug 1984 p355-366.

116) D. Fingerle, W. Gundel, H. Olapinski. Cer. for Engines, Proc. 2nd Int Conf. on Mat. for Engines. Lubeck-Travemunde. 1986, p1191.

117) U. Dworak, H. Olapinski, D. Fingerle, U. Krohn. Advances in Ceramics Vol 12. Science and Technology of Zirconia 2. (1983) p480.

118) K. F. Dufrane, W. A. Gleaser. Wear of Materials 1987. Proc. Int. Conf. Houston. Texas. ASME. p285.

119) R. Rice, C. Wu. 13th Automotive Materials Conf. 1985, Ceram. Eng. & Sci. Proc. Vol 7, No9,10.

120) M. Marmach, M. V. Swain. Proc. Int. Sym. On Ceram. Comp. in Engines. Japan. 1983. p650.

121) H. G. Scott. Wear of Materials. 1985. Proc. Int. Conf. Vancouver, Canada. ASME. p8.

122) T. A. Libsch, P. Becker, S. Rhee. Wear 110 (1986) p263-283.

123) L. J. Lindberg, D. W. Richerson. Cer. for Engines, Proc. 2nd Int Conf. on Mat. for Engines. Lubeck-Travemunde. 1986, p20.

124) J. Breznak, E. Breval, N. Macmillan. J. Mat. Sci. 20 (1985) p4657-4680.

125) T. E. Fischer, M. Anderson, S. Jahanmir, R. Salher. Wear of Materials 1987. Proc. Int. Conf. Houston. Texas. ASME. p257.

126) N. Wallbridge, to be published.

127) C. Yust. Oak Ridge Report DE 86 003016, 1985.

128) B. Hwang, C. Houska, G. Ice, A. Habenschuss. Advanced Ceramic Materials. 3(2) (1988) p180-183.

129) M. Iwasa, M. Kinoshita. Proc. Japanese Ceram. Soc. 95(9) (1987) p899.

130) M. Woydt, K. Habig. Proc. Conf. on Advanced Ceramics. Jan. 1988. Coral Beach.

131) H. Shimura, Y. Tsuya. Wear of Materials 1977. Proc. Int. Conf. St Louis. ASME. p452-461.

132) N. Wallbridge, D. Dowson, E. Roberts. Wear of Materials 1983. Proc. Int. Conf. Reston, Virginia. ASME. p202.

133) B. Longston. Tribology International. 16 (1983) p221-225.

134) C. Yust, F. Carignan, ASLE Trans. 28(2) 1984 p245.

135) J. Derby, J. Macbeth, S. Seshardri. In 'Combustion Engines-Reduction of Friction and Wear.' London. March 1985. paper c65.

136) T. Fischer, H. Tomizawa. Wear of Materials. 1985. Proc. Int. Conf. Vancouver, Canada. ASME. p22.

137) S. Horton, D. Dowson, F. Riley, N. Wallbridge. Revue de Chemie minerale. 22 (1985) p564.

138) H. Ishigaki, I. Kawaguchi, M. Iwasa, Y. Toibana. Wear of Materials 1985. Proc. Int. Conf. Vancouver, Canada. ASME. p13.

139) J. Denape, J. Lamon, D. Broussaud. Science of Ceramics Vol 12, 1983, p529.

140) E. Breval, J. Breznak, N. Macmillan. J. Mat. Sci. 21 (1986) p931-935.

141) J. Derby, S. Seshadri, M. Srinivasan. Fracture Mechanics of Ceramics Vol 8, 1986, p113.

142) J. Ishigaki, R. Nagata, M. Iwasa. Proc. Int. Conf. 'Tribology-Friction, Lubrication and Wear. Fifty Years On.' London. 1987. C194.

143) T. Fischer, H. Tomizawa. Wear of Materials 1985. Proc. Int. Conf. Vancouver, Canada. ASME. p22.

144) J. Czernuszka, T. Page. J. Mat. Sci. 22 (1987) p3907-3916.
145) J. Czernuszka, T. Page. J. Mat. Sci. 22 (1987) p3917-3923.
146) I. Birkby, P. Harrison, R. Stevens. J. European. Ceram. Soc. 5 (1989) p37-45.
147) T. Fischer, H. Tomizawa. Wear of Materials. 1985. Proc. Int. Conf. Vancouver, Canada. ASME. p22.
148) W. Brown, N. Eiss, H. McAdams. J. Am. Ceram. Soc. 47 (1964) p157.
149) I. Birkby, P. Harrison, R. Stevens. Ceram. Eng. Sci. Proc. 9 (1988) p1431.
150) P. Harrison, I. Birkby, R. Stevens. University of Leeds Report.
151) I. Birkby, unpublished work.
152) P. Warren. Acta Met. 26 (1978) p1759.
153) A. Westwood, D. Goldheim, R. Lye. Phil. Mag. 16(141) (1967) p505.
154) A. Westwood, N. Macmillan. R. Kalyoncu. J. Am. Ceram. Soc. 56 (1973) p258.
155) M. Swain, R. Latanision, A. Westwood. J. Am. Ceram. Soc. 58 (1975) p372.
156) P. Rebinder. Proc. 6th Physics Conf. Moscow. 1928. p29.
157) D. Buckley. Ceramic Bulletin. 51 (1972) p884.
158) A. Evans, D. Marshall. Fundamentals of Friction and Wear of Materials. ASME. (1980) p439-452.
159) R. Steijn. J. Appl. Phys. 32 (1961) p1951.
160) S. Horton. D. Dowson. F. Riley. N. Wallbridge. In 'Combustion Engines-Reduction of Friction and Wear.' London. March 1985.p759.
161) T. Sugita, K Ueda, Y. Kanemura. Wear 97 (1984) p1-8.
162) O. Ajayi, K. C. Ludema. Wear of Materials 1987. Proc. Int. Conf. Houston. Texas. ASME. p349.
163) J. Hines, R. Bradt, J. Biggers. Wear of Materials 1979. Proc. Int. Conf. Dearborn, Michigan. ASME. p540.
164) N. Eiss, R. Fabiniak. J. Am. Ceram. Soc. 49 (1966) p221.
165) J. Czernuszka, T. Page. Proc. Brit. Ceram. Proc. No. 34 (1984) p145.
166) P. Ramsey, T. Page. Br. Ceram. Trans. J. 87 (1988) p47-80.
167) R. F. King, D. Tabor. Proc. Royal. Soc. A223. (1954) p225.
168) T. Page. Proc. Brit. Ceram. Proc. No 34. 1984. p111.
169) M. Swain. Wear. 35 (1975) p185-189.
170) N. Wallbridge. Review of the Wear of Ceramics. 1987.
171) H. Frie, G. Grathwohl. Inst. Phys. Conf. No93, EUREM 88, York. 1988 p529.
172) E. Duwell. J. Appl. Phys. 33 (1962) p584.
173) E. Duwell, H. Butzke. J. Appl. Phys. 35 (1964) p3385.
174) C. Brookes, J. O'Neill, B. Redfern. Proc. Royal. Soc. A322. (1971) p73-88.
175) J. A. Kirk, W. Syniuta. Wear. 27 (1974) p367-381.
176) S. Toh, R. McPherson. Fracture Mechanics of Ceramics Vol 8, 1986, p723.
177) I. Cutter, R. McPherson. Wear. 71 (1981) p255-258.
178) D. Cranmer. J. Mat. Sci. 20 (1985) p2029-2037.
179) J. Griffioen, S. Bair, W. Winer. Proc. 12th Leeds-Lyon Symp. on Tribology. London, 1985.
180) J. Challen, D. Dowson. Proc. 3rd Leeds-Lyon Symp. on Tribology. MEP. 1978. p87-93.
181) J. Congleton, N. Petch. Acta Met. 14 (1966) p1179.
182) J. Congleton, N. Petch, S. Shiels. Phil. Mag. 19 (1969) p795.
183) K. Kendall. Proc. Royal Soc. A361 (1978) p245-263.
184) R. Rice. Proc. Brit. Ceram. Soc. 20 (1972) p205-207.
185) R. Rice. In ' Ceram. Eng. & Sci. Proc. Conf. on Automotive Mat. Westerville. 1985. p940-58.

186) B. Lawn. 1988 Gordon Research Conf. 'Toughening of Ceramics'.

187) M. Moore, F. King. Wear. 60 (1980) p123-140.

188) N. Wallbridge, D. Dowson. Wear of Materials 1987. Proc. Int. Conf. Houston. Texas. ASME. p101.

189) M. Gee, E. Almond. Mat. Sci & Technol. 4 (1988) p877.

190) C. Donadille, R. Valle, P. Dervin, R. Penelle. Acta Met. 37 (1989) p1547-1571.

191) J. G. Sevillano, P. van Houtte, E. Aernoudt. Progress in Materials Science, Vol 25, 1982, p60.

192) I. Saunders, J. Nutting. Metal Science, 18, Nov 1984, p571.

193) J. Nutting, P. Pollard. Mat. Sci. & Technol. 3 (1987) p462.

194) S. Hecker, M. Stout. In 'Deformation, Processing and Structure' ASM St Louis, 1982 p1.

195) G. Langford, M. Cohen. Trans ASM, 62 (1969) p623.

196) A. Razavi, G. Langford. Strength of Metals & Alloys, Proc. 5th Int. Conf. 1979, p831.

197) J. Nuttall, J. Nutting. Metal Science, Sep 1978, p430.

198) M. Mecking, B. Nicklas, N. Zarubova, U. Kocks. Acta Met. 34 (1986) p527-535.

199) J. Nuttall, PhD Thesis. Leeds. 1984.

200) M. Hatherly, A. S. Malin. Metal Technol. Aug 1979, p308.

201) J. D. Embury, A. Keh, R. Fisher. Trans. Met. Soc. AIME, 236, Sep 1966, p1252.

202) T. Tabata, S. Yamanaka, J. Fujita. Acta Met. 26 (1978) p405.

203) A. S. Malin, M. Hatherly. Metal Science, Aug 1979, p463.

204) I. L. Dillamore, J. Roberts, A. Bush. Metal Science, Feb 1979, p73.

205) R. L. Aghan, J. Nutting. Metal Science, Feb 1981, p41.

206) W. Osterle, H. Wever, H. Bunge. Metal Science, 17 July 1983, p333.

207) J. Nutting, 8th Int. Cong. on Electron Micro. 1974, vol1, p580.

208) J. Cairns, J. Clough, M. Dewey, J. Nutting. J Inst. Met. 99, 1971, p93.

209) A. S. Malin, M. Hatherly. Metal Science. July 1983 p582.

210) W. B. Hutchinson, B. Duggan, M. Hatherly. Metals Technol., Oct 1979, p398.

211) M. Blicharski, S Gorczyca. Metal Science, July 1978, p303.

212) M. Hatherly, A. S. Malin, Scripta Met. 18 (1984) pp449-454.

213) J. Nutting. Personal Communication.

214) B. J. Duggan, M. Hatherly, W. Hutchinson, P. Wakefield. Metal Science. Aug 1978, p343.

215) E. Rabinowicz. Friction and Wear of Materials. J. Wiley & Sons. 1965.

216) A. de Gee. International Metals Review. No2 1979 p57.

217) E. Rabinowicz. J. Lubric. Technol. April 1975 p217.

218) T. F. Quinn. Tribol. Intern. 16 (1983) p257.

219) P. Dawson. J. Mech. Eng. Sci. 4 (1962) p300-319.

220) J. F. Archard. J. Appl. Phys. 1955 p981.

221) N. Suh. Wear. 44 (1977) p1-16.

222) N. Soda, Y. Kimura, A. Tanaka. Wear. 43 (1977) p165.

223) P. Heilman, J. Don, T. Sun, D. Rigney, W. Gleaser, Wear. 91 (1983) p171.

224) J. K. Lancaster. Wear. 10 (1967) p103-107.

225) N. Suh. Wear. 25 (1973) p111.

226) T. Sadada, S. Norose, N. Mura, K. Mabuchi. Proc. 20th Jap. Cong. on Mat. Sci. (1977) p215.

227) E. Hornborgen. Wear. 33 (1975) p251.

228) J. A. Greenwood, J. Williamson. Proc. Royal Soc. A295 (1966) p300.

229) W. Hirst, A. Hollander. Proc. Royal. Soc. A337 (1974) p397.

230) T. Childs. 'Controlling Component Wear in Difficult Conditions' Nat.

Centre Trib. Risley 1985 p111.
231) H. Krause, T. Senuma. Wear 74 (1981) p67-83.
232) N. Soda, Y. Kimura, A. Taraka. Wear 35 91975) p1-16.
233) S. Rice, H. Nowotry, S. Wayne. Wear 77 (1982) p13-28.
234) M. Moore, R. Douthwaite. Met. Trans. 7A (1976) p1833.
235) D. A. Rigney, M. Naylor, R. Divakar, L. Ives. Mat Sci & Eng. 81 (1986) p409-425.
236) A. Ruff. Wear 40 (1976) p59-74.
237) R. Richardson. Wear 10 (1967) p353-382.
238) D. Kuhlmann-Wilsdorf. Fundamentals of Friction and Wear, ASM, 1981. p119.
239) J. H. Dautzenburg, J. Zaat. Wear 23 (1973) p9.
240) P. Heilmann, W. T. Clarke. D. Rigney. Acta Met. 31(8) (1983) p1293.
241) A. Ruff, L. Ives, W. A. Glaeser. Fundamentals of Friction and Wear, ASM, 1981. p235.
242) D. A. Rigney, L. Chen, M. Naylor, A. Rosenfield. Wear 100 (1984) p195-219.
243) P. Heilmann, J. Don, T. Sun, D. Rigney, W. Glaeser. Wear 91 (1983) p171-190.
244) C. Rao, T. Kosei. Wear of Materials. 1985. Proc. Int. Conf. Vancouver, Canada. ASME. p364.
245) K. Kato, T. Kayaba, Y. Ono. Wear of Materials. 1985. Proc. Int. Conf. Vancouver, Canada. ASME. p463.
246) J. Dautzenburg. Wear 60 (1980) p401-411.
247) M. Beaton, C. Brookes. Wear 11 (1977) p295-308.
248) K. Nakajima, Y. Mizutani. Wear 13 (1969) p283-292.
249) L. Ives. Wear of Materials 1979, Proc. Int. Conf. ASME p245-56.
250) L. Ives, A. Ruff. ASTM STP 664, 1979, p5-35.
251) L. Samuels, E. Doyle, D. Turley. Fundamentals of Friction and Wear, ASM, 1981. p13.
252) A. Thompson. Acta Met. 23 (1975) p1337-1342.
253) W. Salesky, R. Fisher, R. Ritchie, G. Thomas. Wear of Materials. 1983. Proc. Int. Conf. Reston, Virginia. ASME. p434.
254) I. Garber, J. Skorinin. Wear 51 (1978) p327-336.
255) L. K. Ives. Wear of Materials 1979, Proc. Int. Conf. ASME p246.
256) K. Hsu, T. Ahn, D. Rigney. Wear 60 (1980) p13-37.
257) W Gleaser, Wear of Materials 1987. Proc. Int. Conf. Houston. Texas. ASME. p155.
258) M. Inman, E. Kohn. Wear 17 (1971) p33.
259) Z. Yang. Wear of Materials. 1985. Proc. Int. Conf. Vancouver, Canada. ASME. p155.
260) B. D. Cullity. Elements of X-ray Diffraction. Addison-Wesley 1978.
261) T. Kosmac, R. Wagner, N. Claussen. J. Am. Ceram. Soc. (1981) C72.
262) H. Toraya, M. Yoshimura, S. Somiya. Comm. Am. Ceram. Soc. Sep. 1984 C183.
263) H. Toraya, M. Yoshimura, S. Somiya. Comm. Am. Ceram. Soc. June 1984 C119.
264) R. Garvie, P. Nicholson. J. Am. Ceram. Soc. 55 (1972) p303.
265) A. Paterson, R. Stevens. Int. J. High Technol. Ceram. 2 (1986) p134-142.
266) S. Newcomb, W. Stobbs. Mat Sci & Eng. 66 (1984) p195-204.
267) M. J. Manning, P. C. Rowlands. Br. Corros. J. 15(4) (1980) p428.
268) G. Anstis, P. Chantikul, B. R. Lawn, D. B. Marshall. J. Am. Ceram. Soc. 64(9) (1981) p533.
269) J. Wang. PhD Thesis. Leeds University. 1986.
270) R. Steinbrecht. 1988 Gordon Research Conference. 'Toughening of Ceramics. New England.
271) N. Bhathena, R. Hoagland, G. Meyrick. J. Am. Ceram. Soc. 67(12)

(1984) p799.

272) W. M. Rainforth, I. Nettleship. Unpublished work.

273) M. Yang. PhD Thesis. Leeds University. 1989.

274) N. Claussen, K. Weisskopf, M. Ruhle. J. Am. Ceram. Soc. 69 (1986) p288-292.

275) S. Nutt. J. Am. Ceram. Soc. 67 (1984) p428.

276) R. Schramm, R. Reed. Met. Trans. 6A (1975) p1345.

277) P. Brofman, G. Ansell. Met. Trans. 9A (1978) p879.

278) S. Yang, J. Spruiell. J. Mat. Sci. 17 (1982) p677-690.

279) F. B. Pickering. International Metals Reviews. Dec 1986 p227.

280) P. R. Swann. Corrosion 19 (1963) p103t.

281) F. B. Pickering. International Metals Reviews. Dec 1986 p227.

282) I. Dillamore, J. G. Roberts, A. C. Bush. Metal Science 13 (1979) p73.

283) R. Honeycombe. The Plastic Deformation of Metals. Arnold. 1968.

284) W. Heye, G. Wassermann. Phy. Status Solidi. 18 (1966) K107.

285) A. F. Smith. Wear 110 (1986) p151-186.

286) A. F. Smith. Wear 105 (1985) p91-107.

287) A. F. Smith. Wear 96 (1984) p301-318.

288) J. P. Evans, W. Borland, P. G. Morgan. Powder Met. 1 (1976) p17.

289) T. F. Quinn, L. R. Wallace. Wear of Materials. 1985. Proc. Int. Conf. Vancouver, Canada. ASME. p578.

290) S. N. Monteiro, H. Kestenbach. Met. Trans. A. 6A (1975) p938.

291) T. S. Eyre, A. Baxter. Met. Mater. 6 (1972) p435.

292) J. F. Archard. Wear 2 (1958/9) p438.

293) H. Block. In 'General Discussion on Lubrication. Inst. Mech. Eng. London. Vol 2. 1937 p222.

294) J. C. Jeager. Proc. Royal Soc. N.S.W. 56 (1942) p203.

295) D. Kuhlmann-Wilsdorf. Mat. Sci. & Eng. 93 (1987) p107-117.

296) D. Kuhlmann-Wilsdorf. Mat. Sci. & Eng. 93 (1987) p119-133.

297) J. F. Archard. J. Appl. Phys. 24 (1953) p981-988.

298) A. Rosenfield. Wear of Materials 1983. Proc. Int. Conf. Reston, Virginia. ASME. p390.

299) D. Kuhlmann-Wilsdorf. Wear of Materials. 1983.p Proc. Int. Conf. Reston, Virginia. ASME.p402.

300) D. Kuhlmann-Wilsdorf. Fundamentals of Friction and Wear, ASM, 1981. p119.

301) N. Soda, Y. Kimura. A. Tanaka. Wear 40 (1976) p23.

302) T. J. Walker, M. C. Shaw. Proc. 10th Conf. on Machine Tool Design & Research. Pergamon Press. 1970 p241.

303) L. Flamand, D. Berthe. In 'Surface Roughness Effects in Lubrication.' Ed D. Dowson, C. Taylor, M. Godet, D. Berthe. Proc. 4th Leeds-Lyon Symp. on Tribology. Sept1977. p239.

304) J. J. Wert, S. A. Singerman, S. G. Caldwell, D. K. Chaudhuri. Wear 92 (1983) p213-229.

305) H. Krause, E. Ocalan. Wear 108 (1986) p337-343.

306) D. Wheeler, D. H. Buckley. Wear 33 (1975) p65-74.

307) J. P. Hirth, D. A. Rigney, 'Dislocations in Solids' ed. F. R. N. Nabarro. North Holland Publ. Co. 1982.

308) G. E. Dieter. Mechanical Metallurgy. McGraw-Hill. Japan. 1976.

309) F. P. Bowden, D. Tabor. 'The Friction and Lubrication of Solids' Part 1. Clarendon Press. Oxford. 1954.

310) T. F. J. Quinn. Brit. J. Appl. Phys. 13 (1962) p33.

311) T. F. J. Quinn. Tribology International 16 (1983) p305.

312) T. F. J. Quinn. J. L. Sullivan, D. M. Rowson. Wear of Materials 1983. Proc. Int. Conf. Reston, Virginia. ASME. p1.

313) R. H. J. Hannink, M. J. Murray, M. Marmach. Wear of Materials 1983. Proc. Int. Conf. Reston, Virginia. ASME. p181.

314) H. Schubert. J. Am. Ceram. Soc. 69 (1986) p270-271.
315) W. M. Rainforth, A. Parmer, A. Dogget, G. R. Armstrong. T.I.
     Research. Internal Report.
316) W. M. Rainforth. Unpublished Work.
317) R. L. Fleishcer. Acta Met. 35 (1987) p2129-2136.
318) P. F. Becher, M. V. Swain, M. K. Ferber. J. Mat. Sci. 22 (1987)
     p76-84.
319) Phase Diagrams for Ceramicists. ASM. 1964-1981. Fig. 4377.
320) J. Alper. N. McNally. ibid. Fig. 4378.
321) G. Kalonji, J. McKittrick, L. W. Hobbs. Advances in Ceramics Vol
     12. Science and Technology of Zirconia 2. (1983) p816.
322) R. Duclos, J. Crampon, B. Amana. Acta Met. 37 (1989) p877-883.
323) F. Wakai, S. Sakaguchi, Y. Matsuno. Adv. Ceram. Mater. 1 (1986)
     p259.
324) F. Wakai, N. Murayama, S. Sakaguchi, H. Kato, K. Kuroda. Advances in
     Ceramics Vol 24. Science and Technology of Zirconia 3. (1986) p583.
325) Y. Okamoto, J. Ieuji, K. Hayashi, T. Nishikawa. ibid. p565.
326) J. Lankford, R. A. Page, L. Rabenberg. J. Mat. Sci. 23 (1988)
     p4144.
327) M. F. Ashby, R. A. Verrall. Acta Met. 21 (1981) p149.
328) P. Boch, G. Kapelski, F. Platon. Proc. 1st Europ. Ceram. Soc. Conf.
     Maastricht, Holland. June 1989. In press.
329) V. C. Pandolfelli, W. M. Rainforth, R. Stevens. J. Mat. Sci. 1990.
     In press.
330) G. Bansal, A. H. Heuer. Acta Met. 20 (1972) p1281.

APPENDIX 1

CRYSTALLOGRAPHY OF ZIRCONIA

Summary of observed crystal structures [330]

MgO – ZrO_2 solid solution	cubic	Fm3m	$a_c = 0.50778$nn

ZrO_2	tetragonal	$P4_2/nmc$	$a_t = 0.50803$nm $c_t = 0.51903$nm

(diff patterns indexed by convention
according to a face centred tetragonal
unit cell)

ZrO_2	monoclinic	$P2_1/c$	$a_m = 0.51172$nm $b_m = 0.51770$nm $c_m = 0.63031$nm $\beta = 98.91°$

determined for PSZ aged 6hr at 1420°C, 9.4 mol% Mg, 20°C

The cubic phase has the fluorite structure of crystal group m3m of order 48. Precipitates of tetragonal are coherent with the cubic and therefore has principal axes parallel to those of the cubic. The crystal group of the body centred tetragonal is 4/mmm of order 16. Symmetry requires that there be 48/16 = 3 variants of the t phase [330]. The c_t axis is normal to the precipitate habit plane (in an attempt to minimise the strain energy from precipitate matrix mismatch). If, for example, these precipitates are imaged in the TEM using B =$[010]_C$ then only two variants will be observed since the third variant is normal to the beam. This variant may be inferred, however, from strain contrast.

The transformation of the tetragonal phase to the monoclinic structure occurs martensitically. The characteristic of any martensitic transformation is, of course, the shape deformation which provides, for a constant composition, a definite and constant orientation relationship between the parent and product phases, for which there exists a definite habit plane [35]. In a simple cubic system the exact orientation relationships are quite easily determined. In zirconia the general relationship may be found [11,330]:

$(100)_m$ // $\{100\}_t$; $[001]_m$ // $<100>_t$

From this, three possible lattice correspondances may arise, depending on which monoclinic axis a_m, b_m or c_m is parallel to the tetragonal axis c_t. Direct evidence for each relationship is provided by Muddle & Hannink [11] for monoclinic particles dispersed in a cubic matrix with domains parallel to the particle habit plane; the boundary between variants is $(001)_m$ and the orientation relationship t/m is:

$(001)_m$ // $(001)_t$; $[100]_m$ // $[100]_t$

for particles with transverse domains, the domain boundaries are parallel to $(100)_m$ and orientation relationship t/m is:

$(100)_m$ // $(100)_t$; $[001]_m$ // $[001]_t$

In a PSZ the twinning which accompanies transformation occurs on the $(001)_m$ plane, with reports of $(110)_m$ and $(100)_m$ also occurring.

As noted earlier there are three tetragonal variants. There are two possible variants depending on whether the twins are transverse or parallel to the precipitate habit plane. In addition, there are two variants depending on whether the product was derived from a_t or b_t which gives in all twelve different monoclinic variations with a given cubic matrix – See Fig A.1.

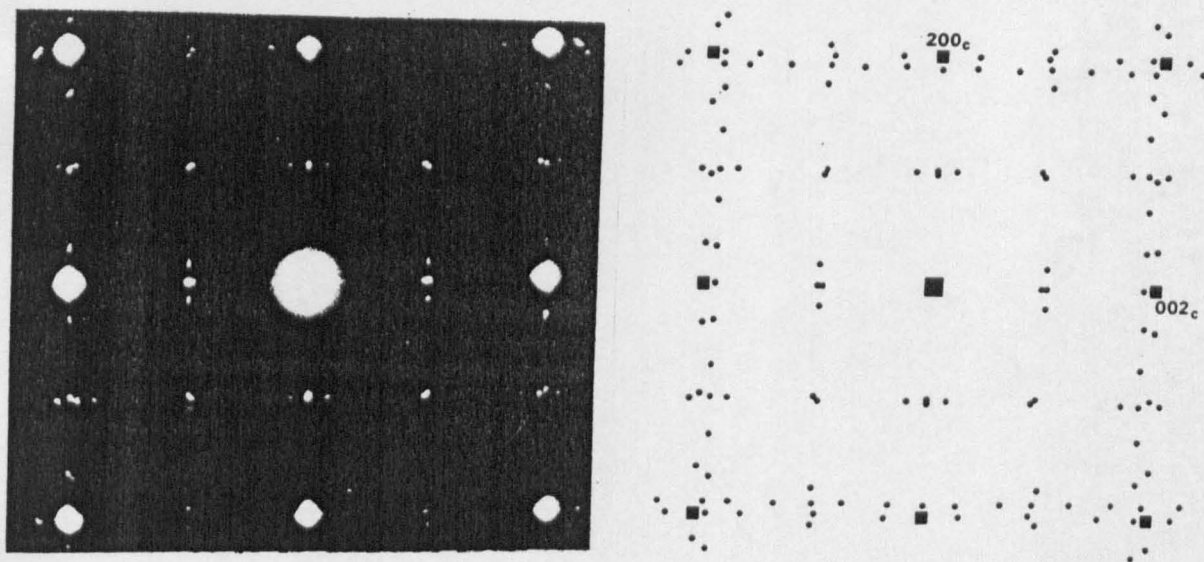The manner in which the twinning promotes microcracking is illustrated in Fig A.2.

Fig. A1. Comparison of observed $<100>_C$ SAED pattern with schematic pattern formed by superimposing single-crystal patterns expected of 12 permitted monoclinic orientations and their twin variants [11].
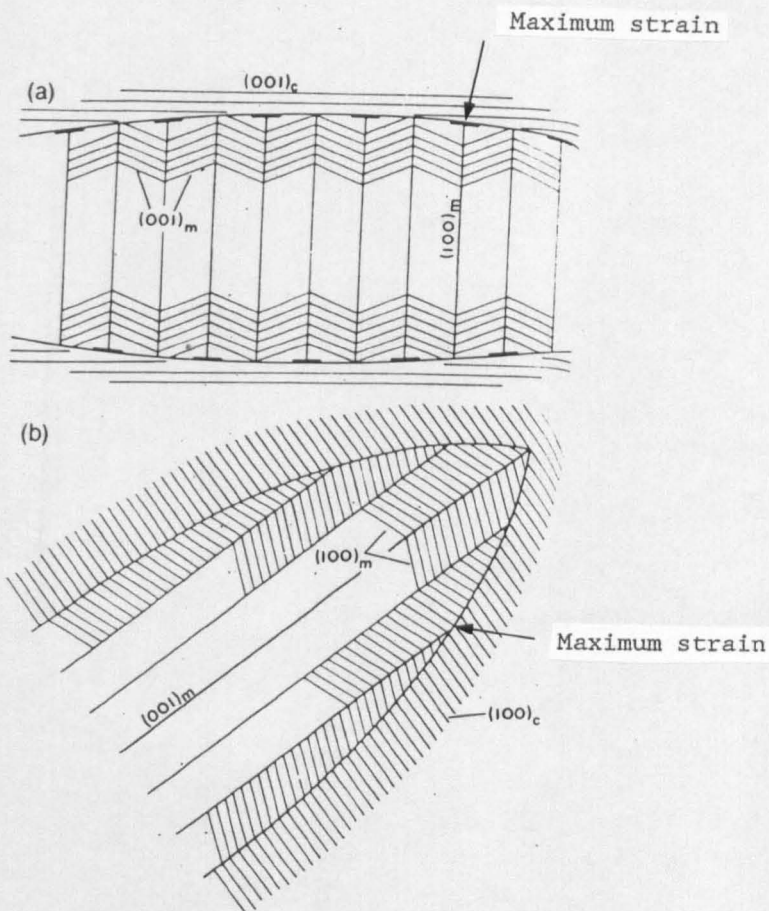
Fig. A2. Schematic representation of lattice displacements developed at the particle-matrix interface as a result of the tetragonal → monoclinic transformation. Particles have domain boundaries parallel to (a) $(100)_m$ planes and (b) $(001)_m$ planes. Positions of maximum strain are potential sites of microcrack nucleation [11].